SLAC-R-720

The Proceedings of the 28th SLAC Summer Institute on Particle Physics: Neutrinos From The Lab, The Sun, And The Cosmos (SSI 2000)

28th SLAC Summer Institute On Particle Physics: Neutrinos From The Lab, The Sun, And The Cosmos (SSI 2000) , 14-25 Aug 2000, Stanford, California

Stanford Linear Accelerator Center, Stanford University, Stanford, CA 94309

Work supported by Department of Energy contract DE–AC03–76SF00515.

XXVIII SLAC Summer Institute on Particle Physics

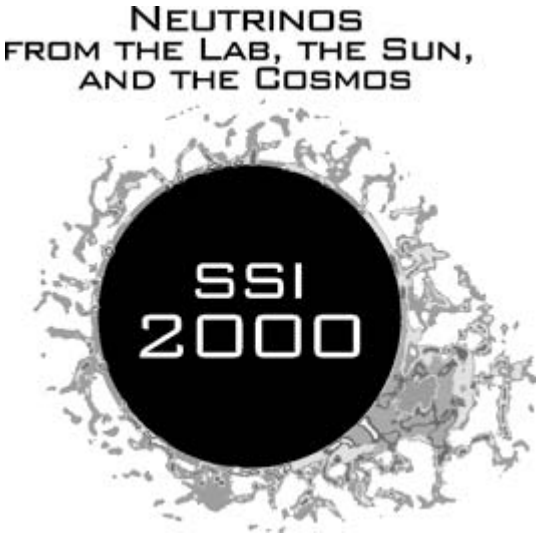

August 14-25, 2000
Stanford Linear Accelerator Center
Stanford, California, U.S.A.

Sponsored by Stanford University and Stanford Linear Accelerator Center under contract with the U.S. Department of Energy, Contract DE-AC03-76SF00515.

Printed in the United States of America. Available from National Technical Information Service, U.S. Department of Commerce, 5285 Port Royal Road, Springfield, VA 22161.

Table of Contents

List of School Lecturers

List of Topical Conference Speakers

ASTROPARTICLE PHYSICS WITH HIGH ENERGY NEUTRINOS

Steven W. Barwick*
Department of Physics and Astronomy
University of California
Irvine, CA 92697

ABSTRACT

Interest in cosmic sources of high energy neutrinos dates back to the late 1950's. This paper outlines the interdisciplinary scientific agenda, which span the fields of astronomy, particle physics, and cosmic ray physics. While the general detection principles based on optical Cherenkov radiation have been understood for many years, the unusual geographic locations of suitable detector sites have challenged the ingenuity of experimentalists. Two high energy neutrino programs are now operating (NT200 in Lake Baikal and the AMANDA detector), with the expectation of ushering in the era of multi-messenger astronomy. Two Mediterranean-based programs have made impressive progress. These detectors are optimized to detect neutrinos with energies of the order of 1-10 TeV, although they are capable of detecting neutrinos over a much broader range of energies. For $E_\nu > 10^{15}$ eV, several new ideas are being exploited to expand the effective volume of the detector. These techniques are based on the detection of neutrino-initiated cascades. We describe the ongoing worldwide efforts to develop expandable techniques and offer an assessment of their relative capabilities.

*Supported by NSF Grants PHY-9722641 and OPP- 9512196. Lectures presented at the SLAC Summer Institute.

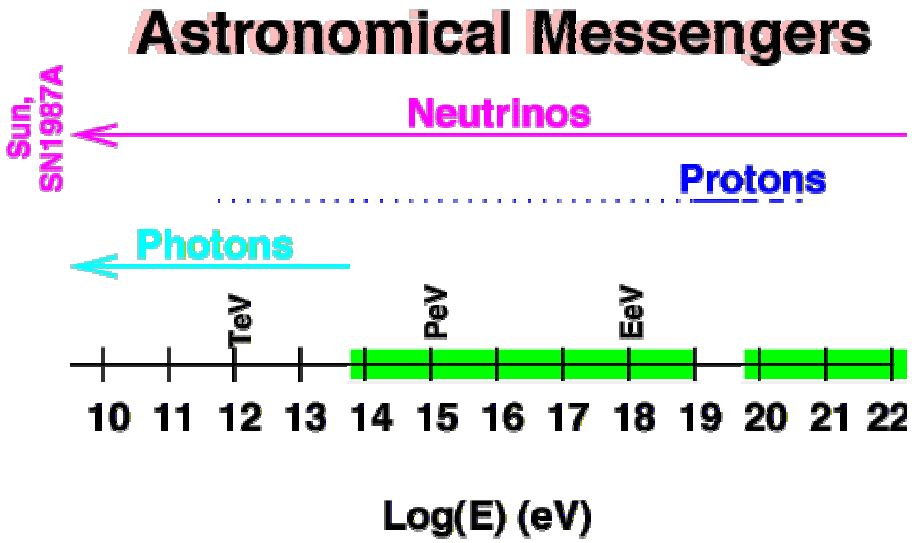

Fig. 1. Relevant energy scales for various cosmic messengers. Due to the weak interaction strength, the neutrino can propagate throughout the Universe without attenuation. The diffuse infrared background attenuates photons with energies above 10 TeV. Cosmic rays point back to the sources if they have sufficiently high energy, but interactions with the cosmic microwave background photons limit the propagation length to less than 50 Mpc.

1 Introduction

The Universe is opaque to photons above several tens of TeV, so information must be carried by different messengers. Soon after the discovery of the neutrino in the 1950's, Reines, Greisen, Markov and others[1] immediately recognized the tremendous potential of the neutrino messenger for astronomy. At high energies, only neutrinos can directly convey astrophysical information from the most distant reaches of the Universe (Fig. 1) or from deep inside the most breathtakingly powerful regions of the sky we know.

Neutrinos provide a unique view of how nature accelerates particles. In particular, they clarify the role of strongly interacting particles in the astrophysical milieu. Once produced, neutrinos are unaffected by intervening matter or photons. Being uncharged, they propagate through the universe undisturbed by magnetic fields. The neutrino messenger may provide the only clear route to the sources of extremely energetic cosmic rays. The great versatility of the neutrino messenger is revealed by the richness of the science goals proposed for neutrino astronomy, which span the fields of cosmology, particle physics, and astrophysics. At the highest energies yet measured, neutrinos may be the only experimental probe of the critical physics mechanisms affecting the

evolution of the early Universe.

Approximately fifty years after the neutrino was first suggested as a powerful new messenger, detectors in Lake Baikal and the South Pole were commissioned to provide the first exploratory views of the neutrino sky at $\sim$ TeV energies. Their success, and the rapid progress by similar efforts in the Mediterranean, suggest that high energy neutrino telescopes are ready to inaugurate the field of multi-messenger astronomy. This paper attempts to summarize the science motivation and experimental progress achieved thus far, and to describe various ideas on how to improve the sensitivity of neutrino detection. The highest energy frontier holds great promise for dramatic advances.

Theorists have identified a variety of potential sites of high energy (HE) neutrino production, and several extensive reviews of this topic have appeared recently in the literature.[2–4] For example, Protheroe has summarized the astrophysical predictions of diffuse neutrino intensities between 1 TeV and the GUT scale. During the mid-1980s, theoretical work concentrated on galactic sources such as X-ray binaries or pulsars. This work was inspired by encouraging reports from underground muon detectors and air shower arrays sensitive to $\sim$PeV gamma rays. Unfortunately, more sensitive devices did not confirm those observations, and consequently, the early optimism has faded. However, the field of extra-galactic gamma ray astronomy has rapidly grown during the past decade. Recently, Gamma Ray Bursts (GRBs) have occupied the theoretical spotlight with the discovery that they are distant extragalactic phenomena and therefore the most energetic transient phenomenon observed in the Universe. On time scales of 0.1 - 100 seconds, these bursts can release of order 10^{52} ergs at x-ray/soft gamma-ray wavelengths. Waxman and Bahcall[5] have argued that GRBs are *the* sources of the extremely high energy (EHE: for the purposes of this lecture, the EHE regime occurs at particle energies in excess of 10^{18} eV) cosmic rays and prodigious sources of high energy neutrinos. The predicted flux is tied to the measured power density of EHE cosmic rays, which also has been used to constrain the neutrino flux in proton blazar models of AGN.[6] Though this procedure is still generating significant debate,[7,8] there is no doubt that models should not over-produce cosmic rays.

Just as multi-wavelength studies have provided unparalleled insight on many astronomical sources, multi-messenger studies by neutrino, gamma ray, and gravity wave detectors may be the Rosetta stone of cosmic accelerators. For example, the AMANDA neutrino facility, located at the South Pole, contemporaneously observes the same sky as new, powerful gamma ray telescopes in the northern hemisphere. Coincidence experiments can also be contemplated with space-based gamma ray observatories and gravi-

tational wave detectors such as LIGO or VIRGO. At the very highest energies, charged cosmic rays are expected to deviate only slightly from line-of-sight trajectories. Should the HiRes and Auger Observatories identify sources of extremely energetic particles, then concurrent observations by neutrino telescopes can provide additional information on the local environment of the accelerator.

Due to the interdisciplinary nature of this field, it is not practical to fully review all related science issues, so no attempt is made to cover low energy neutrino phenomena and those detectors which address these issues (e.g. MACRO, Soudan-II). A large water Cherenkov experiment called SuperKamiokande has provided wonderful results on low energy neutrino physics. It was the subject of several speakers at this school and will not be discussed in great detail here. Also, this paper will not discuss recent ideas to use large arrays of photomultiplier tubes in long baseline oscillation experiments. Out of necessity, we provide a rather incomplete summary of cosmic ray physics and only outline recent advances in our understanding of dark matter, but fortunately, several excellent reviews have recently appeared in the literature.[9,10] Finally, the reader will notice that the discussion is biased toward the AMANDA detector, since the author is most familiar with the strengths and weaknesses of this program. In any case, in this short lecture series, it is impossible to provide a satisfactory account of the remarkable achievements by the current generation of the HE neutrino projects.

2 Science Overview

With very few exceptions, the majority of models of particle acceleration predict that the flux decreases with energy. Currently known technologies for neutrino detection cannot fully compensate for this expected dependence on energy. In addition, the Earth attenuates the flux of neutrinos with energies above $\sim 10^{15}$ eV (or 1 PeV), which mitigates the substantial advantages of using the muon mode of neutrino detection. This leads to a strategy to develop experimental techniques best suited for neutrino energies between 1 TeV and 1 PeV. At these energies, neutrinos act as surrogate messengers for the extremely energetic, but far rarer, cosmic rays. Recently, the potential of neutrino telescopes to observe ν_μ at energies $> 10^{18}$ ($>$1 EeV) has been emphasized.[11,12] At these energies, background from cosmic ray muons is not significant. The authors argue that it may be possible to extract signal events from the enormous flux of lower energy background particles.

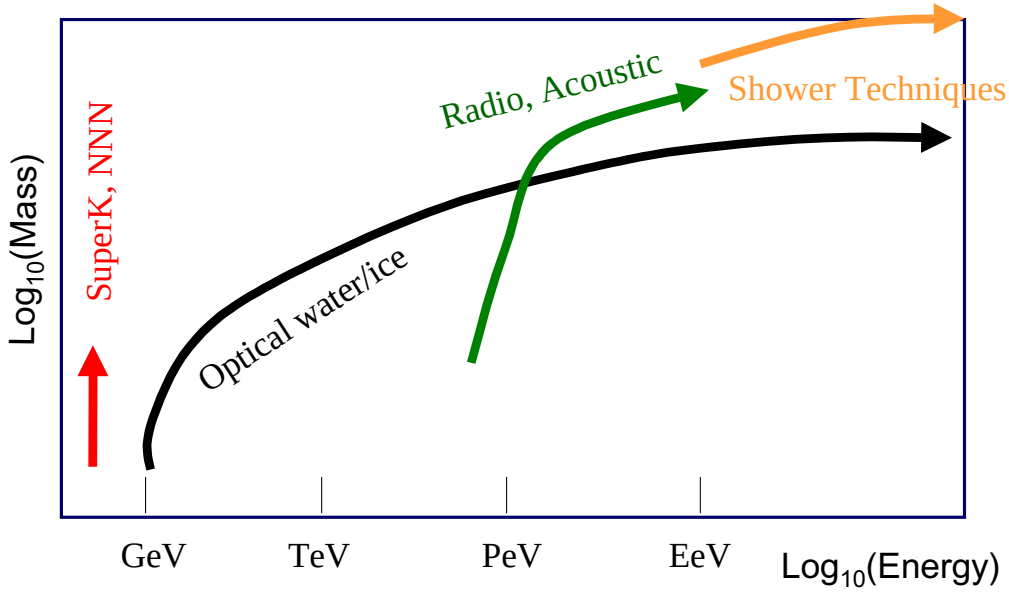

Fig. 2. Neutrinos can be detected over an enormous interval of energies, spanning many orders of magnitude. However, if the energy distribution obeys an inverse power law, as expected from shock acceleration mechanisms, then the technology must change to compensate for the decreasing flux. We illustrate the techniques that have been implemented or suggested by sketching the effective volume of the technology as a function of the neutrino energy. Water and ice Cherenkov techniques dominate the lower energies, but cascade and shower techiques become more attractive at extreme energies. The signal to noise ratio for cascade events is significantly improved by the relatively localized deposition of macroscopic quantities of energy. Consequently, much sparser and cheaper systems can be used to detect these events.

2.1 Astrophysical Sources

The primary motivation to construct very large neutrino telescopes is driven by the dream to identify galactic or extragalactic sources, which may be point-like or diffuse. The high energy frontier holds the most promise to achieve this scientific priority. The atmospheric neutrino and muon backgrounds decrease with energy, the effective area of the detector increases with energy, and angular resolution is likely to improve with energy. Detection of diffuse sources requires good energy resolution with well understood tails, but only marginal angular resolution.

Theoretical activity has centered on modeling two classes of objects: galaxies with active nuclei, or AGN, and gamma ray bursts (GRBs). These objects are known to emit high energy photons, and may also be the accelerators of the highest energy cosmic rays. At TeV energies, the luminosities of some AGN are observed to flare by an order of magnitude in about a day, suggesting very compact central engines. Models of the acceleration mechanism within AGN differ ingeniously. The intensity of neutrino emission ranges from negligible in models that rely solely on electron acceleration to detectable in the most optimistic models based on hadron acceleration. Neutrino observatories are likely to play a key role in settling the debate.

If hadronic acceleration is present in AGN, then a diffuse glow of neutrino emission should be observed uniformly over the sky, originating from distant (and more powerful) AGN. Fig. 3 shows the energy spectrum for a representative sample of neutrino models.

Figure 4, taken from Protheroe,[3] converts the neutrino intensity predictions into an event rate for a detector with an effective area of 0.1 km^2. The calculations include absorption by the Earth, which becomes important for energies $\geq$100 TeV (Ref. **?**). Several models predict more optimistic rates shown in Fig. 4. For example, quasar core models[16] predict 340 events per year which could be observed by AMANDA-II, but this rate violates the Waxman-Bahcall limit. As Fig. 3 shows, present experimental limits from Frejus,[25] Baikal NT-200 (Ref. 107), and AMANDA[20] rule out one of the earliest models for neutrino emission from the core of AGN, and they are beginning to constrain other core models for AGN.

Diffuse sources can be distinguished from the atmospheric neutrino background by a flattening energy spectrum above $\sim$100–1000 TeV. Some models can be differentiated by the their cutoff at the highest energies and spectral shape. The lower energy atmospheric neutrino background can be eliminated by energy-dependent selection cri-

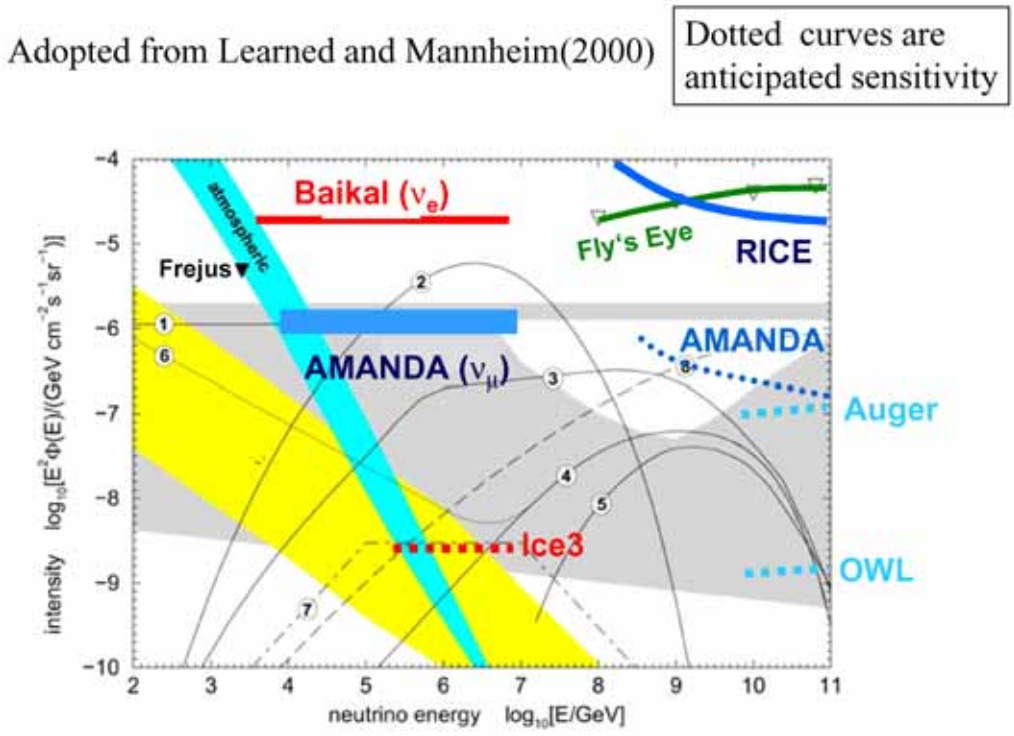

Fig. 3. Figure adapted from Learned and Mannheim.[4] Representative survey of models predicting $\nu_\mu + \bar{\nu}_\mu$ emission from sources diffusely distributed in the sky. The fluxes of $\nu_e + \bar{\nu}_e$ are similar in most models. In the absence of neutrino oscillations, ν_τ are highly suppressed. The atmospheric neutrino fluxes are from Agrawal *et al.*,[13] for both vertical (lower boundary) and horizontal (upper boundary) fluxes. The curves include prompt neutrinos from charm production,[14] but this contribution is not well known at the higher energies. Numbered lines: (1) Model of Nellen *et al.*[15] for the core emission from 3C273 due to p+p interactions; (2) model[16] for p+γ interactions in the core of AGN; (3) model for p+γ interactions in extragalactic sources[7]; (4) representative model for blazar jets according to Mannheim *et al.*[17]; (5) model of neutrino production by GZK mechanism[18]; (6) low energy extention of blazar jet model due to p+p interactions in host galaxies of blazar jets[17]; (7) GRB model by Waxman and Bahcall[5]; (8) representative prediction[19] of a class of topological defect (TD) models. Experimental limits: The energy bounds on the AMANDA-B10 limit[20] are restricted to the approximate region of sensitivity of the detector for an assumed spectrum of E^{-2}. Fly's Eye[21] limit from upward going events. Radio Cherenkov techniques were applied to obtained the RICE[22] limit. Dotted curves are expected sensitivity from operating[11] and planned detectors[23,24] assuming several years of operation.

teria only if the non-gaussian tails of the energy response function are understood with excellent precision. It remains to be seen if the muon response function can be determined with sufficient precision. The "observed" energy corresponds to the local muon energy, not the energy at the interaction point which may be kilometers distant from the center of the detector, nor the energy of the neutrino. Muons with energy above several TeV will radiate a few bursts per kilometer which deposit $\sim 10\%$ of the energy. The highly stochastic nature of the energy deposition may be a useful signature in water detectors, but it is mitigated by scattering in ice detectors. Fortunately, energy information gathered by HE neutrino telescopes does not need to be extremely precise. As the representative models in Fig. 4 show, there is little reduction in signal until the energy threshold exceeds 10-100 TeV.

At the most extreme energies shown in Fig. 3, EHE neutrinos are produced with near certainty by interactions between the ultra-high energy cosmic rays (UHECR) and microwave photons.[26] The flux predictions vary by an order of magnitude, depending on somewhat uncertain assumptions related to the cosmologic evolution of sources of UHECR production and the assumed extrapolation of the charged-current (CC) cross section. The most optimistic predictions may be testable by the current generation of HE neutrino detectors such as AMANDA-II. The absence of signal can be used to constrain the neutrino cross section, which can approach strong interaction cross sections in some models.[27–29]

More speculative mechanisms of EHE neutrino production include topological defects created during grand unified phase transitions or superheavy relic particles. The decay spectrum of topological defects is consistent with all present observational constraints.[30] The decay of superheavy relic particles (SHP) has been a subject of intense activity. The flux of SHPs can be normalized under the Z-burst scenario, where the observed trans-GZK events are produced locally by the interaction of ultra high energy relic neutrinos with the cosmic neutrino background radiation.[31,32] In other models, SHPs decay directly to EHE neutrinos.[33]

The observation of EHE cosmic rays or neutrinos may be the most straightforward path to verify these remnant phenomena. Therefore, the search for EHE neutrinos provides a beautiful example of how HE neutrino telescopes can be used to probe the structure and physics of the early Universe, and perhaps the best opportunity for discovery with the potential to alter our "world view". Since neutrinos do not penetrate the Earth, neutrino observatories must rely on specialized signatures induced by downgoing neutrinos in the atmosphere or limited column density above the buried detectors.

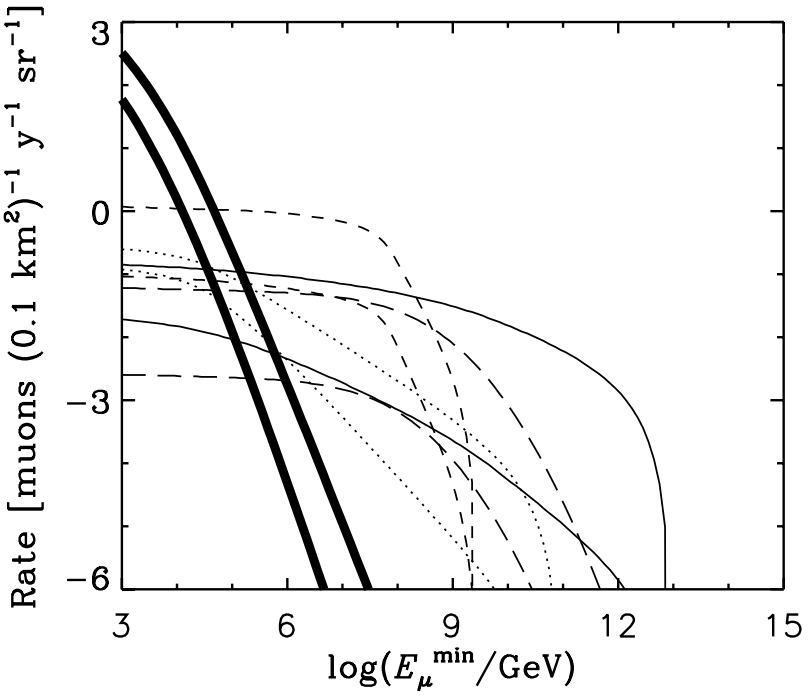

Fig. 4. Rates for diffusely distributed neutrino sources. Atmospheric neutrino-induced muons (thick black lines); GRBs (dotted curves); $p\gamma$ proton blazar (shortdashed curves); topological defect model (thin solid curve), cosmic ray on CMBR (long dashed curves). Upper curves show horizontal signals and lower curves show upward vertical signals. For details, see Protheroe review.[3]

This topic will be covered in the "Detection Modes" chapter.

A few caveats should be kept in mind when interpreting figures of differential diffuse flux. (1) The only "background" shown in Fig. 4 is due to upgoing atmospheric neutrinos, but the rejection of down-going atmospheric muons represents a non-trivial hurdle that must be surmounted. Since atmospheric muons completely dominate the neutrino-induced muons in the downgoing direction, the atmospheric neutrino background is only relevant for 2π steradians of the upgoing hemisphere. (2) Point sources can be located to within a small fraction of a steradian, and the atmospheric neutrino background decreases accordingly. Signal significance increases as $\sim \sqrt{\Delta A_{eff}}/\delta(\theta)$, where $\delta(\theta)$ is the angular extent of the source (or if considering a point source, proportional to the angular resolution of the detector) and ΔA_{eff} is the relative increase in effective area due to the relaxed rejection criteria. (3) Correlated photon observations of GRBs by BATSE provide a special opportunity. Events rates are determined by inte-

grating over all GRB events, and predicted to be $\sim 50/\text{year}$.[5] However, the background livetime is only integrated over the duration of the bursts, which is $\sim 10^{-5}$ years. In addition, the search for neutrino emission from GRBs is greatly simplified by the contemporaneous direction measurements by satellites. Assuming a directional accuracy of 6 degrees, the background is reduced by a factor $d\Omega/(2\pi) = 5 \times 10^{-3}$. Combining directional and temporal information leads to a background reduction of $\sim 5 \times 10^{-8}$ relative to a search for steady diffuse sources. The relaxed rejection criteria increases the effective area of the detector. The increase in effective area is constrained primarily by the requirement to maintain sufficient angular resolution. Alternatively, by raising the energy threshold of the events, angular correlation may not be necessary to reduce the background to manageable levels. It is apparent that searches for transient phenomena enjoy many experimental advantages due to the reduced background (and consequent improvement in sensitivity).

2.1.1 Physics at the Extreme

The origin of the cosmic rays remains one of the most enduring mysteries in astrophysics. It is generally believed that the sources of the highest energy cosmic rays are extragalactic, or at the very least, not confined to the plane of the galaxy due to the isotropic distribution of the detected events. There is some evidence that a new component becomes important at energies above $E > 10^{18}$ eV, primarily the hardening of the spectrum and changes in the average depth of shower maximum. The energy at which the extragalactic component dominates the cosmic ray spectra is critical to the calculation of the total power required by a putative class of sources.

Many "beam dump" models of neutrino production postulate hadronic acceleration to very high energies. A survey of energetic objects reveals several classes (e.g. AGN, quasars, GRBs) of sources that supply the necessary power to create the highest energy cosmic rays. Several calculations assume a transition energy of $\sim 3 \times 10^{18}$ eV and normalize the extragalactic component at an energy that is relatively well measured. However, the uncertainty in value for the transition energy may be an order of magnitude or more. Equally, important is the extrapolation to lower energies where galactic contributions dominate. Even if the extragalactic fluxes are smaller than galactic fluxes, most of the energy content is at lower energies if the spectral index, Γ, is larger than 2.0 (for simple power law approximation, $dN/dE \sim E^{-\Gamma}$). Recent measurements of cosmic particles that exceed 10^{20} eV, the so called trans-GZK events, require relatively

nearby sources. These too may contribute power at lower energies, and therefore must be subtracted from the measured cosmic ray spectrum.

We present a simple argument based on energetics to set the scale for event rates from putative neutrino sources (which follows the treatment of Ref. 50). It is generally assumed that the sources of the highest energy cosmic rays generate an E^{-2} differential spectrum, as predicted (approximately) by shock acceleration models. Normalizing the total integrated energy density for a steeply falling energy spectrum is fraught with uncertainty, but several authors obtain $\rho_{EG} \sim 2 \times 10^{-19}$ erg/cm^3 using

$$\rho_E = \frac{4\pi}{c} \int E\phi(E) dE \tag{1}$$

and $\phi(E) = dN/dE$. In the source region, the average energy density in cosmic rays is related to the average production rate per unit volume, $q(E)$, by

$$\rho_E = q(E) \times \tau_{esc}(E) = q(E) \times \tau_{diff}(E) = q(E) \times \tau_H, \tag{2}$$

where $\tau_{esc}(E)$ is the time spent in the accelerating region, which we replace with the Hubble time, τ_H in this estimate. Assuming a cosmological distribution of sources, Eqn. 2 leads to an estimate of $q_{EG} \sim 10^{37}$ erg/Mpc^3/s. Several classes of extragalactic sources satisfy this numerical relationship. For example, the density of active galaxies[18] is $\sim 10^{-7}$/Mpc^3 and the typical emitted power is 10^{44} erg/s. Gamma ray bursts flash at a rate of 1000 per year. If the average energy per burst[34,35] is 3×10^{52} ergs, then GRBs become suitable candidate sources of EHE cosmic rays. In terms of energetics, both GRBs and AGNs are plausible sources of EHE cosmic rays if they accelerate particles to sufficiently high energies, which also is plausible.

The result for q_{EG} assumes that the extragalactic spectrum includes particles with energies down to $\sim$1 GeV and is exponentially cut off at energies above 5×10^{19} eV (to allow for yet another source of trans-GZK events). The injected power density can be estimated by assuming that the extragalactic cosmic rays diffuse through the Universe with a diffusion time scale comparable to the Hubble time, $\tau_H \sim 10^{10}$ years. The diffusion velocity is assumed to be close to the speed of light. This assumption neglects evolution at large redshift and possible effects due to intergalactic magnetic fields (so particles can travel as much as one Hubble distance in the age of the Universe). The possibility of large intergalactic magnetic fields and local concentration of sources has been considered in more thorough treatments of this issue.[19,36]

The connection between EHE cosmic rays and neutrino fluxes is given by

$$q_\nu(E) = f \times q_{EG}(E) = f \times 30 \text{ events/km}^2\text{/yr}, \tag{3}$$

where f is the efficiency for neutrino production in cosmic ray interactions either within the source or intergalactic medium. The last expression was generated by assuming that the spectral index is 2.0 for both the neutrino and cosmic ray energy spectrum. The Waxman-Bahcall upper bound,[6] which applies to sources that are transparent to neutrons, is obtained by setting $f = 1$. If evolution is included, the estimate produced in Eqn. 3 may be increased by a factor of five if the cosmic ray sources evolve in the same way as star formation. The bound is weakened because photoproduction and pair production attenuate ultra-high energy protons from large redshift, but neutrinos propagate without attenuation.

The trans-GZK events motivated Weiler[31] to propose a new mechanism for cosmic ray production. If there was an abundant source of ultra high energy neutrinos from the early universe, they would annihilate with relic neutrinos to produce high energy cosmic rays locally. The absorption cross section at the Z resonance is very large, so the event rates can be made consistent with observation. The required energy to produce the resonant interaction is greatly reduced if the relic neutrinos have mass, as suggested by recent atmospheric and solar data,

$$E_\nu^R = M_Z^2/2m_\nu = 4 \times 10^{21}\,(\mathrm{eV}/m_\nu)\ \mathrm{eV}. \tag{4}$$

Neutrinos with the requisite energy are thought to be produced in the early universe. If they annihilate within the GZK cutoff distance of 50 Mpc to produce a Z-boson, then the decay products ($\sim 30\ \gamma$, 3 nucleons, 28 e^++e^- pairs, and 80 ν) can propagate to the Earth. The rate of "Z-bursts" may be enhanced by local accumulation of relic neutrinos, but phase space constraints set an upper bound. Of course, the source of the high flux of neutrinos is unknown. To explain the trans-GZK events, the flux of ν at the resonant energy must be approximately the same as the GZK flux at 10^{20} eV, a rather discomforting requirement. Nevertheless, using only standard model physics, the Weiler process simultaneously solves the GZK mystery and provides the first observation of relic neutrinos.

Horizontal air shower techniques can be employed to explore the neutrino sky at extremely high energies.[37] Conceivably, with ~ 10 km^3 of water equivalent target volume for $E_\nu > 10^{19}$ eV, the Auger air shower array will have the sensitivity to search for neutrinos from cosmic ray interactions with the cosmic microwave background and more speculative signals from topological defects.

2.2 Point Sources

The term "point sources" refers to those objects that have sufficient intensity to generate a statistically significant enhancement of ν_μ-induced muon events from the same direction in the sky. The angular direction of the muon can be measured with $0.5 - 3.0$ degree precision (depending on the detector architecture, muon energy at the detector, and propagation parameters). The angular correlation between the neutrino and the outgoing lepton produced in charge current interaction is similar to the experimental precision ($\delta\theta \sim 1.5/\sqrt{E_\nu}$, where θ is in degrees, and E_ν has units of TeV). In this section, we describe the theoretical motivation for both galactic and extragalactic sources of point emission. Obviously, such a survey cannot cover all of the interesting ideas in the literature.

The production mechanism for cosmic rays is not yet fully understood. Shocks from galactic supernova are widely believed to accelerate cosmic rays to $\sim 10^{15}$ eV, while the sources of cosmic rays at the most extreme energies are produced by accelerators outside our galaxy. Plausible models of particle acceleration exist for both galactic and extra-galactic sites, but supporting evidence is largely circumstantial. The observation of high-energy (HE) neutrinos from point sources would unequivocally confirm the hadronic nature of those accelerators. Once the basic mechanism is established, models can evolve quickly in detail and predictive power. Unfortunately, the neutrino flux from galactic and extra-galactic point sources, such as active galactic nuclei (AGN), is predicted to be very low, although the uncertainties in the model parameters lead to considerable variation in the flux predictions. An independent estimate of neutrino flux can be derived by naively scaling the observed gamma spectrum of sources of TeV photons (assuming that they are produced by hadronic interactions), but we caution that this scenario produces an optimistic value for the neutrino flux if proton synchrotron radiation is responsible for a sizeable fraction of the observed TeV photons.[38]

It appears that supernova remnants (SNR) are one of the few classes of galactic sites that have the capability to supply the power to accelerate the galactic cosmic rays, but even these sites must convert the energy of the shock wave into relativistic particles with suspiciously high efficiency (10-30%). The diffusive shock mechanism naturally produces a power law spectrum of $dN/dE \sim E^{-2.1}$, which is consistent with the deduced spectral index of cosmic rays. [The measured spectral index is $E^{-2.7}$, but the local measurements must be corrected for nuclear interactions as cosmic rays propagate in the galaxy]. Recent observations of TeV gamma rays from plerions such as the Crab

Nebula and supernova remnants (e.g., SN1006) provide direct evidence for particle acceleration to TeV energies. However, these observations do not provide compelling evidence for hadronic acceleration due to an unfortunate ambiguity: it is possible (and even probable) that electrons are solely responsible for these observations. In particular, HE gamma rays from SNR may be generated by electrons accelerated by the SN shock. But if SNRs are the sources of cosmic rays, they must accelerate hadrons, and a class of models exploits this idea. They suggest that both protons and electrons are accelerated by the supernova shock. High energy photons are generated by proton collisions with ambient material in the accelerating region. Pions, both neutral and charged, are produced in the nuclear collisions, which in turn decay to HE gamma rays and neutrinos.

While the notion of particle acceleration by supernova shocks provides a credible and largely consistent picture, not all observations neatly fit this scheme. For example, the site(s) of cosmic ray acceleration are expected to generate significant fluxes of gamma rays via π^0 decay,[39] but only one of the nearby SNR, SN1006,[40] generates an observational flux of high energy photons. Moreover, the inferred energy spectrum for photons between GeV and TeV energies does not support an E^{-2} distribution. For most of the SNR, upper limits by the Whipple collaboration[41] imply a spectral break between MeV and TeV energies, which is not expected if they were the sites of galactic cosmic rays. This moderately disconcerting state-of-affairs has motivated at least one author[42] to suggest that most cosmic rays originate from extragalactic sources. The close connection between neutrino production and hadron acceleration reduces some of the speculative uncertainty associated with the information provided by the study of sources of high energy gamma rays. Alternative sites for cosmic ray acceleration may emerge from a detailed study of the neutrino sky.

Even though the cosmic ray puzzle provides powerful motivation to explore the sky for neutrino emission, not all sources of high energy neutrinos need to contribute to the cosmic ray flux. In particular, a powerful galactic accelerator may be surrounded by too much material to emit high energy photons or cosmic rays (they would interact and cascade down to lower energies), but the high energy nature of this accelerator could be discovered by exploiting the neutrino messenger. For example, a one solar mass black hole accreting at the Eddington limit releases $\sim 10^{38}$ ergs. If 10% of this energy is converted into neutrino emission with an E^{-2} spectrum, a source at a distance of 10 kpc would produce of order 1 neutrino event per year in AMANDA-B10. A more massive black hole in the galactic center could conceivably produce a much bigger signal, but this galactic location is not visible to neutrino telescopes in the southern

hemisphere.

Turning to extra-galactic sources, active galactic nuclei (AGNs) are among the most luminous objects in the Universe and promising sources of neutrinos. Present models construct a central engine that consists of a supermassive black hole surrounded by an accretion disk. In these models, high energy neutrino fluxes are generated near the central engine or in the jets of radio-loud AGNs (e.g., Blazars, a class of objects where the jet intersects the line of sight of the observer). Neutrino energies may extend to $\sim 10^{10}$ GeV. The fact that gamma ray emission has been detected[43] from nearby blazars Markarian 421 and 501* provides strong evidence for particle acceleration to high energies. The time averaged energy spectrum from Mk501 during 1997 is consistent with an unbroken power law up to 20 TeV.[43] In general, high-energy photons at TeV scales may interact with material or photon fields in the source, or interact with the diffuse infrared background photons during their flight, losing energy by the mechanism $\gamma + \gamma \rightarrow e^+ + e^-$. Due to this reprocessing, the measured photon energy spectrum may not trace the energy spectrum of the source. Recent measurements of the diffuse infrared background are much larger than theoretically expected.[44] Consequently, the attenuation length for photons in excess of 10 TeV is much shorter than the distance to Mk501. After correction for absorption by the infrared background, the energy spectrum at the source rises dramatically above 10 TeV.[45] If the energy spectrum of neutrinos is similar in shape, then relatively modest sized detectors such as AMANDA-B10 and NT-200 possess sufficient sensitivity to test this assumption.

Recently, it has been argued[46] that the rapid time variability of the high energy photon emission from AGN Blazars and the correlated variation between X-ray and TeV regimes disfavors hadronic acceleration models for this particular class of objects, but others have shown that rapid and correlated variability can be accommodated by modest extensions to the existing hadronic acceleration models.[47,48] At least one model for blazar emission[49] can produce comparable fluxes for ν and γ. High energy photons and neutrinos are produced by the decay of pions. The pions are generated during the collision between clouds of gas with relativistic velocities and the interstellar medium of the host galaxy near the central engine of the AGN. In any case, the vigorous debate suggests that high energy neutrino detectors can play a central role in deciphering the acceleration mechanism, but the challenge is not easy. In general, the sensitivity of kilometer scale detectors should improve linearly with A_{eff}, but the energy response

*See the recent review by Catanese and Weekes[43] for a complete list of detected VHE gamma-ray sources.

must improve commensurately to take full advantage of this capability. To illustrate the general difficulty, Fig. 5 (from Ref. 50) shows the differential signal of neutrino-induced muons from a source with $\phi_\nu = \phi_\gamma$ where ϕ_γ is the measured flux from Markarian 501 *during a period of maximum intensity*. For this particular source, the period of maximum intensity was about six months during the last 3 year interval, but it is always possible that this situation can change to more favorable conditions. Also shown is the steeply falling background from atmospheric neutrinos. The integral under the dotted curve gives a small, but measurable, rate of 30 events per year in a kilometer scale detector. However, the curves do not include the dispersion introduced by the convolution of the finite energy resolution. It is clear that non-gaussian tails on the energy response must be controlled with (perhaps unrealistically) high precision and this remains an open question. The signal events are assumed to be fully contained within a circular patch on the sky with a radius of 1 degree. This may be realistic for water detectors which expect to achieve angular resolution substantially better than 1 degree, but it is probably optimistic by a factor of a few for kilometer scale ice detectors for muon energies of 1 TeV.

Figure 6 provides a summary of model predictions for the flux of high energy neutrinos. It also contains the flux limit reported by the AMANDA collaboration for sky bins with declinations greater than 30 degrees. As mentioned, most theoretical models of potential astrophysical sources of neutrinos predict that the energy spectrum is very hard, approximately E^{-2}.[51] Due to the hard energy spectrum and the energy dependence of σ, the cross section for the weak interaction, the range of the muon, and the effective area of the detector, the most probable energy of the detected neutrino is well above 1 TeV (typically 10–30 TeV for hard spectra).

2.3 Physics Potential

Obviously, the desire to understand the optical and physical properties of the local environment create many interdisciplinary opportunities. Underwater neutrino observatories provide the facilities to monitor the time variability of bioluminescence, temperature, salinity, water currents, biofouling, etc. The NESTOR collaboration has secured funding to deploy an optical cable from shore to the site off Pylos instrumented with sensors of interest to oceanographers and neutrino physicists.[56] Multidisciplinary opportunities encourage interactions between seismologists and neutrino physicists to construct a large seismic array for tomographic studies of the Earth's interior. The

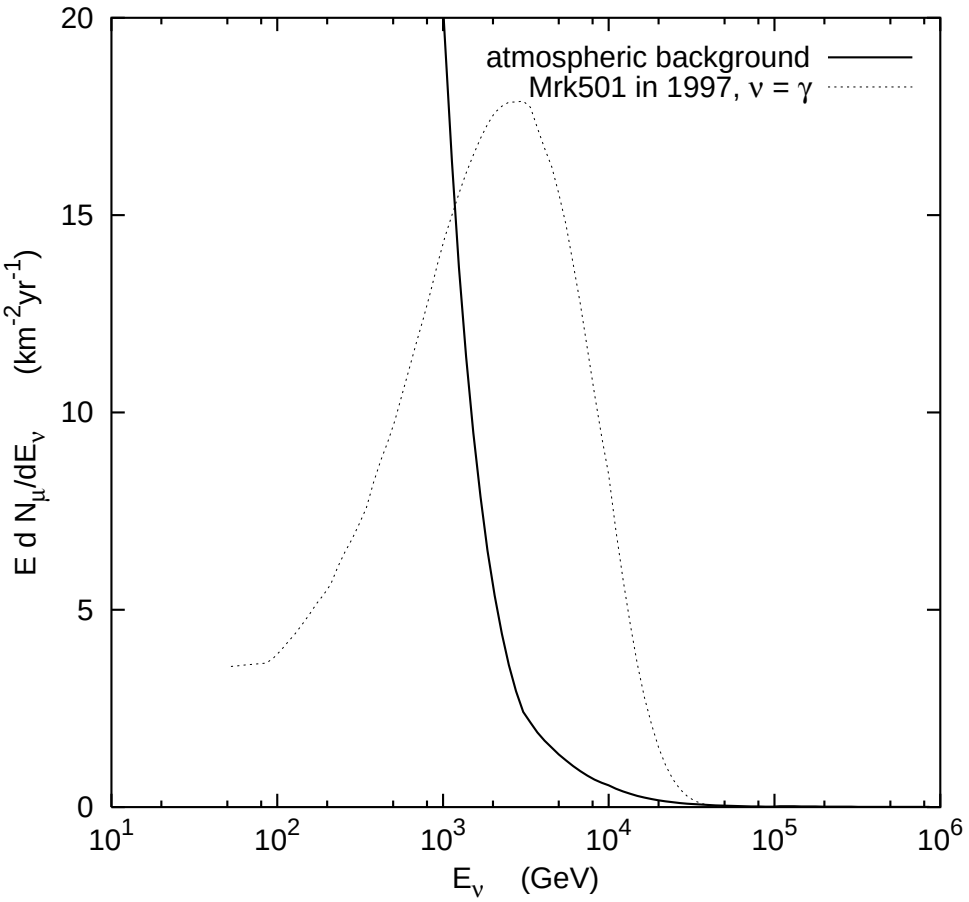

Fig. 5. Differential signal of neutrino-induced muons from a source with $\phi_\nu = \phi_\gamma$, where ϕ_γ is set to the gamma flux from Markarian 501 that was observed *during a period of maximum intensity*. Detector resolution is not included. See text and Gaisser[50] for discussion.

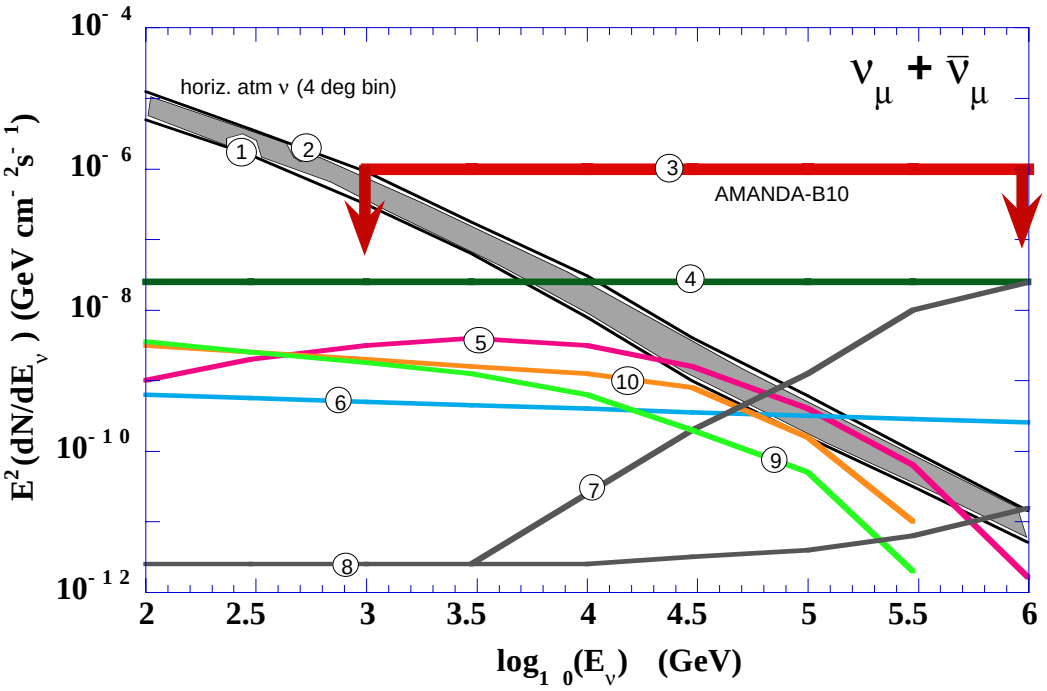

Fig. 6. Survey of $\nu + \bar{\nu}$ flux predictions from cosmic accelerators of high energy neutrinos (adapted from the recent review by Learned and Mannheim[4]). The atmospheric neutrino fluxes are from Agrawal *et al.*,[13] for both vertical (1) and horizontal (2) fluxes within a circle defined by a half angle of 4 degrees (labeled "4 deg bin"). The curves do not include the normalization uncertainty, possibly 20% in magnitude. Numbered lines: (3) AMANDA-B10 limit reported here. (4) Model of Nellen, *et al.*[15] for the core emission from 3C273 due to pp interactions. It also represents neutrino emission from the AGN Blazar Mk501 during 1997 if it emits half of its TeV gamma ray flux in neutrinos. (5) Crab Nebula, Model I from Bednarek, *et al.*.[52] (6) Coma cluster according to Cola, *et al.*.[53] (7) Core emission from 3C273 due to p-γ interactions.[16] (8) Model[54] for the relativistic jet of 3C273 including p-p and p-γ interactions. Supernova remnant gamma-Cygni (9) and IC 444 (10) according to Gaisser, *et al.*.[55] The energy bounds on the AMANDA limit are restricted to the approximate region of sensitivity of the detector.

Baikal detector monitors the seasonal water exchange processes in this unique Siberian lake.[57]

In the next few subsections, we briefly comment on the potential of HE neutrino arrays to contribute to questions in particle physics.

2.3.1 GRB-related science

It is now known that most Gamma Ray Bursts occur at cosmological distances with redshift near unity[58] (although different GRB scenarios do exist[59]). Evidence is accumulating that photon emission is produced by a relativistically expanding fireball.[60] If particles are accelerated to ultrahigh energies, then HE neutrinos may be produced by the decay of pions generated in photonuclear interactions. The neutrinos from GRBs would arrive at the Earth in a burst coincident with the photons. Waxman and Bahcall[5] point out that observations of HE neutrinos from GRBs can test special relativity and the weak equivalence principle with unmatched precision by measuring the time delay between photon and neutrino signals. It is conceivable that the neutrino mass can be extracted from the time delay between the photon and neutrino signals. Assuming photons travel at the speed of light, the time delay is given by:

$$\Delta t \sim 10 \text{ ms} \left(\frac{E_\nu}{5 \text{ GeV}} \right)^{-2} \left(\frac{L}{\text{Gpc}} \right) \left(\frac{m_\nu}{1 \text{ eV}} \right), \tag{5}$$

where L is the distance to the GRB. The duration time for HE neutrino emission is unknown, but models predict values of the order of ms. The time delay between GeV ν emission and MeV γ emission is also not known. If the energy threshold of HE neutrino arrays can be reduced to $\sim$5 GeV for tagged GRB events, and the ν fluxes are large enough to produce signals, then the mass of the heaviest neutrino species can be determined with reasonable accuracy. At these energies, the detection probabilities and event topologies of all neutrino flavor interactions are similar, so the maximum time delay is related to the largest mass. GRBs offer the exciting possibility to study neutrino oscillation over cosmological baselines. As in any astrophysical environment which produces neutrinos from $p + p$ or $p + \gamma$ interactions, the direct production of ν_τ is expected[61] to be $\sim 10^{-5}\Phi(\nu_\mu)$. Scenarios which transform ν_μ into ν_τ provide a reasonable mechanism to dramatically boost the flux of ν_τ to a level comparable to the other neutrino flavors. Therefore, the appearance of ν_τ provides strong evidence for oscillation over baselines of a Gigaparsec or more.

Unfortunately, unambiguous detection of ν_τ is very difficult in HE neutrino detectors, as discussed in section 3.1.3. Several potential signatures have been proposed,

but all face rather long odds for success unless current HE ν detectors soon observe an astrophysical source. This is beautifully illustrated by Alvarez-Muniz, Halzen, and Hooper.[12] They show that the probability to observe the Double Bang signature is very low; typically a few percent of the probability to detect ν_μ-induced muons with similar energies. Unless current generation detectors soon discover ν_μ emission from GRBs, the limited effective volume for Double Bang events strongly disfavors their detection in kilometer scale arrays. Without adequate statistics, it will be difficult to use angular or energy dependent handles to confirm ν_τ detection.

Halzen and Saltzberg[62] have proposed another mechanism for ν_τ detection, but the backgrounds are severe if a comparable flux of ν_μ exist. They point out that the Earth is not opaque to ν_τ at any energy because charged current and neutral current interactions produce a τ in the final state, which in turn decays back to a ν_τ before losing a significant fraction of its energy. Eventually, the energy of the ν_τ decreases to the point where the Earth is no longer opaque. The characteristic "transparency" energy is $\sim$1 PeV, depending weakly on the column depth through the Earth. At these energies, the shower separation between the initial interaction and subsequent decay of the tau lepton is too short to be identified in HE neutrino arrays. However, a small excess (or pile-up) of events is expected at the transparency energy. The angular distribution of these events is somewhat flatter than expected from the other neutrino flavors. The Halzen-Saltzberg signature must be extracted from a background generated by charged current ν_μ interactions. (Obviously, at the characteristic transparency energy, ν_μ can propagate through the Earth without attenuation.) Since the detection probability for muons from ν_τ decays below the detector is only 17% of the probability from ν_μ, due to the branching ratio of the τ to μ channel, the background rate is substantial. In the distant future, the slight difference between angular distributions of ν_τ- and ν_μ-induced muons may be exploited if the acquired statistics is very high.

Can ν_τ from GRB be revealed by measuring cascade events? The superior energy resolution of the cascade mode may be sufficient to show the pile-up feature at the transparency energy. Unfortunately, the reconstructed angular resolution is poor, so the subtle difference in the angular distributions cannot be exploited. The background from NC interactions and ν_e CC interactions compounds the problem.

2.3.2 WIMP searches

Neutrinos may be emitted from the center of the Sun or Earth as a consequence of the annihilation of weakly-interacting cold dark matter particles (WIMPs) that accumulate at the centers of these objects. Galactic WIMPs, scattering off nuclei, lose energy and may become gravitationally trapped. One interesting class of WIMP candidates arise from minimal supersymmetric (SUSY) theory. Within this framework, Bergstrom *et al.*[63] and recently, Feng, *et al.*[9] have calculated the discovery potential for neutrino observatories and beautifully illustrate their power to complement other search methods. Apparently, the parameterized ignorance of SUSY models is too vast to be completely constrained by a single search technique. Bergstrom *et al.* have attacked this worrisome deficiency by combining the limits from cosmic ray antiproton instruments with the anticipated sensitivity of gamma ray satellites and neutrino observatories. A comprehensive search strategy for SUSY particles benefits enormously from the complementary information provided by neutrino telescopes. Combining astrophysical data from special purpose and multipurpose survey instruments creates an intriguing blueprint for future search strategies.

The AMANDA and Baikal collaborations restrict their atmospheric neutrino analysis to the nearly vertical direction to search for high energy neutrinos from the decay of weakly interacting massive particles (WIMPS) from the center of the Earth (see Fig. 7 for one example). The detectors are very efficient for $\cos(\theta_{rec}) < -0.9$. Therefore, the effective area is somewhat larger than achieved by the all sky measurement of atmospheric neutrinos. From the lack of excess of events in the nearly vertical angular bins, flux limits can be obtained. Figure 8 compares the AMANDA limits with existing limits for a broad class of supersymmetric models, illustrating the potential of the technique.

2.3.3 Relativistic Monopoles

A magnetic monopole with Dirac charge $g = (137/2)e$ emits Cherenkov radiation if its velocity exceeds $0.75c$ in water or ice. The particle would emit more photons than a single charged particle by a factor of $\sim 10^4$, and the linear variation in the photon emission rate is quite small compared to an equivalently bright muon. Figure 9 summarizes the current status of experimental limits. The AMANDA and Baikal limits were obtained by searching for upward going particles.[67] A rather large lower limit on the mass of the monopole is required to have the requisite kinetic energy to traverse the

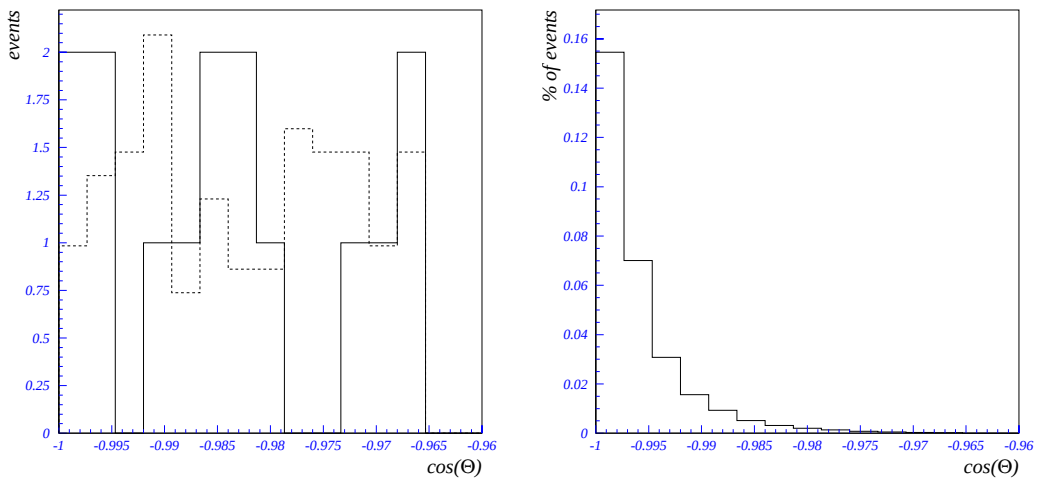

Fig. 7. **Left:** Angular distribution of the data (full line) and simulated atmospheric neutrino events (dashed line) after the application of strong selection criteria. The angular range is between 165 and 180 degrees. The atmospheric neutrino sample has been normalized to the live-time of the experiment. **Right:** Angular distribution of the fraction of simulated WIMP signal for the same selection criteria. The WIMP properties were assumed to produce hard neutrino spectra. Its mass was taken to be 250 GeV.

Earth.

2.3.4 Supernova Detection

A transient burst of low energy neutrino emission from supernova explosions or Gamma Ray Bursts (GRBs) can be detected by AMANDA-II by summing the random noise signals from the photomultiplier tubes in the optical modules within the array. A supernova burst would manifest itself as a statistically significant increase in the summed signal due to the excess photons generated by the low energy neutrino interactions. Sensitivity to transient events is improved by embedding the array in an environment such as polar ice, where the random noise level is low because the internally generated noise of a photomultiplier tube is reduced at cold temperatures and the externally generated background light from radioactive impurities is negligible. The AMANDA collaboration agreed to join the Supernova Early Alert Network[69] to confirm galactic supernovae and determine the direction by triangulation of the neutrino wavefront, which can precede the photon signal by several hours or more. The polar location of AMANDA simplifies the task of triangulation, but the angular resolution of elastically scattered electrons

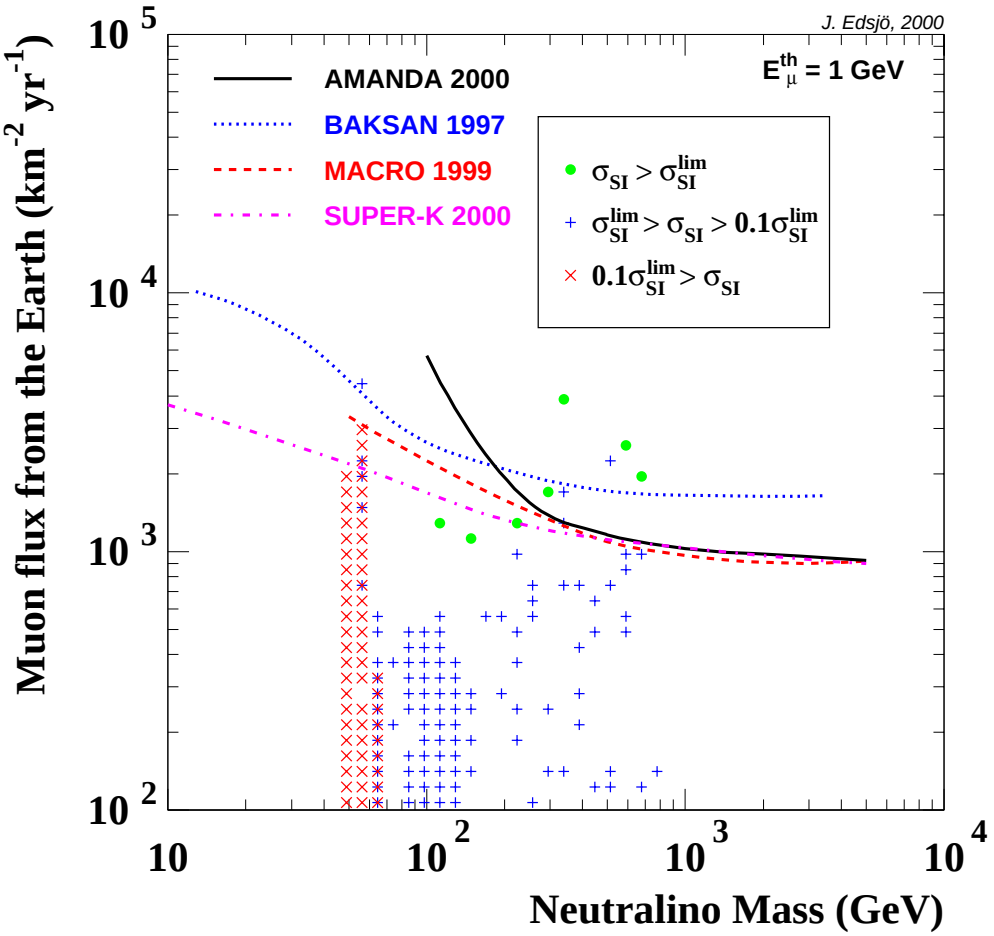

Fig. 8. Experimental limits from AMANDA,[20] SuperK,[64] MACRO,[65] and Baksan.[66] High energy neutrino flux predictions and experimental limits due to the annihilation of supersymmetric particles in the center of the Earth. See Bergstrom, *et al.*[63] for explanation of symbols and corrections applied to normalize the various experimental limits to the same energy threshold. The AMANDA result does not include systematic error, which is expected to weaken the limit.

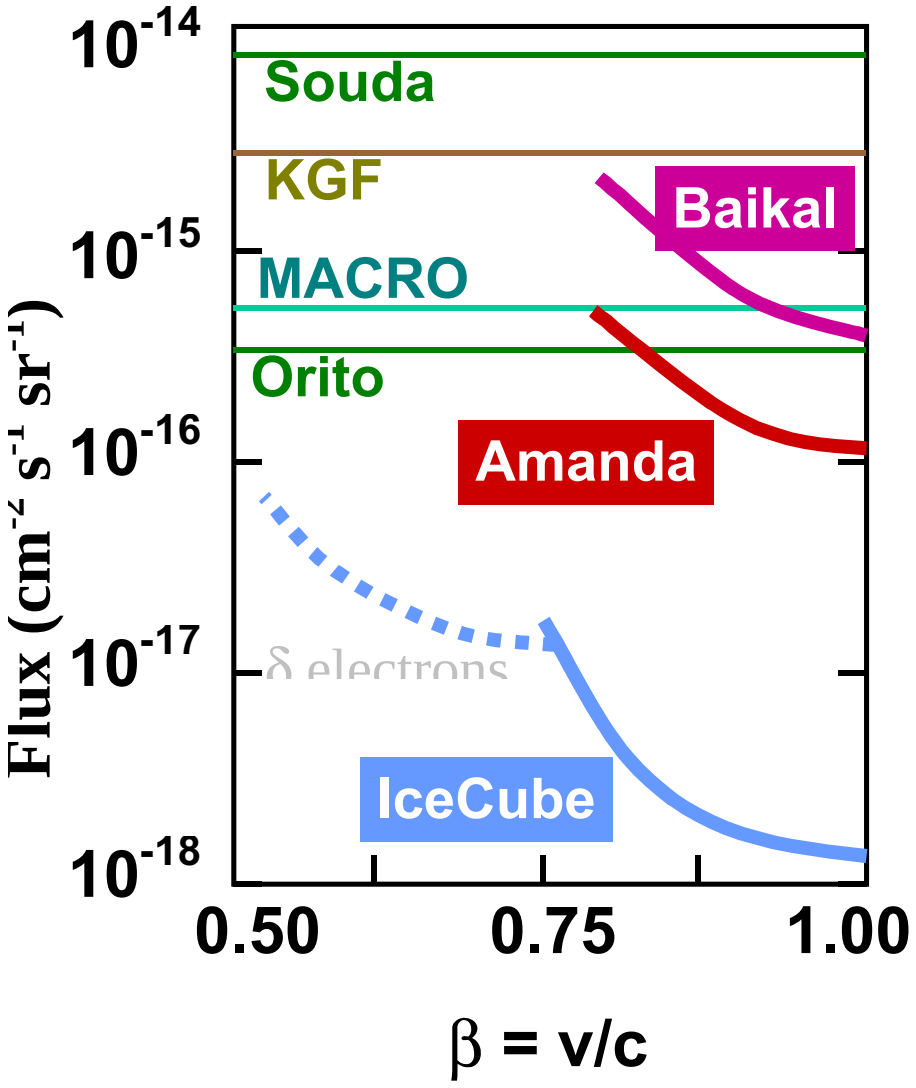

Fig. 9. Experimental flux limits (in units of $cm^{-2}s^{-1}sr^{-1}$) for relativistic monopoles.[68] The AMANDA and Baikal results assume that the monopole is supermassive. The dashed line shows that limits may be extended below the velocity threshold for Cherenkov emission because sub-threshold monopoles will scatter high energy electrons (delta-rays) that will emit Cherenkov photons.

in the SuperKamiokande experiment[70] may be superior. Future neutrino observatories could search for nearby extragalactic bursts by increasing the collection efficiency of the optical sensors (larger PMTs, use of wavelength shifters), implementing techniques to reduce the intrinsic noise, and increasing the number of sensors in the array beyond several tens of thousand.

The low rate of intrinsic noise generated by photomultiplier tubes in Antarctic ice is a unique feature of the AMANDA detector. It results from two effects. First, the concentration of radioactive contaminants in the ice is very low compared to sea-water. Second, thermionic emission from the photocathode is minimized due to the low ambient temperatures. AMANDA-II has sufficient sensitivity to see to the center of our galaxy,[71] whereas IceCube is expected to extend the reach by a factor of 2.5 in distance to cover the most of galaxy. The rather modest improvement in sensitivity is a consequence of the $\sqrt{N_{OM}}$ scaling,[72] where N_{OM} is the number of optical modules in the array.

2.3.5 Neutrino Oscillation

The growing evidence for neutrino oscillation[73] in the atmospheric neutrino data has triggered the neutrino telescope community to investigate the physics capabilities of their detectors for this particular science objective. The energy spectrum of atmospheric neutrinos (hashed box, figure taken from Protheroe's review paper[3]) is a steep power law, suggesting that the detected events will be predominantly medium energy and the rate will be influenced by the energy threshold. Therefore, using atmospheric neutrinos to search for neutrino oscillation requires energy thresholds of 5–20 GeV. Detectors, such as Baikal NT-200 and NESTOR, or the insertion of high density strings into the AMANDA-II array, are designed to achieve this goal.

Atmospheric neutrinos reveal oscillation physics in several ways. A deviation from the expected angular distribution would be strong evidence for oscillations. HE neutrino detectors can contribute to this science by virtue of their large detection area and consequent increase in statistical significance. Unfortunately, these are difficult measurements for neutrino arrays. For the simplest case of two oscillating neutrino species, the probability that a neutrino ν of flavor i (e, μ, τ) will oscillate into a different flavor x is given by

$$P(\nu_i \rightarrow \nu_x) = \sin^2 2\theta \, \sin^2\Big(1.27\Delta m^2 \frac{L(\mathrm{km})}{E_\nu(\mathrm{GeV})}\Big), \tag{6}$$

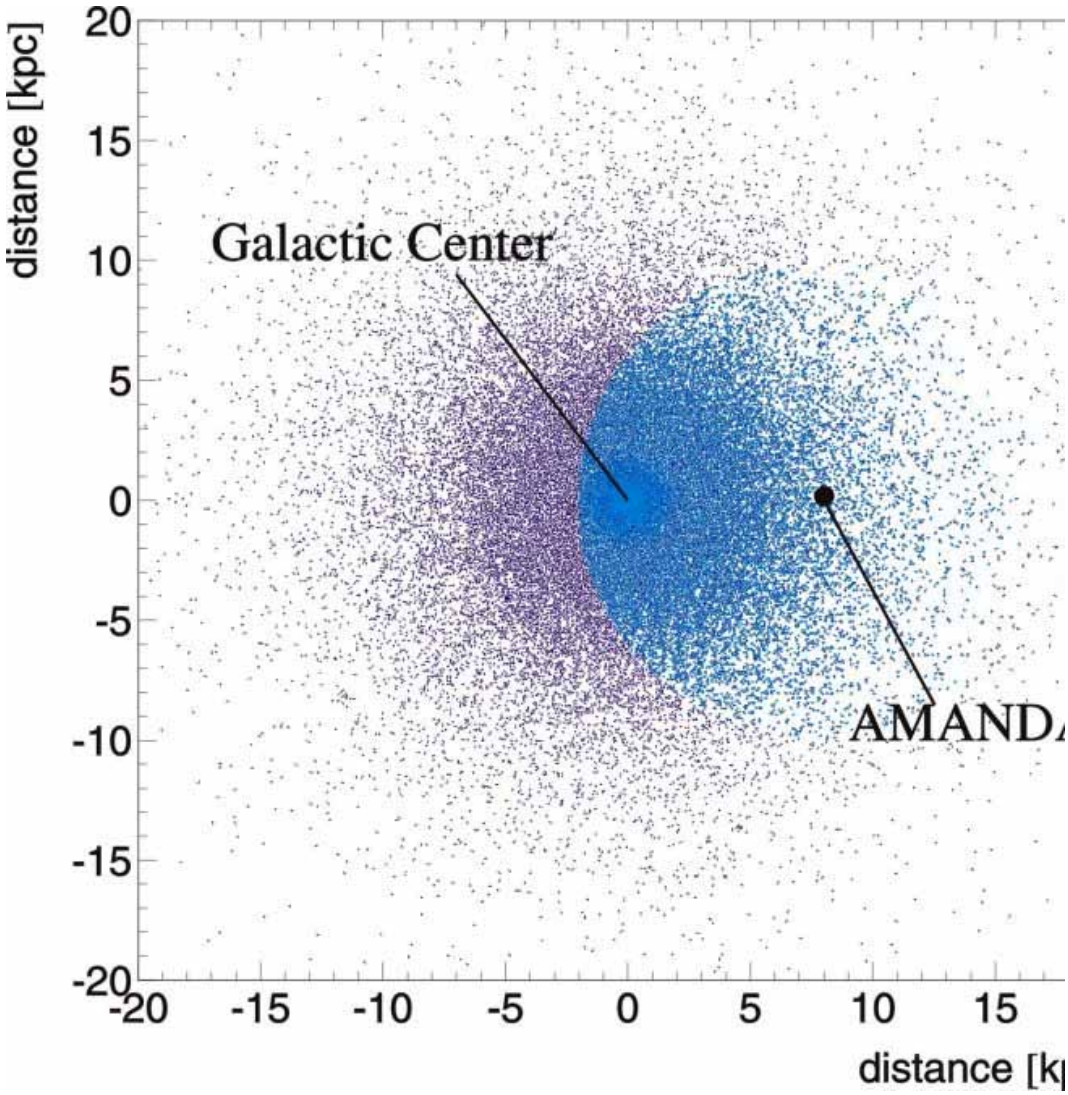

Fig. 10. Expected viewing distance for supernovae similar to SN1987a. For these calculations, the ambient noise rates and non-poissonian fluctuations are taken from measurements by the AMANDA collaboration. The colors correspond to arrays with N_{OM}=100, 1000, 5000.

where θ is the mixing angle, Δm^2 is the difference in mass squared in eV^2 of the two mass eigenstates, L is the pathlength between generating vertex and detector, and E_ν is the energy of the neutrino.

Unless the neutrino-induced muon event is completely contained within the detector, the neutrino energy is not well measured. For the current generation of neutrino detectors, through-going upward muons are the most likely detection mode, but this only establishes a lower limit on the neutrino energy. Moreover, the energy threshold for muons which traverse the array is relatively high, so as E_ν increases, angular deviations become very subtle. For parameters of $\Delta m^2 = 2.5 \times 10^{-3}$ eV^2 and maximal mixing, the angular and energy dependence of the detector area must be determined to 5% or better. It remains to be seen if this accuracy can be achieved in practice. Also ν_e events must be differentiated from ν_μ events, which has yet to be shown conclusively.

A second idea takes advantage of the particular strengths of the existing neutrino arrays. The linear symmetry of string-based designs results in excellent sensitivity to nearly vertical tracks. The long lengths of instrumentation can contain neutrino-induced events over a large interval of energies. By concentrating on nearly vertical tracks, backgrounds are easier to reject. The small vertical spacing of optical sensors (compared to the horizontal spacing of the strings) reduce the energy threshold to interesting levels. The detection efficiency as a function of energy can be calculated more accurately than for the entire hemisphere. In addition, the AMANDA array can calibrate its vertical sensitivity with a well defined muon beam using coincidence events that simultaneously trigger another array at 900 meters. If the vertex is contained within the central part of the array, then the light from the interaction vertex and outgoing muon can be modeled to establish the energy of the neutrino with sufficient accuracy. Obviously, the event rates are much lower for a restricted solid angle, but the large detection area results in sufficient statistics. However, the same concern about being able to differentiate ν_e and ν_μ events applies to this technique. For kilometer-scale detectors, a significant fraction of neutrino-induced atmospheric muons will be contained within the actively instrumented volume, so a calorimetric measurement of the neutrino energy is possible. However, the larger spacing between sensors results in higher energy thresholds which may be above the energies of interest. Medium energy physics objectives can be retained if the kilometer-scale array surrounds a first generation neutrino array. The composite detector can identify and reject atmospheric muons, reducing background rejection requirements in the denser central region of the composite array.

A third method to search for neutrino oscillation over long pathlengths (or base-

lines) utilize accelerators to direct a beam of ν_μ particles with a known energy spectrum toward the detector.

Perhaps the best method to study ν_μ oscillation parameters involves dedicated long baseline experiments with high intensity and well-characterized neutrino beams and large volume detectors placed at great distances. Long-baseline programs such as K2K and Minos are currently investigating oscillation parameters deduced by atmospheric neutrino studies. Next generation long baseline experiments are considering several energy ranges for neutrino beams. At large distances or at low energies, the meager event rates dictate both large intensity beams and large volume for the end detectors. It has been suggested that HE neutrino telescopes located at distances between 1000 and 10000 km could play a role.[74] While most discussion has involved CERN and planned neutrino telescopes in the Mediterranean, the idea works the same for any accelerator and neutrino observatory as long as a neutrino beam can be pointed in the right direction. Even without flavor or charge sign ID, conventional wide band neutrino beams directed at HE neutrino telescopes could measure the sign and magnitude of Δm^2_{13}, and θ_{13}, θ_{23}.

Several new ideas for the end detector are under discussion with performance characteristics more suitable for long baseline physics than are available from HE neutrino arrays, such as low energy threshold, reliable discrimination between $\mu - e$, and charge sign identification of the lepton. The UNO detector[75] extends the water Cherenkov technique, used in SuperKamiokande and other large nucleon decay experiments, to a very large fiducial mass. The initial design envisions a fiducial mass of $\sim 10^6$ tons, making it an attractive target for high-intensity neutrino beams from anywhere on Earth. Two scenarios for long-baseline physics are being explored.[76] Using a beam from a 30–50 GeV muon storage ring (or "neutrino factory") several thousand km away, hundreds of thousands of neutrino interactions would be recorded for each year of running. In addition to a very precise measurement of ν_μ disappearance, wrong-sign muon appearance could be observed by placing large magnets between sub-segments of the detector to measure the charge of energetic muons. A difference in rate between $\nu_e \to \nu_\mu$ and $\bar{\nu}_e \to \bar{\nu}_\mu$ transitions would be clear evidence of CP violation in the leptonic sector. At the other end of the energy scale, a 100–500 MeV ν_μ beam could be exploited to detect ν_e appearance with negligible background, apart from ν_e contamination present in the initial beam. The cross section for neutrino interactions at such energies is small, but the very large target mass of UNO would allow a measurable signal to be observed even 2000 km from the source. At that distance, the δm^2 region corresponding to the large-

mixing angle solution to the solar neutrino problem would be accessible. At shorter distances, where matter effects in the Earth are unimportant, CP violation could also be probed.

3 Detection Principles

The essential characteristics of a neutrino telescope have been known for more than two decades.[1,77] Markov suggested in 1960 that the ocean would be a suitable site for constructing a large neutrino detector based on the detection of Cherenkov light, and most important features were discussed and specified during a series of workshops devoted to developing the DUMAND concept. Halzen and Learned[78] introduced a twist on the general scheme by promoting polar ice as a suitable medium. Until recently, workable implementations of these sensible ideas have been thwarted by unusual technical and logistical challenges associated with the remote deployment of hardware in media that differ from ordinary purified water in several important details. All current architectures for high energy neutrino facilities bury a sparse array of optical sensors within deep ice, ocean or lake waters. The optical sensors respond to the UV dominated Cherenkov radiation emitted by neutrino-induced muons or neutrino-induced hadronic and electromagnetic cascades. Large detector volumes are required because the predicted flux of cosmic neutrinos and the known interaction probabilities at the energies of interest are relatively small. The detection probability, defined as the ratio between the range of the muon to the interaction mean free path of the neutrino, is only 10^{-6} for a ν_μ with an energy of 1 TeV. Moreover, the rare signal events must be extracted from a large flux of atmospheric muon background. For example, at sea level the number of background muons per unit area exceeds the expected neutrino-induced muon signal by $\sim 10^{11}$, so neutrino detectors are constructed at large depths to reduce this unwanted signal. Even at depths of 2 km of water equivalent, down-going background exceeds predicted signal by a factor of $\sim 10^5$. The combination of large volume, large overburden, and desire to minimize material costs leaves experimentalists with few options other than to construct a detector within a remote, naturally occurring, transparent medium such as ice or water (no excavated caves or mines are large enough). The formidable technical challenge of remote operation distinguishes high energy neutrino facilities from existing solar and accelerator-based neutrino detectors. It is one factor which has spurred the continuing discussion of surface detectors (e.g., GRANDE and HANUL[79]) despite the daunting background difficulties.

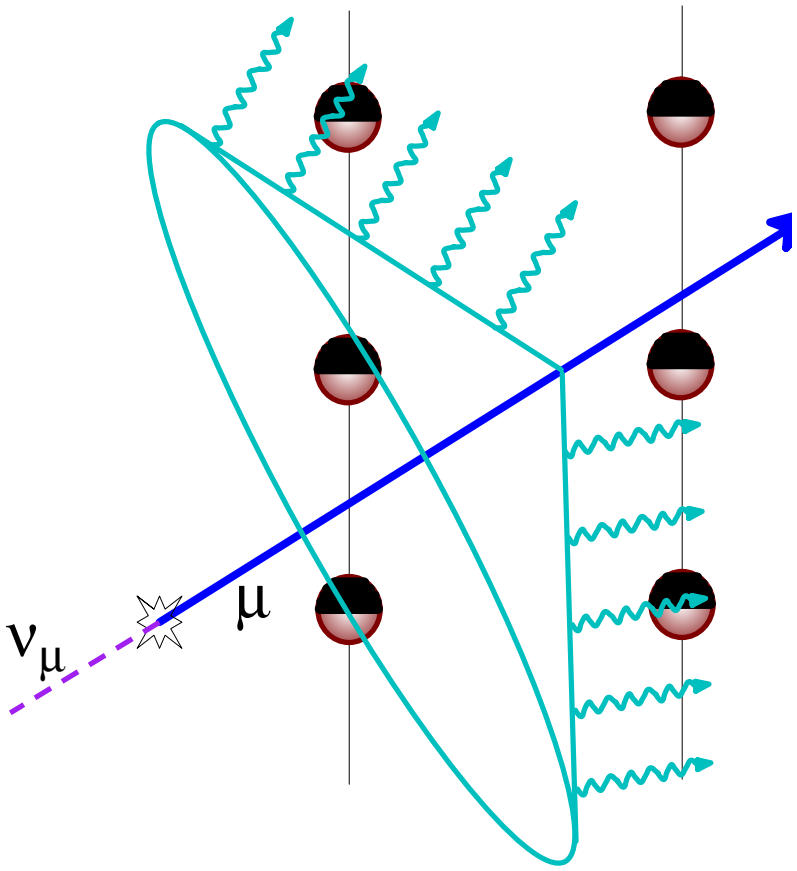

Fig. 11. Schematic of detection method for charged current ν_μ signature. Muon trajectories can be reconstructed by timing the passage of the Cherenkov wavefront.

Cherenkov techniques are now well understood and are illustrated in Fig. 11. A high energy neutrino can be detected only if it converts to a charged lepton, such as a muon, or induces a cascade. Astronomy is possible because the muon direction is aligned with the incident neutrino to within a degree, if the energy is greater than 1 TeV. The angular correlation between charged lepton and neutrino improves as the $1/\sqrt{E}$, so eventually multiple Coulomb scattering becomes the dominant factor in the angular resolution. Conceivably, neutrino directions can be determined to $\sim 0.1^\circ$ in some designs.[80] Source localization can be improved by the detection of multiple events, but unless the event rate is unexpectedly large, the angular resolution is not competitive with conventional astronomy. Therefore sources must be identified statistically - by searching for a class of objects that lie within the angular error boxes. Confidence will be bolstered if theoretical models of that class of objects are consistent with high energy neutrino production. The relatively limited number of potential sites of high energy neutrino production suggests that source confusion is unlikely to be a problem.

The muon is detected by distributing photon sensors (large diameter photomultiplier tubes — PMTs) over the largest possible volume of transparent medium and recording the arrival times and intensity of the Cherenkov wavefront. Accurate reconstruction relies on actively tracking events over linear dimensions exceeding tens of meters and measuring the arrival of the Cherenkov wavefront to tens of nanoseconds or better. Geometries of the arrays are optimized according to the optical properties of the detector media – those media that generate less precision in the arrival time of the Cherenkov wavefront can be compensated by larger detectors with greater average pathlength. The instrumented volume can be increased by utilizing a medium with a large optical attenuation length. Naturally, volumes increase with with additional sensors, so per unit costs become an important design factor.

Muons from neutrino interactions are distinguished from the vastly more numerous atmospheric muons by direction; upward-traveling muons (through the detector) can only originate from nearby neutrino interactions. The Earth filters out all other known particles. Great care must be taken to reject the "down-going" atmospheric muons. In practice, muons are properly reconstructed if they traverse typically ~ 100 m of pathlength within the boundaries of the array defined by the outermost strings, although dense arrays have demonstrated good reconstruction with shorter tracks. Complications arise from the lack of fixed fiducial volume, the presence of events containing multiple muons, decaying muons in flight, and fluctuations in the generation of Cherenkov photons resulting from high energy physics processes. Muon trajectories can pass near

enough to trigger the array, but too far outside the detector boundary for proper reconstruction.

Reconstruction is tied to specific assumptions about the event topology. For example, it is usual to assume that the characteristics for a neutrino-induced muon event are: 1) one and only one particle traversing the array, 2) continuous, uniform production of photons from a minimally ionizing charged particle, 3) propagation at the speed of light, and 4) traversal of the entire instrumented volume of the detector. Deviation from these assumptions, such as stopping muons or decays-in-flight, multiple-muon events, or energetic muon-bremsstrahlung, result in poorer reconstruction of the event trajectory and energy. Once the event is reconstructed, selection criteria are applied to reject events that are likely to be poorly reconstructed. It is obviously desirable to develop selection criteria that maintain good efficiency for signal events.

As mentioned, the dominant source of background in high energy neutrino detectors is downward muon tracks generated by cosmic ray interactions in the atmosphere. This background can be avoided by constructing a detector at $\geq$10 kmwe (kilometers of water equivalent) depths, but such depths are logistically impossible to attain. Rather, large volume detectors are constructed at intermediate depths, and the background must be removed by other methods. In principle, the angular direction distinguishes astrophysical neutrino signals from the background of atmospheric muons — muons originating from below the horizon must originate from neutrino interaction. However, errors in the reconstructed direction of the muon trajectory can result in misinterpreting down-going muons as upward going muons. For detector sites at depths between 1 and 4 kmwe, and energy thresholds of $\sim$10 GeV, the rate of down-going muons exceeds potential signal rates by factors of $10^3 - 10^5$ (assuming atmospheric neutrinos are the baseline signal). Therefore, an important design specification involves the rejection factor, R, defined as $R = A_{eff}(signal)/A_{eff}(mis)$, where $A_{eff}(mis) = F_m \times A_{eff}(\mu_{atm})$, $A_{eff}(\mu_{atm})$ is the effective area for the detection of down-going muons, and F_m is the fraction of down-going muons misidentified as upward going. The rejection factor must be greater than 10^3 for the best case conditions, and typically 10^6 for detectors located at depths of 2 kilometers water equivalent (kmwe). In the simplest description, F_m is a constant, but it may be treated as an angular dependent scattering probability $P(\theta, \theta^{'})$ in more complex descriptions. As the energy threshold of the detector is increased to $\sim 10^{15}$ eV, the ratio of downgoing atmospheric muons to expected signal decreases, reaching unity in the vicinity of 1 PeV. Since the required level of rejection is less at higher energy thresholds, event selection criteria can be optimized to achieve much larger effective

areas than could be achieved with larger rejection requirements. Detection methods with sufficient energy resolution to identify PeV events can be used to search the entire sky. Simulations show[81,82] that the energy of ν_e-induced cascades may be measured with sufficient accuracy, assuming the vertex is contained within the volume of the array. The quoted values in the literature for effective detection area cause much confusion because they are a function of lepton energy, zenith angle, and required rejection factor which differs between physics objectives. The effective volume becomes useful when the range of the muon is comparable to the largest dimension of the array. For muon detection at medium energies (and for all cascade events), the effective volume becomes a convenient parameter of detector sensitivity, but it too depends on energy and rejection factor.

Atmospheric neutrinos form an irreducible background in the sense that they cannot be differentiated from non-terrestrial neutrino signals on an event by event basis. Since the energy spectra and angular distributions of atmospheric neutrinos are reasonably well known from measurement and calculation, statistical techniques using energy spectra, spatial and temporal correlation, etc. can confirm or reject a hypothesis involving atmospheric neutrinos.

3.1 $E_\nu < 1$ PeV: Detection Modes of Optical Cherenkov Arrays

In this section, we discuss the most common detection signatures for HE neutrino telescopes. The neutrino signature depends on flavor and whether the neutrino initiates a charged current or a neutral current interaction.

1. Charged current (CC) interactions initiated by ν_μ. For $E_\mu > 1$ TeV, the range of the muon exceeds several kilometers and the effective volume can greatly exceed the instrumented volume, which is the reason why this mode has been the primary focus of recent detector designs utilizing optical Cherenkov radiation.

2. Cascades initiated by neutral current (NC) interactions, ν_e and $\sim$ 80% of ν_τ charged current interactions.

3. Double Bang events are generated by ν_τ. For $E_\nu > 10^{16}$ eV, the decay length of the tau lepton is comparable to the scale of the instrumented volume of high energy neutrino arrays. The initial interaction produces a large hadronic cascade as does the eventual decay of the tau lepton. The distinct separation of two large cascade events provides a unique signature. However, since the vertices of both cascades must be contained, the effective volume of this mode is a few percent of the CC ν_μ signature.

Table 1 summarizes the primary backgrounds, advantages, and disadvantages for the most common detection modes.

Table 1. Primary modes of detection available to HE neutrino telescopes.

Mode	Background	Advantages	Disadvantages
ν_μ	atm. ν_μ, downgoing atm μ	Best V_{eff}	
ν_e cascades	μ-brem, ν_μ^{NC}	BG systematics	$\sim 0.1 V_{eff}^{\mu}$
		$E_{th} > 10$ TeV	poor angular resolution
ν_τ Double Bang	little	clean downgoing signature	must be contained, $\sim 0.01 V_{eff}^{\mu}$
		long baseline oscillation	E_ν =1-10 PeV, only downgoing
ν_τ by excess ν_e	ν_e and ν_μ^{NC}	low energy ν_τ	very challenging signature

The following sections give more detail on each detection mode.

3.1.1 Muon Detection

The largest effective detector volumes are achieved by measuring the flux of high energy muons. For energies between 0.1 TeV and 1000 TeV, the enormous flux of atmospheric muons, generated cosmic ray collisions in the atmosphere, overwhelms the meager signal expected from neutrinos. Restricting the observations to upgoing directions can eliminate this background. The Earth filters out the atmospheric muons, leaving only muons induced by neutrinos that happen to interact near the active volume of the detector. Assuming that the range of the muon is larger than the characteristic dimension of the active volume of the detector, the signal rate is the convolution

$$Signal \sim A_{eff} \otimes R_\mu \otimes \sigma_\nu(E, y) \otimes \phi_\nu, \tag{7}$$

where R_μ is the muon range in g/cm^2, $y = \frac{E_\nu - E_\mu}{E_\nu}$ is the mean inelasticity so $1-y$ is the fraction of energy transferred to the muon, and A_{eff} is the energy dependent effective area of the detector. The range and cross section both increase linearly with energy into the TeV region. Stochastic processes begin to dominate over continuous ionization losses at energies above 0.5 TeV, and therefore the energy loss per unit length also increases. Assuming a linear scaling between Cherenkov emission and dE/dx, high energy muons become "brighter" and more readily detected. The effective area increases with energy because the muon can be detected from greater distances. Since muons can be detected beyond the instrumented volume, it is possible for the effective area to be larger than the instrumented cross-sectional area of the array of photomulitplier tubes. In practice, strong background rejection requirements usually result in effective areas that are smaller than the geometric area. The energy dependence of A_{eff} must be included in the calculations of the event rate.

The usual procedure for calculating the flux involves several simplifying approximations to estimate the event rate (and avoid the convolution calculation). First, the charged-current cross section is usually averaged over the y-distribution, and small differences in the average between ν and $\bar{\nu}$ are ignored. This approximation is excellent for $E_\nu > 10^{15}$ eV. The mean value of y converges to 0.2 for the neutrino and anti-neutrino, and only weakly depends on energy. Second, the energy dependence of the detector can be factored out of the convolution by calculating the neutrino induced muon spectrum *at the detector*, dN_μ/dE. The flux of muons with energy E_μ induced by neutrinos with energy E_ν is

$$\frac{d^2N_\mu}{dE_\mu dE_\nu} = \int_0^\infty dX \int_{E_\mu}^{E_\nu} dE_\mu^{'}\, g(X, E_\mu, E_\mu^{'})\, N_A \frac{d\sigma}{dE_\mu^{'}} \frac{dN_\nu}{dE_\nu} \tag{8}$$

where the last two factors are, respectively, the charged current cross section and the differential energy spectrum of the neutrinos. The factor, g, is the differential probability that a muon produced with energy $E_\mu^{'}$ travels a distance X and retains an energy E_μ. By ignoring range straggling[†] of the muon, g can be written:

$$g(X, E_\mu, E_\mu^{'}) \cong \frac{\delta(X - X_0)}{\alpha(1 + \beta E_\mu^{'}/\alpha)} \tag{9}$$

where the constants in rock are $\alpha \cong$2 MeV/(g/cm^2) and $\epsilon = \alpha/\beta$ =510 GeV. These parameters vary by less than 20% from 10^{12}–10^{20} eV. Lipari and Stanev[83] have discussed a more accurate treatment of muon propagation at high energy. If the small variations in these parameters are ignored, then X_0 is determined by

$$\beta X_0 = \ln\left[\frac{E_\mu^{'} + \epsilon}{E_\mu + \epsilon}\right]. \tag{10}$$

Using these approximations, we see that the differential muon energy spectrum at the detector is related to the differential neutrino spectrum, ϕ_ν=dN_ν/dE_ν, by

$$\frac{d^2N_\mu}{dE_\mu dE_\nu} \cong \frac{dN_\nu}{dE_\nu}\frac{dP_\nu}{dE_\mu} = \frac{dN_\nu}{dE_\nu}\frac{N_A}{\alpha(1 + \beta E_\mu/\alpha)} \int_{E_\mu}^{E_\nu} \frac{d\sigma}{dE_\mu^{'}} dE_\mu^{'}\,, \tag{11}$$

where the probability that a neutrino of energy E_ν directed toward a detector produces a detectable muon is P_ν. The event rate can now be calculated from Equation 11:

$$Signal \;\; = \;\; \int_{E_\mu^{th}}^\infty \int_0^\infty \frac{d^2N_\mu}{dE_\mu dE_\nu} A_{eff}(E_\mu)\, dE_\nu\, dE_\mu \tag{12}$$

[†] Range straggling refers to the variation in range due to fluctuations in energy losses. Therefore, a beam of particles with identical energy will not travel the same distance for the same energy loss.

$$= \int_{E_\mu^{th}}^{\infty} \int_0^{\infty} \frac{dN_\nu}{dE_\nu} \frac{dP_\nu}{dE_\mu} A_{eff}(E_\mu)\, dE_\nu\, dE_\mu \tag{13}$$

$$= \int_0^{\infty} \int_{E_\mu^{th}}^{\infty} \frac{dN_\nu}{dE_\nu} \frac{dP_\nu}{dE_\mu} A_{eff}(E_\mu)\, dE_\mu\, dE_\nu. \tag{14}$$

According to Eqn. 14, the integrated probability of detection must be weighted according to the effective area of detection. If the energy dependence of A_{eff} is assumed small, then A_{eff} can be removed from the integral:

$$Signal = A_{eff} \int_0^{\infty} \int_{E_\mu^{th}}^{\infty} \frac{dN_\nu}{dE_\nu} \frac{dP_\nu}{dE_\mu}\, dE_\mu\, dE_\nu \tag{15}$$

$$= A_{eff} \int_0^{\infty} \frac{dN_\nu}{dE_\nu} P_\nu\, dE_\nu, \tag{16}$$

where E_μ^{th} is the minimum detectable muon energy for a given detector, which in general depends on the zenith angle and the rejection requirements of the analysis (i.e, it is analysis specific). Note that the probability, $P_\nu(E_\nu) = \int_{E_\mu^{th}}^{\infty} \frac{dP_\nu}{dE_\mu} dE_\mu$ only depends on the minimum detectable muon energy, not the initial neutrino spectrum. Graphical illustrations[84] and analytical expressions for P_ν can be found in literature for several values for E_μ^{th}, with the assumption of constant effective area. These analytical expressions are useful for order-of-magnitude estimates, but it is important to keep in mind the restrictions.

For the energy interval $10^{-3} < E_\nu < 1$ TeV, the probability is averaged for identical fluxes of neutrinos and anti-neutrinos

$$P_\nu \simeq 1.3 \times 10^{-6}\, (E/\mathrm{TeV})^{2.2}. \tag{17}$$

The scaling with energy directly reflects the energy dependence of the neutrino cross section and the average range of the muon. The cross section is proportional to energy below 1 TeV, but then changes to a weaker energy dependence due to the effect of the W propagator. A similar change in the energy dependence occurs for the range of the muon, so for $1 < E_\nu < 10^3$ TeV, the probability becomes

$$P_\nu \simeq 1.3 \times 10^{-6}\, (E/\mathrm{TeV})^{0.8}. \tag{18}$$

For energies greater than 10 PeV, the effect of the W propagator becomes more pronounced, and the cross sections[85] scale with energy approximately as $E^{0.36}$. Unfortunately, the cross sections are not well determined because different assumptions about the parton distribution functions at very small x lead to uncertainties of a factor of 2

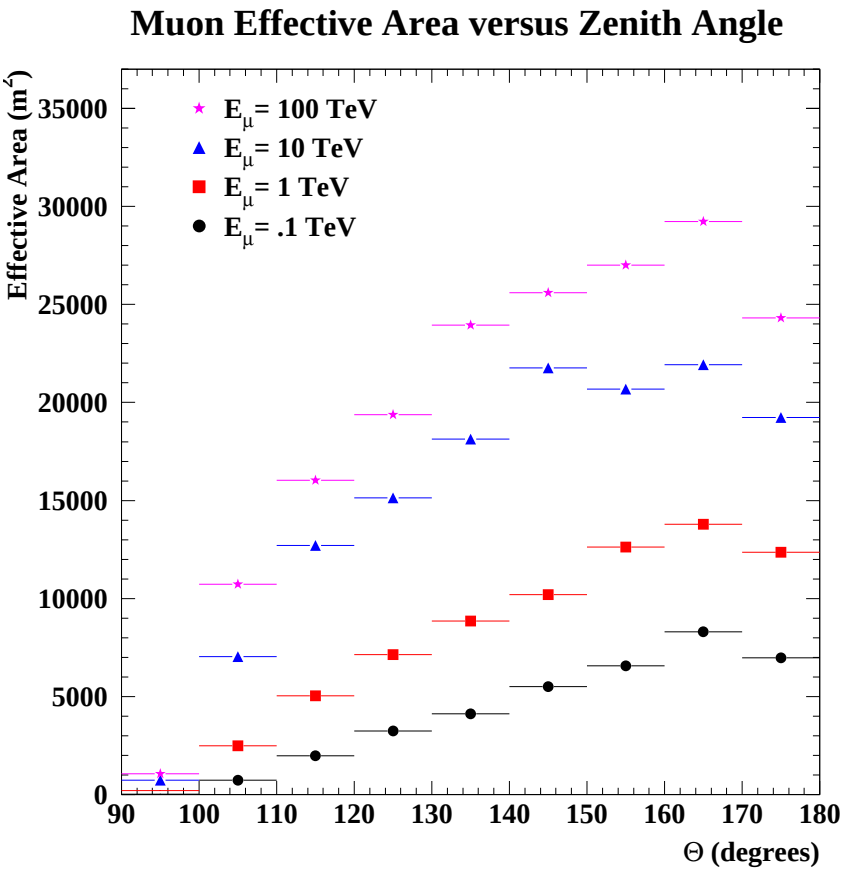

Fig. 12. The effective area for muon detection as a function of zenith angle for E_μ between 0.1 TeV and 100 TeV (180° is vertically up in local detector coordinates).

at 10^{20} eV. Keeping these limitations in mind, the probability for muon detection is approximated as:

$$P_\nu \simeq 10^{-2}\,(E/\mathrm{EeV})^{0.4}, \tag{19}$$

where E is now in units of EeV (10^{18} eV).

The current generation of HE neutrino detectors are constructed with approximate cylindrical symmetry, and oriented vertically. This leads to angular dependence in the effective area, $A_{eff}(\theta)$, where θ is the zenith angle. As figure 12 shows, this is certainly the case with AMANDA. Moreover, the energy dependence of A_{eff} cannot be ignored. To allow for these effects, we can write Eqn. 12 more generally as

$$Signal = \int_{E_{\mu^{th}}(\theta)}^{\infty}\int_0^\infty \frac{dN_\mu}{dE_\mu dE_\nu} A_{eff}(E_\mu,\theta)\,dE_\nu\,dE_\mu. \tag{20}$$

Neutrinos with $E_\nu < 100$ TeV are not strongly attenuated by the Earth, and much of the solid angle near the horizon remains accessible to energies as large as 1 PeV. Although the Earth is transparent to low energy neutrinos, an Earth diameter (1.1×10^5 kmwe) exceeds the interaction length of neutrinos with energy higher than about 40 TeV. It is convenient to introduce an exponential factor to account for the absorption of neutrinos as they travel along the chord of the Earth, $X(\theta)$,

$$f(E_\nu, \theta) = \frac{dN_\nu}{dE_\nu} e^{-\sigma_{tot}(E_\nu) N_A X(\theta)} , \tag{21}$$

which assumes that the reaction products generate no detectable signal. The attenuation factor can be averaged over azimuth angle[85] to produce a "differential shadow factor" that is equivalent to the effective solid angle for upward traveling muons. Uncertainties in the density profile of the Earth and the neutrino cross section contribute to the error in this calculation. For neutrino energies above 10^{20} eV, horizontal and slightly downgoing neutrinos encounter sufficient material to attenuate the flux (keep in mind that we are discussing underground detectors with overburdens of several kilometers of water equivalent or more). There is one notable exception to these conclusions. Tau neutrinos will regenerate themselves because both the charged and neutral current interactions produce a tau neutrino in the final state. Regeneration causes the tau neutrino to lose energy until $\sim 10^{15}$ eV, the energy at which the Earth becomes transparent to all neutrino flavors. In practice, this signature is difficult to use to identify ν_τ if the cosmological sources produce nearly equal fluxes of ν_μ and ν_e with power law spectra. Under these assumptions, the high energy ν_τ signal will be overwhelmed by the signal from lower energy ν_μ. At this point, statistical discriminants must be employed based on angular dependence of the signal or a rare high energy event traveling vertically upward. Unfortunately, the statistics of high energy events by current or next generation detectors is unlikely to be high enough to utilize this discriminant effectively.

The calculations above ignore range straggling and other details of muon energy loss. They are valid only if the range of the muon is less than the column density of matter surrounding the detector. For upgoing neutrinos penetrating the Earth, this condition is valid, but does not hold for detectors at relatively shallow depths for neutrino-induced muons in the downward direction. As a consequence, downgoing signals from neutrinos are concentrated near the horizontal direction, where the column density is greatest.

3.1.2 Cascade Detection

There are several important processes that generate cascades of high energy particles, which are summarized below:

$$\nu_e(\bar{\nu}_e) + N \rightarrow e^-(e^+) + \text{hadrons}, \quad (22)$$

$$\nu_l(\bar{\nu}_l) + N \rightarrow \nu_l(\bar{\nu}_l) + \text{hadrons}, \quad (23)$$

$$\bar{\nu}_e + e^- \rightarrow W^- \rightarrow X. \quad (24)$$

Neutrino-induced electrons produce electromagnetic cascades that generate very bright, localized bursts of Cherenkov photons. The longitudinal development of hadronic and mixed cascades is somewhat less localized on average, and they occasionally produce muons that travel for 50 m. The narrow resonance reaction indicated by the third line[86] can be used to calibrate the energy response of the detector, but the event rates induced by atmospheric neutrinos is negligible for kilometer scale detectors.[2] However, if astrophysical sources of 6.4 PeV neutrinos exist, then this reaction may become important in kilometer scale detectors. While the energy resolution for cascade events is expected to be much better than that for muon tracks, whether it is sufficient to extract resonant events from the continuum induced by charged current reactions on nuclei remains an open issue. Initial studies of the IceCube detector performance[82] shows that this requirement represents a non-trivial challenge.

Although the directional information is poor compared to muon tracks, the energy resolution is far superior. In media with moderate scattering, the sensors nearest the cascade vertex provide the directional information, while distant sensors sample from a expanding diffusive wavefront to provide a calorimetric measurement. The spherical topology of the cascade events readily distinguishes them from the most common atmospheric muon backgrounds. For example, atmospheric ν_e are highly suppressed at these energies because the muons produced in the air shower are far more likely to interact than decay. At energies above 1 TeV, the irreducible flux of atmospheric ν_e is less than ν_μ because fewer atmospheric muons decay before reaching the detector as the muon energy increases. Therefore, neutral current interactions by ν_μ-induced bremsstrahlung and pair production are the dominant background, apart from instrumental enhancement of the more abundant, lower-energy phenomena. Recent work has shown that the latter two physics backgrounds can be eliminated while retaining good efficiency for signal events. Once these backgrounds are rejected, neutral current interactions by atmospheric ν_μ form an irreducible background. In this sense, the techniques of detecting

ν_μ and ν_e are complementary. The good angular precision and superior sensitivity of muon detection is traded for improved energy resolution and lower background rates. For kilometer-scale detectors, the large spacing between strings leads to a rather large energy threshold for simple trigger schemes, but fractional energy resolution of $\sim 25\%$ is expected.[82]

One common practice seen in the literature is to present integral limits in plots of differential spectra, which is acceptable if the energy resolution of the detector is rather poor. However, this practice makes it difficult to interpret the results and gives an overly optimistic impression of the sensitivity of the detector. Given the energy resolution expected for cascade events, it is more informative to plot differential sensitivity as a function of neutrino energy. This point is illustrated in Fig. 13, which was taken from Ref. 82. The figure shows that several models can be probed by current and next generation HE neutrino detectors. In general, differential limits convey information more transparently, but in practice, each model must be compared on a case-by-case basis by calculating the expected event rate for each unique flux prediction and then comparing to background rates to obtain flux limits.

Due to the suppression of the atmospheric ν_e flux at high energies (relative to ν_μ), hadronic cascades induced by neutral current interactions of atmospheric ν_μ generate an irreducible background for astrophysical sources, unless it becomes possible to distinguish NC interactions from ν_e-initiated cascades. The background shown in Fig. 13 has several important consequences. First, it is possible to search for a diffuse flux of ν_e by integrating over the complete sky (4π sr) by imposing a software energy threshold of 100 TeV. Sensitivity to downgoing neutrinos is particularly important for energies above 10^{15} eV because the column depths are too small to significantly attenuate the neutrino signal. It will be very difficult to use the muon mode to search for downgoing muons with comparable energies, so cascades may be the only mechanism for a single detector to integrate signal from the complete sky. Second, Wu[82] estimated the effective volume for ν_e in a typical kilometer-scale detector after the application of background rejection criteria. It is comparable to the effective volume for the ν_μ mode in AMANDA-II. Since the best studied mechanisms for high energy neutrino production predict comparable fluxes of ν_μ and ν_e, most models accessible to study by the ν_e mode in kilometer scale detectors will be tested by the current generation of HE neutrino detectors. Discovery by current generation detectors will provide strong incentive to optimize the next generation detector for flavor composition studies of neutrino emission.

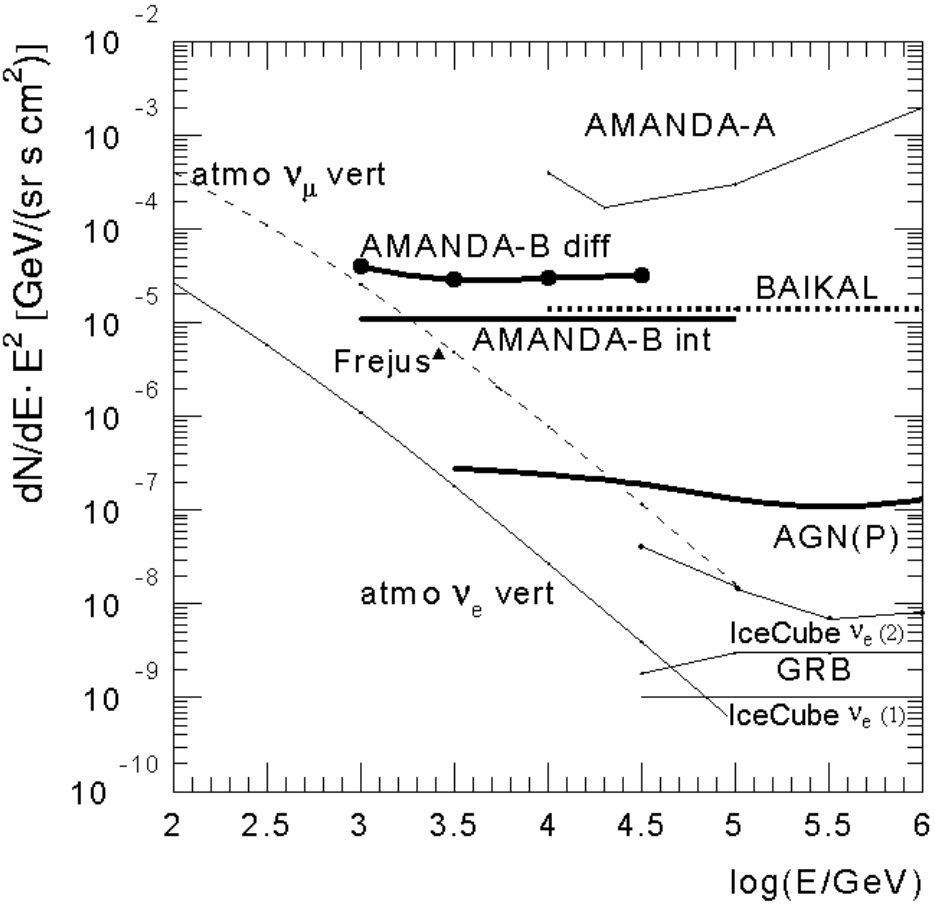

Fig. 13. Diffuse flux predictions and experimental limits for cascade events initiated by ν_e. The experimental limits were obtained from AMANDA-A,[81] Frejus[25] (triangle), and the Baikal NT detector.[67] AMANDA-B diff and AMANDA-B int are the differential and integral limits.[87] The curve labeled IceCube ν_e(1) corresponds to the minimum detectable flux for one year of livetime, assuming an E^{-2} differential spectrum and ignoring atmospheric background. The curve labeled IceCube ν_e(2) is the minimum detectable differential flux, taking into account the irreducible background from NC interaction. The atmospheric neutrino flux,[83] GRB flux[5] and AGN flux[88] are shown for comparison.

3.1.3 ν_τ detection using Double Bang mode

The strong interest in neutrino oscillation and flavor composition of the neutrino flux from astrophysical sources strongly motivates experimentalists to find a mechanism to identify tau neutrinos. Learned and Pakvasa[62] suggested that the tau neutrino may be identified by observing an event characterized by pair of energetic cascades separated by the flight distance of the tau lepton. The signature is known as the "Double Bang" mechanism.

The flight distance, L, of the tau lepton produced in CC interactions is given by

$$L = c\tau E/m_\tau = \left(\frac{87\,\mathrm{m}}{1.8}\right)\left(\frac{E_\tau}{1\,\mathrm{PeV}}\right). \quad (25)$$

The flight distance is approximately 100 m for E_τ = 2 PeV, which is large enough to observe with a HE neutrino facility. The initial cascade from the charged current interaction contains $\sim$ 30% of E_ν. The energy lost by the tau lepton is largely ionization, since the heavy mass suppresses bremsstrahlung and pair production. The subsequent decay of the tau lepton produces an even more spectacular cascade containing 70% of the neutrino energy. The simultaneous observation of two cascades separated by a minimally ionizing track would be unambiguous and profound.

The backgrounds for the Double Bang signature are expected to be very small, but the effective volume in optical arrays is greatly reduced by the requirement to contain both showers.[61,12] The lack of reconstruction tools for this unusual topology makes it difficult to estimate the minimum and maximum separations that produce sufficient energy resolution and background rejection, but first pass estimates of the effective volume is only a few percent of the volume for ν_μ. Apparently, event rates will be very small compared to other modes accessible to current HE neutrino detectors. Also, the requirement for well-separated showers constrains the lower energy limit to several PeV. At this energy, attenuation by the Earth becomes severe so only half the sky is accessible. Despite these obstacles, the discovery of one or more astrophysical sources by current generation detectors will motivate the development of analysis tools tuned for the Double Bang signature.

At EeV energies, the Double Bang signature is more readily detected by facilities employing the air fluorescence techniques such as HiRes, Auger, and EUSO/OWL. In this case, the detection strategy utilizes a variant of the horizontal air shower method.

3.2 $E_\nu > 1$ PeV: Optical Cherenkov

The AMANDA collaboration[11] has recently suggested that present generation optical arrays can be used to detect ν_μ with energies above 10^{18} eV. The muon is ejected with 80% of the neutrino energy and propagates for tens of kilometers. Except near the horizon, the limited column thickness above the detector suggests that the energy losses are modest. Since the muons are detected with energies close the production energy, the effective area of AMANDA is very large. Simulations show that muons with E_μ = 10^{18} eV can be detected more than 500 m from the center of the array. The arrival time distribution of photons characterizes the distance, while the quantity and topology characterizes the energy. Atmospheric muon backgrounds are small at these energies, but instrumental artifacts (from cross-talk in the electronics, for example) must be understood. The response of the optical sensors to large light levels can be calibrated by *in situ* light sources. An early stage of analysis, which includes background rejection criteria, shows that the aperture of AMANDA is $\sim$5–10 km^{3}sr, comparable to the Auger sensitivity from horizontal air showers. The expected sensitivity for AMANDA at EHE energies is indicated by the dotted curves in Fig. 3 and compared to Auger, OWL, and RICE.

Most of the EHE events are detected well outside the instrumented volume so angular reconstruction and energy resolution are not likely to be very good. Since signal events tend to arrive from the horizon while background events cluster near zenith, the lack of angular reconstruction eliminates this powerful statistical test. Fortunately, it is probable that IceCube can reconstruct the angular parameters of EHE muons with much better accuracy. The energy threshold could be reduced relative to AMANDA-II because background topologies are easier to recognize. Even though the overall sensitivity of IceCube will be comparable to AMANDA and Auger, it can verify discovery claims with improved performance (relative to AMANDA) or with independent systematic errors (relative to Auger).

3.3 $E_\nu > 1$ PeV: Alternative Techniques

Above ~ 10 PeV, the predicted event rates for optical arrays are rather meager.[89] Alternative techniques for 10^9 GeV neutrinos are being considered through coherent radio[90–92] or acoustic[93] pulses. At EHE energies, acoustic and ice-based radio techniques run out of rate unless an enormous extrapolation in size is assumed. Instead, new techniques which utilize the enormous energy deposition by EHE ν's interactions are under

development. We briefly discuss horizontal air shower measurements with conventional arrays[23] or with fluorescent light either from the ground[94] or from orbiting detectors.[24]

3.3.1 Radio and Acoustic Techniques

Nearly 40 years ago, Askaryan[95] predicted that the development of high energy electromagnetic cascades in normal matter should produce a charge excess. Photon and electron scattering processes[‡] that pull electrons from the surrounding material into the cascade create an excess negative charge of 20-30%. This effect has been confirmed by a beautiful measurement at SLAC Final Focus Test Beam Facility.[96]

Techniques based on the detection of coherent radio emission from neutrino-induced electromagnetic cascades are being pursued in several ways. The RICE experiment exploits the dielectric properties of cold Antarctic ice. At radio wavelengths, the attenuation length in ice is approximately 1 km, nearly an order of magnitude larger than optical absorption lengths, suggesting that much larger volumes of ice can be instrumented for a given number of sensors. Relatively little of the neutrino energy is transformed into radio power, so the energy threshold of this technique is rather high. However, the large attenuation lengths at radio wavelengths assures that once the signal to noise exceeds unity for a given receiver, it will remain detectable to large distances between cascade and receiver. At the moment, more than a dozen radio receivers are buried in the same holes used by the AMANDA collaboration. The sensors are placed at depths of several hundred meters, which stems from two competing conditions. At increasing depths, the ice temperature increases (so attenuation length is reduced) and the transmission of high frequency signals becomes more difficult. At shallow depths, the index of refraction changes rapidly due to the changing density of the firn ice layer. The primary aim of the RICE collaboration is to study reliability, backgrounds, calibration, and the position resolution of vertex reconstruction.[22] Present analysis shows that the vertex of the cascade can be determined with a resolution of 10 m. The RICE collaboration is developing higher gain antennas and new transmission technologies based on optical fibers to increase the bandwidth. D. Seckel[97] has speculated that radio techniques may be the best technique with the capability to achieve an effective volume of 100 km^3. Long term issues such as power, signal transmission, servicing, and triggering over vast distances on the Antarctic plateau remain to be solved.

The interaction of EHE neutrinos near the surface of the lunar regolith may produce

[‡] positive charge is removed by in-flight annihilation of positrons in the cascade

radio frequency pulses.[92] The large target mass compensates for the small solid angle and limited exposure time on large telescopes. The acceptance of this technique is $\sim 10^3$ km^{3}sr for $E_\nu > 10^{20}$ eV, which is a factor of 100 larger than expected for optical arrays. However, the exposure time for optical arrays is typically years whereas time allocation on radio telescopes is typically a few days. Backgrounds from high energy cosmic rays may pose a problem. Recent work scanned the limb of the moon. It was thought that total internal reflection would suppress radio emission by cascades initiated by cosmic rays. However, recent work which has included the LPM effect has shown the detection probabilities for cosmic ray events dominate near the limb.[98] Imperfections from sphericity on the lunar surface may create background "hot spots" as well. Fortunately, the neutrino detection probabilities dominate cosmic ray probabilities near the center of the moon, but refraction reduces the acceptance.

Both water and ice media can be used to detect acoustic pulses which are generated by cascades when ionization energy losses are converted into heat. While heat is deposited into the medium very quickly (a few nanoseconds), it dissipates very slowly. The approximate step function expansion creates a coherent bipolar pressure wave. The signal strength scales linearly with energy, as given by

$$P \propto \frac{KE}{CRd^2}\,, \tag{26}$$

where P is the amplitude of the pressure wave, K is the expansion coefficient, C is the heat capacity, d is the diameter of the cascade development, R is the distance between the cascade and detector, and E is the energy of the neutrino. Note that the "seeing distance" is linearly proportional to deposited energy for a fixed receiver sensitivity. This explains why acoustic techniques become attractive at $>$PeV energies. One critical parameter is the bulk coefficient of thermal expansion, K, which increases with water temperature, which makes the relatively warm water of the Mediterranean an excellent site.

The pressure amplitude from background noise (which is highly variable due to surface waves) decreases as $1/f$, whereas thermal noise in the receivers scales linearly with frequency. Thermal noise dominates above 20 KHz, which sets an upper bound for the optimal frequency of operation. The recent review by Learned and Mannheim[4] summarizes the current experimental efforts to develop this technique.

3.3.2 Horizontal Air Shower Technique

Given the general power law dependence of the neutrino flux expected from most models, the lowest energies are best explored by optical Cherenkov detectors. Radio and acoustic techniques have the potential to extend the search to the energy interval 10^{15}–10^{18} eV because they can detect downgoing neutrinos with greater sensitivity than optical methods. The upper limit is approximate, determined by event rate, even though the effective volume for these techniques is potentially several orders of magnitude greater than kilometer scale arrays. At the highest energies, large area sparse arrays of particle detectors are sensitive to the macroscopic quantities of energy deposited in the atmosphere during the development of extensive air showers (EAS). We use the word "shower" instead of "cascade" to remind us that the event extends laterally over several kilometers. At these energies, impressively large areas are required to observe a few events per year. For example, the Auger project[37] is now constructing a 3000 km^2 array in Argentina, and plans to duplicate that effort in the northern hemisphere.

The previous method requires "contained" events in the sense that particles must strike the detectors in the active volume, necessitating large areas of instrumentation. Alternatively, pixellated optical telescopes have the sensitivity to detect optical photons generated in the air shower due to nitrogen fluorescence and Cherenkov radiation. The de-excitation of the nitrogen atoms is isotropic, while Cherenkov radiation is co-aligned with the direction of the shower. Therefore, telescopes designed to search for $\sim$ TeV particles rely on Cherenkov radiation, whereas higher energies are best probed by fluorescence techniques because the particle trajectory need not point at the telescope. Compared to surface arrays, far fewer optical telescopes are required to achieve the same aperture, but they are much more sophisticated and operate only on moonless nights ($\sim$ 10% duty cycle). The Auger project employs both techniques.

Horizontal air shower techniques can be employed to explore the neutrino sky at extremely high energies.[37,23] In the vertical direction, the atmosphere is about 10 interaction lengths thick, but the column thickness grows with zenith angle. No shower initiated by a strongly interacting particle can penetrate to the detector from near the horizon. Therefore, horizontal air showers can only be created by deeply penetrating particles, such as neutrinos and muon-induced bremsstrahlung cascades. Even at EHE energies, the interaction length of weakly interacting particles is very long compared to the column thickness, so cascade vertices will be uniformly distributed throughout the atmosphere. In particular, a large fraction of neutrino interactions occur at large depths.

Neutrino showers can be differentiated from electromagnetic showers by exploiting differences in the shape and timing parameters of the shower front, but systematic difficulties involved in both the detection and analysis of inclined showers has hampered efforts in the past.[99] Conceivably, with an acceptance ~ 20 km^{3}sr of water equivalent target volume for $E_\nu > 10^{19}$ eV, the Auger air shower array will have the sensitivity to search for neutrinos from cosmic ray interactions with the cosmic microwave background, and for more speculative signals from topological defects.

Fluorescence techniques measure the longitudinal development of the shower, so energy determination and background rejection are straightforward given an accurate trajectory, and the EUSO/OWL project[24] is designed to take advantage of this. Initially, a large field-of-view mirror with pixellated light sensors is installed on the International Space Station. Flying at altitudes of $\sim$400 km, downward-oriented mirrors can scan a very large volume of the Earth's atmosphere. Preliminary simulations of performance show that the neutrino aperture is sufficient to detect of order 10 events per year from GZK or from the more optimistic parameterizations of topological defect and Z-burst models. The effective volume of the detector system can be increased by eventually launching several mirrors on free-flying satellites to higher altitudes. Potentially, this system increases the sensitivity to HE particles by several orders of magnitude beyond Auger if the technical hurdles are overcome. The "Double Bang" signature for tau neutrinos is quite striking at EHE energies. For $E_\nu = 10^{19}$ eV, the shower pairs are separated by 500 km. In addition to fluorescence photons from horizontal air showers, Cherenkov photons from upward traveling vertical events can be used to identify tau neutrinos. As mentioned in section 2.3.1, the Earth filters all known particles with energies above 1 PeV except ν_τ. At the transparency energy, tau leptons produced in CC ν_τ interactions will travel a distance $\gamma c\tau$ of approximately 50 m (or $\sim$50 mwe since most of these interactions occur in the ocean). For interactions less than 50 m beneath the surface, the tau lepton will emerge and decay to generate an extensive air shower. This process yields a target mass of 10^{14} metric tons at a transparency energy of 10^{15} eV for a baseline target area of 10^6 km^2.

Since the Cherenkov photons are strongly peaked in the forward direction, the energy threshold is greatly reduced for those events that travel toward the instrument. The vertical trajectory suggests that few pixels detect light, so backgrounds and triggering will be challenging. For example, the event rate of upward traveling muons from CC ν_μ will dominate the ν_τ flux due to the much longer range. A fraction of these muons may radiate high energy photons that may confuse flavor indentification.

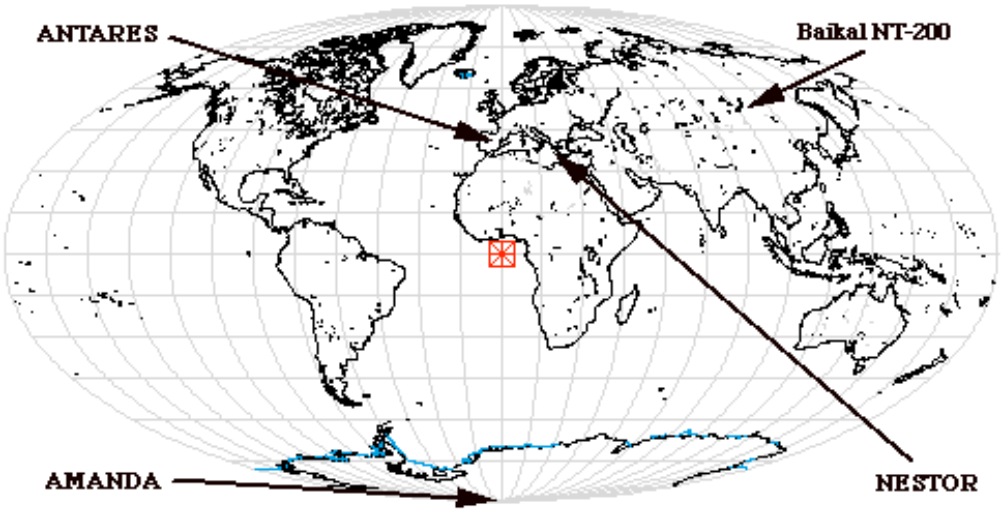

Fig. 14. Geographical location of operating or planned high energy neutrino facilities.

4 High Energy Neutrino Detectors

4.1 General Considerations

The visionary decision by the DUMAND collaboration over 25 years ago to construct a large telescope nearly 5000 m under the ocean and 40 km from shore launched the experimental effort to construct a neutrino observatory. The design goals then were much the same as they are now: threshold energy of $\sim 10 - 100$ GeV, optimized for muon energies of 1–10 TeV, effective detection area = 20,000 m^2, number of optical sensors = 200. Unfortunately, this pioneering effort fell victim to expensive logistical difficulties and was de-funded.

At present, four groups are competing in the construction of high energy neutrino observatories: two in the Mediterranean — NESTOR[100,56] and ANTARES[101]— one in Lake Baikal, Siberia, called NT-200[102] — and one in deep ice at the South Pole called AMANDA.[103–105] Baikal's NT-200 and AMANDA-II are taking data, and feasibility studies are being carried out at the Mediterranean sites. The geographical location is shown in Fig. 4.1.

AMANDA anchors the effort in the southern hemisphere and complements the sky coverage of the Siberian and planned Mediterranean observatories, as shown in fig. 15. Several new concepts for surface neutrino observatories are being discussed,[79] and a new effort to study undersea sites near Sicily and Ponza Island in Italy (NEMO),[106] but I will not cover those ideas here.

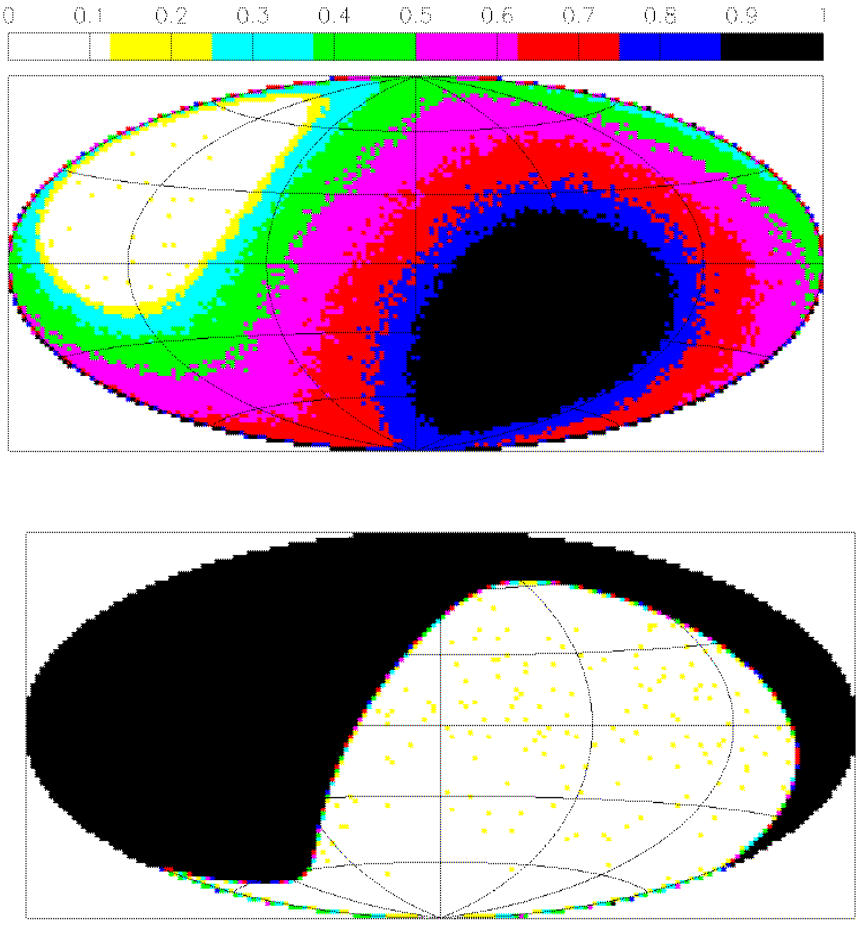

Fig. 15. Comparsion of sky coverage by northern hemisphere detectors (top) and AMANDA (bottom). The top scale indicates the fraction of time observing a given region of the sky. The darkest patches show the regions of greatest efficiency. The figure shows that both northern and southern hemisphere detectors are required for uniform sky coverage.

The relative merits of each site and technological implementations are sufficiently attractive to warrant several on-going efforts because the decision tree is not yet mature. Many factors contribute to a complex matrix of project cost. These include optical properties, temporal and spatial variability of the medium, deployment complexity, logistical support, physics emphasis, sensor density and overall geometry, *in situ* component reliability, system architecture, signal transport, sophistication of front end electronics and data acquisition system, repair, maintenance, etc. Photon scattering concerns strongly favor water, but absorption lengths are largest in ice. There is little doubt that track reconstruction is easier in water, but AMANDA has shown that they can cope with the scattering properties of ice. Intrinsic noise rates in the photomultiplier tubes are higher in sea-water, but local coincidence techniques provide a robust solution. Larger depths reduce background but strain mechanical and penetrator connections. In addition, the Baikal NT-200 and AMANDA have shown that background rejection is possible for the shallower depths, so great depths are not necessary. Short distances to the surface offer greater freedom in the choice of architectures to avoid single point failures, but standard engineering practices provide redundant reliable solutions for long distance communication. Given sufficient time and resources, there is no reason to doubt eventual success for any of the programs discussed in the next few sections. At the end of the day, what matters most is reliable operation of deployed sensors.

4.2 NT-200 at Lake Baikal

The Baikal collaboration has been accumulating experience with the construction and operation of water-based neutrino observatories since 1993, the longest track record of any group. Those initial efforts were followed by intermediate stages of construction that included configurations with 96 and 144 optical sensors and culminated with NT-200, which was completed in April 1998 (see figure 16). It consists of 192 optical sensors positioned at a depth of 1.1 km below the surface of the lake. The sensors are arranged in pairs and operated in coincidence to suppress unrelated signals from bioluminescence and internally generated random noise. Deployment, the “Achilles Heel” of remotely located neutrino observatories, has been solved by utilizing the seasonal ice cover on Lake Baikal. The solid platform can be accessed for significant periods of time, enabling reliable detector assembly and repair of detector elements.

An umbrella-like frame maintains eight vertical strings of optical sensors, consist-

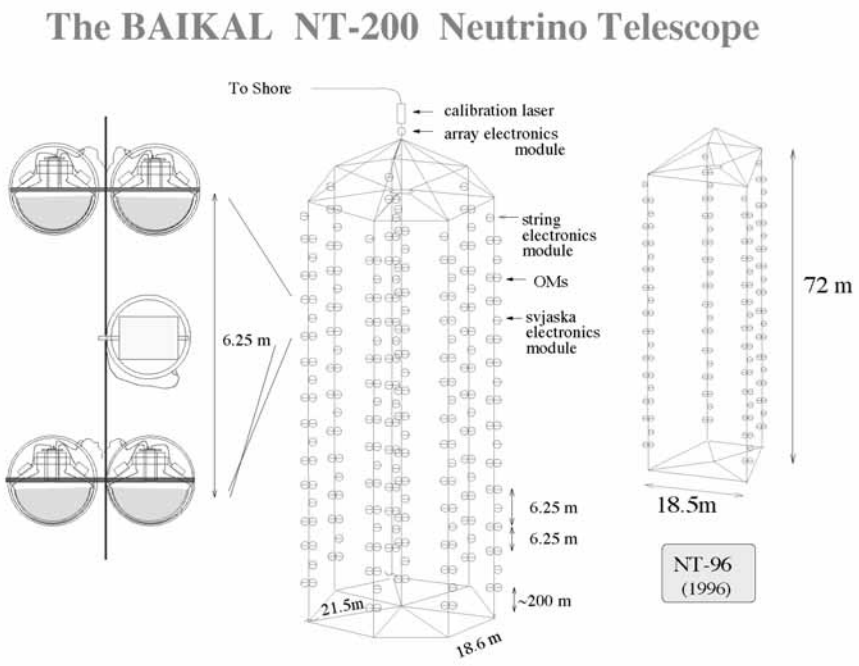

Fig. 16. Schematic diagram of the NT-200 neutrino array located in Lake Baikal. The smaller array on the right is a view of the partial detector deployed in 1996.

ing of a glass pressure vessel and a photomultiplier tube (PMT) with a diameter of 37 cm. The operation and performance of the Baikal detector is understood. They have shown that the optical properties of the water medium and 1.1 km depth are adequate to measure the angular spectrum of atmospheric muons with good accuracy and to identify atmospheric neutrinos (Fig. 17). This result bodes well for the Mediterranean sites because they are deeper (so less background from atmospheric muons) and the optical properties are better. Neutrino events were extracted from 234 days of livetime. After reconstruction, neutrino events were selected by imposing a restriction on the chi-squared of the fit and requiring consistency between the reconstructed trajectory and the locations of sensors registering photons. In this context, sensors that do not register photons carry important information as well. Finally, the non-gaussian tails of the angular distribution were reduced by imposing the condition that events must traverse more than 35 m within the array.

The high PMT density of the NT-200 design results in a low energy threshold — advantageous for medium-energy science goals — but limits the effective area at high energies to $\sim 5 \times 10^3$ m^2, presumably too small to detect neutrinos from non-terrestrial sources. A strawman design for a 2000 sensor array has been presented. The effective area would be $\sim 10^5$ m^2, while retaining a 10–20 GeV energy threshold. It could fill the niche between the current generation of neutrino detectors and future kilometer-scale arrays with, presumably, much higher energy thresholds.

4.3 ANTARES

A flurry of research and development activities have occupied the ANTARES (Astronomy with a Neutrino Telescope and Abyss environmental RESearch — hopefully, it sounds better in French) collaboration as they assess the relevant physical and optical parameters of their site. Deployment methods are being developed and refined through a series of operations using barges, research and military vessels. The NESTOR and ANTARES groups envision quite different deployment schemes, array designs, and signal processing. Technological solutions are being sought which are affordable, reliable, and expandable.

Over the past few years, the ANTARES collaboration has methodically determined the critical optical parameters of a 2400 m deep site off the coast of Toulon, France. Significant R&D has concentrated on string deployment and retrieval. They have reported that one string has been installed at the site and recovered after one year of flawless op-

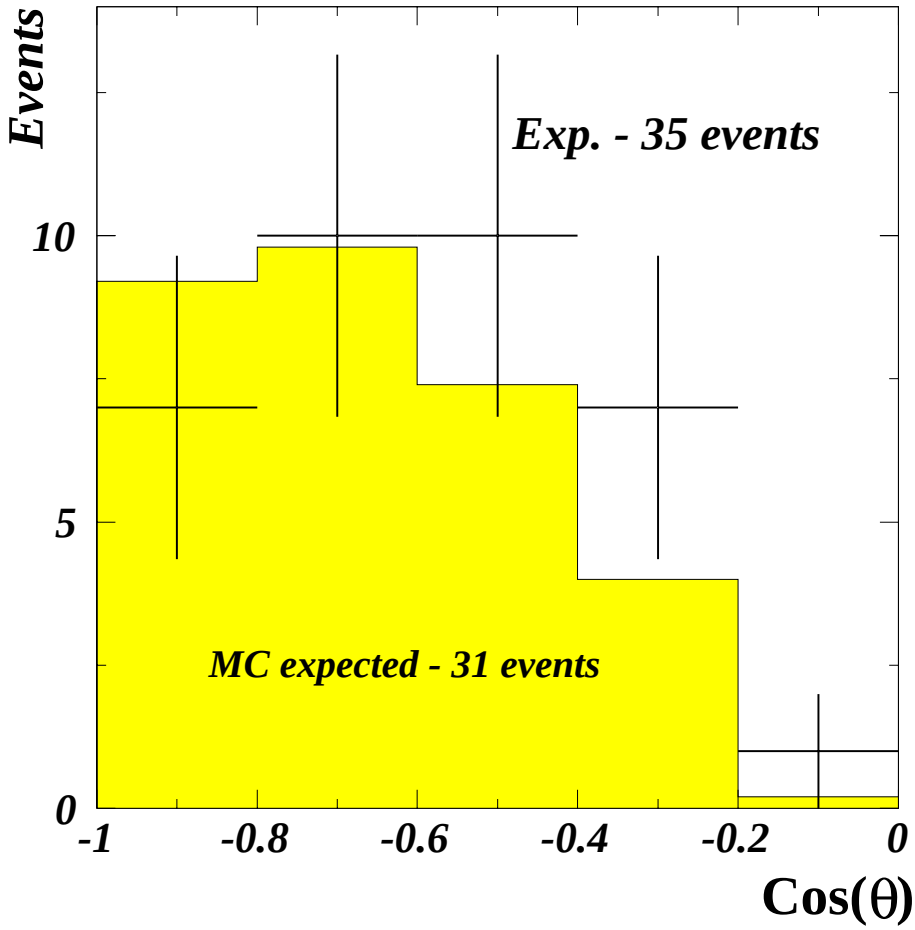

Fig. 17. Angular distribution of atmospheric neutrino signal by NT-200 experiment.[107] The shaded histogram is the distribution expected from Monte Carlo simulations.

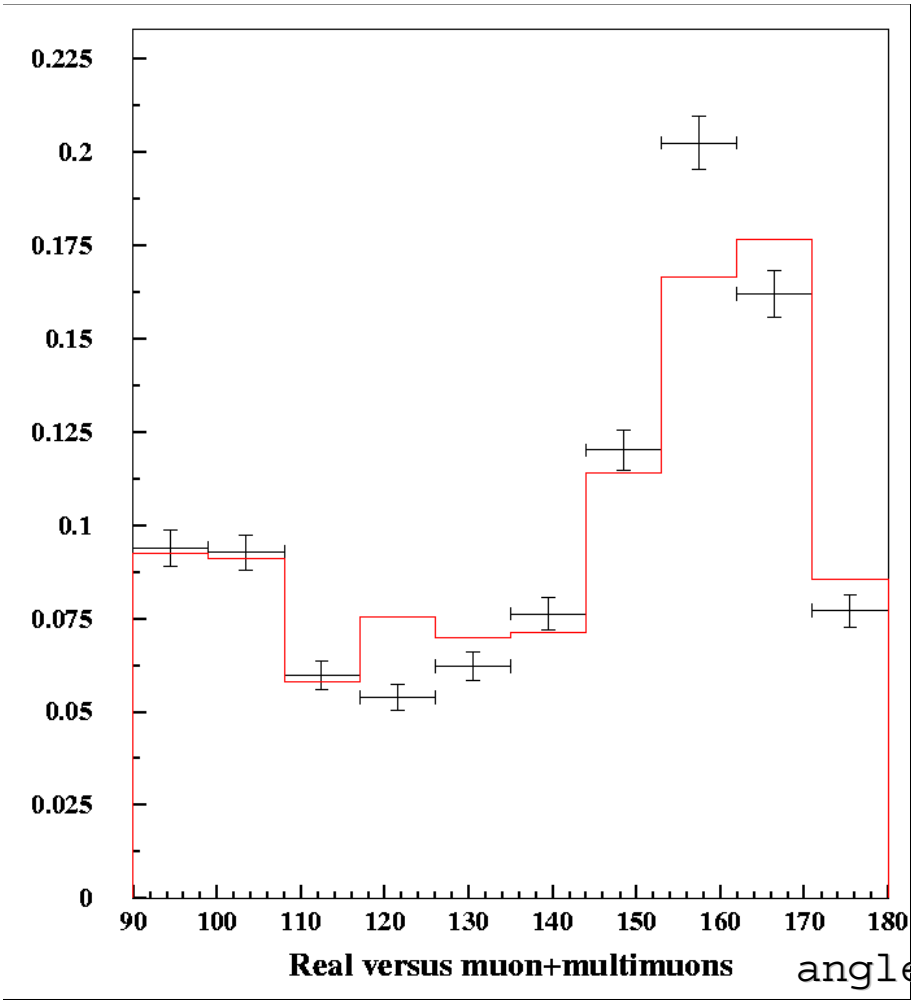

Fig. 18. Downgoing angular distribution of cosmic ray muons from the ANTARES single string prototype.[108] The figure shows good agreement between the expected and measured distributions.

eration. This success paves the way for more complex and difficult operations, such as the deployment of a fully functional string of sensors, deployment of multiple strings, or the insertion of a string within an existing array.

Precision attenuation and scattering measurements at a wavelength of 450 nm are extremely encouraging. The collaboration has reported an absorption length greater than 50 m and scattering length greater than 200 m for blue wavelengths.[109,110] Environmental studies at the Toulon site show that upward facing PMTs lose sensitivity over time due to the accumulation of organic debris, so the ANTARES design consists of only downward looking PMTs. Deep sea currents have been measured over a period of a year and show no unusual excursions from expected values. The collaboration concludes that the optical and environmental properties at the selected site satisfy the requirements of their telescope design.

Simulations of an array consisting of 15 triads of strings (~ 1000 PMTs) indicate that neutrino events can be cleanly identified. Random noise exceeding 50 kHz per optical sensor has been measured, but can be eliminated by straightforward coincidence requirements between neighboring elements in the array. Bioluminescent flashes do not affect local coincidence rates due to the relatively weak intensity of the output and the relatively long duration of the burst. Muon directions should be identified with sub-degree angular resolution.

To gain experience with the complex deployment procedures, a demonstrator line was deployed. This 350 m line consists of two vertical cables supporting 16 frames of a pair of optical modules. It was equipped with appropriate sensors for precise positioning of the detector elements and measuring environmental parameters. A series of deployment operations in 1998 demonstrated reliable solutions for deployment, positioning, and recovery of strings in the deep sea.[110] The string was then equipped with 8 optical modules and signal transmission electronics and deployed to a depth of 1100 m for long term operation. Signals were transmitted to shore using an electro-optical cable 37 km in length. Figure 18 shows the angular distribution of downgoing atmospheric muons that were reconstructed from a subset of data collected since November, 1999. The excellent agreement between the measured and predicted angular distributions represents an important milestone[108] for undersea detectors.

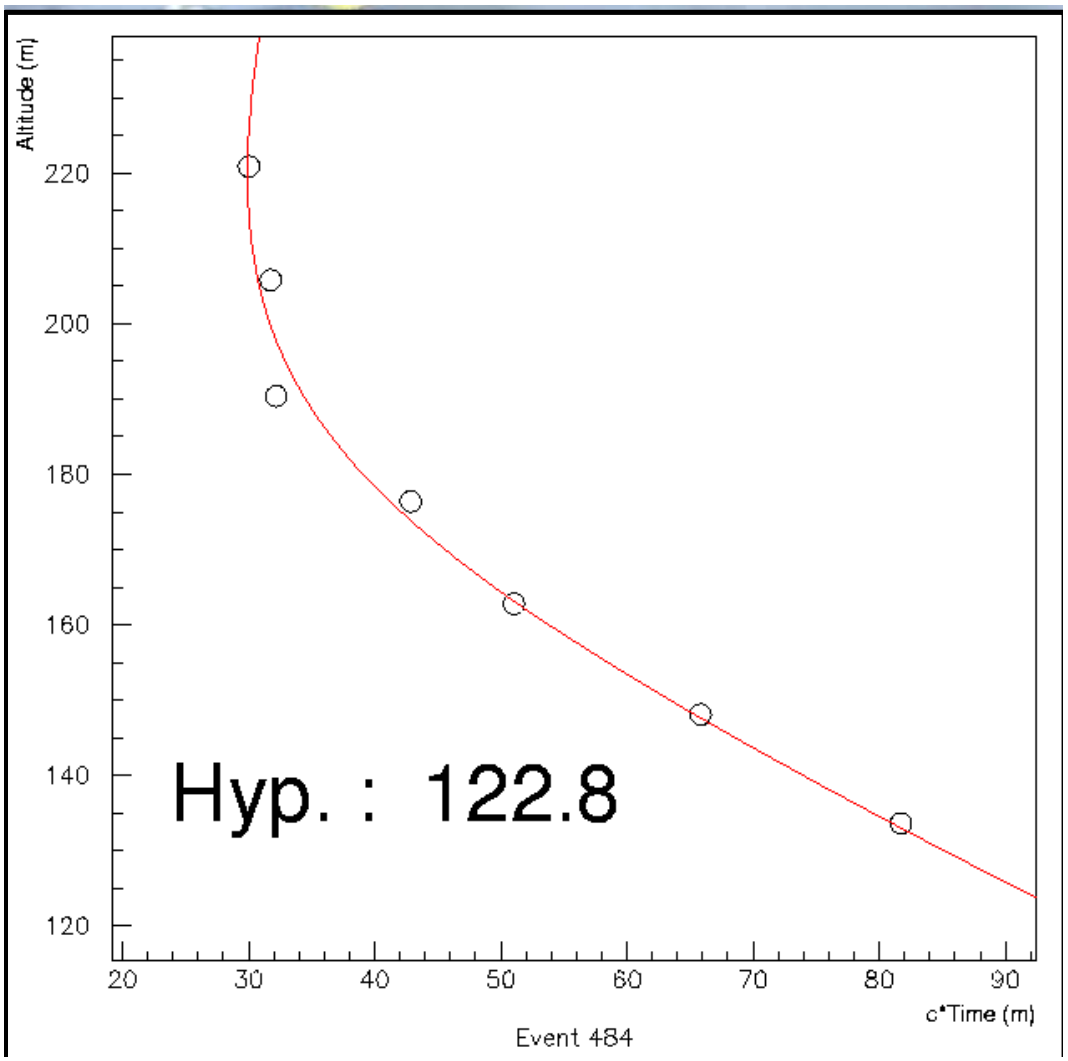

Fig. 19. Reconstructed downgoing muon event.[108] Data collected by the single string prototype installed by the ANTARES collaboration in Mediterranean.

4.4 NESTOR

NESTOR[100,111] plans to deploy an array of 168 optical sensors at a depth of 3.5–4.0 km. The site is located 7.5 miles off the coast of Pylos, Greece. The large depth significantly reduces the background of down-going atmospheric muons, but places greater stress on the penetrator connections. Hexagonal floors, rather than strings, comprise the basic unit. The array consists of 12 floors, fixed in place with an extensive network of wire guides, and assembled to form a 200 m tall tower. Horizontal separations between optical modules on a given floor are slightly larger than 34 meters. At each corner of the hexagonal floor is a pair of two photomultiplier tubes, 15 inches in diameter (one facing up and the other facing down). The NESTOR collaboration plans to deploy the complete array in 2001.

The NESTOR collaboration has been active since 1991. The flux and angular distribution of atmospheric muons was measured at depths as great as 4200 m. Site testing is complete, showing excellent optical properties. For example, the attenuation length at blue wavelengths is 55 m. Like the Baikal design, a symmetric up-down arrangement of PMT orientations will insure better uniformity in its angular acceptance. At the NESTOR site, it is believed that upward facing PMTs will not suffer from obscuration due to sedimentation or biological growth. The array design is expected to achieve a low energy threshold due to the relatively high density of optical sensors.

Recently, the NESTOR collaboration has performed mechanical tests by successfully towing a single floor out to sea and deploying it to a depth of ~ 2600 m. In the near future, they have a far more ambitious plan to deploy two, fully instrumented, floors to depth. It is hoped that these tests will establish the electro-mechanical durability of the signal processing and transmission systems. Assuming operational success of the first tower, the collaboration anticipates seeking funding for six additional towers. They would be deployed in a hexagonal pattern around the first tower, at a radial distance of 150 m. This array would have an effective detection area of 10^5 m^2 for 1 TeV muons, and provide 1 degree pointing resolution.

4.5 AMANDA

The AMANDA-B10 high energy neutrino detector was constructed between 1500–2000 m below the surface of the Antarctic ice sheet where the optical properties are suitable for track reconstruction[71] (see Fig. 20). The instrumented volume forms a cylinder with outer diameter of 120 m. The surface electronics are located within a kilometer

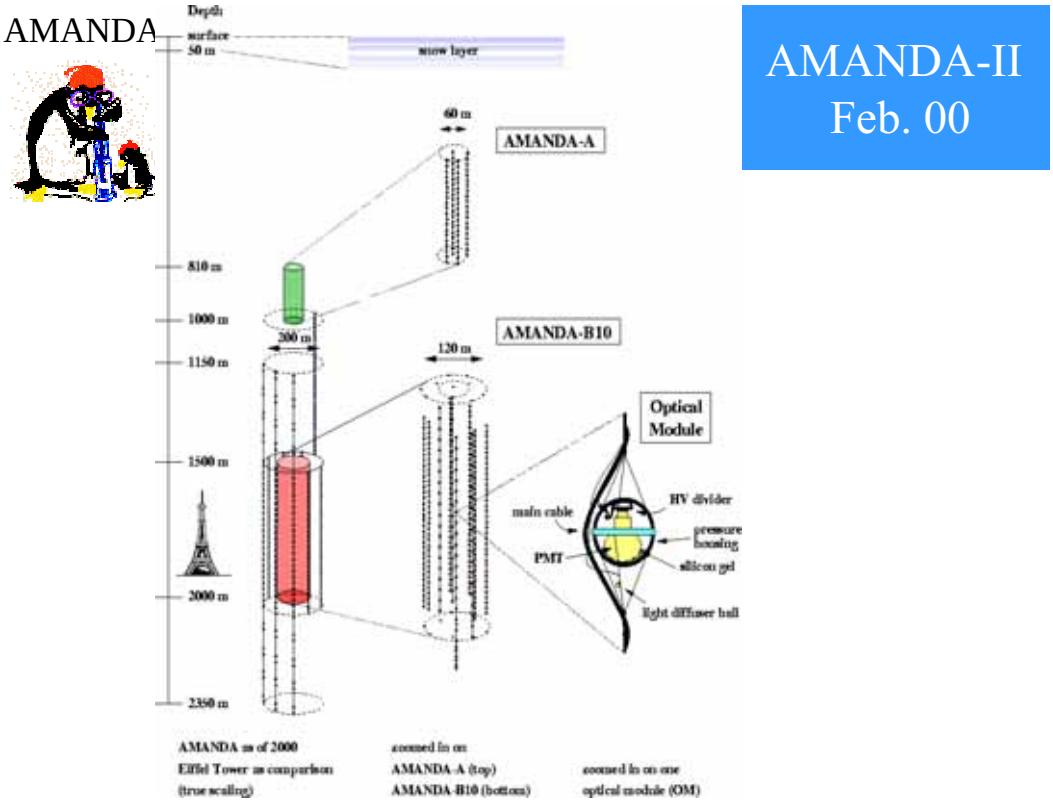

Fig. 20. Schematic representation of the AMANDA detector. AMANDA-A consists of 80 optical modules (OMs) deployed to a depth between 800–1000 meters. It was the first array deployed in Antarctica. AMANDA-B10 is the central 10 strings of 302 OMs deployed between 1500–2000 meters. An exploded view of AMANDA-A and AMANDA-B10 appears in the center column. The first phase of AMANDA-II construction began with the deployment of three strings between 1150–2350 m. Data was collected with the 13-string array during 1998 and 1999. AMANDA-II was completed in January, 2000. It consists of 19 strings (677 OMs), but does not include AMANDA-A.

of the Amundsen-Scott Research Station at the geographic South Pole. The detector was commissioned in February 1997,[112,113] and initial scientific results were presented at the XXIVth International Cosmic Ray Conference.[71] Reconstruction methods and detector calibration techniques were introduced in a previous publication.[104]

AMANDA-B10 consists of 302 optical modules (OMs) that contain an 8 inch diameter photomultiplier tube controlled by passive electronics and housed in a glass pressure vessel. They are connected to the surface by an electrical cable that provides high voltage and transmits the signals from the OM. The simple, reliable system architecture is responsible for the low fraction of OM failure ($<$ 10% after several years of

operation, although most of the failures occur within a week of deployment).

In January, 2000, AMANDA-II was completed. It consists of 19 strings with a total of 677 OMs arranged in concentric circles, with the ten strings from AMANDA-B10 forming the central core of the new detector. New surface electronics consolidates several triggering functions and adds functionality. New scalers were installed that provides millisecond resolution — important for supernova studies. Several technologies were deployed to evaluate their utility and readiness for future expansion to larger systems. The analysis procedure utilizes two essential characteristics of the signal to simplify the analysis relative to atmospheric neutrino measurements. First, the sources are assumed to be point sources in the sky, so only events within a selected angular region are considered. Secondly, we use the topological characteristics of a spectrally hard neutrino signal to reject poorly reconstructed atmospheric muons and atmospheric neutrinos, both of which have softer spectra. Topological variables include an estimate of muon energy and an assessment of the spatial fluctuation of the detected signals in a given event. The complete suite of variables was able to differentiate signal events from several classes of background topologies. Several important results from the simulation programs were tested by comparing the background simulation to the experimental data at various steps along the analysis chain.

Monte Carlo based simulation programs determined the effective area for background and neutrino-induced muons. Simulations for upgoing signals of several energies are shown in Fig. 21. AMANDA-B achieved an important milestone by becoming the first 10,000 m^2-class detector, while AMANDA-II is expected to break the 30,000 m^2 barrier for 1 TeV muons. The space angle resolution should improve to 1–2 degrees, and the fractional energy resolution for muon events is expected to improve to a factor of 2–3.

The search for point sources of HE neutrino emission used an iterative analysis procedure to maximize the $S/\sqrt{BG}$, where the signal, S, was computed with an energy spectrum proportional to E^{-2} for the source. BG is background from atmospheric muons. After optimizing the analysis parameters, the sensitivity was evaluated for power law spectra with indices between 2.0 and 3.0.

The space angle resolution is determined from simulation. The upper panel of Figure 22 shows that the median resolution is 3 degrees, and the lower panel indicates that this value only weakly depends on neutrino energy. Two studies were used to check the angular resolution and absolute offset. First, events that simultaneously trigger the GASP ACT[114] and AMANDA provide a “test beam” containing single muons with

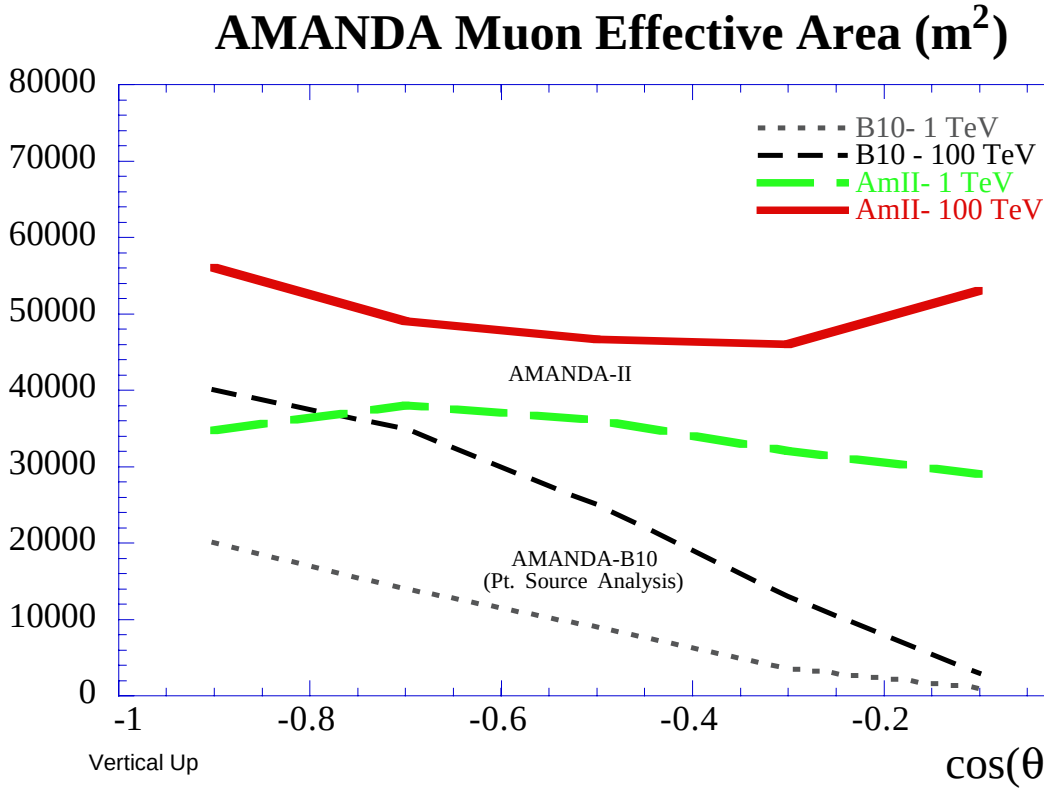

Fig. 21. The effective area of AMANDA II as a function of zenith angle, θ. The area is computed for neutrino-induced muons with either 1 TeV or 100 TeV of energy at the interaction vertex. Selection criteria from the point source analysis in AMANDA-B10 were applied. The different curves correspond to muon energies of 1 TeV and 100 TeV at the detector.

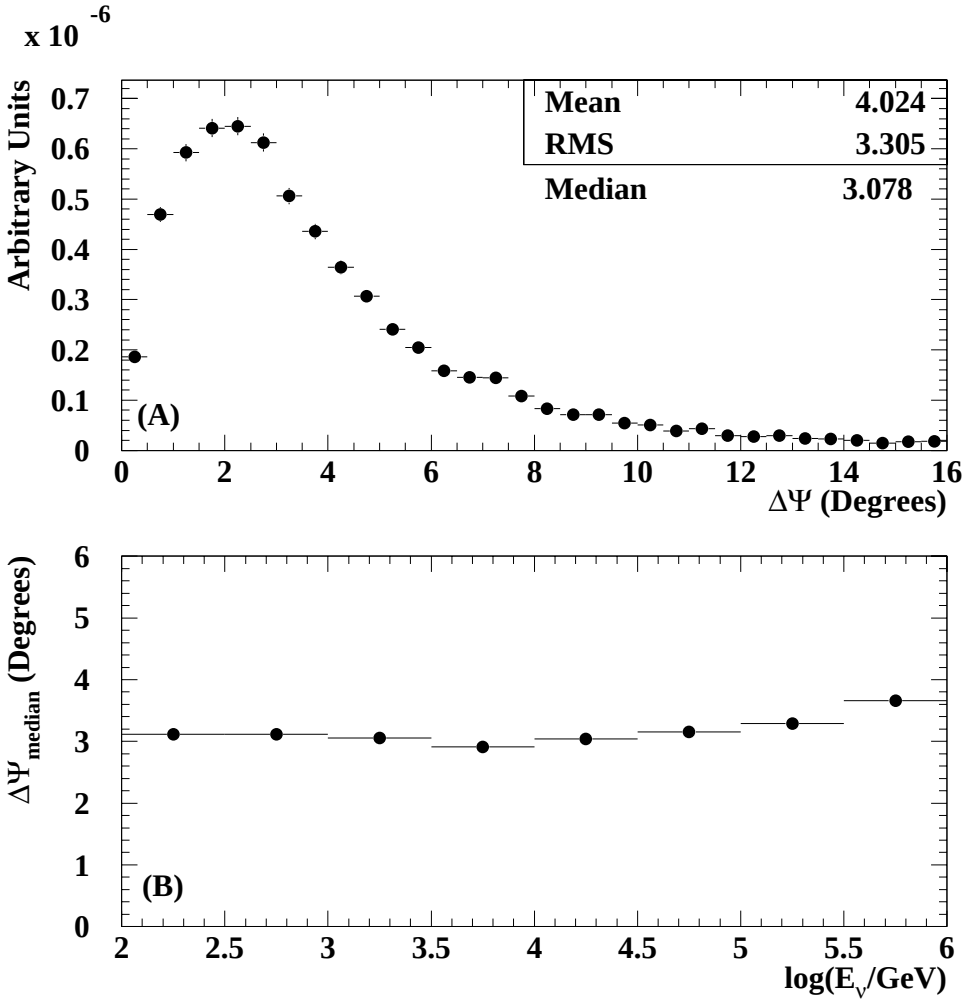

Fig. 22. (Plot taken from talk presented by the author at Neutrino 2000.) Error in the space angle for simulted signal events with energy spectra proportional to $E_\nu{}^{-2}$. **Top:** distribution of error averaged over declination. **Bottom:** Space angle error as a function of neutrino energy.

directional information provided by GASP. To improve the statistical accuracy of the investigation, a second study involved events which simultaneously trigger the SPASE air shower array[115] and AMANDA. The geometric relationship between SPASE and AMANDA is shown in Fig. 23. Although the interpretation of these special events is complicated by the presence of multiple muons, which tend to reconstruct with worse angular precision than single muon events, the response of the detector to these events appears to be correctly modeled.

The point source analysis yields an event sample of 1097 events which are dis-

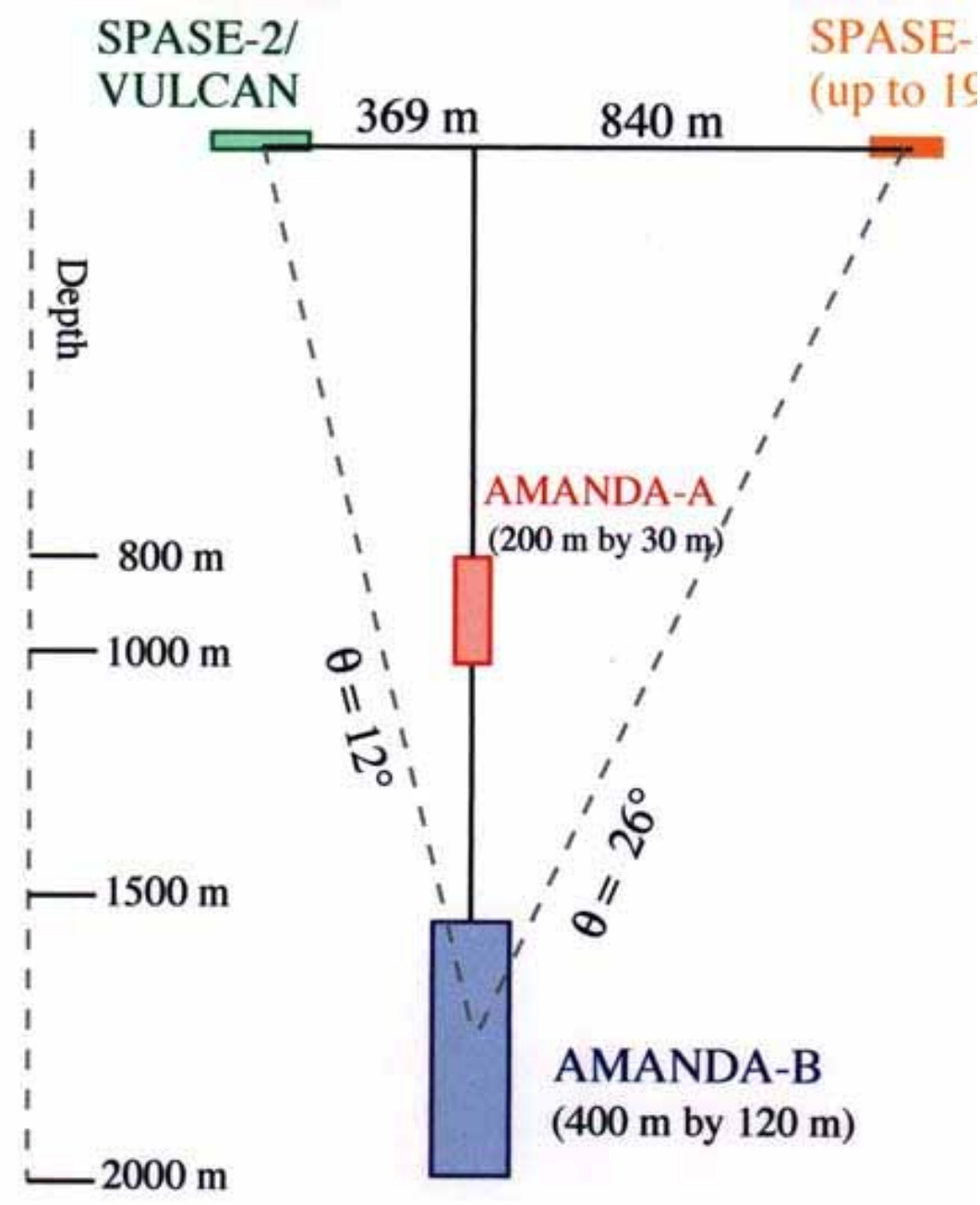

Fig. 23. Side view of the geometric relationship between surface air shower arrays (SPASE1 and SPASE2) and AMANDA. Events that have simultaneously triggered both the SPASE and AMANDA detectors were used to confirm that the angular response of the AMANDA array is well described by the detector simulation programs.

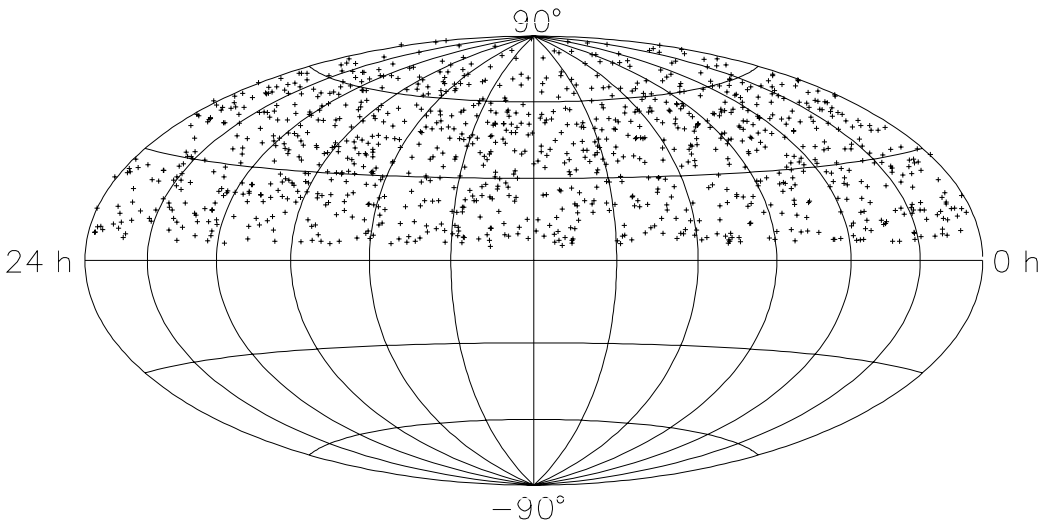

Fig. 24. Sky distribution of 1097 events in point source analysis. Coordinates are Right Ascension (RA) and declination (dec).

tributed on the sky as shown in Fig. 24.

Guided by the estimate of angular resolution, the sky was divided into 319 non-overlapping angular bins. The distribution of counts per sky bin is consistent with random fluctuations, which were determined by selecting all events within a declination band and randomly redistributing them in Right Ascension.

The neutrino limits were computed according to

$$\phi_\nu^{limit}(E_\nu > E_\nu^{min}) = \frac{\mu(N_b, N_0)}{T_{live} \cdot \epsilon \cdot \overline{A}_{eff}^{\nu}}\,, \tag{27}$$

where $\overline{A}_{eff}^{\nu}$ is the neutrino effective area weighted by the assumed neutrino energy spectrum. This quantity is related to the muon effective area shown in Figure 12. The factor T_{live} is the livetime, and ϵ is the efficiency due to finite angular resolution and also accounts for non-central source placement within an angular bin. The term $\mu(N_b, N_0)$ generates the 90% CL according to Feldman and Cousins[116] for signal events given the measured number of events in the bin, N_0 and the expected background N_b determined

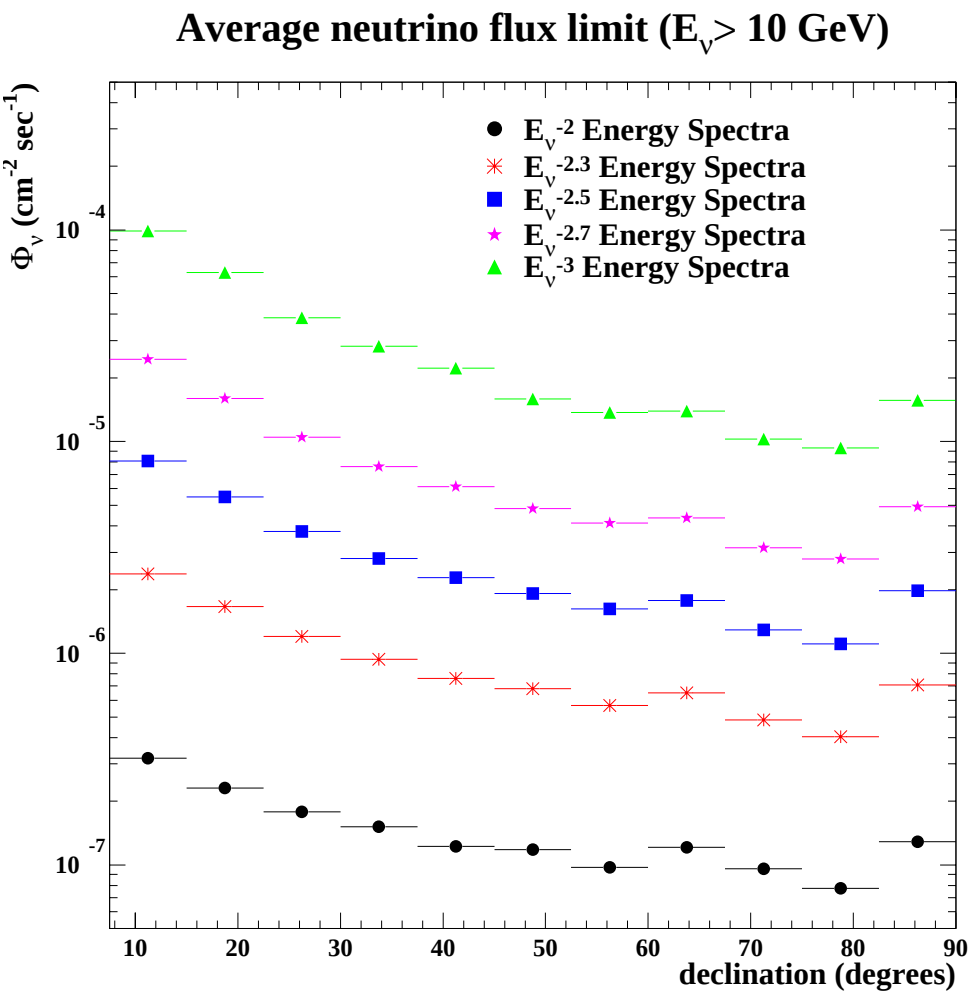

Fig. 25. Preliminary neutrino flux limit (90% CL) on point sources of high energy neutrinos as a function of declination, averaged over RA.[20,113] The limit is computed for a lower energy threshold of 10 GeV. Note that the power law exponent refers to the neutrino energy spectrum. Also, neutrino absorption by the Earth is taken into account.

from the events in the declination band containing the source bin. The results of this calculation are shown in Figure 25 for various assumed spectral indices.

One example of particular interest is the search for neutrinos from Markarian 501 (see Fig. 26). The limit clearly contradicts a model where the neutrino spectrum at the source is identical to a photon spectrum inferred by Protheroe and Meyer.[45] If the results of Protheroe and Meyer are confirmed, the neutrino limit provides additional evidence that nonstandard physics is involved in either the production or transit of the

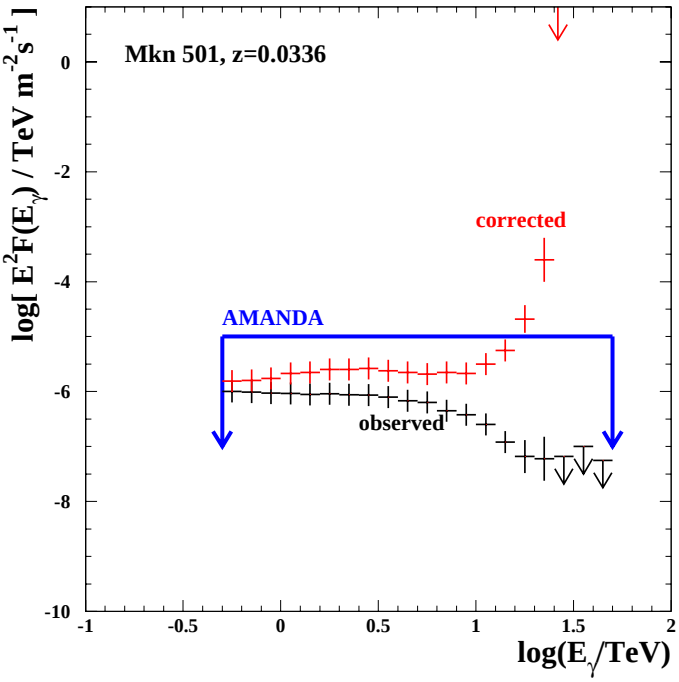

Fig. 26. (Plot taken from talk presented by the author at Neutrino 2000.) Time averaged spectrum of gamma rays from Markarian 501 observed in 1997[117] and corrected for absorption in the infrared background.[45] Several models of neutrino flux from Markarian 501 are compared to the AMANDA limit assuming an energy dependence proportional to E^{-2}. The models assume that the time averaged neutrino flux is identical to the gamma ray flux observed in 1997.[117] A second model assumes that the neutrino flux is identical to the gamma ray flux after correction for absorption by the infrared background.[45]

gamma rays.

The inferred limits on neutrino flux apply to point sources with continuous emission (or episodic emission averaged over a time interval of approximately 0.6 years) and power law energy spectra with a fixed spectral index above the energy threshold of the detector. The limits for sources at large positive declination are comparable to the best published limits in the Southern sky.[65]

The known source of atmospheric neutrinos can be used to confirm the absolute sensitivity of the AMANDA detector, to within a systematic error of $\pm 30\%$. In a recent paper,[118] the AMANDA collaboration provided evidence for the detection of atmospheric neutrinos. The absolute rate and angular distribution of events is consistent with predictions generated by computer simulation. The distributions of simulated

background events agree with data at low rejection levels, but disagree after stronger rejection criteria are applied. A large number of "event quality" distributions were compared at the strongest selection criteria, and they agree with atmospheric neutrino simulations, including the distribution of the number of optical modules participating in an event, N_{OM}. This parameter is crudely related to the energy deposited near the array. The final event sample in the search for point sources contains both atmospheric neutrinos and poorly reconstructed downgoing muons. The fraction of atmospheric ν in the sample can be enhanced at the expense of sensitivity. Experimental data is dominated initially by background events — typically downward going atmospheric muons with poorly known directions. This can be seen in figure 27, as indicated by the flat behavior for less restrictive selection criteria (quality < 4.2). As selection criteria become progressively more restrictive (increasing values along the x-axis), the asymptotic flattening of the ratio (experimental data)/(Signal MC Atm. ν) indicates that the evolution of the experimental data becomes consistent with signal expectation in the vicinity of the plot where the (BG MC)/Exp ratio approaches zero. From this evidence (and visual inspection on the individual events), they conclude that the contamination in the atmospheric neutrino sample from known physics effects is small ($< 15\%$) for values of the event quality parameter greater than five. Background simulations with much greater statistical precision are underway.

Figure 28 shows that the angular distribution of 188 events is also consistent with the simulated distribution of atmospheric ν events. Due to the elongated cylindrical geometry of AMANDA-B10, the acceptance shows strong dependence on zenith angle.

Thus, the angular dependence of the atmospheric neutrino sample is consistent with expectation and background simulations indicate that contamination from known physics backgrounds is small. Finally, the distribution of the number of OMs in an event is also consistent with expectation (see figure 29).

Unlike detectors with well-defined triggers that insure that particles travel within a fixed geometry, the effective area for high-energy neutrino detectors depends on muon energy and zenith angle. Also, the energy threshold of the detector must be understood in great detail for those physics objectives that involve steeply falling power law spectra, since the detected muon signals are mostly from the lowest energy neutrinos. This is particularly true for the measurement of atmospheric neutrinos. Since the designs for high energy neutrino detectors involve no obvious fiducial volume, the effective areas must be estimated by detector simulation programs. The predictions of the programs can be confirmed by studying known physics signals such as downgoing atmo-

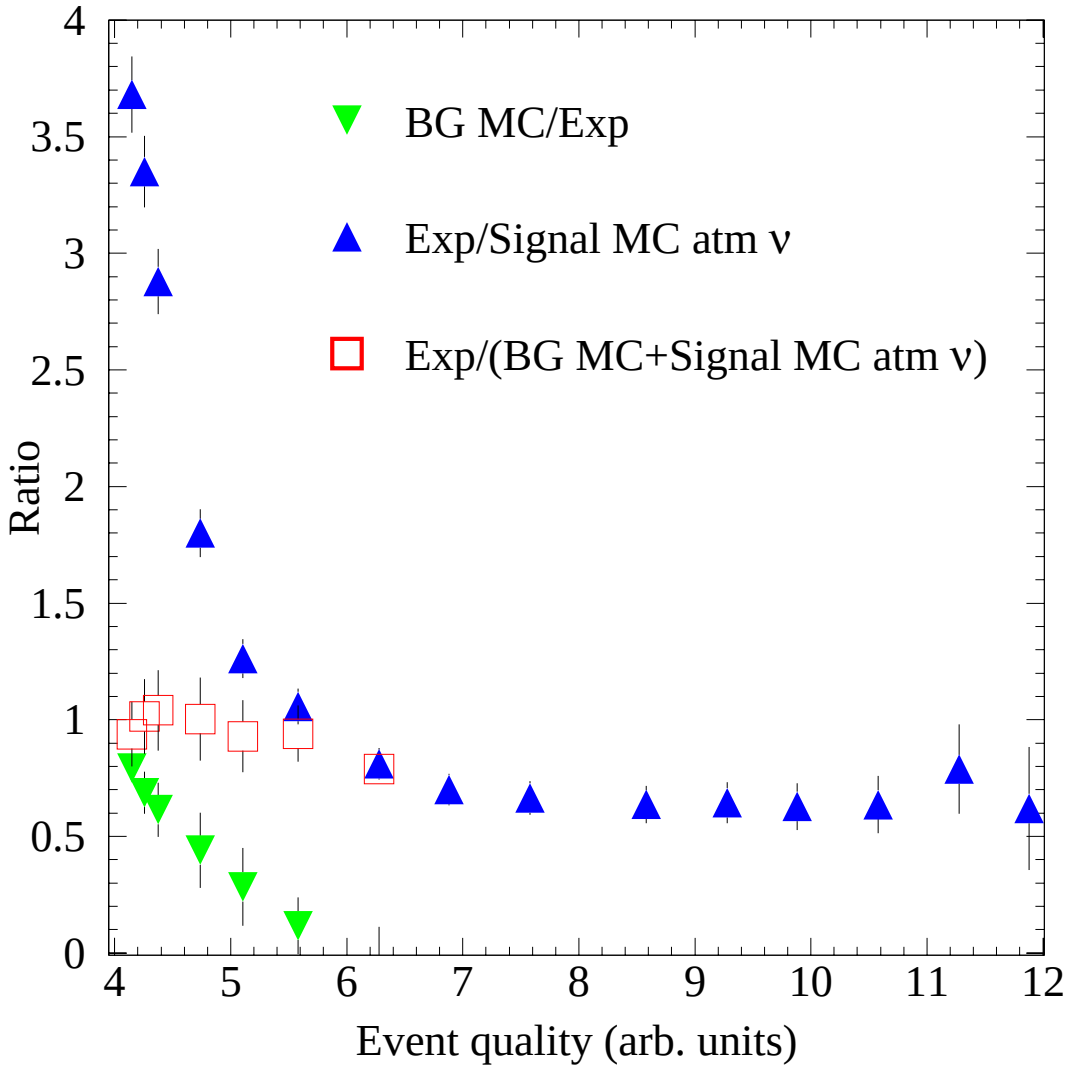

Fig. 27. Ratios of passing rates for simulated background (BG MC), simulated atmospheric neutrino signal (Signal MC atm. ν), and reconstructed experimental data (Exp) as a function of "event quality", a variable which measures the severity of the selection criteria.[20]

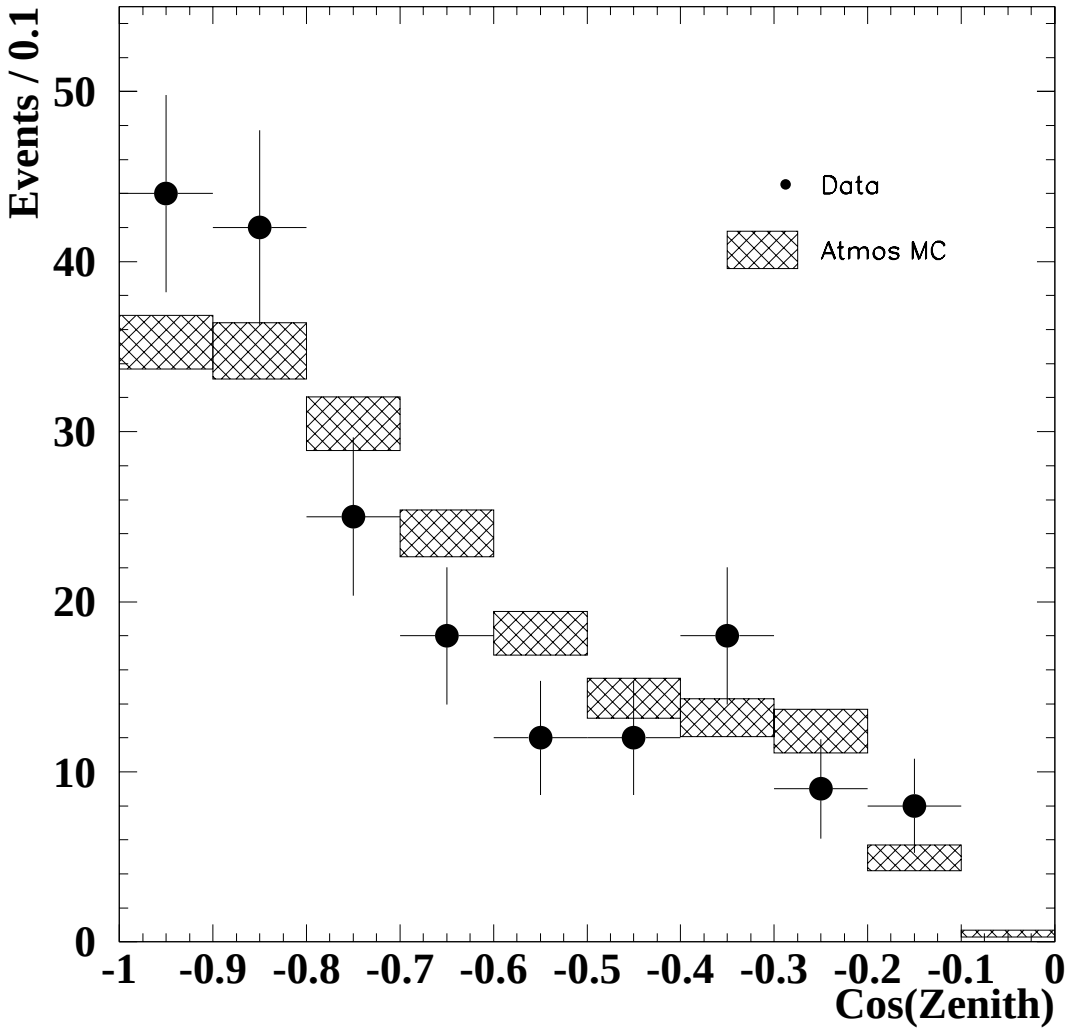

Fig. 28. Reconstructed zenith angle distribution.[20] The simulated atmospheric neutrino events (shaded boxes) are normalized to data (filled circles). The vertical widths of the boxes indicate the errors computed using binomial statistics.

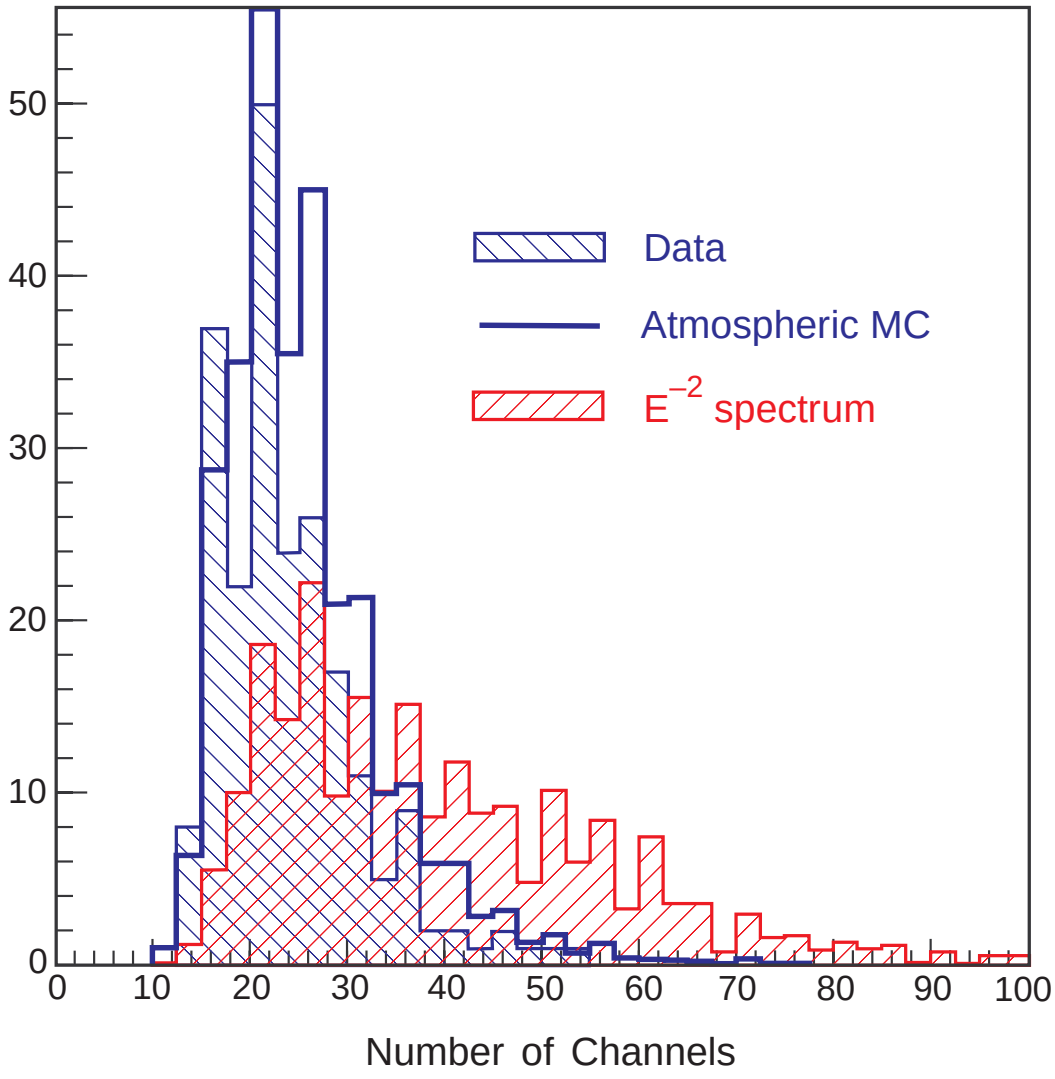

Fig. 29. Distribution of the number of optical modules (or "channels") participating in each event in the atmospheric neutrino sample.[20] The MC simulation for atmospheric and a generic spectrum $10^{-5}E^{-2}$ cm^{-2}s^{-1}sr^{-1}GeV^{-1} are also shown. The channel number provides a simple, although not very precise, measure of the muon event within the array. Note that the experimental data agree with the atmospheric neutrino spectrum. From the non-observation of an excess of events with high channel counts, the AMANDA collaboration presented a preliminary limit shown in Fig. 3. The collaboration is evaluating systematic errors.

spheric muons and atmospheric neutrinos, although the systematic uncertainties in flux are rather large at the energies of interest. T. Gaisser[119] has estimated the uncertainty in the absolute neutrino flux to be $\pm 30\%$, which is dominated by two components: the uncertainty in the flux of the primary cosmic rays and uncertainty in the kaon production cross section. AMANDA captures neutrino-induced muons with energies between 50 GeV and somewhat larger than 2 TeV (see fig. 30). The energy of the primary cosmic ray particles (which are 85% protons at these energies) responsible for the production of these neutrinos spans from 1 TeV to 10 TeV. Unfortunately, relatively few measurements of the cosmic ray spectrum exist for energies above 100 GeV, so the systematic uncertainty is $\sim 25\%$, if estimated from the variation in the absolute flux measurements.

The primary cosmic ray spectrum is not the only source of uncertainty in the flux calculations. Several sources of theoretical uncertainty are introduced due to inadequate understanding of the proton-nucleus interaction cross section. In particular, the differential kaon production cross sections are not well measured are the relevant values of Feynman x, and theoretical uncertainties due to model variations are relatively large. This limitation becomes important for HE neutrino detectors because kaon decay (not pion decay!) is the dominant source of atmospheric neutrinos for energies above 200 GeV. It appears that uncertainties introduced by muon tracking programs (such as Muprop or Mudedx) are relatively small except near the horizon.

Additional systematic errors are generated by uncertainties in description and implementation of detector response. Although these uncertainties are detector specific, in general, it may be instructive to discuss the issues for one of the architectures. For AMANDA, the spatial and wavelength variation of the optical parameters of the bulk ice creates distinct calibration challenges. Additional complication arises from the modification of the local optical properties associated with the re-frozen hole. Water-based detectors have a distinct advantage due to the uniformity of the optical properties. All detectors must contend with uncertainty from obscuration by cables and harness hardware, wavelength-dependent quantum efficiency and absorption by glass and optical coupling materials. The collection efficiency (the fraction of photoelectrons produced at the cathode that strike the first dynode in the photomultiplier tube) is not easy to measure in practice[120] and it may be affected by ambient magnetic fields. The efficiency is correlated with the direction of the magnetic field relative to the dynode structure, but this information is not easily obtained for remotely deployed strings of sensors. Nor is it easy to control the azimuth angle during deployment of long strings

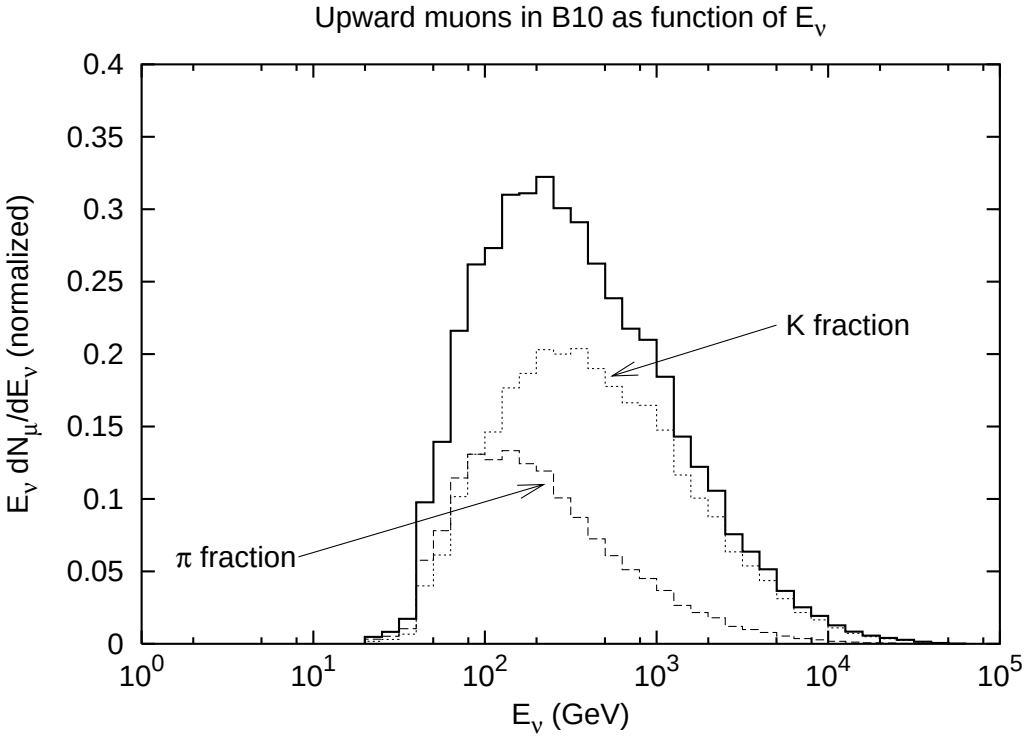

Fig. 30. Energy spectrum of the neutrinos responsible for the muon signal in the AMANDA detector. Figure taken from Gaisser.[119]

of cables, and no effort was made by the AMANDA collaboration to control the azimuthal orientation. Underwater detectors may be able to reduce this systematic by placing magnetometers at several locations along each string or floor. Experience has shown that the uncertainty in the *detection efficiency* of 1 photoelectron signals[§] and uncertainties in the *in situ* geometry of the array and transit time calibration are small compared to the other uncertainties. The combined detector-related uncertainty is likely to be comparable to the flux uncertainties, but these details require additional study.

[§]Detection efficiency is defined as the fraction of 1 photoelectron signals from the PMT that exceed a minimum discriminator threshold. Typically, this efficiency is greater than 85%.

5 New techniques

5.1 Kilometer scale arrays

It may not be strictly accidental that deployment methods based on solid surfaces have enjoyed greater success at this moment, but there is no reason to doubt that present off-shore, deep-water efforts will develop appropriate deployment methods. In the long term, they will be challenged to demonstrate that reliability and budget issues remain competitive with AMANDA and NT-200. While the current generation of neutrino observatories represent remarkable achievements, they are only a fraction of the size ultimately required to probe the hadronic sky. In fact, all current programs have the potential for expansion to kilometer scales — it is one of the important design requirements of the current generation of neutrino detectors. Several arguments have been used to coalesce around a detector with kilometer dimensions. A survey of theoretical models of neutrino emission from GRBs and AGN produce fluxes that could be detectable with kilometer-scale detectors — with orders of magnitude bracketing the maximum and minimum flux predictions. Given the current state of theoretical uncertainty, the bigger the detector, the better the chances, although the improvement can be modest for several objectives. More persuasively, the symmetric shape and larger volumes offer significant experimental advantages: particle trajectories are reconstructed with much higher efficiency, down-going atmospheric muon background will be simpler to reject, and energy resolution will be improved, perhaps dramatically. The simulated event topologies shown in Fig. 31 and Fig. 32 illustrate the point that it may be possible to distinguish each of the three known neutrino flavors.[121]

Several workshops have been held worldwide to discuss ideas for future expansion of the neutrino observatories. Scientific goals and priorities were actively debated, and the sensitivity of several strawman designs were studied. The relatively mature IceCube concept was optimized within the rough constraint of 5000 OMs distributed on fewer than 80 strings. A reasonable estimate of cost, scaling from the default analog-based technology, is $7000 per optical sensor. Systems with superior technical capabilities are being evaluated during the concept study and design phases of the project. Deployment, logistics, quality assurance, data management, data processing, data acquisition, and project management tasks introduce non-trivial extrapolations from present systems. Remotely located systems, by their very nature, tend to be manpower intensive. After engineering and technical reviews which evaluated design, construction,

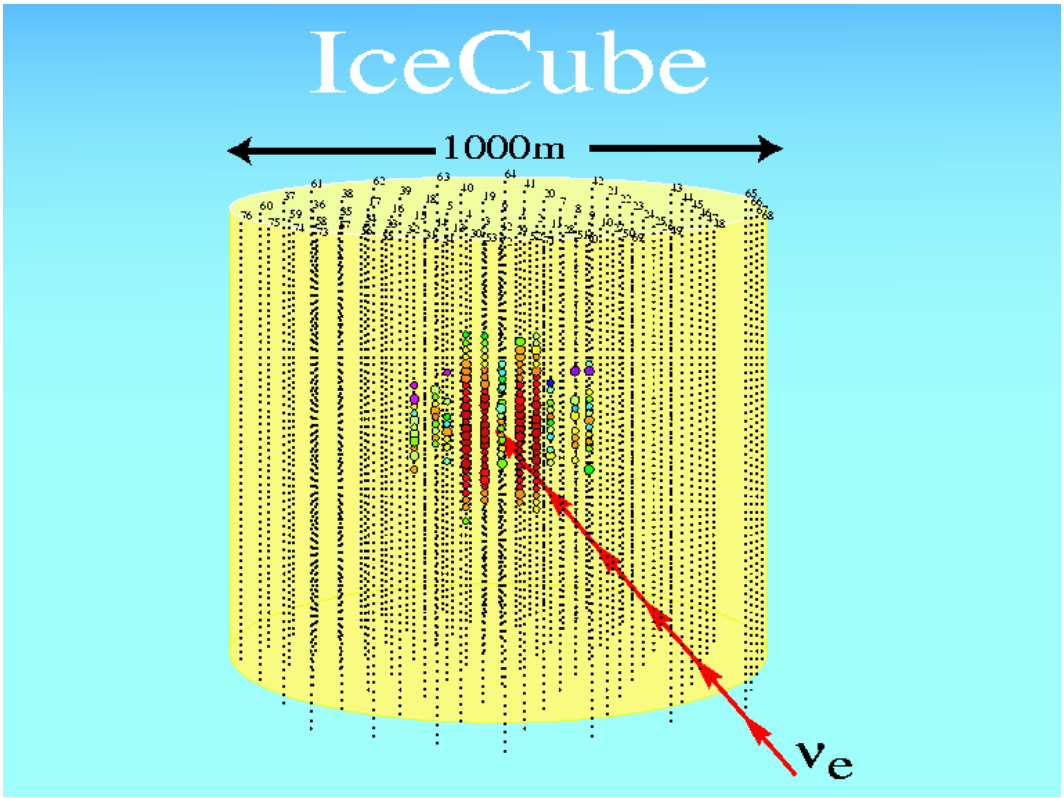

Fig. 31. Schematic of a 1 PeV electron neutrino event in IceCube. The energy is contained within the volume, resulting in excellent energy resolution. The effective detection volume for this signature is 10 percent of the volume for ν_μ.

personnel, inflation, risk and contingency issues, the IceCube project is expected to cost ∼$250M. This figure represents a reasonable lower limit for the baseline cost for any future kilometer-scale array, unless system designs require little R&D. The construction of IceCube should be completed before the end of the decade, given a reasonable projection of the drilling capacity and standard contingency estimates for construction delays. The Baikal collaboration envisions an expansion to 2000 OMs. Similarly, the NESTOR and ANTARES groups anticipate significant expansion after successful operation of the first generation detectors.

We summarize the performance and sensitivity of kilometer scale detectors to various astrophysics and physics goals. If the scaling is linear, then limits should improve by an order of magnitude or more if the system is operated for 5–10 years. If the presently operating arrays are capable of "background limited" operation, then the minimum detectable flux of future arrays scales as the square root of the product of exposure time and $V_{eff} \propto A_{eff} \times R_\mu$. Of course, there are caveats that may improve

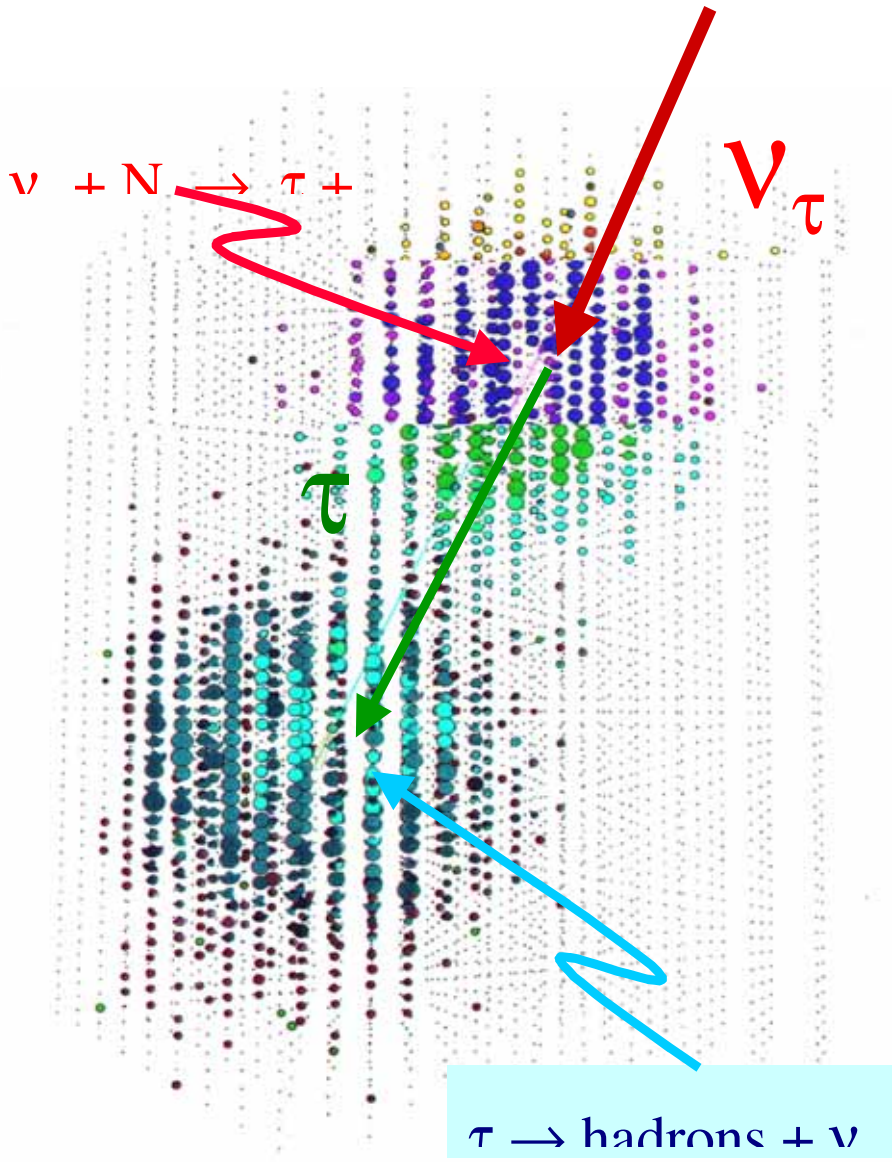

Fig. 32. Schematic of a 10 PeV tau neutrino event in IceCube. The energy is contained within the volume, resulting in excellent energy resolution. The effective detection volume for this signature is a few percent of the volume for ν_μ.

the scaling relationship.

A few comments are in order. From table 2, it is clear that transient and point source physics provides the main experimental motivation for kilometer-scale arrays. The background can be reduced to negligible levels for transient sources with external tags from satellites or surface monitors, so sensitivity should improve linearly for kilometer-scale and larger arrays. The promise of flavor ID depends on the results of present generation of neutrino telescopes. Assuming approximately equal fluxes, then detectable fluxes of ν_e or ν_τ should be revealed by the ν_μ mode in the near future with present arrays. On the other hand, the lack of signal in current and next generation detectors would begin to constrain models that predict dissimilar flavor composition. Clearly, discovery by present generation detectors is preferred. If so, the next generation detectors should measure energy and angular parameters with much better resolution. Finally, the sensitivity to cascades induced by ν_e interactions is listed with a $\sqrt{}$ because next generation detectors face a background from NC interactions by atmospheric ν_μ.

Table 2. Summary of scaling relationships for various physics objectives proposed for kilometer-scale detectors relative to present generation detectors (*e*.g., AMANDA-II, ANTARES). The $\sqrt{}$ symbol indicates that the minimum detectable flux improves as the square root of the product of exposure time and effective volume.

Physics Goal	Scaling of Sensitivity
GRB	linear
$<$PeV diffuse	$\sqrt{}$
$<$PeV point	linear
WIMP from Earth	$\sqrt{}$
WIMP from Sun	linear
SNa	$\sqrt{}$
EHE diffuse	$\sqrt{}$
ν oscillation (atm.)	requires low energy threshold
ν oscillation (Long Baseline)	not optimal
ν_τ	few % of ν_μ
ν_e, cacades	$\sim$ 10% of ν_μ
γ-ray astronomy with muons	$\sqrt{}$
Glashow $\bar{\nu}_e$	$\sqrt{}$
exotica (PBH, monopoles, etc.)	?

6 Conclusions

The late Fred Reines, father of neutrino physics, was fond of saying that one should choose to work on physics topics worthy of a lifetime's study. The broad diversity of

scientific capabilities and enormous potential of high energy neutrino astrophysics certainly qualifies. In view of the large number of possible sources discussed by theorists and even larger variation in their predicted intensity of neutrino emission, it is plausible that some will be detected by current, or soon-to-be upgraded, neutrino detectors such as AMANDA-II. If history is a guide, there will be surprises as well, as these detectors begin to survey the great canvas of the unknown.

High energy neutrino facilities are developing during an era of exciting discoveries in related areas of particle astrophysics: the detection of rapidly varying multi-TeV gamma ray signals from AGN, the discovery that GRBs are extremely distant, the reports of cosmic rays exceeding 10^{20} eV — beyond the Greisen-Zatsepin-Kuzmin limit — and strong evidence for neutrino oscillation from atmospheric neutrino data. At the close of the millennium, the hadronic sky is being probed with first generation neutrino detectors. They constitute bold, essential, first steps toward the realization of multi-messenger astronomy.

The recently commissioned AMANDA-II detector should achieve several important milestones. For diffusely distributed sources and WIMP searches from the Earth, its sensitivity after several years of operation will be limited by the atmospheric neutrino background up to energies of $\sim$1 PeV. Future arrays can only improve as the square root of the exposure, which is proportional to $\sim A_{eff} \times$livetime. At EHE energies, the sensitivity of AMANDA-II will be comparable to Auger (now under construction) and to future kilometer scale arrays, because the muon can be detected at great distances from the instrumented volume of the detector. Optical telescopes in space, such as the EUSO/OWL concept, represent the next real leap in sensitivity at these energies. The effective volume of AMANDA-II for ν_μ is comparable or larger than the effective volume of cubic kilometer arrays for the ν_e or ν_τ detection modes. Therefore, AMANDA-II (or ANTARES or NESTOR, when completed) must detect astrophysical sources of neutrinos in order for the next generation detector to determine the flavor composition of neutrino emission, unless a reasonable model can be constructed to produce ν_τ with significantly greater efficiency than the other flavors. Just as importantly, the lack of signal in AMANDA-II offers critical guidance for the design of the next generation kilometer-scale detector. Cubic architectures may need to be re-evaluated if the horizontal ν_μ mode becomes the most effective tool to extend the sensitivity. However, the sensitivity for GRBs, WIMPs from the Sun, and point sources should grow linearly with exposure and A_{eff} because these science objectives are not background limited at the energies of interest. In some scenarios, the factor of ten or so improvement in

sensitivity can be achieved on time scales much shorter than suggested by the 7–10 year construction schedule. For example, placing 20% of the strings envisioned for IceCube around AMANDA-II creates a composite system with an effective area of ~ 0.5 km^2. Consideration of "background free" science objectives argues for optimized sensitivity for E_ν between 10–100 TeV, and fortunately, these objectives can be attacked in the short term by modest extensions to existing arrays or detectors under construction. This fortuitous condition is a consequence of the slow growth of A_{eff}, approximately as the square root of the number of optical sensors for fixed length strings, and the presence of powerful arrays of 200-700 OMs. Not surprisingly, it is conceivable that the results from the current generation of HE neutrino detectors will strongly impact the optimal architectures for the next generation array. However, this prudence must be balanced by the competing desire to develop the next generation device as quickly as possible. Fortunately, the multi-year construction schedule anticipated for kilometer scale arrays provides an opportunity for significant modification during the latter phases of construction, if consistent with standard engineering practices. Given a carefully designed architecture for the next generation detector, it is not unreasonable to imagine that the insights revealed by the neutrino messenger will soon rival those deduced by observing the electromagnetic sky. This is the challenge for this millennium.

References

[1] K. Greisen, Ann. Rev. Nucl. Science, **10** (1960) 63; F. Reines, Ann. Rev. Nucl. Science, **10** (1960) 1; M.A. Markov and I.M. Zheleznykh, Nucl. Phys. **27** (1961) 385; M.A. Markov in *Proceedings of the International Conference on High Energy Physics at Rochester*, E.C.G. Sudarshan, J.H. Tinlot, and A.C. Melissinos, Eds. (1960), p. 578; Proceedings of the DUMAND Summer Workshop, Bellingham, Washington (1975); A. Roberts, Rev. Mod. Phys. **64** (1992) 259.

[2] For a review, see T.K. Gaisser, F. Halzen and T. Stanev, Phys. Rep. **258**(3) (1995) 173; R. Gandhi, C. Quigg, M.H. Reno and I. Sarcevic, Astropart. Phys., **5** (1996) 81.

[3] R.J. Protheroe, in Proceedings of 18th International Conference on Neutrino Physics and Astrophysics(Neutrino 98), Takayama, Japan (1998), astro-ph/9809144.

[4] J.G. Learned and K. Mannheim, to appear in Ann. Rev. Nucl. Part. Phys. (2000).

[5] E. Waxman and J. Bahcall, Phys. Rev. Lett. **78** (1997) 2292.

[6] E. Waxman and J. Bahcall, Phys Rev. **D59** (1999) 023002.

[7] K. Mannheim, R.J. Protheroe, and J.P. Rachen, Phys. Rev. **D63** (2001) 023003 [astro-ph/9812398].

[8] F. Halzen, Lectures presented at TASI School, July 1998, astro-ph/9810368.

[9] J.L. Feng, K.T. Matchev, and F. Wilczek, submitted for publication, astro-ph/0008115.

[10] See rapporteur summaries from 26th Inter. Cosmic Ray Conf. (Salt Lake City, Utah, 1999): S. Yoshida, p. 180; J. Beatty, p. 169.

[11] See http://www.physics.ucla.edu/˜ moonemp/radhep/barwick.pdf

[12] J. Alvarez-Muñiz, F. Halzen, and D.W. Hooper, Phys.Rev. **D62** (2000) 093015 [astro-ph/0006027].

[13] V. Agrawal, T.K. Gaisser, P. Lipari, and T. Stanev, Phys. Rev. **D53** (1996) 1314.

[14] M. Thunman, G. Ingelman, and P. Gondolo, Astropart. Phys. **5** (1996) 309 [hep-ph/9505417].

[15] L. Nellen, K. Mannheim, P.L. Biermann, Phys. Rev. **D47** (1993) 5270.

[16] F.W. Stecker, M.H. Salamon, Sp. Sci. Rev. **75** (1996) 341.

[17] K. Mannheim, Astropart. Phys. **3** (1995) 295.

[18] J.P. Rachen and P.L. Biermann, Astron. Astrophys. **272** (1993) 161.

[19] G. Sigl, M. Lemoine, and P. Biermann, Astropart. Phys. **10** (1999) 141; and G. Sigl, astro-ph/0008364.

[20] E. Andres, et al., Proc. XIX Int. Conf. Neut. Phys. Astrophys., “Neutrino 2000” (Sudbury, Canada, June 2000) [astro-ph/0009242].

[21] R.M. Baltrusaitis, *et al.*, Phys. Rev. **D31** (1985) 2192.

[22] D. Besson, talk presented at Work. Radio Emiss. High Energy Physics(UCLA, November, 2000); see http://www.physics.ucla.edu/˜ moonemp/radhep/

[23] J.J. Blanco-Pillado, R.A. Vazquez, and E. Zas, Phys. Rev. Lett. **78** (1997) 3614; K. S. Capelle, J.W. Cronin, G. Parente, and E. Zas, Astropart. Phys. **8** (1998) 321.

[24] D.B. Cline and F.W. Stecker [astro-ph/0003459]; http://lheawww.gfsc.nasa.gov/docs/gamcosray/hecr/OWL/

[25] W. Rhode, *et al.*, Astropart. Phys. **4** (1996) 217.

[26] F.W. Stecker, *et al.*, Phys. Rev. Lett. **66** (1991) 2697.

[27] G. Domokos and S. Kovesi-Domokos, Phys. Rev. Lett. **82** (1999) 1366.

[28] P. Jain, D.W. McKay, S. Panda, and J. P. Ralston, Phys. Lett. **B484** (2000) 267 [hep-ph/0001031].

[29] G. Burdman, F. Halzen, and R. Gandhi, Phys. Lett. **B417** (1998) 107.

[30] R.J. Protheroe and T. Stanev, Phys. Rev. Lett. **77** (1996) 3708; Erratum **78** (1997) 3420.

[31] T. Weiler, Astropart. Phys. **11** (1999) 303; D. Fargion, B. Mele and A. Salis, Astrophys. J. **517** (1999) 725.

[32] G. Gelmini and A. Kusenko, Phys. Rev. Lett. **84** (2000) 1378.

[33] V. Berezinsky, M. Kachelreis, and A. Vilenkin, Phys. Rev. Lett. **79** (1997) 4302.

[34] E. Waxman, Phys. Rev. Lett. **75** (1995) 386.

[35] M. Vietri, Ap. J. **453** (1995) 883.

[36] P. Blasi and A.V. Olinto, Phys. Rev. **D59** (1999) 023001.

[37] J. Cronin, Nobel Symposium on Particle Physics and the Universe (Haga Slott, Sweden, 1998); see also http://www.fnal.gov/pub/pierreauger.html for more information.

[38] R.J. Protheroe and A. Mucke, [astro-ph/0011154].

[39] L.O.C. Drury, F. Aharonian, and H. Völk, Astron. and Astrophy., **287** (1994) 959; T. Naito and F. Takahara, J. Phys. G: Nucl. Part. Phys., **20** (1994) 477.

[40] T. Tanimori, *et al.*, Astrophy. J., **L25** (1998) 497.

[41] J.H. Buckley, *et al.*, Astron. Astrophys., **329** (1998) 639; J. H. Buckley, *et al.*, Mon. Not. Roy. Astron. Soc. **289** (1997) 371 [astro-ph/9906118].

[42] R. Plaga, Proc. Workshop on TeV Gamma Ray Astrophysics (Kruger National Park, South Africa, 1997), ed. O.C. de Jager, p. 152.

[43] M. Catanese and T.C. Weekes, Publ. Astron. Soci. of the Pacific (submitted for publication), astro-ph/9906501; F.A. Aharonian, *et al.*, Astron. Astrophys. **349** (1999) 11.

[44] D.P. Finkbeiner, M. Davis, D.J. Schlegel, submitted to Astrophys. J., astro-ph/0004175.

[45] R.J. Protheroe and H. Meyer, Phys. Lett. **B493** (2000) 1 [astro-ph/0005349].

[46] J.H. Buckley, *et al.*, Adv. Space Res., **21** (1998) 101; J.H. Buckley, Science, **279** (1998) 676.

[47] J.P. Rachen, astro-ph/0003282.

[48] C.D. Dermer, Proc. Workshop on TeV Astrophysics of Extragalactic Sources (Cambridge, Mass., 1998) eds. M. Catanese, J. Quinn, T. Weekes, Astropart. Phys. **11** (1999) 1 [astro-ph/9901324].

[49] M. Pohl and R. Schlickeiser, Astron. Astrophys. **354** (2000) 395.

[50] T.K. Gaisser, Proc. Intern. Work. Observ. Ultra High Energy Cosmic Rays from Space and Earth (Metepec, Puebla, Mexico) August, 2000 [astro-ph/0011525].

[51] F.W. Stecker and M.H. Salamon, Space Sci. Rev. **75** (1996) 341-355; J.P. Rachen and P. Meszaros, Phys. Rev. **D58** (1998) 123005; V.J. Stenger, J.G. Learned, S. Pakvasa, and X. Tata, eds., Proc. High Energy Neutrino Astrophysics Workshop(U. Hawaii), World Scientific, Singapore; A.P. Szabo and R.J. Protheroe, Astropart. Phys. **2** (1994) 375 [astro-ph/9405020].

[52] W. Bednarek and R.J. Protheroe, Mon. Not. Roy. Astro. Soc. **287** (1997) 560.

[53] S. Colafrancesco, and P. Blasi, Astropart. Phys. **9** (1998) 227.

[54] K. Mannheim, Phys. Rev **D48** (1993) 2408.

[55] T.K. Gaisser, R.J. Protheroe, and T. Stanev, Ap. J. **492** (1998) 219.

[56] A. Capone, in Proceedings of the 25th International Cosmic Ray Conference (Durban, South Africa) **7** (1997) 49; S. Sotiriou, Proc. Simul. Analy. Meth. Large Neut. Tel., Zeuthen Germany (July, 1998, C. Spiering, ed.), p. 337 [DESY-PROC-1999-01].

[57] C. Spiering, Proceedings of the Ringberg Neutrino Workshop, Germany (1998); C. Spiering, Prog. Part. Nucl. Phys. **40** (1998) 391.

[58] S.T. Scully and F.W. Stecker, submitted to Phys. Rev. Lett. [astro-ph/0006112]

[59] C. Dermer, Presentation at 2nd Rome Workshop on Gamma Ray Bursts in the Afterglow Era (17-20 October 2000). Shortened version to appear in the Proceedings of the Heidelberg 2000 High-Energy Gamma-Ray Workshop, eds. F. A. Aharonian and H. Völk (AIP: New York) [astro-ph/0005440].

[60] For a recent review, see T. Piran, Phys. Rep. **314** (1999) 575.

[61] A. Husain, Nucl. Phys. **B** (Proc. Suppl.) **87** (2000) 442.
See also transparencies at http://taup99.in2p3.fr/TAUP99/; H. Athar [hep-ph/0004191]; H. Athar, G. Parente, and E. Zas, Phys. Rev. **D62** (2000) 093010.

[62] J.G. Learned and S. Pakvasa, Astropart. Phys. **3** (1995) 267; F. Halzen and D. Saltzberg, Phys. Rev. Lett. **81** (1998) 430.

[63] L. Bergstrom, J. Edsjo, and P. Gondolo, Phys.Rev. D**58** (1998) 103519 [hep-ph/9806293].

[64] A. Okada, for the SuperKamiokande Collaboration, astro-ph/0007003.

[65] T. Montaruli, *et al.*, Proc. 26th Intern. Cosmic Ray Conf. (1999), HE 4.2.03; M. Ambrosio, *et al.*, submitted to Astrophys. J., (2000), astro-ph/0002492.

[66] M.M. Boliev, *et al.*, Nucl. Phys. **B** (Proc. Suppl.) **48** (1996) 83; O.V. Suvorova, hep-ph/9911415.

[67] V. A. Balkanov, et al., Astropart. Phys. **14** (2000) 61.

[68] C. Spiering, Proc. XIX Int. Conf. Neut. Phys. Astrophys. “Neutrino 2000” (Sudbury, Canada, June 2000) [astro-ph/0012532].

[69] For more information, see
http://www-ussk.icrr.u-tokyo.ac.jp/~ kate/snnet/snnet.html

[70] J.F. Beacom and P. Vogel, Phys. Rev. **D60** (1999) 033007 [astro-ph/9811350].

[71] See contributions in Proc. 26th Inter. Cosmic Ray Conf. (ICRC99), Salt Lake City, UT, (Aug 1999). HE 3.1.06, HE 6.3.07, HE 4.2.06, HE 6.3.01, HE 4.1.15, HE 5.3.05, HE 4.2.05, HE 6.3.02, HE 4.1.14, HE 4.1.14, HE 3.2.11, HE 4.2.07, HE 5.3.06, at
krusty.physics.utah.edu/~ icrc1999/proceedings.html

[72] F. Halzen and J. Jacobsen, Phys. Rev. **D49** (1994) 1758.

[73] Y. Fukuda, *et al.*, Phys. Rev. Lett. **81** (1998) 1562; H. Gallagher, *et al.*, in Proceedings of the 29th Intl. Conf. on High Energy Physics (Vancouver, July, 1998); D.G. Michael, *et al.*, in Proceedings of the 29th Intl. Conf. on High Energy Physics (Vancouver, July, 1998).

[74] K. Dick, M. Freund, P. Huber, and M. Lindner, Nucl. Phys. **B588** (2000) 101; see also hep-ph/0008016.

[75] Chang Kee Jung, Proceedings of the Next generation Nucleon decay and Neutrino detector Workshop (NNN99), Sept. 23-25, 1999, Stony Brook, New York [hep-ex/0005046].

[76] D. Casper, http://meco.ps.uci.edu/lepton_workshop/talks/casper/uno.pdf.

[77] V.S. Berezinskii and G.T. Zatsepin, Sov. Phys. Usp., **20** (1977) 361.

[78] F. Halzen and J. Learned, in *Proceedings of the International Symposium on Very High Energy Cosmic Ray Interactions*, University of Lodz Publishers, M. Giler, ed. (1989); F. Halzen, J. Learned, and T. Stanev, AIP Conference Proceedings **198** (1989) 39.

[79] D. Normile, Science **279** (1998) 802.

[80] F. Hubaut, Proc. Simul. Analy. Meth. Large Neut. Tel., Zeuthen, Germany (July, 1998, C. Spiering, ed.), p. 328 [DESY-PROC-1999-01].

[81] R. Porrata, *et al.* in Proceedings of the 25th International Cosmic Ray Conference, Durban, South Africa **7** (1997) 9; R. Porrata, *The Energy Spectrum of Pointlike Events in AMANDA-A*, dissertation, U.C. Irvine (1998).

[82] W. Wu, Ph.D. dissertation, U.C. Irvine (2000), http://www.physics.uci.edu/˜ wenqingw/cascade/thesis/

[83] P. Lipari and T. Stanev, Phys. Rev. **D44** (1991) 3543.

[84] T.K. Gaisser and T. Stanev, Phys. Rev. **D31** (1985) 2770.

[85] R. Gandhi, C. Quigg, M.H. Reno, and I. Sarcevic, Phys. Rev. **D58** (1998) 093009 [hep-ph/9807264].

[86] S.L. Glashow, Phys. Rev. **118** (1960) 316; V.S. Berezinsky and A.Z. Gazizov, JETP Lett. **25** (1977) 254.

[87] M. Kowalski, "On the Construction of Cascade-like Events in the AMANDA Detector", Diplomarbeit, Humboldt-Universitat zu Berlin, Berlin, 2000.

[88] R.J. Protheroe, Accretion Phenomena and Related Outflows, IAU Colloq. 163 (1996), astro-ph/9607165.

[89] J. Alvarez-Muñiz and F. Halzen, Phys. Rev. **D63** (2001) 037302 [astro-ph/0007329].

[90] C. Allen, *et al.*, in Proceedings of the 25th International Cosmic Ray Conference, Durban, South Africa **7** (1997) 85; See also http://kuhep4.phsx.ukans.edu/˜ iceman/index.html.

[91] P.B. Price, Astropart. Phys.**5** (1996) 43.

[92] P. Gorham, K.M. Liewer, and C.J. Naudet, Proc. Of 26th Intern. Cosmic Ray Conf., **2** (Salt Lake City, Utah, 1999) 479; see also astro-ph/9906504.

[93] L.G. Dedenko, *et al.*, in Proc. of 25th Intern. Cosmic Ray Conf., eds. M.S. Potgieter, B.C. Raubenheimer, and D.J. VanDerWalt, **7** (Durban, South Africa, 1997) 89.

[94] S.C. Corbato, *et al.*, Nucl. Phys. **B** (Proc. Suppl.) **28** (1992) 36; N. Hayashida, *et al.*, astro-ph/9804043.

[95] G.A. Askaryan, Sov. Phys. JETP, **14** (1962) 441; G.A. Askaryan, Sov. Phys. JETP **21** (1965) 658.

[96] D. Saltzberg, *et al.*, submitted to Phys. Rev. Lett., hep-ex/0011001.

[97] See http://www.physics.ucla.edu/˜ moonemp/radhep/seckel.pdf

[98] See http://www.physics.ucla.edu/˜ moonemp/radhep/alvarez.pdf

[99] E. Zas, Proc. Intern. Work. Observ. Ultra High Energy Cosmic Rays from Space and Earth (Puebla, Mexico, 2000) [astro-ph/0011416].

[100] L. Trascatti, Nucl. Phys. **B** (Proc. Suppl.) **70** (1998) 442.

[101] F. Feinstein, in Proc. Simul. Analy. Meth. Large Neut. Tel., Zeuthen, Germany (July, 1998, C. Spiering, ed.), p. 68 [DESY-PROC-1999-01]; F. Feinstein, Nucl. Phys. **B** (Proc. Suppl.) **70** (1998) 445; see also http://antares.in2p3.fr/antares/antares.html

[102] I.A. Belolaptikov *et al.*, Astropart. Phys. **7** (1997) 263; L. Kuzmichev, in Proceedings of the 25th International Cosmic Ray Conference (Durban, South Africa) **7** (1997) 21; S. Klimushin, Proc. Simul. Analy. Meth. Large Neut. Tel., Zeuthen, Germany (July, 1998, C. Spiering, ed.), p. 38. [DESY-PROC-1999-01]; G.V. Domogatsky, Nucl. Phys. **B70** (Proc. Suppl., 1998) 439; see also http://www.ifh.de/baikal/baikalhome.html

[103] S.W. Barwick, *et al.*, *The status of the AMANDA high-energy neutrino detector*, in Proceedings of the 25th International Cosmic Ray Conference, Durban, South Africa (1997); see also `http://amanda.berkeley.edu/`

[104] E. Andres, et al., Astropart. Phys. **13** (2000) 1.

[105] S.W. Barwick, *et al.*, in Proceedings of the *International Conference on High Energy Physics(ICHEP98)*, Vancouver, Canada, July, 1998.

[106] C. De Marzo, Nucl. Phys. **B** (Proc. Suppl.) **87** (2000) 433.

[107] V.A. Balkanov, et al., presented at Neutrino 2000, astro-ph/001131.

[108] L. Thompson, et al., Proc. XIX Int. Conf. Neut. Phys. Astrophys. “Neutrino 2000” (Sudbury, Canada, June 2000).

[109] L. Moscoso, Nucl. Phys. **B** (Proc. Suppl.) **87** (2000) 377.

[110] F. Montanet, Nucl. Phys. **B** (Proc. Suppl.) **87** (2000) 436.

[111] L.K. Resvanis, Nucl. Phys. **B** (Proc. Suppl.) **87** (2000) 448.

[112] R. Wischnewski, *et al.*, Nucl. Phys. **B** (Proc. Suppl.) **75A** (1999) 412.

[113] S.W. Barwick, for the AMANDA collaboration, Nucl. Phys. **B** (Proc. Suppl.) **87** (2000) 402.

[114] G. Barbagli, *et al.*, Nucl. Phys. **B** (Proc. Suppl.) **32** (1993) 156.

[115] J.E. Dickinson, *et al.*, Nucl. Inst. Meth. **A440** (2000) 95.

[116] G.J. Feldman and R.D. Cousins, Phys. Rev. **D57** (1998) 3873.

[117] F.A. Aharonian, *et al.*, Astron. Astrophys. **349** (1999) 11.

[118] E. Andres, et al., submitted to Nature (2000).

[119] T. Gaisser, private communication, 2000.

[120] A.G. Wright, Nucl. Inst. Meth. **A442** (2000) 452.

[121] F. Halzen, Proc. of Snowmass 94 (E.W. Kolb and R. Peccei, eds.).

LABORATORY NEUTRINO MASS EXPERIMENTS

Jochen Bonn*
Institute of Physics, University of Mainz
55099 Mainz, Germany

ABSTRACT

Current experiments yield convincing evidence for neutrino mass differences $|\Delta m_{\rm i}^2|$ and mixing. The results are discussed in this SSI. The question of the masses themselves, however, is the domain of laboratory neutrino mass experiments. The "mass' of a weak interaction eigenstate, determined by investigating the kinematics of weak decays, is given by $m_{\rm w}^2 = \sum_{\rm i} |U_{\rm wi}|^2 m_{\rm i}^2$ with $m_{\rm i}$ = mass eigenstates and $U_{\rm wi}$ elements of the mixing matrix.
The second approach to the investigation of neutrino masses, neutrinoless double β decay, is sensitive to an effective mass $m_{\rm ee} = |\sum {\rm e}^{i\phi_{\rm i}} U_{\rm ei}^2 \cdot m_{\rm i}|$ with ${\rm e}^{i\phi_{\rm i}}$ = Majorana phases. The mixing matrix elements $U_{\rm ei}^2$ are complex in general, so cancellation can occur and $m_{\rm ee}$ can become zero or close to it even when the mass values $m_{\rm i}$ are non-zero. Therefore this parameter is complementary to $m_{\rm w}^2$ as detected in weak decays.
The main task of laboratory neutrino mass experiments is to fix the mass scale. This is very important information for elementary particle physics and cosmology which is not accessible by other means.

*Supported by BMBF.

1 Introduction

The lectures summarized below describe laboratory experiments to gain information on neutrino masses from neutrino sources specific to the experiment. The alternative approach to look for oscillations of neutrinos produced outside the laboratory is covered by other lectures. The access to neutrino masses is provided by a weak decay emitting the neutrino in question.

Limits on the mass of the tau neutrino are derived from tau decays into 5 pions, in order to carry as much energy away as possible and facilitate the determination of the missing mass associated with the unobserved neutrino. Limits on the mass of the muon neutrino are derived from the 2 body decay of the pion into a muon and a muon neutrino. To derive a limit on the neutrino mass the masses of the muon and the pion, as well as the momentum of the muon from pion decay at rest, have to be precisely known. At present the main contribution to the uncertainty in the ν_μ mass stems from the uncertainty in the pion mass. A new experiment to reduce this uncertainty will be presented. Limits on the electron neutrino mass are derived from nuclear β decays. Different approaches will be presented: the investigation of the decay of rhenium with cryogenic detectors, and the investigation of tritium beta decay with dedicated spectrometers.

If neutrinos are identical to their antiparticles (Majorana particles), which is possible for neutral elementary particles, then neutrinoless double β decay is a very sensitive probe for an effective electron neutrino mass. Proposals for new experiments in double β decay and in tritium decay will be presented.

1.1 Present Knowledge of Neutrino Masses

In the Standard Model neutrinos are assumed to be massless. We have however learned in the lectures on solar and especially on atmospheric neutrinos that there is very strong evidence for neutrino oscillations, from which differences in the squared neutrino masses and mixing parameters can be derived. Therefore neutrinos are not massless and the neutrinos observed, directly or indirectly, are combinations of different mass eigenstates. The different mass eigenstates are linked together by the small mass squared differences derived from the oscillation experiments. The lowest bound on a neutrino mass is of special interest as, in combination with the differences in the squared masses, it limits the sum of all masses. The lowest bound for a neutrino mass

adopted by the Particle Data Group is the limit on the mass of the electron anti-neutrino from tritium β decay.

1.2 Aims of the Experiments and Implications of Possible Results

The analysis of experimental data in search for a signature of the masses of ν_μ and ν_τ are predominantly motivated by the fact that there is no firm evidence that these neutrinos are stable. In addition, solar and atmospheric neutrino experiments are disappearance experiments and until recently there was no experimental evidence that the neutrinos oscillate into each other and not into some sterile neutrino. Experiments in search for the mass of the electron neutrino are dedicated experiments, the main task of which is to set the mass scale. This can not be achieved by oscillation experiments as a difference in the square of the mass is not experimental evidence for a small mass, as demonstrated in the K $\bar{\text{K}}$ system.

The most direct approach is nuclear β decay. Double β decay is less direct as it asks for nontrivial properties of the neutrino, namely that it is a Majorana particle. In addition the interpretation of a $\beta\beta0\nu$ result would not be straightforward. The aim of the next generation experiments is to reach a sub-eV sensitivity to be able to discriminate between different models for neutrino masses and to contribute to the question of dark matter in the universe. The determination of the contributions of the different mass eigenstates to the electron neutrino weak eigenstate is beyond present-day proposals. The lectures given at the 2000 SLAC Summer Institute, and this contribution, reflect the status of the experiments described. To update their knowledges the readers are referred to the homepages of the experiments:

`http://www.hep.anl.gov/ndk/hypertext/nuindustry.html`

and links therein. For details of the transparencies shown see:

`www.slac.stanford.edu/gen/meeting/ssi/2000/video.html`

2 Limits on the Mass of ν_τ

Experiments to set limits on m_{ν_τ} are special in the sense that the decay involved has an extraordinary signature. To be able to determine the fraction of energy and momentum carried away by the neutrino it is necessary to study decays into 5 pions and a τ

neutrino,

$$\tau \rightarrow 5\pi(+\pi^0) + \nu_\tau, \qquad \mathrm{BR} = 10^{-3}. \tag{1}$$

This mode is essentially free of background and the information on m_{ν_τ} can be derived from only a few events. Each event can be fully reconstructed and the neutrino mass can be calculated by using the invariant mass of the 'visible' 5(6) π's:

$$M^2_{5\pi} = \left(\sum E_{\mathrm{i}}, \sum \vec{p_{\mathrm{i}}}\right)^2 \tag{2}$$

The drawback is that the accuracy achievable is rather poor due to low statistics and a still very high energy available. The present best limit, from ALEPH,[1] is $m_{\nu_\tau} \leq 18.2$ MeV/c^2. The ultimate limits attainable at BaBar and BELLE are expected to be about 3 MeV/c^2.

3 High Precision Measurement of the Pion Mass, and Implications for m_{ν_μ}

The limits on m_{ν_μ} are extracted from the two body decay of a pion at rest into a muon and a muon neutrino.

$$\pi^+ \rightarrow \mu^+ + \nu_\mu \tag{3}$$

From kinematics one easily derives the formula for the neutrio mass and its uncertainty:

$$m^2_\nu = m^2_\pi + m^2_\mu - 2 \cdot m_\pi \cdot \sqrt{p^2_\mu + \pi^2_\mu} \tag{4}$$

$$\Delta m^2_\nu = 2p_\mu \sqrt{(\Delta m_\pi)^2 + 1.6(\Delta p_\mu)^2 + 0.9(\Delta m_\mu)^2} \tag{5}$$

The values for the masses of the muon and pion, and for the momentum of the muon, are determined in individual experiments. Using the values adopted by the Particle Data Group[2]:

Mass of the pion: m_π = 139.570180(350) MeV/c^2,

Mass of the muon: m_μ = 105.658357(5) MeV/c^2,

Muon momentum: p_μ = 29.791998(110) MeV/c,

one immediately recognises that the uncertainty is mostly due to the error in the pion mass. A redetermination of this value with lower uncertainties would hence significantly reduce the uncertainty in the mass of the muon neutrino.

The principle of the new experiment is to determine the pion mass from a gaseous source of a mixture of oxygen and nitrogen in which pionic and muonic atoms are formed simultaneously in the same volume. In a gas the captured muon or pion will blow off the electronic shell and create a hydrogen-like atom with no electrons present as the refilling of the electronic levels will be too slow. Because of this fact, one of the major sources of systematic uncertainties of the former experiment will be avoided.

The wavelength of a photon emitted from such an H like exotic atom is given by

$$\lambda = \frac{1}{R_\infty Z^2} \cdot \frac{m_\mathrm{e}}{m_\pi} \cdot \left(1 + \frac{m_\pi}{M}\right) \cdot L \tag{6}$$

with R_∞: Rydberg constant,

L : contains information about the transition,

M : atomic mass.

Inserting the masses and charges for muonic oxygen and pionic nitrogen we find that the ratio of the wavelengths is extremely close to unity (1.0083). One can therefore record both lines simultaneously and thus relate the pion mass to the muon mass which is extremely well known. The pions are stopped in the cyclotron trap at PSI[3]; the muons are created from pion decay in flight. At a mixture of 90% of oxygen and 10% of nitrogen, equal source strength for both lines is achieved. By avoiding two major sources of systematic uncertainties of the former experiments, refilling of the K shell and calibration uncertainties, it should be possible to considerably reduce the uncertainty of the pion mass.

4 Approaches for Determining the Mass of ν_e

4.1 Neutrinoless Double β Decay

4.1.1 Principle of Double β Decay

Double β decay is a rare second order decay connecting two nuclei which differ in neutron and proton number by two units. It can be observed if the sequential decay is forbidden or strongly suppressed. Starting from a nucleus with even numbers of protons and neutrons (even-even nucleus), a β decay leads to a daughter nucleus with

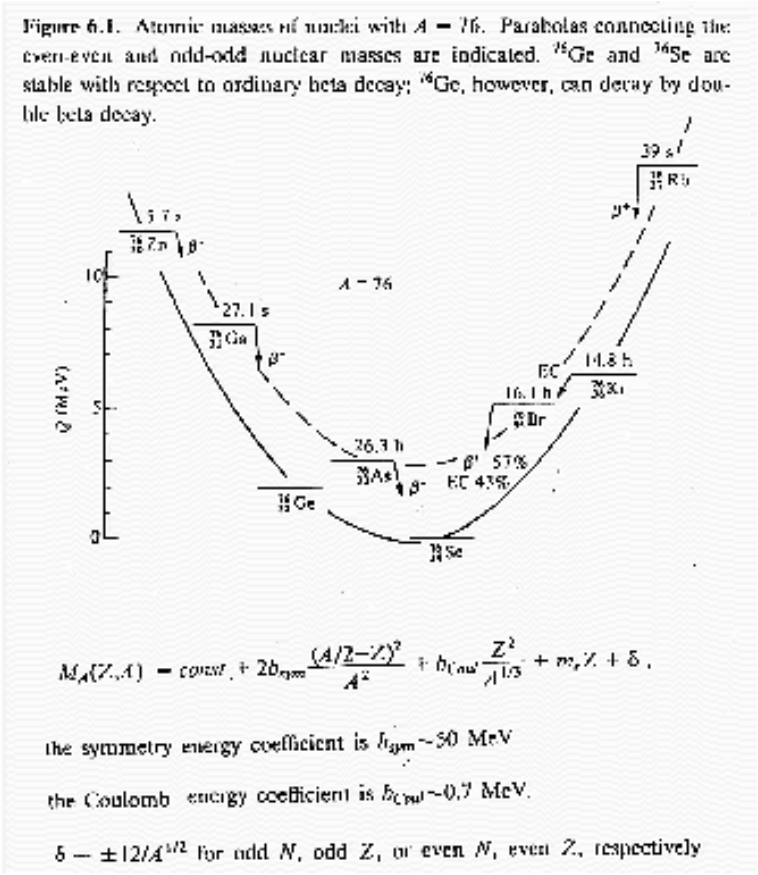

Fig. 1: Atomic masses of nuclei with A=76.

odd numbers of protons and neutrons (odd-odd nucleus). The subsequent decay again results in an even-even nucleus. Due to the pairing of nucleons, even-even nuclei are more bound than odd-odd nuclei. As a result the first decay may be energetically forbidden although the minimum of the energy in the isobaric chain is not reached and the decay from the even-even mother nucleus into the even-even daughter by double β decay is possible (fig. 1).

As shown in fig. 2 there exist two possibilities for double β decay, the allowed 2nd order process in which two electrons and two neutrinos are emitted ($\beta\beta 2\nu$) and neutrinoless double β decay ($\beta\beta 0\nu$) in which the neutrino emitted in one vertex is absorbed at the other vertex. The latter requires physics beyond the Standard Model (SM).

One possibility to allow such a scenario is to require the neutrino to be its own anti-particle (a Majorana particle) and to have a finite mass, because the right-handed anti-neutrino emitted at the first vertex has to be left-handed at the second vertex to be

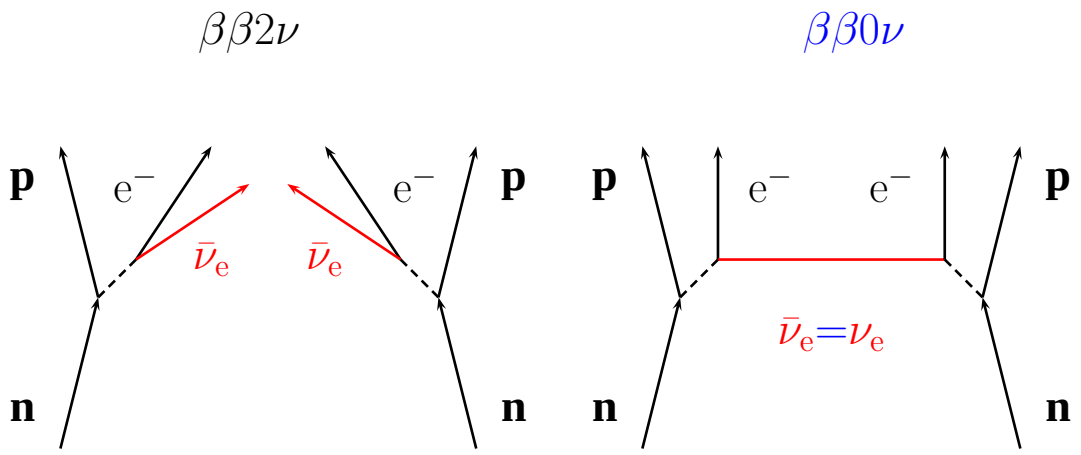

Fig. 2: Double β Decay. Displayed are the two possibilities for double β decay, the allowed 2nd order process ($\beta\beta2\nu$) and the neutrinoless double β decay ($\beta\beta0\nu$). Further explainations are given in the text.

absorbed as a neutrino. Via this mechanism neutrinoless double β decay is sensitive to neutrino masses. Although this is a complicated process involving assumptions about the nature of the neutrino, it is attractive for experimental tests as it has a clear signature. One can either reconstruct the two electrons emerging from the same point or look for the monoenergetic line at the high energy end of the allowed double β decay spectrum.

As a historical remark it should be added that the detection of the decay product, e.g. by geochemical methods, cannot distinguish between the two modes of double β decay and thus does not yield any information on neutrino masses.

An example for an energy spectrum from double β decay is depicted in fig.3, showing a clear $\beta\beta2\nu$ spectrum of the decay of ^{76}Ge into ^{76}Se but no indication of a peak at the position expected for the $\beta\beta0\nu$ mode. As the position is well known from the mass difference of ^{76}Ge and ^{76}Se one can set a rather narrow window on the energy spectrum and compare the count rate in this window with the background given by the count rate outside the window. In the absence of a signal this difference has a 50% probability to be negative. The statistical treatment of such a “negative count rate” is a problem similar to the problem of negative neutrino mass parameters arising from fits to spectra of e.g. tritium β decay.

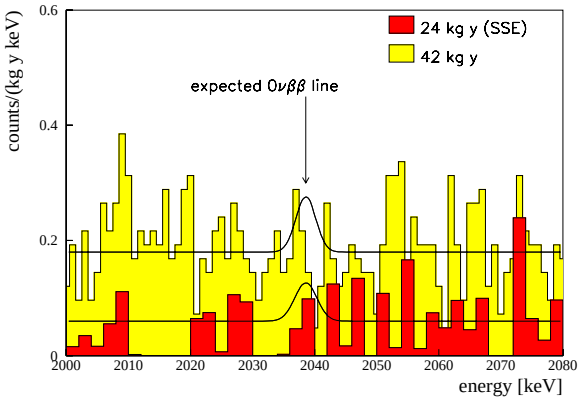

Fig. 3: $\beta\beta 2\nu$ energy spectrum of ^{76}Ge.

4.1.2 Present Limits from $\beta\beta 0\nu$ Experiments

The current status of the different double β decay experiments is given on the homepages of the groups involved. The following data are taken from the homepage of the Heidelberg-Moscow experiment on ^{76}Ge. This experiment claims the present lowest limit; the result of other experiments on different nuclear systems are also given. The half-life reported for the allowed $\beta\beta 2\nu$ decay is[4]

$$T_{1/2} = 1.77 \pm 0.01^{+0.13}_{-0.11} \cdot 10^{21} \text{ y},$$

and the limit for $\beta\beta 0\nu$ derived from the null result is[5]

$$T_{1/2} > 5.7 \cdot 10^{25} \text{ y}.$$

The interpretation of the limit on the partial half-life, in terms of a neutrino mass, more precisely a Majorana neutrino mass, requires knowledge about the structure of the intermediate nucleus. The neutrinos involved are not real, but imaginary particles probing the intermediate nucleus up to very high excitation energies. The relevant nuclear matrix elements are therefore subject to uncertainties. The mass limits deduced from a given set of experimental data using different nuclear matrix elements may differ by about a factor of three.[6–8]

The value derived from the Heidelberg-Moscow collaboration is[9]

$$\langle m_\nu \rangle \leq 0.35 \text{ eV/c}^2, \quad 90\% \text{ C.L.}$$

The discussion of the parameter deduced from double β decay and its comparison with the parameters from weak decays will be given in the section on tritium β decay and its interpretation.

4.1.3 Proposals for Next Generation Double β Decay Experiments

There are eight nuclei which decay via double β decay with electron emission: ^{48}Ca, ^{76}Ge, ^{82}Se, ^{100}Mo, ^{116}Cd, ^{130}Te, ^{136}Xe, ^{150}Nd. An optimum candidate should have a well understood intermediate nucleus to reduce uncertainties in the nuclear matrix element, a high isotopic abundance to have as much active material as possible, and a high Q value to have a relatively short half-life. From the experimental point of view it is important to couple source and detector as close as possible. I will briefly present three proposals for next generation $\beta\beta$ decay experiments.

GENIUS, the large scale version of the Heidelberg-Moscow experiment with isotopically enriched ^{76}Ge.
Germanium is not a good candidate except for its superb properties as a detector. The high quality of Ge detectors compensate the low Q value (2.0 MeV) and the low natural abundance (7.8%), asking for isotopic enrichment. To reduce background to the extremely low values needed to improve the present limit a detector array shall be operated in a huge dewar filled with ultra clean liquid nitrogen. The concept of these naked Ge crystals relies on the fact that liquid nitrogen is one of the materials with the lowest radioactive impurities and that the necessary cables can be reduced to a minimum e.g. 3 g of Kevlar and electrical contacts for a test crystal. The whole collection of detectors shall reach a total active mass of about 1 ton and be housed in an underground laboratory such as the Gran Sasso Laboratory.

CUORICINO and **CUORE**
An alternative concept for detecting the decay electrons are cryogenic detectors as used in the CUORICINO test set up, a precursor of a very large array of TeO_2 crystals coupled to bolometric detectors. As the specific heat capacity is extremely low at temperatures in the 1 K range and below, the energy released in $\beta\beta0\nu$ decay would produce a detectable temperature rise in a large crystal. The system developed for $\beta\beta$ decay consists of TeO_2 crystals of about 200 g each coupled to Si-thermometers. The energy resolution reached in a calibration experiment is 3 keV at 5.4 MeV.

The relatively slow response of cryogenic detectors is of no concern in this experiment.

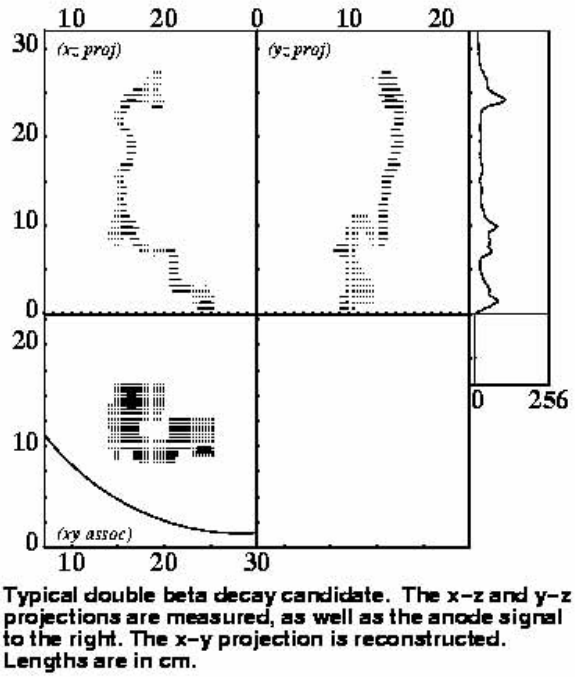

Fig. 4: Operational TPC from Gotthard experiment[10]

Tellurium is a relatively good candidate with a high Q value of 2533 keV and the highest natural abundance (33.8%) of all $\beta\beta$ decay candidates. Te can therefore be used without isotopic enrichment. A first test set up, called CUORICINO with 14 planes and 4 detectors per plane will be built and operated to find the best conditions for the final set up, CUORE with a total of $17 \cdot 60$ crystals. The site to house CUORE will be the Gran Sasso underground laboratory.

EXO

A third proposal is to use several tons of isotopically enriched ^{136}Xe ($Q = 2.5$ MeV) to operate a large time projection chamber (TPC). In addition it is planned to extract the decay product, a single Ba ion or atom and to identify it by laser spectroscopy. As can be seen from fig. 4 taken from the operational TPC from the Gotthard experiment[10] the tracks of the two electrons can be clearly identified. This is a clear advantage. The disadvantage is the relatively poor energy resolution especially of the proposed huge EXO set up. An identification of the Ba ion at the $\beta\beta$ decay vertex would certainly help to reduce background. At present many technical aspects of EXO are still under discussion.

4.2 Nuclear β Decay

Nuclear β decay is the historical ground of neutrino physics. It was in β decay where the neutrino had to be introduced by Wolfgang Pauli to be able to find a description that did not violate the conservation of energy. Up to now the influence of the neutrino mass onto the shape of the β spectrum however could not be measured with high enough precision to find a non-zero value. The most stringent limits from kinematics, however, are derived from tritium β decay. Close to the end point the modification of the spectrum caused by a finite neutrino mass is given by

$$(E_0 - E)^2 \sqrt{1 - \frac{m_\nu^2 c^4}{(E_0 - E)^2}} \; . \tag{7}$$

4.2.1 Criteria for Selecting a Candidate for Neutrino Mass Determination from β Decay

From the above formula it can be seen that a detectable modification of the β spectrum can only be expected very close to its endpoint. It is therefore mandatory to select a decay with a low Q value to have a high fraction of the count rate in the interesting area. A low energy of the electrons to analyse is very helpful to achieve a high resolution $\Delta E/E_0$. To work with a well known β decay spectrum, it is preferable to use a superallowed transition.

If the radioactive source is identical with the detector or at least part of this, the above-mentioned points may be the only relevant criteria. In the case that a spectrometer is used to analyse the energy the following additional criteria apply:

- Precise knowledge of the final state spectrum.
- Low energy loss in the source.
- Low backscattering fraction.
- Short half-life to achieve a high specific activity.

At present two experimental approaches are realised: the investigation of ^{187}Re by bolometric cryo detectors and the investigation of the β decay of molecular tritium (T_2) by dedicated spectrometers.

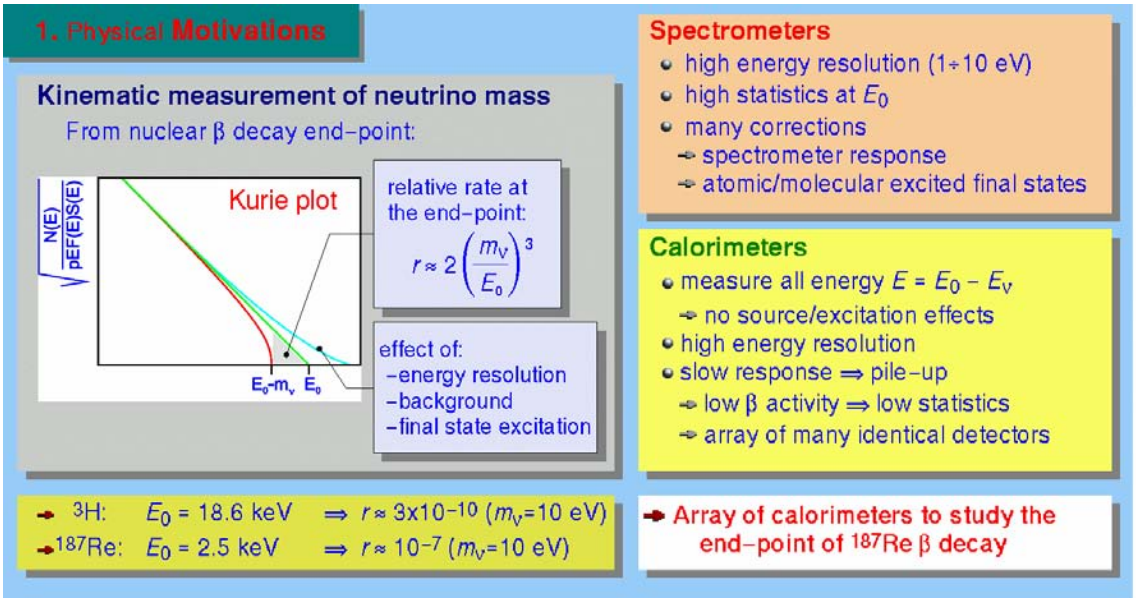

Fig. 5: Milano experiment.

4.2.2 Neutrino mass limit from Re β decay with cryo detectors

At NEUTRINO 2000 the status of the Milano experiment to determine the neutrino mass from ^{187}Re decay was presented and some comments were given to compare this experiment with the experiments with dedicated spectrometers to investigate tritium β decay. Let me comment on the figure given[11] at Neutrino 2000 (fig. 5). In fig. 5 the authors claim an extension of the observed β-spectrum into the region above the endpoint caused by energy resolution, final state excitations and background. It is true that background is present above the endpoint, and it is there that the background can be determined without correlations to the parameters of the β spectrum. In the energy analysing MAC-E filters used to study tritium decay, however, there is no count rate from the β spectrum scattered into the region above endpoint. More generally, no electron will be detected at an energy higher than its real energy. The electrons can only lose energy and, unlike momentum analysing magnetic spectrometers, there is no way to get a misinterpretation caused by scattering inside the spectrometer. This is an important point as one is bound to detect very small changes of the spectral shape in the endpoint region.

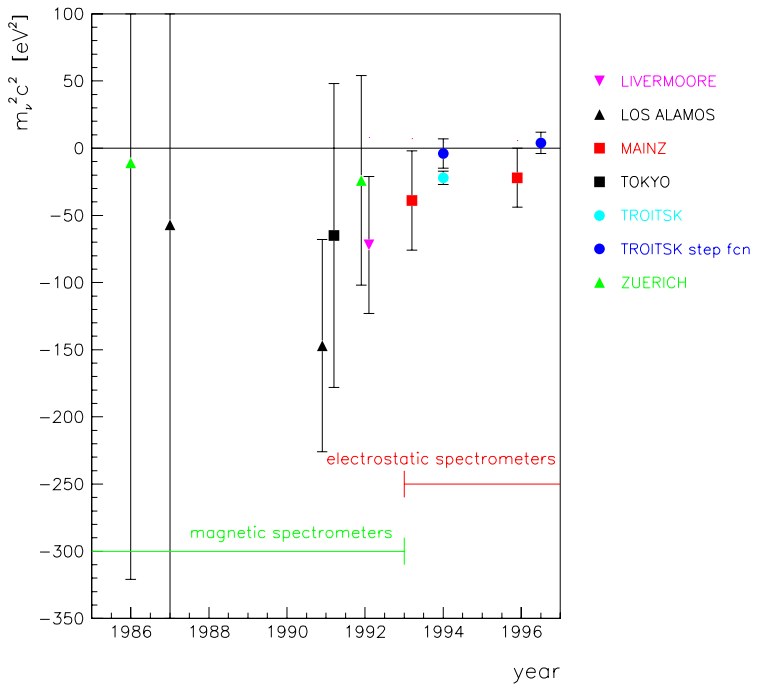

Fig. 6: Results of all tritium-β-experiments since 1986.[12–20]

4.2.3 Neutrino Mass Limit from Tritium β Decay

Another point claimed as being in favor of the Re experiment is the relatively high rate close to the endpoint. This is certainly true. In the real experiments it is however more than compensated by the fact that in the Re experiment all decays have to be analysed with a slow detector of moderate resolution. In the tritium experiments the overwhelming part of the spectrum is not passing the analysing filter such that at 10 eV below endpoint only $3 \cdot 10^{-10}$ of the total activity have to be counted with a fast detector.

In spite of the presently large gap in the performance of Re bolometers and tritium β decay spectrometers the Re detectors may have a chance to contribute substantially to the field. Bolometric detectors are used in many applications, so their technical development and improvement does not depend on experiments on the neutrino mass only. These detectors are very inexpensive compared to spectrometers and it may be possible to operate large arrays once a proof-of-principle experiment is successful. Microbolometers and spectrometers have completely different systematics.

As already indicated the present lowest limits on neutrino masses from the kinematics of weak decays are derived from tritium β decay.

The limits on the mass of the electron neutrino from tritium β decay experiments have been considerably improved and the former trend to unphysically negative values of the mass-squared seems to have vanished. This breakthrough is clearly seen in fig. 6. It is to a large extent based on the properties of a new type of spectrometer. This instrument, dedicated to the investigation of the tritium β spectrum close to its endpoint, is the MAC-E filter containing Magnetic Adiabatic Collimation with an electrostatic Energy analysis.[21,22] It was developed independenly by the groups in Mainz[21] and in Troitsk.[23]

The principle of the spectrometer will be briefly explained and the choice of tritium will be motivated. For details I refer the reader to the literature. For convenience a recent summary of the status of the Mainz experiment is attached to this paper. A description of the joint effort of a new international collaboration to build a new spectrometer to push the sensitivity on the neutrino mass below 0.5 eV/c^2 can be found on the homepage of the collaboration[24] called Karlsruhe Tritium Neutrinomass Experiment KATRIN.

Basic properties of a MAC-E-filter

Fig. 7 shows the principal setup of a MAC-E filter (or solenoid retarding spectrometer). It basically consists of a magnetic guiding field with a strong variation in its field strength and an electric analysing potential in the minimum of the magnetic field. The source is placed close to one of the magnetic field maxima and the detector close to the other one. Electrons starting from the source into the forward hemisphere are guided by magnetic field lines of the superconducting solenoids onto the detector. In between the two solenoids the fringing field gets rather weak and the electron beam expands accordingly. When passing from high to low magnetic field the electrons experience a gradient force acting on the orbital motion around the field line and transforming the energy in this motion into energy in the longitudinal motion. In the case of adiabatic conditions the resulting quasi-parallel electron beam in the center of the spectrometer has the same emittance as the source.

The energy of the electrons in this quasi-parallel beam is analysed by an electrostatic filter. Electrons with an energy large enough to pass the filter potential are transmitted and counted by the detector. The relative width of the filter is given by the ratio of the magnetic fields in the center of the solenoid and in the analysing plane. It is typically 5000 at the present spectrometer. For KATRIN it is planned to work with a resolution $E/\Delta E$ of up to 20000.

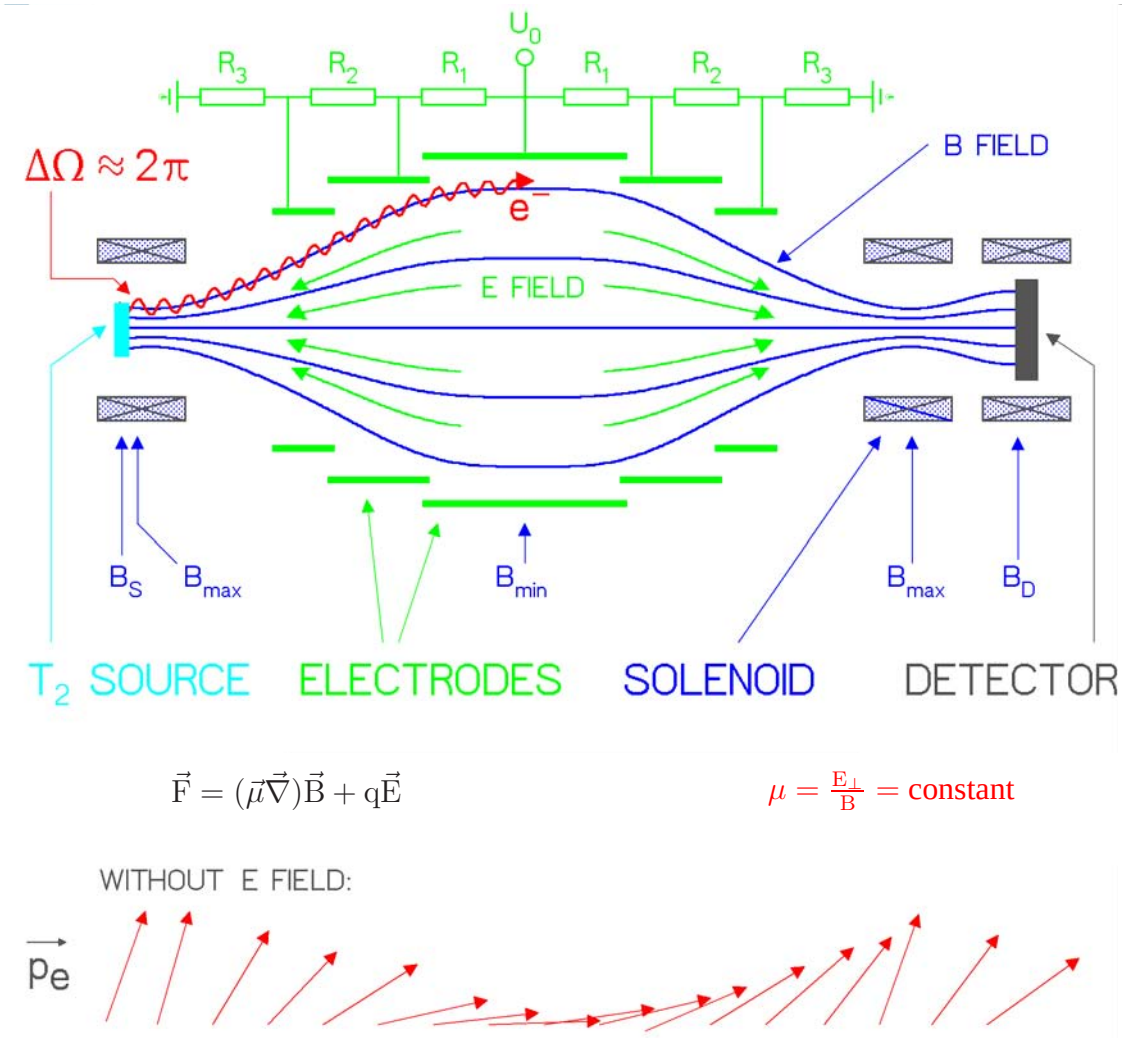

Fig. 7: Principle of the Mainz MAC-E Filter.

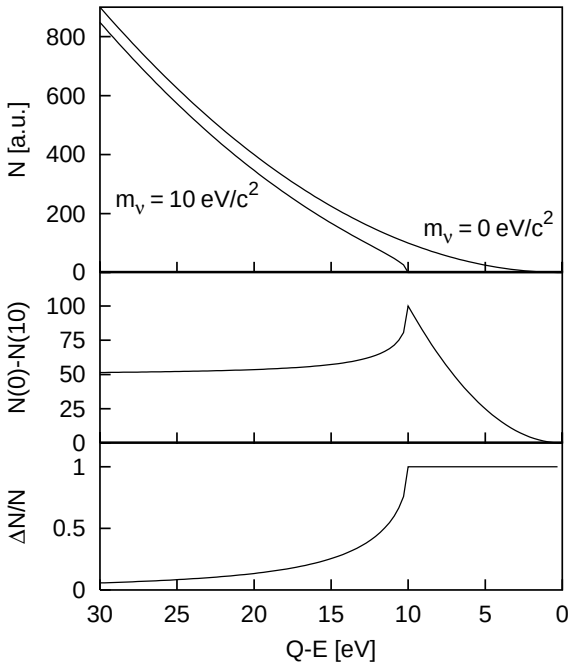

Fig. 8: Signature of a non-zero neutrino mass. In the upper part the endpoint region of the tritium β-spectrum is displayed for two neutrino masses, 0 eV/c^2 and 10 eV/c^2. In the middle part the absolute difference of the spectra is shown, and in the lower part the relative difference. The strongest signature for a non-zero neutrino mass can be found in the region close to the β endpoint.

Consideration that led to the choice of tritium to be studied with a MAC-E filter.
To detect the change of the shape of the β-spectrum due to a non-zero neutrino mass several considerations are important.

1. The signal is given by a correction factor to the standard β-spectrum,

$$\frac{dN}{dE} = const \cdot |M|^2 \; F(Z,E) \; p \; (E + m_{\mathrm{e}}c^2) \; \sum_{\mathrm{n}} W_{\mathrm{i}\rightarrow \mathrm{f_n}} \varepsilon_{\mathrm{n}} \sqrt{\varepsilon_{\mathrm{n}}^2 - m_\nu^2 c^4} \qquad (8)$$

   with $|M|$: matrix element of β decay,
   $F(Z,E)$: Fermi function,
   $W_{\mathrm{i}\rightarrow \mathrm{f_n}}$: transition probability in the nth final state,
   ε_{n}: $E_0 - V_{\mathrm{n}} - E$,
   V_{n}: energy of nth final state.

   For values of $\varepsilon >> m_\nu c^2$ the correction approaches a constant (see fig. 8). As we are looking for an effect of a neutrino mass in the range of 1 eV/c^2 or even below, $\Delta\dot{N}$ is in the order of $10^{-13} \cdot I_0$ eV/c^2 (I_0 = total accepted decay intensity under investigation) * . In the case of an integrating spectrometer the influence of m_ν will increase linearly with the distance from the endpoint, the slope being $\Delta\dot{N}_{\mathrm{diff}}$.

2. A constant background (in a differential spectrum) or a slope in the background (in an integrating spectrum) directly correlate with the neutrino mass. It is therefore extremely important to be able to gain information on the background. In the MAC-E spectrometers the recorded β-spectrum definitively ends at its endpoint. There is no tail to the high energy side. This allows one to extract the background, and its possible dependence on the effective retarding voltage, undisturbed by the β-spectrum.

3. As the relative change of the β-spectrum is very small, a high total decay rate and a high accepted solid angle are necessary to achieve the statistics needed to emerge from background. In this respect the MAC-E filter spectrometers win by orders of magnitudes over the previously used magnetic spectrometers.

4. The arguments 1) to 3) are technical and apply to any β-spectrum. The choice of tritium is governed by

   - its high specific activity, i.e. by the fact that a thin source within a limited energy loss fraction of the β-particles results in a relatively high count rate.

*In the case of tritium β decay with $E_0 = 18.6$ keV.

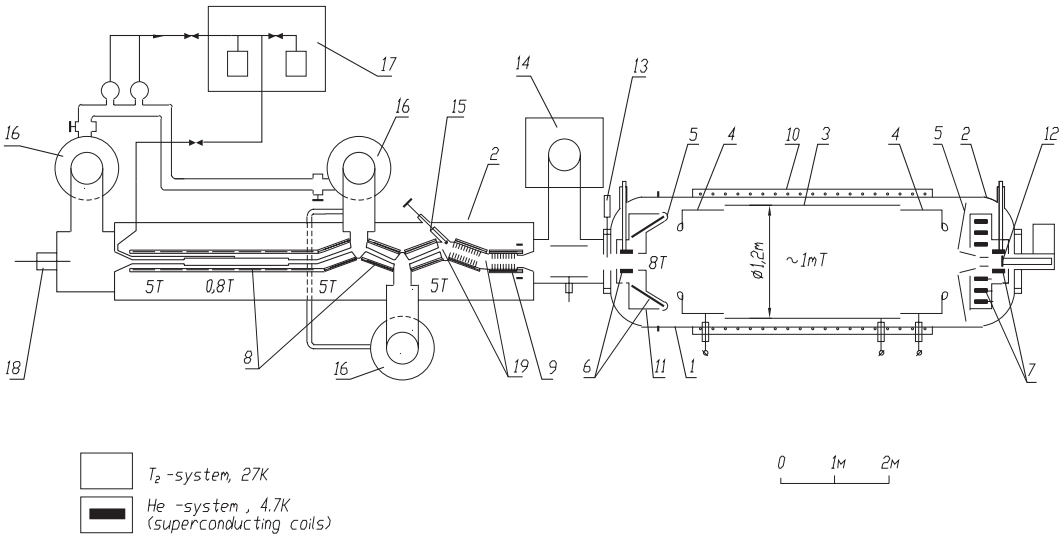

Fig. 9: Schematic view of the Troitsk experimental setup.

- its well-known slope as a superallowed mirror transition.
- the fact that the spectrum of molecular final states is rather well understood.

In spite of the fact that tritium is the easiest and best understood candidate, the systematic uncertainties are serious and will grow with the attempt to detect smaller neutrino masses. Really helpful is that the extreme end of the β-spectrum, i.e. $(E - E_0)$, is smaller than the excitation energy of the first excited state in T_2, and therefore is free of energy loss and corresponding systematic uncertainties.

4.2.4 The Mainz and the Troitsk experiments

The experiments at Troitsk[25] and Mainz[26] use similar MAC-E-Filters differing slightly in size: The diameter and length of the Mainz (Troitsk) spectrometers are 1 m (1.5 m) and 4 m (7 m). The major differences between the two setups are the tritium sources.

The Troitsk experiment uses a windowless gaseous tritium source (WGTS) which is based on adiabatic transportation of electrons in a strong longitudinal magnetic field and circulation of tritium gas at low pressure by means of a differential pumping system[23] (see fig. 9). This approach was first pioneered in an experiment at Los Alamos.[14] An essential refinement made at Troitsk was the use of the strong magnetic field for transportation, which permits the use of multiple bends of the transportation channel

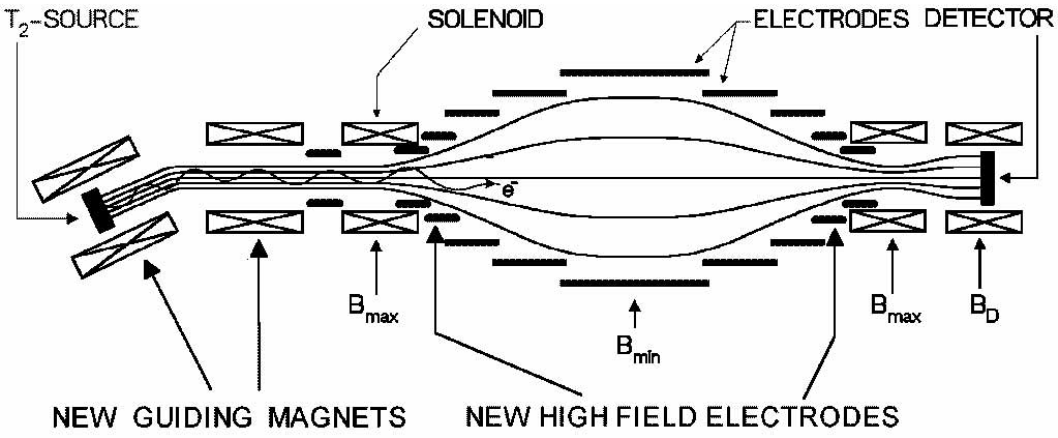

Fig. 10: The upgraded and improved Mainz setup (schematically, not in realistic scale). The outer diameter amounts to 1 m, the distance from the source to the detector is 6 m.

(a 3 m long tube of 50 mm diameter filled with 0.01 mbar of T_2), providing better differential pumping and smooth coupling to the MAC-E-filter spectrometer. The WGTS provides a number of beneficial features for the study of the tritium β spectrum, such as guaranteed homogeneity over the cross section of the source, and reliable on-line control of inelastic energy losses of electrons in the source. It further allows one to use theoretical calculations of free molecular final state corrections and totally suppresses backscattering.

Mainz uses a film of molecular tritium quench-condensed onto a highly oriented graphite substrate (HOPG). The film has a diameter of 17 mm and a typical thickness of 40 nm, which is measured by laser ellipsometry. In the years 1995–1997 the Mainz setup was upgraded to enhance the count rate and to decrease the background rate. As a second substantial improvement, a new cryostat now provides temperatures of the tritium film below 2 K to avoid a roughening transition of the film, which was a source of systematic errors of earlier Mainz measurements. The roughening process is a temperature activated surface diffusion process; therefore low temperatures are necessary to get time constants much longer than the duration of the measurement.[27,28] The full remote control of the apparatus allows one to perform long term measurements of several months per year. Figure 10 gives a sketch of the Mainz setup. Since this upgrade, the count rate, background and energy resolution of the Mainz setup are nearly the same as the ones of the Troitsk experiment.

Results of the Troitsk Neutrino Mass Experiment

The Troitsk experiment has taken 200 days of tritium data from 1994 on. Since the first measurement in 1994, the Troitsk experiment has observed a small anomaly in their experimental spectrum a few eV below the β endpoint E_0, which resembles a sharp step of the count rate. Since a MAC-E-Filter is integrating, a sharp step corresponds to a narrow line in the primary spectrum. The data indicate a relative intensity of about 10^{-10} of the total decay rate. From 1998 on, the Troitsk group reported that the position of this line seems to oscillate with a frequency of 0.5 years between 5 eV and 15 eV below E_0.[25] The cause for such an anomaly is not known. Detailed investigations as well as synchronous measurements with the Mainz experiment are under way and will help to clarify this effect.

Fitting a standard β spectrum to the Troitsk data results in significantly negative values of $m_\nu^2 \approx -10$ to -20 eV^2/c^4. However, describing the anomaly phenomenologically by adding a monoenergetic line with free amplitude and position to a standard β spectrum results in values of m_ν^2 compatible with zero. The average over all Troitsk runs until 1999 then amounts to[29]

$$m_\nu^2 = -1.0 \pm 3.0 \pm 2.5 \text{ eV}^2/\text{c}^4,$$

which corresponds to an upper limit of

$$m_\nu^2 \leq 2.5 \text{ eV/c}^2 \quad (95\ \%\ \text{C.L.}).$$

Results of the Mainz Neutrino Mass Experiment

Figure 11 shows the endpoint region of the Mainz 1998 and 1999 data in comparison with the former Mainz 1994 data. An improvement of the signal-to-background ratio by a factor of 10, as well as a significant enhancement of the statistical quality of the data, is clearly visible. The main systematic uncertainties of the Mainz experiment are originating from the physics and the properties of the quench-condensed tritium film and are the inelastic scattering of the β electron within the tritium film, the excitation of neighbor molecules due to the β decay, and the self-charging of the tritium film due to the radioactivity. As a result of detailed investigations,[30–32] these systematic uncertainties were improved significantly. The data of the last runs of 1998 and 1999 (see fig. 11) neither show a Troitsk-like anomaly nor any residual problem. The most sensitive analysis on the neutrino mass, in which only the last 70 eV of the β spectrum

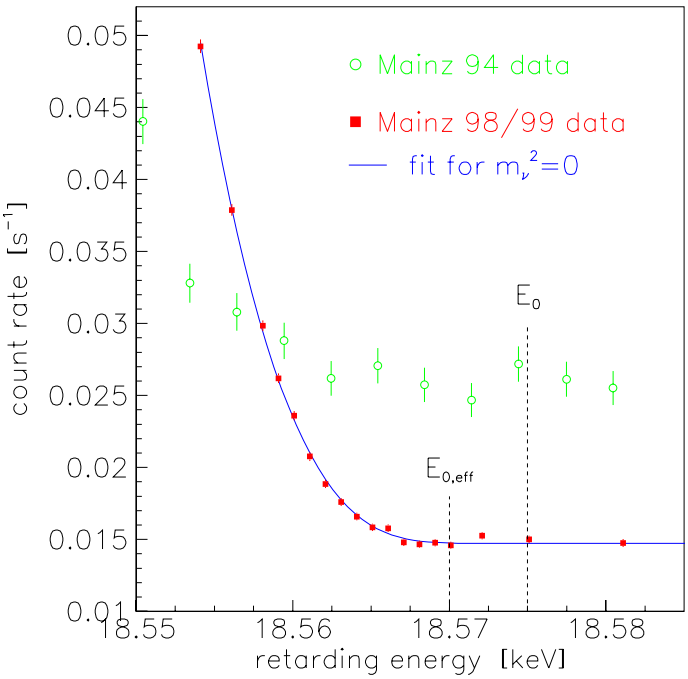

Fig. 11: Averaged count rate of the Mainz 1998 and 1999 data (points) in comparison with previous Mainz data from 1994[20] . Displayed is the count rate as a function of the retarding energy near the endpoint E_0. The line describes the fit and $E_{0,eff}$ the effective endpoint. The position of the latter takes into account the width of response function of the setup and the mean rotation-vibration excitation energy of the electronic ground state of the $^3\mathrm{HeT}^+$ daughter molecule.

below the endpoint are used, results in

$$m_\nu^2 = -1.6 \pm 2.5 \pm 2.1 \text{ eV}^2/\text{c}^4,$$

which is compatible with a zero neutrino mass and corresponds to an upper limit on the electron neutrino mass of:

$$m_\nu \leq 2.2 \text{ eV/c}^2 \quad (95\ \%\ \text{C.L.}).$$

These new Mainz 1998 and 1999 data and analysis,[33] improved the published former upper limit of $m_\nu < 2.8\,\text{eV/c}^2$,[26] which was based on the Mainz 1998 data alone. Together with the Troitsk results, they represent the world's best sensitivity on a neutrino mass in a direct neutrino mass experiment.

5 A next generation tritium β-decay experiment

The present tritium β decay experiments at Troitsk and Mainz have already reached their intrinsic sensitivity limit. One can estimate that future measurements of both experiments will improve the current mass limits only marginally to $m_\nu < 2\,\mathrm{eV/c^2}$. This implies that the interesting sub-eV/c^2 neutrino mass region can only be investigated by a new experimental set-up with much higher ν-mass sensitivity.

In the following we present a design study for a next-generation tritium β decay experiment with sub-eV/c^2 sensitivity for the electron neutrino mass. With an estimated sensitivity of $m_\nu = 0.3\,\mathrm{eV/c^2}$ (95 % C.L.) the experiment will have the potential to improve the existing limits by a *factor of ten*.

The study is based on the long-term experience with the existing spectrometers of the MAC-E type and has been done in collaboration by groups from Mainz, Troitsk, Karlsruhe and Fulda, following first ideas presented in Refs. 31,22.

5.1 Definition of experimental parameters

The neutrino mass sensitivity of a tritium experiment depends on the design values of two key experimental parameters: the relative energy resolution $R = \Delta E/E$ of the electrostatic spectrometer and the luminosity $\mathcal{L}$. While $\Delta E/E$ is given by the ratio $B_{\mathrm{min}}\,/\,B_{\mathrm{max}}$ of the magnetic field B_{min} in the analyzing plane of the spectrometer and the maximum magnetic field B_{max}, the luminosity $\mathcal{L}$ is proportional to the source area A_{S} and the maximum allowed starting angle θ_{max} of β decay electrons in the tritium source.

To reach a sub-eV/c^2 sensitivity, the energy resolution ΔE of the electrostatic spectrometer at the tritium β decay endpoint at 18.6 keV should be $\Delta E = 1$ eV, implying a ratio of magnetic fields $B_{\mathrm{min}}\,/\,B_{\mathrm{max}} = 5 \times 10^{-5}$. This resolution requires an improvement by a *factor of about 4* compared to the ΔE values of the experiments in Troitsk and Mainz. With regard to the luminosity $\mathcal{L}$ one has to keep in mind that the relative influence of a finite neutrino mass on the count rate scales with m_ν^2, hence the luminosity should be increased by *nearly two orders of magnitude* relative to present experiments (see also figure 12).

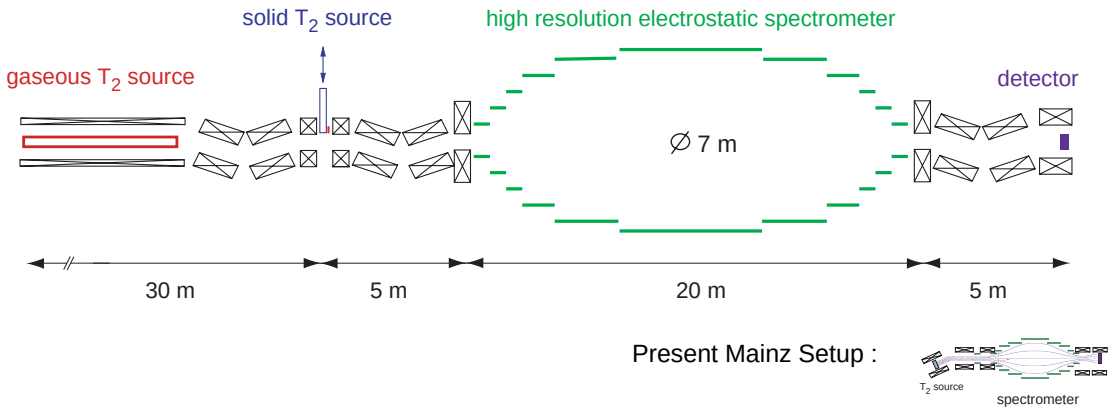

Fig. 12: Schematic view of the proposed next-generation tritium β decay experiment in a linear configuration. The main components of the system comprise a windowless gaseous tritium source (WGTS), a quench condensed tritium source (QCTS), and a large electrostatic spectrometer of 7 m diameter and 20 m length with an energy resolution of 1 eV. Electrons passing the MAC-E filter are recollimated onto a segmented solid state detector. The electron transport section adiabatically guides β decay electrons from the source to the spectrometer (and further on to the detector) while at the same time eliminating all tritium molecules in a two stage process: a first differential (active) pumping part at LN_2 temperature, which is followed by a second (passive) cryotrapping part at LHe temperature. The overall length of this linear set-up amounts to about 60 m. Shown for comparison is the present Mainz setup at same scale.

In this context it is advantageous to define a single overall quality factor Q by the ratio of both parameters with $Q = \mathcal{L}/R$, which can also be expressed as[22]

$$Q = \frac{A_{\mathrm{A}}}{2 \cdot (1 + \cos\theta_{\mathrm{max}})} \quad .$$

The quality of a MAC-E filter is proportional to the area of the analyzing plane A_{A} of the spectrometer and thus will improve quadratically with the up-scaling of its linear dimensions. To meet the improvements on energy resolution and source luminosity defined above, a large electrostatic spectrometer with an analyzing plane of 7 m diameter and a T_2 source with column density of $5 \cdot 10^{17}$ molecules/cm^2 and a maximum accepted starting angle $\theta_{\mathrm{max}} = 51^\circ$ are considered.

In addition to these requirements, a low background rate at the tritium β-decay endpoint region at 18.6 keV of the order of 10^{-2} counts/sec is essential for a sensitivity to sub-eV neutrino mass effects. This low background rate implies stringent requirements on the vacuum conditions of the electrostatic spectrometer, and it also calls for a state-of-the-art solid state detector with good energy-, time- and spatial resolution for low energy

electrons in the keV range.

Finally, it is especially important to control all systematic effects which might influence the measurements. As the most important systematic effects are associated with the properties of the tritium source, the design study proposes to use two different tritium sources with entirely different systematics: a WGTS, following the design of the Troitsk experiment, and QCTS, following the Mainz design. Alternate measurements with both sources will minimize systematic uncertainties. Both sources will have to be calibrated and controlled extensively. Calibration of the properties of the WGTS will be provided by means of an electron gun, while a series of ^{83m}Kr-conversion line test measurements will determine the characteristics of the QCTS.

Apart from the standard integrating (MAC-E) mode of operation, short-term measurements with the differential time-of-flight (MAC-E-TOF) mode pioneered in Mainz[22] will play an important role in the planned measuring program of the new experiment. These additional runs will help to investigate possible systematic effects arising from local distortions of the energy spectrum close to the endpoint. Effects such as the anomaly reported in the Troitsk experiment[19] can thus be investigated in detail. Moreover, as an effect such as the Troitsk anomaly corresponds to a narrow line in the energy spectrum, the resulting distortion in the energy spectrum will stay *local* in the MAC-E-TOF mode. This in turn will allow one to disentangle the effects due to m_ν^2 from any narrow spectral anomaly close to the endpoint. Apart from the search for massive neutrinos, the detailed spectral information to be obtained with the new setup will also allow the search for other non-SM physics like tachyonic neutrinos or small right-handed contributions to the electroweak interactions.

6 Summary

- Tritium is the best candidate for the investigation of a β-spectrum to extract information on the neutrino mass with a β-spectrometer.
- The MAC-E filters used in Mainz and in Troitsk are the best spectrometers ever used to investigate β-spectra close to their endpoint.
- The proposed next generation experiment KATRIN has a chance to detect the neutrino mass if $m_\nu > 0.5$ eV/c^2.

Acknowledgement

I would like to thank SLAC for the invitation to SSI2000 and for the hospitality, and B. Bornschein for the help in preparing this manuscript.

References

[1] J.M. Roney, Neutrino2000, http://nu2000.sno.laurentian.ca

[2] Particle Data Group, Eur. Phys. J. **C15** (2000) 1.

[3] K. Assamagan et al., Phys. Rev. **D53** (1996) 6065.

[4] M. Guenther et al., Phys. Rev. **D55** (1997) 54.

[5] L. Baudis et al., Phys. Rev. Lett. **83**, 41 (1999) [hep-ex/9902014].

[6] S.M. Bilenky, S. Pascoli and S.T. Petcov, hep-ph/0102265.

[7] M. Moe and P. Vogel, Ann. Rev. Nucl. Part. Sci. **44** (1994) 247.

[8] A. Faessler and F. Šimkovic, J. Phys. **G24** (1998) 2139.

[9] A. Dietz, talk at DARK2000.

[10] http://www.unine.ch/phys/corpus/Gothard/got_art.html

[11] http://crio.mib.infn.it/wig/

[12] M. Fritschi et al., Phys. Lett. **B173** (1986) 485.

[13] J.F. Wilkerson et al., Phys. Rev. Lett. **58** (1987) 2023.

[14] R.G.H. Robertson et al., Phys. Rev. Lett. **67** (1991) 957.

[15] H. Kawakami et al., Phys. Lett. **B256** (1991) 105.

[16] E. Holzschuh et al., Phys. Lett. **B287** (1992) 381.

[17] W. Stoeffl et al., Phys. Rev. Lett. **75** (1995) 3237.

[18] Ch. Weinheimer et al., Phys. Lett. **B300** (1993) 210.

[19] A.I. Belesev et al., Phys. Lett. **B350** (1995) 263.

[20] H. Backe et al., Proc. XVII Conference on Neutrino Physics and Astrophysics, Neutrino 96, Helsinki, Finland (World Scientific, Singapore, 1996).

[21] A. Picard et al., Nucl. Instrum. Meth. **B63** (1992) 345.

[22] J. Bonn et al., Nucl. Instrum. Meth. **A421** (1999) 256.

[23] V.M. Lobashev and P.E. Spivak, Nucl. Instrum. Meth. **A240** (1985) 305.

[24] KATRIN homepage, `http://www-ik1.fzk.de/tritium/`

[25] V.M. Lobashev et al., Phys. Lett. **B460** (1999) 227.

[26] Ch. Weinheimer et al., Phys. Lett. **B460** (1999) 219.

[27] L. Fleischmann et al., J. Low Temp. Phys. **119** (2000) 615.

[28] L. Fleischmann et al., Eur. Phys. J. **B16** (2000) 521.

[29] V.M. Lobashev et al., Proc. of the Int. Conf. Neutrino 2000, Sudbury, Canada, Nucl. Phys. **B** (Proc. Suppl.), in press.

[30] V. N. Aseev et al., Eur. Phys. J. **D10** (2000) 39.

[31] H. Barth et al., Prog. Part. Nucl. Phys. **40** (1998) 353.

[32] B. Bornschein, Ph.D. thesis, Mainz University, 2000.

[33] J. Bonn et al. , Proc. of the Int. Conf. Neutrino 2000, Sudbury, Canada, Nucl. Phys. **B** (Proc. Suppl.), in press.

[34] IMEC vzw, B-3001 Leuven, Belgium (`http://www.imec.be`), private communication.

REACTOR-BASED NEUTRINO OSCILLATION EXPERIMENTS

Giorgio Gratta
Physics Department, Stanford University, Stanford CA 94305-4060

ABSTRACT

We review the status of neutrino oscillation searches employing nuclear reactors as sources. This technique, a direct continuation of the experiments that proved the existence of neutrinos, is today an essential tool in investigating the indications of oscillations found in studying neutrinos produced in the sun and in the earth's atmosphere. The low energy of the reactor $\bar{\nu}_{\rm e}$ makes them an ideal tool to explore oscillations with small mass differences and relatively large mixing angles. In the last several years the determination of the reactor anti-neutrino flux and spectrum have reached a high degree of accuracy. Hence measurements of the $\bar{\nu}_{\rm e}$ flux at a given distance L can be readily compared with the expectation at $L = 0$, thus testing the disappearance. While two experiments with baselines of about 1 km, sensitive to the neutrino mass differences associated with the atmospheric neutrino anomaly, have collected data and published results in the last two years, an ambitious project with a baseline of more than 100 km is preparing to take data. This ultimate reactor experiment will have sensitivity sufficient to explore part of the oscillation phase space relevant to solar neutrino scenarios. It is the only envisioned experiment with a terrestrial source of neutrinos capable of addressing the solar neutrino puzzle.

Contents

1 Introduction

Neutrinos have the distinction of being the first elementary particles whose existence was predicted by a theorist in order to explain seemingly unrelated phenomena.[1] Pauli made such prediction in 1930 in his famous letter in order to explain the continuous electron energy distribution in nuclear beta decay. It became immediately clear that neutrinos will be difficult to observe, because the corresponding cross sections are so tiny. But in a series of experiments in 1953-56 Cowan, Reines and collaborators were able to prove convincingly that electron anti-neutrinos from nuclear reactors are able to cause the inverse neutron beta decay, $\bar{\nu}_{\rm e} + {\rm p} \to {\rm e}^+ + {\rm n}$, and hence that they are real particles. Shortly afterwards, in 1962, the separate identity of the muon neutrinos, ν_μ, was demonstrated. Another decade later, in 1975, the tau lepton was discovered and the observation of its decay properties implied the existence of the third neutrino, ν_τ, which was directly observed only in the last year.[2] Precise measurements of the decay width of the Z have shown that just three neutrino flavors participate in the weak interactions (at least for neutrinos with masses less than $1/2\, M_{\rm Z}$).

Ironically, while our knowledge of intrinsic neutrino properties remains quite poor, these particles have been used as tools to understand other phenomena. The tradition of underground detectors began thirty years ago when Davis and his collaborators were first able to detect neutrinos from the Sun. This was, and still is, the only clear proof that the basic energy generation in stars is understood. The birth of neutrino astronomy can be associated with the observation of the neutrino burst from the supernova 1987A. Neutrino-induced reactions played an important role in establishing what is now known as the Standard Model of electroweak interactions when in 1973 the neutral currents were discovered via the observation of the $\nu_\mu + e \to \nu_\mu + e$ scattering as well as the neutral current scattering of neutrinos on nucleons. Finally, neutrinos have been extensively used in deep inelastic scattering experiments at CERN and FNAL, exploring the quark structure of nucleons.

The main problem in neutrino physics today is the question whether neutrinos, like the charged fermions, have a mass.[3,4] The experimental hints for neutrino mass are at present based on the phenomenon of neutrino oscillations. If neutrinos are massive particles which behave in analogy to quarks, the states with a definite mass (i.e., the "mass eigenstates" which propagate as plane waves in a vacuum) are not necessarily the partners of the charged leptons that couple to the vector bosons $\rm W^\pm$ in doublets

(i.e., the weak eigenstates)

$$\left(\begin{array}{c} \nu_{\rm e} \\ {\rm e}^- \end{array} \right) , \left(\begin{array}{c} \nu_\mu \\ \mu^- \end{array} \right) , \left(\begin{array}{c} \nu_\tau \\ \tau^- \end{array} \right) . \tag{1}$$

The weak eigenstates $|\nu_l\rangle$ will be in such a case linear superpositions of the mass eigenstates $|\nu_i\rangle$

$$|\nu_l\rangle = \sum_i U_{l,i} |\nu_i\rangle \ , \tag{2}$$

where the coefficients $U_{l,i}$ form the leptonic mixing matrix. If we assume that only three neutrinos can contribute in the Eq. (2) above, then U is a unitary 3×3 matrix.

If Eq. (2) is valid, we encounter the phenomenon of neutrino oscillations in which a neutrino which was initially in the weak eigenstate l can be spontaneously transformed, at least in part, into another weak eigenstate neutrino of flavor l'. To see how that happens, consider the time development of the mass eigenstate $|\nu_i\rangle$

$$|\nu_i(t)\rangle = e^{-i(E_i t - p_i L)} |\nu_i(0)\rangle \simeq e^{-i(m_i^2/2E)L} |\nu_i(0)\rangle \ , \tag{3}$$

where L is the flight path and in the last expression we assumed that the laboratory momenta and energies are much larger than the neutrino rest masses m_i. Let us consider now the propagation of a neutrino which was created at $L = 0$ as a weak eigenstate $|\nu_l\rangle$. At a distance L this state is described by

$$|\nu_l(L)\rangle \simeq \sum_i U_{l,i} e^{-i(m_i^2/2E)L} |\nu_i\rangle \ \simeq \ \sum_{l'} \sum_i U_{l,i} e^{-i(m_i^2/2E)L} U^*_{l',i} |\nu_{l'}\rangle \ . \tag{4}$$

Thus, the neutrino of flavor l acquired components corresponding to other flavors l'. This is a purely quantum mechanical effect, a consequence of the coherence in the superposition of states in Eq. (2). The probability that the "transition" $l \to l'$ happens at L is obviously

$$P(\nu_l \to \nu_{l'}, L) = |\sum_i U_{l,i} U^*_{l',i} e^{-i(m_i^2/2E)L}|^2 \ . \tag{5}$$

This is an oscillating function of the distance L. The oscillation length depends on the neutrino masses m_i (actually on the differences of mass squares), and the oscillation amplitude depends on the mixing matrix U.

Neutrino oscillation experiments are often analyzed in a simplified way by assuming that only two neutrino flavors mix, e.g. e and μ. The mixing matrix U then depends only on one mixing angle θ, and the oscillation probability, Eq. (5), is also simplified,

$$U = \left(\begin{array}{cc} \cos\theta & \sin\theta \\ -\sin\theta & \cos\theta \end{array} \right) \ , \ P(\nu_{\rm e} \to \nu_\mu, L) = \sin^2 2\theta \sin^2(\Delta m^2 L/4E) \ . \tag{6}$$

Here $\Delta m^2 \equiv m_1^2 - m_2^2$. The probability that $\nu_{\rm e}$ remains $\nu_{\rm e}$ is obviously $P(\nu_{\rm e} \to \nu_{\rm e}, L) = 1 - P(\nu_{\rm e} \to \nu_\mu, L)$.

In this two-flavor scenario the oscillation amplitude is $\sin^2 2\theta$ which vanishes if $\theta = 0$ or 90° and is maximum if θ =45°. The oscillation length is

$$L_{osc} = 2\pi \frac{2E_\nu}{\Delta m^2} = \frac{2.48 E_\nu({\rm MeV})}{\Delta m^2({\rm eV}^2)} {\rm meters}\ . \tag{7}$$

To test for oscillations, one can perform either an *appearance* search in which one looks for new neutrino flavor, or a *disappearance* test in which one looks for a change in the flux normalization. In either case, tests performed at distance L are only sensitive to the values of Δm^2 for which $L \geq O(L_{osc})$.

So far we have considered only propagation of neutrinos in a vacuum. When neutrinos propagate in matter, such as in the solar interior, the oscillation pattern may be modified. This happens because electron neutrinos can forward scatter on electrons by charged current interactions, and other neutrino flavors cannot. Under favorable circumstances a resonance enhancement of the oscillation amplitude, the so-called Mikheyev-Smirnov-Wolfenstein (MSW) effect,[5] can take place.

2 Physics motivation of modern experiments

Numerous searches for neutrino oscillations were performed during the last two decades using nuclear reactors as well as particle accelerators as sources. Most of them resulted in an "exclusion plot", i.e., based on them certain ranges of the parameters Δm^2 and $\sin^2 2\theta$ can be excluded from further considerations as shown in Figure 1. However, at the present time there are three groups of measurements that suggest the existence of neutrino oscillations. (And, at the same time, the parameter ranges suggested by them are not excluded.) Only these *positive* results will be briefly discussed here (other experiments are listed in the Review of Particle Properties[6]).

2.1 Experimental indications for neutrino oscillations

The most prominent group of measurements which are commonly interpreted as evidence for neutrino oscillations are usually referred to as the "atmospheric neutrino anomaly".[7] Primary cosmic rays impinging on the nitrogen and oxygen nuclei at the top of the earth's atmosphere produce mostly pions, which subsequently decay via the chain $\pi \to \mu\bar{\nu}_\mu, \mu \to {\rm e}\bar{\nu}_{\rm e}\nu_\mu$. At sufficiently low energy, when such a chain can

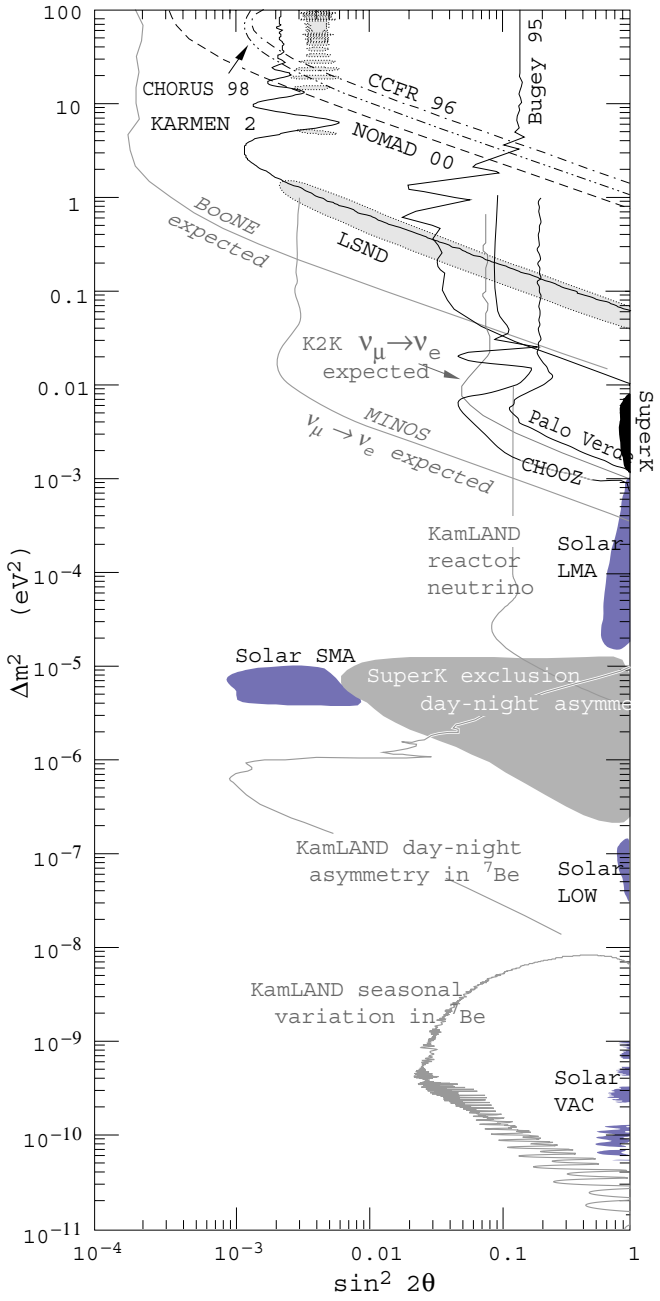

Fig. 1. Phase-space for neutrino oscillations. The existing limits on $\nu_e - \nu_\mu$ are compared with current and future experiments and the regions obtained by interpreting the solar, atmospheric and LSND neutrino anomalies as due to oscillations (note that some of these three effects are not necessarily to be regarded as oscillations of the $\nu_e - \nu_\mu$ type). The MSW mechanism is used in plotting some of the solar neutrino regions. The sensitivity of reactor experiments is the same for $\nu_e - \nu_\tau$ oscillations. Limits are at 90% CL. The two bottom KamLAND sensitivity curves refer to direct solar neutrino observations that are not discussed in this paper.

fully develop, the resulting atmospheric neutrinos therefore are expected to follow the $\nu_\mu : \nu_{\rm e} = 2 : 1$ ratio, which is essentially independent of the details of the complicated process that created them. In addition, in an underground detector, one can deduce the direction of the incoming neutrinos from the direction of the leptons (e and μ) created by the charged current interactions. Again, one is reasonably confident that this zenith angle distribution can be accurately predicted. If the ν_μ and/or $\nu_{\rm e}$ neutrinos oscillate, one expects deviations from the 2:1 ratio mentioned above. Also, since the zenith angle is simply related to the neutrino path length, one expects deviations from the expected zenith angle dependence of the lepton yield.

Both signatures of neutrino oscillations were in fact observed. The ν_μ/ν_e ratio is noticeably smaller, only about 60%, than the expected value. This result has been confirmed in four detectors thus far. The anomalous zenith angle dependence was first observed in Kamiokande, and has been now confirmed, with much better statistical significance, by SuperKamiokande. If these effects indeed signify neutrino oscillations (and we do not have another viable explanation) then the corresponding mixing angle is large, $\sin^2 2\theta \approx 1$. The value of the mass parameter Δm^2 remains uncertain, but is clearly in the range 10^{-2} - 10^{-4} eV^2.

The second set of measurements that can be interpreted as evidence for neutrino oscillations deals with the "missing" solar neutrinos.[8] The Sun produces an intense flux of electron neutrinos as a byproduct of the fusion reactions which generate solar power. It is believed that the solar structure is understood sufficiently well so that the flux and energy spectrum of the solar neutrinos can be confidently predicted. The solar neutrino fluxes have been measured in five experiments so far. All of them report a deficit, i.e., the measured flux is less than the expected one. Moreover, the reduction depends on the neutrino energy, inferred experimentally from the thresholds of the individual detectors. The only viable explanation of the deficit appears to be neutrino oscillation (ν_e disappearance). By contrast to the attempts to explain the deficit by modification of the solar model, which are unsuccessful, all existing data can be simply and elegantly explained by invoking neutrino mass. In particular, the solution based on the MSW effect offers the most popular scenario. Treating the problem in the two-flavor framework explained above, one arrives at two isolated islands in the Δm^2 – $\sin^2 2\theta$ plane. Both solutions correspond to $\Delta m^2 \approx 10^{-5}$ eV^2. One of them has rather small $\sin^2 2\theta \approx 10^{-2}$. The other one has much larger mixing angle, $\sin^2 2\theta \geq 0.5$. This solution also spans a larger interval of Δm^2 extending up to 10^{-4} eV^2.

Finally, the only indication for oscillations involving man-made neutrinos comes

from the LSND experiment which finds evidence for the $\bar{\nu}_\mu \rightarrow \bar{\nu}_\mathrm{e}$ and, with more limited statistics, also for $\nu_\mu \rightarrow \nu_\mathrm{e}$.[9] The former channel uses neutrinos from the pion and muon decay at rest, with energies less than $m_\mu/2$. The latter channel uses neutrinos from the pion decay in flight which have somewhat higher energies. These are appearance experiments; the observed signal should be absent if neutrinos do not oscillate. The well determined quantity is the oscillation probability, which has the value of about 3×10^{-3}. This result has not been independently confirmed but it is not contradicted by other evidence either.

As we can see from this brief discussion, the last decade brought us a number of clues. With the exception of the LSND signal, they all came from measurements involving neutrinos produced by natural sources outside of our control. A number of new experiments has been performed or is in various stages of planning in order to investigate further these tantalizing effects. Reactor experiments play an all-important role in this quest, owing to their unique ability to investigate very small neutrino-mass differences.

Like in many other aspects of neutrino physics there is a fundamental difference between the past reactor oscillation experiments[10–13] and the more recent experiments with baselines of 1 km or more: experiments in this last category are designed to further investigate in a controlled environment, with man-made neutrinos, particular regions of the oscillation parameter space where we do have indications for oscillation from other experiments. Hence the results from this new generation of detectors directly impact our understanding of the neutrino mixing matrix.

2.2 Reactor versus accelerator-based oscillation experiments

Nuclear reactors produce isotropically $\bar{\nu}_\mathrm{e}$ in the β decay of the neutron-rich fission fragments. All detectors optimized for oscillation searches take advantage of the relatively large cross-section and specific signature of the inverse-β-decay reaction $\mathrm{p} + \bar{\nu}_\mathrm{e} \rightarrow \mathrm{n} + \mathrm{e}^+$. This cross-section is shown in Figure 2 as a function of the neutrino energy along with the the neutrino flux at the reactor and the resulting interaction rate in a detector. We note here that the detection reaction has a threshold of about 1.8 MeV, as will be discussed in more detail later. Many of the merits and limitations of reactor-based experiments can be understood observing that the energy of $\bar{\nu}_\mathrm{e}$ is rather low, in the few-MeV range. It directly follows that reactor-based experiments can only be of $\bar{\nu}_\mathrm{e}$-disappearance type since the neutrino "beam" does not have sufficient energy to

produce muons (or τs !) and the neutral-current reaction of an "oscillated" $\bar{\nu}_\mu$ or $\bar{\nu}_\tau$ on electrons has too low a cross-section and is indistinguishable from the many backgrounds present. This first limitation makes reactor-based experiments well suited only for investigating relatively large mixing parameters. In practice experiments have reported mixing sensitivities around 10% at large Δm^2 (although the proposal for a very ambitious experiment with sensitivity better than 2% at a particular Δm^2 will be discussed later). The second limitation of reactor-based oscillation searches derives from

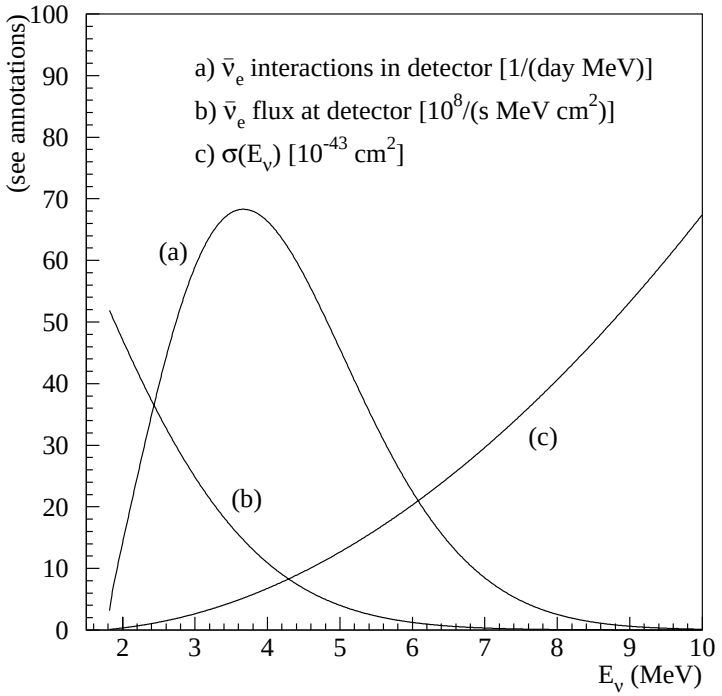

Fig. 2. $\bar{\nu}_e$ flux, inverse beta decay cross section, and $\bar{\nu}_e$ interaction spectrum at the detector.

the fact that the only known method of collimating neutrino beams employs the Lorentz boost of the parent particles from which decay the neutrinos are produced. For this reason low energy neutrinos are generally produced over large solid angles while high energy ones may come in relatively narrow beams. Obviously a reactor emits $\bar{\nu}_\mu$ in a completely isotropic way, and this, together with the modest interaction cross-sections available at low energy, make the specific signal rather low. At the same time, however, the low energy neutrinos provide us with a unique opportunity to probe the lowest regions of Δm^2 that are otherwise beyond the reach of accelerator-based searches. Some

of these tradeoffs are well illustrated by Figure 3 where the Δm^2 sensitivity is shown, together with the necessary baseline, versus the reactor power and detector fiducial mass for different statistical accuracies.

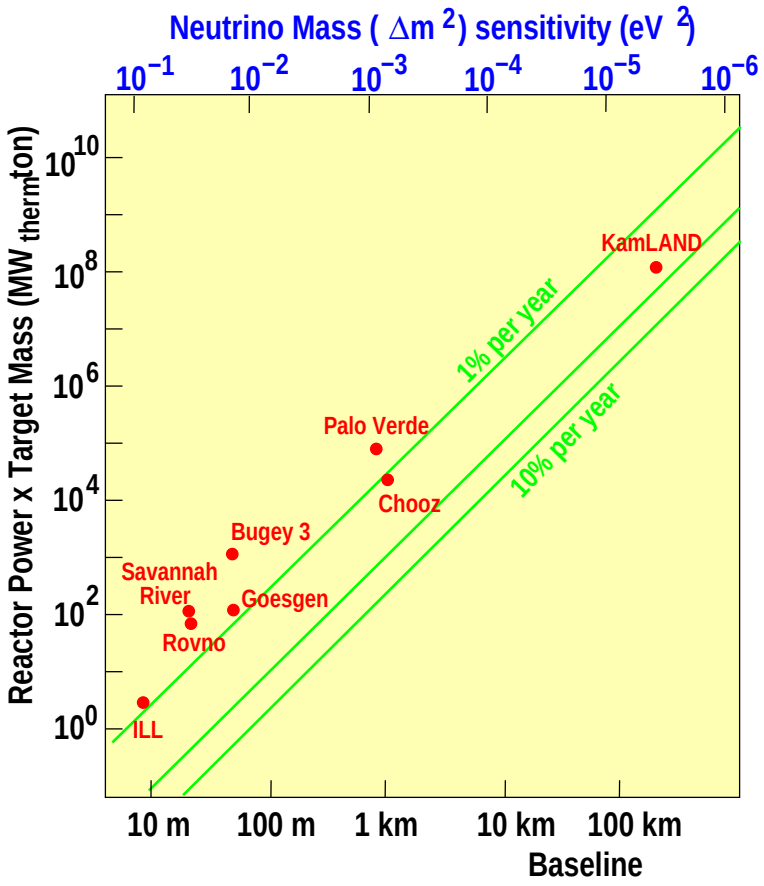

Fig. 3. Neutrino Δm^2 sensitivity as a function of total reactor power and detector fiducial mass for detection based on the inverse-β reaction discussed in the text. The baseline scales with the Δm^2 sensitivity sought, according to Eq. 7. The fiducial-mass$\times$power necessary for the experiment grows with the square of the baseline.

Oscillation searches using reactors as sources are particularly important today since several of the indications for neutrino oscillations shown in Figure 1 point to regions of the parameter space at very small Δm^2 and nearly-full mixing. Hence two reactor-based experiments were performed to investigate the phenomenon of atmospheric neutrinos as $\bar{\nu}_{\rm e} - \bar{\nu}_{\rm X}$-oscillations. Such experiments, described in detail below, had baselines of about 1 km and fiducial masses of the order of 10 tons. In comparison the

accelerator-based Minos project between FNAL and the Soudan mine[9] will access similar Δm^2 values with GeV-energy neutrinos and a baseline of the order of 1000 km. However the 5.4 kton Minos detector will be able to investigate also oscillation channels not including $\bar{\nu}_{\rm e}$ and reach a mixing parameter sensitivity substantially better than 1%.

The reactor-based KamLAND experiment, with a baseline larger than 100 km, will offer the unique opportunity of testing, with man-made neutrinos, the large-mixing-angle MSW solution of the solar neutrino puzzle. In this case the restriction to $\bar{\nu}_{\rm e} - \bar{\nu}_{\rm X}$-oscillations does not limit the interest of the experiment (since solar neutrinos do certainly involve $\nu_{\rm e}$!), while its Δm^2 sensitivity is well beyond what can be practically achieved by accelerators. (For comparison, similar Δm^2 sensitivity could be achieved in an accelerator-based experiment with baselines of order 10^5 km, larger than the diameter of the earth.)

Of course the relatively lower energy of neutrinos from reactors pushes the optimization of reactor-based experiments to concentrate on the reduction and rejection of backgrounds from natural radioactivity that is, on the other hand, hardly an issue in accelerator-based detectors. In this respect the correlated signature from the inverse-β process described plays a very important role, as will be described in detail later.

While in the case of neutrinos produced by accelerators the experimenter has full control over the status of the beam, the flux of $\bar{\nu}_{\rm e}$ cannot be changed at will in commercial power nuclear reactors. However, in practice, typical reactor optimization requires a refueling shutdown every 12 to 24 months. Such shutdowns usually last about a month, providing a rather convenient flux modulation that can be used to validate background subtraction methods. As explained in detail later, even in the case of KamLAND, which observes the neutrinos from about 70 reactor cores, a substantial flux modulation is provided by the coincidence of scheduled refueling outages in the Spring and Fall periods, when electricity demand is lowest.

Finally we remark here that the fully isotropic flux produced by nuclear reactors eliminates the problems related with beam pointing that are present in experiments using accelerators. While the pointing accuracy required in these experiments is well within the present technology, a fool-proof cross check of the beam-detector alignment is certainly not trivial to obtain.

In conclusion, reactor-based and accelerator-based experiments offer complementary approaches to the quest for neutrino oscillations. It is likely that only the combined efforts on these two fronts, together with other studies such as the search for

neutrino-less double-β decay, will allow us to elucidate the problem of mixing in the lepton sector.

3 Neutrino spectrum and flux determination

Since reactor-based oscillation experiments are of the disappearance type, the accurate determination of the $\bar{\nu}_{\rm e}$ spectrum and absolute normalization at the reactors is an essential ingredient of the measurements. We note here that for oscillation parameters well within the experiment's sensitivity the evidence for oscillations would manifest itself as a deficit of events accompanied by a distortion of the energy spectrum, as shown by the example[14] in Figure 4. However, as the true value of the oscillation parameters moves closer to the sensitivity boundary of the experiment, the spectral shape loses power and the accuracy of the measurements essentially relies on the total event count and, hence, the knowledge of the absolute reactor flux. This last scenario also corresponds to the more usual case in which no oscillations are observed and an upper limit is set.

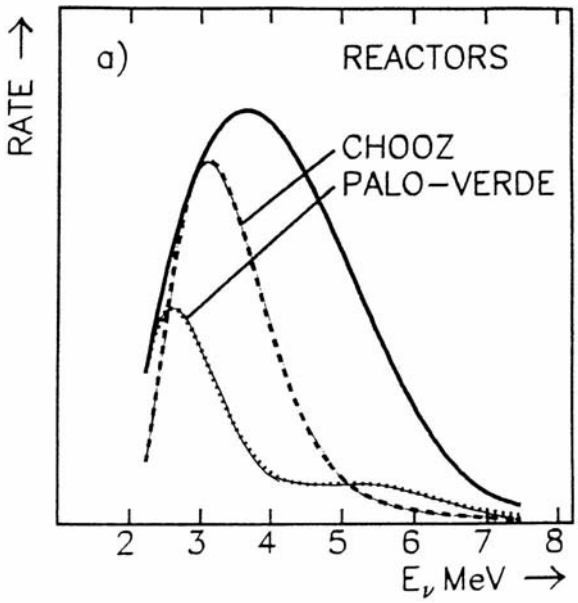

Fig. 4. Expected energy spectra[14] for no oscillations and oscillations with parameters $\Delta m^2 = 7.2 \times 10^{-3}$ eV^2 and $\sin^2 2\theta = 1$ at the Chooz ($L \simeq 1$ km) and Palo Verde ($L \simeq 0.8$ km) experiments.

While in this section we will concern ourselves mainly with *a priori* reactor $\bar{\nu}_{\rm e}$ yield determinations, multiple-baseline measurements are possible and have been performed

in the past at the Goesgen[11] and Bugey[12,13] reactors. Indeed such measurements helped in gaining confidence in the reactor yield estimates, and, although they were not attempted by Palo Verde and Chooz, they have been recently proposed for a more accurate determination of the mixing angle θ_{13} for the atmospheric neutrino region $\Delta m^2 \approx 10^{-3}$ eV^2.[15]

We note that, while the methods described here are very general, most of the details discussed in this section specifically derive from the Palo Verde experiment.[16]

3.1 Anti-neutrino production

The estimate of the $\bar{\nu}_{\rm e}$ yield proceeds, schematically, in three steps. First the thermal power of each reactor core is measured, generally daily, so that, starting from the initial fuel composition, the burn-up state can be computed as function of time. Small corrections due to other reactor parameters that modify the criticality of the core are also introduced at this time. Reactor simulation codes are often used at this stage and produce an accurate instantaneous fission rate throughout the fuel cycle. In a second step the neutrino spectrum is derived from the fission rate. Generally both data from direct β^- measurements for three of the dominant fissile isotopes and theoretical estimates are used. These two approaches give consistent results. In the final step an experimental e^+ spectrum in the detector is derived and compared with data.

It should be stressed that a good over-all cross check of this procedure is provided by the inspection of older (shorter baseline) experiments. The coincidence of their measured spectrum with the prediction based on the procedure described above can be interpreted as if the older experiments were, as far as many of the errors are concerned, near detectors in a two baseline measurement. This is so because, unlike for the case of accelerator-produced neutrinos, most commercial reactors are remarkably similar to each other in terms of neutrino production and there are no beam focusing or steering effects. All this notwithstanding, there are certain advantages in real two-baseline measurements, as will be discussed in a later section.

It is useful here to mention that typical modern commercial Light Water Reactors (LWR) have thermal powers of the order of 3 GW$_{th}$. This figure applies to both Pressurized Water Reactors (PWR) and to the less common Boiling Water Reactor (BWR) designs. In both cases the fuel is enriched to $2-5\%$ ^{235}U. Since on average a fission produces $\sim$ 200 MeV and ~ 6 $\bar{\nu}_{\rm e}$ we conclude that the typical yield is $\sim 6 \times 10^{20}$ $\bar{\nu}_{\rm e}$ core^{-1} s^{-1} (of course part of this flux will be below the detection

threshold, see Figure 2).

The existence of a 1.8 MeV threshold in the detection process $\bar{\nu}_{\rm e} + {\rm p} \rightarrow {\rm n} + {\rm e}^{+}$ insures that the observed $\bar{\nu}_{\rm e}$ signal tracks very closely in time the power excursions in the reactor. In fact only $\bar{\nu}_{\rm e}$ from large Q-value, and hence short half-life, β-decays are detected. This is of some practical importance as large quantities of spent fuel are usually stored on-site by reactor operators. There is no need to track the inventory of spent fuel and, in fact, after a few hours from reactor turn on/off the $\bar{\nu}_{\rm e}$ flux can be considered to be at regime.

3.2 Fission-rate estimates

The four isotopes whose fission and decay chains are the source of virtually all the power and neutrino yields are ^{235}U, ^{238}U, ^{239}Pu, and ^{241}Pu. The fission rates deriving from their evolution during a typical fuel cycle in one of the Palo Verde reactors is shown in Figure 5 as calculated by a core simulation program.[16] For comparison we also show the evolution of ^{240}Pu and ^{242}Pu which give the next-to-leading contributions. The contribution of these isotopes is of order 0.1% or less and will not be considered further.

Each isotope produces a unique neutrino spectrum through its decay chain, so plutonium breeding results in a significant change in the emitted neutrino spectrum.

Two types of errors can be attributed to the isotope compositions described in Figure 5: errors deriving from uncertainties in the initial fuel composition and in the measurement of the plant parameters that are used as input to the simulation, and errors due to imperfect core and neutronics modeling by the simulation program itself. The errors intrinsic to the simulation are known to contribute substantially less than 1% to the neutrino yield uncertainty, from tests in which fuel is sampled and analyzed for isotopic composition at the end of a fuel cycle. The results usually agree well with the predictions from the cycle simulation.

The correlation between the $\bar{\nu}_{\rm e}$ yield and the plant parameters used as input to the simulation is shown in Figure 6. Apart from the obvious correlation with the thermal power, other parameters enter the simulation because they affect the criticality by altering the neutron transport in the core (generally by the water density and boron absorber concentration). In general we see that for the parameter with largest correlation besides power, the cold legs water temperature (“T inlet”), an error of 10% produces an uncertainty of only 0.15% in the $\bar{\nu}_{\rm e}$ yield. Of course the inlet temperature is known to much

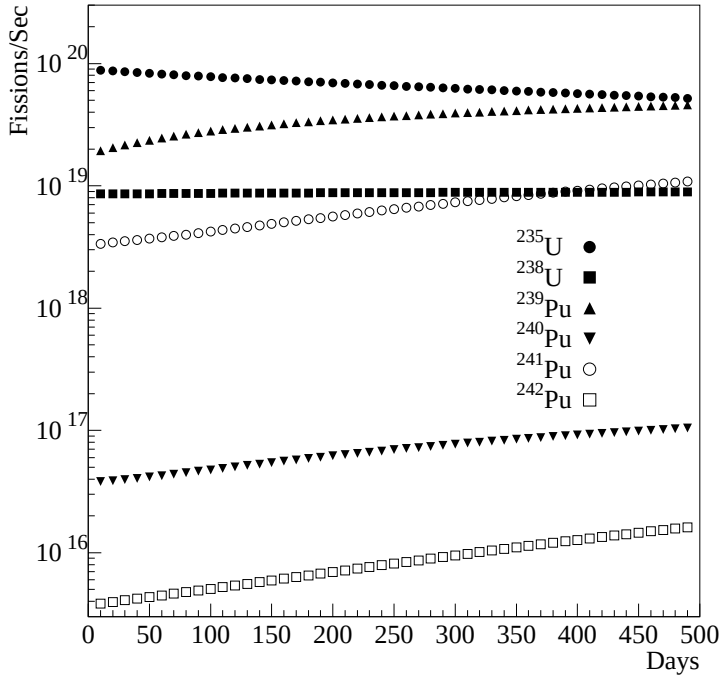

Fig. 5. Time evolution of fission rates for each of the six most important isotopes in one of the Palo Verde reactor cores. The horizontal scale covers a full fuel cycle, at the end of which about 1/3 of the core is replaced with fresh fuel. Only the four most important isotopes are normally used to predict $\bar{\nu}_e$ yields.

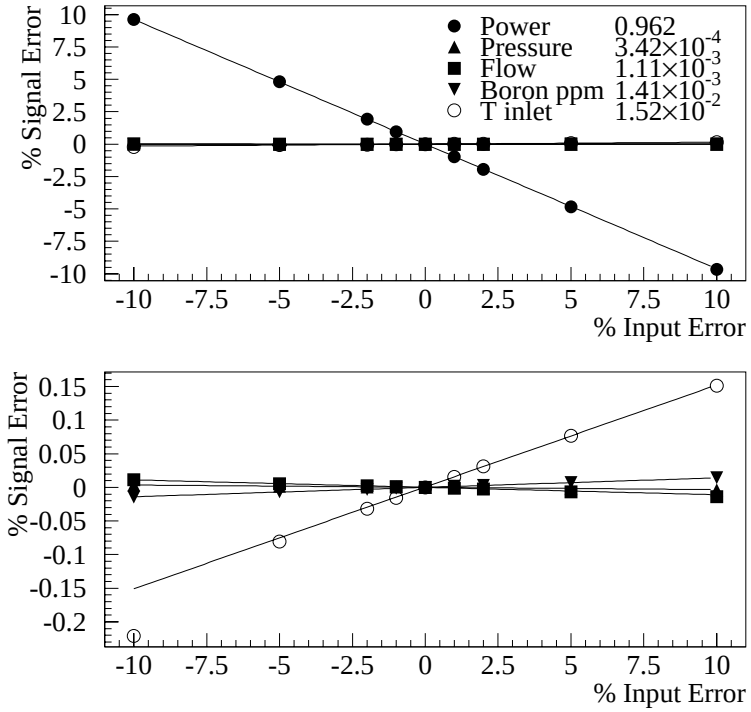

Fig. 6. Correlation between $\bar{\nu}_e$ yield and the five most important inputs to the core simulation for a PWR. The numbers in the key are the slopes of the fitted lines. Note that a variation of even 10% in any of the parameters, except power, has little effect on the output of the simulation.

better than 10%.

Economic reasons and safety provide plant operators with an incentive to accurately measure the thermal power of the reactors. Indeed, usually more than one method is used and the results are compared to understand the size of the uncertainties. Generally calorimetric methods (simultaneous measurement of temperature and flow-rate of the water outlet in the secondary cooling loop) give the smallest error (0.7% at Palo Verde) and are used as the primary power estimate.

3.3 From fission rates to $\bar{\nu}_e$ and e^+ spectra

The instantaneous fission rates of the four isotopes ^{235}U, ^{238}U, ^{239}Pu, and ^{241}Pu found above are then converted into a $\bar{\nu}_e$ spectrum. For all but ^{238}U direct measurements of the beta spectrum from fissioning by thermal neutrons exist.[17,18] These are converted to neutrino spectra by fitting the observed β spectra to a set of 30 hypothetical β-branches. However, Refs.[17,18] do not include ^{238}U fission, which requires faster neutrons than were available for those measurements. While this is unfortunate and a measurement

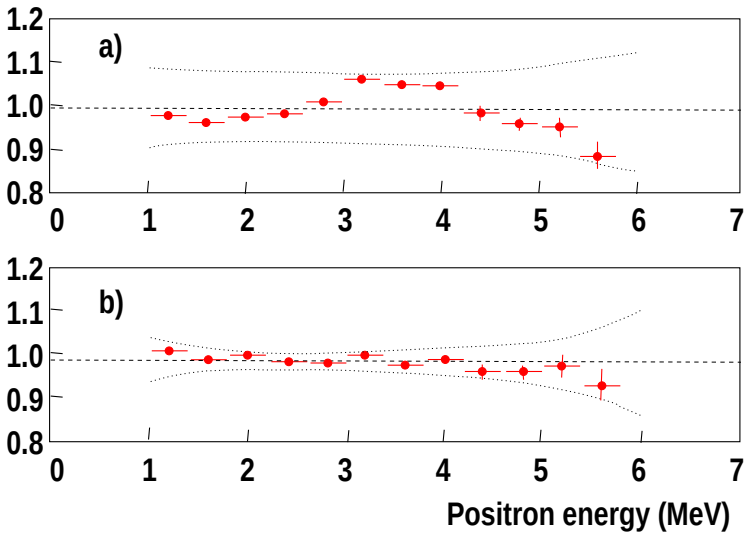

Fig. 7. Ratio between Bugey 3 measurements and different predictions.[13] In a) the measurements are compared to *a priori* calculations.[20] In b) Bugey 3 data is compared to the prediction obtained using β spectra measurements[17,18] (and the calculation mentioned for ^{238}U). The dashed envelopes are estimates of the overall systematics.

would certainly be welcome, the lack of data is of no major practical consequence

since ^{238}U only contributes $\sim 8\%$ to the total power and $\sim 11\%$ to the neutrino signal. *A priori* theoretical calculations of the β spectrum have been performed[19,20] for each of the four isotopes discussed here. These calculations typically consider the decays of ~ 750 isotopes, of which ~ 250 have measured β spectra. As shown in Figure 7 a), a rather good agreement was found between the calculated spectra and the ones measured, as described above, for ^{239}Pu, ^{241}Pu and ^{235}U. In terms of integrated flux above threshold the agreement is certainly better than 10%. Hence it is assumed that using the calculation for ^{238}U should produce an additional error of the order of better than 1%.

Finally the neutrino spectrum emitted by the reactors must be converted into an estimate of the experimental observable, the positron spectrum in the detector. Assuming no oscillations, there are three contributions to this calculation: the distance to each core, the cross section for $\mathrm{p} + \bar{\nu}_\mathrm{e} \longrightarrow \mathrm{n} + \mathrm{e}^+$, and the number of target protons.

The distance to the reactors is of course trivially obtained with negligible uncertainty. The cross section for inverse-β decay has been calculated[21] and also the angular distribution.[22] The lowest order cross section was modified for several effects such as neutron recoil, weak magnetism, and radiative corrections. The estimated accuracy of the resulting modified cross section is about 1%.

The number of protons in the target requires knowledge of the chemical composition and mass of both scintillator and possible other detector materials where $\bar{\nu}_\mathrm{e}$ can be captured and recorded with finite efficiency. Typically errors smaller than 1% are achievable for this parameter.

3.4 Accuracy of the flux and spectrum predictions

The ultimate check of the accuracy of the prediction outlined above consists of comparing the results, in terms of the $\bar{\nu}_\mathrm{e}$ energy spectrum, with the measurements performed in short baseline reactor oscillation experiments. Since such experiments have not reported the observation of oscillations we can assume that their measurements represent the direct observation of the reactor spectrum at production. This statement is reinforced by the fact that some of the short baseline experiments such as Gösgen[11] or Bugey[12,13] did measurements at different baselines, observing no difference between the spectra. This is shown for Gösgen in Figure 8. In particular the relatively recent Bugey 3 measurements were performed at 15-40 m distance from the core and recorded very high statistics (some 1.5×10^5 $\bar{\nu}_\mathrm{e}$ events). The good agreement between Bugey 3

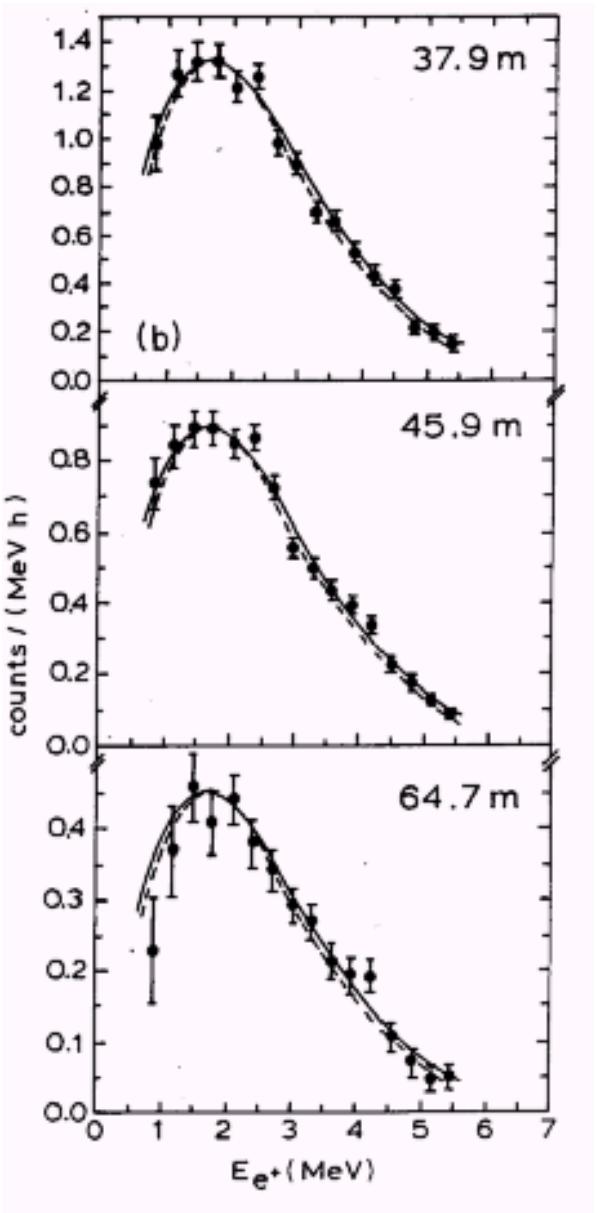

Fig. 8. Positron spectrum observed by the Gösgen experiment for three different baselines. The continuous lines represent fits to the predictions obtained, as described in the text, using ILL data and theoretical calculations.

data and the non-oscillation predictions is shown in Figure 7. In panel a) the prediction is generated purely from theory. Of more practical importance is panel b) where the prediction derives from β spectra (except for ^{238}U where theory is used). In this case a fit to an horizontal line gives a level of 0.99 with $\chi^2/d.o.f. = 9.2/11$. The final Bugey 3 result is quoted as having a 1.4% total uncertainty.

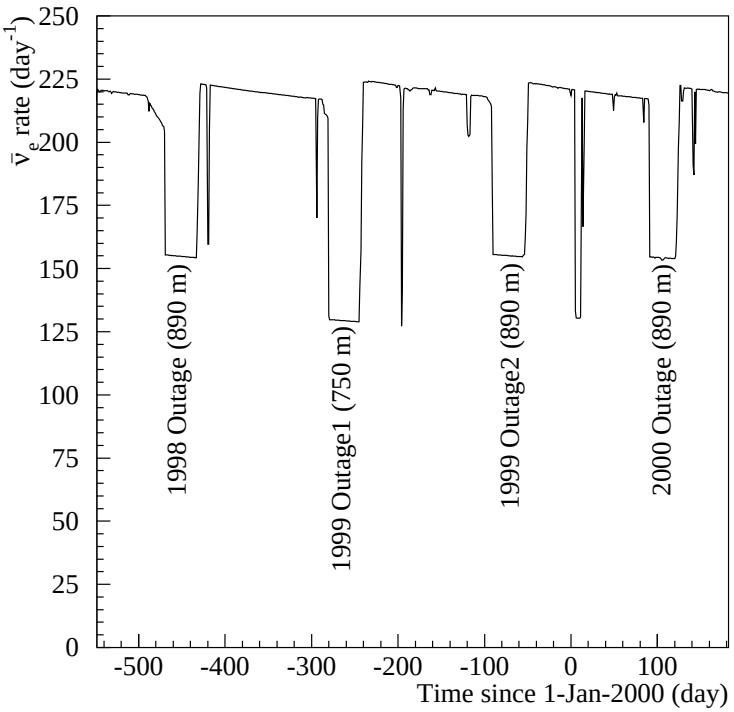

Fig. 9. Expected number of $\bar{\nu}_e$ interactions in the Palo Verde detector during the $\sim$2 years of data-taking of the experiment. The history displayed is rather typical for a multi-core power plant with regular refueling periods (about 1 month-long each) and unscheduled reactor trips. Note that one reactor is closer to the experiment while the other two are equidistant, this explains the different excursion for one of the refuelings. The steady decline in $\bar{\nu}_e$ interactions during the cycle is the effect of fuel burn-up.

For reference we give in Figure 9 the time evolution of the $\bar{\nu}_e$ interaction rate expected in the Palo Verde detector, calculated as described above from the plant data. The time evolution is typical of a plant with more than one reactor. Refueling outages (about 1 month long each) have different amplitudes because of the different distances between the reactors and the detector. Short accidental reactor trips are also visible along with the steady rate decline through the reactor cycle due to fuel burn-up.

4 Experiments motivated by the atmospheric neutrino anomaly

Two experiments have been built with the specific purpose of testing the hypothesis that neutrino oscillations occur with the parameters found by the atmospheric neutrino measurements. While Chooz is completed and all their data is published,[23,24] data-taking at Palo Verde finished in the summer 2000 and results from the first half of the data-set are published.[25,26] Palo Verde data presented here refers to this first half of the data-set, while the analysis of the second half should be published soon.

As can be seen from Figure 3, in order to access $\Delta m^2 \approx 10^{-3}$ eV^2 with reactor neutrinos, a baseline of order 1 km and a mass in excess of a few tons are needed. Indeed the backgrounds from cosmic radiation and natural radioactivity are a major consideration in the design of such large, low-energy detectors, and different background situations led the two groups to rather different designs.

The Chooz detector was built in a pre-existing underground cavity under a $\simeq 100$ m rock overburden ($\simeq 300$ m.w.e). This substantial cosmic radiation shielding allowed the use of a homogeneous detector where inverse-β events were tagged as a double (delayed) coincidence between the e^+ (prompt) signal and the n (delayed) one. In turn this simple event signature can be identified with large efficiency, so that a 5 ton active mass was sufficient for the experiment. The Palo Verde detector, on the other hand, was located in an underground bunker excavated for the purpose. Economic considerations limited the overburden to 12 m ($\simeq 32$ m.w.e.) sufficient only to eliminate the hadronic component of the cosmic radiation and reduce the muon flux by a factor of five. The rather large remaining muon flux produced a substantial quantity of secondary neutrons, so that a segmented detector was needed to take full advantage of the triple coincidence given by the e^+ ionization and subsequent γ's from annihilation. This more elaborate topological signature reduced the detector efficiency and pushed the fiducial mass to 12 ton. Both detectors were built with materials selected for low radioactivity and included a passive γ and neutron shield and an active cosmic-ray veto counter.

While the 3-reactor plant of Palo Verde produces a larger power (11.6 $GW_{\rm ther}$) than the 2-reactor one at Chooz (8.5 $GW_{\rm ther}$), more important is the fact that, unlike in the case of Palo Verde which was a plant running at regime, the Chooz reactors were commissioned after the start of data taking at the experiment. This endowed the collaboration with the rather unique opportunity of observing the backgrounds at reactor-off for a substantial period and the slow ramp-up of power. On the other hand

the need to cope with a much more stable operation, with the periodic $\sim 2/3$ refueling power excursions shown in Figure 9, motivated the Palo Verde group to develop new methods for background subtraction that will be important for future experiments that will be likely to run in similar steady-state situations.

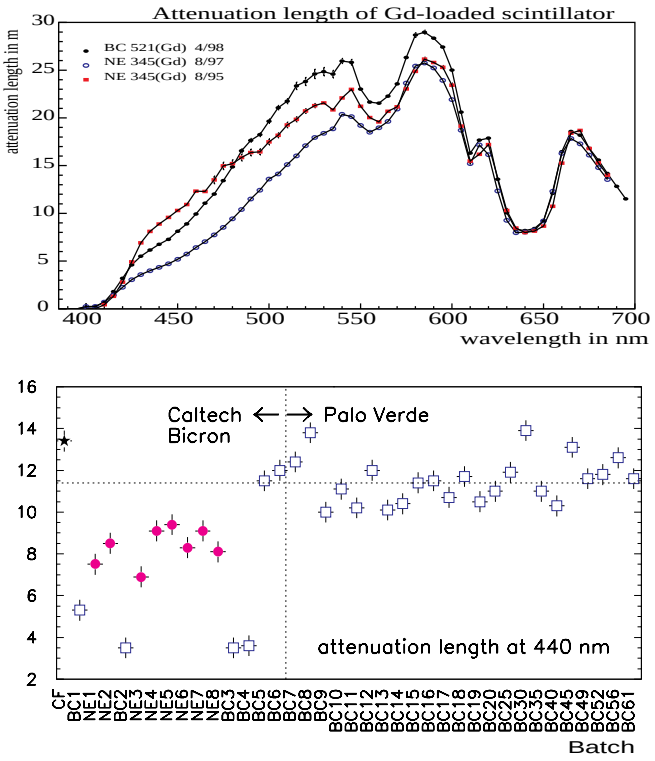

Fig. 10. Initial light attenuation length in Palo Verde scintillator. Top: attenuation length as function of wavelength in three scintillator batches. Bottom: attenuation length at $\lambda = 440$ nm for the initial batches of scintillator. Production batches are to the right of the vertical dashed line, while on the left we show various test batches not used in the detector. The first point ("CF") refers to a standard (non Gd loaded) scintillator fluid. Typical production scintillator had an attenuation length better than 11 m.

Both detectors used liquid scintillator loaded with 0.1% natural gadolinium, which has a high thermal neutron capture cross-section and releases a large amount of energy in the capture. In this way the neutron capture time is reduced to $\sim$27 μs from $\sim$170 μs for the unloaded scintillator, proportionally reducing the uncorrelated background. Furthermore, Gd de-excitation after the capture releases a 8 MeV γ cascade, whose summed energy gives a robust event tag well above natural radioactivity. In contrast, neutron capture on protons releases only a single 2.2 MeV γ. While the Gd loading offers obvious advantages in suppressing backgrounds, it is not easy to achieve

in the stable and sufficiently transparent form needed for a large detector. Both groups invested substantial resources in scintillator development. In Figure 10 we show initial attenuation length data for the Palo Verde scintillator, which was a cocktail of 60% mineral oil, 36% pseudocumene (1,2,4 trimethylbenzene) and 4% alcohol (used to keep the Gd compound in solution), with PPO as primary fluor. This scintillator had a H:C ratio of $\simeq 2$ and a light yield of 56% of anthracene, with typical light attenuation length greater than 11 m at $\lambda = 440$ nm.[27] The time stability of the same scintillator is shown

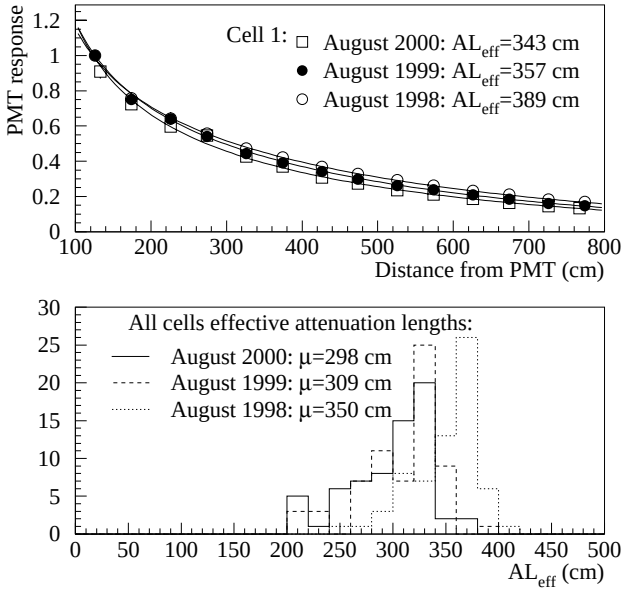

Fig. 11. Evolution of scintillation-light attenuation-length in Palo Verde scintillator during the two years of life of the detector. Top: the attenuation curve for scintillation events at different locations along one of the 9 m-long cells. Bottom: *effective* attenuation values for all detector cells. Note that the shorter value of the effective attenuation length reflects the non-trivial optics of the cells.

in Figure 11 where the light attenuation curve for one cell and the *effective* attenuation length for all cells are presented as measured three times, at one year intervals. The 12% loss in the first year decreases to 3% in the second, possibly indicating a gradual stabilization.

4.1 Chooz

The Chooz detector was built at a distance of $\simeq 1000$ m from the two reactors of the new Chooz power plant of *Électricité de France* in the Ardenne region of France. The plant, shown in Figure 12, has a total thermal power of 8.5 GW_{th} and the two reactors reached full power in, respectively, May and August 1997. The experiment took data from April 1997 until July 1998, in the conditions specified in Table 1. The

Fig. 12. Aerial view of the Chooz power plant. The detector is located in a tunnel under the hills on the bottom right of the photograph.

detector, schematically shown in Figure 13, consisted of a central volume of 0.1% Gd-loaded scintillator with a mass of 5 tons, where $\bar{\nu}_{\rm e}$ were detected. This scintillator was contained in an acrylic vessel which separated it from a 70 cm thick shielding layer of mineral oil. 192 eight-inch photomultipliers (PMT's) were mounted onto a steel vessel which in turn isolated, mechanically and optically, the central detector from the outer veto counter. The central detector had a photocathode coverage of 15% and a light yield of ~ 130 photoelectrons/MeV (p.e./MeV).[28] The 90 ton veto scintillator was at least 80 cm thick and was read out with two rings of 24 eight-inch PMT's, the

	Time (h)	$\int W_{th} dt$ (GWh$_{th}$)
Total run	8761.7	
Live	8209.3	
Dead	552.4	
Reactor 1 ON only	2058.0	8295
Reactor 2 ON only	1187.8	4136
Both reactors ON	1543.1	8841
Both reactors OFF	3420.4	0

Table 1. Summary of the Chooz data-taking conditions.

outer containment tank being painted with white reflective paint. An outer layer (75 cm thick) of low-activity sand provided primary shielding from the rock. Laser flashers were installed to monitor the detector performance and radioactive sources could be inserted into the central region of the detector through special pipes. The detector energy response was calibrated daily with ^{60}Co, ^{252}Cf and AmBe γ- and n-sources in order to accurately track the aging of the scintillator. As an example we show in Figure 14 the results of a Cf calibration run with the source placed in the middle of the detector. Data is compared with a Monte Carlo simulation for the reconstruction of the x, y and z positions and total energy in the detector. Both the peaks for n-captures on p (2.2 MeV) and Gd (8 MeV) are clearly visible. The very good energy resolution ($\sigma(E)/E = 5.6$ % at 8 MeV) allows one to verify that the 8 MeV line is in fact the superposition of a 7.77 MeV line with 77% weighting from capture on ^{157}Gd and a 8.31 MeV line with 23% weighting from capture on ^{155}Gd. The fit to these two Gaussians gives $\chi^2/\mathrm{d.o.f.} = 67.6/55$ while the fit to a single Gaussian is very poor with $\chi^2/\mathrm{d.o.f.} = 875/58$. The position resolution was found to be $\sigma_x = 17.5$ cm.

4.2 Palo Verde

The Palo Verde experiment was built at the Palo Verde Nuclear Generating Station, the largest nuclear plant in the Americas, ~ 80 km west of Phoenix, in the Arizona desert. The total thermal power from three identical pressurized water reactors is 11.6 GW. Two of the reactors were located 890 m from the detector, while the third was at 750 m. The shallow underground bunker housing the detector is shown in Figure 15 at the

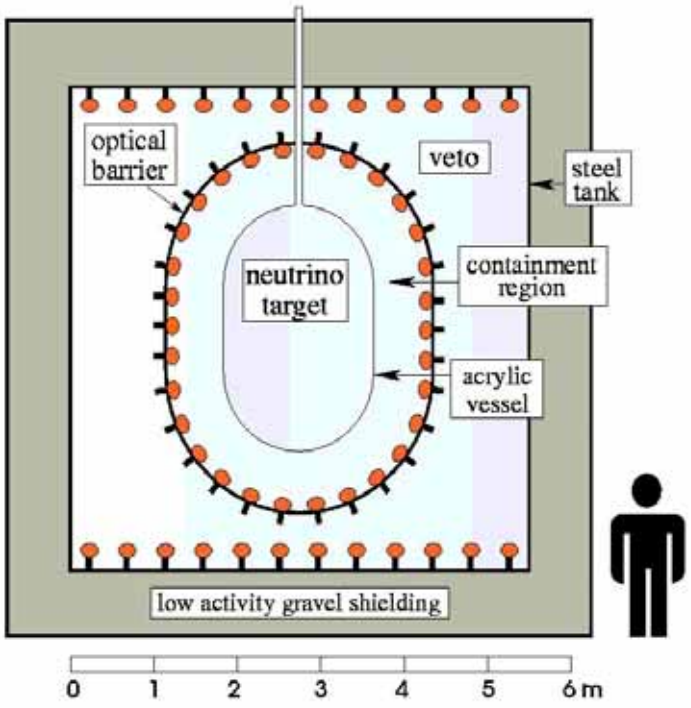

Fig. 13. Schematic drawing of the Chooz detector.

time of construction. In total 353.10 days of $\bar{\nu}_{\rm e}$ data were collected at Palo Verde in the period between October 1998 and July 2000, covering four scheduled refueling outages as indicated in Figure 9 above. 243.65 days were at full power while 22.25 days (87.19 days) had the reactor(s) at 750 m (890 m) off. This data was complemented by frequent calibration runs.

The fiducial mass, segmented for active background rejection, consisted of 66 acrylic tanks filled with 0.1% Gd-loaded scintillator and arranged as shown in Fig. 16. Each cell was 9 m long, with a 12.7×25.4 cm^2 cross section, and it was viewed by two 5-inch photomultiplier tubes, one at each end. A $\bar{\nu}_{\rm e}$ is identified by space- and time-correlated $\rm e^+$ and n signals. Positrons deposit their energy in a scintillator cell and annihilate, yielding two 511 keV γ's that, in general, will be detected in different cells, giving a triple coincidence. Neutrons thermalize and are captured in Gd, giving a γ-ray shower of 8 MeV total energy also detected in more than one cell. The central detector was surrounded by a 1 m-thick water shield to moderate background neutrons produced by muons outside the detector and to absorb γ's from the laboratory walls. Outside

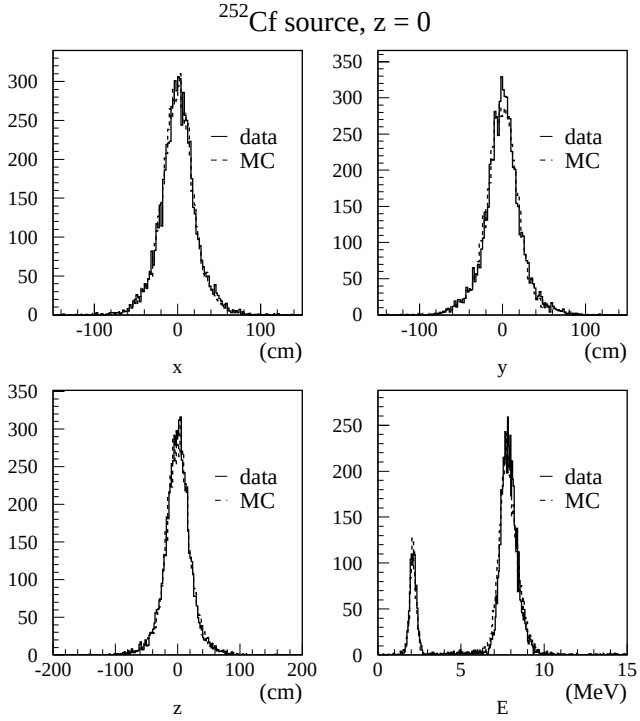

Fig. 14. Visible energy and position reconstructed for a calibration ^{252}Cf source placed inside the Chooz detector.

of the water tanks were 32 large liquid scintillator counters and two end-caps to veto cosmic muons. The rate of cosmic muons was approximately 2 kHz. The pattern of muons traveling through veto counters and their timing relative to the central detector hits were recorded for subsequent off-line analysis. The central detector was equipped with a system of tubes which allows the insertion of calibration sources in the small spaces between cells. In addition, a set of blue LEDs and optical fibers was used to produce flashes of light inside each of the cells. In order to reduce natural radioactivity, all building materials for the detector were carefully selected, including the aggregate (marble) used in the concrete of the underground laboratory.

Both the positron and the neutron were triggered by a triple coincidence requiring at least one cell above a "high" threshold set at about 600 keV (positron ionization or neutron shower core), and two cells above a "low" threshold set at about 40 keV (Compton scattering from annihilation photons or neutron shower tails). The triple coincidences were required to be within 3×5 matrixes anywhere in the detector as

Fig. 15. The Palo Verde underground laboratory at the time of construction (Fall 1996).

recognized by a custom-made trigger processor.[29]

The efficiency calibration was based upon a primary measurement performed a few times per year with a calibrated ^{22}Na e^+ source and an Am-Be neutron source. The ^{22}Na source was placed in the calibration pipes, mimicking the effects of the positron from the $\bar{\nu}_e$ interaction by providing annihilation radiation and a 1.275 MeV photon which simulates the e^+ ionization in the scintillator. The source was placed at 18 positions in the detector deemed to be representative of different conditions. The results of this procedure were then rescaled to the e^+ case using a Monte Carlo simulation. A final calibration using a ^{68}Ge source dissolved in the scintillator of one cell was performed at the end of the data-taking. The neutron detection efficiency was measured by scanning the detector with an Am-Be source where the 4.4 MeV γ associated with the neutron emission was tagged with a miniaturized NaI(Tl) counter. Other calibrations, used to measure the detector energy response, were performed using the Compton edges from ^{137}Cs, ^{65}Zn and ^{228}Th sources. The same Th source was also used more frequently to track the scintillator transparency, as already shown in Figure 11. Weekly runs of the fiber-optic and LED flasher systems were used, respectively, to monitor the gain and linearity of photomultipliers and the timing/position relationship along the cells.

Since the energy deposition of the 511 keV γ's in one cell has a sharply falling spec-

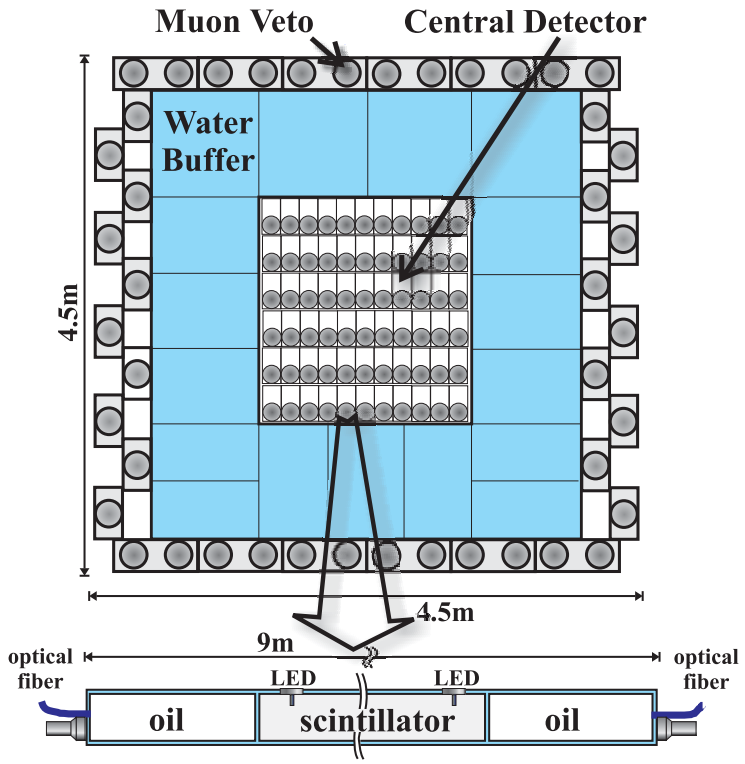

Fig. 16. Schematic view of the Palo Verde neutrino detector.

trum (Compton scattering) it was vital to have the lowest possible "low" thresholds in the trigger and to understand the behavior of such thresholds with great accuracy. This second task was complicated by the fact that the trigger used voltage amplitudes, while only charge from integrating ADCs was available off-line. For this reason the detector simulation included a detailed description of the signal development in time. This code correctly described the shape of pulses, taking into account scintillator light yield, attenuation length and de-excitation time; photomultiplier rise-time, fall-time and gain; and event position along a cell. The simulation of the detector response to the ^{22}Na source is shown in Figure 17 and correctly describes the 40 keV (600 keV) threshold position to within 1.4 keV (2.6 keV), resulting in an uncertainty on the positron (neutron) efficiency of 4% (3%).

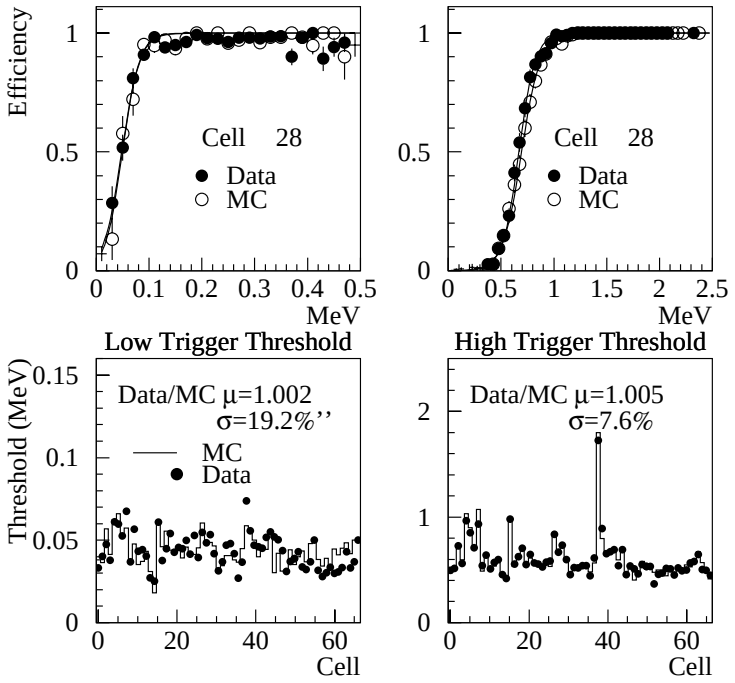

Fig. 17. A comparison of the trigger thresholds from data and Monte Carlo. The data were taken with a ^{22}Na source at the center of each cell. The top portion shows the efficiency of the trigger thresholds (low and high) for a typical cell as a function of energy deposited; the bottom shows the energy at 50% efficiency for low and high thresholds in all 66 cells.

4.3 Backgrounds

There are generally two types of background affecting long baseline reactor experiments: uncorrelated hits from cosmic-rays and natural radioactivity, and correlated ones from cosmic-μ-induced neutrons. The first type can be measured by studying the time difference between positron-like and neutron-like parts of an event. More insidious are cosmic-μ-induced neutrons, which present the same time correlation between prompt and delayed parts of the event as in $\bar{\nu}_{\rm e}$. Such events are schematically shown in the Palo Verde detector, in Figure 18. Neutrons are produced by cosmic-μ spallation and capture on the materials outside the veto counter. Both production mechanisms can result in either neutron thermalization and capture, where the thermalization process fakes the prompt triple coincidence, or secondary neutron production, where one of the captures fakes the prompt triple coincidence. Conceptually the same situation holds for

Chooz (and KamLAND, as will be discussed later), although differences in overburden and the simpler scheme of coincidence, numerically change the relative importance of different backgrounds. It is useful to point out that direct neutrons from the reactors have a totally negligible effect at the distances discussed here.

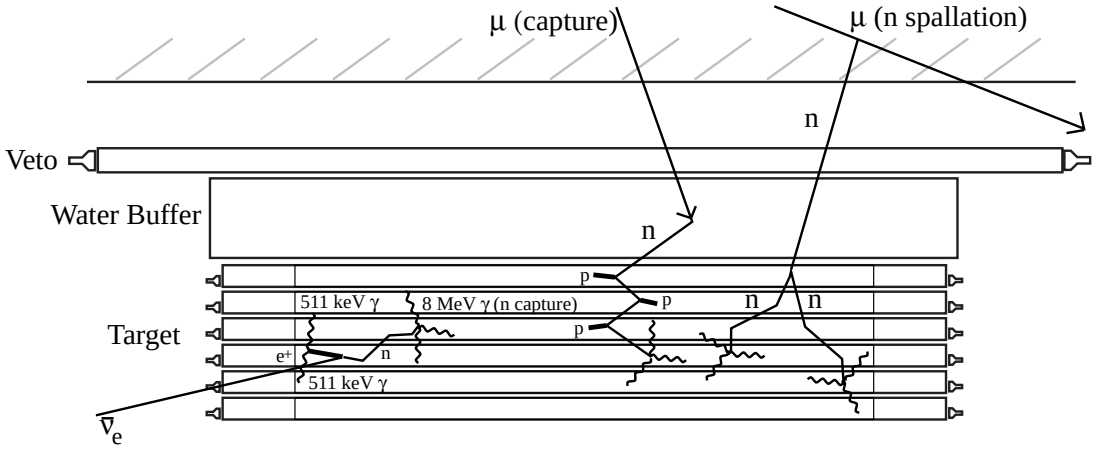

Fig. 18. Schematic view of two types of cosmic-μ-induced backgrounds compared with a signal event (far left) in the Palo Verde detector. Neutrons are produced by cosmic-μ spallation (right) and capture (left) on the materials outside the veto counter. Both production mechanisms can result in either neutron thermalization and capture (left), where the thermalization process fakes the prompt triple coincidence, or secondary neutron production (right), where one of the captures fakes the prompt triple coincidence. The μ represented to the left is an example of veto inefficiency, higher for the case of μ stopping in the detector (only one hit in the veto counter). A conceptually similar situation holds for Chooz, where, while the rate of cosmic-μ-induced events is substantially lower, events are only tagged as double coincidences.

Both experiments pre-select $\bar{\nu}_e$ candidates by requiring an appropriate topology (in space and time) for the prompt and delayed parts of each event and their relative position. Such cuts insure that the spatial and temporal extents of the events are compatible with the $\bar{\nu}_e$ hypothesis and that events are well contained and measured in the detector. A general classification in terms of signal and different backgrounds can be conveniently done by studying the correlation between prompt and delayed energy in Chooz for such a pre-selected sample, as shown in Figure 19. The region marked “B” in the Figure contains cosmic-ray muons stopping in the detector after entering undetected by the veto counter. Both prompt energy (muon ionization) and delayed energy (Michel electron) are large. Indeed events in region “B” show a fast time correlation between prompt and delayed part, consistent with the muon lifetime. Region “C” is populated

by the muon-spallation events discussed above: large prompt energy deposit from proton recoils in neutron thermalization is accompanied by a fixed 8 MeV energy deposit characteristic of neutron capture. Regions “A” and “D” are populated by random coincidences of natural radioactivity hits, sometimes including a high-energy proton recoil from neutron scattering in the delayed part (region “A”). Neutrino candidates populate the region framed by the darker line, as can be seen by comparison between the scatter plots with reactors ON and OFF.

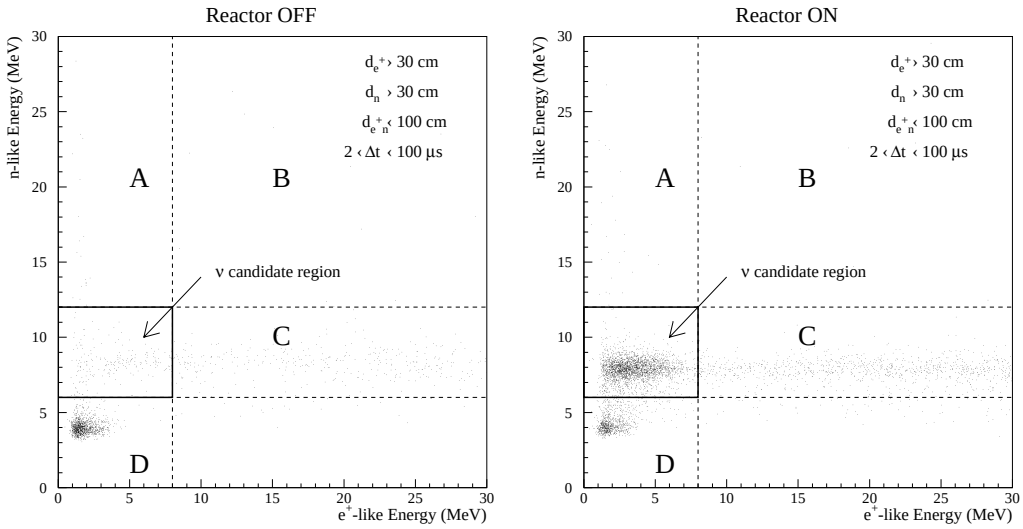

Fig. 19. Delayed energy vs. prompt energy in pre-selected Chooz events. The selection cuts are listed in the figure. On the left is shown the case of reactors OFF, while on the right is the case of reactors ON. A description of the event-types in the different regions of the plot is given in the text.

The time elapsed between the prompt and delayed parts of the events is shown in Figure 20 for the Palo Verde data. We note that the process of n-capture in the segmented detector requires the sum of two exponentials to be fit properly. This is due to the fact that a fraction of the neutrons stop, after thermalization, in passive materials (mainly acrylic for Palo Verde) where there is no Gd and the capture is a slower process. While the Monte Carlo gives a good fit with two exponentials, for data a third exponential, with longer time constant, is needed in the fit. This exponential accounts for events initiated by an uncorrelated background, having the delayed part triggered by cosmic rays, crossing the detector with a 2 kHz rate. Timing cuts are applied by both experiments to insure that events are consistent with a neutron capture. In addition

events are rejected for a period of time following tracks detected in the veto counters. This last cut is particularly important at Palo Verde where the cosmic-ray rate is high.

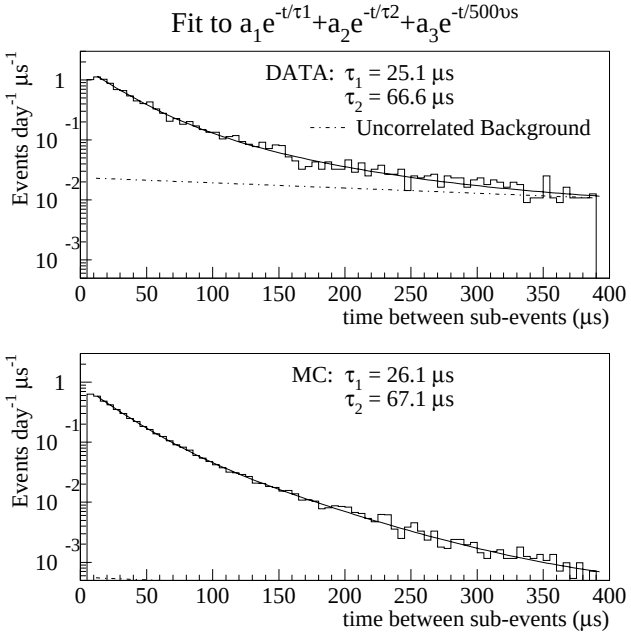

Fig. 20. Time elapsed between the prompt and delayed parts of events in Palo Verde data and Monte Carlo. The simulated data are fit to two exponentials. Data are fit to three exponentials of which the third accounts for the random background.

The availability for Chooz of data at zero power and with the reactors ramping up provides, of course, an independent way to check the magnitude of backgrounds, as shown in Figure 21 where all cuts were applied. The background estimate from the Figure is 1.1 ± 0.25 events/day. A simple subtraction of the e^+ spectra with reactor ON and OFF gives for Chooz the spectrum shown in Figure 22. The comparison of the observed distribution with the expected one for no-oscillations already shows very good agreement.

The same procedure can be repeated for Palo Verde using the thermal power excursions due to refueling. However in this case this technique substantially magnifies the errors since: 1) the periods of low power still have about 2/3 of the full flux, so that in the subtraction most of the signal is lost, 2) the statistical errors are dominated

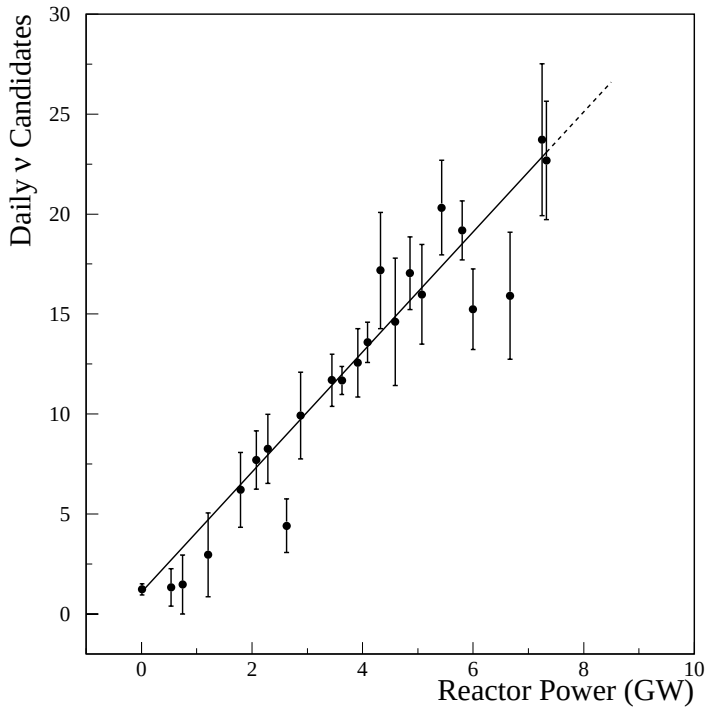

Fig. 21. Chooz data during the reactors commissioning. The background at reactors off is of 1.1 ± 0.25 events/day.

by the relatively short periods of low power. In addition, for any experiment, the subtraction used above is only justified under the assumption that the data quality (and, particularly, the efficiencies for signal *and* backgrounds) remains constant through the experiment. An alternative method[30] was developed for the Palo Verde analysis, starting from the evidence that, for their depth and detector configuration, the dominant correlated background has at least two neutrons, each triggering the detector with its capture. Such intrinsic symmetry can be used to cancel most of the background directly from data and compute the remaining components from Monte Carlo simulations. This technique makes the best possible use of the statistical power of all data collected. The rate of candidate events after all cuts can be written as $N = B_{\rm unc} + B_{\rm nn} + B_{\rm pn} + S_\nu$, where the contribution of the uncorrelated $B_{\rm unc}$, two-neutron $B_{\rm nn}$ and other correlated backgrounds $B_{\rm pn}$ are explicitly represented, along with the $\bar{\nu}_{\rm e}$ signal S_ν. The dominant background $B_{\rm nn}$ (along with $B_{\rm unc}$) is symmetric under exchange of sub-events, so that an event selection with the requirements for the prompt and delayed event parts

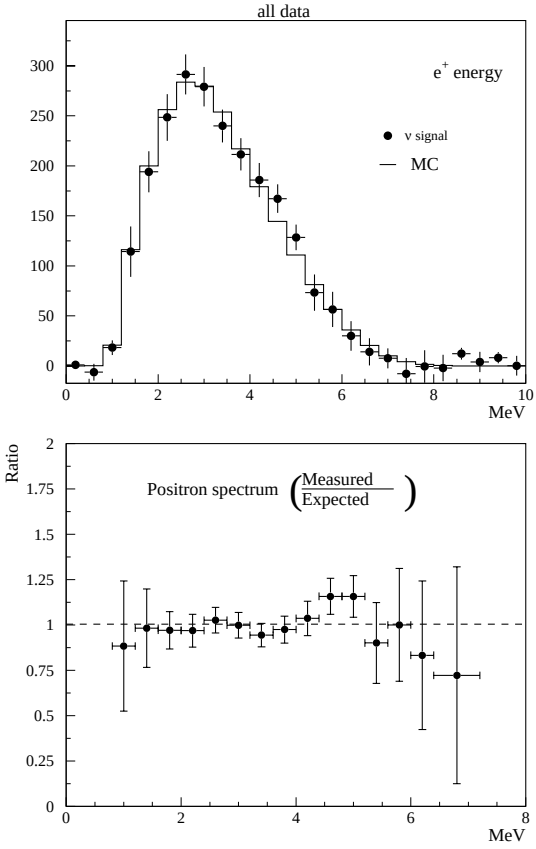

Fig. 22. Background subtracted positron energy spectrum in Chooz data. Error bars represent statistical errors only. The solid histogram represent the expectation for the case of no oscillations. The ratio between the two curves is shown on the bottom panel.

swapped, will result in a rate $N' = B_{\rm unc} + B_{\rm nn} + \epsilon_1 B_{\rm pn} + \epsilon_2 S_\nu$. Here ϵ_1 and ϵ_2 account for the different efficiency for selecting asymmetric events after the swap. One can then calculate $N - N' = (1-\epsilon_1)B_{\rm pn} + (1-\epsilon_2)S_\nu$ where the efficiency correction $\epsilon_2 \simeq 0.2$ can be estimated from the $\bar{\nu}_{\rm e}$ Monte Carlo simulation. The Palo Verde group found that the processes of μ-spallation in the laboratory walls and capture of the μ's that are not tagged by the veto counter, contribute to $(1-\epsilon_1)B_{\rm pn}$, while other backgrounds are negligible. Using Monte Carlo simulation, they obtain $(1-\epsilon_1)B_{\rm pn} = -0.9 \pm 0.5$ d^{-1} (-1.3 ± 0.6 d^{-1}) for μ-spallation in the 1998 (1999) data-set; the same figures for μ-capture are 0.6 ± 0.3 d^{-1} (0.9 ± 0.5 d^{-1}) in 1998 (1999). This represents only a small correction to $N - N'$ since the error on $B_{\rm pn}$ is de-magnified by the fact that ϵ_1 is close

to 1. While the Monte Carlo model is accurate for the capture process, in the case of spallation the broad range of spectral indexes for the n-recoil energy reported in literature was simulated.[30] The average between different predictions is then used for $B_{\rm pn}$ while the spread is used as an extra systematic error. Since no $\bar{\nu}_{\rm e}$ signal is present above 10 MeV, the observed integrated rate above this energy is used as a normalization of the Monte Carlo.

The Palo Verde results obtained in this way are shown in Table 2 for different running periods. Clearly also in this case there is good agreement with the no-oscillation hypothesis.

Period	98 "on"	98 "off"*	99 "on"	99 "off"†
Duration (d)	36.0	31.3	111.0	23.4
η	0.0746	0.0772	0.112	0.111
N (d^{-1})	38.2 ± 1.0	32.2 ± 1.0	52.9 ± 0.7	43.9 ± 1.4
S_ν (d^{-1})	16.5 ± 1.4	13.4 ± 1.4	25.2 ± 0.9	15.1 ± 1.9
B (d^{-1})	21.7 ± 1.0	18.8 ± 1.0	27.7 ± 0.6	28.8 ± 1.3
$R_{\rm Obs}$ (d^{-1})	221 ± 18	174 ± 17	225 ± 8	136 ± 17
$R_{\rm Calc}$ (d^{-1})	218	155	218	130

Table 2. Summary of results from the Palo Verde experiment. * Reactor at 890 m distance off. † Reactor at 750 m distance off. Statistical uncertainties only.

4.4 Results and systematics

A summary of systematic errors for both Chooz and Palo Verde is given in Table 3. Although the Table does not include the final calibration at Palo Verde, the systematic error given for Chooz should probably be considered as some sort of ultimate limit for reactor-based oscillation experiments, at least when only one detector is present. Indeed the intrinsically high efficiency ($\simeq 70\%$) of the homogeneous detector, together with the unique opportunity of studying the zero power case, are important advantages (for comparison the efficiency of the larger but segmented Palo Verde detector is $\simeq 11\%$).

The (energy averaged) ratio between $\bar{\nu}_{\rm e}$ detected and expected was found to be

$$R = 1.01 \pm 2.8\%({\rm stat}) \pm 2.7\%({\rm syst}) \qquad {\rm Chooz} \tag{8}$$

and

$$R = 1.04 \pm 3\%(\mathrm{stat}) \pm 8\%(\mathrm{syst}) \qquad \mathrm{PaloVerde} \tag{9}$$

in both cases consistent with 1.

Systematic	Chooz (%)		Palo Verde (%)	
$\sigma(\bar{\nu}_{\mathrm{e}} + \mathrm{p} \rightarrow \mathrm{n} + \mathrm{e}^{+})$	1.9		-	
Number of p in target	0.8		-	
$P_t h$	0.7		-	
Energy absorbed per fission	0.6		-	
Total rate prediction		2.3		3.0
e^{+} det. eff.	-		4.0	
n det. eff.	-		3.0	
$\bar{\nu}_{\mathrm{e}}$ selection cuts	-		4.0	
B_{pn} estimate	-		4.0	
Total $\bar{\nu}_{\mathrm{e}}$ efficiency		1.5		7.5
Total		2.7		8.0

Table 3. Origin and magnitude of systematic errors in Palo Verde and Chooz. Note that the two experiments offer different breakdowns of their systematics. For simplicity we do not show the systematics for the Palo Verde ON-OFF analysis. As usual the Palo Verde results only include the first half of their data set and do not include the final detector calibration.

Both experiments were able to exclude $\bar{\nu}_{\mathrm{e}}$ - $\bar{\nu}_{\mathrm{X}}$ oscillations as being mainly responsible for the atmospheric neutrino anomaly. This is evident from the exclusion contours obtained by both experiments using the unified approach[31] and shown in Figure 23 for Chooz and Figure 24 for Palo Verde.

4.5 Are smaller mixing angles within experimental reach ?

The current data on neutrino oscillations suggests the need to include at least three neutrino flavors when studying results from experiments. The most general approach would involve five unknown parameters, three mixing angles and two independent mass differences. However, an intermediate approach consists of a simple generalization of the two flavor scenario, assuming that $m_3^2 \gg m_1^2, m_2^2$ (i.e. $\Delta m_{13}^2 = \Delta m_{23}^2 = \Delta m^2$, while $\Delta m_{12}^2 \simeq 0$). In such a case the mixing angle θ_{12} becomes irrelevant and one is

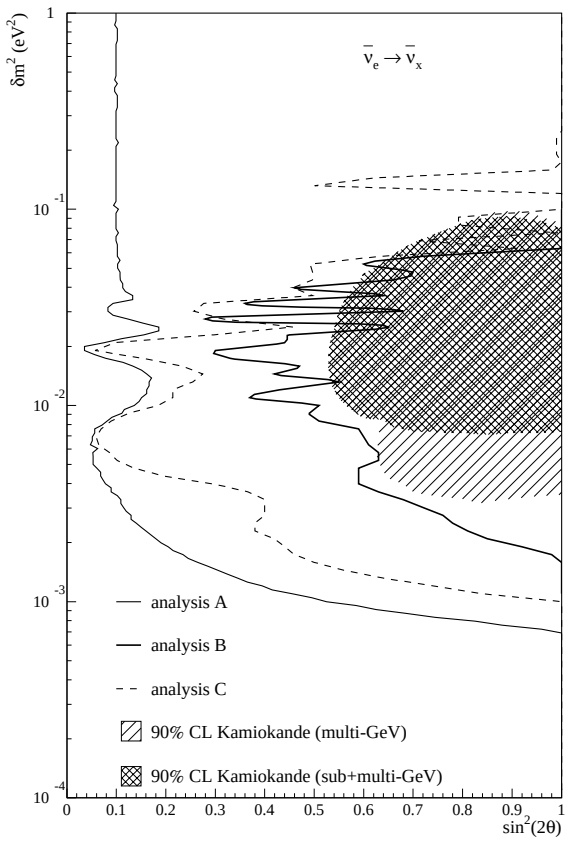

Fig. 23. Limits on mass difference and mixing angle from Chooz (90% CL) obtained with the unified approach.[31] Analysis A refers to the curve obtained by a fit to the background-subtracted spectrum in which both shape and normalization are used. Analysis C uses only the shape of the spectrum. Finally analysis B uses the difference of baselines between the two reactors ($\Delta L = 116.7$ m). While in this last case most systematics cancel, the statistical errors are larger, and the Δm^2 sensitivity rather poor due to the short baseline difference. The Kamiokande $\nu_{\rm e} - \nu_\mu$ atmospheric neutrino result is also shown.

left with only three unknown quantities: $\Delta m^2, \theta_{13}, \text{and } \theta_{23}$. With this parameterization, and assuming that ν behave like $\bar{\nu}$, the $\bar{\nu}_e$ disappearance is governed by

$$P(\bar{\nu}_e \to \bar{\nu}_x) = \sin^2 2\theta_{13} \sin^2 \frac{\Delta m^2 L}{4E_\nu} \ , \tag{10}$$

while the $\nu_\mu \to \nu_\tau$ oscillations, assuming that this scenario is responsible for the atmospheric neutrino results, are described by

$$P(\nu_\mu \to \nu_\tau) = \cos^4 \theta_{13} \sin^2 2\theta_{23} \sin^2 \frac{\Delta m^2 L}{4E_\nu} \ . \tag{11}$$

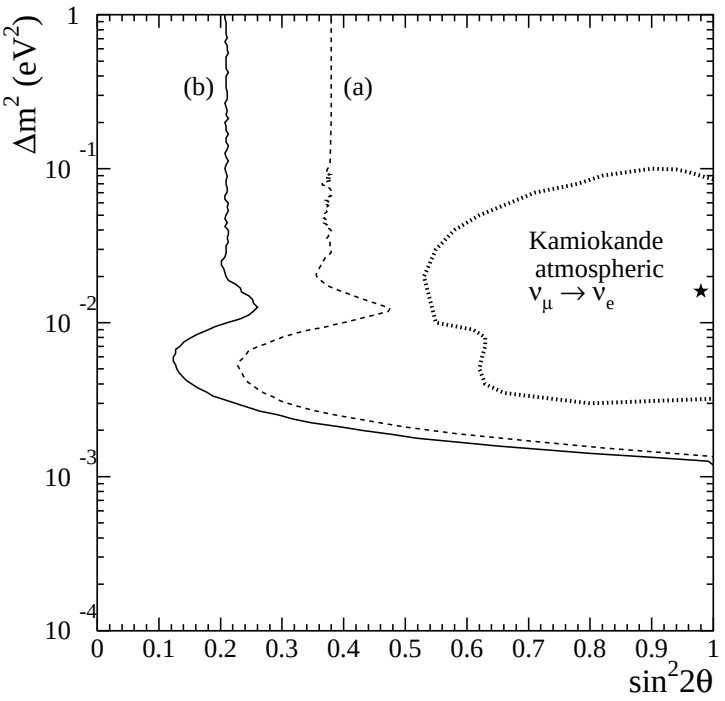

Fig. 24. Limits on mass difference and mixing angle from Palo Verde (90% CL) obtained with the unified approach.[31] Curve (a) is obtained by using the reactor power changes to estimate and subtract the background, while curve (b) is obtained with the alternative background subtraction method described in the text. The Kamiokande $\nu_\mu - \nu_e$ atmospheric neutrino result is also shown.

A preliminary analysis of the atmospheric neutrino data based on these assumptions has been performed[32] and its results are shown in Figure 25 for the ν_e disappearance channel. One can see that, while the relevant region of the mass difference Δm^2 is determined by the atmospheric neutrino data, the mixing angle θ_{13} is not constrained very much. Here the reactor-based neutrino oscillation experiments play a decisive role.

It is interesting to ask whether such a role can be extended to address regions of even smaller mixing parameter $\sin^2 2\theta_{13}$. A simple inspection of Table 3 shows that, using the Chooz systematics, if all flux and cross-section related errors could be set to zero one would be left with an error of $\simeq 1.5\%$. Assuming a detector large enough to produce negligible statistical error the total error would shrink from the present 3.9% to 1.5%.

This scenario is considered by Ref. 15, which proposes to use an underground reac-

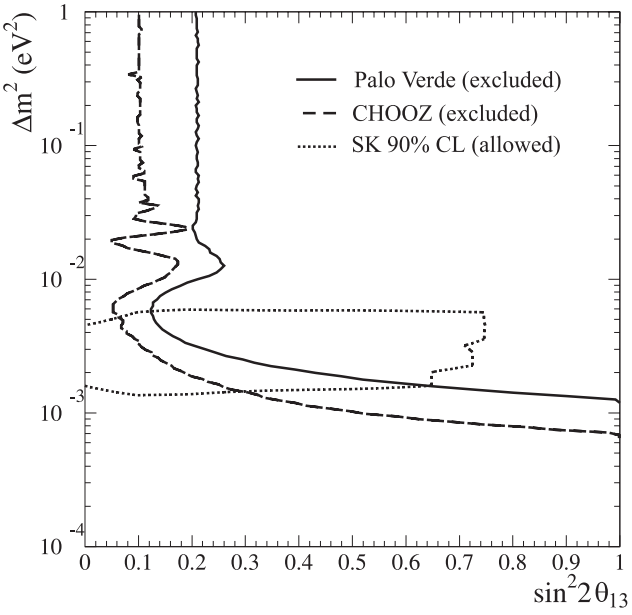

Fig. 25. Exclusion plot showing the $allowed$ region of θ_{13} and Δm^2 based on the Super-Kamiokande preliminary analysis (the region $inside$ the dotted curve). The region $excluded$ by the neutrino reactor experiments is to the right of the corresponding dashed and continuous curves.

tor at Krasnoyarsk in Russia as a source, and two identical detectors placed at distances of $\simeq 1100$ m and $\simeq 250$ m. The interesting feature of the Krasnoyarsk site is that there are substantial facilities available underground, with an overburden of ~ 600 m.w.e., twice the depth of Chooz. Indeed it might even be conceivable to locate the detectors on rail-cars and periodically switch their position to further reduce some of the systematics related to detector efficiency. The proposal discusses the use of 50 tons of Gd-loaded scintillator for each of the two homogeneous detectors, so that the far detector would collect 50 events/day (the thermal power of the reactor is in this case lower than at Chooz or Palo Verde. The background is estimated to be 5 events/day or less.

This proposal estimates that such an experiment could reach a sensitivity in mixing strength of better than 0.02 in the Δm^2 region relevant for atmospheric neutrinos. While the idea certainly looks interesting, it would be useful to explore how practical it is in general to push the errors of the absolute $\bar{\nu}_{\rm e}$ flux to the 1% domain, even with the measurements considered here. Finally one should understand the schedule for operation of the Krasnoyarsk reactors which, according to the Gore-Chernomyrdin[33] agreement, are supposed to be shutdown for re-coring in some future.

5 Exploring the solar ν anomaly on earth: KamLAND

While historically solar neutrinos have provided us with the first hint for oscillations, most people consider today that the strongest evidence for oscillation is provided by the atmospheric neutrino anomaly. Indeed the azimuthal dependence of the anomaly has substantially helped to reduce the effect to some property of neutrinos, and the advent of K2K, to be followed soon by the Minos and CERN to Gran Sasso programs,[9] are bringing the study of oscillations in this regime to a laboratory activity with both source and detector well under control.

While in the case of solar neutrinos none of the effects that would be generally considered "smoking guns" for oscillations has clearly emerged from the data, their exploration "in a laboratory setting" is made particularly challenging by the huge L/E_ν required. It is probably a safe prediction that it will take a very long time before an accelerator-based experiment will be able to tackle the solar neutrino problem! However, the very low energy of reactor neutrinos make a reactor-based oscillation experiment able to reach the Large Mixing Angle (LMA) MSW solution possible — albeit rather challenging. While we prefer to leave to others the assessment of how likely this solution is to be the right one, we find the chance to study solar neutrino oscillations "in the lab" absolutely amazing and compelling. We note here that, unlike in the case of atmospheric neutrinos, where it turned out that electron neutrinos were not involved in the dominant mixing, the solar neutrino problem, if due to oscillations, has to be related to $\nu_{\rm e}$ disappearance. So, unless $\bar{\nu}_{\rm e}$ behave drastically differently from $\nu_{\rm e}$ (which would be a worthwhile discovery anyway!) a reactor experiment is an exact replica of the astrophysical experiment, only built on earth.

5.1 Nuclear reactors in Japan

The "easier" solution of the solar neutrino problem (LMA MSW) is shown in Figure 1. In order to completely explore this solution one needs a Δm^2 sensitivity of at least 10^{-5} eV^2 at large mixing angle. As is now customary we refer to Figure 3 as a first step in designing our experiment: we see that a ≈ 100 km baseline is needed and this drives the power$\times$fiducial-mass product between 10^7 and 10^9 $\mathrm{MW_{th}} \times \mathrm{tons}$. Clearly a large detector has to be used in conjunction with very many nuclear reactors. A cursory look at the placement of nuclear power plants on the earth, Figure 26, reveals that such an experiment could only be placed in Europe, the eastern United States, or Japan.

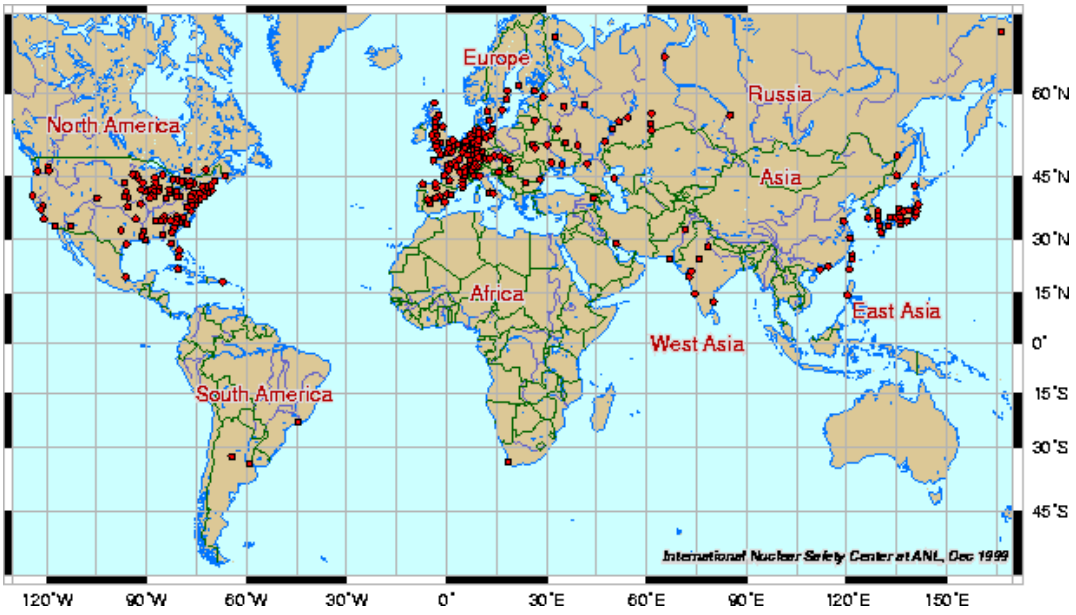

Fig. 26. Location of nuclear power plants in the world. Substantial concentrations of reactors are in Europe, the eastern US, and Japan.

There are 16 commercial nuclear power plants in Japan, their location being shown in Figure 27. They supply about 1/3 (or 130 $\mathrm{GW_{th}}$) of the total electric power in the country. At the Kamioka site there is an anti-neutrino flux of $\simeq 3 \times 10^6\,\mathrm{cm^{-2}s^{-1}}$ (or $\simeq 1.3 \times 10^6\,\mathrm{cm^{-2}s^{-1}}$ for $E_{\bar{\nu}} > 1.8$MeV) from these reactors. 80% of this flux derives from reactors at a distance between 140 km and 210 km, so that there is a limited range of baselines. The breakdown of this data by power plant (several plants have on site more than one reactor) is given in Figure 28. We note that some 2% of the flux derives from power plants in South Korea that will have to be included (albeit only as a crude estimate) to provide an exact flux prediction.

While the table in Figure 28 assumes the nominal power for each of the cores, an average over one year, taking into account scheduled and unscheduled down times, gives an expected non-oscillation rate of $\simeq$750 $\mathrm{kton^{-1}year^{-1}}$ for a $\mathrm{C}_n\mathrm{H}_{2n+2}$ target. Although the signal is provided by a very large number of cores, it turns out that a modulation of the $\bar{\nu}_\mathrm{e}$ flux is expected at KamLAND[34] thanks to the refueling and maintenance schedule of nuclear power plants in Japan. Such shutdowns, in fact, are concentrated in the Fall and Spring when the power demand is lowest, as illustrated in Figure 29. Hence, from the point of view of the tools available to study backgrounds, KamLAND is in a

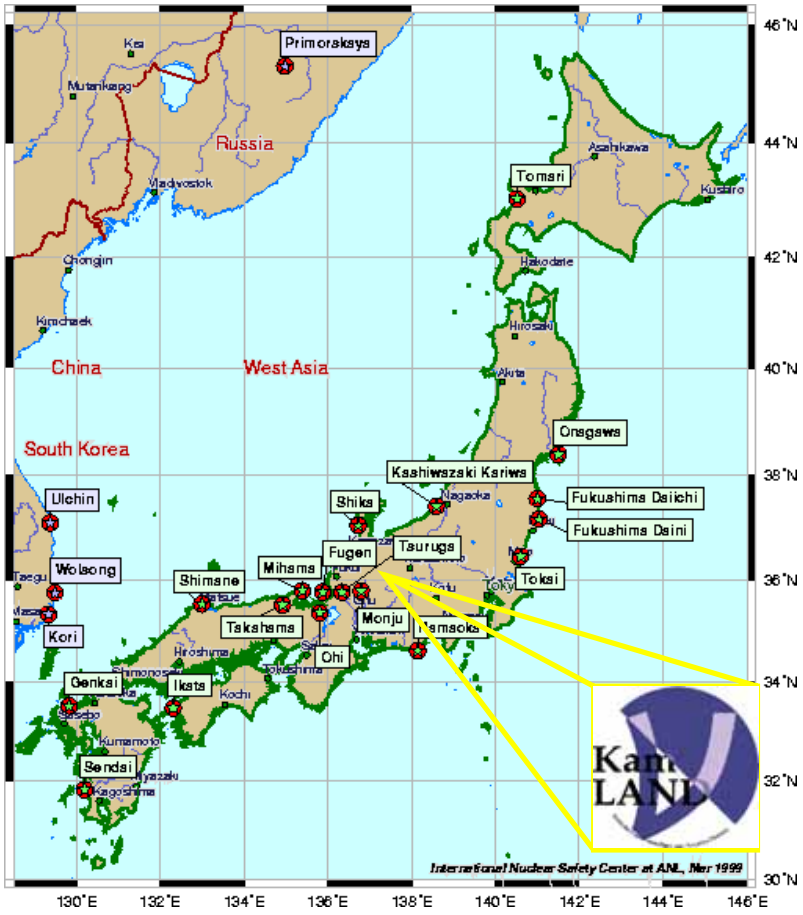

Fig. 27. Location of large nuclear power plants in Japan, Korea and eastern Russia.

situation very similar to that of Palo Verde, with 2 dips in the flux from full to $\approx 2/3$ expected every year.

5.2 Detector design

The KamLAND detector is housed in the cavity built for the Kamiokande detector under the summit of Mt. Ikenoyama in the Japanese Alps, about 50 km east of the town of Toyama. The layout of the laboratory is shown in Figure 30. The rock overburden is more than 1,000 m in any direction with an average rock density of 2.7 g/cm^3. The site is at 500 m distance from SuperKamiokande.

A cutout view of the KamLAND detector is shown in Figure 31. The fiducial volume consists of a sphere containing 1000 tons of liquid scintillator. The scintillator

Site	Distance	# of	P(ther.)	flux	Signal
Japan	(km)	cores	(GW)	($\bar{\nu}$ cm^{-2}s^{-1})	($\bar{\nu}$/yr)
Kashiwazaki	160.0	7	24.6	4.25×10^{5}	348.1
Ohi	179.5	4	13.7	1.88×10^{5}	154.0
Takahama	190.6	4	10.2	1.24×10^{5}	101.8
Hamaoka	214.0	4	10.6	1.03×10^{5}	84.1
Tsuruga	138.6	2	4.5	1.03×10^{5}	84.7
Shiga	80.6	1	1.6	1.08×10^{5}	88.8
Mihama	145.4	3	4.9	1.03×10^{5}	84.5
Fukushima−1	344.0	6	14.2	5.3×10^{4}	43.5
Fukushima−2	344.0	4	13.2	4.9×10^{4}	40.3
Tokai−II	294.6	1	3.3	1.7×10^{4}	13.7
Shimane	414.0	2	3.8	9.9×10^{3}	8.1
Onagawa	430.2	2	4.8	9.8×10^{3}	8.1
Ikata	561.2	3	6.0	8.4×10^{3}	6.9
Genkai	755.4	4	6.7	5.3×10^{3}	4.3
Sendai	824.1	2	3.3	3.5×10^{3}	2.8
Tomari	783.5	2	5.3	2.4×10^{3}	2.0
Korea					
Ulchin	~750	4	11.2	8.8×10^{3}	7.2
Wolsong	~690	4	8.1	7.5×10^{3}	5.2
Yonggwang	~940	6	16.8	8.4×10^{3}	6.9
Kori	~700	4	8.9	8.0×10^{3}	6.6
Total		69	175.7	1.34×10^{6}	1102

Fig. 28. List of relevant parameters for power reactors in Japan and South Korea.

container is a thin plastic-walled balloon of 6.5 m radius that is not supposed to take the weight of the scintillator but only to isolate it from an outer 2.5 m thick layer of non-scintillating, radiation shielding, fluid. The balloon is also designed to be impermeable to radon that mainly originates from Th and U contaminations inside the PMT's glass. The buffer fluid and the liquid scintillator are contained and mechanically supported by a stainless steel spherical vessel which also provides the mechanical structure where the photomultipliers for the fiducial volume are mounted. The sphere is solidly mounted inside the cylindrical rock cavity and the space between them is filled with water and used as a veto Čerenkov counter. The scintillator, based on mineral oil and pseudocumene, is designed to achieve sufficient light yield and n-γ discrimination by pulse-shape analysis, yet complying with rather strict flammability requirements from the Kamioka mine. Given the cost and stability issues for a detector of the size of KamLAND, it was chosen not to Gd-load the scintillator. As will be discussed later, simulations indicate that sufficient signal-to-noise ratio will be achieved with unloaded scintillator. Events will be localized inside the fiducial volume using the light propaga-

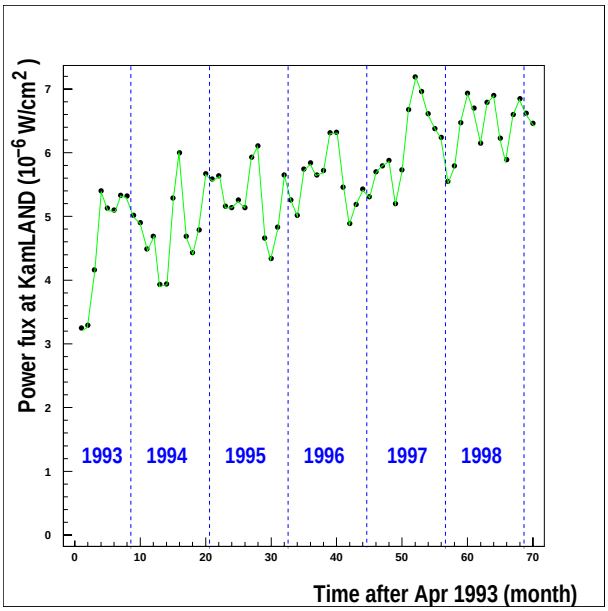

Fig. 29. Power-flux level at Kamioka from Japanese reactors as a function of time. Low power periods in the Fall and Spring seasons are alternated with peaks of high power in the Summer and Winter.

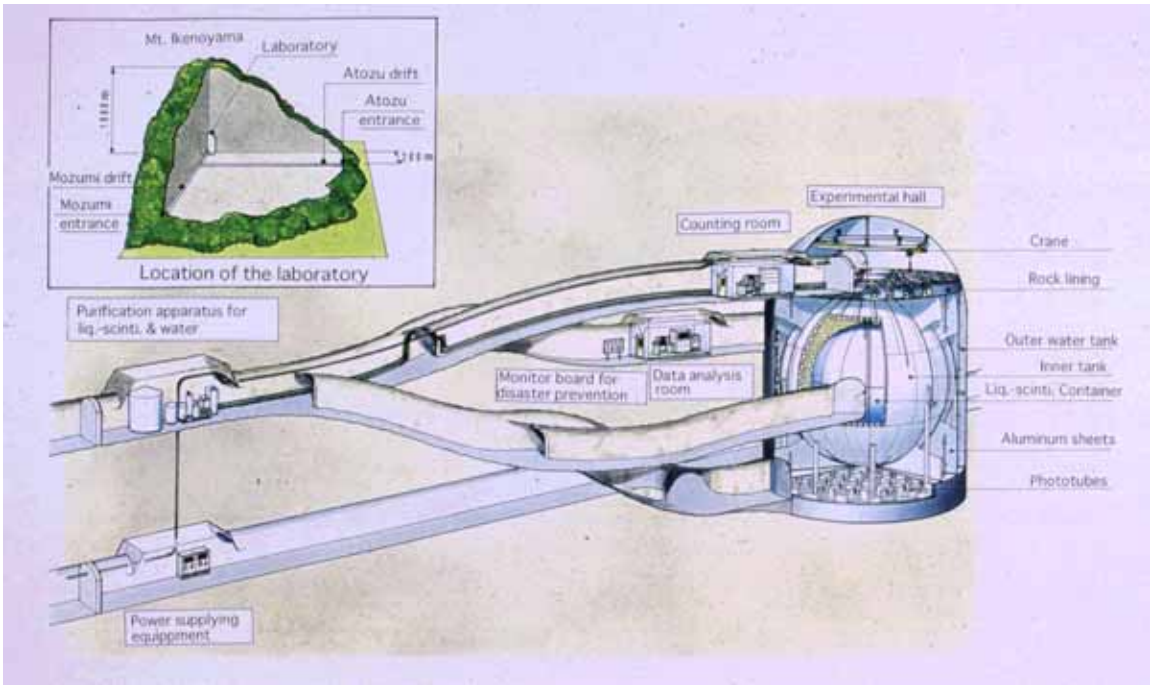

Fig. 30. Partial view of the system of tunnels inside Mount Ikenoyama with the locations of KamLAND and its main services.

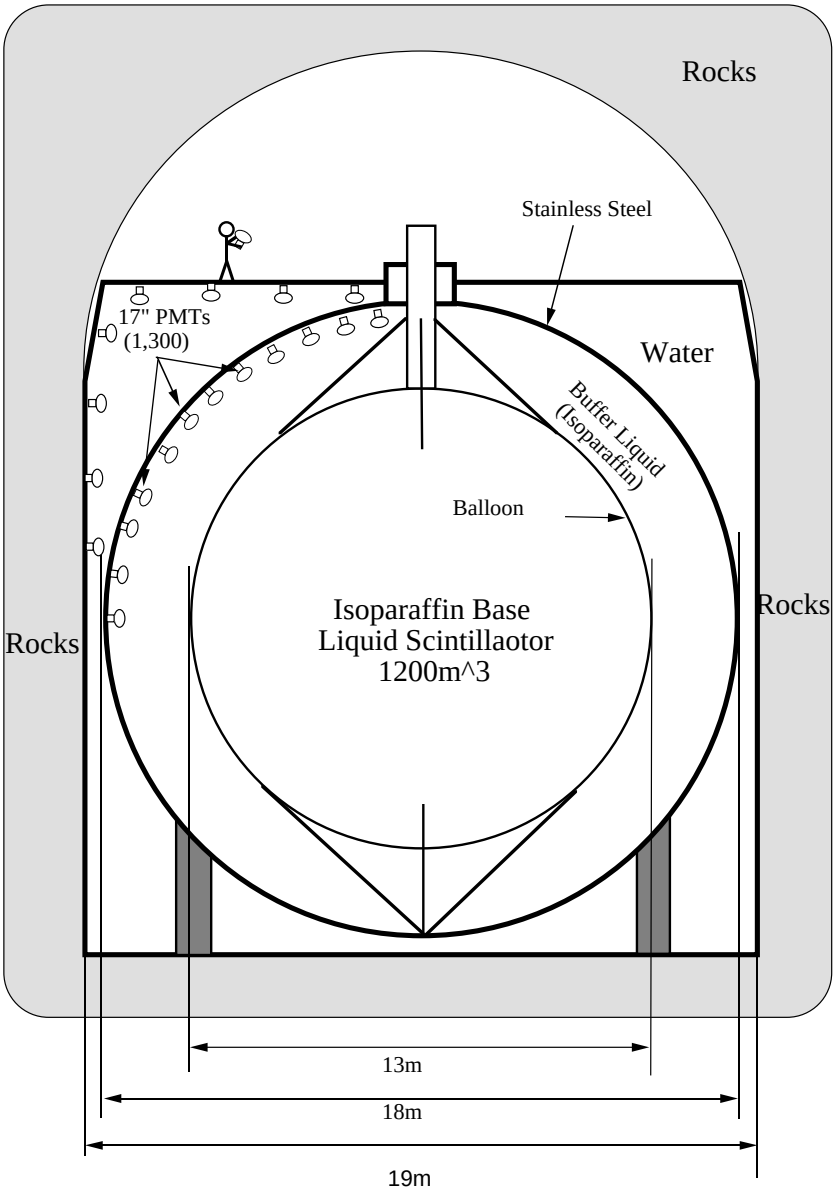

Fig. 31. Schematic cross-section of the KamLAND detector.

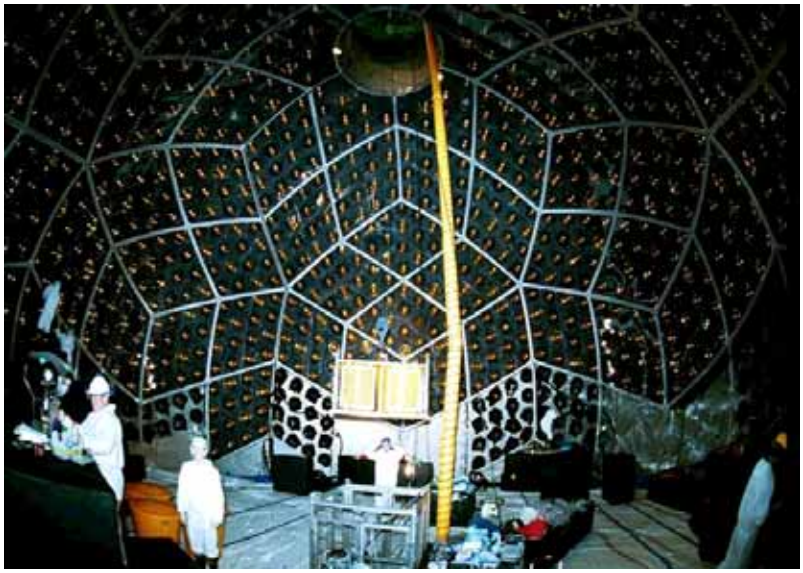

Fig. 32. View of the internal volume of the sphere during the central detector installation. A modular styrofoam raft is used as a platform for workers. The installation began from the top of the sphere and moved down, as the water level in the sphere was reduced. PMTs, black shades, acrylic plates, monitoring LEDs and cables were mounted in place for each level before lowering the water.

tion delays to the different photomultipliers so that large area, fast tubes are required. While the veto counter will be read out using 20-inch photomultipliers dismounted from the Kamiokande detector, new, faster, tubes with 17-inch active photocathode have been developed for KamLAND in order to allow for proper vertex reconstruction from timing. Such tubes have an average transit-time-spread of $\simeq 3$ ns (to be compared to $\simeq 5$ ns for the Kamiokande/SuperKamiokande tubes). The central detector has a 30% photocathode coverage obtained using about 1280 17-inch tubes complemented, for energy measurements, by 642 20-inch Kamiokande tubes. A spherical shell of acrylic panels (not shown in Figure 31) is mounted at a radius immediately inside the position of the PMT's and is used as the primary barrier against radon migration into the active scintillator. A cylindrical stainless steel chimney of 3 m diameter protrudes from the top of the sphere to permit access to the central detector during installation. Buffer fluid and scintillator lines as well as calibration ports will be mounted in the chimney along with all the electrical cabling.

The readout of KamLAND is designed to provide waveform analysis information for each of the PMT's in the detector with essentially no dead-time for several consecu-

Background source	Rate (day^{-1})
Cosmic-muon-induced neutrons	0.1
Natural radioactivity (random coincidence)	0.15
Natural radioactivity (correlated)	0.005
Total predicted background	0.25
Reactor $\bar{\nu}_e$ signal (no oscillation)	2

Table 4. Summary of background rates for the $\bar{\nu}_e$ signature. A signal-to-noise ratio of about 10/1 is expected for reactor $\bar{\nu}_e$.

tive events. This allows for clean event reconstruction and enables the off-line study of the pre-history of interesting events. For example, multiple neutron events, described above as the most dangerous background at Palo Verde, will be fully reconstructed by KamLAND. Similarly, cosmogenic activation giving short half-life nuclei will be clearly recorded. Deep digital buffering will allow the detector to sustain substantial bursts of events like that expected from supernovae.

In Figure 32 we show a phase of the central detector PMT installation that was concluded in September 2000. The KamLAND installation schedule calls for scintillator filling to start in early Spring 2001 and data taking to begin in the Summer 2001.

5.3 Expected performance

Similarly to previous experiments, both random hits from natural radioactivity, and correlated events from neutron production in cosmic-ray-muon spallation and capture, contribute to the background to reactor $\bar{\nu}_e$ in KamLAND. The results of Monte Carlo full detector simulation using the measured Kamioka cosmic ray flux and the activities of various components as sampled during construction are given in Table 4. For the purpose of this background estimate we have used U and Th contaminations in the scintillator of 10^{-14} g/g that have already been achieved in samples of the KamLAND scintillator. Monte Carlo studies have shown that cosmogenic activation gives negligible contribution to the background for doubles. A discussion of backgrounds to single signatures, not considered here, can be found elsewhere.[34]

In Figure 33 we show the predicted energy spectra for reactor neutrinos at KamLAND for no oscillations and different oscillation parameters consistent with the LMA

MSW solar neutrino solution. We can use one of these curves and add to it fluctuations consistent with a 10/1 signal-to-noise ratio and three years of data to investigate the sensitivity of the experiment. Assuming that oscillations with $\Delta m^2 = 2 \times 10^{-5}$ eV^2 and $\sin^2 2\theta = 0.75$ are indeed the cause of the solar neutrino anomaly, we obtain the measurement of the oscillation parameters shown in Figure 34. On the other hand, no evidence for oscillation after three years of data would result in the exclusion curve shown in Figure 1 and would rule out the LMA MSW solution to the solar neutrino problem.

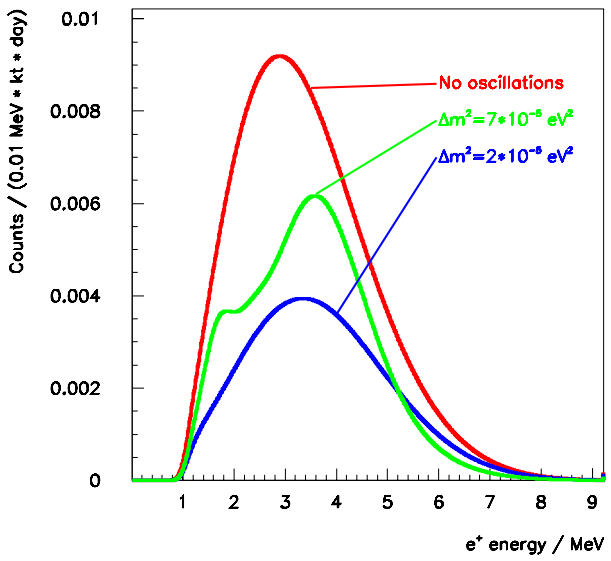

Fig. 33. Positron energy spectra expected at KamLAND for no oscillations and oscillations with parameters in the LMA MSW solar neutrino solution.

5.4 Other physics with a very large $\bar{\nu}_{\rm e}$ detector

KamLAND will be the largest detector specifically optimized to detect low-energy $\bar{\nu}_{\rm e}$ with good efficiency and low background. This opens a number of interesting opportunities beyond the measurement of oscillations from reactors. In addition, such a large detector with a low energy threshold can be used to directly measure neutrinos from the Sun, particularly the ^{7}Be line that is below the threshold of the water Čerenkov detectors. The presence of large amounts of carbon in KamLAND's scintillator opens the possibility of detailed flavor studies in neutrinos coming from supernovae. Finally

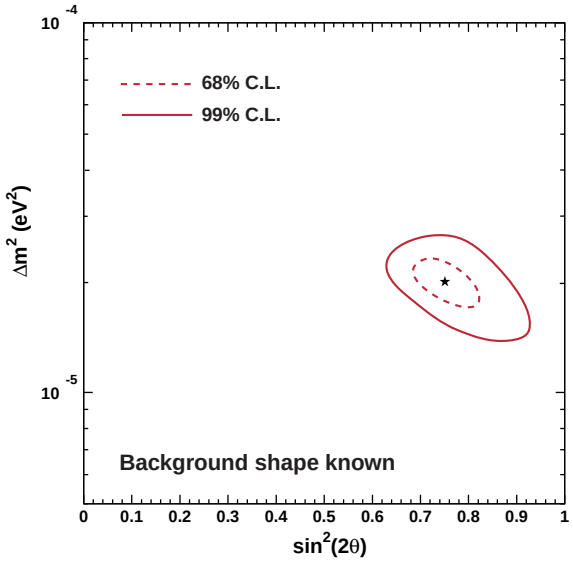

Fig. 34. Simulated measurement of neutrino oscillation parameters from three years of data at KamLAND assuming $\Delta m^2 = 2 \times 10^{-5}$ eV^2 and $\sin^2 2\theta = 0.75$. A signal-to-noise ratio of 10/1 was assumed (see text).

KamLAND represents such a large step in size and backgrounds relative to the previous detectors that we should be ready for the possibility that it will discover completely new and unexpected phenomena in physics or astrophysics.

Given our space limitations we will only mention here the topic of terrestrial $\bar{\nu}_{\rm e}$ that is somewhat unusual and directly relates to the experiment's ability to detect $\bar{\nu}_{\rm e}$'s. The reader interested in the direct detection of solar neutrinos or neutrinos from supernovae is referred to the KamLAND design report.[34] A description of the new and unexpected phenomena mentioned above will be hopefully provided at a later stage.

Although the study of terrestrial anti-neutrinos was proposed as early as 1966[35] practical difficulties, due to the very small cross-sections and very low energies involved, have made this physics impractical until now. KamLAND has the ability to detect energy depositions of the order of 1 MeV in a unprecedented amount of liquid scintillator and is therefore ideally suited for this study. It is important to realize that low energy $\bar{\nu}_{\rm e}$ are easily detected with very low background in KamLAND thanks to their very specific signature.

The cooling rate of our planet and its contents of heavy elements are central issues

in the earth sciences. The earth radiates about 40 TW of heat from its surface. About 40% of this energy (or 16 TW) is believed to have radiogenic origin with 90% of it deriving from decays of ^{238}U and ^{232}Th. Radiogenic heat is therefore an essential component of the present dynamics of our planet. As discussed by several authors,[35–37] the concentration of these isotopes can be mapped, at planetary scale, by direct detection of $\bar{\nu}_e$ deriving from the β-decay processes. Since neutrinos have a mean free path many orders of magnitude larger that the size of our planet, the neutrino field is analogous, except for directionality information, to a gravitational field, where the sources are represented by radioactive density (as opposed to mass density).

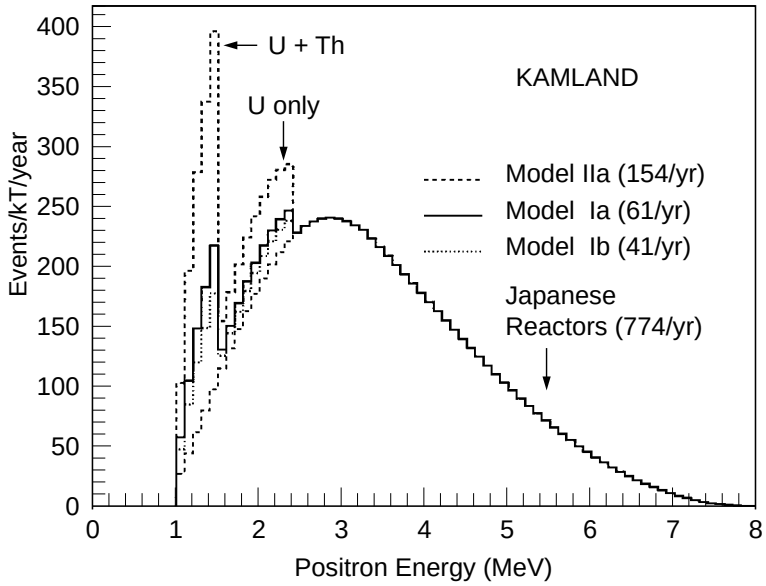

Fig. 35. Energy spectrum from terrestrial anti-neutrinos compared with reactor signal as expected in KamLAND. Three different geophysical models[38] are shown for the terrestrial anti-neutrinos and no oscillations are assumed for all the spectra shown.

Since the maximum energy carried by terrestrial neutrinos is[37] 3.27 MeV and the capture threshold is 1.8 MeV, the maximum in the energy spectrum detected in the prompt part of the events will be 2.49 MeV (including the 1.02 MeV from positron annihilations). For energies above threshold only the Thorium and Uranium decay chains give a detectable amount of events. ^{234}Pa from the U chain and ^{228}Ac and ^{212}Bi of the Th chain have similar endpoints (respectively 2.29 MeV, 2.08 MeV and 2.25 MeV) while ^{214}Bi from the U chain has an endpoint of 3.27 MeV. Therefore the energy spectrum

observed for the prompt part of the event has a characteristic double-hump structure shown in Figure 35. This will also allow the measurement of the U/Th ratio. Anti-neutrinos from nuclear reactors give, as described above, a similar signature, but their energy is substantially higher and, as shown in the Figure, they can be easily separated from the terrestrial anti-neutrinos.

The two lower spectra (Ia and Ib) superimposed in Figure 35 for the terrestrial anti-neutrino component correspond to two different possible geophysical models with different heavy elements concentration in the oceanic and continental crusts.[38] The highest curve (IIa) is given as a reference and shows what the spectrum would be in the extreme case where the entire 40 TW of heat escaping from the Earth's interior was generated by the Th and U decay chains.

In one year of data-taking, model Ia would give an integral of 61 events while model Ib would give only 41 events, and a differentiation between the two at 3σ level could be obtained in five years of data-taking, taking into account the fluctuations of the background due to the reactor neutrinos.

6 Conclusions

The use of nuclear reactors to study neutrino properties has a long and glorious history. While the first experiments devoted to oscillation searches were motivated by the generic principle to "look where the light is", many of the modern hints for neutrino oscillations point to parameters that match very well the capabilities of reactor-based experiments. At the same time the understanding of the flux and spectrum of $\bar{\nu}_{\rm e}$ from power reactors has reached substantial sophistication. The first two "long baseline" experiments, Chooz and Palo Verde, have amply demonstrated the capability of this new breed of detectors, while providing solid evidence that $\nu_{\rm e} - \nu_{\mu}$ is *not* the dominant channel in the atmospheric neutrino oscillation. KamLAND, scheduled to begin data-taking in less than one year, will extend our reach for small mass-differences to unprecedented levels. Its size and background will move reactor-based experiments to a new dimension, with several new physics opportunities in the essentially background-less detection of $\bar{\nu}_{\rm e}$ from a number of natural sources. Direct observation of solar neutrinos is also among the future goals of this "ultimate" reactor experiment.

7 Acknowledgments

This review is rooted in the many daily discussions that accompanied the design, construction, data-taking and analysis of the Palo Verde experiment. Each one of the collaborators in a remarkably small and effective group contributed importantly to some of the results described here. They are Felix Boehm, Jerry Busenitz, Brian Cook, Herb Henrikson, Janos Kornis, David Lawrence, K.B. Lee, Kevin McKinny, Lester Miller, Vladimir Novikov, Andreas Piepke, Barry Ritchie, Dillon Tracy, Petr Vogel, Yi-Fang Wang and Joachim Wolf. I would also like to thank Junpei Shirai, Fumihiko Suekane and Atsuto Suzuki for bringing me up-to-speed quickly in many exciting early discussions on KamLAND. I am also indebted to Alessandro Baldini and Carlo Bemporad for interesting discussions on the Chooz data. Finally I would like to thank the organizers of the Summer Institute for the opportunity to present the subject and the flawless organization.

This work was supported in part by the US DoE grant DE-FG03-96ER40986.

References

[1] For early developments in neutrino physics see, for example, Chapter 1 in "Neutrino Physics", K. Winter, Ed., Cambridge University Press, 1991.

[2] G. Rameika, these Proceedings.

[3] For an up-to-date discussion of the neutrino masses and the relevant experiments see, for example P. Fisher, B. Kayser and K.S. McFarland, Ann. Rev. Nucl. Part. Sci. 49, 481 (1999) or K. Zuber, Physics Reports, 305 (1998) 296.

[4] See H. Murayama, these Proceedings, for an extensive discussion of the theoretical implications of finite neutrino masses.

[5] L. Wolfenstein, these Proceedings.

[6] D.E. Groom *et al.*, Europ. Phys. J. C15 (2000) 1.

[7] E. Kearns, these Proceedings.

[8] J. Wilkerson, these Proceedings.

[9] G. Feldman, these Proceedings.

[10] For a general discussion of short-baseline reactor experiments see F. Boehm and P. Vogel, Physics of Massive Neutrinos, Cambridge 1992.

[11] G. Zacek *et al.*, Phys. Rev. D34 (1986) 2621.

[12] B. Achkar *et al.*, Nucl. Phys. B434 (1995) 503.

[13] B. Achkar *et al.*, Phys. Lett. B374 (1996) 243.

[14] P.F. Harrison, D.H. Perkins and W.G. Scott, Phys. Lett. B349 (1996) 137.

[15] L. Mikaelyan, arXiv:hep-ex/0008046v2 25 Aug 2000, to appear in Proceeding of Neutrino 2000, Sudbury, Canada.

[16] L. Miller, PhD thesis, Stanford Sept 2000, unpublished.

[17] A.A. Hahn *et al.*, Phys. Lett. B218 (1989) 365.

[18] K. Schreckenbach *et al.*, Phys. Lett. B160 (1985) 325.

[19] Davis *et al.* Phys. Rev. C19 (1979) 2259;
P. Vogel *et al.* Phys. Rev. C24 (1981) 1543.

[20] H-V. Klapdor *et al.* Phys. Rev. Lett. 48 (1982) 127;
H-V. Klapdor *et al.* Phys. Lett. B112 (1982) 22.

[21] P. Vogel, Phys. Rev. D29 (1984) 1918.

[22] P. Vogel and J.F. Beacom, Phys. Rev. D60 (1999) 053003.

[23] M. Apollonio *et al.*, Phys. Lett. B420 (1998) 397.

[24] M. Apollonio *et al.*, Phys. Lett. B466 (1999) 415.

[25] F. Boehm *et al.*, Phys. Rev. Lett. 84 (2000) 3764.

[26] F. Boehm *et al.*, Phys. Rev. D62 (2000) 072002.

[27] A. Piepke *et al.*, Nucl. Instr. and Meth. A432 (1999) 392.

[28] A. Baldini *et al.*, Nucl. Instr. and Meth. A372 (1996) 207.

[29] G. Gratta *et al.*, Nucl. Instr. and Meth. A400 (1997) 456.

[30] Y-F. Wang *et al.*, Phys. Rev. D62 (2000) 013012.

[31] G.J. Feldman and R.D. Cousins, Phys. Rev. D57 (1998) 3873.

[32] Preliminary result, SuperKamiokande Collaboration; see K. Okamura, Ph.D. Thesis, University of Tokyo (1999).

[33] “US-Russian Plutonium Production Agreement is Signed”, Statement by the White House office of the Vice President, 23 Sept. 1997.

[34] P. Alivisatos et al. ”KamLAND: a liquid scintillator Anti-Neutrino Detector at the Kamioka site”, Stanford-HEP-98-03, Tohoku-RCNS-98-15.

[35] G. Eders, Nucl. Phys. 78 (1966) 657.

[36] G. Marx, Czech. J. of Phys. B19 (1969) 1471;
G. Marx and I. Lux, Acta Phys. Acad. Hung. 28 (1970) 63;
C. Avilez *et al.*, Phys. Rev. D23 (1981) 1116.

[37] L. Krauss *et al.*, Nature 310 (1984) 191.

[38] R.S. Raghavan *et al.*, Phys. Rev. Lett. 80 (1998) 635.

FEASIBILITY STUDY OF A NEUTRINO SOURCE BASED ON A MUON STORAGE RING

N. Holtkamp*
Fermi National Accelerator Laboratory
P.O. Box 500
Batavia, IL, 60150

ABSTRACT

One of the first applications of an intense muon source could be a muon storage ring. The muon beam is injected into the ring and decays while circulating. The neutrinos from the decay muons form a very intense and well collimated beam ($\nu_{\rm e}$,ν_{μ}) that could be used for future neutrino experiments. The idea for such a neutrino source has been described many times, but only recently with the progress on ionization cooling concepts being made within the muon collider/neutrino source collaboration, such a source seems feasible. With a new proton driver and a target that can withstand the intense radiation and the power density from the impinging proton beam, the source will produce enough muons through pion decay to achieve approximately 2x10^{20} muons decaying into neutrinos in one of the straight sections of the storage ring. In order to achieve this goal very efficient and large aperture focusing and rf accelerating systems have to be developed. The biggest advantage though comes from the fact, that the transverse emittance for a neutrino source has to be reduced by only a factor of approximately ten in both transverse dimensions. The longitudinal emittance coming from the source is of no importance, which makes longitudinal cooling unnecessary. Following the goal of 2x10^{20} muons/year decaying in one straight section an attempt has been made to investigate the technical feasibility of such a facility as a whole.

*The work presented here has been performed by the members of the Muon Collider/Neutrino Source Collaboration coordinated by Fermilab and by many collaborators from different institutes and organizations, like CERN, Thomas Jefferson National Accelerator Facility, Oak Ridge National Laboratory, INP Protvino (Russia), JINR Dubna (Russia), Michigan State University and Cornell University with support from NSF. The author summarizes the results from this study which has been been published in April 2000: FNAL-pub-00/08-E, May 2000

1 Introduction

A muon storage ring as a source of intense neutrino beams supersedes a standard neutrino source in many ways. Classical neutrino sources have long decay channels which are used to generate $\bar{\nu}_{\mu,\tau,\mathrm{e}}$,$\nu_{\mu,\tau,\mathrm{e}}$ beams from pions coming from a target that is hit with an intense proton. In a muon storage ring the muons circulate after injection until they decay. A major fraction of these muons will decay in the straight section, which will produce an intense, very well collimated and clean ν_{e},$\bar{\nu}_{\mathrm{e}}$ beam.

1.1 Physics with a Neutrino Factory

Recent measurements of atmospheric muon neutrino (ν_μ) fluxes from the Super–Kamiokande (SuperK) collaboration have shown an azimuth–dependent ($\rightarrow$ baseline dependent) depletion that strongly suggests neutrino oscillations of the type $\nu_\mu \rightarrow \nu_x$. Since the atmospheric ν_{e} flux is not similarly depleted, ν_x cannot be ν_{e} and must therefore be either ν_τ , or ν_{s} (a sterile neutrino). These observations have inspired many theoretical papers, several neutrino oscillation experiment proposals, and much interest in the physics community. This interest is well motivated. Understanding the neutrino-mass hierarchy and the mixing matrix that drives flavor oscillations, may provide clues that lead to a deeper understanding of physics at very high mass-scales and insights into the physics associated with the existence of more than one lepton flavor. Hence, there is a strong incentive to find a way of measuring the neutrino flavor mixing matrix, confirm the oscillation scheme (three–flavor mixing, four–flavor, n-flavor ?), and determine which mass eigenstate is the heaviest (and which is the lightest). This will require a further generation of accelerator based experiments beyond those currently proposed.

High energy neutrino beams are currently produced by creating a beam of charged pions that decay in a long channel pointing in the desired direction. This results in a beam of muon neutrinos ($\pi^+ \rightarrow \mu^+ + \nu_\mu$) or muon anti–neutrinos ($\pi^- \rightarrow \mu^- + \bar{\nu}_\mu$). In the future, to adequately unravel the mixing matrix, we will need $\nu_{\mathrm{e}}$and $\bar{\nu}_{\mathrm{e}}$ (as well as ν_μ and $\bar{\nu}_\mu$) beams. To illustrate this, consider neutrino oscillations within the framework of three-flavor mixing, and adopt the simplifying approximation that only the leading oscillations contribute (those driven by the largest $\Delta \mathrm{m}^2_{ij}$, defined as $\Delta \mathrm{m}^2_{32} \equiv \Delta \mathrm{m}^2_3 - \Delta \mathrm{m}^2_2$, where m_i is the mass associated with mass eigenstate **i**. The probability that a neutrino of energy E $\approx$ GeV and flavor α oscillates into a neutrino of flavor β whilst traversing a distance L $\approx$ (km) is given by:

$$P(\nu_{\rm e} \rightarrow \nu_\mu) = sin^2(\theta_{23})\, sin^2(2\theta_{13})\, sin^2(1.267\Delta {\rm m}^2_{23}\frac{L}{E}), \quad (1)$$

$$P(\nu_{\rm e} \rightarrow \nu_\tau) = cos^2(\theta_{23})\, sin^2(2\theta_{13})\, sin^2(1.267\Delta {\rm m}^2_{23}\frac{L}{E}), \quad (2)$$

$$P(\nu_\mu \rightarrow \nu_\tau) = cos^4(\theta_{13})\, sin^2(2\theta_{23})\, sin^2(1.267\Delta {\rm m}^2_{23}\frac{L}{E}). \quad (3)$$

Each of the oscillation probabilities depend on $\Delta {\rm m}^2_{32}$ and two mixing angles θ_{ij}. To adequately determine all the θ_{ij} and sort out the various factors contributing to the P($\nu_\alpha \rightarrow \nu_\beta$) will require $\nu_{\rm e}$ as well as ν_μ beams. In addition, there is a bonus in using $\nu_{\rm e}$ beams since electron neutrinos can elastically forward scatter off electrons in matter by the charged current (CC) interaction. This introduces a term in the mixing matrix corresponding to $\nu_{\rm e} \rightarrow \nu_e$ transitions that is not present for neutrinos of other flavors. Hence, if electron–neutrinos travel sufficiently far through the Earth, matter effects modify the oscillation probabilities. This modification depends on the sign of $\Delta {\rm m}^2_{32}$, and provides a unique way of measuring which mass eigenstate is heaviest, which is lightest. In conclusion, if one can find a way of producing $\nu_{\rm e}$ beams *of sufficient intensity* a strong motivation exists. The obvious way to attempt to produce high energy $\nu_{\rm e}$ beams is to exploit muon decays. Since muons live 100 times longer than pions, we need to avoid the use of a linear decay channel, which would be impractically long for high energy muons. The solution is to use a muon storage ring with long straight sections, one of which points in the desired direction. This yields a neutrino beam consisting of 50% $\nu_{\rm e}$ and 50% $\bar{\nu}_\mu$ if μ^+ are stored, or 50% ν_μ and 50% $\bar{\nu}_{\rm e}$ if μ^- are stored. Using a storage ring to produce secondary beams of Koshkarev[2] in 1974. The idea (also ascribed to refs.[3] and[4]) therefore dates back to the early days of the ISR at CERN. The key questions that need to be addressed in order to produce a viable proposal for the production of secondary beams by this method are:

- **How can enough particles be stored ?**
- **How can their phase-space be compressed to produce sufficiently intense beams for physics ?**

The calculated beam fluxes using the proposed scheme were too low to motivate the construction of a secondary beam storage ring. A viable solution to the key question (how to make sufficiently intense beams) was implemented at the beginning of the 1980's for antiproton production, leading directly to the CERN proton–antiproton collider and the discovery of the weak Intermediate Vector Bosons. The solution to

the intensity question involved using lithium lenses to collect as many negative particles as possible, and stochastic cooling to reduce the phase-space of the $\bar{\mathrm{p}}$ beam before acceleration. In 1980 it was suggested[4] that the negative particle collection ring (the Debuncher) at the proposed Fermilab antiproton source could be used to provide a neutrino beam downstream of one of its long straight sections. The Debuncher collects negative pions (as well as antiprotons), which decay to produce a flux of captured negative muons. The muon flux in the Debuncher was not considered to be sufficient.

In order to make progress a method of cooling muon beams is required together with an increase in yield for muon production. Stochastic cooling cannot be used since the cooling time is much longer than the muon lifetime. Therefore ionization cooling was proposed as a possible solution.[5] A way of collecting more pions (that subsequently decay into muons) using a very high-field solenoid was proposed[6] in 1989. Thus by the end of the 1980's the conceptual ingredients required for very intense muon sources were in place, but the technical details had not been developed. Beginning with the 1990's the desire to exploit an intense muon source to produce muon beams for a high energy muon collider motivated the formation of a collaboration (back then called *The Muon Collider Collaboration*, subsequently renamed *The Neutrino Factory and Muon Collider Collaboration*). The work going on since has resulted in a more complete technical understanding of the design of an intense muon source.[7] In 1997 it was proposed[8] to use an intense muon source, together with a dedicated muon storage ring with long straight sections, to produce a very intense neutrino source. It was shown that such a **Neutrino factory** would be sufficiently intense to produce thousands of events per year in a reasonably sized detector at large baseline length. In addition, it was shown that if the ring could be tilted at large angles it would provide beams for very long (trans–earth) neutrino oscillation experiments. This proposal came at a time of increasing interest in neutrino oscillation experiments due to the SuperK results.[8] At the same time several articles considering the direction of high physics were published (e.g. Ref. 9). Thus, the neutrino factory concept quickly caught the imagination of the physics community. This interest led to the first NUFACT workshop at Lyon in 1999, a yearly series continuing since then, and to a number of technical feasibility studies investigating several overall schemes to optimize the total muon flux.[10,11] Most of the results presented here have been taken from a study[12] to explore an explicit neutrino factory design and identify the associated R&D issues. Together with a parallel 6 month physics study[13] to explore the physics potential of a neutrino factory as a function of its energy, intensity, and the baseline for oscillation experiments a comprehensive description of the facility

and the physics is available.

1.2 The Accelerator Facility

A muon storage ring used to produce very intense and clean neutrino beams is most probably the first application of an intense muon source. After being generated from pion decay and cooled in an ionization cooling channel, the muon beam is accelerated and injected into a storage ring, where the muons decay while circulating. The neutrinos from the decay muons in the storage ring form a very intense and well collimated beam of electron and muon neutrinos ($\nu_{\mathrm{e}}, \nu_{\mu}$). The summary addresses four basic question and the answers are of general interest. They will help to define the R&D program. Specificially defined by the Fermilab directorate, the report tried to answer the following questions.

- **A design concept for a muon storage ring and associated support facilities that could, with reasonable assurance, meet performance goals required to support a compelling neutrino based research program.**
- **Identification of the likely cost drivers within such a facility.**
- **Identification of an R&D program that would be required to address key areas of technological uncertainty and cost/performance optimization within this design, and that would, upon successful completion, allow one to move with confidence into the conceptual design stage of such a facility.**
- **Identification of any specific environmental, safety, and health issues that will require our attention.**

Table 1. Charge for the study of the Neutrino Factory based on a Muon storage ring

If the μ-beam divergence in the straight section is small compared to the decay angle, the opening angle of the neutrino beam is completely dominated by the decay kinematics. Given the energy of the muons this angle basically equals $1/\gamma_{\mathrm{muon}}$. From the requirement to have the divergence of the muon beam in the straight section to be small compared to the divergence of the neutrino beam, a goal emittance for the muon source can easily be defined. The divergence of the muon beam due to beam focusing ($\propto \sqrt{\epsilon/\beta}$ was chosen to be 10 % of the natural divergence and assuming a reasonable maximum β-function of $\approx$400 m, the design emittance the cooling had to produce is

$\approx 2 \times 10^{-3}\pi$ mm rad. This emittance is only a factor of 10 smaller than the typical emittance of the pion beam if it is generated in a 20 T solenoidal field. Transverse emittance requirements (only a factor of ten) and longitudinal emittance requirements (many bunches instead of one or two) are for these two reasons signficantly relaxed in a neutrino factory as compared to a muon collider. Other beam parameters that were chosen for the neutrino factory study are based on various assumptions, some of which are summarized in table 2.

1. Given the experience in the simulations being done for the Muon Collider, and based on an earlier paper on this subject, a reasonable assumption had to be made for the number of muons one could expect per incident proton on target. This would have to include all the decay losses and the beam loss during cooling and acceleration.
2. Because this is a pulsed accelerator, the average current that has to be accelerated to achieve the 2×10^{20} neutrinos/year, critically depends on the total operating time. More operating time reduces the investment cost on the high power rf systems. An optimistic assumption here led to 2×10^{7} sec/year assumed for the purpose of this study.
3. The intense proton source being considered would be based on the results of the design study going on at Fermilab.
4. In the simplest version of a racetrack shaped storage ring with two long straight sections, approximately one third of the muons will decay in each straight.

Table 2. List of basic assumptions being made for the purpose of this feasibility study.

Given the large number of different and technically demanding sub-systems required for such a facility the charge for the feasibility study was focused on basic questions one would have to answer for such an accelerator facility. Given the large variety of possibilities for short (≈500 km), long (≈3000 km) and very long baseline (≈8000 km) experiments and based on somewhat preliminary assumptions in September 1999 on the potential physics goals, a number of boundary conditions had to be taken into account, before a specific set of accelerator parameters was picked. The final list for this study is given in table 3.

This table, together with a number of assumptions that were made (see table 2), defined a set of specifications that were used to start the design of the accelerator complex.

Energy of the storage ring	GeV	50
Number of neutrinos per straight section	1/year	2×10^{20}
Baseline length (FNAL to SLAC/LBN)	km	3000
no polarization		
capability to switch between μ^+ and μ^-		

Table 3. List of basic assumptions being made for the purpose of this feasibility study.

These specifications are given in table 4.

Nevertheless many of these parameters were based on an earlier study[14] and on feasibility considerations that were done in the framework of the muon collider work.[7] It was recognized very early in the study, that because of the comparatively high energy (50 GeV) and high average current with 6x10^{20} muons per year in 2x10^{7} seconds the average beam power would be 240 kW. This would be the highest pulsed power lepton beam in the world, exceeding the SLAC linac by more than a factor of two in its final 1999 run. The basic sketch of such a storage ring, as well as a list of storage ring parameters chosen for this study, is given in figure 1 and table 5.

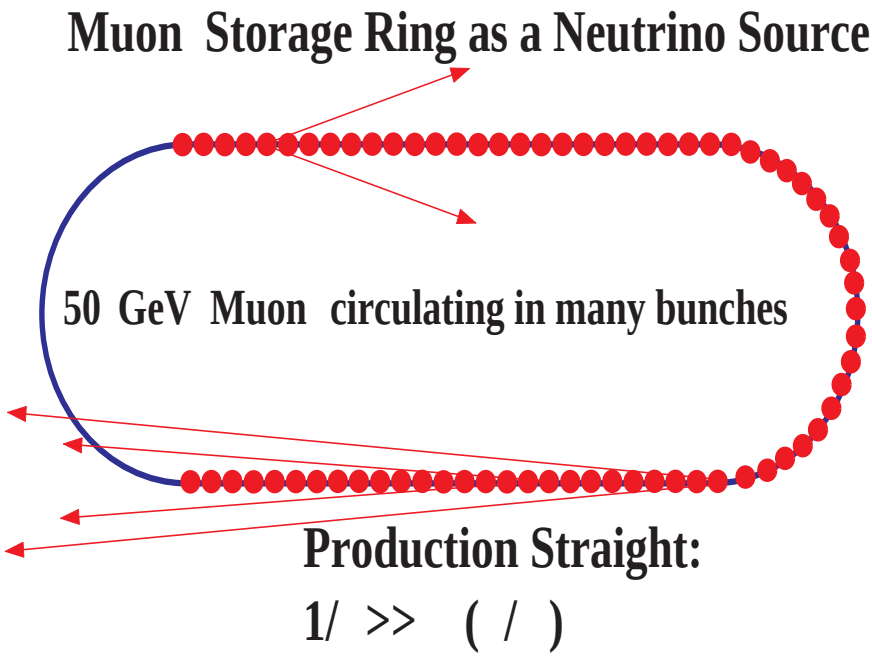

Fig. 1. Sketch of a Muon storage ring with two long straight sections.

The acceptance of the storage ring is designed for 3σ of 3.2 π mm rad. This allows

1. Given the ongoing study at Fermilab for a fast cycling proton synchrotron (15 Hz) with 16 GeV extraction energy, the number of protons per pulse required on target is at least 2×10^{13}. This is approximately 1 MW beam power on target.
2. The transverse emittance of the muon beam after the cooling channel has to be small enough that the beam divergence in the straight section is less then 1/10 of the decay angle, which is $1/\gamma$=2 mrad. At an invariant emittance of $\gamma \cdot \varepsilon$=1.6π mm rad the β-function would be $\approx$ 400m. This seemed reasonable.
3. Following the assumption of having ten protons per one muon injected in the storage ring, 2×10^{12} muons per pulse are required after the cooling channel and have to be accelerated.
4. Abandoning polarization for this study had two advantages. The very low frequency rf system that was proposed directly after the target is not necessary, because forward and backward polarized pions do not have to preserve their correlation in longitudinal phase space. For the same reason the proton bunch length in the proton accelerator could go up to 3 nsec instead of 1 nsec, which is a significant relief.
5. Fermilab to SLAC/LBNL with a distance of $\approx$3000 km defines the slope of the storage ring with respect to the earth surface, which is 22% or 13 deg in our case. This slope is gentle enough to think of conventional installation methods.

Table 4. Parameters for the facility following from table 2 and table 3.

a total emittance growth of approximately a factor of 2 in the accelerating systems once the muon beam has been cooled down to the goal value of 1.6 π mm rad. The straight section pointing towards the west coast would have the large β-functions to provide the smallest possible opening angle for neutrino beam. The upward pointing straight section would feed a surface experiment with a very intense neutrino beam. In order to correct the nonlinear and off-energy beam dynamics, the β-function is significantly smaller ($\approx$ 150m).

Energy	GeV	50
decay ratio per straight	%	39
Designed for inv. emittance	π·m·rad	0.0032
Emittance at cooling exit	π·m·rad	0.0016
β in straight	m	440
N_μ/pulse	10^{12}	6
typical decay angle of μ (= 1/γ)	mrad	2.0
Beam angle ($\sqrt{\epsilon/\beta} = \sqrt{\epsilon \cdot \gamma}$) $\gamma = (1-\alpha^2)/\beta$	mrad	0.2
Lifetime (c γ τ)	m	3x10^5

Table 5. Parameters for the 50 GeV storage Ring.

2 The General Layout of the Facility

The footprint of the total facility is comparatively small and fits easily under several existing laboratory sites. This is considered a big advantage compared to other large scale accelerator studies going on. A sketch which is basically made to scale is shown in figure 2. The largest subsystems are the accelerating linacs and recirculating accelerators (RLA1 and RLA2).

The total area required in order to provide a 50 GeV muon beam to a storage ring is approximately 1.0 km$\times$2.0 km only. In contrast to other High Energy physics programs proposed, the site constraints can hardly be a limitation. The philosophy behind the given geometric layout is that bending between the different subsystems is minimized, which will minimize muon loss because of the large transverse emittance of the beam. The same number of passes through each linac (both sides) of the RLA's is another criterion that was applied to make the beam loading and the rf system requirement the same for both sides. Coming out of the last RLA, the muon beam would be gently bent downwards into the storage ring tunnel and injected into the straight section pointing to the long baseline experiment. Although this might take up a certain fraction of the main decay straight, injecting in this direction is much easier than injecting into the upward arm.

Another remarkable result of this layout, given the earlier boundary conditions, is that the direction the proton beam hits the target defines the direction of the neutrino beam going to the experiment. Therefore once the location of the detector is fixed, the

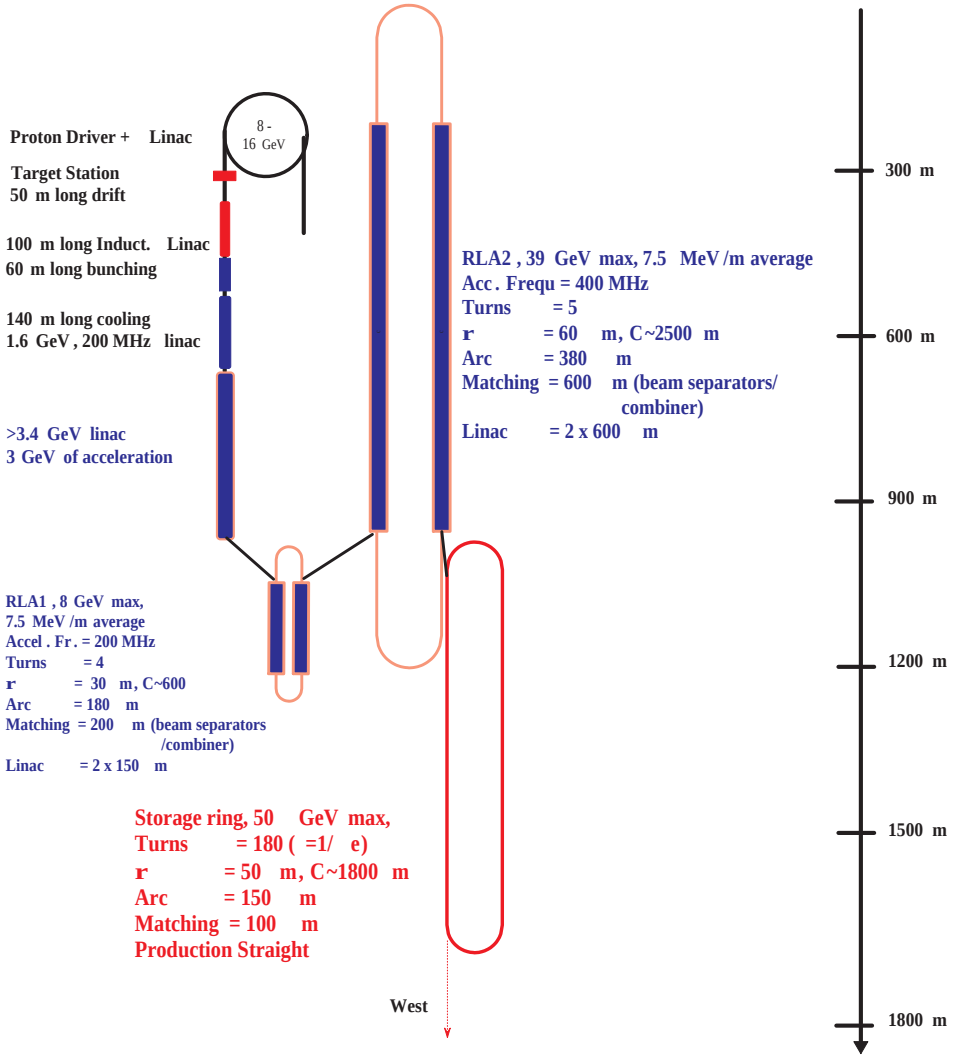

Fig. 2. Footprint (approximately to scale) of the whole facility.

layout is constrained, or else one of the boundary conditions have to be given up, which will most probably increase cost or decrease performance.

3 The subsystems of a the Neutrino Factory

The different subsystems of such a Neutrino Factory are in principle very similar to what is required for a Muon Collider, although they are not identical and in many ways not as demanding. The relaxation of having the muons in each pulse distributed over many bunches, together with the reduced transverse emittance cooling required, are the most obvious ones. The beam dynamics and performance of these subsystems, as well

as their technical feasibility, are now described further.

3.1 The Proton Driver

The design of an intense proton source as part of a possible upgrade within the baseline program at Fermilab is under investigation.[15] A fast cycling synchrotron operating at 16 GeV is under study. It would produce a high power proton beam, with four bunches per pulse at a repetition rate of 15 Hz. Given the infrastructure at Fermilab, the existing linac in combination with a minor upgrade program would be capable of providing enough protons for injection. In the course of the study two things became evident:

- The required proton intensity is more likely to be 3×10^{12} per pulse due to smaller efficiency of the low Z target.
- This intensity can be distributed over four bunches but not many more, given the limitation of the induction linac (used later in in the accelerator chain) which has to produce a number of high voltage pulses within one acceleration cycle of the synchrotron ($\approx$2 μsec).

Given the advantages of a low Z target (see later in this paragraph) the optimization showed in addition that there is a 15-20% advantage in the pion yield per unit proton beam power as the energy of the protons drop. From the engineering point of view and given the higher yield, a lower energy proton driver operating at 6-8 GeV would therefore be preferable. It became also quite clear that a proton synchrotron that is capable of delivering a 4 MW proton beam is one of the larger consumers of wall plug power within the facility.

3.2 The Target

Extensive studies on target yield[16] as well as on radiation damage have been performed. The basic system considered as a first generation target consists of a strained graphite rod, which would operate at approximately 2200C$^{\circ}$.[17] The advantages of graphite are the lower atomic number and the capability of withstanding very high thermal and mechanical stress. While the power deposited in the target per incident beam power goes down by a factor of five, the yield only drops by $\approx$1.5. The target would be radiation cooled and based on present knowledge would have to be exchanged every 3 months. An intense R&D program together with the collaborating institutions is necessary to justify these statements. The design of the 20 Tesla capture solenoid is a

technical enterprise by itself. The combination of a 11 Tesla superconducting coil with an 8 Tesla normal conducting coil set additional constraints on feasibility. The normal conducting coil requires approximately 10 MW dc power and the lifetime is limited to about 2500 hours because of erosion due to excessive cooling requirements.[18] A sketch of the target set-up can be seen in figure 3. The approximately one meter long grpahite rod is mounted within the normal conducting Bitter solenoid. In addition to this massive copper device more shielding is added around and the super-conducting target solenoid can be seen in the outer shell. The radiation level during operation at the target is of the order of $10^{10} - 10^{11}$ Gray.

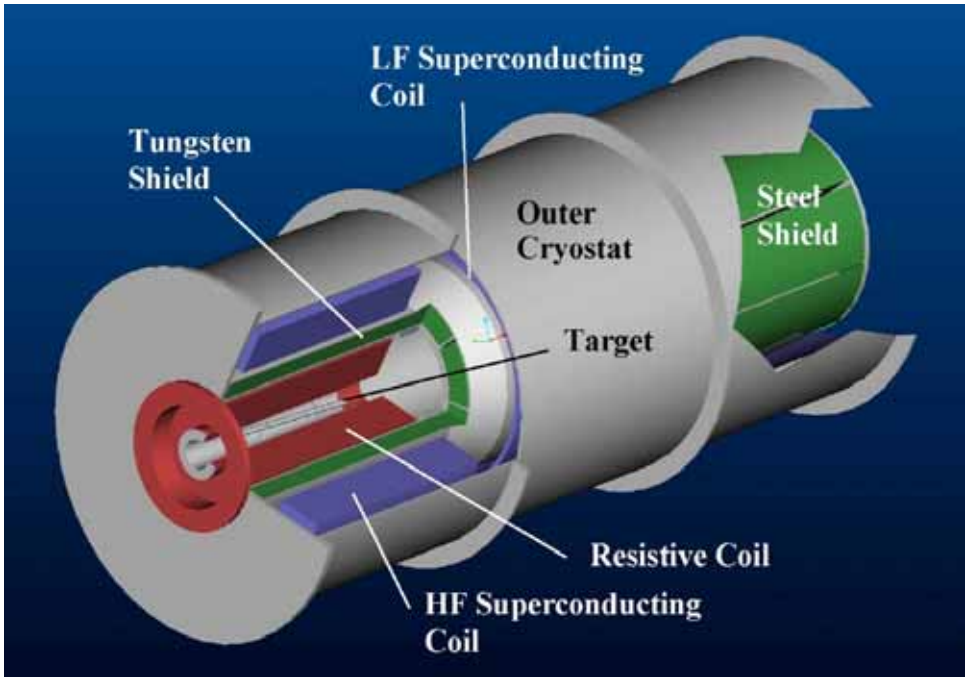

Fig. 3. Sketch of the target set-up: the graphite rod placed within the normal conducting magnet, the shielding, and in the outer shell the sc-solenoid.

The target area, remote handling procedures and facilities are very similar to what has been proposed for the **Spallation Neutron Source** in Oak Ridge. Having a solid target even reduces the operational risk according to the experts. The target hall itself on the other hand is impressive. Remote handling procedures, shielding and target and component exchange has to be integrated into the design to make it viable.

3.3 The Phase Rotation

In order to reduce the energy spread of the muon beam, the muons have to be rotated in phase space. The fifty meter long decay channel is not only used to let the pions decay into muons but also to develop a correlation between the energy of the muons and their longitudinal position along the muon bunch. With a total length of more than 200 nsec per bunch, each of the four bunches coming from the target should be de-accelerated at the head and accelerated at the tail[19] to reduce the energy spread before rebunching. An induction linac naturally provides voltage pulses of that order, while rf cavities with a low enough frequency either become excessively large or too power intensive. A 100 meter long induction linac operating at 15 Hz with 4 pulses per cycle and a not yet achieved gradient of -1 to 1 MV/m (2MV/m total) would be required. A sketch of an induction cell together with a superconducting coil operating at 1.3-3 Tesla is shown in figure 4. Coming out of the decay channel the required beam aperture is 60 cm, which dominates the core size of the induction cell.

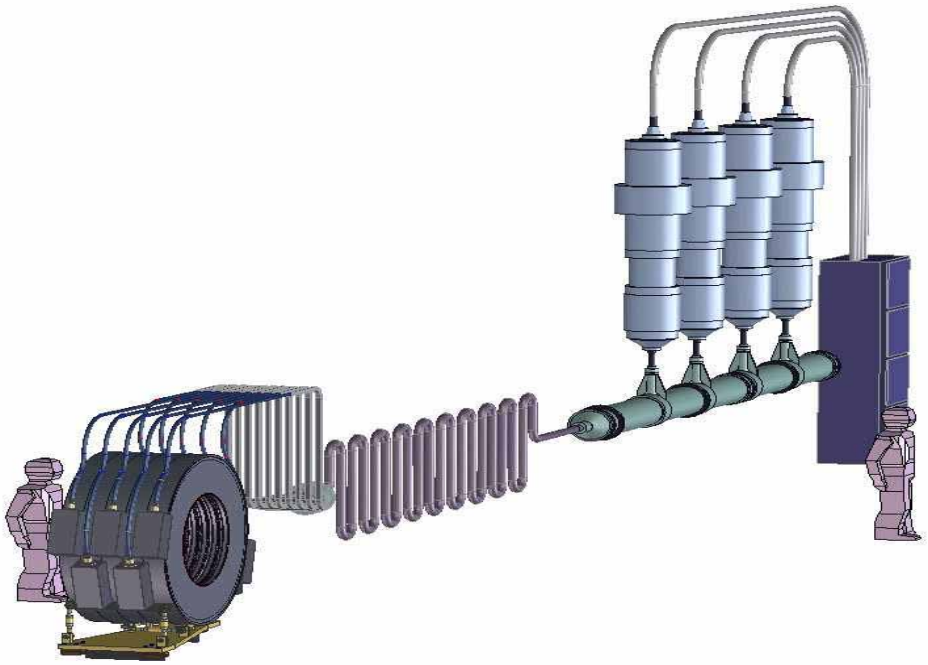

Fig. 4. Sketch of an induction cell with integrated superconducting 3 T coils for muon focusing. A delay line pulser with switches to produce four pulses per cycle is connected to a single one meter long induction cell.

Each unit is approximately one meter long and driven by an individual power supply.[19,20] The accelerating gradient is large compared to existing induction linacs and is

certainly an R&D item. Technical feasibility on the other hand is less of a concern than investment cost, power consumption and reliability.

3.4 Mini Cooling, Bunching and the Cooling Channel

Mini cooling and re-bunching of the muon beam after the phase rotation is the first intrinsically non-efficient step. Four muon pulses with a length of ≈200 nsec each drift through an approximately two meter long liquid hydrogen absorber into high gradient cavities and then further on into the cooling channel. While so called mini-cooling reduces the transverse emittance by ≈30% the cooling channel has to reduce the emittance by almost an order of magnitude. The high gradient 200 MHz cavities have to reaccelerate and longitudinally focus the growing muon bunch while strong alternating solenoids with a field of 3.6 Tesla on axis produce small enough β-functions for transverse cooling.[21] The performance of the cooling channel is shown in figure 5. Significant beam loss occurs immedeately at the entrance of the cooling channel. The main reason is that the energy spread reduction in the phase rotation section is far from perfect and after rebunching the rf-bucket is already completely filled. Any further disturbance, like straggling and scattering in the cooling cells, will increase the longitudinal emittance and cause particles to fall out of the bucket. For the channel shown here the cooling channel increases the number of particles that would fit into the acceptance of the accelerators by only a factor of 2, while for an ideal beam coming (small energy spread) this factor is more like 6-8. New designs that are being explored come much closer to this number.[11]

The main challenges here are certainly the unrivaled gradient in normal conducting cavities at 200 MHz and the rf source that is necessary to provide enough peak power at this frequency.[23] The high field superconducting coils on the other hand are more than challenging due to the very large stored energy and the enormous forces (2000 tons) they have to sustain. A rule of thumb correlates the achievable current density (J) with the field at the coil (B) and the radius (R): $B \times J \times R < 350$ MPa. As a result, the coils used for focusing in the cooling channel become rather large and expensive.[22] A sketch of the cooling channel segment, with the hydrogen absorber, the cavity and the solenoids is shown in figure 6.

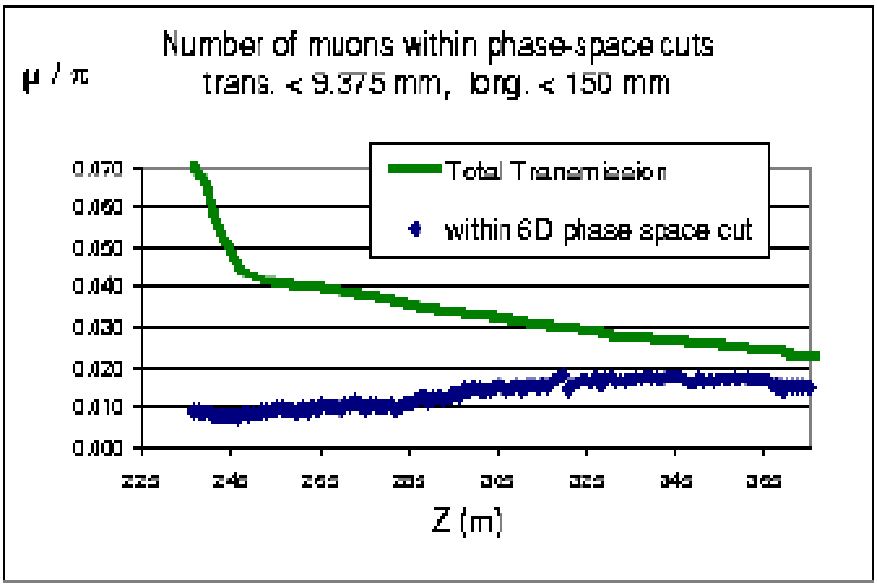

Fig. 5. Cooling performance of the cooling channel being used in this study.

3.5 The Acceleration

Coming out of the cooling channel, the muons have a kinetic energy of ≈ 110 MeV and have to be accelerated to 50 GeV. The transverse invariant emittance is ideally $1.6\,\pi$ mm rad. The longitudinal phase space is diluted due to scattering in the cooling channel as well as energy and position dependent drift differences. In order to capture the beam the first part of the acceleration can only be done in a low frequency high gradient rf system operating far off crest to form a stable bucket. 200 MHz is the maximum possible frequency because that is the bunching frequency used early on after phase rotation and in the cooling channel. The main difference between this linac and the cooling channel is that distributed focusing (solenoids or quads) can be used, which makes possible the use of superconducting rf cavities between the focusing elements. Shown in figure 2 is a 3 GeV superconducting linac in which the phase angle for acceleration is gradually increased to capture and stabilize the beam. Afterwards two cascaded recirculating linacs (RLAs) boost the energy to 50 GeV, with the first RLA having four recirculations and the second RLA having five. The large energy spread of the beam in combination with the large beam size requires long matching sections in order to go into and out of the arcs, which are normal conducting for the first RLA and superconducting in the second. The aperture that is required in the arc cells is

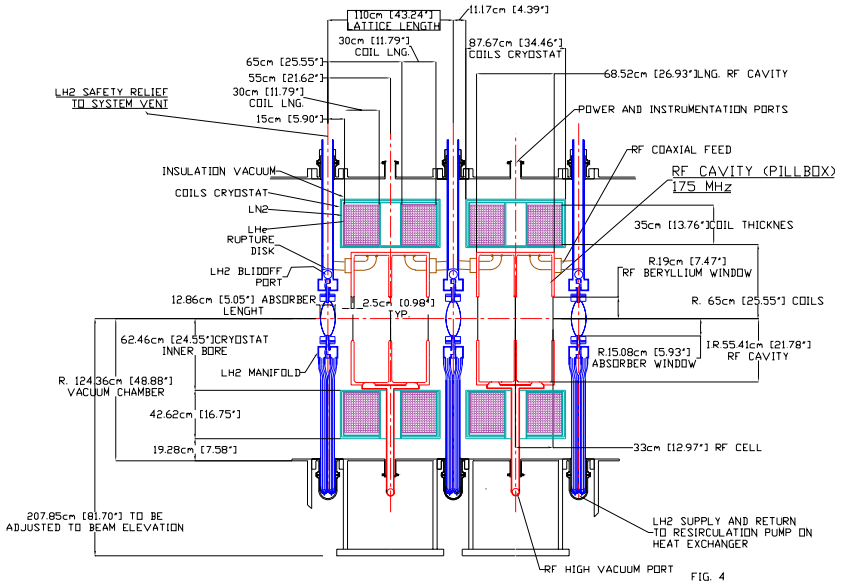

Fig. 6. Sketch of a cooling cell showing one period of the magnetic channel, the hydrogen absorber and the 200 MHz cavities mounted inside.

dominated by the off energy particle orbits (given $\sim$10% energy rms spread coming from the cooling channel) and goes up to several tenths of centimeters. The number of recirculations is limited by the fact that the separation from turn to turn becomes more difficult as the number of turns increases, and also by balancing the cost of the arcs with the cost of the rf systems.

For these reasons the second RLA, with five turns and 8 GeV/turn, certainly dominates the required real estate requirement. Developing the low frequency high gradient superconducting cavities for these accelerators is clearly a high priority R&D item. Based on the technology at CERN, where sputtered niobium on copper cavities are used for acceleration at 350 and 400 MHz, this seems feasible, but has not been demonstrated yet. The first linac as well as RLA1 is based on 200 MHz rf. RLA2 though would have twice the frequency (400 MHz) in order to save investment and operational cost. The rf power sources that would be used to drive these cavities have to be developed as well. Providing peak power at low frequency using standard technology leads to excessively large structures. Multi-beam klystrons are one possibility to avoid such pitfalls.[25]

3.6 The Storage Ring

The muon storage ring represents neither a cost driver not a real technological issue, given the boundary conditions from table 5. The racetrack shape with the superconducting 6 T arcs brings the efficiency per straight to almost 40%. The circumference is ≈1800 meters and given the angle of 13°, the ring dips 260 m into the earth on one side. The available depth for reasonably good tunneling conditions is the only real site-dependent part of this study. A sketch of the geology under the Fermilab site demonstrates the boundary conditions. Starting almost at the surface of the earth, the ring goes down to the top of the underlying aquifer which should be avoided due to largely increased tunneling cost (see figure 7).

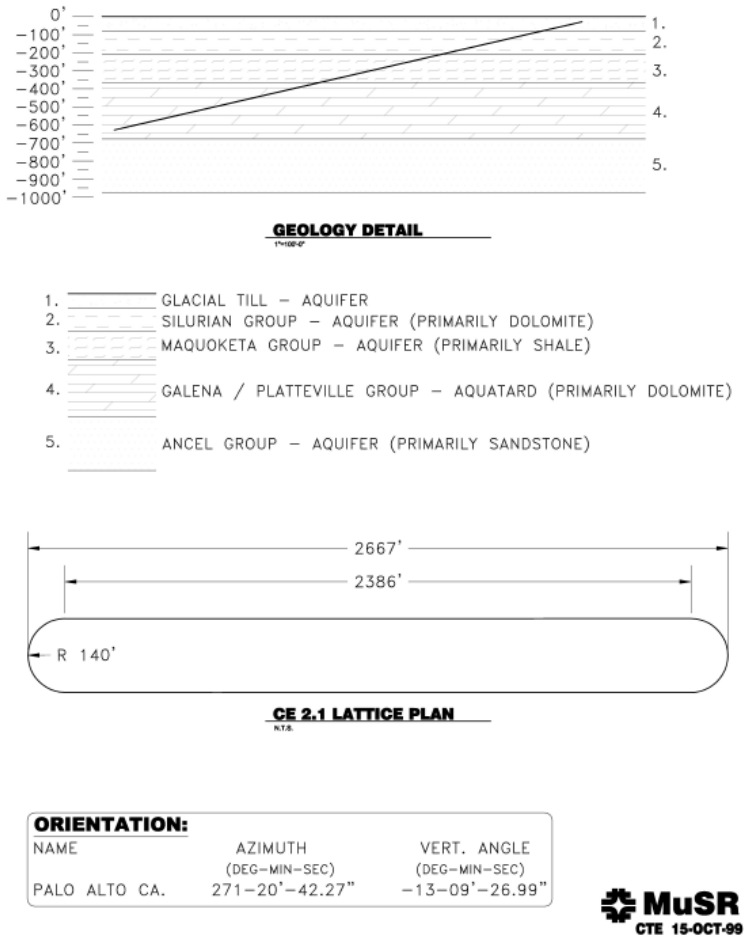

Fig. 7. Location of the storage ring under the Fermilab site tilted at an angle of 13 degree. The geological layers determine the available depth for tunneling under reasonable conditions.

Maximizing the yield from each straight section on the other hand requires maximum circumference. The gain that can be made by following this philosophy is shown in figure 8. Bending magnets with a field larger than 6 Tesla do not significantly increase the yield but are technically more challenging, given the fact that a large aperture is required: a) for the beam due to the large emittance, b) due to the tungsten shield to protect the magnet from decay electrons. Normal conducting dipoles on the other hand (1.8 T) would reduce the muon yield per straight from 39% to 28%. The production of the muon beam is much too expensive and too difficult to accept such a large factor for the ring design. As a result of this study, the storage ring certainly seems not to be much of an R&D issue[26] compared to the other subsystems.

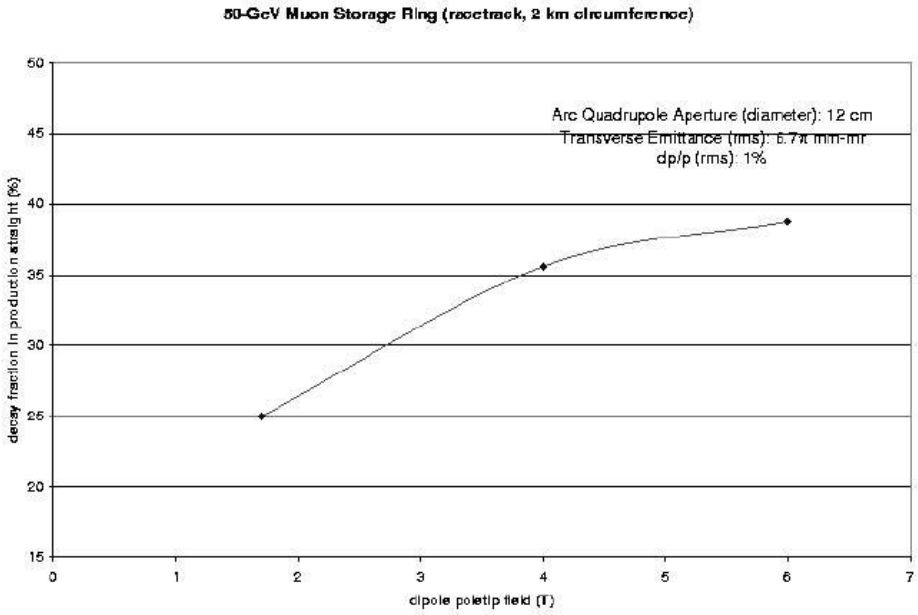

Fig. 8. Muon yield versus bend strength assuming the maximum depth to be used for the storage ring tunnel at an angle of 13°.

3.6.1 Environment, Safety and Health Issues

For the Muon Storage ring there are four major subsystems where significant ES&H issues have to be addressed. Some of them are very common, others are not. For the proton source, a 16 GeV synchrotron, 4 MW of average proton beam power is produced. Residual radiation, etc., will be a major design, and later on operational, issue. The target, the place where 4 MWatts of proton beam are dumped, is the second area where

remote handling, radiation environments and operational aspects have to be part of the design. Both areas though are not uncommon, and the procedures being in place for the Spallation Neutron Source project in Oak Ridge will provide a lot of input on how to handle those. The same is true for the operation of cryogens for the different superconducting systems, magnets and rf cavities. Again, this is a familiar subject.

On the other hand, the large amount of neutrino radiation produced by an intense neutrino beam coming from the straight section of a storage ring is very uncommon. The well collimated neutrino beam, with an opening angle of 2 mrad, and the intense flux of neutrinos into this cone produces enough interaction with matter, so that 100 mrem per year can be achieved being close to the ring. In order to avoid any legal matter discussion on this subject, a boundary condition applied by the project team was to design the ring so that by the time the neutrino beam exits the west boundary (the down-going beam) or the east boundary (the up-going beam), the integrated radiation per year will not exceed this amount. Given the integrated design flux per year (2×10^{20} ν's), this determines the location of the storage ring with respect to the site boundaries. For the Fermilab site this boundary can be seen in figure 9.

For the east boundary, a large (so far nonexistent) building with a height of 600 feet was assumed. The neutrino beam, if it hit the walls, would produce radition for the same reason as in the soil. Three boundaries for different conditions (30 GeV, 50 GeV, 10 mrem/y, 100 mrem/y) have been plotted. The final location of the storage ring can be seen as well.

3.7 Summary

Presented here is a preliminary summary of the feasibility study on a muon storage ring used as a new intense source for long baseline neutrino beams. The study was done in close collaboration with the Neutrino Source/Muon Collider collaboration and has focused much more closely on the engineering aspects of such a facility. As a result, many R&D issues have been identified. All of them seem solvable if an aggressive R&D program could be started, but it would have to happen almost simultaneously. All of these solutions are extrapolations of existing and well understood technologies. One of the real challenging subjects, the beam diagnostics, which will be crucial for the performance especially of the cooling channel, has not been addressed. Here really new inventions are required. Given the results from this study it certainly seems feasible to build a Neutrino Source if intensity and energy can be compromised for the first step.

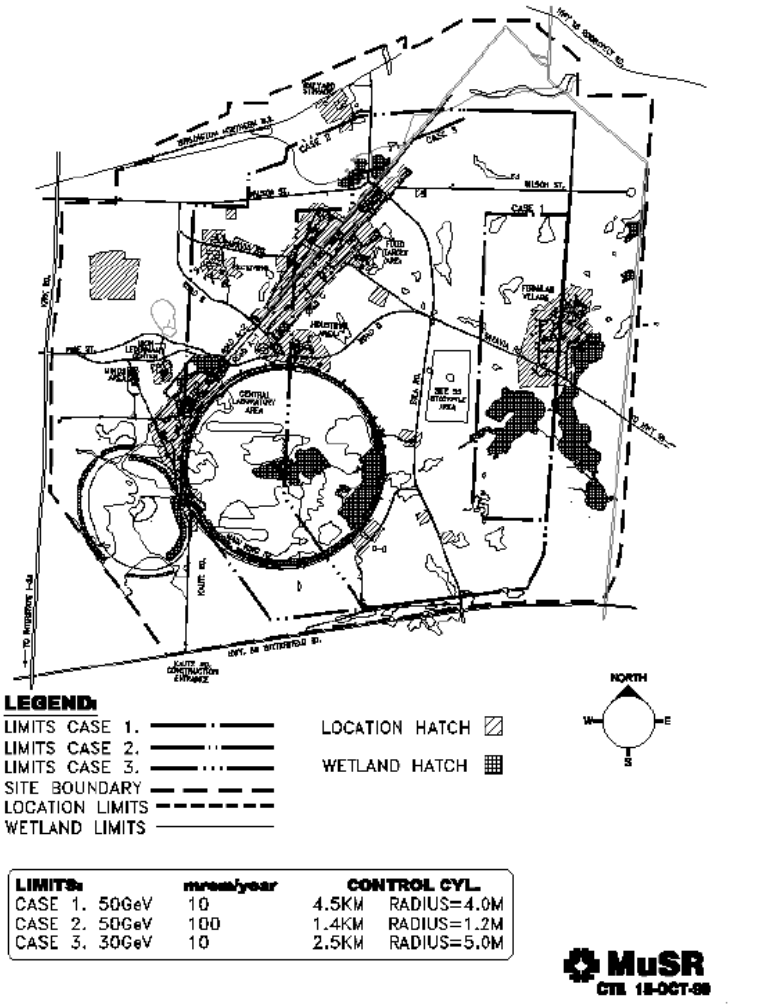

Fig. 9. Fermilab site boundaries and possible locations for the muon storage ring, without exceeding exposure limits outside the Fermilab boundary.

4 Acknowledgement

I would like to thank all the contributors to this study for the enthusiasm they have shown. Especially I want to thank Robert Palmer who contributed many of the ideas that were used as the basis of this study. Andy Sessler, for focusing the Neutrino Source/Muon Collider collaboration on this subject and Jonathan Wurtele and Mike Zisman for organizing the simulation effort for the cooling channel. I want the thank the contributors from the different laboratories (INP, Protvino, TJNAF, Oak Ridge, Michigan State University, National High Magnetic Field Laboratory etc) and their management for their support and interest. (Presenting the list of names would be too long.) I

also would like to express my gratitude to the Fermilab management for their support and for giving me the opportunity to organize this study.

References

[1] J. Tinlow (1960); G. Budker (1969); A. Skrinsky (1971); D. Neuffer (1979,1985); R. Palmer (1994); S. Geer, Phys. Rev. D57, 6989 (1998).

[2] D.G. Koshkarev, Preprint ITEP-33, 1974 and *Proposal for a decay ring to produce intense secondary particle beams st the SPS*, CERN/ISR-DI/74-62.

[3] S. Wojcicki, unpublished (1974).

[4] T. Collins, unpublished (1975).

[5] A.A. Kolomensky, Sov. Atomic Energy Vol. 19, 1511 (1965).

[6] R.M. Djilkibaev and V.M. Lobashev, Sov. J. Nucl. Phys. 49(2), 384 (1989).

[7] C. Ankenbrandt et al. (Muon Collider Collaboration), Phys. Rev. ST Accel. Beams 2, 081001 (1999).

[8] S. Geer, *Neutrino beams from muon storage rings: characteristics and physics potential*, FERMILAB-PUB-97-389, 1997; Presented in the Workshop on Physics at the First Muon Collider and Front-End of a Muon Collider (Editors: S. Geer and R. Raja), November, 1997; S. Geer, Phys. Rev. D57, 6989 (1998).

[9] J. Ellis, E. Keil, G. Rolandi, *Options for future colliders at CERN*, CERN–SL/98-004 (1998); B. Autin, A. Blondel, J. Ellis (editors), *Prospective study of muon storage rings at CERN*, CERN 99-02, April (1999).

[10] Ongoing study at CERN on a Neutrino Source Based on a Muon Storage Ring, H. Haseroth, CERN, private communication and talk given at NuFact'00 conference, Monterey, Ca., May 2000.

[11] Ongoing study at Brookhave in Collaboration with the Neutrino Factory and Muon Collider Collaboration on a Neutrino Source Based on a Muon Storage Ring, B. Palmer (BNL); A. Sessler (LBNL), private communication.

[12] N. Holtkamp, D. Finley, editors, *Feasibility of a Neutrino Source Based on a Muon Storage Ring*, Fermilab pub-00/08-E, May 2000.

[13] C. Albright et al., *Physics at a Neutrino Factory*, Fermilab-FN-692, May 2000.

[14] *The Cost Effective Design for a Neutrino Factory*, R. Palmer, C. Johnson, E. Keil, CERN-SL-99-070-AP, Nov 1999. 22pp, CERN Library Only.

[15] *Common issues of Proton Drivers: How to produce short intense bunches?*, W. Chou et al Collaboration Meeting, Dec.13-15, Berkeley, LBNL, not published.

[16] *Particle Production for a Muon Storage Ring: I. Targetry and PI/MU Yield*, N. Mokhov, Fermilab-Conf-00-209, Sep 2000, to be published in proceedings of Nu-FACT'00: International Workshop on Muon Storage Ring for Neutrino Factory, Monterey, Ca, 22-26 May.

[17] *Design and Layout of a 4 MW Target Facility for a Neutrino Source Based on a Muon Storage Ring*, P.Spampinato et al, Oak Ridge Nat. Lab., to be published; and ref.[12] chapter 4.

[18] *Design and Layout of a 20 T Target Solenoid*, J. Miller,et all, to be published; and ref.[12] chapter 4.

[19] *Design and Layout of a 100 MV Induction Linac for Phase Rotation*, V. Balbekov et al. (Fermlilab), S. Yu et al. (LBNL).

[20] *Design and Layout of a High Field Induction Cell and a Pulser System*, I. Terechkine, V. Kazacha, A. Sidorov, Joint Inst. of Nuclear Research, Dubna to be published; and ref.[12] chapter 5.

[21] *Simulation Results on the Relative Performance of RF Cavities used in Cooling Channels*, P. Lebrun, J. Monroe, see for example MuCool Notes, see: http: www-mucool.fnal.gov/notes/mcnoteSelMin.html, not published.

[22] *Design and Layout of Various High Field Large Aperture Solenoidal Channels for a Neutrino Factory*, I. Terechkine (Fermilab), S. Kozub, L. Tkachenko, INP Protvino, MuCool Note Nr ?; and ref.[12] chapter 6.

[23] *RF Systems for a the cooling channel of the Muon Source*, J. Reid and D. Sprehn, et al., see ref.[12] chapter 10.

[24] *Concept and Beam Dynamics for a Muon Accelerator Driver (MAD) for a Neutrino Factory*, D. Douglas, L. Harwood, V. Lebedev, talk given at Fermilab, Feb. $15^{th}/16^{th}$, 2000, to be published and ref.[12] chapter 7.

[25] D. Sprehn, G. Caryotakis, Stanford Linear Accelerator Center, talk given at Fermilab, Feb. $15^{th}/16^{th}$, 2000, to be published and ref.[12] chapter 10.

[26] *Storage Ring Design for a 50 GeV Muon Storage Ring*, C. Johnstone et al, to be published; and ref.[12] chapter 8.

MATTER EFFECTS ON NEUTRINO PROPAGATION

Lincoln Wolfenstein*
Carnegie Mellon University, Pittsburgh, PA 15213

ABSTRACT

Neutrino oscillations can be different in matter than in vacuum due to the index of refraction. Examples discussed are the MSW effect for solar neutrinos and effects of passage through the Earth on solar and atmospheric neutrinos.

*Supported by DOE Contract DE-FG02-91ER40682.

Neutrino interactions appear to be well described by the Standard Model. There are the charged current (CC) interactions due to $W^{\pm}$ exchange with quarks

$$\begin{aligned} &\nu_i + d \to \ell_i^- + u, \\ &\bar{\nu}_i + u \to \ell_i^+ + d, \qquad i = e, \mu, \tau, \end{aligned}$$

as well as neutral current (NC) interactions due to Z exchange with quarks

$$\nu_i + q \to \nu_i + q, \qquad i = e, \mu, \tau.$$

The scattering on electrons is slightly more complicated; for ν_μ and ν_τ there is only NC, but for ν_e there is both NC and CC, which can interfere with each other. The Z exchange is in the t-channel, for ν_e-e scattering W exchange is in the u-channel, for $\bar{\nu}_e$-e scattering the W is in the s-channel. Of importance for experiments the cross-sections for elastic scattering on electrons follow approximately

$$\sigma(\nu_e\, e) : \sigma(\bar{\nu}_e\, e) : \sigma(\nu_x\, e) = 6 : 2.5 : 1,$$

where $\nu_x = \nu_\mu$ or ν_τ.

For neutrino energies of 10-20 MeV, the highest energy for solar neutrinos

$$\sigma \sim 10^{-41}\,\mathrm{cm}^2$$

so that the mean free path $L \sim 10^{12}\mathrm{km}/\rho$ where ρ is the density in gm/cc. For ν_μ with energies from 1 to 100 GeV as for accelerator and also atmospheric neutrino experiments

$$\sigma \sim 10^{-38}\ \mathrm{cm}^2\text{-E(GeV)}$$

so that $L \sim 10^9\mathrm{km}/\rho E$. In all these cases the Earth and Sun are essentially transparent. The matter doesn't matter.

Twenty years ago I discovered that in some circumstances the matter could matter.[1] The basic point is that transparent media may have significant indices of refraction. The key is the optical theorem

$$n = 1 + \frac{2\pi N}{p^2} f(0),$$

where N is the number of scatterers per cc, $f(0)$ is the forward scattering amplitude and p is the momentum. The imaginary part of this equation yields $\mathrm{Im}\, n$,

which is the absorption coefficient, corresponding to the well-known relation between $\mathrm{Im}\, f(0)$ and the cross-section. However, we are interested in the real part. For a weak interaction, $f(0)$ is real in the first approximation; $\mathrm{Im}\, f(0)$ occurs only in second order and is proportional to G^2, but $\mathrm{Re}\, f(0)$ is proportional to G. Specifically, we find

$$p(n-1) \sim GN,$$

where G is Fermi's constant. Since $p(n-1)x$ determines a phase change, GN defines the inverse of a length over which there is a large phase change. Multiplying G times Avogadro's number determines a length which is approximately the radius of the Earth!

My original idea was to consider massless neutrinos with an off-diagonal neutral current. That is, I considered the possibility that Z exchange changed the flavor so that, for example,

$$\nu_\mu + q \to \nu_\tau + q.$$

My motivation was to find a method to check the Standard Model statement that neutral currents were diagonal. The off-diagonal NC corresponds to an off-diagonal index of refraction, analogous to the case of optical rotation. Thus, as a ν_μ beam passed through the Earth it could "rotate" into ν_τ. As one observed neutrinos coming through the Earth at different angles the transmission probability would oscillate, or, if the angular resolution was bad one would find an average survival probability of about 50%.[2] Exactly this was found 20 years later in the Super Kamiokande experiment. The possibility that the experiment could be explained in this was has been explored by several authors.[3] This is probably not the explanation; in particular, it predicts that the disappearance is energy-independent.

Let me turn now to the case of massive neutrinos with oscillations due to mixing. Considering only two flavors of neutrinos ν_a and ν_b

$$\nu_a = \nu_1 \cos\theta_v + \nu_2 \sin\theta_v, \qquad \nu_b = -\nu_1 \sin\theta_v + \nu_2 \cos\theta_v,$$

where ν_1, ν_2 are mass eigenstates and θ_v is the vacuum mixing angle, one finds the oscillation probability in vacuum

$$\begin{aligned} P(\nu_a \to \nu_b) &= \sin^2 2\theta_v \sin^2(\pi x/\ell_v), \\ \ell_v &= 4\pi p/\Delta m^2 = 2.5\,\mathrm{meters}\,\frac{p(\mathrm{MeV})}{\Delta m^2(\mathrm{eV}^2)}. \end{aligned} \tag{1}$$

In the case of oscillations involving ν_e, the effect of matter can be important. This is because n is different for ν_e than for ν_μ or ν_τ since there is a contribution to ν_e-e scattering from W exchange. (The phase due to Z exchange is the same for all ν_i and so is just an overall phase.) This contribution is

$$p(n-1) = -\sqrt{2}GN_e. \tag{2}$$

The propagation equation then becomes

$$\begin{aligned} i\frac{d}{dt}\begin{pmatrix}\nu_e\\ \nu_\mu\end{pmatrix} &= \frac{1}{2E}\begin{bmatrix} m_{ee}^2 + 2\sqrt{2}GN_eE & m_{e\mu}^2 \\ m_{e\mu}^2 & m_{\mu\mu}^2\end{bmatrix}\begin{pmatrix}\nu_e\\ \nu_\mu\end{pmatrix}, \\ m_{ee}^2 &= \frac{1}{2}\left(\mu^2 - \Delta m^2\cos 2\theta_v\right), \\ m_{\mu\mu}^2 &= \frac{1}{2}\left(\mu^2 + \Delta m^2\cos 2\theta_v\right), \\ m_{e\mu}^2 &= \frac{1}{2}\Delta m^2 \sin 2\theta_v. \end{aligned} \tag{3}$$

Thus, for values of ℓ_v that are comparable to $(GN_e)^{-1}$ or larger, oscillations in matter can be very different in the mixing angle and oscillation length than in vacuum. For uniform matter the oscillation length ℓ_m and mixing angle θ_m are given by[1]

$$\begin{aligned} \sin 2\theta_m &= \sin 2\theta_v(\ell_m/\ell_v), \\ \ell_m &= \ell_v\left[1 - 2\ell_v/\ell_0\cos 2\theta_v + \left(\frac{\ell_v}{\ell_0}\right)^2\right]^{-\frac{1}{2}}, \\ \ell_0 &\equiv 2\pi/\sqrt{2}GN_e = 16,000\text{km}/\rho_e, \end{aligned}$$

where ρ_e is N_e in units of Avogadro's number.

An example of particular interest was pointed out by Mikheev and Smirnov.[4] This was the case in which θ_v is relatively small and one considers ν_e emerging from the Sun, thus passing through a region of continuously changing density. One assumes that in the vacuum the lower mass state is mainly ν_e ($m_{ee}^2 \ll m_{\mu\mu}^2$). In the center of the Sun the ee term in Eq. (3) dominates because of large N_e, but this term gradually decreases until it equals $m_{\mu\mu}^2$. This they refer to as a resonance; it can also be called a "level crossing". If we consider the "eigenstates" for propagation we see that for large N_e the top eigenstate is overwhelmingly ν_e but outside the Sun this eigenstate is primarily ν_μ. In the adiabatic approximation the neutrino stays in the top eigenstate and so starting out as ν_e it emerges as

mainly ν_μ. This is called the MSW effect. The adiabatic approximation requires that the two "levels" not get too close at crossing; since they are kept apart by the $m^2_{e\mu}$ term ($= \frac{1}{2}\Delta m^2 \sin 2\theta_v$), this requires that θ_v be not *too* small. Solar neutrino disappearance rates have been fitted with $\sin^2 2\theta_v \sim 10^{-2}$ and $\Delta m^2 \sim 5\times 10^{-6}\mathrm{eV}^2$. (See the talks by Wilkerson[5] and Murayama.[6]) Even though θ_v is very small the oscillation probabilities end up greater than 50%. It is also possible to exploit this matter effect and fit the data with large $\sin^2 2\theta_v \sim 0.7$ (LMA − MSW).

An important aspect of the MSW effect in the adiabatic approximation is that the neutrinos leave the Sun in a vacuum eigenstate. There are no oscillations between Sun and Earth. However, once these neutrinos enter the Earth they are not in a matter eigenstate; therefore oscillations start again. Thus the flux of solar ν_e coming through the Earth and detected at night can be different than that detected during the day. In particular, it is possible that the ν_e shine more brightly at night than during the day. For certain values of Δm^2 and $\sin^2 2\theta_v$ for the LMA-MSW it is found[7] that a 20% asymmetry ((Night-Day)/Sum) would be possible at Super Kamiokande. Such large asymmetries have been ruled out, but small asymmetries are possible.

Note that this Earth effect is not the MSW effect since the density of the Earth does not vary continuously. It is constant for neutrinos that miss the core and there is an almost discontinuous change for those that go through the core. Note also that the day-night effect could occur even if the ν_e suppression factor is exactly $\frac{1}{2}$, maximal mixing.[8] This is because if the adiabatic condition holds, the neutrinos arrive at the Earth in the eigenstate $(\nu_e + \nu_\mu)/\sqrt{2}$ and in the Earth they oscillate in part to $(\nu_e - \nu_\mu)/\sqrt{2}$ so that they emerge as a coherent mixture

$$\cos\varphi(\nu_e + \nu_\mu)/\sqrt{2} + e^{i\alpha}\sin\varphi(\nu_e - \nu_\mu)/\sqrt{2}$$

Returning now to the atmospheric neutrinos, the question has been raised whether the disappearing ν_μ oscillate to ν_τ or possibly to a new kind of non-interacting "sterile" neutrino ν_s. For the case of $\nu_\mu \to \nu_s$ the oscillations can be affected by matter because ν_μ has an index of refraction

$$p(n-1) = GN_n/\sqrt{2},$$

where N_n is the neutrino number density whereas ν_s does not. As the energy increases the mixing terms proportional to $\Delta m^2/E$ become less important relative

to the GN_n term; as a result, the mixing is suppressed. Thus, data on the energy dependence of the ν_μ disappearance has been used as evidence against ν_μ-ν_s possibility. (See the talk by Kearns.[9])

For the value of $\Delta m^2 \sim 3 \times 10^{-3}\text{eV}^2$ which we assume is associated with ν_μ-ν_τ oscillations it is important whether there is some mixing with ν_e described by $\sin\theta_{e3}$. So far we only know that this is small. For atmospheric neutrinos the appearance of upward going ν_e from $\nu_\mu \to \nu_e$ oscillations can be affected by matter. In particular, it is possible that even for small values like $\sin^2\theta_{e3} = 0.03$ the oscillation of $\nu_\mu \to \nu_e$ in the Earth could be almost 50% but only for those of a particularly energy coming through the core. However, even averaging over a range of energies and angles it is possible that a significant enhancement could be present in future atmospheric neutrino data.[10]

One of the reasons for the interest in θ_{e3} is the possibility of CP violation in the neutrino mixing matrix. As in the case of quarks (CKM matrix) it is necessary to consider the full 3×3 matrix. If θ_{e3} is not too small there is the possibility of having a CP-violating difference between $\nu_\mu \to \nu_e$ and $\bar{\nu}_\mu \to \bar{\nu}_e$. Such an experiment would be conceivable in the future in long baseline experiments with beams from Fermilab or CERN. However, you expect some difference anyway because the matter effect is different for ν_e and $\bar{\nu}_e$. Thus, it is necessary to separate out the matter effect to find CP violation.[11]

In summary, we have considered a number of cases where matter effects could be important:

1. Solar neutrinos:
   - Matter effects inside the Sun could enhance the oscillations (MSW effect).
   - Matter effects inside the Earth could then cause a day-night effect.
2. Atmospheric neutrinos:
   - An off-diagonal neutral current could induce oscillations even for massless neutrinos.
   - Matter effects allow to distinguish $\nu_\mu \to \nu_\tau$ from $\nu_\mu \to \nu_s$.
   - Matter effects could enhance $\nu_\mu \to \nu_e$ transitions.
3. Long baseline experiments:

- Matter effects cause a difference between $\nu_\mu \to \nu_e$ and $\bar{\nu}_\mu \to \bar{\nu}_e$, thus simulating CP violation.

References

[1] L. Wolfenstein, Phys. Rev. D **17**, 2369 (1978).

[2] L. Wolfenstein in *Long Distance Neutrino Detection*, AIP Conference Proceedings No. 52, p. 108 (1978).

[3] M.C. Gonzalez-Garcia *et. al.*, Phys. Rev. Lett. **82**, 3202 (1999), hep-ph/9809531; P. Lipari and M. Lusignoli, Phys. Rev. D **60**, 013003 (1999), hep-ph/9901350.

[4] S.P. Mikheev and A.Yu. Smirnov, Sov. J. Nucl. Phys. **42**, 913 (1985) (Yad. Fiz. **42**, 1441 (1985)).

[5] J. Wilkerson, in these proceedings.

[6] H. Murayama, in these proceedings.

[7] J.N. Bahcall and P.I. Krastev, Phys. Rev. C **56**, 2839 (1997), hep-ph/9706239.

[8] A. H. Guth, L. Randall and M. Serna, JHEP **8**, 018 (1999), hep-ph/9903464.

[9] E. Kearns, in these proceedings.

[10] E.K. Akhmedov, A. Dighe, P. Lipari and A.Y. Smirnov, Nucl. Phys. **B542**, 3 (1999), hep-ph/9808270.

[11] J. Arafune, M. Koike and J. Sato, Phys. Rev. D **56**, 3093 (1997); Erratum *ibid.* D **60**, 119905 (1999), hep-ph/9703351; H. Minakata, H. Nunokawa, Phys. Rev. D **57**, 4403 (1998), hep-ph/9705208; M. Koike and J. Sato, Phys. Rev. D **61**, 073012 (2000); Erratum *ibid.* D **62**, 079903 (2000), hep-ph/9909469.

LEP ELECTROWEAK PHYSICS

Robert Clare*
Department of Physics
University of California, Riverside
Riverside, CA 92521

ABSTRACT

The LEP Collaborations have been taking data for over 10 years. In this talk just a small number of hopefully interesting results on electroweak physics will be presented. These are neutrino counting, heavy flavor (b quark) cross-sections and asymmetries, final-state interaction effects in W pair events, and results on the global electroweak fit: where do we stand on the Higgs boson.

1 Introduction

The LEP experiments, ALEPH, DELPHI, L3 and OPAL, accumulated data at the Z resonance between 1989 and 1995. In this time, more than 16 million Z decays were recorded by the four experiments. The bulk of the data was at the peak of the Z resonance; however, significant fractions were also accumulated approximately 2 GeV below and above the peak. These data were used to determine the so-called "Z lineshape", that is, the mass, width of the Z boson and its couplings to fermion pairs.

In 1995, the LEP machine left the Z resonance for higher energies. The energy has been increased in steps, by the addition of new RF cavities, starting at 130 GeV in the last half of 1995 to 208 GeV in 2000 (well, actually a *very* small amount of data has been recorded at 209 GeV). These data have been used to study fermion-pair production at high energy. Since 1996, the LEP energy has been greater than 160 GeV, above the threshold for pair-production of W bosons. With these data the properties of the W boson have been studied. An example of the various cross-sections that have been measured at LEP is shown in Figure 1.

Of course, additional measurements have been made using the LEP data sets, such as QCD studies, and searches for new phenomena. These measurements are beyond the scope of this talk, although the latest results on new particle searches was presented at this conference.[1]

Rather than giving a whirlwind tour of all of the electroweak results that have been made at LEP, I'll concentrate on just a few measurements which I think are interesting and important. These are: neutrino counting (particularly relevant for this conference); the measurements in the heavy quark sector, especially R_{b} and $A_{\mathrm{FB}}^{\mathrm{b}}$; the effects on the W mass measurement of final state interactions in fully-hadronic W decays; and finally the global fit: what do we know about the Higgs boson.

2 Neutrino Counting

At LEP, the number of neutrino species is measured by determining the invisible width of the Z boson. The width of the Z into a pair of fermions is given by the formula:

$$\Gamma_{\mathrm{f\bar{f}}} = \frac{G_F m_{\mathrm{Z}}^3}{6\pi\sqrt{2}}(g_{\mathrm{Vf}}^2 + g_{\mathrm{Af}}^2) \tag{1}$$

where

$$g_{\mathrm{Af}} \;=\; I_{3\mathrm{f}} \tag{2}$$

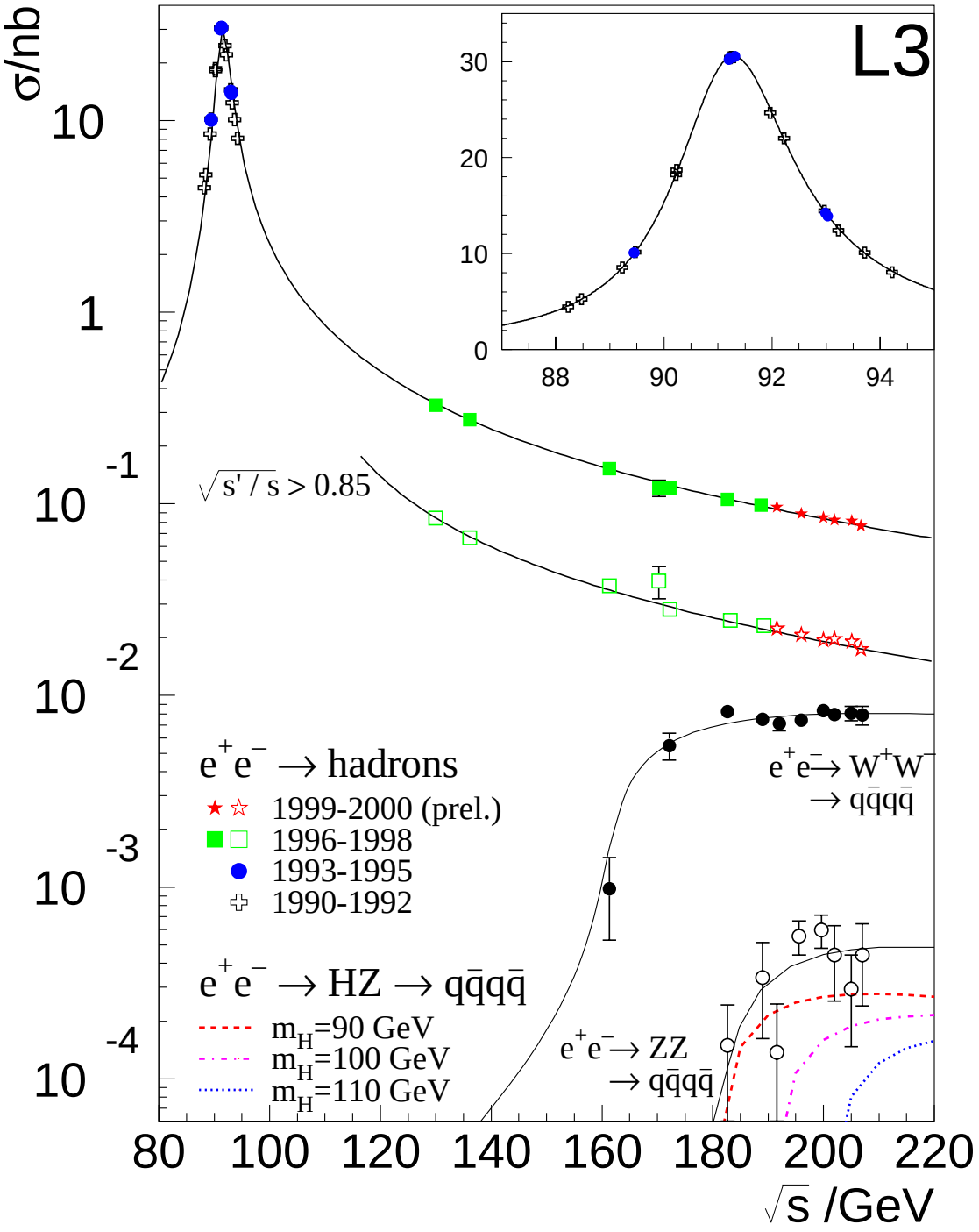

Fig. 1. Hadronic cross-sections as measured by L3 at LEP. Shown are the $q\bar{q}$, the W-pair and Z-pair (with all W's and Z's decaying hadronically) cross-sections, compared with the Standard Model expectations as a function of the center-of-mass energy, $\sqrt{s}$. Also shown is the expected cross-section for a Higgs boson with various masses.

$$g_{\mathrm{Vf}} \quad = \quad I_{3\mathrm{f}} - 2Q\sin^2\theta_{\mathrm{W}}. \tag{3}$$

Thus, the width of the Z into a pair of neutrinos, $\Gamma_{\nu\bar{\nu}}$, is approximately 167 MeV (which can be compared to 84 MeV for the width into a pair of charged leptons). To determine the number of neutrino species, one simply divides the measured invisible width by $\Gamma_{\nu\bar{\nu}}$.

There are two techniques to measure the invisible width, each with their advantages and disadvantages. The first is the "direct" method which actually measures the rate of invisible Z decays. The Z decays are tagged using a photon from initial state radiation. The second is more indirect, as it derives the invisible width by taking the measured total width and subtracting off the measured partial widths. All that is left over is "invisible".

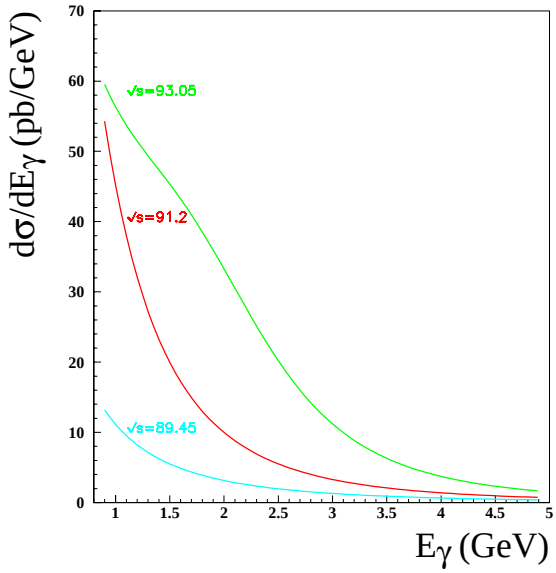

Fig. 2. The differential cross-section for $\mathrm{e^+e^-} \to \gamma\mathrm{Z} \to \gamma\nu\bar{\nu}$ for three different center-of-mass energies.

For the "direct" method, it is important to tag using photons with as small an energy as possible, as the photon energy follows a bremsstrahlung distribution. This can be seen in Figure 2 which shows the differential cross-section for center-of-mass energies around the Z peak. As can also be seen, although the measurement is best performed above the Z peak, it is still possible, albeit difficult, to measure the cross-section *below*

the peak, because of the width of the Z resonance.

One must also take into account t-channel W exchange and W–Z interference (Figure 3). Although W exchange also produces neutrinos in the final state, only the electron neutrino is produced, and thus this process yields no information about the number of species. At the Z resonance, the W exchange and W–Z interference contribute about 5% to the total cross-section.[2]

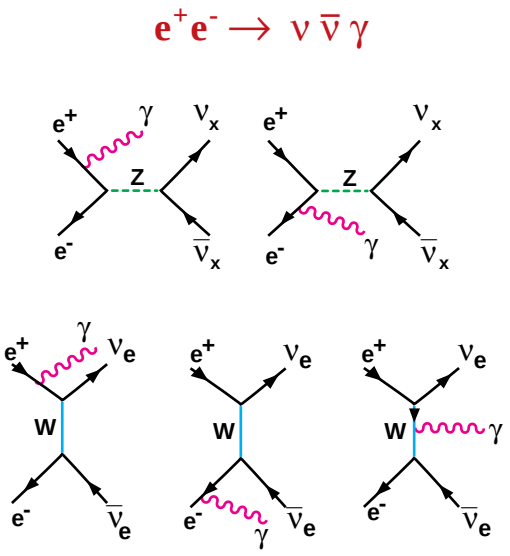

Fig. 3. The lowest order diagrams contributing to $\mathrm{e^+e^-} \to \nu\bar{\nu}\gamma$.

Examples of measured single γ spectra are shown in Figure 4, with comparisons of the data to the expectations of $\nu\bar{\nu}\gamma$ production with 3 neutrino species. One can see the importance of accepting photons with very low energies.

The final results of the LEP experiments[3–6] using the direct technique is shown in Figure 5. The LEP average results in a 3% measurement of the number of neutrino species.

The "indirect" method relies on the knowledge of the measured cross-section as a function of center-of-mass energy, the so-called "Z lineshape". The bulk of the information is contained in the hadronic cross-section, shown in Figure 6. That the cross-section depends on the number of neutrinos can be seen by examining the form of the peak cross-section:

$$\sigma^0_{\mathrm{had}} = \frac{12\pi}{m_{\mathrm{Z}}^2}\frac{\Gamma_{\mathrm{ee}}\Gamma_{\mathrm{had}}}{\Gamma_{\mathrm{Z}}^2}.$$

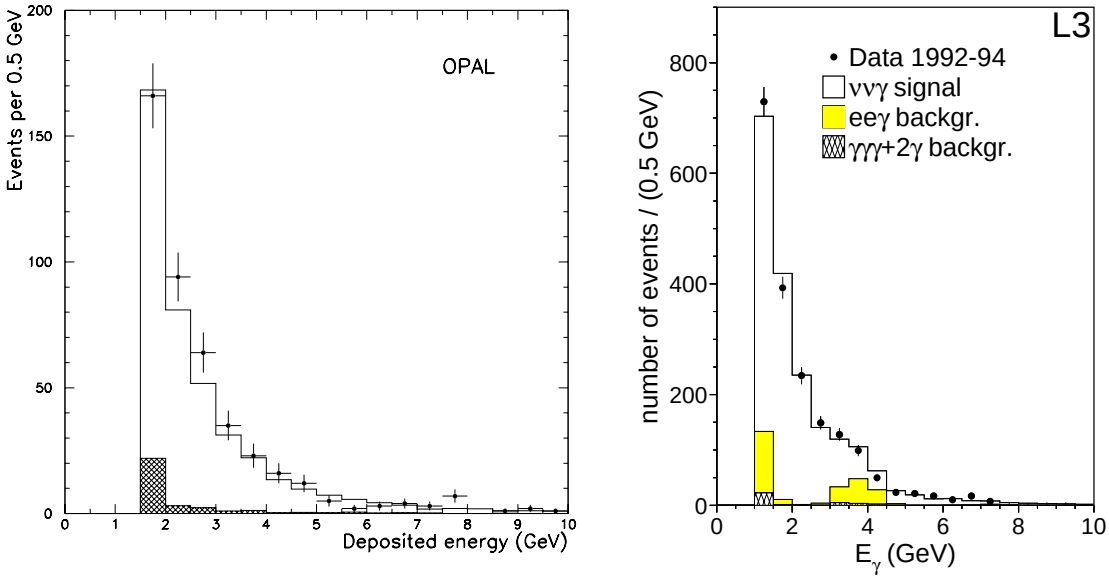

Fig. 4. The measured single photon energy spectra for OPAL (left) and L3 (right). The open histograms are the expectations for $\nu\bar{\nu}\gamma$ production with 3 neutrino species. The solid histograms are the background.

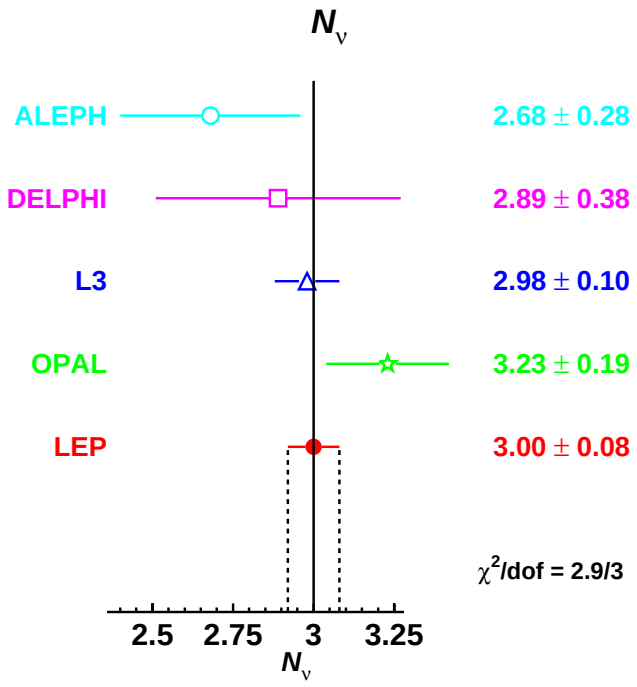

Fig. 5. The results of the four LEP collaborations, as well as the combination, on the direct measurements of N_ν at the Z.

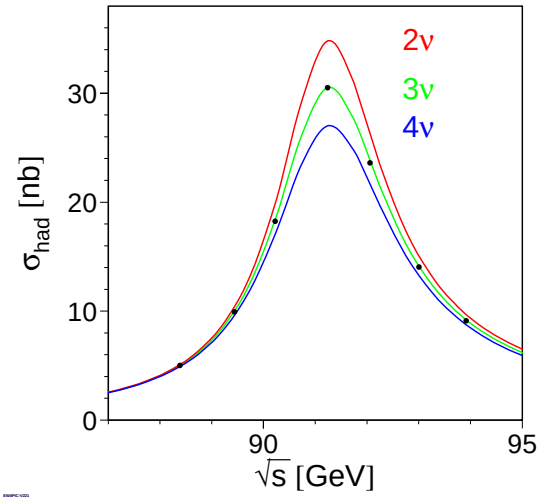

Fig. 6. The measured hadronic cross-section (all 4 experiments combined) compared to the expectations for 2, 3 and 4 neutrino families.

As the number of neutrino families decreases, the invisible width decreases, decreasing the total width and increasing the peak cross-section. The detailed shape of the cross-section is critical for this measurement. Radiative corrections are large: the first order corrections change the peak cross-section by 25%. However, they appear to be under control at better than 0.1%, as shown in Figure 7.

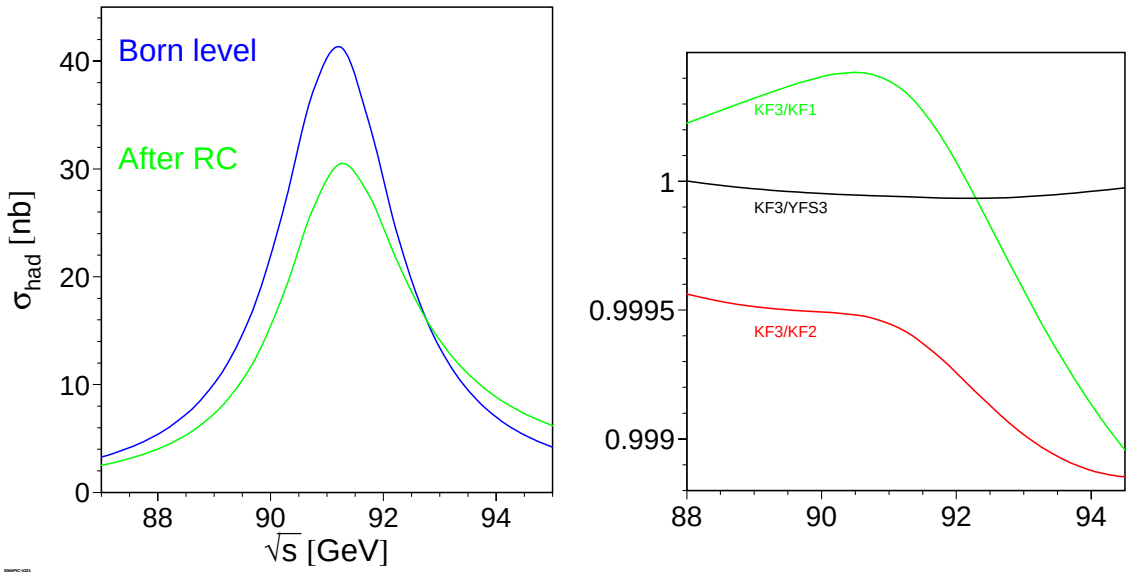

Fig. 7. On the left, the Born-level and first-order-corrected hadronic cross-section; on the right, the ratio of first, second and third order corrections.

From the combined LEP lineshape fit results,[7]

$$\sigma^0_{\rm had} = 41.540 \pm 0.037 \ \text{nb} \quad (4)$$

$$\Gamma_{\rm Z} = 2495.2 \pm 2.3 \ \text{MeV} \quad (5)$$

$$m_{\rm Z} = 91187.5 \pm 2.1 \ \text{MeV} \quad (6)$$

$$R_\ell \equiv \Gamma_{\rm had}/\Gamma_{\ell\ell} = 20.767 \pm 0.025, \quad (7)$$

the experiments derive

$$\frac{\Gamma_{\rm inv}}{\Gamma_{\ell\ell}} = 5.942 \pm 0.016. \quad (8)$$

Using the Standard Model expectation of $\frac{\Gamma_{\nu\bar{\nu}}}{\Gamma_{\ell\ell}} = 1.992 \pm 0.0012$, one finally arrives at

$$N_\nu = 2.984 \pm 0.008. \quad (9)$$

This is a bit below an integral value of three, due mainly to the fact that all four collaborations measure a hadronic cross-section higher than the Standard Model prediction.

If, on the other hand, one assumes that there are 3 neutrino families, then this result can be translated into a limit on additional invisible width:

$$\Gamma_{\rm inv}^{\rm new} < 2.0 \ \ {\rm MeV}, \tag{10}$$

or about 1% of the width of a "standard" neutrino family.

3 Electroweak Heavy Flavor Physics

There are a few aspects of the b-quark that make electroweak studies using b-quarks both interesting as well as possible. First of all, because the b-quark has a relatively long lifetime, the use of displaced vertices allows for efficient and effective tags. In addition, about 20% of the time, a b-quark will decay semi-leptonically resulting in a high momentum electron or muon. Finally, the large mass of the b-quark allows a separation of b- and c-quark events based on the invariant mass of the particles associated with the displaced vertex.

The rate for $Z \rightarrow b\bar{b}$ is interesting because of the extra diagrams involved (Figure 8). Because of these diagrams, the ratio $R_{\rm b} \equiv \Gamma_{\rm b\bar{b}}/\Gamma_{\rm had}$ is uniquely sensitive to the top-quark mass, and is practically insensitive to other parameters of the Standard Model, including the Higgs mass.

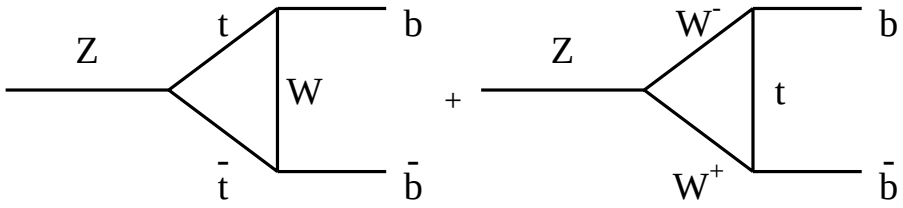

Fig. 8. The extra diagrams for the $Zb\bar{b}$ vertex involving the t-quark.

The current status[8] of the $R_{\rm b}$ measurements is shown in Figure 9. The results are quite consistent with each other, and with the expectations of the Standard Model. It should be noted that $R_{\rm b}$ all by itself yields a prediction of $m_{\rm t}$ of 150 ± 25 GeV, in very good agreement with the measured value of 174.3 ± 5.1 GeV. This was not always the case, as also shown in Figure 9. There have been a number of changes in the last five years.

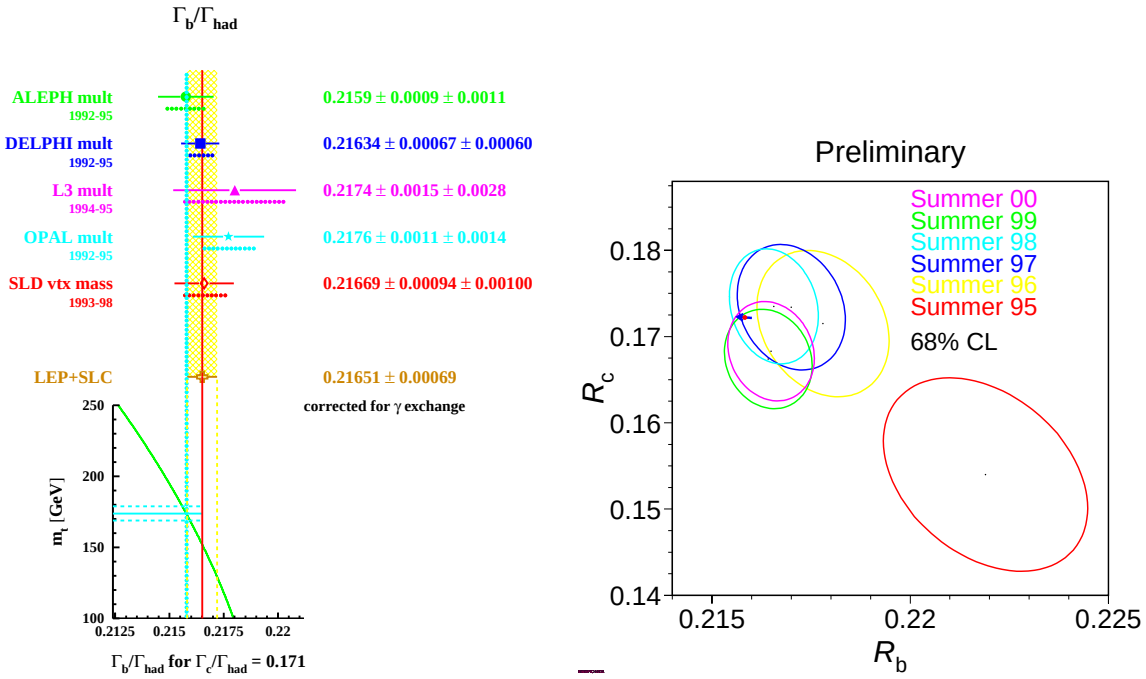

Fig. 9. On the left, the current measurements of R_{b}. On the right, the history over the last few years of R_{b} and R_{c}, compared to the Standard Model prediction (small arrow).

In 1995, only about one half of the full LEPI data set had been analysed. Thus, the current values, which are very close to the final results, include twice the statistics.

The techniques used to measure $R_{\rm b}$ have improved significantly. In 1995, only a few measurements used multiple-tags. The use of multiple-tags allows the determination of many efficiencies directly from the data, reducing significantly the reliance on Monte-Carlo models. This has made the results more robust.

Much work has gone into studying correlations between hemispheres. These correlations can arise through the underlying physics, for example through gluon radiation which can reduce the available phase-space for both b quarks, or can even flip both quarks into the same hemisphere. They can also arise through experimental measurement systematics, for example mis-measuring the primary event vertex and thus affecting the measured decay length of both b's. These effects are also under better control, also partially through the use of multiple types of tags which are affected differently by the various systematic uncertainties.

Finally, a very important element in the measurement of $R_{\rm b}$ has been improvements in related measurements. As can be seen, in 1995 there was a strong correlation between $R_{\rm b}$ and $R_{\rm c}$. The correlation is much smaller now (due to the improved $R_{\rm b}$ techniques), but measurement of $R_{\rm c}$ has also improved at the same time, also through the use of new methods. In addition, some ancillary measurements, such as D meson branching ratios and gluon splitting fractions ($g \to {\rm b\bar{b}}$ and $g \to {\rm c\bar{c}}$) have been better measured, or in some cases measured for the first time, again reducing the reliance on Monte-Carlo.

The upshot is that $R_{\rm b}$ appears to no longer be a concern. However, the b sector is not completely out of the woods yet, as the forward-backward asymmetries are making life interesting now.

The b-quark asymmetry has always provided an interesting and important measurement of $\sin^2\theta_{\rm W}$. This can be seen by examining the structure of the forward-backward asymmetry on the Z peak:

$$A_{\rm FB} = \frac{3}{4}\mathcal{A}_{\rm e}\mathcal{A}_{\rm f} \tag{11}$$

where

$$\mathcal{A}_{\rm f} = \frac{2g_{\rm Vf}g_{\rm Af}}{g_{\rm Vf}^2 + g_{\rm Af}^2} \tag{12}$$

or, equivalently

$$\mathcal{A}_{\rm f} = \frac{2(1-4|Q_f|\sin^2\theta_{\rm W})}{1+(1-4|Q_f|\sin^2\theta_{\rm W})^2}. \tag{13}$$

Since the b-quark has charge $-\frac{1}{3}$, $\mathcal{A}_{\rm b}$ is fairly *insensitive* to $\sin^2\theta_{\rm W}$. On the other hand, $A_{\rm FB}^{\rm b}$ is *more* sensitive than $A_{\rm FB}^{\ell}$ to $\sin^2\theta_{\rm W}$, as shown in Figure 10. Thus, $A_{\rm FB}^{\rm b}$ provides an excellent measurement of $\sin^2\theta_{\rm W}$ at the *electron* vertex.

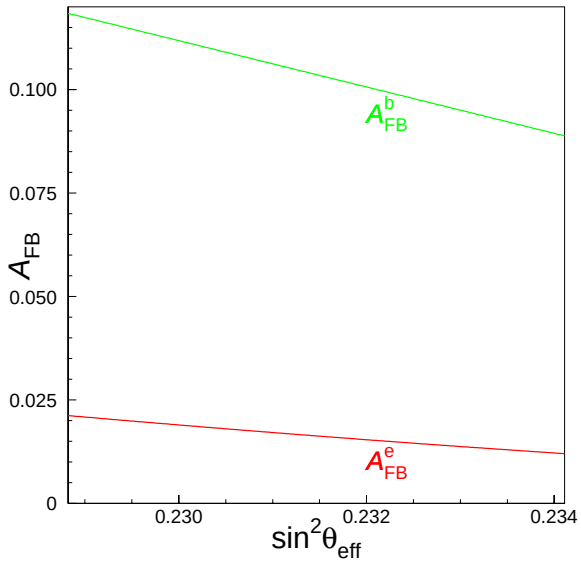

Fig. 10. The forward-backward asymmetry as a function of $\sin^2\theta_{\rm W}$. As can be seen, $A_{\rm FB}^{\rm b}$ is more sensitive to $\sin^2\theta_{\rm W}$ than the electron (or any other unit charged particle) asymmetry.

The measurement of $A_{\rm FB}^{\rm b}$ is conceptually very simple: one tags $\rm b\bar{b}$ events, measures the charge of at least one of the quarks, and then counts the number of b quarks and $\bar{\rm b}$ quarks in the forward hemisphere and takes the difference. The tagging techniques are similar to those used for the $R_{\rm b}$ measurement, relying on high p_t leptons and lifetime information. To measure the quark charge, the charge of the lepton is used for the leptonic tags. For the lifetime tags, as well as for the leptonic tags, one can use the "jet charge". The idea here is that the charge of the primordial quark is "remembered" by the sum of the charges of all particles in the jet, especially if one weights the particles according to their momentum.

There are a number of corrections which must be applied to the measured asymmetry. One source which has been studied in some detail in the recent past arises from QCD radiative corrections. Examples of the effects of QCD corrections are shown in Figure 11. There have been a number of recent calculations.[9] The current understanding is that these effects result in a 1 – 2.5% correction which is somewhat dependent on the analysis and experimental cuts. The correction is larger for the leptonic tags than

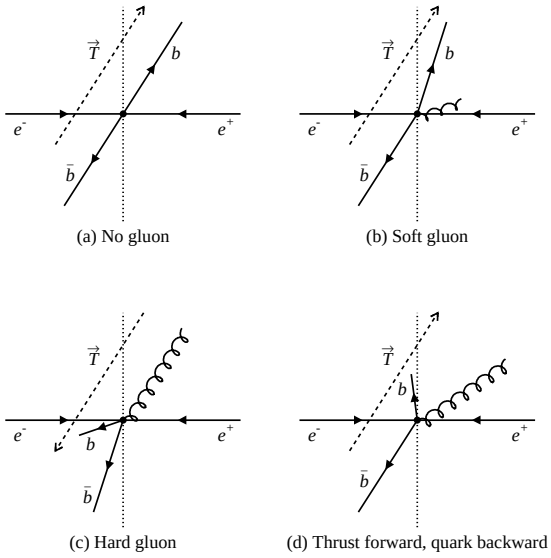

Fig. 11. Examples of event distortions due to QCD radiative corrections. As can be seen, in some cases the quark can be "flipped" to the wrong hemisphere.

for the jet-charge tags, as the jet-charge method compensates for some of the effects.

The resulting measurements[10–13] are shown in Figure 12 (Ref. 14), grouped by measurement type. As can be seen, there is very good agreement among the experiments as well as between the two methods. The average of all leptonic tags yields $A_{\rm FB}^{\rm b} = 0.0971 \pm 0.0026$ whereas the average jet-charge tag is $A_{\rm FB}^{\rm b} = 0.1021 \pm 0.0031$, consistent with the overall average of $A_{\rm FB}^{\rm b} = 0.0990 \pm 0.0020$. Note that because of correlations, these results are not a straight-forward average of the individual measurements.

Although the measurements of $\rm b\bar{b}$ asymmetry are consistent with each other, one can ask whether they are consistent with other measurements. This can be seen graphically in Figure 13. On the left, the $A_{\rm FB}^{\rm b}$ measurements (diagonal band) are compared to the $\mathcal{A}_\ell$ measurements from the leptonic asymmetries, tau polarization and $A_{\rm LR}$ (vertical band) and the direct $\mathcal{A}_{\rm b}$ measurements (horizontal band). There *is* a region where all measurements overlap; it is, however, not where the Standard Model would like to have them. Viewed another way, if one assumes that the b couplings are those given by the Standard Model, then the $\mathcal{A}_\ell$ value extracted from $A_{\rm FB}^{\rm b}$ does not agree with that from the leptonic asymmetries. This is the "standard" interpretation when using $A_{\rm FB}^{\rm b}$ to extract $\sin^2\theta_{\rm W}$ which yields significantly different values for the two. On the other

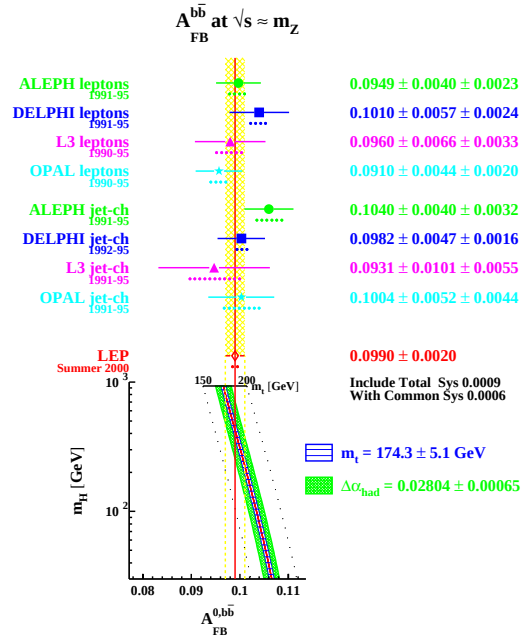

Fig. 12. The various measurements of $A_{\mathrm{FB}}^{\mathrm{b}}$, compared to the Standard Model expectation as a function of the Higgs mass.

hand, if one assumes that the leptonic asymmetries are correct, and uses $\mathcal{A}_\ell$, $A_{\mathrm{FB}}^{\mathrm{b}}$, $\mathcal{A}_{\mathrm{b}}$ and R_{b} to extract the b couplings (the right half of Figure 13), the agreement between the measured b couplings and the Standard Model is not very good.

This is one of the very few sets of measurements that disagree with the Standard Model. Is this physics or just a statistical (or systematic) effect? We will probably have to wait a while to discover this, as essentially all of the available data have been analysed, and all of the results are now final or close to final, and both the LEP and SLC programs are finished.

4 Final State Interactions in W decays

When both W bosons in $\mathrm{e^+e^-} \to \mathrm{W^+W^-}$ decay hadronically, the two hadronic systems may interfere. This is because the typical hadronization scale is about 1 fm, whereas the typical separation between the W's at the time of their decay (at LEP energies) is about 0.1 fm. Because of this, the two systems have the potential to cross-talk, which might influence the measured W mass distributions. Only the fully hadronic (qqqq)

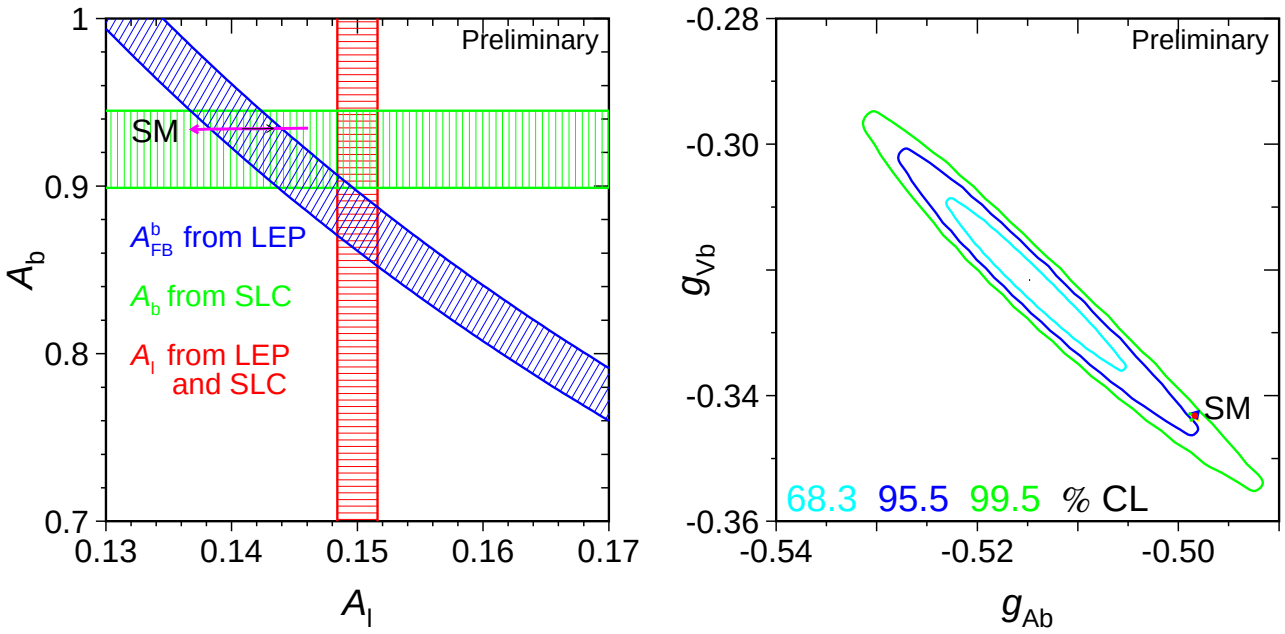

Fig. 13. On the left, the comparison of the $A_{\mathrm{FB}}^{\mathrm{b}}$ (diagonal band), $\mathcal{A}_{\mathrm{b}}$ (horizontal band) and $\mathcal{A}_{\ell}$ (vertical band) measurements. On the right, the extracted b couplings using all available measurements. In both cases, the arrow indicates the Standard Model expectation for Higgs masses between 100 GeV (back end of arrow) to 1000 GeV (head of arrow).

events are affected; events where only one W decays hadronically (qq$\ell\nu$) events are not affected.

There are two sources of final state interactions which might affect the W mass, "color reconnection"[15] and Bose-Einstein correlations.[16] They are schematically represented in Figure 14. Color reconnection involves a change of the color flux, which

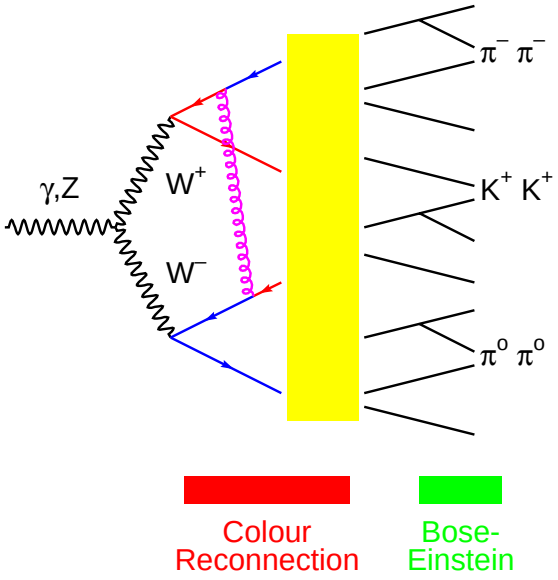

Fig. 14. The different types of final state interactions which can affect the W mass measurements.

could be brought about by the exchange of low energy gluons between quarks from different W decays. Bose-Einstein correlations which affect the distributions of final state pions and kaons are only bad if particles from different W decays are involved.

As all of these processes occur at low momentum transfer, perturbative QCD cannot be used to evaluate them. Until recently, the only available method was to use various Monte-Carlo models. This was not a good situation, as the various models gave a wide range of results: one[17] predicted mass shifts of several hundred MeV! As the final statistical uncertainty on the W mass is expected to be 25 MeV, this could be a show-stopper.

However, with the increasing statistics available, the collaborations are now reporting measurements of these effects using data. These can be used to constrain the available models, placing a limit on the size of any mass shift.

There is ample evidence for Bose-Einstein correlations (BEC) in Z decays.[18] Thus BEC should also occur within a single W decay (*intra*-W BEC). Furthermore, given the arguments above, they could also occur between the two W decay products (*inter*-W BEC).

All four experiments have studied BEC in W decays.[19] All see indications for intra-W BEC. An example of this evidence is shown in Figure 15. However, the fact

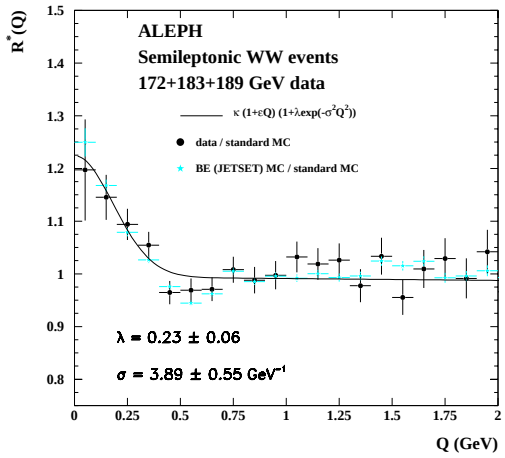

Fig. 15. An example of the evidence for Bose-Einstein correlations in W boson decays.

that BEC do exist makes it more difficult to see if the dangerous inter-W BEC also exist. The experiments have gotten around this by comparing distributions of pions with those from qq$\ell\nu$ events (with only intra-W BEC) or from pions from completely different qq$\ell\nu$ events (with no BEC at all by construction).

The results at the moment are inconclusive.[20] ALEPH disfavor inter-W BEC by about 2 sigma; DELPHI favor inter-W, but also only at 2 sigma. L3 disfavor them at 4 sigma (see Figure 16), whereas OPAL can not say either way (the data are compatible with no inter-W BEC). Clearly more work is needed on this. Fortunately the experiments have not yet analyzed the full data set. With the current situation, the experiments have estimated that BEC effects contribute a systematic uncertainty on the W mass of about 25 MeV.

Color reconnection can be viewed as a situation where the QCD string between the two quarks in one W decay flips to connect two quarks from different W's, as shown diagrammatically in Figure 17. Predicted effects include a change of particle multiplicities, as the dynamics of the fragmentation process have changed, and a change of particle and energy flow between jets, following the string. Also here, with only

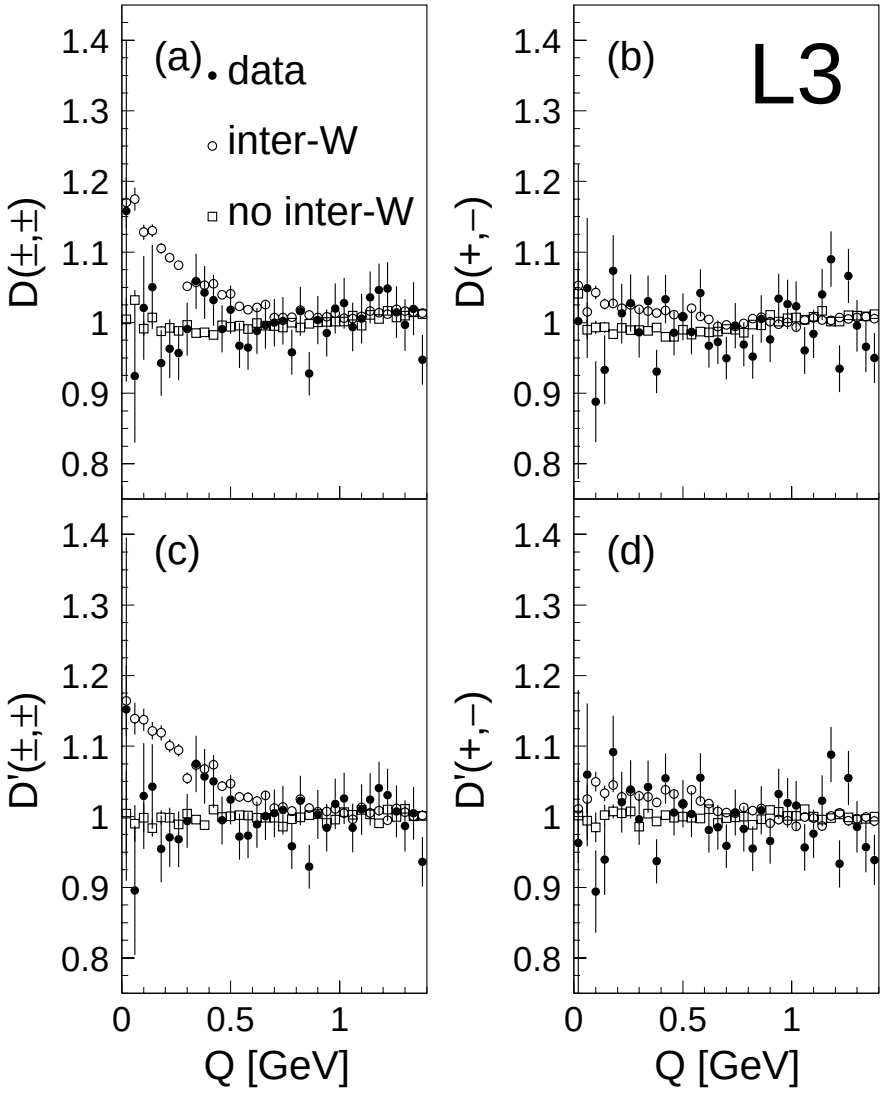

Fig. 16. Distributions of the variables D and D' as a function of Q, the 4-momentum difference between pairs of particles. D and D' are constructed to be one in the absence of inter-W BEC. The data are in agreement with no inter-W BEC (a and c). The control samples of unlike-sign particles (b and d) show no effect.

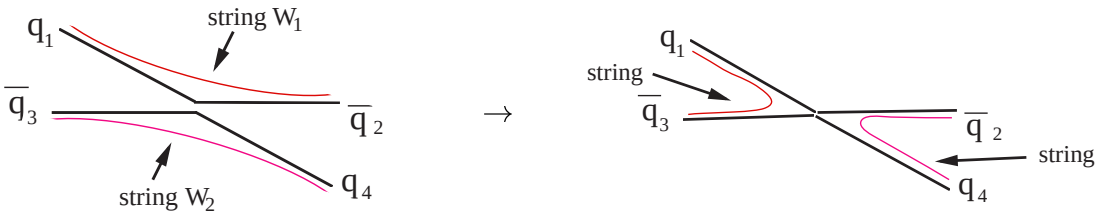

Fig. 17. A diagrammatic view of color reconnection.

models to rely on, the experimenters have tried to infer as much as possible by studying the data, comparing qqqq events to qq$\ell\nu$ or to mixed events.

The study of particle multiplicities has been inconclusive to date.[21] The experiments have compared the inclusive multiplicity in qqqq to twice the multiplicity in qq$\ell\nu$ (after correcting for the leptons). Most models predict a shift between -0.3 and 0.2. As can be seen in Figure 18, it will be very difficult to exclude any models using this method. There is ongoing work to study heavy hadrons (K, p) which are expected[22] to show

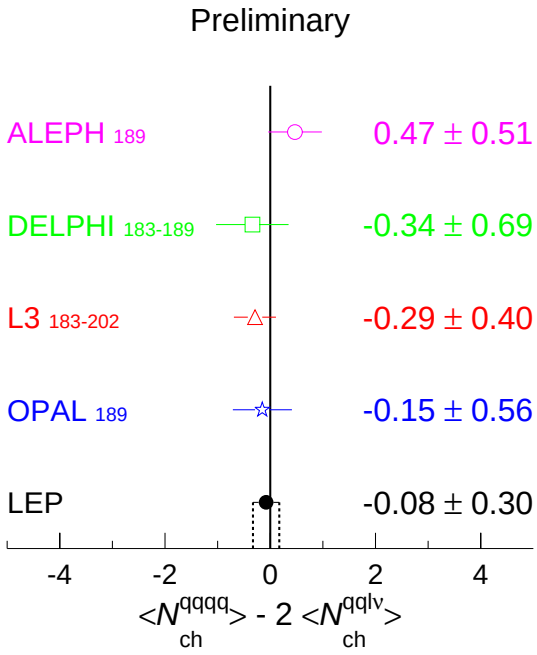

Fig. 18. The difference between the multiplicities in fully hadronic WW decays and semileptonic WW decays.

larger effects.

A more promising method is the study of the inter-jet particle and energy flows,[23]

which was successfully used to establish the "string effect". Here one takes fully hadronic WW events and applies a very tight selection, requiring a very clean and well defined 4 jet topology. With these requirements, one can achieve a very high probability ($\approx$ 87%) of pairing the jets to the correct W boson. After normalizing the inter-jet angles, the energy or particle flow is plotted as a function of the normalized angle, as shown in Figure 19. One then takes the ratio of the intra-W regions to the inter-W

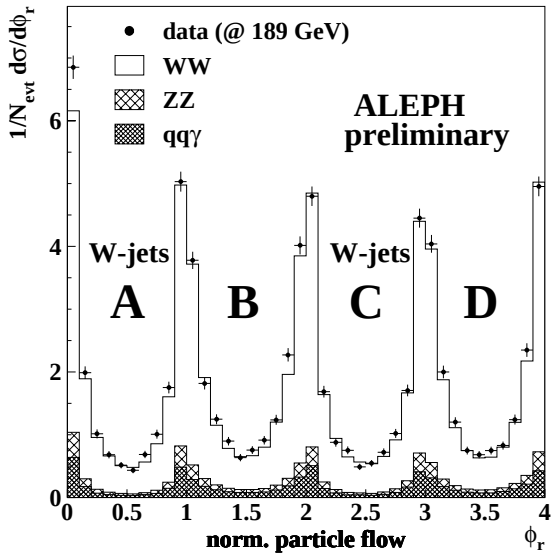

Fig. 19. The particle flow as a function of normalized inter-jet angle. The events are oriented such that regions A and C correspond to the region between the quarks arising from a W (intra-W).

regions, to better isolate the effects of color reconnection. This analysis has been performed by L3,[24] ALEPH[25] and OPAL.[26] Examples are shown in Figure 20. As can be seen, this quantity can be used to distinguish the various models. The experiments have parameterized their results as a function of the reconnection probability: 0% means that reconnection never occurs (the two W's decay independently) and 100% means that reconnection always occurs. The L3 data prefer a 40% reconnection probability and disfavors no reconnection at the 1.7 sigma level. ALEPH prefer 15% reconnection and put the 1 sigma limit at 45%. The OPAL results are inclusive, with one analysis preferring some reconnection and another preferring no reconnection.

The experiments have also studied the relationship between the reconnection probability and the expected mass shift. This is shown in Figure 21. With the current results indicating around 40% reconnection probability, the current estimate is at most 50 MeV

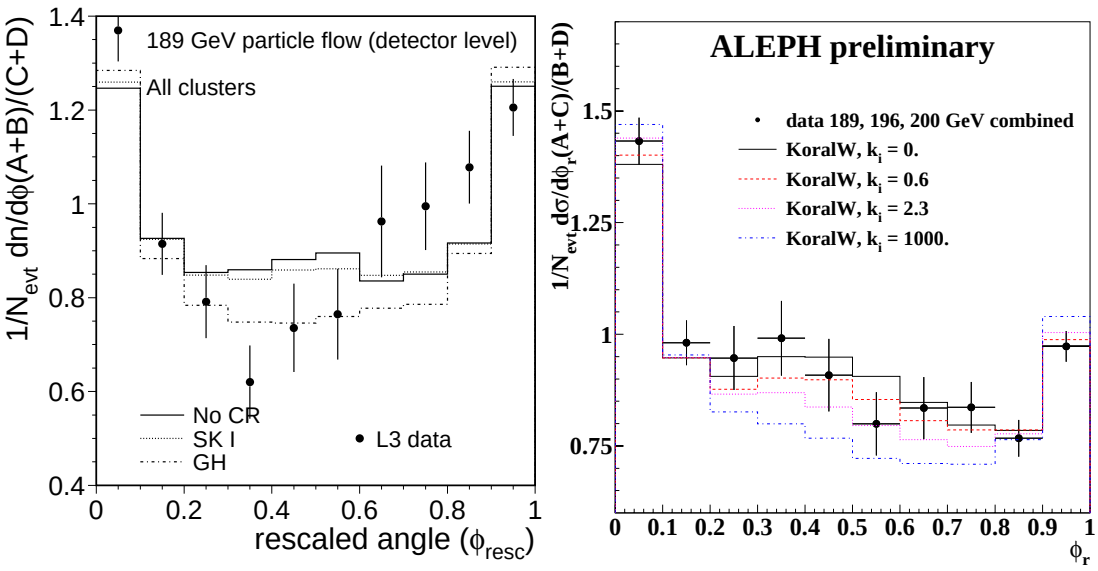

Fig. 20. The ratio of intra-W to inter-W particle flows as a function of the angle for L3 (left) and ALEPH (right). The points are the data and the lines various Monte-Carlo models with varying reconnection probabilities. In each plot, the solid line corresponds to no color reconnection.

for the difference in masses. On the other hand, the mass shift can also be experimentally determined by comparing the difference in masses using fully hadronic events and semileptonic events, as also shown in Figure 21. The result is currently consistent with no mass shift, as well as a 50 MeV shift. With more statistics all results will improve.

5 The Global Fit

The many electroweak measurements performed at LEP, SLC and elsewhere can be used to test the Standard Model. Within the Standard Model they can be used to extract information about the Higgs boson mass through the effects of radiative corrections. An example of the comparison of measurement to SM predictions is shown in Figure 22. There are several things that can be gleaned from this figure. Firstly, electroweak radiative corrections are indeed needed; secondly, the SM appears in good shape, and thirdly, the uncertainty on the running of α directly affects the ability of the data to say something about the Higgs mass.

The fine structure coupling "constant", α, runs because of virtual fermion loops in

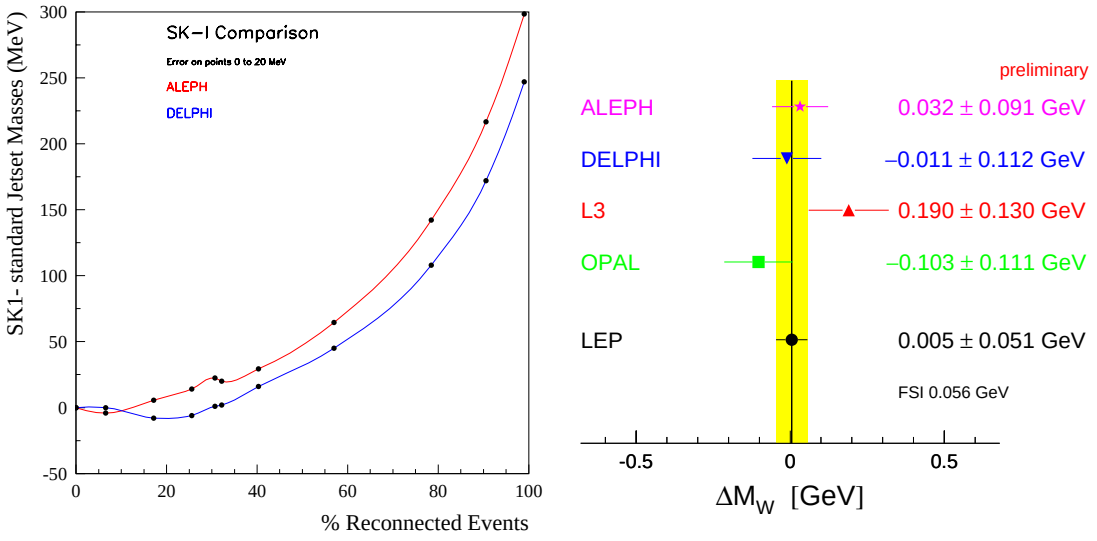

Fig. 21. On the left, the W mass difference as a function of the reconnection probability. On the right, the experimentally determined mass shifts.

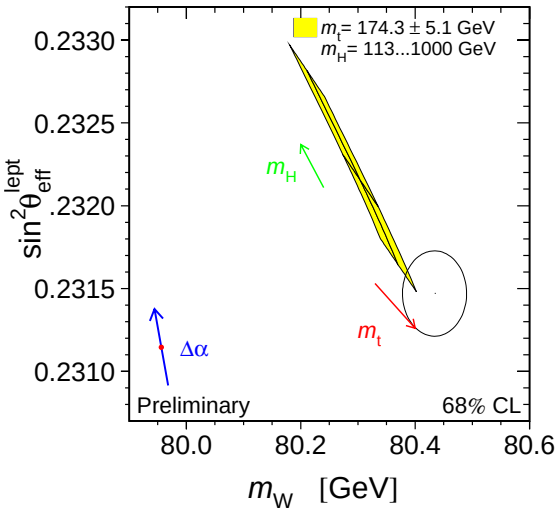

Fig. 22. The measurement of m_{W} and $\sin^2\theta^{\mathrm{lept}}_{\mathrm{eff}}$ (contour) compared to the SM prediction (shaded region). The size of the region reflects the uncertainty on the top quark mass, and the range allowed for the Higgs mass, with the arrows indicating the regions of higher mass. Also shown is the prediction if only the effects of the running of α are considered. The size of the arrow on that point reflects the uncertainty on $\Delta\alpha$.

the photon propagator, resulting in

$$\alpha(m_{\rm Z}) = \frac{\alpha(0)}{1-\Delta\alpha}. \tag{14}$$

For leptonic loops, QED can be used, and the radiative corrections are known to high order.[27] On the other hand, the contributions from quark loops are more problematic, since QCD at low energy is non-perturbative. One can get around this by relating the hadronic component of $\Delta\alpha$ to the hadronic cross-section measured in $\mathrm{e^+e^-}$ annihilation (R):

$$\Delta\alpha_{\rm had}(m_{\rm Z}^2) = -\frac{\alpha m_{\rm Z}^2}{3\pi}\int_{4m_\pi^2}^{\infty} ds \frac{R(s)}{s(s-m_{\rm Z}^2-i\epsilon)}. \tag{15}$$

There have been two choices for evaluating R: using the data[28] or using QCD.[29] The

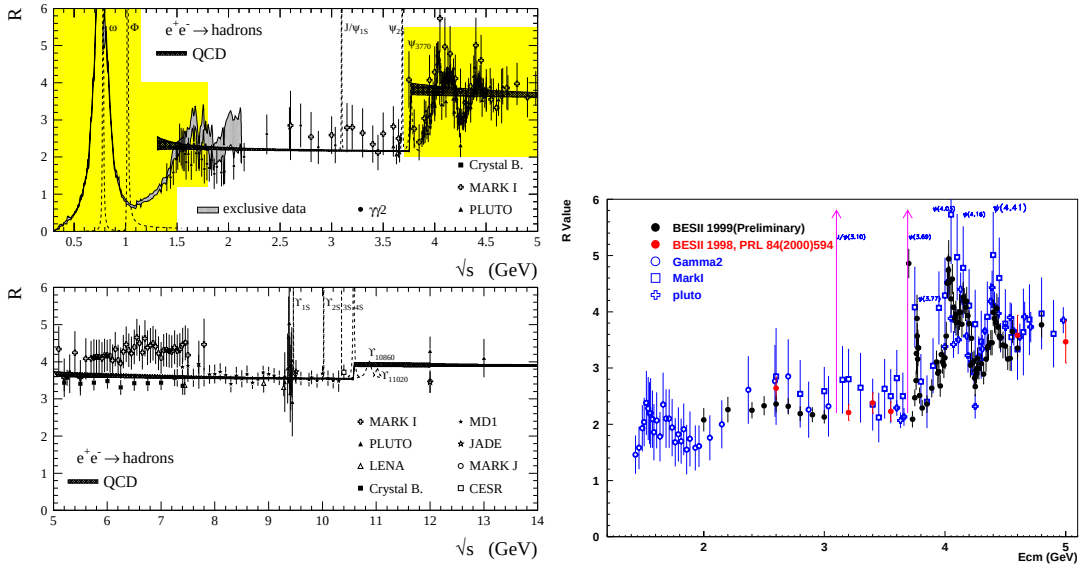

Fig. 23. On the left, the measurements (points) of R as a function of the center of mass energy compared to the QCD calculations (narrow hatched band). On the right, the new measurements from the BES experiment (solid points) compared to older results (open points).

situation until this year has not been very satisfactory, as seen in Figure 23. The data below 10 GeV, which is important, is not very consistent, and the uncertainties are often rather large. The uncertainties from the QCD calculations are much smaller, but QCD and the data do not always agree. The value of $\Delta\alpha$ determined from data is larger, with a larger uncertainty than that from QCD. This in turn yields a smaller value of the Higgs mass, but also with a larger uncertainty (*i.e.*, higher mass limit).

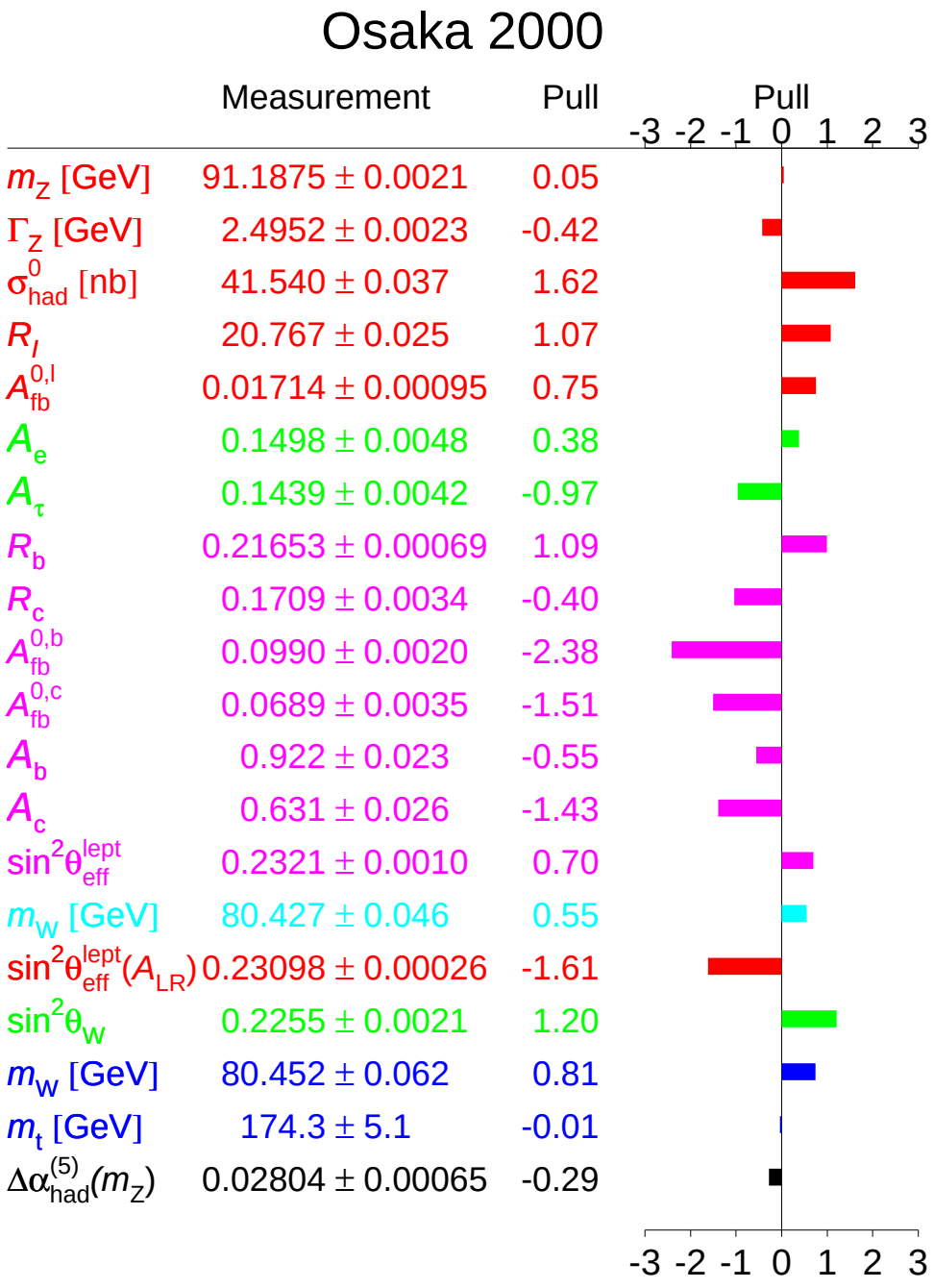

Fig. 24. The data measurements used in the global SM fit for the Higgs mass. Also shown is the deviation from the SM fit (labeled “pull”).

Fortunately, there has been a significant improvement in the data this year, with the new preliminary BES results,[30] as also shown in Figure 23. The data uncertainties have been reduced significantly, and the results seem to agree with QCD better. The preliminary value of $\Delta\alpha$ obtained with the new data is 0.02755 ± 0.00046[31] compared to the old data result of 0.02804 ± 0.00065.[28]

The complete data set used for the fit to determine the Higgs mass in the context of the SM is shown in Figure 24. As can be seen, the biggest deviations occur for $A_{\rm FB}^{0,\,\rm b}$ and $A_{\rm LR}$, as discussed earlier.

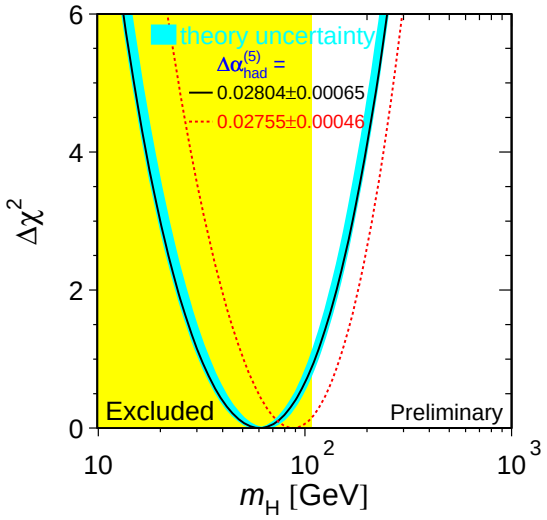

Fig. 25. The χ^2 of the SM fit as a function of the Higgs mass. The solid curve shows the result using the older value of $\Delta\alpha$; the dashed curve results from the new preliminary value. The band around the solid curve indicates the theoretical uncerntainties in the fit. The shaded region below about 113 GeV indicates the limit from the direct searches at LEP.[1]

The resulting fit for the Higgs mass is shown in Figure 25, for the old and new data evaluations of $\Delta\alpha$. Using the old $\Delta\alpha$, the central value for the Higgs mass is 60 GeV, with the 95% confidence level limit of 165 GeV. Using the new value of $\Delta\alpha$, these numbers move up to 88 GeV and 210 GeV, respectively. This shows how important the low energy $\rm e^+e^-$ data is! Nevertheless, it is clear that the electroweak measurements prefer a low mass Higgs.

6 Summary

The LEP program has been fantastically successful. The LEP machine has performed both as a Z factory as well as a W factory. A wealth of information has been obtained concerning the Standard Model. This talk has just focused on a very small number of these results:

- The number of light neutrino families has been determined to be three at the sub-percent level, from measurements of the width of the Z. Any additional "invisible" contributions to the Z width are limited to the per-mil level. Perhaps more relevant for this conference, any new invisible particles are limited to have less than one percent of a standard neutrino coupling.
- The heavy flavor electroweak sector has been and continues to be very interesting. The only relatively significant deviations from the Standard Model are in the b quark couplings, driven by a combination of the $A_{\rm FB}^{\rm b}$ measurements and the leptonic asymmetries ($A_{\rm FB}$, τ polarization and SLD's $A_{\rm LR}$). Unfortunately, all of the available data has been analyzed, the experiments have stopped taking data, and the results are essentially final. It will be a while before we learn anything new here.
- Final state interactions were once seen as potential "show-stoppers" in the determination of the W mass. New studies, and especially new techniques using the data, indicate that FSI is probably not a problem.
- The Higgs boson appears to be light.

References

[1] C. Mariotti, in these proceedings (SLAC Summer Institute, 2000).

[2] L. Trentadue *et al.*, *Neutrino Counting*, in Z Physics at LEP I, ed. G. Altarelli, R. Kleiss, and C. Verzegnassi, volume 1, CERN, 1989.

[3] ALEPH Collaboration, D. Buskulic *et al.*, Phys. Lett. **B 313** (1993) 520.

[4] DELPHI Collaboration, P. Abreu *et al.*, Zeit. Phys. **C 74** (1997) 577.

[5] L3 Collaboration, M. Acciarri *et al.*, Phys. Lett. **B 431** (1993) 199.

[6] OPAL Collaboration, R. Akers *et al.*, Zeit. Phys. **C 65** (1995) 47.

[7] G. Duckeck, in Proceedings of the XXXth International Conference on High Energy Physics, (World Scientific, July 2000), to be published.

[8] D. Su, in Proceedings of the XXXth International Conference on High Energy Physics, (World Scientific, July 2000), to be published.

[9] S. Catani and M. H. Seymour, JHEP **9907**, 023 (1999);
V. Ravindran and W.L. van Neerven, Phys. Lett. **B445** (1998) 206.

[10] ALEPH Collaboration, D. Buskulic *et al.*, Phys. Lett. **B384** (1996)414;
ALEPH Collaboration, *Measurement of the b and c forward-backward asymmetries using leptons* ALEPH 99-076 CONF 99-048, contributed paper to EPS 99 Tampere **HEP'99 #6-65**;
ALEPH Collaboration, R. Barate *et al.*, Phys. Lett. **B426**, (1998) 217.

[11] DELPHI Collaboration, P.Abreu *et al.*, Z. Phys **C65** (1995) 569;
DELPHI Collaboration, *Measurement of the Forward-Backward Asymmetries of* $e^+e^- \rightarrow Z \rightarrow b\bar{b}$ *and* $e^+e^- \rightarrow Z \rightarrow c\bar{c}$ *using prompt leptons* DELPHI 2000-101 CONF 4000, contributed paper to ICHEP 2000, #377;
DELPHI Collaboration, P.Abreu *et al.*, Eur. Phys. J. **C9** (1999) 367.

[12] L3 Collaboration, M. Acciarri *et al.*, Phys. Lett. **B448** (1999) 152;
L3 Collaboration, M. Acciarri *et al.*, Phys. Lett. **B439** (1998) 225.

[13] OPAL Collaboration, G. Alexander *et al.*, Z. Phys. **C70** (1996) 357;
OPAL Collaboration, *Updated Measurement of the Heavy Quark Forward-Backward Asymmetries and Average B Mixing Using Leptons in Multihadronic Events*, OPAL Physics Note PN226 contributed paper to ICHEP96, Warsaw, 25-31 July 1996 **PA05-007**;
OPAL Collaboration, *QCD corrections to the bottom and charm forward-backward asymmetries* OPAL Physics Note PN284;
OPAL Collaboration, K.Ackerstaff *et al.*, Z. Phys. **C75** (1997) 385.

[14] E. Migliore, in Proceedings of the XXXth International Conference on High Energy Physics, (World Scientific, July 2000), to be published.

[15] G. Gustafson, U. Pettersson, and P. Zerwas, Phys. Lett. **B 209** (1988) 90.

[16] G. Goldhaber, Phys. Rev. Lett. **3** (1959) 181.

[17] J. Ellis and K. Geiger, Phys. Rev. **D54** (1996) 1967.

[18] OPAL Collaboration, P. Acton *et al.*, Phys. Lett. **B 267** (1991) 143; ALEPH Collaboration, D. Decamp *et al.*, Z. Phys. **C 54** (1992) 75; DELPHI Collabo-

ration, P. Abreu *et al.*, Phys. Lett. **B 286** (1992) 201; DELPHI Collaboration, P. Abreu *et al.*, Z. Phys. **C 63** (1994) 117; OPAL Collaboration, G. Alexander *et al.*, Z. Phys. **C 72** (1996) 389; L3 Collaboration, M. Acciarri *et al.*, Phys. Lett. **B 458** (1999) 517; DELPHI Collaboration, P. Abreu *et al.*, Phys. Lett. **B 471** (1999) 460; OPAL Collaboration, G. Abbiendi *et al.*, *Transverse and Longitudinal Bose-Einstein Correlations in Hadronic Z^0 Decays*, Preprint CERN-EP-2000-004, CERN, 2000, (submitted to Eur. Phys. J.), submitted to E. Phys. J. **C**.

[19] ALEPH Collaboration, R. Barate *et al.*, Phys. Lett. **B 478** (2000) 50; L3 Collaboration, M. Acciarri *et al.*, Phys. Lett. **B493** (2000) 233; DELPHI Collaboration, P. Abreu *et al.*, Phys. Lett. **B 401** (1997) 181; OPAL Collaboration, G. Abbiendi *et al.*, Eur. Phys. J. **C 8** (1999) 559; OPAL Collaboration, G. Abbiendi *et al.*, *Bose-Einstein Correlations in $\mathrm{e^+e^-} \to \mathrm{W^+W^-}$ Events at 172, 183 and 189 GeV*, OPAL Physics Note PN393, contrib. to HEP-EPS'99 conference, Tampere, Finland, 1999; DELPHI Collaboration, P Abreu *et al.*, *Correlations between Particles from Different Ws in $\mathrm{e^+e^-} \to \mathrm{W^+W^-}$ Events*, DELPHI 99-159 CONF 330, contrib. to Moriond 2000 QCD, Les Arcs, France, 2000.

[20] A. Valassi, in Proceedings of the XXXth International Conference on High Energy Physics, (World Scientific, July 2000), to be published.

[21] P. de Jong, in Proceedings of the XXXth International Conference on High Energy Physics, (World Scientific, July 2000), to be published.

[22] V. Khoze and T. Sjöstrand, Eur. Phys. J. **C 6** (1999) 271.

[23] D. Ducheseau, *New method based on energy- and particle-flow in $\mathrm{e^+e^-} \to \mathrm{W^+W^-} \to$ hadrons events for colour reconnection studies*, Preprint, 2000, LAPP-EXP 2000-02.

[24] L3 Collaboration, *Search for Colour Reconnection Effects in $\mathrm{e^+e^-} \to WW \to$ hadrons*, Preprint, 2000, L3 Note 2560, contributed paper to ICHEP 2000, #511.

[25] ALEPH Collaboration, *Colour Reconnection studies using particle flow between W bosons*, Preprint, 2000, contributed paper to ICHEP 2000, #282.

[26] OPAL Collaboration, *Colour reconnection studies in WW events at LEP*, Preprint, 2000, OPAL Physics Note 448, contributed paper to ICHEP 2000, #575.

[27] M. Steinhauser, Phys. Lett. **B429** (1998) 158.

[28] S. Eidelmann and F. Jegerlehner, Z. Phys. **C67** (1995) 585; M. L. Swartz, Phys. Rev. **D53** (1996) 5268; A.D. Martin and D. Zeppenfeld, Phys. Lett. **B345** (1994) 558.

[29] R. Alemany, *et al.*, Eur. Phys. J. **C2** (1998) 123; M. Davier and A. Höcker, Phys. Lett. **B419** (1998) 419; J.H. Kühn and M. Steinhauser, Phys. Lett. **B437** (1998) 425; J. Erler, Phys. Rev. **D59** (1999) 054008.

[30] Z. Zhao, in Proceedings of the XXXth International Conference on High Energy Physics, (World Scientific, July 2000), to be published.

[31] B. Pietrzyk, in Proceedings of the XXXth International Conference on High Energy Physics, (World Scientific, July 2000), to be published.

RECENT RESULTS FROM SLD

Mark Convery*
Stanford Linear Accelerator Center
Stanford University, Stanford, CA 94309

Representing the SLD Collaboration

ABSTRACT

New results from the SLD collaboration in the fields of electroweak, QCD and heavy flavor physics are presented. The analyses make use of all or part of SLD's final data sample of 550,000 Z^0 decays collected between 1993 and 1998. Many of the analyses exploit the large longitudinal polarization provided by the SLC's e^- beam. The precision vertexing provided by the CCD-based vertex detector is similarly key to many of the analyses.

Final results are presented for the total cross section asymmetry A_{LR}, the final state asymmetries A_c and A_s, and the B fragmentation function $D(x_B)$. Preliminary results are presented for A_b, for the final state branching ratios R_b and R_c and for B_s mixing.

*Supported by DOE Contract DE-AC03-76SF00515.

	SLC	LEP (Z^0 Running)
Center of Mass Energy	92 GeV	92 GeV
Circumference	3 km	27 km
Beam Size at IP	$3 \times 1\mu\mathrm{m}$	$400 \times 16\mu\mathrm{m}$
e^-/bunch	4×10^{10}	30×10^{10}
Crossing Rate	120 Hz	45 kHz
Z's/day/experiment	3000	30,000
e^- Polarization	0.75	0

Table 1. Table of beam parameters comparing SLC to LEP.

1 Introduction

The SLD experiment,[1] located at the interaction point of the Stanford Linear Collider (SLC), finished taking data at the Z^0 resonance in June of 1998. The total data sample taken in the years 1993 to 1998 consists of 550,000 Z decays. In this paper I will describe a number of analyses that have been performed using the SLD Data. These analyses cover topics in the fields of electroweak, QCD and heavy flavor physics. Many of them benefit from the unique beam conditions available at the SLC.

2 The Stanford Linear Collider (SLC)

The SLC, the world's first linear collider, produced Z^0 bosons by colliding electron and positron beams accelerated in the SLAC Linac. It ran between and 1989 and 1998 and by 1998, SLC's luminosity had improved to the point that it was producing 20,000 Z's per week of running. Table 1 compares the parameters of the SLC to those of CERN's Large Electron Positron Collider (LEP).

SLD is clearly at a statistical disadvantage to experiments running at LEP. However, in many cases, the advantages provided by the electron beam polarization - possible only at a linear collider, as well as the tiny beam spot of the SLC, can more than make up for the lower statistics.

fermion	$I^3_{L,f}$	Q_f	$g_{L,f}$	$g_{R,f}$	A_f	$\frac{\delta A_f}{\delta \sin^2_{\theta_W}}$
ν	1/2	0	0.5	0.0	1	0
e, μ, τ	-1/2	-1	-0.27	0.23	0.16	-7.9
u, c, t	1/2	2/3	-0.35	-0.15	0.69	-3.5
d, s, b	-1/2	-1/3	-0.42	0.07	0.94	-0.6

Table 2. Born Level couplings of the fermions to the Z.

3 Electroweak Asymmetries

The left- and right-handed couplings of the Z^0 to the various fermions at Born Level are given by

$$g_{L,f} = I^3_{L,f} - Q_f \sin^2 \theta^{eff}_W \quad (1)$$

$$g_{R,f} = Q_f \sin^2 \theta^{eff}_W, \quad (2)$$

where $I^3_{L,f}$ is the third component of weak isospin, Q_f is the charge of each fermion, and θ^{eff}_w is the *effective* value of the Weinberg angle at the Z^0.

This parity-violating difference in left- and right-handed coupling leads to a coupling asymmetry defined as

$$A_f \equiv \frac{g^2_{L,f} - g^2_{R,f}}{g^2_{L,f} + g^2_{R,f}} \quad (3)$$

Table 2 lists I^3_L, f, Q_f, $g_{L,f}$, $g_{R,f}$ and A_f for each of the fermions.

Expressed in terms of A_f, the differential cross-section for production of fermion pairs at the Z^0 is given by

$$\frac{d\sigma}{d\cos\theta_f} \sim (1 + P_e A_e)(1 + \cos^2\theta_f) + 2\cos\theta_f (A_e - P_e) A_f, \quad (4)$$

where θ_f is the dip angle of the final state fermion (not anti-fermion) and P_e is the longitudinal polarization of the incoming electron beam. From the first term, it is evident that there is a "production asymmetry" in the rate of Z^0 production for right-($P_e > 0$) and left-handed ($P_e < 0$) electrons. Clearly, it is necessary to have control of P_e in order to measure this asymmetry. Also, note that this production asymmetry is independent of final state. Therefore, it is not necessary to measure the type or charge of the final state fermions.

The second term in equation 4, since it is odd in $\cos\theta$, describes a forward-backward "decay asymmetry". To measure this asymmetry it is necessary to identify the type of

fermions in the final state, as well as their charge. The asymmetry is present even if ($P_e = 0$), although it is enhanced if $P_e \neq 0$.

Experimentally, we define three observables that are sensitive to to A_f:

$$A_{FB}^f \equiv \frac{\sigma_F^f - \sigma_B^f}{\sigma_F^f + \sigma_B^f} = \frac{3}{4} A_e A_f \tag{5}$$

$$A_{LR} \equiv \frac{\sigma_L - \sigma_R}{\sigma_L + \sigma_R} = |P_e| A_e \tag{6}$$

$$A_{FB_{LR}}^f \equiv \frac{(\sigma_{FL}^f - \sigma_{BL}^f) - (\sigma_{FR}^f - \sigma_{BR}^f)}{(\sigma_{FL}^f + \sigma_{BL}^f) + (\sigma_{FR}^f + \sigma_{BR}^f)} = \frac{3}{4} |P_e| A_f, \tag{7}$$

where σ is the rate for $Z^0 \rightarrow hadrons$, σ^f is the rate for $Z^0 \rightarrow f\bar{f}$, "F" and "B" refer to forward ($\cos\theta_f > 0$) and backward ($\cos\theta_f < 0$) and "L" and "R" refer to left- and right-handed electron beams.

Equation 5 describes the unpolarized forward-backward asymmetry that can be measured even without electron polarization (e.g. at LEP). Equation 6 describes the production asymmetry that requires control of the electron polarization and is the most sensitive way to measure A_e at SLD. Equation 7 describes a polarization-enhanced forward-backward asymmetry that can be used to measure A_f for fermions other than electrons. The polarized asymmetries are useful both because they allow A_e and A_f to be measured independently and also because they give a large statistical enhancement of $(\frac{P_e}{A_e})^2 \approx 25$, which more than makes up for the factor 10 statistical advantage that LEP experiments have.

4 The SLD Detector

The SLD detector is a 4π multi-purpose detector that has many features in common with other e^+e^- detectors. Figure 1 shows a cutaway drawing of the SLD detector. Tracks emerging from the primary Interaction Point first pass through the precision vertex detector (called VXD3). They then pass through the Central Drift Chamber, where their momentum and direction are measured. They then enter the Cherenkov Ring Imaging Detector (called CRID), which is used to identify charged hadrons. A calorimeter made of lead and liquid argon (called the LAC) is used for photon energy measurements and electron identification. The Warm Iron Calorimeter (WIC) surrounds the detector and is used for muon identification and hadronic energy measurements. Also, a polarimeter based on Compton scattering is located just downstream of SLD and is used to measure

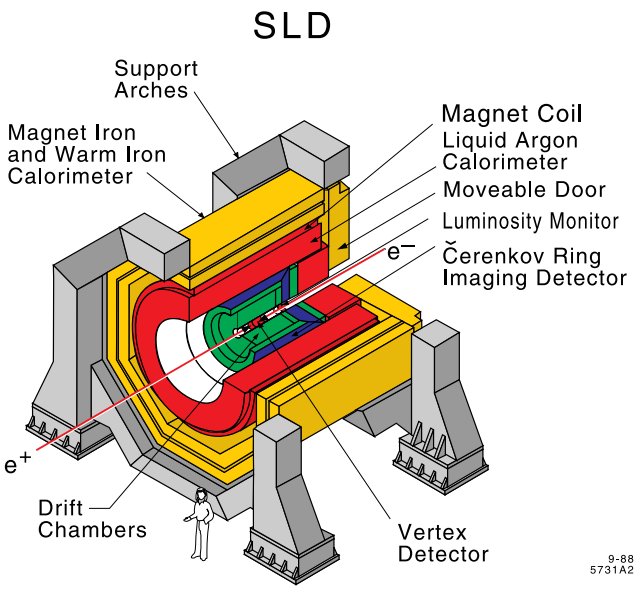

Fig. 1. Cutaway view of the SLD detector, located at the interaction point of the SLC.

the polarization of the electron beam. Since this polarimeter and the Vertex Detector are unique devices, they will be described in more detail in the following sections.

4.1 Vertex Detector

Since the SLC provides a very small and stable primary interaction point ($\sigma_{r\phi,measured} = 4\ \mu$m), it is desirable to have a vertex detector with similar resolution. This is provided by the upgraded vertex detector VXD3, which was installed in 1996. It is based on CCD technology and contains 307 million pixels. The achieved resolutions of this device are $\sigma_{r\phi} = 7.8\ \mu$m in the $r-\phi$ plane and $\sigma_{rz} = 9.8\ \mu$m in the $r-z$ plane. Topological vertexing and inclusive reconstruction algorithms exploit this excellent resolution.

4.2 Polarization Measurement

In order to exploit the electron beam polarization provided by the SLC, it is necessary to measure the average polarization, $\langle P_e \rangle$. This is done primarily with a Compton Polarimeter, shown in Figure 2. The counter collides the electron beam with a circularly polarized laser beam and measures the scattered electrons. Then, by measuring the Compton asymmetry, it is possible to extract the electron polarization. The counter can run during collisions so that P_e can be constantly monitored.

There are also two other counters, called the Quartz Fiber Calorimeter and Polarized

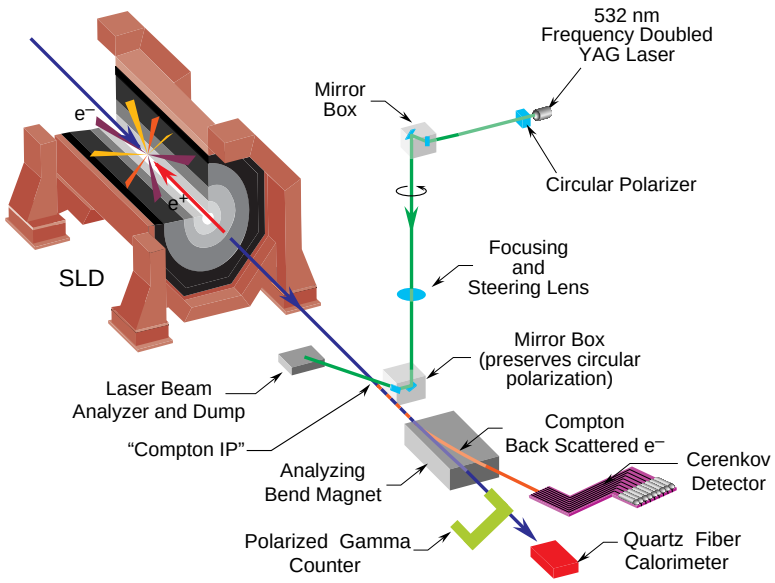

Fig. 2. Schematic of the electron polarization measuring devices located just downstream of the SLD.

Gamma Counter, which can only run during single beam running. These counters, however, provide a useful cross-check of the polarization measurement.

In '98 a separate test was performed to measure the polarization of the positron beam, which is not measured during colliding beam running and is normally assumed to be zero. The test found $P_{e^+} = -0.02 \pm 0.07\%$, which is so small as to be negligible in the electroweak measurements.

5 Electroweak Measurements

5.1 Measurement of A_{LR}

The measurement of A_{LR} is an extraordinarily simple and elegant one. All that it requires of from the SLD detector is a measurement of the number of $Z \rightarrow hadrons$ for left- and right-handed electrons. This leads to a cancellation of many possible systematic effects and hence a very small systematic error.

5.1.1 Experimental Corrections

The first step in the measurement of A_{LR} is the measurement of the raw asymmetry A_m, defined as:

$$A_m \equiv \frac{N_L - N_R}{N_L + N_R} \tag{8}$$

where N_L is the number of hadronic events produced with a left-handed electron beam N_R is the number produced with a right-handed beam.

To obtain the measurement of A_{LR} it is necessary to divide the raw asymmetry by the luminosity-averaged polarization of the electron beam ($\langle P_e \rangle$). This is defined as

$$\langle P_e \rangle = (1 + \xi) \frac{1}{N_Z} \sum_{i=1}^{N_Z} P_i, \tag{9}$$

where P_i is the beam polarization at the time of production of the ith Z^0 and ξ is a factor that corrects for the difference in polarization between the Compton interaction point and the Z^0 production interaction point. ξ is found to be quite small ($\xi = 0.0012 \pm 0.0015$).

We can then calculate the value of A_{LR} at the beam energy as

$$A_{LR}(E_{beam}) = \frac{A_m}{\langle P_e \rangle}. \tag{10}$$

Since the SLC does not run exactly on the Z^0 pole, it is necessary to extrapolate to that energy and to correct for electroweak interference. These two corrections are treated together and parameterized by a single correction factor, ϵ:

$$A^0_{LR} = (1 + \epsilon) A_{LR}(E_{beam}), \tag{11}$$

where A^0_{LR} is the inferred asymmetry at the Z^0 pole.

5.1.2 Systematic Errors

The systematic errors of the A_{LR} measurement come from uncertainties in the correction factors described in the previous section. Table 3 gives their numerical values. The largest systematics are related to the polarization measurement and to knowledge of the beam energy.

5.1.3 A_{LR} Result

Combining statistical and systematic errors, the final result on A_{LR}, using data taken between 1993 and 1998, is found to be $A^0_{LR} = 0.15138 \pm 0.00216$.[2] This corresponds to a measurement of $\sin^2 \theta^{eff}_W = 0.23097 \pm 0.00027$. Clearly, the measurement is still statistically dominated. When combined with SLD's results on the leptonic coupling asymmetries,[3] the final value of $\sin^2 \theta^{eff}_W$ is 0.23098 ± 0.00026.

Factor	Systematic Error
Polarization Measurement, $\langle P_e \rangle$	0.5%
Polarization Shift, ξ	0.15%
Experimental and Background Asymmetry	0.07%
Electroweak and Beam Energy Correction	0.39%
Total	0.65% ($\sigma_{syst}(A_{LR}^0) = 0.001$)

Table 3. Table of systematic errors for the A_{LR} measurement.

5.1.4 $\sin^2\theta_W^{eff}$ Comparisons

Figure 3 shows the world's measurements of $\sin^2\theta_W^{eff}$. The A_{LR} measurement has the lowest error. Since $\sin^2\theta_W^{eff}$ is sensitive to radiative corrections, it can be used in conjunction with the measured values of $\alpha(M_Z)$, G_F, M_Z and M_t to measure the Higgs Mass (m_H). See section 5.5 for more details on this.

5.2 Measurement of R_b

Measurements of R_b and R_c ($R_q \equiv \frac{\Gamma(Z\to q\bar{q})}{\Gamma(Z\to hadrons)}$) are also performed at SLD.

5.2.1 Radiative Corrections to R_b

Measurements of R_b are especially interesting because of its sensitivity to vertex corrections such as the one shown in Figure 4. In the Standard Model, the top quark diagram changes the value of R_b by:

$$\delta_{R_b} \approx -\frac{20}{13}\frac{\alpha}{\pi}\left[\frac{M_t^2}{M_Z^2} + \frac{13}{6}\ln\frac{M_t^2}{M_Z^2}\right] \approx -0.025. \tag{12}$$

Other new physics may change the value of R_b by similar amounts and so precision measurements of R_b become very interesting.

5.2.2 Inclusive b and c Reconstruction

The first step in measuring R_b and R_c is developing a highly pure and efficient method of tagging event hemispheres that contain b or c quarks. At SLD, this is done using an inclusive reconstruction technique. Figure 5 illustrates this technique. After splitting the event into hemispheres, the technique selects tracks that are considered to have

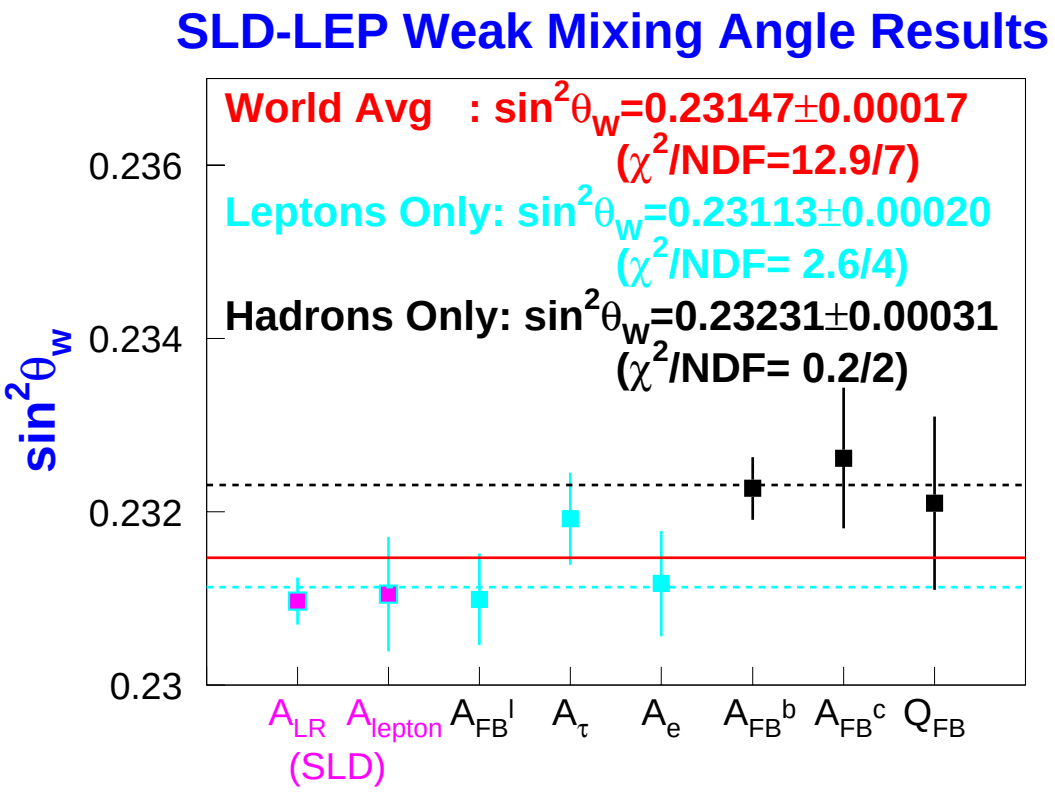

Fig. 3. The world's measurements of $\sin^2\theta_W^{eff}$ at the Z^0 pole.

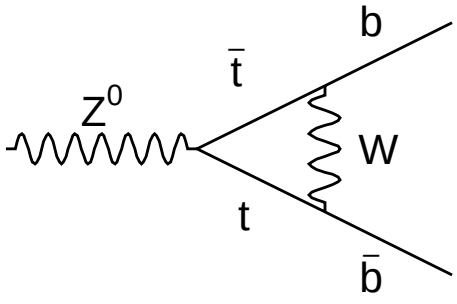

Fig. 4. The Feynman diagram for a Standard Model radiative correction to R_b. New physics may couple in a similar way.

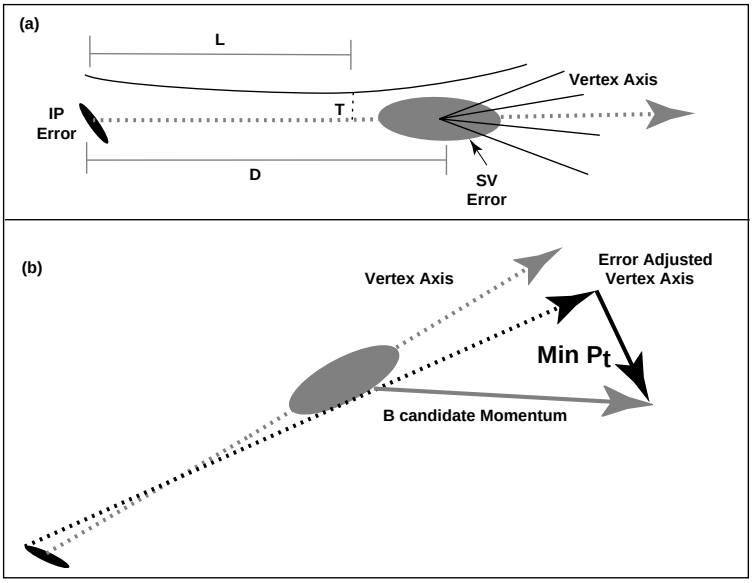

Fig. 5. Illustration of the inclusive b and c reconstruction technique. In (a), a seed vertex (SV) is topologically identified and tracks are attached to it based on their values of L, T and D. In (b), the calculation of M_{pt} is demonstrated.

come from the b or c quark. This is done by topologically identifying a "seed" vertex (as shown in Figure 5(a)) in each hemisphere.[4] Due to the finite charm lifetime, not all of the tracks coming from the b decay are expected to come from a single point. Therefore, a "track attachment" algorithm is needed to attach tracks to this seed vertex. A neural net based on the variables T, L and D as defined in Figure 5(a) is used to perform this attachment. Roughly speaking, tracks with $T < 1\,\text{mm}$, $L > 0.5\,\text{mm}$ and $L/D > 0.25$ are attached to the vertex.

Then, the mass (M_{raw}) of this set of "b-tracks" is calculated under the assumption that each track is a pion. To correct for the effect of missing tracks and neutrals, a "P_t corrected mass" is calculated as:

$$M_{pt} = \sqrt{M_{raw}^2 + P_t^2} + |P_t|, \tag{13}$$

where P_t is the momentum of the b-tracks transverse to the flight direction. This flight direction is chosen so as to minimize the P_t within one-sigma vertex errors, as shown in figure 5(b). Figure 6(a) shows a plot of M_{pt} for Monte Carlo and data. Clearly, there is good separation between b, c and uds quarks in this variable alone. In the Monte Carlo, cutting at $M_{pt} > 2$ GeV gives a b purity of 98% and a b efficiency, $\epsilon_{b\to b}$, of 57%.

A Neural Net based on M_{pt} and other related variables is used to improve the ef-

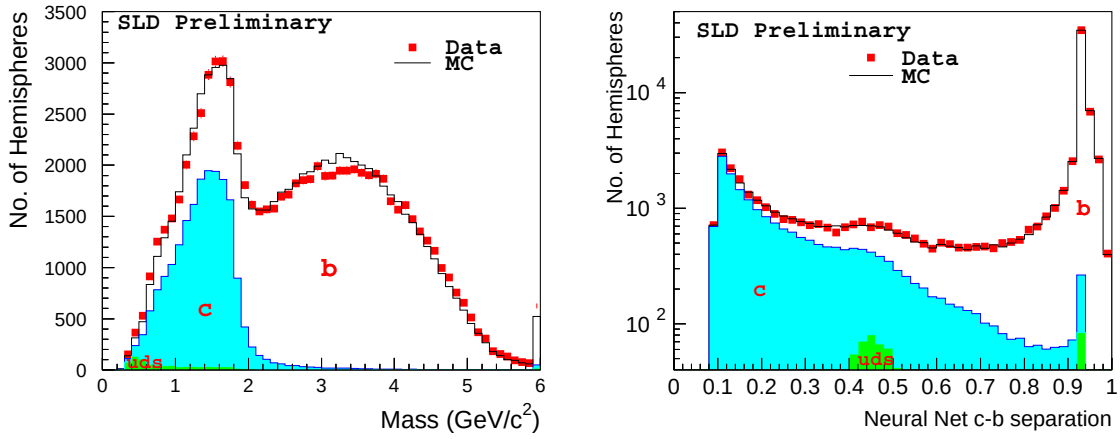

(a) (b)

Fig. 6. (a) shows the distribution of M_{pt} in data and for Monte Carlo. (b) shows the output of the Neural Net based on M_{pt} and other related quantities. The output is close to zero for c quarks and close to one for b quarks.

ficiency of the b-tag. Figure 6(b) shows the output of the neural net, which is ideally close to one for b hemispheres and close to zero for c hemispheres. Figure 7 shows the efficiency and purity of a b-tag based on this neural net as a function of the cut position. At a cut position of 0.75, the efficiency is improved to 63% while maintaining a purity of 98%.

5.2.3 Double Tag Method

In order to measure R_b, it is necessary to know the efficiency of the single hemisphere b-tag ($\epsilon_{b\to b}$). To measure $\epsilon_{b\to b}$, and hence R_b, with the lowest possible systematic error, we use a "double tag method". This allows us, essentially, to measure $\epsilon_{b\to b}$ in data without relying on Monte Carlo. This reduces possible systematic errors due to lack of knowledge of the b production spectrum (fragmentation function), b decay modeling and detector modeling.

In the limit that the mistagging of charm ($\epsilon_{c\to b}$) and light quarks ($\epsilon_{uds\to b}$) are both zero, and that there are no hemisphere correlations, we can write the the efficiency of the b-tag as

$$\epsilon_{b\to b} = 2\frac{N_{double}}{N_{hemi}}, \tag{14}$$

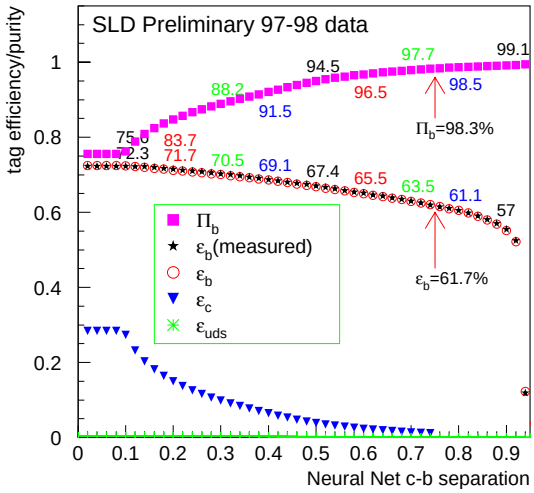

Fig. 7. Efficiency (ϵ_b) and purity (π_b) for b tagging as a function of the cut position on the Neural Net output.

Factor	Systematic Error
Running b mass	0.00067
Tracking	0.00041
D Modeling	0.00042
Total	0.00094

Table 4. Table of the largest systematic errors for the R_b. Several other smaller contributions are included in the total.

where N_{double} is the number of events with two tagged hemispheres and N_{hemi} is the number of tagged hemispheres. Knowing $\epsilon_{b\to b}$, the calculation of R_b is straightforward.

In the actual measurement, the Monte Carlo is used to make corrections for mistagging and for hemisphere correlations.

5.2.4 R_b Result

Figure 8 shows the measured value R_b for a range of values of the cut on the output of the Neural Net. The stability of the measurement gives us confidence that the Neural Net output is well understood. Table 4 lists the largest of the systematics involved in the measurement.

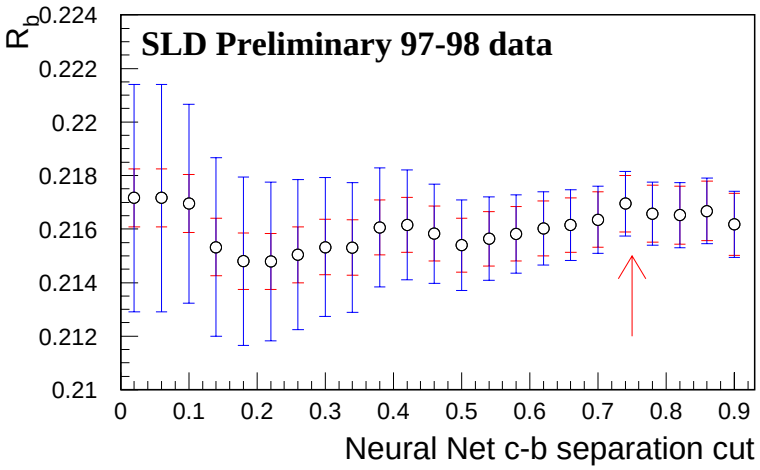

Fig. 8. Measured value of R_b as a function of the Neural Net cut.

The preliminary result using data taken from '93 to '98 is $R_b = 0.21669 \pm 0.00094_{stat} \pm 0.00101_{syst}$. This is to be compared to the world average as of Summer 2000 — $R_b = 0.21653 \pm 0.00069$ and the Standard Model value of 0.2157.[5]

5.3 R_c Measurement

The measurement of R_c is quite similar to R_b. As shown in Figure 6(b), the same Neural Net that is used for b-tagging can also be used for charm tagging. This tag has an efficiency for correctly tagging charm quark jets of $\epsilon_{c\to c} = 17.4\%$, and a purity of $\pi_{c\to c} = 84.5\%$ at the nominal cut position. Figure 9 shows the efficiency and purity as a function of cut position. Also, a double tag technique is used to minimize the systematic errors.

The largest systematics of the measurement are related to charm decay modeling ($\delta R_c = 0.0017$) and Interaction Point correlations ($\delta R_c = 0.00116$). The preliminary result based on data taken between '96 and '98 is $R_c = 0.1732 \pm 0.0041_{stat} \pm 0.0025_{syst}$. This is to be compared to the world average as of Summer 2000 of $R_c = 0.1709 \pm 0.0034$ and the Standard Model value of 0.1725.[5]

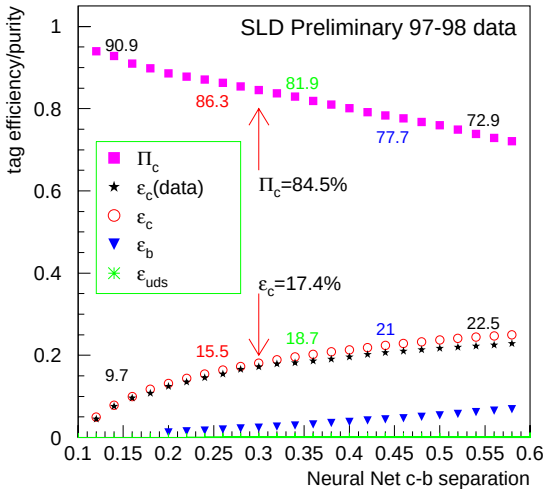

Fig. 9. Efficiency (ϵ_c) and purity (π_c) for $c-$tagging as a function of the cut on the Neural Net Output.

5.4 Measurement of A_b, A_c and A_s

The measurement of the quark asymmetries takes advantage of the polarized cross-section for quark production:

$$\frac{d\sigma}{d\cos\theta_f} \sim (1 + P_e A_e)(1 + \cos^2\theta_f) + 2\cos\theta_f (A_e - P_e) A_f, \tag{15}$$

where θ_f is the dip angle of the final state fermion (not anti-fermion) and P_e is the polarization of the electron beam. Therefore, to measure the quark asymmetries, we need to be able to tag not only the *quark flavor* (u, d, s, c, b), but also the *quark charge* (*e.g.* b or $\bar{b}$). For A_b and A_c, SLD has developed a number of techniques for tagging quark flavor. In this paper, we will cover only those with recent new results.

5.4.1 A_b with Lepton Tag

This analysis begins by identifying hemispheres with with b or $\bar{b}$ quarks using the Neural Net Mass Tag described in section 5.2.2. Then, it uses identified muons and electrons among the vertex tracks to tag the quark charge via the decay $b \to l$. The largest background to this process is the cascade decay $b \to c \to \bar{l}$, which produces oppositely charged leptons and thus incorrect tags. These cascade decays can be distinguished from the direct ones by examining their total momentum (p), their momentum trans-

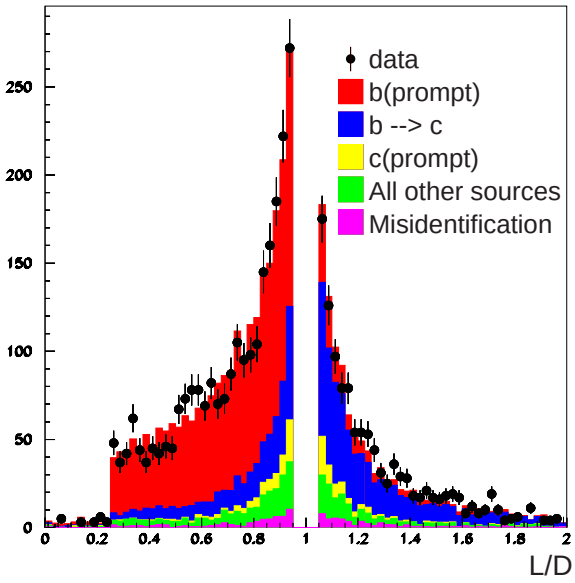

Fig. 10. Distribution of $\frac{L}{D}$, as defined in Figure 5, for direct (prompt) and cascade leptons.

verse to the the jet direction (p_t) and by using vertexing information. The vertexing information is incorporated by noting that leptons coming from direct $b \to l$ decays should tend to come from closer to the primary vertex, whereas those coming from cascade decays should come from farther away. In terms of the variables defined in Figure 5(a), this means that direct decays should have $L/D < 1$ and cascade decays should have $L/D > 1$. Figure 10 shows the Monte Carlo distributions of L/D for direct and cascade decays. Clearly, there is good separation in this variable.

A Neural Net is used to combine the three types of information used in the tagging. Figure 11 shows the output of this Neural Net, which returns values close to one for direct leptons and close to zero for cascade.

Using this tag, the preliminary result for data taken between '93 and '98 is[6] $A_b = 0.922 \pm 0.029_{stat} \pm 0.024_{syst}$.

5.4.2 A_b with Vertex Charge

An alternative method of tagging the quark charge is to use the total charge of the tracks associated to the b-vertex as described in section 5.2.2. Clearly, this method will work only for charged b-hadrons. To improve the charge reconstruction, tracks which were found in the Vertex Detector, but not in the drift chamber are included in the charge calculation. Figure 12 shows how the charge purity is improved by using these tracks.

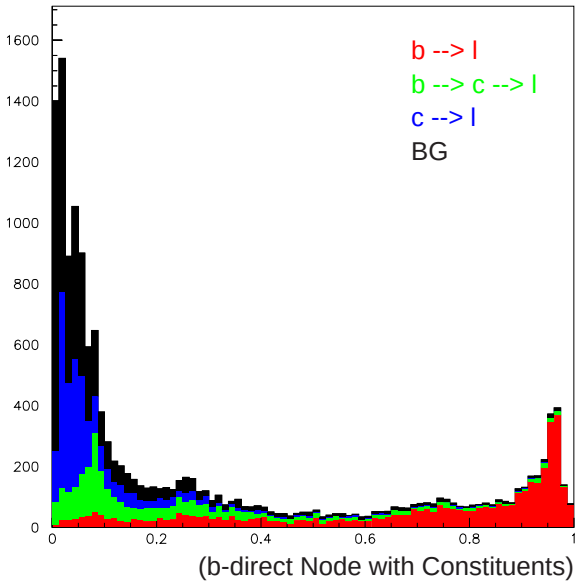

Fig. 11. Output of the Neural Net used for distinguishing direct and cascade leptons.

The analyzing power is improved from 0.58 to 0.64.

Figure 13 shows the asymmetry separately for left and right handed polarized electron beams. The preliminary result based on data taken between '97 and '98 is[7] $A_b = 0.926 \pm 0.019_{stat} \pm 0.027_{syst}$.

5.4.3 A_b Combined Average

Combining A_b measured with the lepton tag and with the vertex charge tag, along with two other SLD measurements based on a Kaon tag and on a jet charge tag, we find an SLD average of $A_b = 0.914 \pm 0.024$. This is to be compared with the the LEP average as of Summer 2000 of 0.880 ± 0.020 and the Standard Model value of 0.926.[5]

5.4.4 Measurement of A_c Using Exclusive Reconstruction

The most straightforward way to measure A_c is by directly reconstructing the charmed mesons produced. In the SLD analysis, we reconstruct D decays in the following exclusive modes (and their charge conjugates):

- $D^{*+} \to D^0\pi^+(D^0 \to K^-\pi^+)$
- $D^{*+} \to D^0\pi^+(D^0 \to K^-\pi^+\pi^0)$
- $D^{*+} \to D^0\pi^+(D^0 \to K^-\pi^+\pi^+\pi^-)$

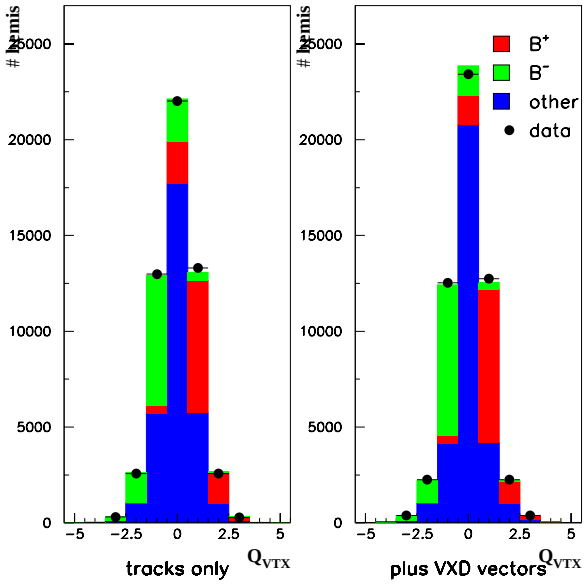

Fig. 12. (a) shows the vertex charge when using only tracks reconstructed in the vertex detector *and* the Drift Chamber. (b) shows the same quantity when tracks reconstructed only in the vertex detector are included.

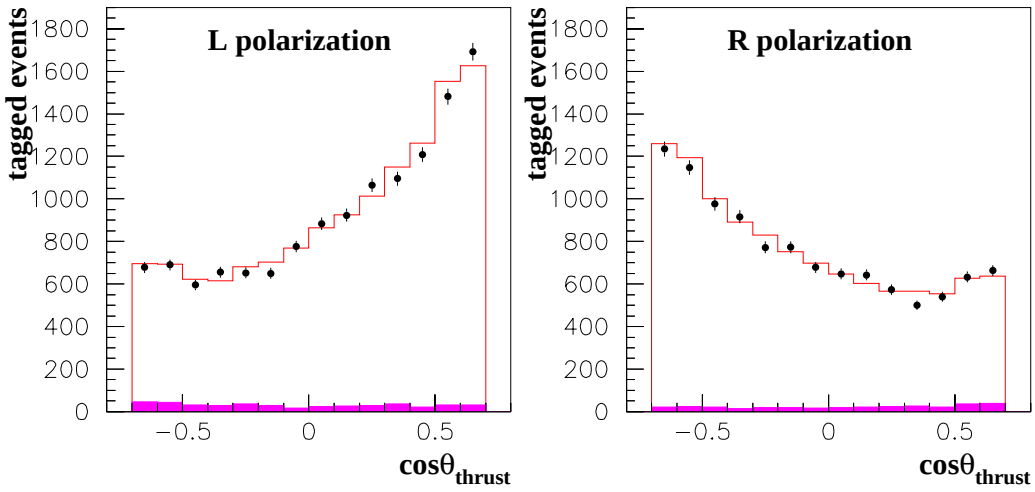

Fig. 13. The *b*-production asymmetry using a vertex charge tag shown separately for left- and right- electron polarizations.

- $D^{*+} \to D^0\pi^+(D^0 \to K^-l^+\nu)$
- $D^+ \to K^-\pi^+\pi^-$
- $D^0 \to K^-\pi^+$

Figure 14 shows plots of $\Delta m \equiv m_{D^{*+}} - m_{D^0}$ for each of the D^{*+} modes. A clear signal is seen for each mode.

A large background that needs to be rejected in this analysis is D mesons coming from $b \to c$ decays. These can be rejected by requiring that the D come directly from the primary interaction point, and by applying a b-veto to the opposite hemisphere.

The final result from this analysis for data taken between '93 and '98 is $A_c = 0.690 \pm 0.042_{stat} \pm 0.021_{syst}$.[8]

Combining this result with other SLD results based on leptons, on inclusive reconstruction with Kaon and vertex charge tagging and of a soft π^+ tag, we find an SLD average result of $A_c = 0.635 \pm 0.027$. This is to be compared with the LEP average of $A_c = 0.612 \pm 0.032$ and the Standard Model value of 0.675.[5]

5.4.5 Measurement of A_s

The measurement of A_s relies on the QCD "Leading Particle" effect, which predicts that very high momentum kaons will come preferentially from $Z \to s\bar{s}$ decays. The analysis uses identified $K^{\pm}$'s with $p > 9$ GeV, which are 92% pure, and K^0_s's with $p > 5$ GeV, which are 91% pure. Events with either a K^+K^- combination, or a $K^{\pm}K^0_s$ combination are selected. In the Monte Carlo, 66% of these events are $Z^0 \to s\bar{s}$ and they have an 82% analyzing power.

Figure 15 shows the asymmetry separately for left and right handed electron polarizations. The final result for data taken between '93 and '98 is[9] $A_s = 0.895 \pm 0.066_{stat} \pm 0.062_{syst}$.

5.5 Global Electroweak Comparison

The consistency of the world's measurements of electroweak parameters with the Standard Model can be checked in Figure 16. The SLD measurement of A_b is consistent with the Standard Model. The LEP measurement of A^b_{FB} seems to favor a heavy Higgs. The "orthogonality" of SLD's measurements of A_{LR} and A_b is clearly useful because it minimizes the area of the overlap region between them.

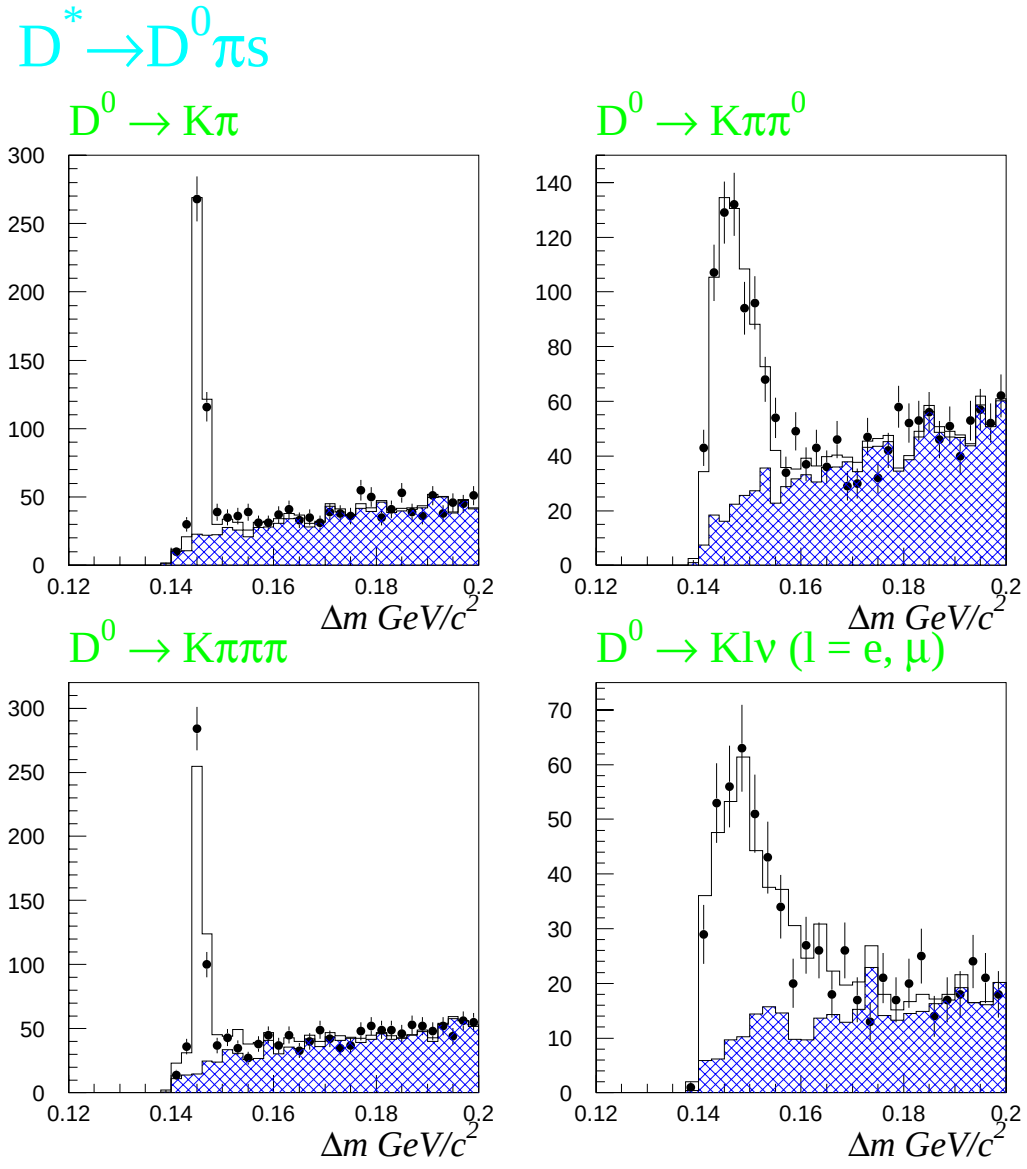

Fig. 14. Plots of Δm for each of the D^{*+} modes reconstructed in the A_c analysis. Clear signals are seen in each mode.

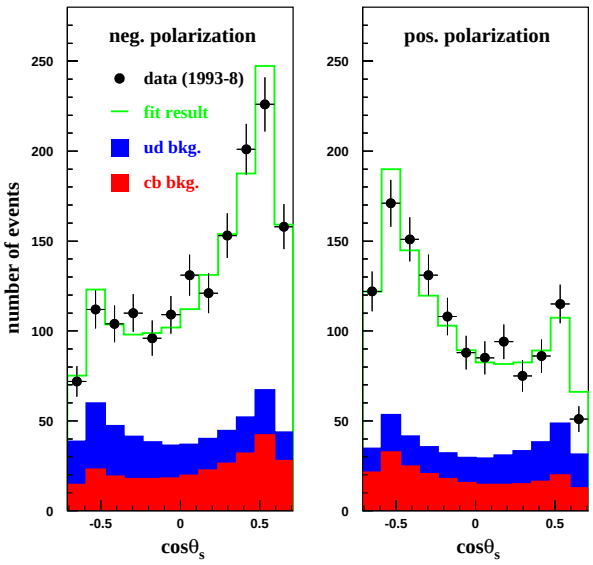

Fig. 15. The s-quark production asymmetry shown separately for left (negative) and right (positive) polarizations.

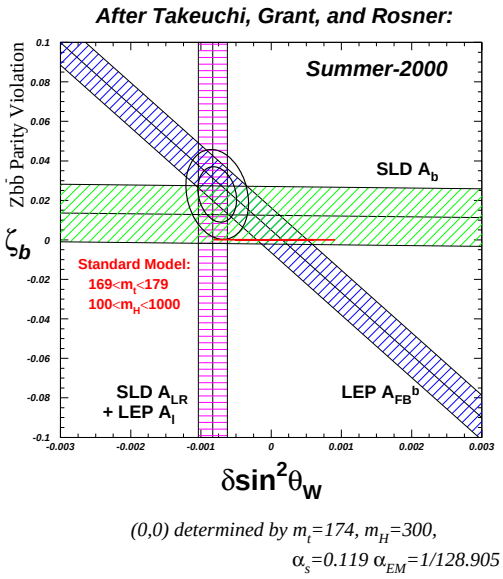

Fig. 16. A check for consistency with the Standard Model of the world's electroweak measurements. The Standard Model lies on a line at $\xi_b = 0$ between $\delta \sin^2 \theta_w \approx -0.001$ and $\delta \sin^2 \theta_w \approx 0.001$

Alternatively, one can use the various electroweak measurements to calculate the Higgs mass within the Standard Model. Figure 17 shows the Higgs mass limits that can be extracted from each of the electroweak measurements. A very tight limit ($m_H <$

147 GeV at 95% confidence) can be extracted from the SLD measurement of $\sin^2\theta_W^{eff}$ alone. All measurements except A_{FB}^b favor a light Higgs mass.

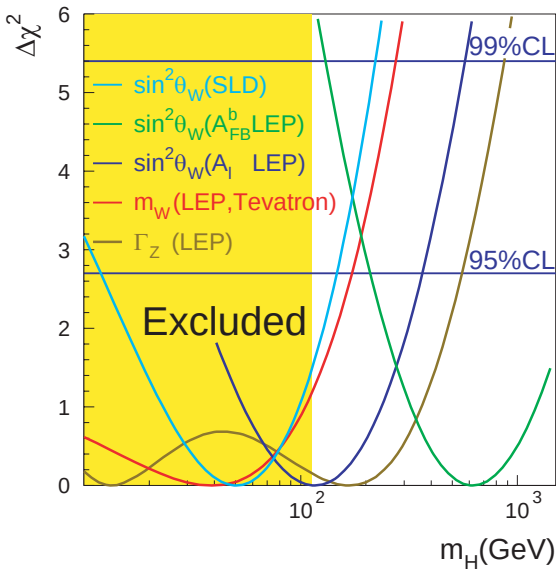

Fig. 17. Using different measurements of $\sin^2\theta_w^{eff}$ to constrain the Higgs Mass. SLD's measurements provide the single tightest limit.

6 Measurement of the B Fragmentation Function

The measurement of the B hadron production spectrum $D(x_B)$, where $x_B \equiv E_b/E_{beam}$, which is called the B Fragmentation Function, is interesting for a number of reasons. It can give useful input to B physics analysis, since $\langle x_B \rangle$ is often a large systematic. Also, it may help in the understanding of the rate of $b\bar{b}$ production in $p\bar{p}$ collisions, which is twice as large as predictions. Finally, it is a good place to test Heavy Quark Effective Theory (HQET).

6.1 x_B Reconstruction

The SLD analysis performs an inclusive reconstruction of x_B based solely on charged tracks.[10] The analysis begins the same as the inclusive B reconstruction algorithm described in section 5.2.2. As shown in Figure 18, the composite system of measured tracks has total momentum (p_{ch}) transverse momentum (p_T) and longitudinal momentum (p_L) defined relative to the vertex direction. The algorithm then defines a "missing

system" whose p_T is equal and opposite to that of the measured system, and whose mass, m_0, and longitudinal momentum p_{0L} are unknown. We can, however, place a limit on m_0 by noting that, in the B rest frame,

$$m_B = \sqrt{m_{ch}^2 + p_T^2 + p_L^2} + \sqrt{m_0^2 + p_T^2 + p_L^2}. \tag{16}$$

So,

$$m_B \geq \sqrt{m_{ch}^2 + p_T^2} + \sqrt{m_{ch}^2 + p_T^2}. \tag{17}$$

Therefore, noting that p_T is a Lorentz invariant, we can set a limit,

$$m_0^2 < m_{0,max}^2 \equiv m_B^2 + m_{ch}^2 - 2m_B\sqrt{m_{ch}^2 + p_T^2}. \tag{18}$$

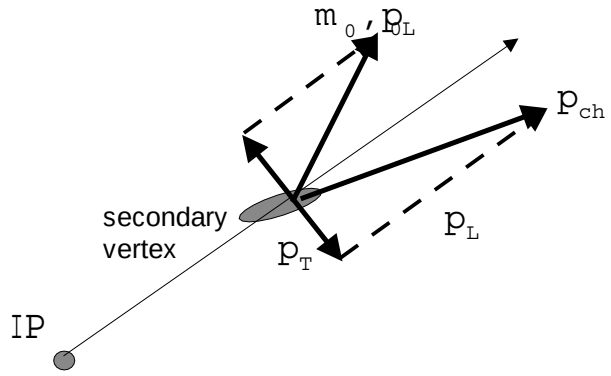

Fig. 18. Illustration of the variables used in the inclusive x_B reconstruction procedure.

Then, if we select hemispheres with small $m_{0,max}^2$, we preferentially select those hemispheres that are close to being fully reconstructed and therefore are measured with good energy resolution. We then set $m_0 = m_{0,max}$ and calculate x_B. Figure 19(a) shows the efficiency of this procedure and 19(b) shows the fractional energy resolution that is achieved.

6.2 Data/Monte Carlo Comparison

Figure 20 shows the results of applying this x_B reconstruction to the data and comparing to Monte Carlo, which was generated with the Jetset program.[11] Clearly, there is a discrepancy between the two.

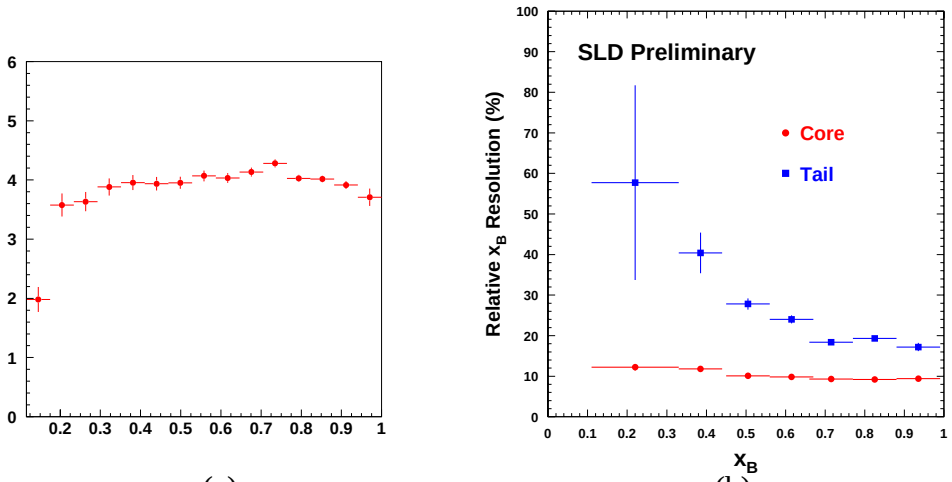

(a) (b)

Fig. 19. (a) shows the efficiency for of the x_B reconstruction procedure as a function of x_B. (b) shows the x_B resolution achieved as as a function of x_B.

6.3 Unfolding and $\langle x_B \rangle$

Ideally, we would like to take out the effects of resolution in order to produce the parent distribution. This "unfolding" procedure is complicated, however, because it depends on the fragmentation model that is used. This model dependence can be reduced by using a procedure called, "Singular Value Decomposition with Regularization".[12] Figure 21 shows the unfolded spectrum that is obtained with this procedure.

We can also extract the average B energy, $\langle x_B \rangle$. The final result based on data taken between '97 and '98 is $\langle x_B \rangle = 0.709 \pm 0.003_{stat} \pm 0.005_{syst}$.

7 Measurement of B_s^0 Mixing

As shown in Figure 22, B_s mixing is very similar to the more familiar B_d mixing. B_d mixing has been rather precisely measured, with a world average value of $\Delta m_d = 0.472 \pm 0.016$ ps^{-1}. B_d mixing is interesting because it is sensitive to the CKM parameter[13] V_{td}

$$\Delta m_d \propto m_{B_d} f_{B_d}^2 B_{B_{B_d}} \eta_{QCD} |V_{tb}^* V_{td}|^2, \tag{19}$$

where m_{B_d} is the mass of the B_d meson, $f_{B_d}^2$ and $B_{B_{B_d}}$ are QCD-related factors that need to be calculated and η_{QCD} is a QCD correction factor that is well known. Naively,

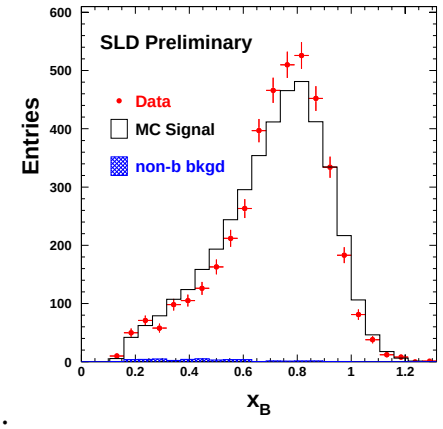

Fig. 20. The B fragmentation function $D(x_B)$ as measured in data compared to Monte Carlo.

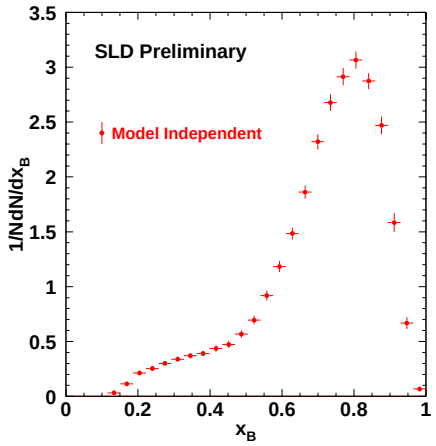

Fig. 21. The "unfolded" $D(x_B)$ spectrum, which has had efficiency and resolution effects removed in a model independent manner.

one might think that one could use the measured value of Δm_{B_d} to measure V_{td}. However, this is complicated because the hadronic factor, $f_{B_d}\sqrt{B_d}$ is not well known. The theoretical estimate is[13]

$$f_{B_d}\sqrt{B_d} = 201 \pm 42 \text{ MeV}. \tag{20}$$

This uncertainty spoils any estimate of V_{td} based on B_d mixing.

B_s mixing provides a way around this uncertainty. As can be seen in Figure 22, the only major difference is that rather than having a factor of V_{td} at the vertices, B_s mixing

Fig. 22. Feynman diagrams for B_d and B_s mixing.

has V_{ts}. The expression for Δm_s is therefore,

$$\Delta m_s = m_{B_s} f_{B_s}^2 B_{B_s} \eta_{QCD} |V_{tb}^* V_{ts}|^2, \tag{21}$$

where the factors are all similar to those for B_d. Since V_{ts} is much greater than V_{td}, we expect B_s mixing to be roughly 15 times faster than B_d mixing. Now, if one takes the ratio $\frac{\Delta m_s}{\Delta m_d}$, many of the theoretical uncertainties cancel and one is left with

$$\frac{\Delta m_s}{\Delta m_d} = \frac{m_{B_s} f_{B_s}^2 B_{B_s}}{m_{B_d} f_{B_d}^2 B_{B_s d}} \left|\frac{V_{ts}}{V_{td}}\right|^2 = (1.11 \pm 0.06) \left|\frac{V_{ts}}{V_{td}}\right|^2. \tag{22}$$

So, by measuring B_s mixing, we can turn B_d^0 mixing into a precision measurement of V_{td}.

7.1 Ingredients

Since B_s mixing is so fast, it is necessary to do time dependent measurements. To do so requires three ingredients.

- Initial State Tag: Determine quark-charge of B_s^0 at the time of production.
- Final State Tag: Determine quark-charge of B_s^0 at the time of decay.
- Proper time of the B_s^0 decay: Requires measurement of decay length and boost of the B_s^0.

The "Moser Formula" for B_s^0 mixing significance[14] is a convenient way of demonstrating the importance of each of these components. It reads:

$$S = \sqrt{\frac{N}{2}} f_{B_s} (1 - 2w) e^{-\frac{1}{2}(\Delta m_s \sigma_t)^2}, \tag{23}$$

where S is the expected significance of a Δm_s measurement, N is the number B_s^0 candidates identified, f_{B_s} is the B_s^0 purity, w is the quark charge mistag rate, and σ_t is the proper time resolution. σ_t can be written as the sum of two terms,

$$\sigma_t^2 = \left(\frac{\sigma_L}{\gamma\beta c}\right)^2 + \left(\frac{\sigma_p}{p}t\right)^2, \tag{24}$$

where σ_L is the decay length resolution, p, γ and β are the usual kinematic variables for the B_s. From equation 23 it is clear that while purity and tagging are important, it is absolutely essential to have excellent proper time resolution. This is because for $\Delta m_s > 10$ ps^{-1}, the significance will be exponentially damped unless $\sigma_t < 0.1$ ps. Since γ is typically 5 at the Z^0 pole the decay length resolution needs to be of order 100 μm or better. SLD's excellent vertex resolution yields excellent σ_t resolution, which makes SLD's measurements competitive at high Δm_s, even with lower statistics than LEP.

The following sections will describe each of the three ingredients in turn.

7.2 Initial State Tag

The initial state tag takes advantage of the forward-backward asymmetry of B mesons produced in Z^0 decay. This asymmetry is enhanced by the polarization of the SLC electron beam. Figure 23 shows the polar angle of b quarks (not $\bar{b}$) produced with left- and right-handed electron beams. Using the polarization as an initial state tag is 100% efficient (since the polarization is known for every event), and provides the correct tag 72% of the time. In order to enhance the initial state tag, information from the b-decay on the "opposite side" is also used. This information includes the jet charge, the vertex charge, the charge of any kaons, the charge of any leptons and the "dipole", which is described in section 7.3.3. This combined tag has a 75 to 78% correct tag probability. Figure 24 shows the output of this tag.

7.3 Final State Tags

The final state tag must identify the quark charge of the B_s^0 (i.e. b or $\bar{b}$) and provide a way to measure the time of the decay. A number of different techniques are used to provide this tag. The quality of each technique is parameterized by its B_s purity (f_{B_s}), its boost resolution ($\frac{\sigma_p}{p}$), its quark charge mis-tag fraction (w_{final}), and its decay length resolution (σ_L), which is calculated from a double gaussian fit with a fixed "core" frac-

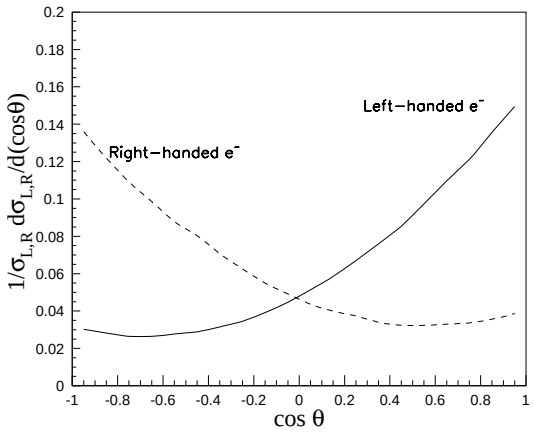

Fig. 23. Polar angle distribution for b-quarks produced at the Z^0, shown separately for right- and left-handed electron beams.

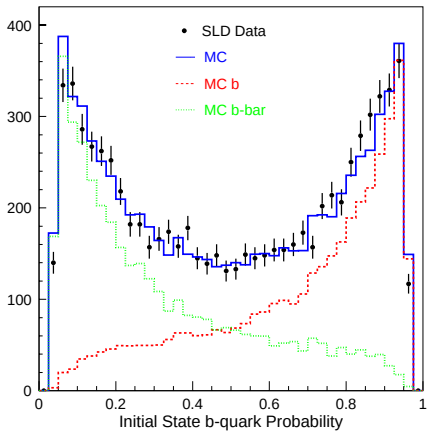

Fig. 24. Distribution of the computed initial state b-quark probability.

tion of 60%. Table 5 lists these parameters for each tagging technique. The following sections describe each tag in more detail.

7.3.1 D_s + Tracks

In the "D_s + Tracks" method, a D_s meson is exclusively reconstructed through either $D_s^- \to \phi\pi^-$ or $D_s \to K^{*0}K^-$. Identifying the charged kaons with the CRID greatly reduces the combinatoric background. The trajectory of the reconstructed D_s is then intersected with the other tracks of the vertex to form the B decay vertex, from which

h

Tagging Technique	f_{B_s}	σ_L (60% Core)	$\frac{\sigma p}{p}$	w_{final}
D_s + Tracks	0.38	48 μm	0.08	0.13
Lepton + D	0.16	54 μm	0.07	0.04
Charge Dipole	0.12	72 μm	0.07	0.24

Table 5. Performance parameters of the three final state tags.

the decay length is calculated. Figure 25 shows the reconstructed mass distribution of the D_s candidates, and a clear D_s signal is seen.

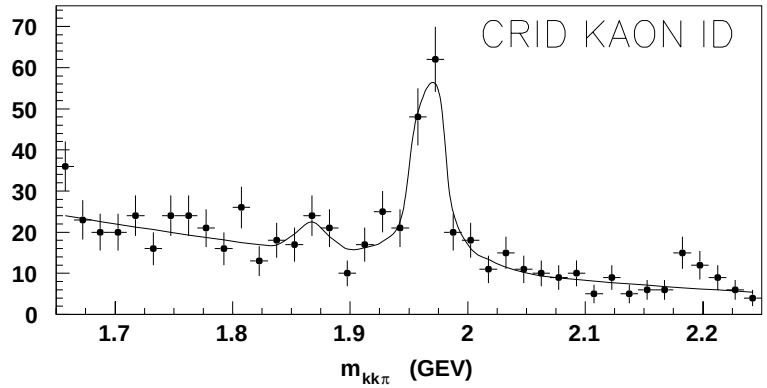

Fig. 25. Plot of the three body mass $m_{KK\pi}$ for D_s candidates. The CRID is used to identify kaons. A clear D_s peak is observed.

7.3.2 Lepton + D

In the "Lepton + D" method, a Neural Network similar to the one used for the A_b measurement (section 5.4.1) is used to select neutral semi-leptonic B decays. This network is also used to suppress "wrong sign" leptons from cascade $b \to c \to \bar{l}$ decays. The tag also requires a separate topologically reconstructed D vertex. The B decay point is then reconstructed by vertexing the lepton with the tracks from the D vertex.

7.3.3 Charge Dipole

The last final state tag is the fully inclusive "Charge Dipole" technique. As shown in Figure 26 this technique exploits the $b \to c$ decay topology of B_s decays. For a B_s decay, the tracks coming from the b decay vertex can have a charge of either 0 or 1,

while the tracks coming the cascade c decay can have a charge of either -1 or 0. For $\bar{B}_s$ decays the situation is reversed. Due to SLD's excellent vertex resolution, the b and c vertices can often be distinguished topologically. The measured distance between the vertices is L and the "charge dipole" is defined as $\delta q = (Q_D - Q_B) \times L$. So, for $\delta q > 0$, it is likely the decay was a $\bar{B}_s^0$. And, for $\delta q < 0$, it is likely that the decay was a B_s^0. Figure 27 shows the separation provided by the dipole.

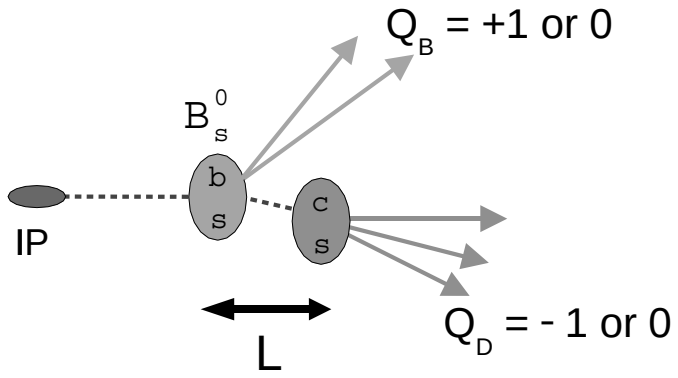

Fig. 26. Illustration the "dipole" technique for final state tagging.

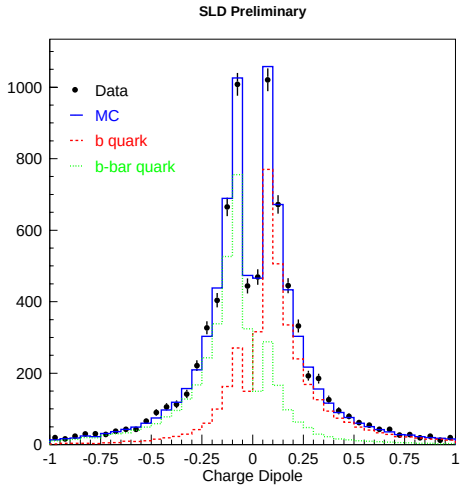

Fig. 27. Distribution of the quantity δq, as defined in the text. There is good separation between b and $\bar{b}$.

7.4 Amplitude Fit Method

In order to extract a signal (or limit) for B_s^0 mixing, the so-called "Amplitude Fit" method is used.[14] In this method the probability for mixing as a function of time is

fitted to the expressions

$$Prob(B_s^0 \to B_s^0) = \frac{1}{2}\Gamma e^{-\Gamma t}(1 + Acos\Delta m_s t) \quad (25)$$

$$Prob(B_s^0 \to \bar{B_s^0}) = \frac{1}{2}\Gamma e^{-\Gamma t}(1 - Acos\Delta m_s t), \quad (26)$$

where Γ is the decay width and A is the mixing amplitude, which is the free parameter in the fit. As we scan through all possible values of Δm_s, we would expect $A = 1$ for the true value Δm_s and $A = 0$ for Δm_s away from the true value. One can think of this method as a "Fourier Transform" of the data. Figure 28 shows the results of this fit for a large Monte Carlo sample of Lepton + D events.

To set a 95% confidence limit on Δm_s we find those values of A for which $A + 1.65\sigma_a < 1$. To determine the "Sensitivity", which is the expected limit if the experiment were repeated many times, we find those values of A for which $1.65\sigma_A < 1$.

Perhaps the most important advantage of this method is that it allows the combination of several samples, such as from different final state tags, or from different experiments. Figure 29 shows the SLD amplitude fit results for the combination of all three final state tags. Based on this fit, SLD excludes at 95% confidence level the region $\Delta m_s < 7.6$ ps^{-1} and the region $11.8 < \Delta m_s < 14.8$ ps^{-1}.

7.5 B_s Mixing World Average

SLD's amplitude fits can also be combined with those of the rest of the world. Figure 30 shows this world average as of Summer 2000. SLD's data is especially important at high Δm_s, due to the excellent σ_t resolution. The sensitivity of the world average is 17.9 ps^{-1} and it is able to rule out the region $\Delta m_s < 14.9$ ps^{-1}.

8 Conclusion

The SLD physics program has made large contributions in the areas of electroweak, QCD and heavy flavor Physics at the Z^0. Table 6 lists some highlights of this program. In addition to these measurements, SLD also has many other interesting results for which there was not space in this paper.

References

[1] SLD Collaboration, K. Abe *et al.*, *Phys. Rev.* D **53**, 1023 (1996).

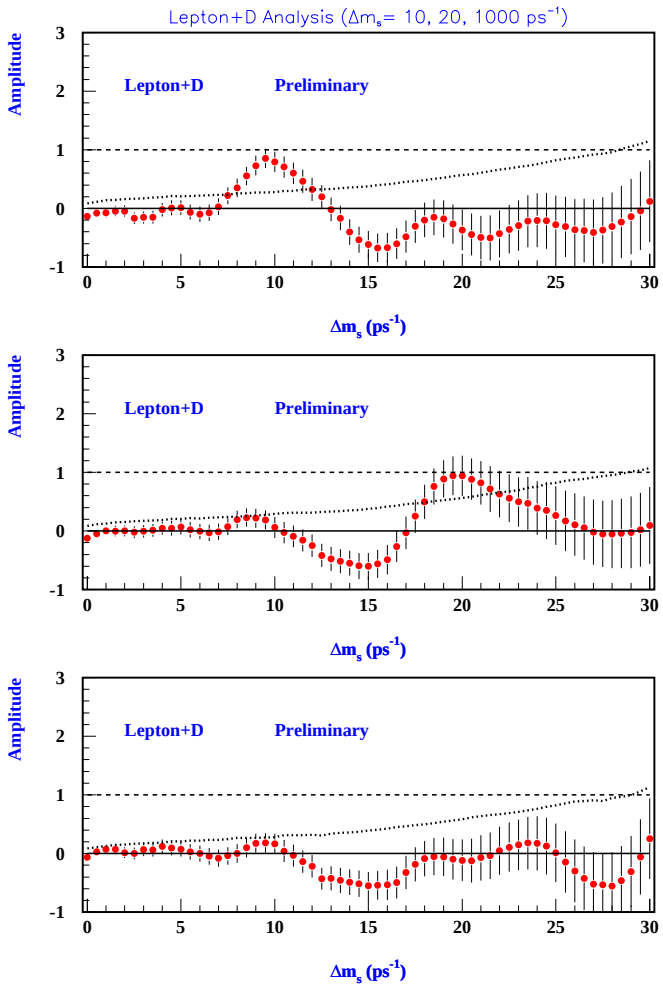

Fig. 28. Monte Carlo demonstration of the Amplitude Fit method for a sample of lepton + D decays. In the top plot, the data was generated with $\Delta m_s = 10$ ps^{-1} and a clear signal is observed there. In the middle plot, $\Delta m_s = 20$ ps^{-1} was used and a somewhat less significant signal is observed. In the bottom plot, $\Delta m_s = 1000$ ps^{-1} was used, which is beyond the sensitivity of the analysis and no signal is observed.

[2] SLD Collaboration, K. Abe *et al.*, *Phys. Rev. Let.* **85**, 5059 (2000).

[3] SLD Collaboration, K. Abe *et al.*, *Phys. Rev. Let.* **86**, 1162 (2001).

[4] D.J. Jackson, *Nucl. Instr. & Meth.* **A86**, 1162 (1997).

[5] The LEP Electroweak Working Group, EP Preprint Summer 2000, CERN-EP/2001-021.

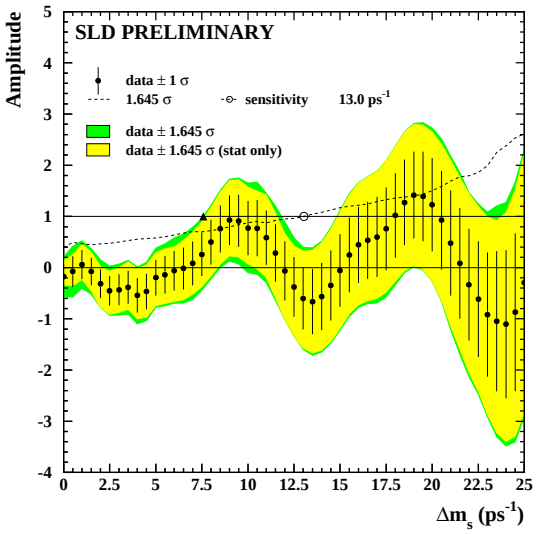

Fig. 29. Combined amplitude fit for the three final state tags.

Measurement	Value
A^0_{LR}	$0.15138 \pm 0.00216 \Rightarrow \mathbf{sin^2\,\theta_w^{eff} = 0.23097 \pm 0.00027}$
R_b	$0.21669 \pm 0.00094 \pm 0.00101$
$\boldsymbol{R_c}$	$\mathbf{0.1732 \pm 0.0041 \pm 0.0025}$
A_b	0.914 ± 0.024
A_c	0.635 ± 0.027
$\boldsymbol{A_s}$	$\mathbf{0.895 \pm 0.066 \pm 0.062}$
$\langle \boldsymbol{x_B} \rangle$	$\mathbf{0.709 \pm 0.003 \pm 0.005}$
Δm_s	Exclude $\Delta m_s < 7.6$ ps^{-1} and $11.8 < \Delta m_s < 14.8$ ps^{-1}

Table 6. Table summarizing the results presented in this paper. Those that are the world's best are indicated in bold.

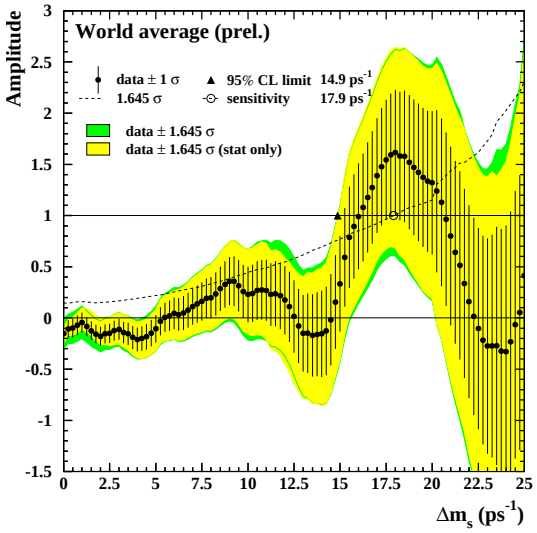

Fig. 30. Combined amplitude fit for the world's B_s mixing data as of Summer 2000.

[6] SLD Collaboration, K. Abe *et al.*, *"Direct Measurement of A_b at the Z^0 Pole Using a Lepton Tag*, SLAC-PUB-8516 (2000) [hep-ex/0009064].

[7] SLD Collaboration, K. Abe *et al.*, *"Direct Measurement of A_b Using Charged Vertices"*, SLAC-PUB-8542 (2000).

[8] SLD Collaboration, K. Abe *et al.*, *Phys. Rev.* D **63**, 032005 (2001).

[9] SLD Collaboration, K. Abe *et al.*, *Phys. Rev. Let.* **85**, 5059 (2000).

[10] SLD Collaboration, K. Abe *et al.*, *Phys. Rev. Let.* **84**, 4300 (2000).

[11] T. Sjostrand, Computer Physics Commun. **82**, 74 (1994).

[12] A. Hoecker and V. Kartvelishvili, NIM **A372**, 469 (1996).

[13] S. Mele, *Phys. Rev.* D **59**, 113011 (1999).

[14] H.-G. Moser and A. Roussarie, *Nucl. Instr. & Meth.* **A384**, 491 (1997).

MEASUREMENTS OF DIRECT CP VIOLATION IN THE NEUTRAL KAON SYSTEM

Alexandre Glazov
Enrico Fermi Institute
University of Chicago, Chicago, IL 60637

Representing the KTeV Collaboration

ABSTRACT

This paper presents new measurements of direct CP violation in the neutral kaon system performed by the two fixed target experiments, NA48 at CERN and KTeV at Fermilab. The data establishes a non-zero value of $\mathrm{Re}(\epsilon'/\epsilon) = (19.3 \pm 2.4) \times 10^{-4}$ (world average). The result is consistent with the Standard Model expectations and rules out Superweak models as the sole source of the CP violation in the neutral kaon system.

The emphasis of this paper is on experimental techniques which made this measurement possible. We describe the KTeV experiment in somewhat more detail than NA48. Similarities and differences between the two detectors are highlighted.

1 Introduction

Since the discovery of the K^0, $\overline{K^0}$ mixing in the 1950s, the system of neutral kaons has attracted the attention of physicists as an outstanding laboratory for precision study of extremely small effects. The observable states, K_L and K_S, have a tiny mass splitting (Δm) but a large lifetime difference. The latter allows the clean separation of K_L particles which led in 1964 to the discovery of the CP violating decay $K_L \to \pi\pi$.[1]

The gross features of the CP violation in the neutral kaon system are due to CP asymmetric mixing or *indirect* CP violation. The CP eigenstates for K^0, $\overline{K^0}$ particles are CP even and CP odd states, K_1 and K_2:

$$\begin{aligned} K_1 &\sim K^0 + \overline{K^0}\,, \\ K_2 &\sim K^0 - \overline{K^0}\,. \end{aligned} \tag{1}$$

If the neutral kaons obeyed CP symmetry, the K_S and K_L particles would coincide with K_1 and K_2, respectively. This actually explains the lifetime difference: K_S is allowed by CP to decay into the $\pi\pi$ state which has a much larger phase space compared to all the CP-allowed K_L decays. Yet the presence of the $K_L \to \pi\pi$ decay means that K_L contains some CP even admixture:

$$\begin{aligned} K_S &\sim K_1 + \epsilon K_2\,, \\ K_L &\sim K_2 + \epsilon K_1\,. \end{aligned} \tag{2}$$

The smallness of CP violation is expressed by the smallness of the CP violating mixing parameter, $2\mathrm{Re}(\epsilon) = 0.00327 \pm 0.00012$.[2]

The other possible source of CP violation comes from the decay process by itself and is usually referred as *direct* CP violation. Assuming CPT conservation, the decay amplitudes into final states with different isospin I are written

$$\begin{aligned} \langle I|T|K^0\rangle &= A_I e^{i\delta_I}, \\ \left\langle I|T|\overline{K^0}\right\rangle &= A_I^* e^{i\delta_I}, \end{aligned} \tag{3}$$

where $I = 0, 2$ and δ_I are final state interaction phase shifts. We can write the ratio of K_L to K_S decay amplitudes into the two 2π final states, $\pi^+\pi^-$ ("charged mode") and $\pi^0\pi^0$ ("neutral mode"), as

$$\begin{aligned} \eta_{+-} &= \epsilon + \epsilon', \\ \eta_{00} &= \epsilon - 2\epsilon'. \end{aligned} \tag{4}$$

Here ϵ' is given by

$$\epsilon' = \frac{i}{\sqrt{2}} e^{i(\delta_2 - \delta_0)} \frac{\mathrm{Re}(A_2)}{\mathrm{Re}(A_0)} \left(\frac{\mathrm{Im}(A_2)}{\mathrm{Re}(A_2)} - \frac{\mathrm{Im}(A_0)}{\mathrm{Re}(A_0)} \right). \tag{5}$$

The phase of ϵ is determined by the K_L-K_S mass difference, Δm, and the lifetime difference. It is about $\phi_\epsilon = 43.5°$. The phase of ϵ', $\phi_{\epsilon'} = \pi/2 + \delta_2 - \delta_0 = 48 \pm 4°$, according to the measurement of the final state phase shifts.[3] Therefore, in the absence of CPT violation, the ϵ and ϵ' vectors are nearly parallel and using equation (4) we can write:

$$\mathrm{Re}(\epsilon'/\epsilon) = \frac{1}{6}\left(1 - \left|\frac{\eta_{00}}{\eta_{+-}}\right|^2\right) = \frac{1}{6}\left(1 - \frac{\dfrac{\Gamma(K_L \to \pi^0\pi^0)}{\Gamma(K_S \to \pi^0\pi^0)}}{\dfrac{\Gamma(K_L \to \pi^+\pi^-)}{\Gamma(K_S \to \pi^+\pi^-)}}\right). \qquad (6)$$

In the Standard Model, the kaon mixing is explained by a box diagram with virtual W exchange. This indirect CP violation is naturally accommodated by the complex phase in the CKM quark mixing matrix. The Standard Model *predicts* existence of the direct CP violation, although exact calculations are difficult and under some circumstances $\mathrm{Re}(\epsilon'/\epsilon)$ may vanish since the dominant diagrams have contributions of the opposite sign. Recent calculations estimate $\mathrm{Re}(\epsilon'/\epsilon)$ between 5×10^{-4} and 30×10^{-4}.

Alternatively, CP violation can be described by the Superweak model,[4] which introduces an additional CP violating interaction, analogously to the standard weak interaction which violates parity. The Superweak model has no direct CP violation, $\mathrm{Re}(\epsilon'/\epsilon)_{SW} = 0$. Therefore, measuring a non-zero value of $\mathrm{Re}(\epsilon'/\epsilon)$ confirms the Standard Model and rules out the Superweak model as a sole source of the CP violation.

In the 1980's and early 1990's two groups, at CERN and at Fermilab, undertook experiments to measure $\mathrm{Re}(\epsilon'/\epsilon)$. The results obtained by NA31 at CERN, $\mathrm{Re}(\epsilon'/\epsilon) = (23. \pm 6.5) \times 10^{-4}$, and by E731 at Fermilab, $\mathrm{Re}(\epsilon'/\epsilon) = (7.4 \pm 5.2) \times 10^{-4}$, are in fair agreement although they carry different messages: the CERN result establishes direct CP violation at about 3.5σ level while the Fermilab result is consistent with $\mathrm{Re}(\epsilon'/\epsilon) = 0$. The average of the experiments, $\mathrm{Re}(\epsilon'/\epsilon) = (15 \pm 8) \times 10^{-4}$, establishes the effect at the 2σ level only. Both groups decided to perform new experiments with a design precision of a few $\times 10^{-4}$ to clarify the matter. The new experiments are KTeV at Fermilab and NA48 at CERN.

The measurement of $\mathrm{Re}(\epsilon'/\epsilon)$ at a sub-per-mil level using formula (6) is challenging. First of all, high intensity kaon beams are needed to detect several million CP violating $K_L \to \pi^0\pi^0$ decays. The double ratio form of equation (6) suggests cancellation of systematic uncertainties, which are common for the decays into the same final state and also for decays of the same particles into different final states. Yet, in general the cancellation is not perfect and requires careful detector design as well as scrupulous

data analysis.

The next section describes the design and basis of the data analysis at the two experiments. We will try to emphasize similarities and alternative paths used by the collaborations. The paper is based on the first $\mathrm{Re}(\epsilon'/\epsilon)$ measurements by the collaborations. These are the KTeV measurement based on 1996 data and the first part of the 1997 data,[5] the NA48 measurement is based on 1997 data,[6] and the NA48 preliminary result is based on 1998 data.[7] The paper also uses some results based on the complete set of 1997 KTeV data, although this analysis has not been finalized in terms of the new measurement of $\mathrm{Re}(\epsilon'/\epsilon)$ yet.

2 Experiments to measure direct CP violation

Both the CERN and Fermilab experiments are fixed target detectors using secondary high energy neutral beams. The kaon energy range is $40 - 160$ GeV for KTeV and $70 - 170$ GeV for NA48. Both detectors are situated about 100 m downstream from the primary target to obtain beams of K_L, neutrons and neutral hyperons with small contamination of K_S. The primary targeting angle and additional beryllium absorbers are used to optimize the kaon to baryon flux ratio.

The key feature for both experiments is the so-called *double beam* technique: decays of K_S and K_L are detected simultaneously, for both the charged and neutral mode. The primary particle is determined using the horizontal decay vertex position (KTeV) or from the timing tagging (NA48). The experiments differ in the way the K_S particles are produced. KTeV uses two parallel K_L beams, one of which has a fully active plastic *Regenerator*, situated close to the decay volume, to produce K_S in a coherent regeneration process. NA48 has a secondary K_S production target. Some of the primary protons are transported to this target; they are detected by an array of scintillator counters to provide timing tagging.

Both experiments have similar setups to detect two track $K \to \pi^+\pi^-$ and four gamma $K \to \pi^0\pi^0$ events. The tracking consists of two stations of drift chambers, before and after an analysis magnet. The calorimetry of the experiments is superb. KTeV uses an array of CsI crystals while NA48 has chosen a quasi-homogeneous liquid krypton calorimeter. Both devices have excellent resolution; they are calibrated to a sub-per-mil level using electrons from numerous semileptonic $K_L \to \pi e \nu$ ($Ke3$) decays.

The next two subsections describe the two experiments in more detail.

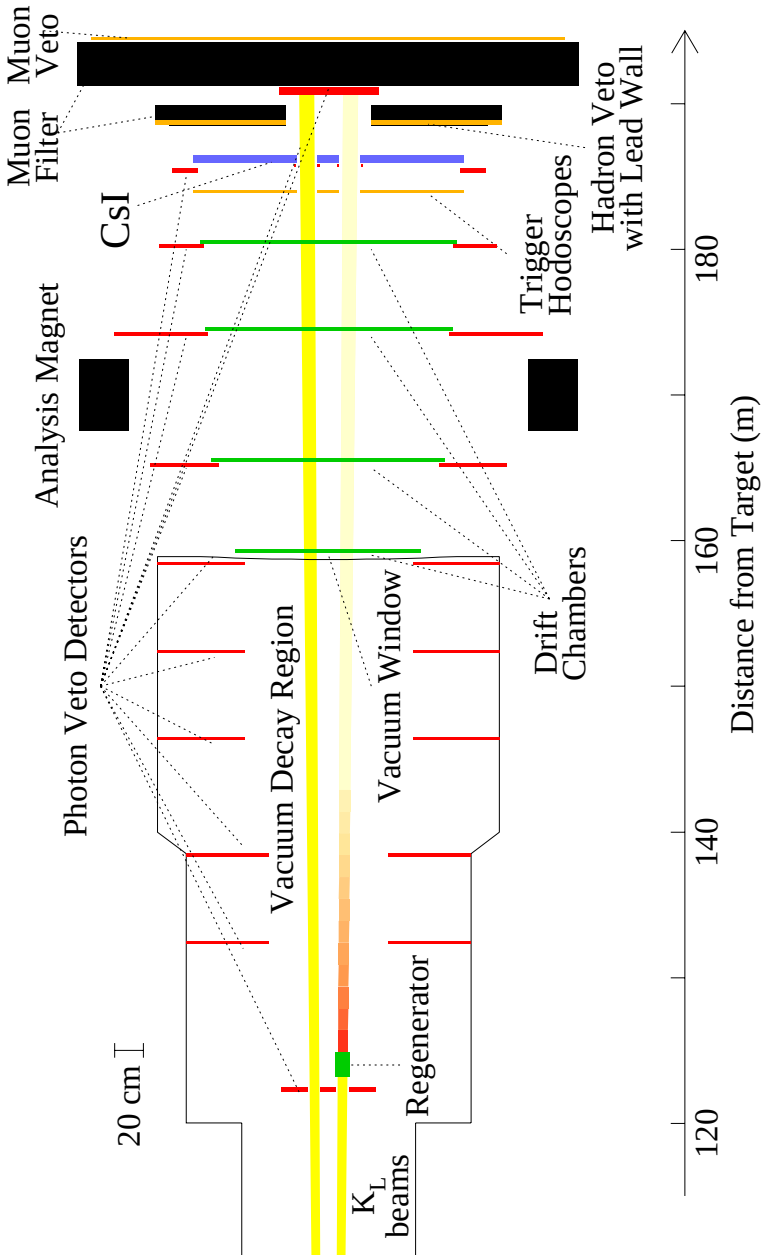

Fig. 1. The KTeV detector configuration used for the $\mathrm{Re}(\epsilon'/\epsilon)$ measurement.

2.1 The KTeV detector

A diagram of the KTeV detector is shown in Figure 1. The kaon beams are produced by an 800 GeV primary proton beam striking a BeO target. About half of $(2-8)\times 10^{12}$ protons per spill interact with the target. A set of sweeping magnets removes a large fraction of the charged particles, reducing the flux of muons reaching the detector to below 100 KHz. A set of collimators produces two identical beams that diverge by ± 0.8 mrad in the horizontal view. Beryllium and lead absorbers are placed into the beams to improve the kaon to neutron flux ratio.

Two identical kaon beams enter the fiducial volume of the detector at about 110 meters downstream from the primary target. The vacuum decay region is from about 110 to 159 meters. The decay volume is surrounded by a set of photon veto detectors to suppress neutral mode background originating from $K_L \to 3\pi^0$ events with missing photons. Inside the decay volume, the beams are separated by about 10 cm in the horizontal (X) view.

At about 125 meters from the primary target, one of the K_L beams passes through about 1.7 meters of plastic scintillator *Regenerator*. We will name this beam *Regenerator* as opposed to the other *Vacuum* beam. Since K^0 and $\overline{K^0}$ particles have different interaction cross sections with ordinary matter, the kaon beam downstream of Regenerator contains some admixture of K_S. The large decay width of the $K_S \to \pi\pi$ process means that K_S decays are dominant in the Regenerator beam. In fact, to balance the rate of $K_{S,L} \to \pi\pi$ decays and also to improve the kaon to neutron flux ratio, an additional beryllium absorber is placed upstream in the Regenerator beam. The total transmission of the Regenerator beam is about 8%; the regeneration amplitude ρ at a kaon energy of 70 GeV is about 1.2%

Once per minute the Regenerator and the additional beryllium absorber are moved from one beam to another, providing identical experimental conditions for collecting decays of K_S and K_L particles.

The length of the Regenerator is optimized to enhance *coherent regeneration* – regeneration without transverse momentum transfer, $P_t^2 = 0$, coherently summed over interactions throughout the Regenerator material. To veto inelastic interactions, the Regenerator is made of blocks of scintillators viewed by photomultiplier tubes providing veto signals at the trigger level. The remaining type of non-zero p_t^2 regeneration, originating from diffractive scattering, is studied in detail for $\pi^+\pi^-$ events, for which a measurement of p_t^2 is possible, modeled and subtracted as a background (see section 3).

The signal from the plastic scintillator is also used to veto $\pi^-\pi^+$ decays occurring inside the Regenerator. The last 2 cm long module of the Regenerator consists of two 0.56 cm lead plates sandwiched with 0.44 cm scintillator plates. This provides eight radiation lengths for four photons (2 radiation lengths for each photon) from $\pi^0\pi^0$ events and defines the sharp boundary of the decay region for the neutral mode.

At 159 meters the kaon decay products leave the vacuum decay volume through a 0.58 mm thick Kevlar window and enter the active detector which consists of drift chambers, analysis magnet, scintillator trigger hodoscope, CsI electromagnetic calorimeter and a set of hadron and muon veto detectors.

The charged particle spectrometer comprises four stations of drift chambers, two before and two after the analysis magnet. Each station contains four planes of drift chambers, two with wires in the horizontal and two with wires in the vertical direction, to measure drift distances in the vertical (Y) and horizontal (X) plane, respectively. To minimize multiple scattering, the space between the drift chambers is filled with helium contained in plastic bags at atmospheric pressure. The analysis magnet provides a horizontal momentum kick of 0.412 GeV/c.

The KTeV electromagnetic calorimeter is a square array consisting of 3100 blocks of cesium iodide crystals. Two sizes of blocks were used: 2.5×2.5 cm in the central region and 5×5 cm on the outside. All blocks are 50 cm long, which corresponds to 27 radiation lengths. The scintillation light from each CsI block is collected by a photomultiplier tube.

The channel gains are calibrated using electrons from $K_L \to \pi e \nu$ decays. For the 1996 running period, a total of 1.9×10^8 electrons was collected during the nominal running. This amount was nearly doubled for the 1997 data, allowing detailed studies of the block by block energy linearity. The results of this calibration are presented in Figure 2. The average energy resolution is below 0.7%, a value which is superior to all large detectors used in high energy physics.

2.2 The NA48 detector[6]

The NA48 detector has two separate production targets for K_L and K_S particles, located 126 m and 6 m upstream of the beginning of the decay region. For each SPS pulse, 1.1×10^{12} protons hit the K_L production target. Some of the non-interacting primary protons impinge on a bent silicon mono-crystal. A small fraction of these protons undergo channeling, and are bent to produce a collimated beam of 3×10^7 protons per

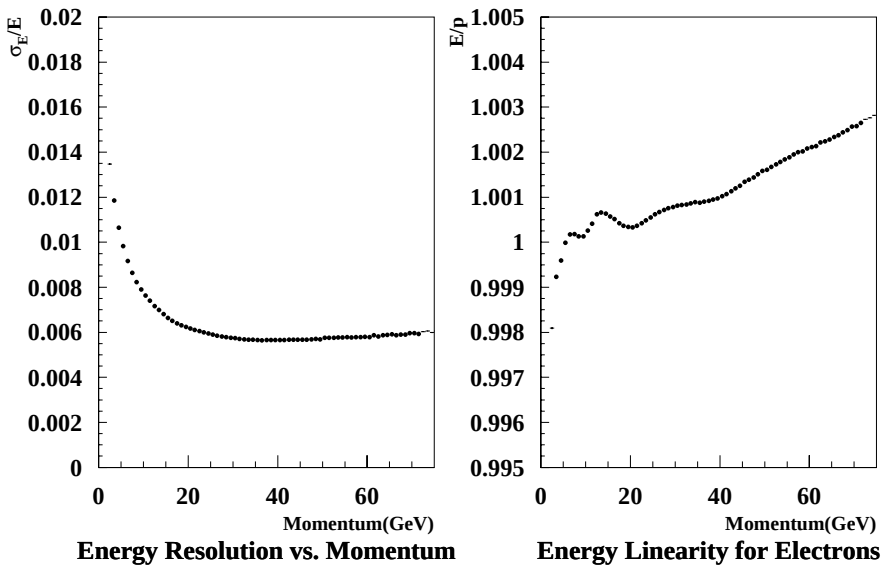

Fig. 2. Results of the KTeV CsI calibration with electrons for the 1997 run period. The left plot represents the measured calorimeter resolution as a function of electron momentum. The right plot shows the linearity of the CsI response.

pulse transported to the K_S production target. The production angles of K_L and K_S are optimized to minimize the difference in momentum spectra. The K_S beam enters the decay volume 68 mm above (Y view) the K_L beam. The beams converge at 0.6 mrad angle such that the axes of the two beams cross at the position of the electromagnetic calorimeter.

The protons directed to the K_S target are detected by an array of scintillator counters. This device is used to tag K_S decays. The presence (absence) of a proton detected in coincidence with the event defines the event as K_S (K_L). The proton time resolution is 120 ps and the double-pulse separation is 4 ns.

The neutral beam produced at the K_S target traverses an anti-counter, formed by a set of three scintillator counters preceded by an aligned 3 mm thick iridium crystal which enhances photon conversion (1.8 effective radiation lengths). This detector is used for an accurate definition of the beginning of the decay region.

The decay volume is contained in an evacuated 90 meter long tank surrounded by photon veto counters. The decay particles enter the detection volume through a 0.9 mm thick Kevlar window; the neutral beam continues in a 16 cm evacuated beam pipe.

The active volume of the NA48 detector has the same components as KTeV. The magnetic spectrometer comprises four drift chambers and a dipole magnet giving a horizontal transverse momentum kick of 0.265 GeV/c. The volume between drift chambers is filled with helium. The drift chambers consist of eight planes of sense wires, two horizontal, two vertical and two along each of 45° directions.

A quasi-homogeneous liquid krypton electromagnetic calorimeter with 127 cm (27 radiation length) long projective tower readout is used to measure photons from $\pi^0\pi^0$ events. The calorimeter has excellent resolution in energy (0.9% at average photon energy) and position (1.2 cm).

The summary of the basic features of the NA48 and KTeV detectors is given in Table 1. The numbers on NA48 performance are compiled from Ref. 6. The proper time resolution is calculated assuming average spatial resolutions along the beam direction (Z coordinate) and average kaon momentum.

One can see that both detectors have similar performance. For the two parameters used to reconstruct event kinematics, momentum/energy resolution and proper time resolution, the KTeV detector has a slight advantage. A better momentum resolution of the KTeV charged spectrometer is due to a larger field in the analysis magnet. Better resolution of the CsI calorimeter translates to a better proper time resolution for $\pi^0\pi^0$ events.

3 Data Analysis

The event reconstruction is similar for the both experiments, since the detector setups are very close. There are only small differences in the way some kinematic quantities are calculated. The main difference is in event tagging. KTeV uses the X position of the event vertex to determine the beam while NA48 relies on timing tagging to select the production target.

For the charged mode, tracks are reconstructed from the hits and drift times in the spectrometer. A vertex is defined as the point of closest approach of two oppositely charged tracks, provided they are separated by less than 3 cm in Z (NA48), or the χ^2 of the vertex fit is below 100 (KTeV). The experiments differ in the way the energy of the event is determined. NA48 ignores absolute track momentum information and reconstructs the energy using the opening angle between the tracks and the ratio of the track momenta, assuming the two tracks originate from $K \to \pi^+\pi^-$. KTeV uses a straight sum of the pion momenta. The NA48 method avoids systematic uncertainties

	KTeV	**NA48**
Beam Line		
Proton energy	800 GeV	450 GeV
Proton intensity per spill	$(2-8)\times 10^{12}$	1.1×10^{12}
Spill/Inactive time duration, sec	20/40	2.4/12.0
Kaon momentum range	$40-160$ GeV	$70-170$ GeV
Average kaon energy	70 GeV	110 GeV
Detector Setup		
Basic design	Double beam technique	
Source of K_S	Coherent regeneration	Secondary target
Event tagging	Vertex position	Timing tagging
Tracking		
Analysis Magnet P_t kick	0.412 GeV/c	0.256 GeV/c
Detector technology	Drift chambers	
Number of stations	2 before and 2 after magnet	
Planes per station	four, 2x2y	eight, 2x2y2u2v
Resolution per plane	100 μm	90 μm
Average per plane efficiency	99.5%	99.5%
Momentum resolution, σ_p/p	$0.2\% \oplus 0.008\% \times p$	$0.5\% \oplus 0.009\% \times p$
P resolution at P_{av}	0.4%	0.7%
Proper time resolution at P_{av}, $\Delta\tau/\tau_S$	6.1%	10.0%
Calorimetry		
Detector technology	CsI crystals	Liquid krypton
Spatial resolution	1.0 mm (small blocks) 1.8 mm (large blocks)	1.3 mm
Energy resolution, σ_E/E	$0.02/\sqrt{E}\oplus 0.005$	$0.125/E \oplus$ $0.032/\sqrt{E}\oplus 0.005$
Energy resolution at E_{av}	0.7%	0.9%
Proper time resolution at E_{av}, $\Delta\tau/\tau_S$	7.4%	8.5%

Table 1. Comparison of the basic parameters of NA48 and KTeV detectors

arising from the imperfect knowledge of the magnetic field flux, and pays the price of larger dependence on multiple scattering in the vacuum window. The magnetic field map is well known in the case of KTeV.

The semileptonic $Ke3$ background is rejected by requiring a low value of the ratio E/p of the energy of a matching cluster in the calorimeter to the track momentum. The cut is $E/p < 0.8$ (NA48) or $E/p < 0.85$ (KTeV). The $K \to \pi\mu\nu$ ($K\mu 3$) background is rejected by requiring no hits in the muon veto detectors.

Good $\pi^+\pi^-$ events are selected by requiring the invariant mass of two pions to be close to the nominal kaon mass. This essentially eliminates differences between the methods used to reconstruct kaon momentum discussed above.

A further reduction of the background is achieved using a cut based on the kaon transverse momentum. NA48 defines p'_t which is the component of the kaon momentum orthogonal to the line joining the production target (K_L or K_S, identified by the Y vertex position) and the point where the kaon trajectory crosses the plane of the first drift chamber. The p'_t resolution is independent of the target from which the event originated. The distributions of p'_t for $\pi^+\pi^-$ events from different targets show similar shape.[6] NA48 selects events with $p'^2_t < 2 \times 10^{-4}$ GeV^2/c^2.

KTeV has only one production target. For the good signal events, the kaon transverse momentum is equal to zero. The dominant source of large p_t^2 events in the Regenerator beam is due to diffractive scattering in the Regenerator. Therefore, p_t^2 is calculated assuming that the kaon scatters at the Z position of the downstream end of the Regenerator. After subtraction of the scattering background, the p_t^2 distributions in both beams are in fair agreement; some residual discrepancy is included in the systematic error. KTeV cuts at $p_t^2 < 2.5 \times 10^{-4}$ GeV^2/c^2. Simple calculations shows that this cut is actually much harder than the NA48 p'_t cut. Assuming the angles to be small, one can get

$$p_t^2 = p'^2_t \times \left(\frac{L}{Z}\right)^2, \tag{7}$$

where L is the distance from the target to the NA48 first drift chamber (about 210 m and 90 m for K_L and K_S target, respectively) and Z is the distance from the target to the decay vertex. For a K_L event decaying in the middle of the decay region, $Z = 140$ m, one gets $p_t^2 = 2.25 \times p'^2_t$. The difference between transverse momentum definitions becomes even larger for K_S events.

The neutral mode reconstruction starts with identifying four clusters in the electormagnetic calorimeter with energies above 3 GeV. The clusters are required to have

photon-like shape and to be in time. Fiducial cuts are applied to ensure the photons are well measured. The minimum distance between photon candidates is required to be greater than 10 cm (NA48) or 7.5 cm (KTeV). The $K_L \to 3\pi^0$ background is reduced by requiring no extra clusters of energy above about 1.5 GeV.

The kaon energy is obtained from the sum of photon energies. To determine the longitudinal position of the decay vertex relative to the front of the calorimeter, NA48 uses the energies and positions of the four selected clusters and assumes that their invariant mass is the kaon mass. Next, three possible combinations of photon clusters into π^0 pairs are tried; the event is selected if one of the combinations has acceptable quality.

KTeV chooses an alternative method. First, all three pairings of photons into π^0 candidates are tried. For each π^0 candidate, the Z vertex is reconstructed using energies and positions of the photons and assuming that their invariant mass is the pion mass. The pairing with the best agreement of the two π^0 vertices is chosen; the event is rejected if the best pairing has a poor quality. The vertex of the kaon decay is determined as a weighted average of the two π^0 vertices. Finally, the invariant mass of the four photon clusters is reconstructed; it is required to be close to the nominal mass of the kaon.

The X and Y position of the decay vertex is determined using the line connecting the production target and the center of energy of the photon clusters. For NA48, the production target is defined by the timing tagging. For KTeV, the X position of the vertex is used to define the beam. KTeV requires that X and Y positions of the vertex are within one of the two beams. Since the separation between the beams is larger than the transverse position resolution (10 cm compared to 1 mm), the X-position tagging always gives the correct beam for a signal, non-scattered event. For events scattered in the Regenerator, there is a certain probability to leave the Regenerator beam and decay in the range of Vacuum beam, contributing as a *cross over* background.

KTeV uses $\pi^+\pi^-$ events, for which complete reconstruction of the kinematics is possible, to study regenerator scattering background. The scattering background consists of an inelastic and a diffractive part. Empirically, the former has a relatively flat p_t^2 spectrum and can be described as a pure K_S state. The latter can be further subdivided into single, double and multiple scattering off Carbon, scattering off Lead and scattering off Hydrogen. Each of the terms has its own p_t^2 dependence and can be represented as a coherent mixture of K_S and K_L states. Other small backgrounds include diffractive dissociation reactions $n + C_{12} \to C_{12} + K_S\Lambda$ and $K_L + C_{12} \to C_{12} + K_S\phi$,

$\phi \to K_S K_L$ with non-reconstructed Λ or one K_S particle missing, as well as Primakoff K^* production: $K_L + Pb \to Pb + K_S^*$, $K_S^* \to K_S + \pi^0$ with missing π^0.

The scattering background is parametrized and put into the Monte Carlo simulation. This simulation is tuned to fit the charged mode data. The same Monte Carlo model is used to predict background shapes for $\pi^0\pi^0$ events. The regenerator scattering background for $K_S \to \pi^0\pi^0$ events is estimated to be about 1%. The contribution of the cross over background for $K_L \to \pi^0\pi^0$ events is about 0.3%. The systematic uncertainty in $\mathrm{Re}(\epsilon'/\epsilon)$ from the background subtraction is about 0.7×10^{-4}. This number includes uncertainties in the charged mode p_t^2 acceptance as well as possible difference in the inelastic background levels between charged and neutral modes because of residual differences in the veto cuts.

The timing tagging is a unique feature of the NA48 experiment.[6] The event is tagged by classifying it as K_S if there is a proton within a ± 2 ns coincidence window centered on the event time; otherwise the event is classified as K_L.

An accidental coincidence between a proton traversing the tagger and a K_L event may cause the event to be wrongly counted as K_S. This probability is measured for $\pi^+\pi^-$ events, using the Y position of the vertex as an alternative tagging technique, to be $\alpha_{LS}^{+-} = (11.05 \pm 0.01)\%$ (1998 data[7]). The measurement of the double ratio is sensitive to the difference in this probability between $\pi^0\pi^0$ and $\pi^+\pi^-$ events. The latter was estimated by various techniques to be $(0.3 \pm 4.2) \times 10^{-4}$.

4 Results

Table 2 summarizes event yields collected by the experiments. So far we have three reported measurements of $\mathrm{Re}(\epsilon'/\epsilon)$: the first published KTeV result based on the 1996 $\pi^0\pi^0$ data and the $\pi^+\pi^-$ data collected in the first quarter of 1997 (**KTeV 96-97a**); the first published NA48 result based on the 1997 data (**NA48 97**) and a preliminary result announced by NA48 based on the data collected in 1998 (**NA48 98**). The last row in Table 2 (**KTeV 97-97b**) shows yields for the KTeV data collected in 1997 (complete 1997 for $\pi^0\pi^0$ events and last three quarters of 1997 for $\pi^+\pi^-$ events). The analysis of this sample is not yet finished.

The next step from event yields is to calculate $\mathrm{Re}(\epsilon'/\epsilon)$ according to formula (6). An obvious problem arises, however. As the K_L and K_S lifetimes are very different, so are the decay Z distributions and thus the event yields, integrated over the large Z range, are different as well. Furthermore, the detector acceptance is not constant in Z;

	$N(K_L \to \pi^+\pi^-)$ $\times 10^6$ events	$N(K_S \to \pi^+\pi^-)$ $\times 10^6$ events	$N(K_L \to \pi^0\pi^0)$ $\times 10^6$ events	$N(K_S \to \pi^0\pi^0)$ $\times 10^6$ events
KTeV 96-97a[5]	2.6	4.5	0.9	1.4
NA48 97[6]	1.1	2.1	0.5	1.0
NA48 98[7]	4.8	7.5	1.1	1.8
KTeV 97-97b	7.1	12.3	2.5	4.2

Table 2. Data sets and event yields. The **KTeV 96-97a** data sample comprises $\pi^0\pi^0$ data collected in 1996 and $\pi^+\pi^-$ data collected in the first quarter of the 1997 running period ("97a"). The **KTeV 97-97b** sample consists of $\pi^0\pi^0$ data collected in the 1997 running period and $\pi^+\pi^-$ data collected in the last three quarters of 1997. The **NA48 97** and **NA48 98** data samples are based on the 1997 and 1998 running periods, respectively.

it is also unequal for $\pi^+\pi^-$ and $\pi^0\pi^0$ events.

The collaborations took alternative paths to resolve this problem. NA48 uses a technique of *weighting* K_L events according to their proper decay time, so that the effective longitudinal vertex distribution of K_L events is made equal to the K_S distribution. The residual acceptance differences, mainly due to difference in production targets and beam divergences, are studied with a full simulation of the beams and detector.

KTeV relies on detailed Monte Carlo simulation to determine the detector acceptance. The collaboration uses the weighting method as a cross check.

Both methods have advantages and disadvantages. An obvious disadvantage of the weighting technique is the increase in statistical uncertainty, since the K_L events reconstructed far from the K_S production target are effectively not counted. An obvious disadvantage of the Monte Carlo correction is an additional systematic uncertainty coming from determination of the detector acceptance in Z.

The quality of the Monte Carlo simulation can be checked by its ability to reproduce the data Z distribution in the Vacuum beam. This can be studied for the signal $\pi^+\pi^-$, $\pi^0\pi^0$ as well as for the high statistics $Ke3$ and $3\pi^0$ events. Figure 3 shows Z distributions of $\pi^+\pi^-$ and $Ke3$ events for KTeV data collected in the last three quarters of 1997 running period ("97b"), compared to the Monte Carlo simulation. A linear slope in the straight line fit to the ratio of the data to the Monte Carlo distributions is a direct measure of the bias in $\mathrm{Re}(\epsilon'/\epsilon)$. Since the average Z position in the Vacuum beam differs by about 6 meters in Z relative to the Regenerator beam, a slope of 1×10^{-4} m^{-1} corresponds to about a 1×10^{-4} shift in $\mathrm{Re}(\epsilon'/\epsilon)$. The 97b data show that the slope is

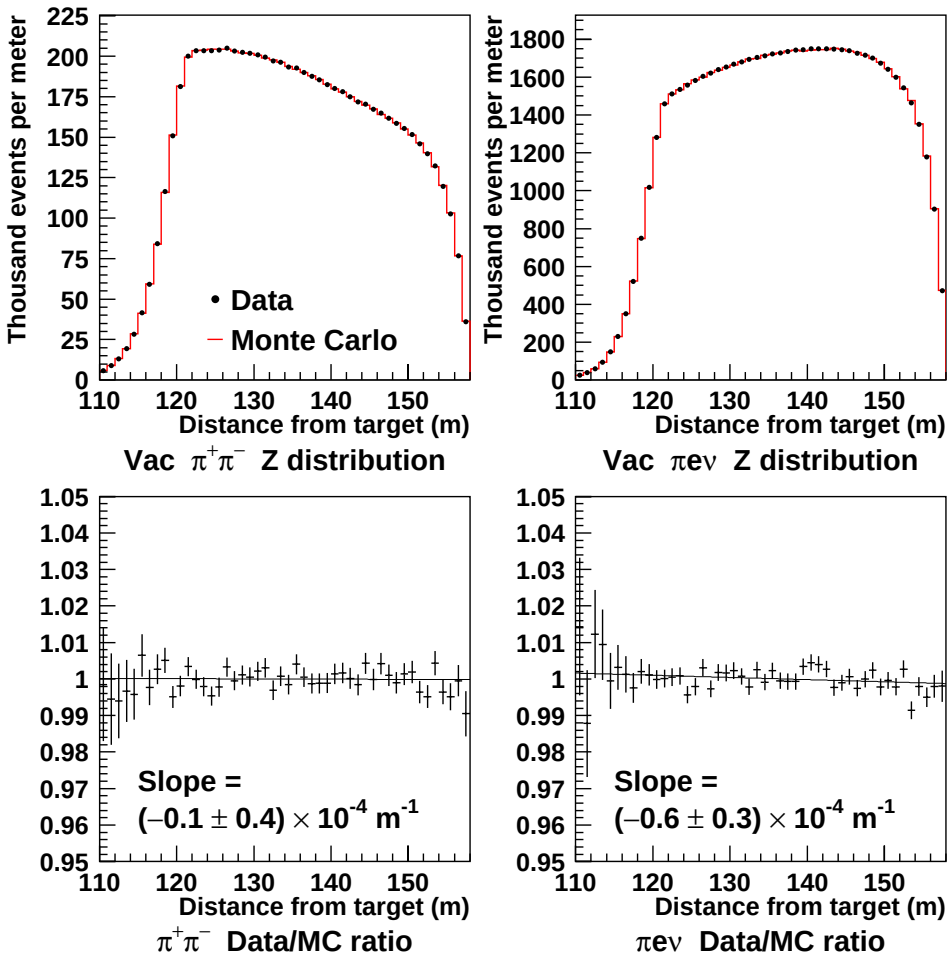

Fig. 3. Distribution of decay vertex position for $K \to \pi^+\pi^-$ events (upper left plot) and for $K \to \pi e\nu$ events (upper right plot). The KTeV $1997b$ data are shown as points with error bars; the histogram represents Monte Carlo simulation. The two bottom plots show the ratio of data to Monte Carlo distributions.

consistent with zero. This was not the case for the data collected in the first quarter of 1997 ("97a") which was used for the first KTeV result on $\mathrm{Re}(\epsilon'/\epsilon)$.[5] In fact, this slope was the dominant source of the systematic uncertainty in the result.

Table 3 gives a summary of systematic uncertainties of the $\mathrm{Re}(\epsilon'/\epsilon)$ measurements. The numbers are combined into groups for an easier comparison between experiments. "Trigger efficiency" includes losses of $\pi^+\pi^-$ and $\pi^0\pi^0$ events during data taking. For KTeV, the largest contribution is from the level 3 software filter. For NA48, it is dominated by level 1 losses of $\pi^+\pi^-$ events.

"$\pi^+\pi^-$ reconstruction" comprises uncertainties arising from the knowledge of the momentum scale, from the detector alignment and calibration and from the analysis cut variation. "$\pi^0\pi^0$ reconstruction" covers calorimeter energy scale and linearity, alignment and cut variation. The key source for the charged mode is the analysis cut variation. For the neutral mode, knowledge of the energy scale and linearity are the most important.

"Acceptance", in the case of KTeV, includes all uncertainties in Monte Carlo simulation: description of the limiting apertures, of the detector resolution, modeling of the drift chamber efficiency. This item also includes overall checks based on the Z-slope in the Vacuum beam; the slope in the charged mode is the dominant source of this uncertainty ($\Delta(\mathrm{Re}(\epsilon'/\epsilon)) = 1.6 \times 10^{-4}$). For NA48, "Acceptance" includes uncertainties in residual differences between K_S and K_L beams, as well as a small contribution from scattering off detector elements.

"Background" includes backgrounds in charged and neutral decay modes. For KTeV, the largest contribution comes from uncertainties in modeling the regenerator scattering background.

"Event tagging" and "Accidental effects" are the sources specific to the NA48 experiment. KTeV is practically insensitive to the biases coming from accidental activity since it uses identical beams for K_L and K_S events. Any extra detector activity is essentially the same for events from Vacuum and Regenerator beam. Residual effects are included in the uncertainty of the drift chamber simulation and the calorimeter energy scale. The situation is different for NA48 since the K_L and K_S beams are very different.

"Regenerator parameters" is the source specific for KTeV. It includes uncertainties in measuring of transmission and regeneration, as well as uncertainties of the external parameters, τ_S and Δm.

The values for the direct CP violating parameter $\mathrm{Re}(\epsilon'/\epsilon)$ measured by KTeV and

	KTeV 96-97a $\times 10^{-4}$	NA48 97 $\times 10^{-4}$	NA48 98 $\times 10^{-4}$
Trigger efficiency	0.6	3.8	1.8
$\pi^+\pi^-$ reconstruction	0.5	0.8	0.3
$\pi^0\pi^0$ reconstruction	1.3	2.0	1.7
Acceptance	2.0	2.1	1.6
Background	0.8	0.7	0.6
Event tagging	–	1.8	1.4
Accidental effects	–	2.3	2.0
Regenerator parameters	0.3	–	–
Total	2.8	5.7	4.0

Table 3. Sources of systematic uncertainty of the $\mathrm{Re}(\epsilon'/\epsilon)$ measurements. The numbers are combined in groups according to the procedure given in the text (see Section 4) for easier comparison between the experiments. The "Total" line shows the total systematic uncertainty given by each experiment.

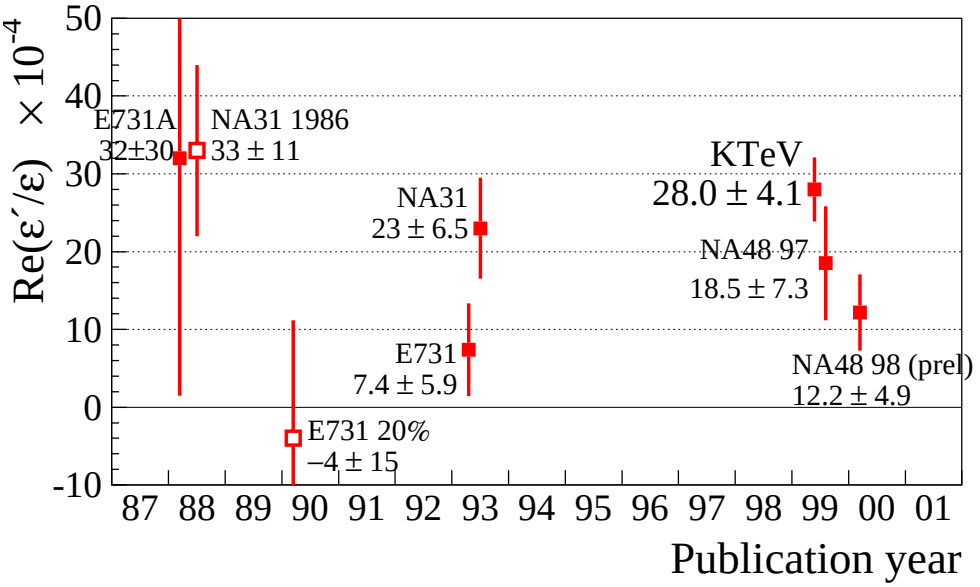

Fig. 4. Recent measurements of $\mathrm{Re}(\epsilon'/\epsilon)$. Open squares show measurements based on subsets of data samples superseded by the subsequent publications.

NA48 are:

KTeV 96-97a:[5]	$(28.0 \pm 3.0\ (stat) \pm 2.8\ (syst)) \times 10^{-4}$	$=$	$(28.0 \pm 4.1) \times 10^{-4}$,
NA48 97:[6]	$(18.5 \pm 4.5\ (stat) \pm 5.8\ (syst)) \times 10^{-4}$	$=$	$(18.5 \pm 7.3) \times 10^{-4,}$
NA48 98:[7]	$(12.2 \pm 2.9\ (stat) \pm 4.0\ (syst)) \times 10^{-4}$	$=$	$(12.2 \pm 4.9) \times 10^{-4}$

NA48 also quotes the combination of their published[6] and preliminary[7] results:

$$\mathrm{Re}(\epsilon'/\epsilon) = (14.0 \pm 4.3) \times 10^{-4} \quad \textbf{NA48 97-98, combined.}$$

Figure 4 shows all world measurements of $\mathrm{Re}(\epsilon'/\epsilon)$. Assuming that systematic errors are uncorrelated between experiments and different experimental results are consistent with each other, we obtain the following value for $\mathrm{Re}(\epsilon'/\epsilon)$:

$$\mathrm{Re}(\epsilon'/\epsilon) = (19.3 \pm 2.4) \times 10^{-4}\ (5\% c.l.) \quad \textbf{World Average}$$

This result definitively establishes the existence of direct CP violation and thus confirms the prediction of the Standard Model. It also shows that a Superweak interaction cannot be the sole source of CP violation in the neutral kaon system.

Further experimental results from both collaborations will be available soon. KTeV is close to completing the analysis of the 1997 data which more than doubles the sample used for the first publication. Another factor of two in statistics will come from the 1999 data. NA48 plans to reduce the systematic uncertainty in $\mathrm{Re}(\epsilon'/\epsilon)$ for the 1998 data sample before publishing the analysis. The detector continues data-taking and analysis of the 1999 data is on the way. The statistical uncertainty of $\mathrm{Re}(\epsilon'/\epsilon)$, combining the data from both collaborations, is expected to be lower than 1×10^{-4}.

After the first exciting news about the existence of direct CP violation the measurement of $\mathrm{Re}(\epsilon'/\epsilon)$ enters the phase of establishing the exact value of this important parameter. Careful detector design, large data samples and assiduous data analysis make this possible.

References

[1] J.H Christenson, J.W. Cronin, V.L. Fitch, and R. Turlay, Phys. Rev. Lett. **13**, 138 (1964).

[2] Particle Data Group, C. Caso *et al.* Eur. Phys. J. C**3**, 1 (1998).

[3] W. Ochs, πN Newsletter **3**, 25 (1991).

[4] L. Wolfenstein, Phys. Rev. Lett., **13**, 562 (1964).

[5] A. Alavi-Harati *et al.*, Phys. Rev. Lett. **83**, 917 (1999).

[6] G. Anzivino *et al.*, Phys. Lett. **B 465**, 335 (1999).

[7] R.G. Cassagnac, Proceedings Rencontres de la vallee d'Aoste, la Thuile (2000).

ep PHYSICS AT HIGH Q^2

Thomas Hadig
Physikalisches Institut, Universität Heidelberg, 69120 Heidelberg, Germany
on behalf of the H1 and ZEUS Collaborations

ABSTRACT

This article summarizes a talk presented at the SLAC Summer Institute 2000, SLAC, Stanford, USA.

The HERA ep collider allows the measurement of the proton structure and tests of the Standard Model in a large region of phase space that has not been accessible before. Such tests provide the framework for the H1 and ZEUS Collaborations to look for physics beyond the Standard Model.

1 Introduction

The HERA collider provides the H1 and ZEUS detectors with electrons or positrons at an energy of 27.5 GeV and protons with 920 GeV making it a unique place to study the proton structure and to search for physics beyond the Standard Model. Each experiment has collected up to now more than 100 pb^{-1}. The largest fraction stems from positron proton collisions.

In this article, processes with large momentum transfer between the incoming lepton and the proton are described. In the next section, the inclusive cross section and the comparison to the Standard Model is presented. Possible extensions of the Standard Model are compared to the data subsequently.

2 Inclusive Cross Section

The beam particles can interact via neutral or charged current events. In the former, a photon or a Z boson is exchanged,

$$NC : e^{\pm}p \to e^{\pm}X. \tag{1}$$

In deep-inelastic scattering events, the four-momentum transfered squared Q^2, is large, i.e. the exchanged boson is highly virtual. The proton structure is resolved and only a fraction x of the proton momentum takes part in the scattering. The double differential cross section can be described by

$$\frac{d^2\sigma^{\pm}_{NC}}{dxdQ^2} = \frac{2\pi\alpha^2}{xQ^4}\left[Y_+\tilde{F}_2(x,Q^2) \mp Y_- x\tilde{F}_3(x,Q^2) - y^2\tilde{F}_L(x,Q^2)\right] \tag{2}$$

with

$$Y_{\pm} = 1 \pm (1-y)^2, \tag{3}$$

where the plus and minus signs apply for an incoming electron respectively positron beam.

There is a strong global dependence on Q^{-4} such that processes at high momentum transfer are strongly suppressed. The main contribution for virtualities well below the Z pole comes from the proton structure function F_2. An additional function xF_3 arises from parity breaking weak interactions which enter through the Z exchange and the γZ interference. The last term describes the longitudinal cross section which is a negligible contribution at high Q^2 and small y.

In charged current processes a $W^{\pm}$ boson with the charge of the incoming lepton is exchanged,

$$CC : e^{\pm} p \rightarrow \overset{(-)}{\nu} X. \tag{4}$$

The double differential cross section is — in leading order — given by

$$\frac{d^2\sigma^{\pm}_{CC}}{dxdQ^2} = \frac{G_F^2}{2\pi x}\left(\frac{M_W^2}{M_W^2+Q^2}\right)^2 x\left[(u+c)+(1-y^2)(\bar{d}+\bar{s})\right] \tag{5}$$

with the W mass M_W, the Fermi constant G_F, and the quark densities $u, c, \bar{d}, \bar{s}$. At low Q^2 the charged current process is strongly suppressed compared to the neutral current processes by the mass term. This is also seen in figure 1 where the single differential neutral and charged current cross sections are plotted.

It can be seen that the data of both experiments agree well with each other and with the prediction of the Standard Model over more than six orders of magnitude.

Figure 2 shows the comparison of the neutral current cross section for both charges of the incoming lepton. While the positron proton data taken in the years 1994 till 1997 have been measured at a center of mass energy of $\sqrt{s} = 300$ GeV, the cms energy for the other data was $\sqrt{s} = 320$ GeV. The data from the lower energy running has been corrected to allow a direct comparison to that from the higher energy running.

At low photon virtualities, the cross sections are similar, while at higher Q^2 the electron cross section is significantly higher than the one for positions. The difference is induced by the Z exchange which does not have a visible influence at low Q^2. This is seen more clearly in figure 3 where the single inclusive cross section is displayed in two different regions of the momentum transfer. In the high Q^2 region (bottom plots) a significant difference between the theory predictions with and without Z exchange is found. The sign of the γZ interference differs for electron and positron induced processes and the data are described well in both cases.

This difference allows the extraction of the structure function xF_3 from HERA data alone as is shown in figure 4. The data are — within the still large statistical errors — consistent with those of the global fits of the CTEQ and MRS groups. The contribution of the longitudinal cross section in this region of phase space at large Q^2 and high x is found to be negligible.

Detailed comparisons of data to QCD theory have been performed. A summary of the results can be found in the talk by J. Engelen in these proceedings.[5]

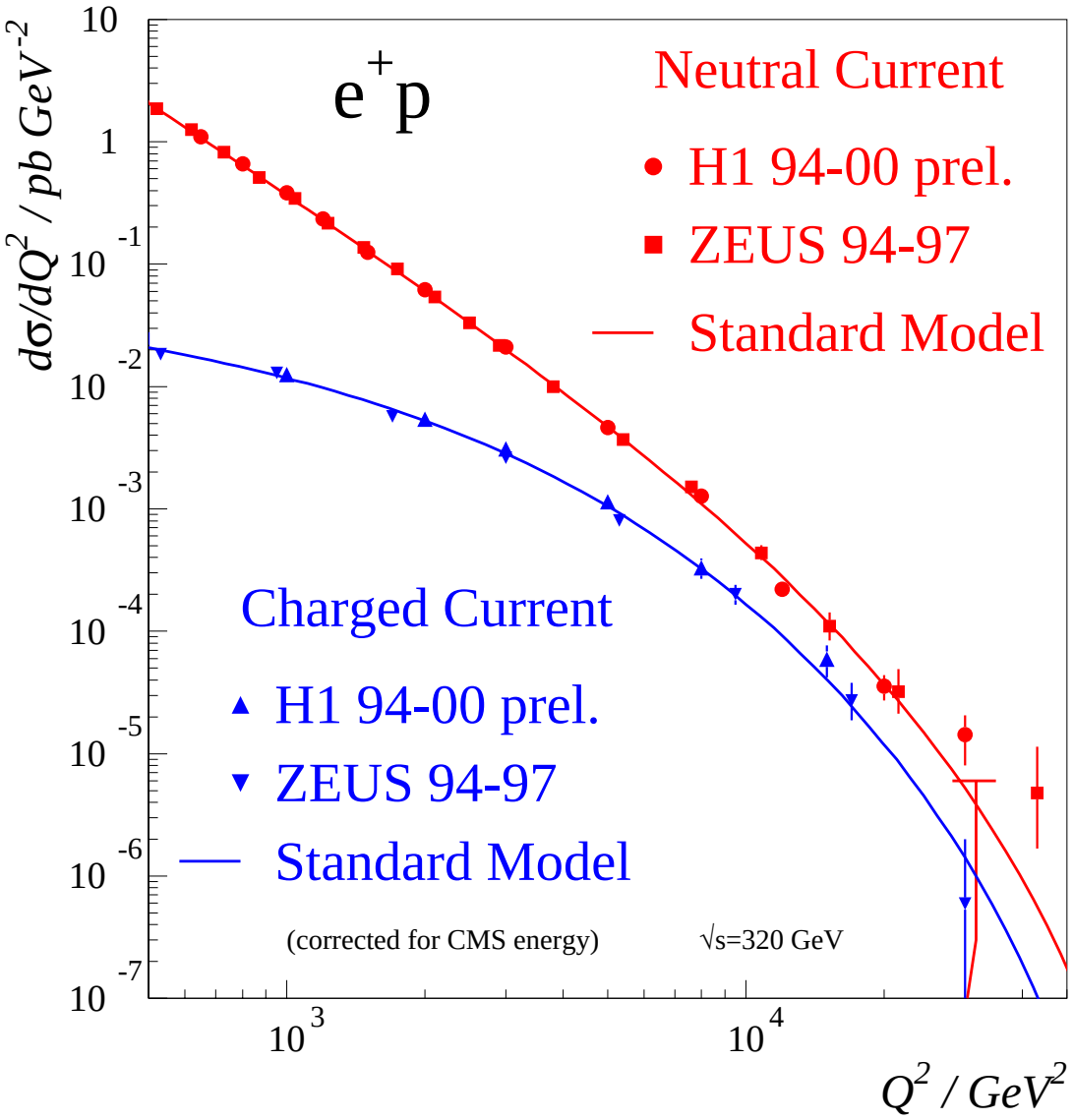

Fig. 1. Comparison of neutral and charged current cross sections for e^+p collisions. The symbols show the data of both experiments and the full line gives the prediction of the Standard Model.[1,2]

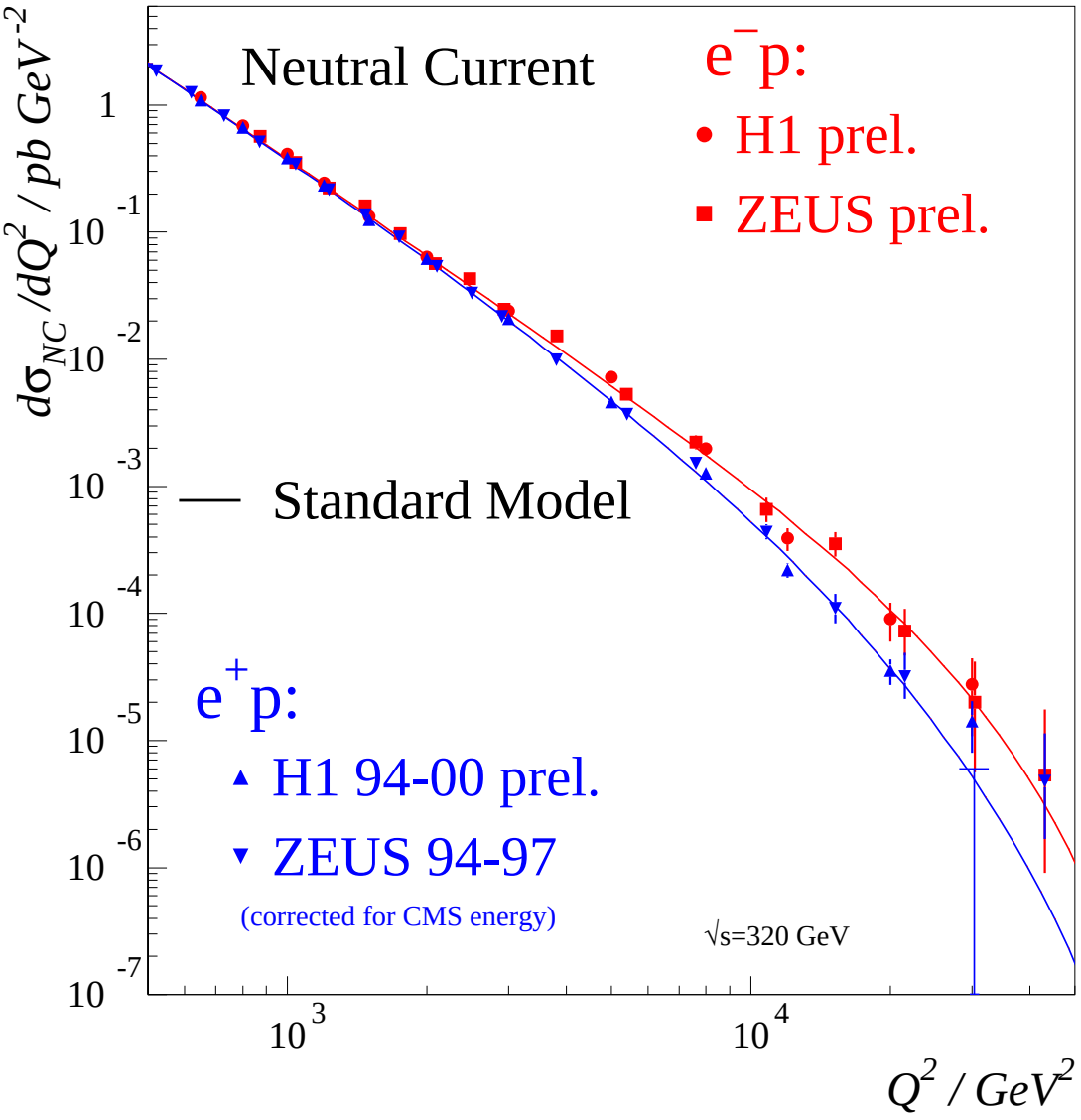

Fig. 2. Comparison of neutral current cross sections for e^+p and e^-p collisions. The e^+p data in the years 1994 till 1997 have been taken at a lower center of mass energy. A correction for the effect of this difference has been applied to allow for a direct comparison (see figure 3). The symbols show the data of both experiments and the full line gives the prediction of the Standard Model.[2–4]

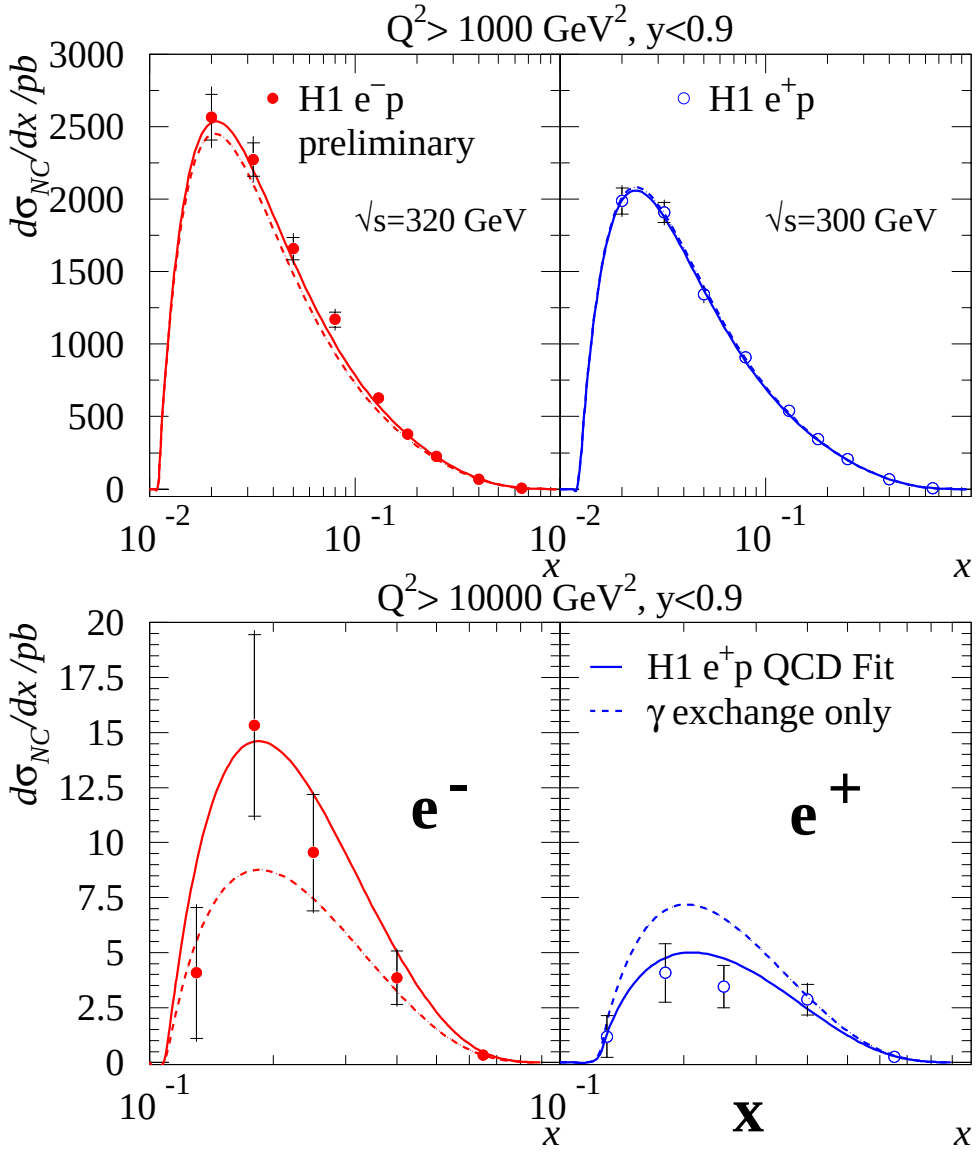

Fig. 3. Influence of the γZ interference in two different regions of four-momentum transfer Q^2. The symbols show the data of the H1 Collaboration and the full line gives a fit of the Standard Model to the data. The dashed line shows the part of the theoretical prediction taking into account the exchange of photons only.[3]

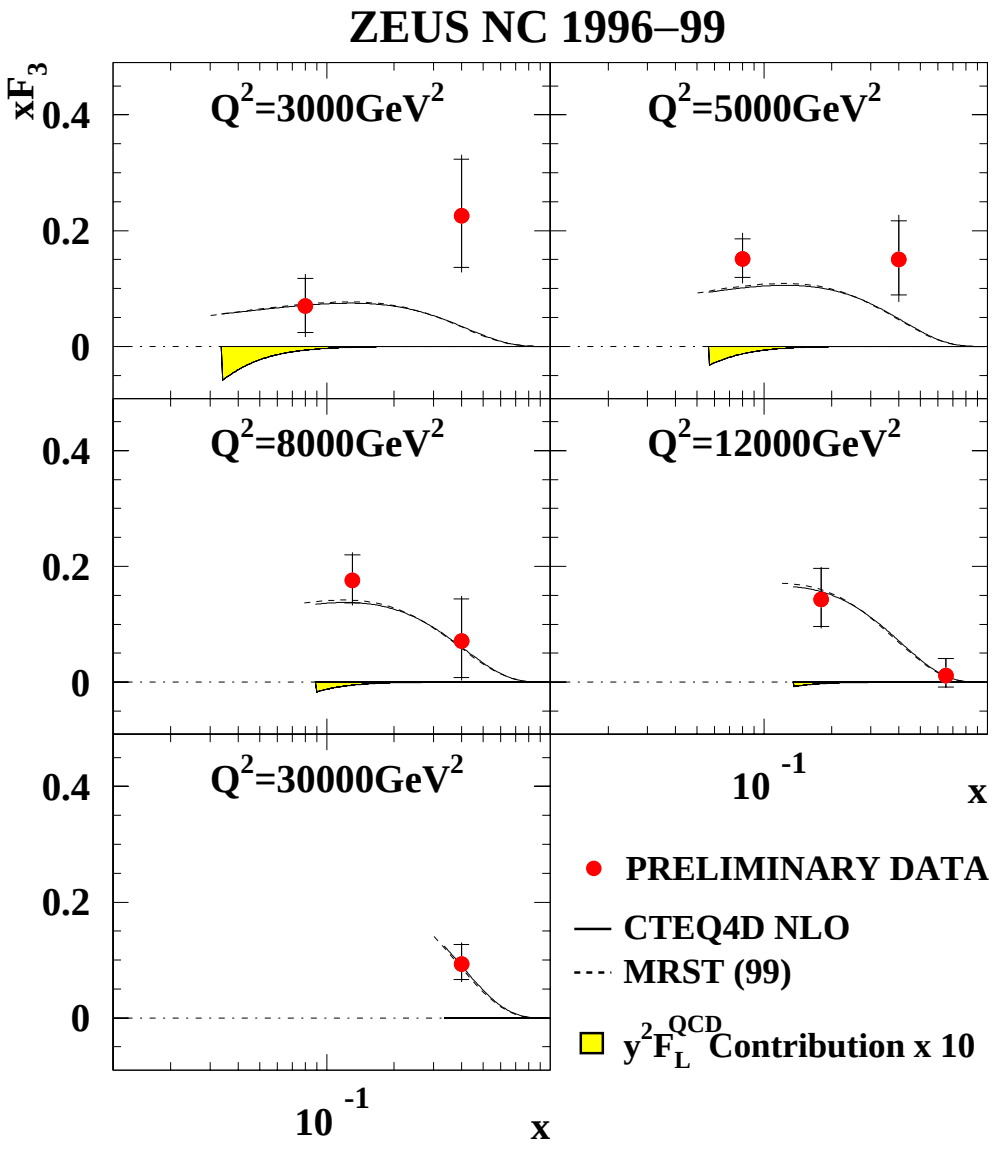

Fig. 4. Extraction of the xF_3 structure function. The symbols show the data of the ZEUS Collaboration. The lines display the value taken from the global parton density fits performed by the CTEQ and MRS groups. The shaded area shows the contribution ($\times$ 10) of the longitudinal structure function.[4]

3 Physics Beyond the Standard Model

One typical signature for physics beyond the Standard Model are mass resonances in the cross section. The center of mass energy squared available in the lepton quark cross section is

$$\hat{s} = xs \tag{6}$$

with the ep center of mass energy $\sqrt{s} = 320$ GeV.

Figure 5 shows the inclusive cross section in different bins of x. The data are well described by a next-to-leading order QCD fit. In figure 6, a more detailed study by the H1 Collaboration is presented with cuts optimized to look for resonances in the lepton quark cross section. While in the early data set a deviation from the Standard Model expectation was seen, the new data set with increased statistics does not confirm this effect. The ZEUS Collaboration also observes, at high Q^2 and x, no significant deviation from the Standard Model expectations in their analysis of 1994-2000 data.[6]

The H1 Collaboration has observed an excess in events containing isolated leptons. A typical event is shown in figure 7. The signature of the events consists of an isolated electron or muon, a significant amount of missing transverse energy and a jet with large transverse momentum (p_T^X). If the missing momentum is attributed to a single neutrino leaving the detector undetected, the transverse mass of the lepton neutrino pair can be extracted and is found to cluster at the mass of the W boson, see figure 8. However, contrary to the distributions of the measured events, the transverse momentum of the jet produced in Standard Model W production is predicted to be small. This is plotted in figures 8 and 9. While the H1 Collaboration observes an excess at high transverse momenta of the jets, the ZEUS Collaboration finds good agreement with the Standard Model expectations. This picture is confirmed by the numbers given in table 1. An analysis with comparable cuts shows that, even though the Monte Carlo expectation is very similar, the H1 Collaboration sees more events than ZEUS.

A possible production of single top quarks by a flavor violating neutral current vertex has been studied by both collaborations in the leptonic and hadronic decay channels. Since no significant excess has been found, limits have been derived for the photon coupling. Since Z exchange is strongly suppressed, no limits on the Z coupling are calculated. The comparison in figure 10 shows that the limits on the photon coupling are the best limits available.

Supersymmetric extensions of the Standard Model predict the existence of new particles: squarks, the supersymmetric partners of the quarks, and sleptons. Standard

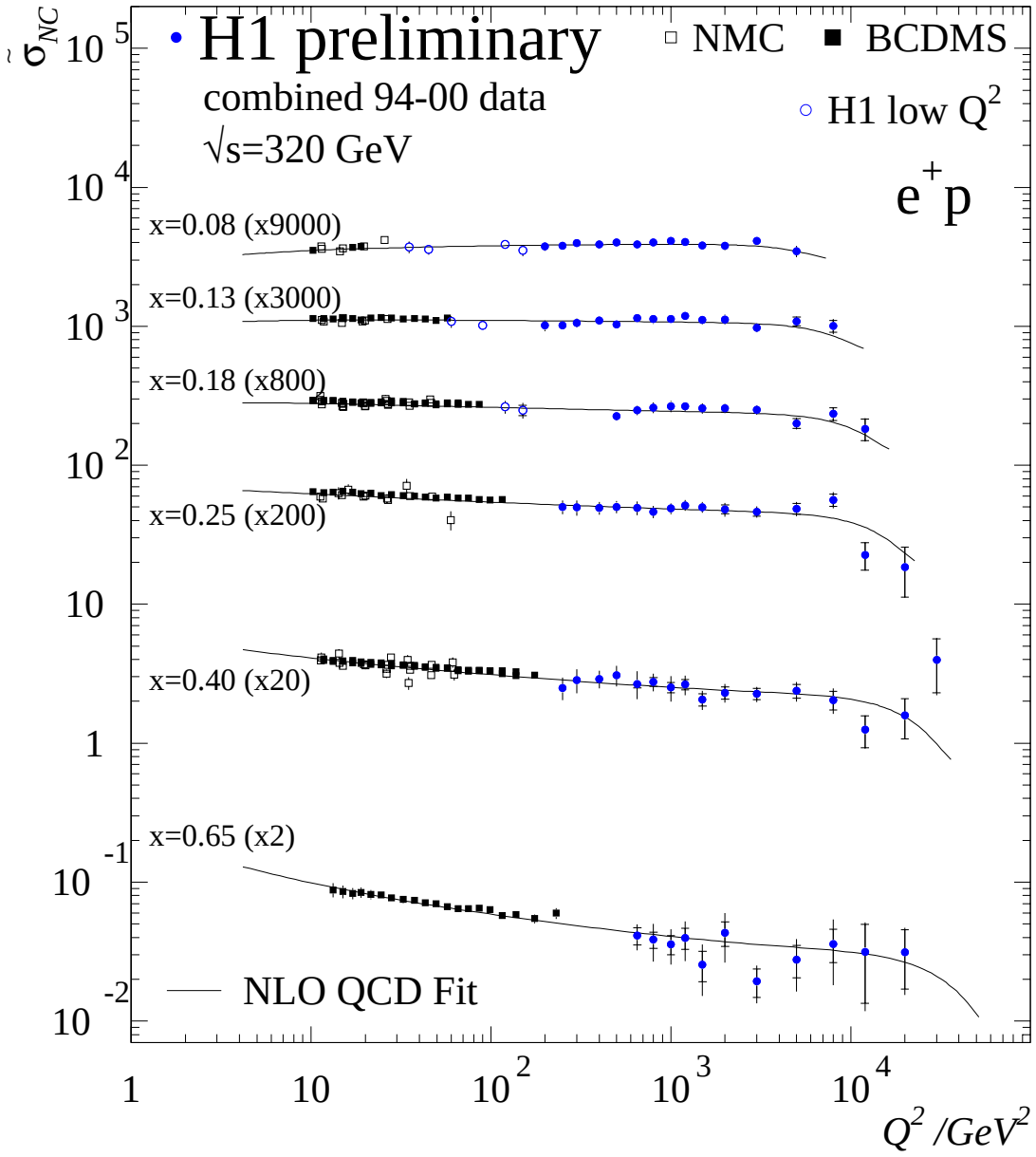

Fig. 5. Double differential inclusive cross section. The symbols show the data of the H1 Collaboration and the fixed target experiments NMC and BCDMS. The lines display a QCD fit to the data.[1]

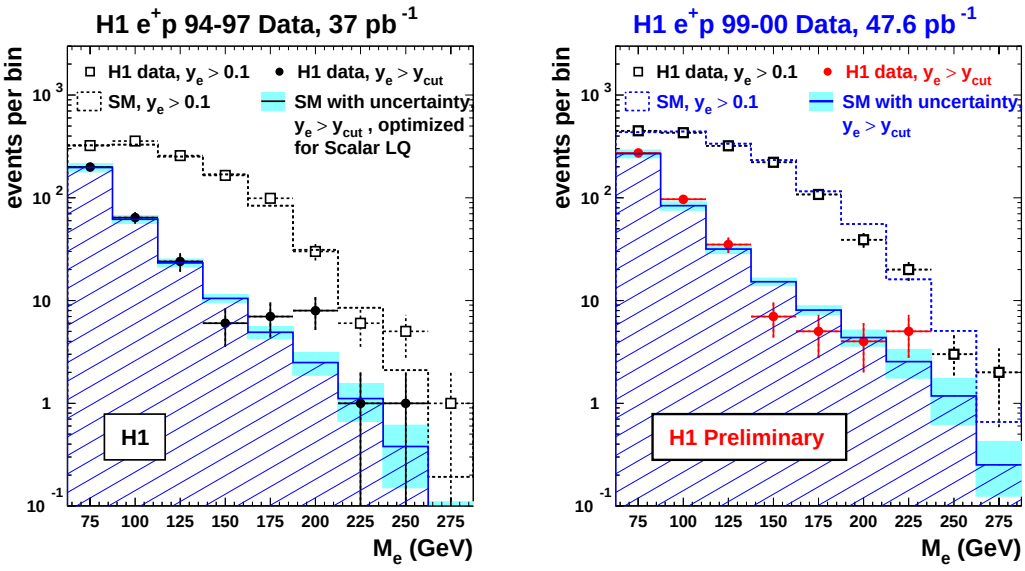

Fig. 6. Cross section as a function of the invariant mass of the lepton quark subprocess. Points show the data of the H1 Collaboration and the histograms give the Standard Model expectation. The left plots show the data of the 1994 to 1997 data taking, the right those of the 1999 and 2000 data set.[7]

Collaboration	Data Set	Events seen	MC expectation
Default analyses of the collaborations			
H1 preliminary	1994-2000 e^+p only, 82 pb^{-1}	9	2.3 ± 0.6
ZEUS prelim.	1994-1999 e^+p and e^-p, 82 pb^{-1}	11	9.8 ± 1.3
Special analyses using similar cuts			
H1 preliminary	1994-2000 e^+p only, 82 pb^{-1}	9	1.78
ZEUS prelim.	1994-1999 e^+p and e^-p, 82 pb^{-1}	1	1.60

Table 1. Comparison of the number of isolated lepton events seen and expected from Monte Carlo simulations of all relevant Standard Model processes. In the upper part, the default analyses of both collaborations are shown. Those are optimized for the detector configurations and specific channels. For comparison, analyses with similar cuts have been performed and are shown in the lower part.[8–10]

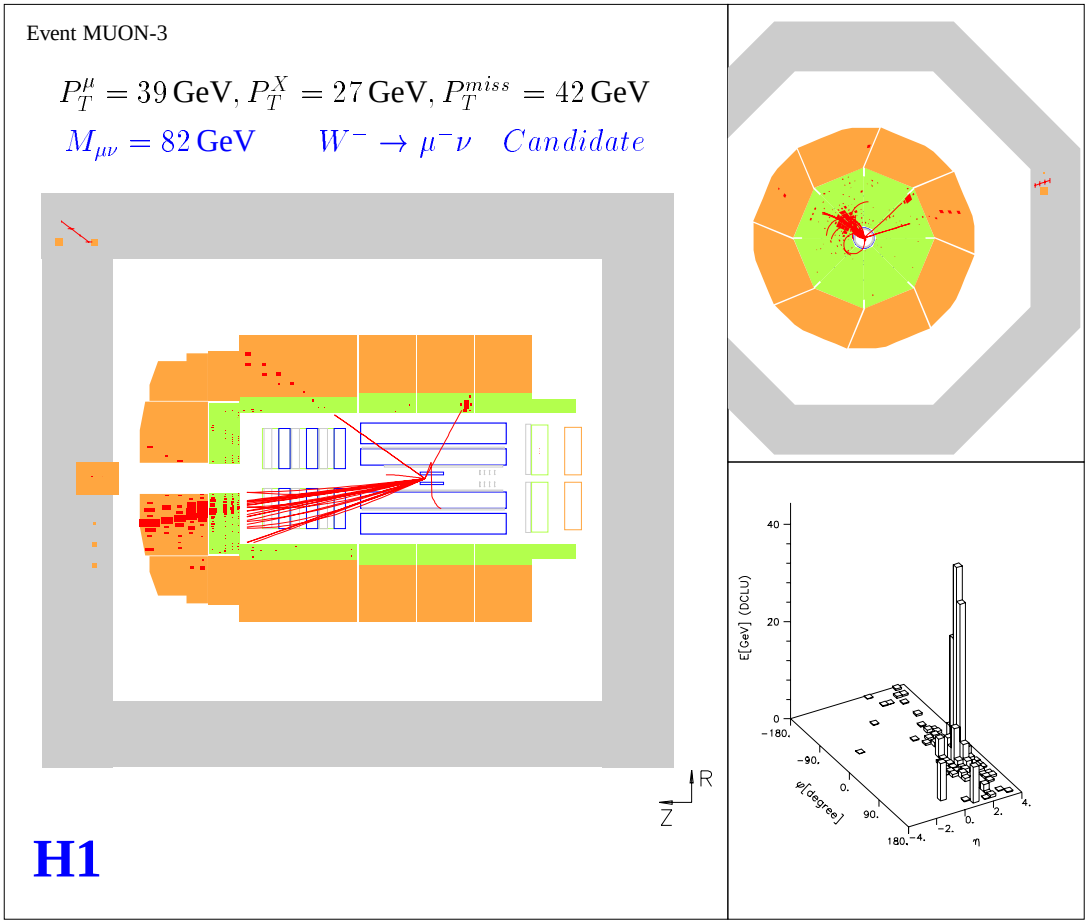

Fig. 7. Event display of an isolated lepton event recorded at the H1 detector.

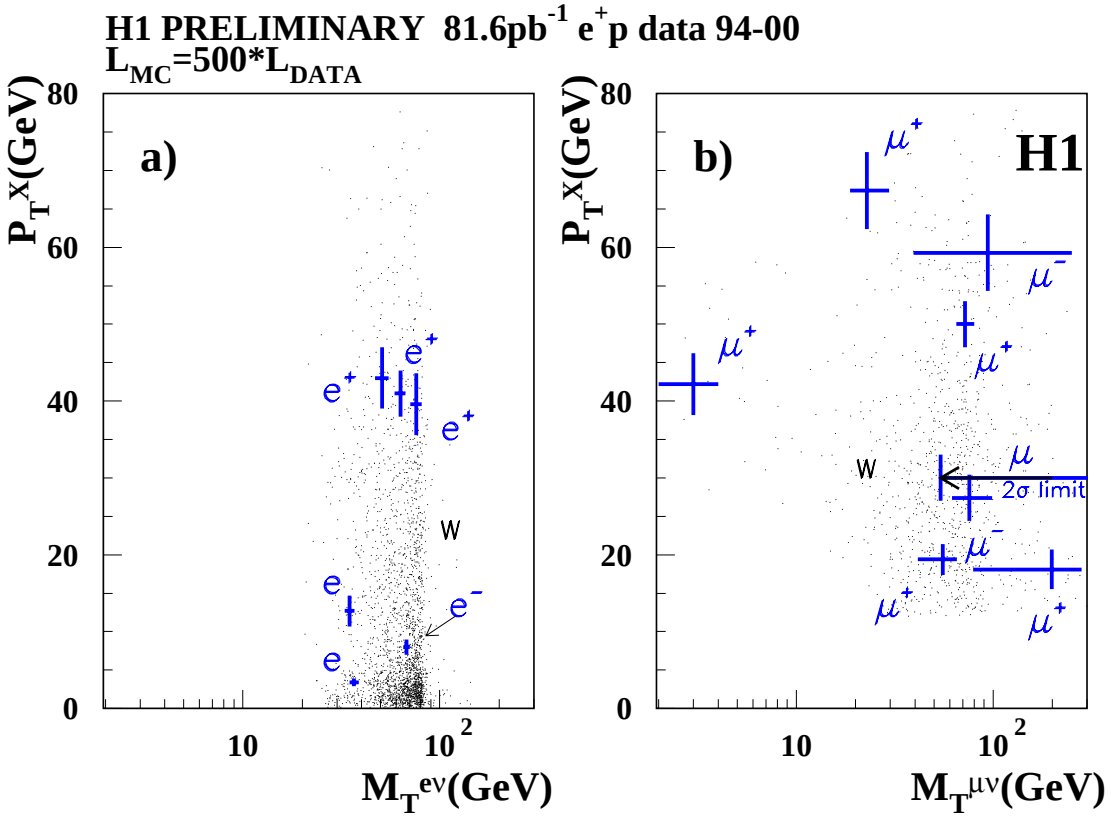

Fig. 8. Event distribution of the isolated lepton events. Shown is the transverse mass of the lepton neutrino pair versus the transverse momentum of the jet for isolated electron and muon events. The events found by the H1 Collaboration are shown as crosses corresponding to the uncertainty in the measurement of the observables. The small points show the event distribution expected from a Monte Carlo simulation of Standard Model W production. The luminosity of the Monte Carlo production exceeds that of the data by a factor 500.[8]

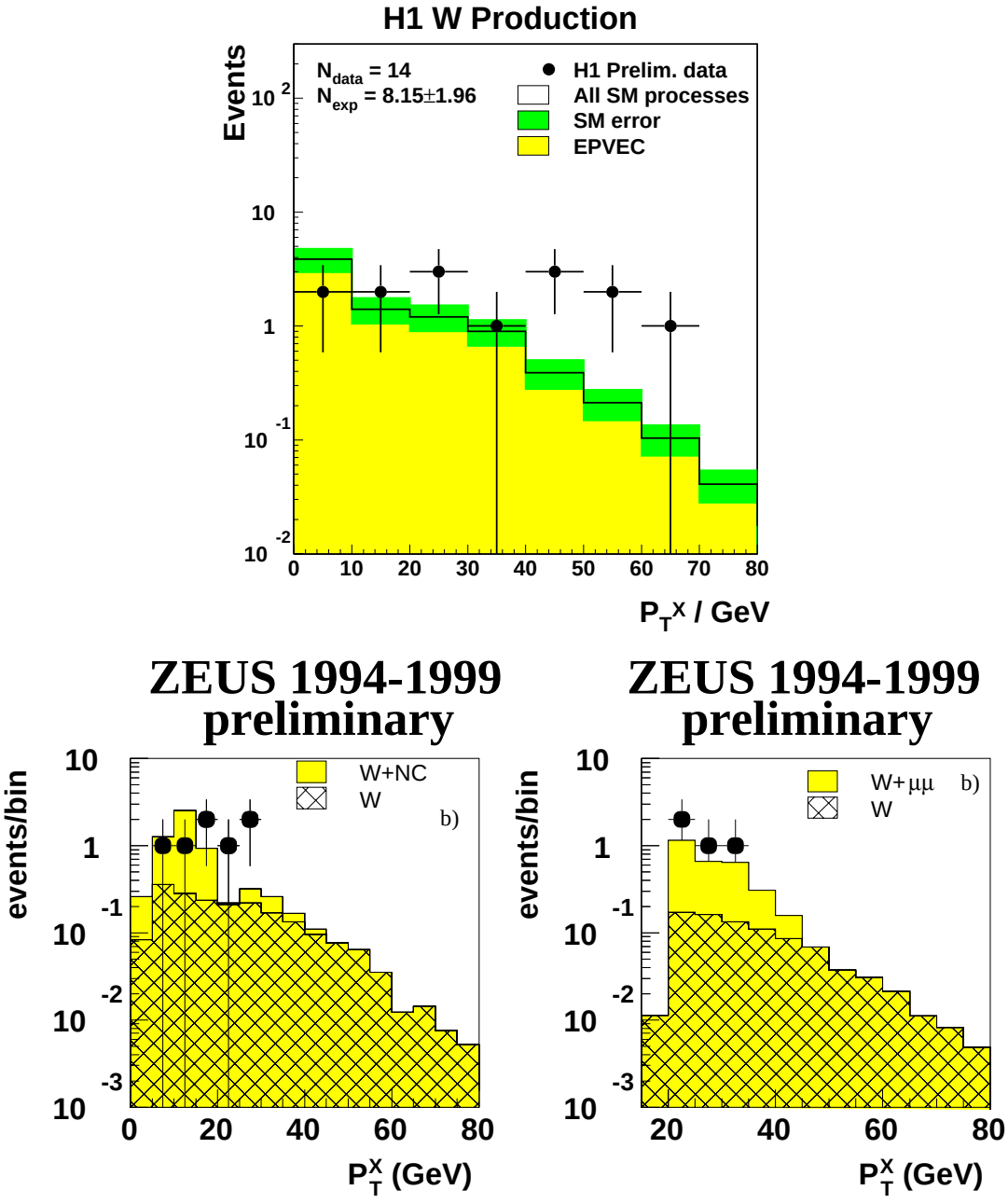

Fig. 9. Distribution of the transverse momentum of the jets in isolated lepton events measured at H1 (top) and ZEUS (bottom, left: electron channel, right: muon channel) Collaboration. Full points show the data, full lines the prediction of the Standard Model.[8,9]

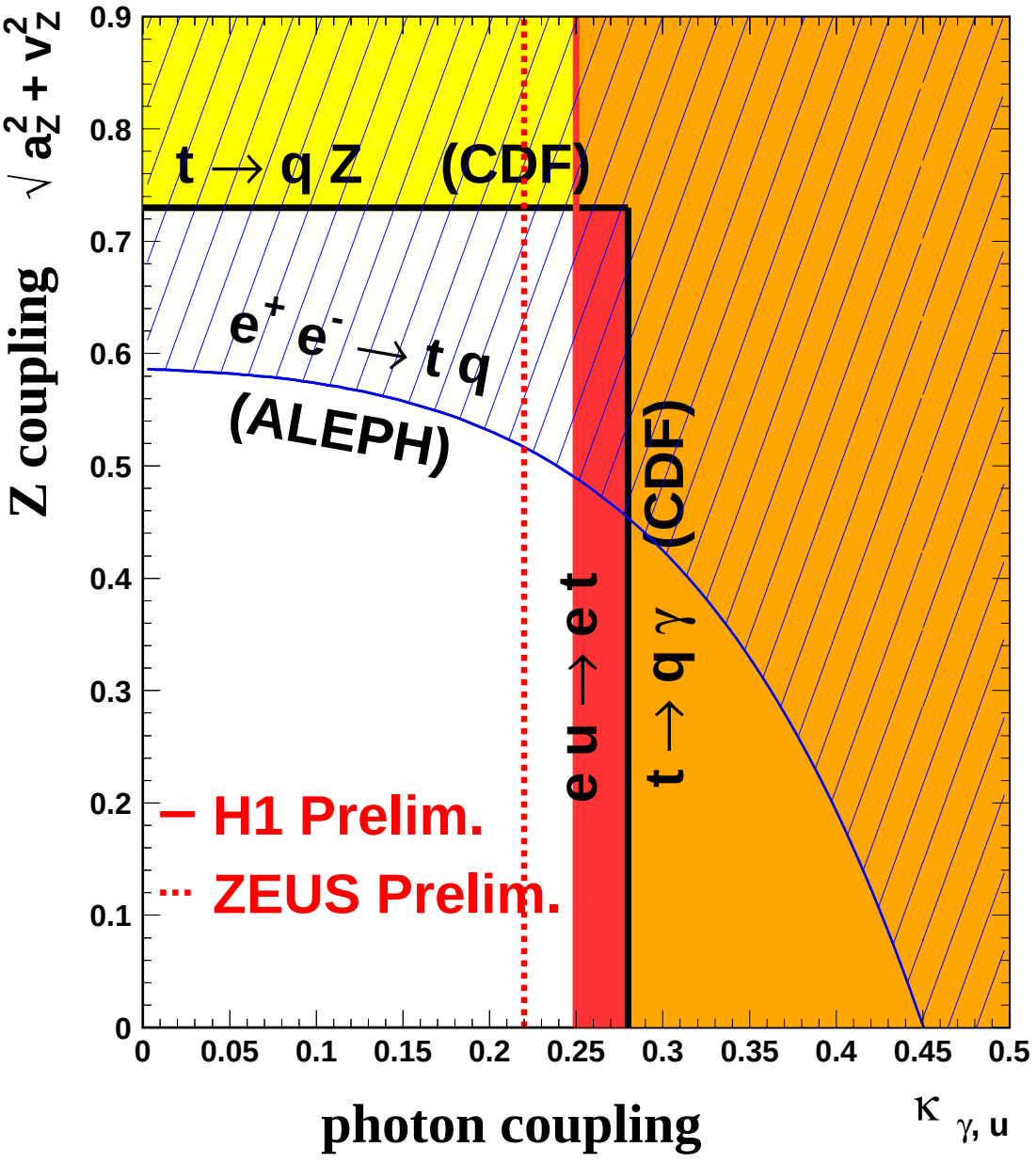

Fig. 10. Limits on the photon coupling for single top production as extracted from the H1 and ZEUS Collaborations. For comparison, the limits of the CDF and ALEPH Collaboration are shown.[9,11]

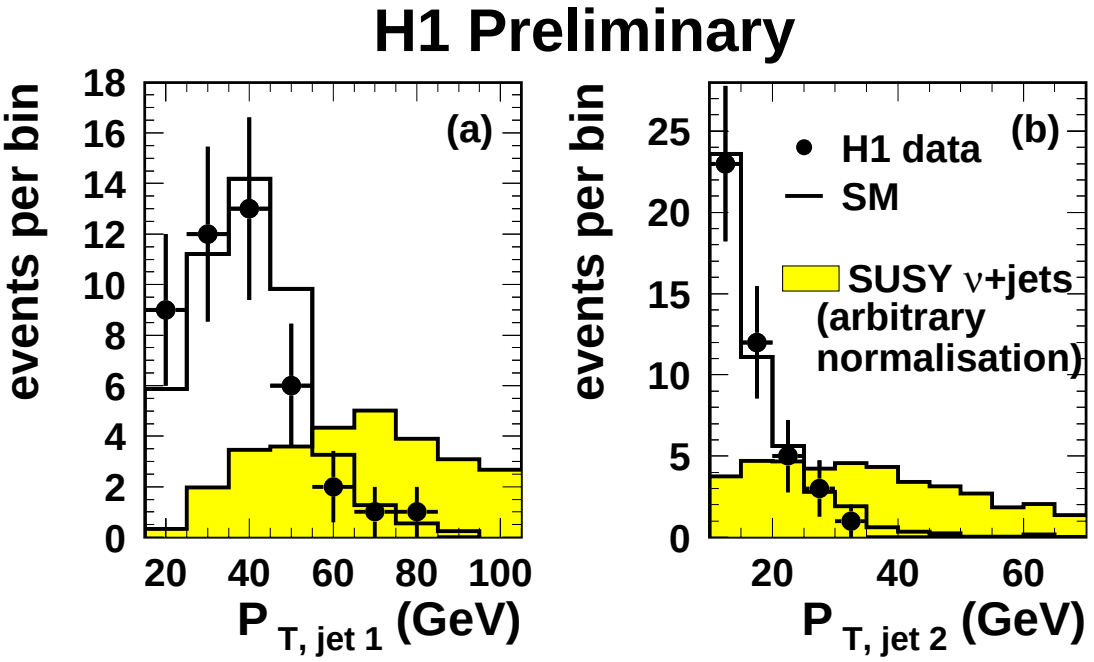

Fig. 11. Distribution of the transverse momentum of the jets in the neutrino plus multiple jet event sample. The full points show the data and the open histograms the expectation of the Standard Model. The filled histogram displays the contribution as calculated by a signal Monte Carlo.[13]

Model particles have an R parity of +1 while SUSY sparticles have -1. In R parity conserving theories, sparticles can only be produced together with their anti-sparticles. In R parity violating theories, sparticles can be produced e.g. at lepton quark vertices where the HERA ep collider has a unique detection potential.

Many decay channels for sparticles have been looked at. As an example, the transverse momentum distribution of the jets in the neutrino plus multiple jet channel is shown in figure 11.

The distributions for all channels are well described by the Standard Model and no excess is found. Therefore, limits on R parity violating couplings have been extracted, see figures 12 and 13. The limits are found to depend only weakly on the SUSY parameters μ and M_2 and are the best limits available.

Additional studies have been performed and limits on e.g. minimal super-gravity theories,[13] contact interactions, extra dimensions,[14] or excited fermions[15] have been extracted.

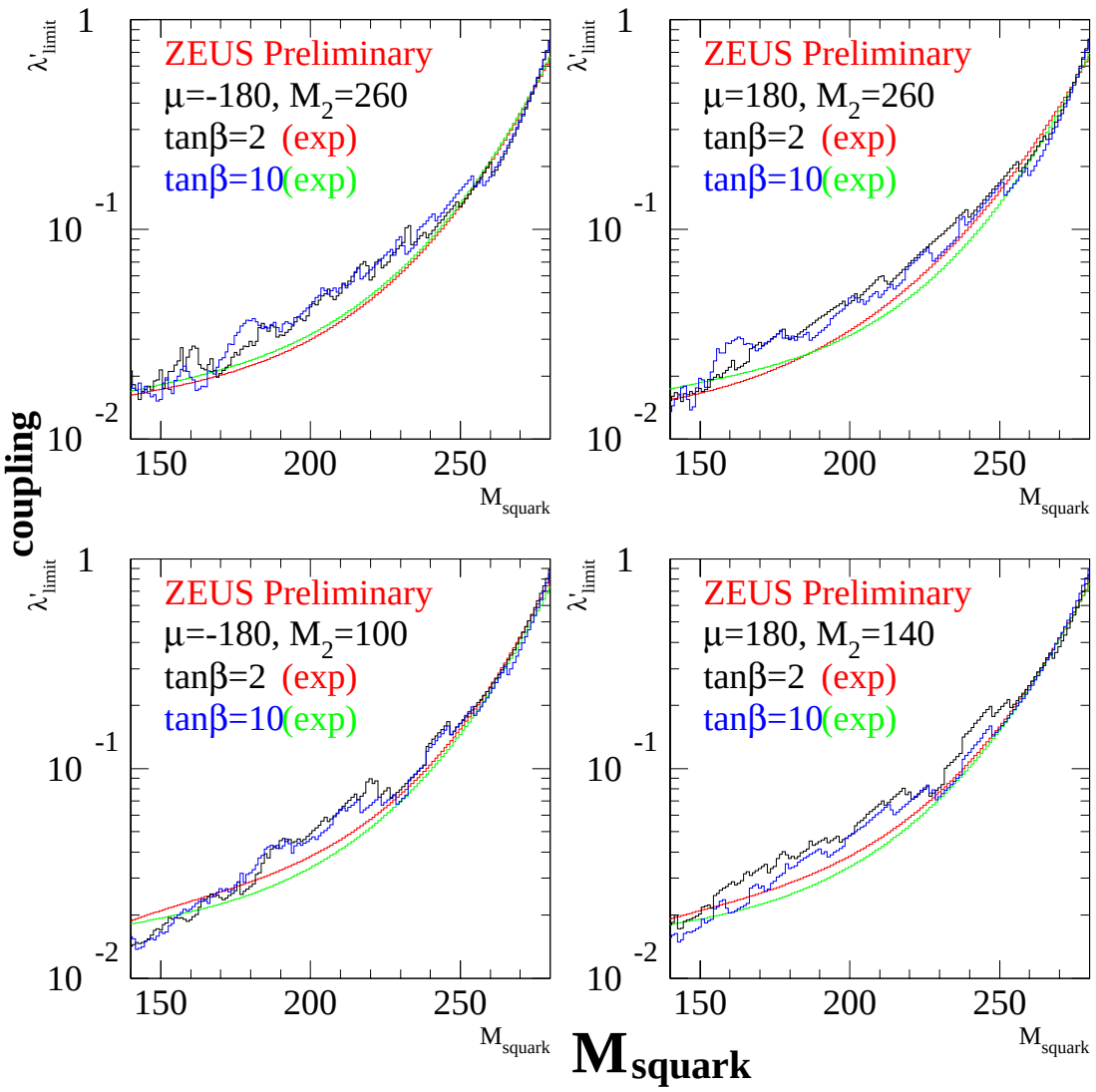

Fig. 12. 95% confidence limits for SUSY processes as extracted by the ZEUS Collaboration. The histograms show the limits for different combinations of the SUSY parameters μ and M_2.[12]

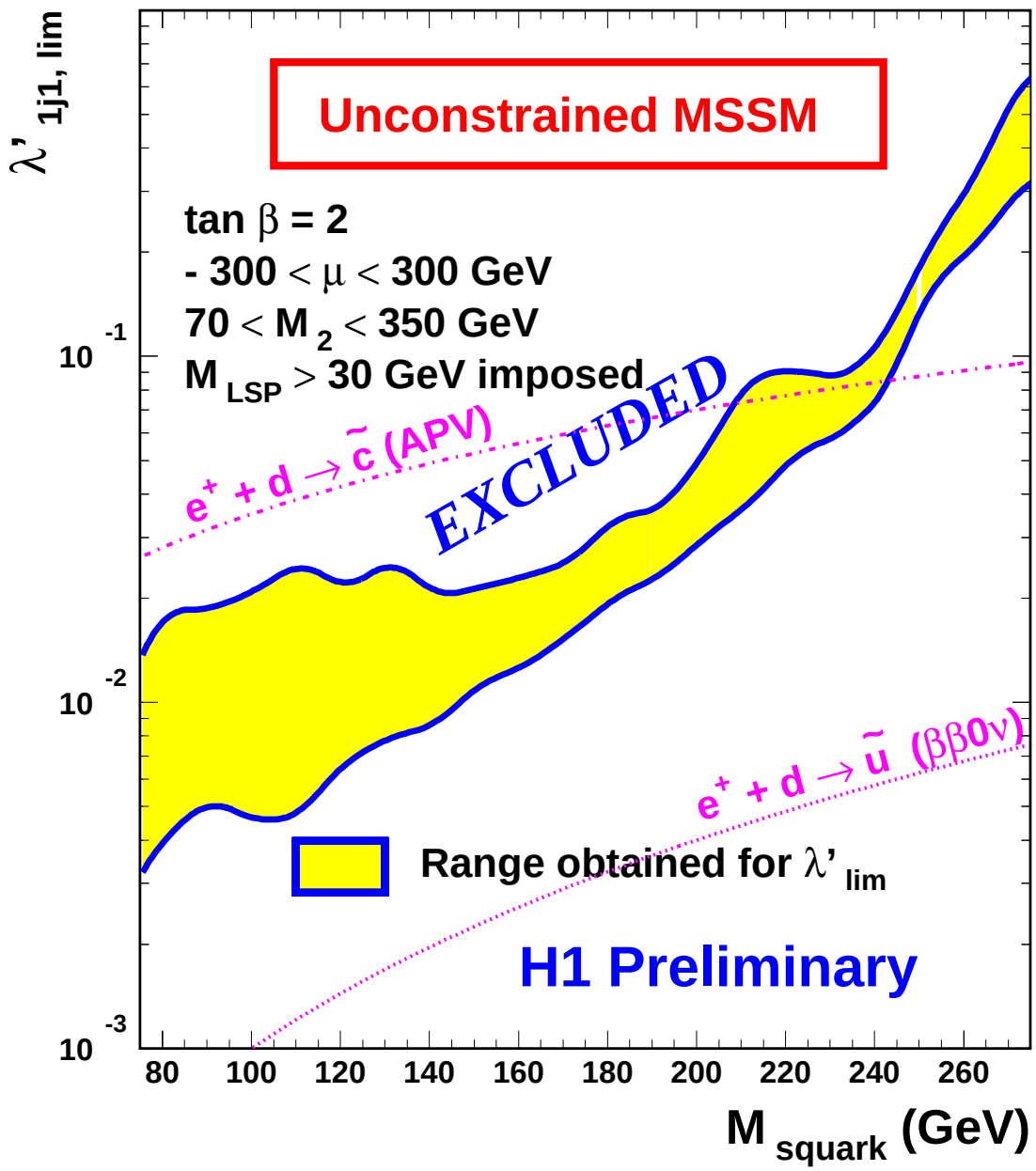

Fig. 13. Limits for SUSY processes as extracted by the H1 Collaboration. The shaded area shows the dependence on the SUSY parameters, the region above the area is excluded for all parameter combinations. For comparison, limits from the neutrinoless double beta decay and atomic parity violations are shown. These are valid for first and second, respectively, generation squarks only, while the H1 limit is valid for all generation of squarks.[13]

4 Summary

The collider experiments at the HERA storage ring have collected a large amount of ep data in the last eight years.

Studies of the proton structure at the H1 and ZEUS Collaborations have shown a remarkable agreement with the Standard Model. The neutral current as well as the charged current inclusive cross section allow the extraction of the proton structure and tests of QCD predictions. The influence of weak contributions is clearly seen.

The HERA ep collider also provides a unique testing ground for physics beyond the Standard Model. No signal was found in searches for leptoquarks, for single top production, and for R parity violating SUSY. Corresponding limits have been extracted and are in large regions of the parameter space the best limits available. The H1 Collaboration has seen an excess of events with an isolated lepton, large missing momentum, and a jet with large p_T^X. This excess is not confirmed by the ZEUS Collaboration. Whether these events are the first signals of physics beyond the Standard Model or a simple statistical fluctuation can only be decided after more data has been collected. The next data taking period will begin after a significant upgrade of both detectors and the storage ring, and startup is expected in the middle of next year.

References

[1] H1 Collaboration, Inclusive measurement of deep inelastic scattering at high Q^2 in positron-proton collisions at HERA, *contributed paper to ICHEP 2000, Osaka, Japan.*

[2] ZEUS Collaboration, J.Breitweg et al., *Eur. Phys. J.* C 12 (2000) 3, 411-428.

[3] H1 Collaboration, Measurement of neutral and charged current cross-sections in electron-proton collisions at high Q^2 at HERA, *contributed paper to ICHEP 2000, Osaka, Japan.*

[4] ZEUS Collaboration, Measurement of high Q^2 neutral-current $e^{\pm}p$ deep inelastic scattering cross sections and a first measurement of the structure function xF_3 at HERA, *contributed paper to ICHEP 2000, Osaka, Japan.*

[5] J. Engelen. QCD at HERA, *talk presented at SSI2000, 14 - 25 August 2000, Stanford, CA, USA.*

[6] ZEUS Collaboration, Resonance search in $e+$jet at HERA, *contributed paper to ICHEP 2000, Osaka, Japan.*

[7] H1 Collaboration, Search for leptoquarks in ep collisions at HERA, *contributed paper to ICHEP 2000, Osaka, Japan.*

[8] H1 Collaboration, W production in ep collisions at HERA, *contributed paper to ICHEP 2000, Osaka, Japan.*

[9] ZEUS Collaboration, Search for events with isolated high-energy leptons and missing transverse momentum at HERA, *contributed paper to ICHEP 2000, Osaka, Japan.*

[10] A. Mehta for the H1 and ZEUS Collaboration, Leptoquarks and flavour violation at HERA, *talk presented at ICHEP 2000, Osaka, Japan.*

[11] H1 Collaboration, Search for single top production in ep collisions at HERA, *contributed paper to ICHEP 2000, Osaka, Japan.*

[12] ZEUS Collaboration, Search for squark production in R-parity-violating interactions at HERA, *contributed paper to ICHEP 2000, Osaka, Japan.*

[13] H1 Collaboration, A search for squarks of R-parity violating SUSY at HERA, *contributed paper to ICHEP 2000, Osaka, Japan.*

[14] ZEUS Collaboration; J.Breitweg et al., *Eur. Phys. J.* C 14 (2000) 2, 239-254;
H1 Collaboration, C. Adloff et al., *Phys. Lett.* B479 (2000) 358-370;
H1 Collaboration, Search for compositeness, leptoquarks and large extra dimensions in e^-q and e^+q contact interactions at HERA, *contributed paper to ICHEP 2000, Osaka, Japan.*

[15] H1 Collaboration, C. Adloff et al., accepted by *Eur. Phys. J.* C, July 2000 [hep-ex/0007035];
H1 Collaboration, A search for excited neutrinos in e^-p collisions at HERA, *contributed paper to ICHEP 2000, Osaka, Japan;*
ZEUS Collaboration, Search for excited fermions in ep collisions at HERA, *contributed paper to ICHEP 2000, Osaka, Japan.*

TOP QUARK STUDIES AND IMPLICATIONS FOR FINDING NEW PHYSICS AT THE TEVATRON

Raymond E. Hall*
Department of Physics
California State University, Fresno, CA 93710

Representing the DØ and CDF Collaborations

ABSTRACT

The top quark was discovered in 1995 by the CDF and DØ collaborations in $p\bar{p}$ collisions at the Tevatron collider, which delivers a center of mass energy of 1.8 TeV. Since then, each experiment has collected a total of roughly 100 top quark candidate events and from these limited statistics comes all experimental knowledge of top quark properties. With five separate measurements between these two experiments the top quark mass is now measured to $\delta\, m_t$ = 2.9%, the most precisely known of all the quark masses. Due to its curiously heavy mass there is hope that the top may be different in other ways that might point to new physics beyond the Standard Model. The Standard Model predicts many other properties of the top quark, including its production and decay, and these proceedings will survey the measurements made with the current data set to see if there is any hint of deviation from Standard Model expectations and hence discovery of new phenomena. The large mass of the top quark also allows CDF and DØ to make indirect measurements of intrinsic spin of a bare quark, and to verify the V-A coupling in its decay to a real W boson. We also look for evidence of predicted single top production and possible competing production processes such as charged Higgs production. Finally we look to the improvement to all these measurements that the upcoming Run II of the Tevatron promises.

1 Top Quark Search and Discovery

Within the current Standard Model, the building blocks of matter are the three generations of fermions. The search for top was ushered in by the discovery in 1977 of the bottom quark, first evidence of a third generation of quarks, seen in a fixed target experiment at Fermilab.[1] With little hint from the Standard Model (SM) on what the top quark mass should be, many years were spent increasing accelerator energies and simultaneously raising the lower limit on the top quark's mass. Finally by 1990, while sitting at the Z^0 resonance, the SLAC[2] and LEP[3] e^+e^- colliders had produced no top quarks among the decay of any Z Bosons. This set a lower limit on the mass of the top of $m_t > 46$ GeV/c^2 at a 95% confidence level, or larger than half the Z boson mass.

At the same time indirect evidence for the existence of the top quark was mounting. The most compelling evidence was the confirmation that the bottom quark has the weak isospin quantum number (I_3^b) of -1/2, exactly what the Standard Model requires for the bottom quark to be in a doublet with the top as its partner. This was determined from four complementary measurements: the forward-backward asymmetry[4] in $e^+e^- \to b\bar{b}$, the absence of flavor-changing neutral currents in bottom quark decays[5,6] , the absence of large tree level $B_d^0\bar{B}_d^0$ mixing[7,8] , and the Z^0 partial decay width into $b\bar{b}$ pairs.

In addition, there also became available many precision measurements of electroweak parameters in the SM. It turns out that the Standard Model provides many indirect constraints on m_t through measurements that are sensitive to box diagrams ($B_d^0\bar{B}_d^0$ mixing), or radiative corrections (to the *W* and *Z* boson masses) which include m_t in the one loop diagrams. By using data from LEP, SLC and νN scattering data, and an estimated range of Higgs mass (M_H), the LEP electroweak working group[9] found that SM assumptions on the above mention processes led to a fitted top quark mass of

$$m_t = 178^{+11}_{-11}(stat)^{+18}_{-19}(syst) \text{ GeV/c}^2. \quad (1)$$

The search then shifted to the more powerful $p\bar{p}$ machines, most importantly the Tevatron $p\bar{p}$ Collider at Fermilab with a center of mass energy of 1.8 TeV, which today still has the highest available collision energy. With the above experimental and theoretical lower limits on m_t , the search signal had become well defined. With the top mass greater than that of the W Boson, pair production would dominate, and its subsequent decays would produce very energetic daughters. In fact with m_t in this range the standard model decay of the top is to a bottom quark and a real W boson. The topology of the event then is determined by the subsequent decay of these two W bosons. The

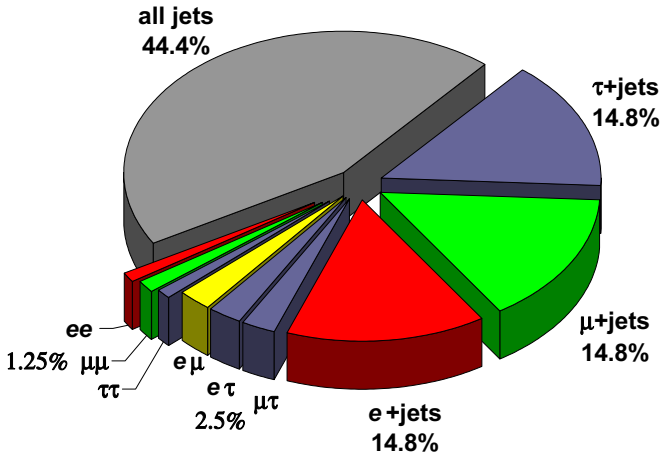

Fig. 1. Branching fraction of a $t\bar{t}$ pair to various final state signatures

decay branching fractions of the W boson are well measured, so with a little algebra we can determine how often a $t\bar{t}$ decay will feature an isolated high p_T lepton in the final state. Figure 1 summarizes the signature decay channels of top pairs which are named according to the daughter leptons from the W boson decays involved. The $dilepton$ channels are those where both W bosons decay to leptons; ee, $\mu\mu$, and $\tau\tau$ are each 1.25% of all $t\bar{t}$ decays, and $e\mu$, $e\tau$ and $\mu\tau$ each comprise 2.5% of all $t\bar{t}$ decays. The $lepton + jets$ channels (one W boson decays to $e\nu$, $\mu\nu$, or $\tau\nu$, and the other to a two jet final state) each make up 14.8% of all $t\bar{t}$ decays. The remaining 44.4% of $t\bar{t}$ decays are from the *all-jets* channel, where both W bosons decay to two-jet final states.

The top quark was finally discovered simultaneously by the CDF[10] and DØ[11] collaborations in 1995 based on a data sample of roughly 60 pb^{-1} for each experiment. The top turned out to be very heavy indeed, and even with collisions at 1.8 TeV the production of top pairs was a very rare process, and to find it entailed a sum of search analyses over all the possible decay signatures.

2 The CDF and DØ Detectors: How to catch a top quark

The daughter W bosons from top decays can result in either high transverse momentum (p_T) leptons or quarks. The daughter b-quarks form jets of hadrons and are also high in p_T. The search for top then entails the detection of the decay of these daughter W bosons and b-quarks.

The detection of W bosons daughters focuses on the leptonic decays $W \to e\nu$ and $W \to \mu\nu$, and to a lesser extent $W \to \tau\nu$ due to difficulties in reconstruction of the τ. The DØ[12] and CDF[13] detectors both have central charged particle tracking detectors and finely segmented sampling calorimeters to detect and measure high p_T electrons. Both detectors are surrounded by proportional drift tube chambers to capture high p_T muons. Both experiments detect the presence of neutrinos through the imbalance of energy in the detector (through assumption of momentum conservation in the plane transverse to the beam), a technique that relies on full coverage and hermetic calorimeters and muon detectors. Decays of W bosons to quarks are also detected with the sampling calorimeter.

The b-quarks are identified by two methods. The first method of 'tagging' the b-quark is based on detection of low p_T muons. Based on the semileptonic branching fractions, approximately 18% of all b-quarks will produce a muon in the final state. Thus a b-quark decay will result in a hadron jet measured in the calorimeter with a low p_T muon coming out the back, a configuration which is detectable with high efficiency. This method is used by both experiments.

The second method is to take advantage of the 1.6 ps lifetime and high p_T of the b-quark. The decay vertex of a b-quark will be displaced by about 0.5 cm from the primary collision vertex. A precise charged particle tracker, such as the CDF silicon based SVX,[14] can locate these displaced vertices and thereby identify the b-quarks.

3 Initial Measurements: Pair Production Cross Section and Mass

3.1 Counting experiments

To discover the top quark we must detect events that fit the $t\bar{t}$ pair decay hypothesis. A complication is that there are of course background processes that can mimic the event characteristics (collectively referred to as the topology of the event) of $t\bar{t}$ decays. The dilepton channels have the least competing background processes, which somewhat compensates for their small branching fraction. The $e\mu$ channel is referred to as the 'golden channel' as the main background is primarily W boson pair production with associated jets, a process with a cross section smaller than that of $t\bar{t}$ production. The dilepton channels ee and $\mu\mu$ have the additional background of Z boson plus associated

jets production. Fortunately this background can be severely reduced by cutting out events where the invariant mass of the lepton pair is near the mass of the Z boson.

Table 1. Number of $t\bar{t}$ candidate events observed and background events expected in the absence of $t\bar{t}$ production.

experiment	DØ		CDF	
dilepton channel	$ee, e\mu, \mu\mu$		$ee, e\mu, \mu\mu$	$e\tau, \mu\tau$
number of events	9		9	4
background	2.6 ± 0.6		2.4 ± 0.5	2.0 ± 0.4
lepton+jets channel	topological	muon b-tag	vertex tag	muon b-tag
number of events	19	11	29	25^a
background	8.7 ± 1.7	2.4 ± 0.5	8.0 ± 1.0	13.2 ± 1.2
all jets channel				
number of events	41		187	
background	24 ± 2.4		151 ± 10	

[a] some events are in both the CDF vertex tag and muon b-tag event sets

The lepton+jets channel is the second best in terms of signal to background, and the higher branching fraction gives better statistics. It is also important to find this channel because, as detailed in the next section, the presence of only one neutrino allows the mass of the two top quarks to be reconstructed with a 2C fit. The primary backgrounds to the lepton+jets channel is the production of W bosons with associated jets and to a lesser extent QCD multijet production where one jet is misidentified as an electron. Although it is rare for a W boson be produced with four jets (as in the $t\bar{t}$ decay) the cross section for W bosons to be produced with this much p_T is greater than the cross section of $t\bar{t}$ production. Figure 2 show a histogram of the W + jets background events as a function of number of jets above 15 GeV for roughly 80 pb^{-1} of data.

Three methods have been developed to separate the $t\bar{t}$ from these backgrounds. The topological analysis selection developed by DØ takes advantage of the fact that a $t\bar{t}$ pair is predominantly produced near rest and that the decay of two such massive bodies produces a spray of particles which is, on average, quite uniformly spherical in distribution. Two variables which can separate signal from background are H_T (defined as the scalar sum of all the jet transverse energies) which is said to be analogous to the 'temperature' of the event, and aplanarity, $\mathcal{A}$, which is the lowest term of the momentum

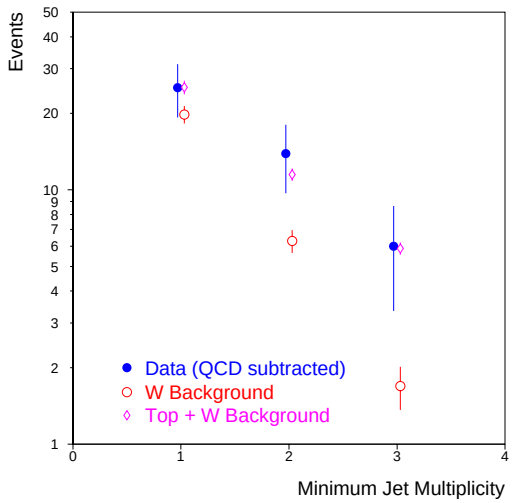

Fig. 2. Number of muon tagged μ + jets events as a function of inclusive number of jets in the event with $E_T > 15$ GeV. The excess due to $t\bar{t}$ production over the W + jets background is seen clearly for the events with three or more jets.

tensor and depicts how spherically symmetric the event products are distributed. The other two methods depend on the identification of b-quarks through the tagging methods describe earlier. Both CDF and DØ use soft muon b-tagging and CDF uses the very elegant technique of vertex b-tagging utilizing their silicon based particle tracker the SVX.

The analyses to detect decay channels that involve taus are more complex and utilize the precision charged particle tracking of CDF.[15] Due to the complexity and inefficiency of identifying taus the signal to background is inferior to the above-mentioned channels.[18] Finally there is the all-jets channel, the six jet final state, where the overwhelming background is QCD multijet production. The discrimination of $t\bar{t}$ events from this background is accomplished on larger statistical samples using a combination of the b-tagging techniques[20] and multivariate and/or neural net analyses.[19] Table 1 lists the number of events found in the DØ and CDF data along with the calculated expected backgrounds, broken down by the described decay channels.

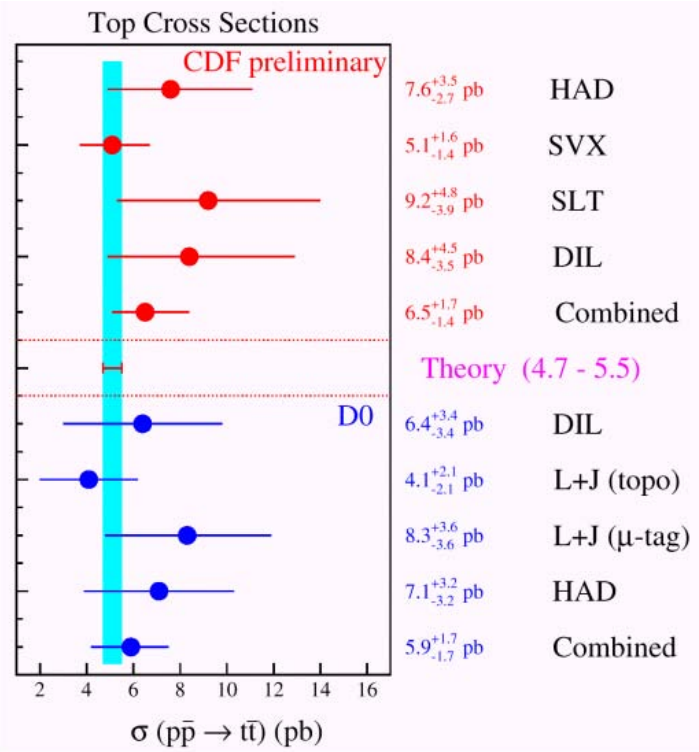

Fig. 3. Cross sections

3.2 Top Quark Pair Production Cross Section

A measurement of the $t\bar{t}$ cross section enables a test of QCD at the high mass scale associated with the top quark ($Q^2 \sim m_t^2$). The acceptances of the DØ and CDF detectors scale as a function of top quark mass since the distributions of lepton p_T and jet E_T spectra change as m_t increases. Thus the $t\bar{t}$ production cross section, $\sigma_{t\bar{t}}$, is determined as a function of m_t from the number of observed events in each of the decay channels. So for a given channel:

$$\sigma_{t\bar{t}} = \frac{N_{obs} - B}{A\mathcal{L}}$$

where N_{obs} is the number of observed events, B is the number of expected background events, A is the total acceptance$\times$efficiency, and $\mathcal{L}$ is the integrated luminosity.

The measured cross sections from the two experiments[16,17] are listed and plotted with relative errors in Figure 3. This figure also demonstrates the agreement of the separate analysis channels as listed in Table 1. Be cautioned that each experiment reports their cross section measurement for a different value of m_t (the respective measured value of each experiment) and thus a true comparison of central values is not possible

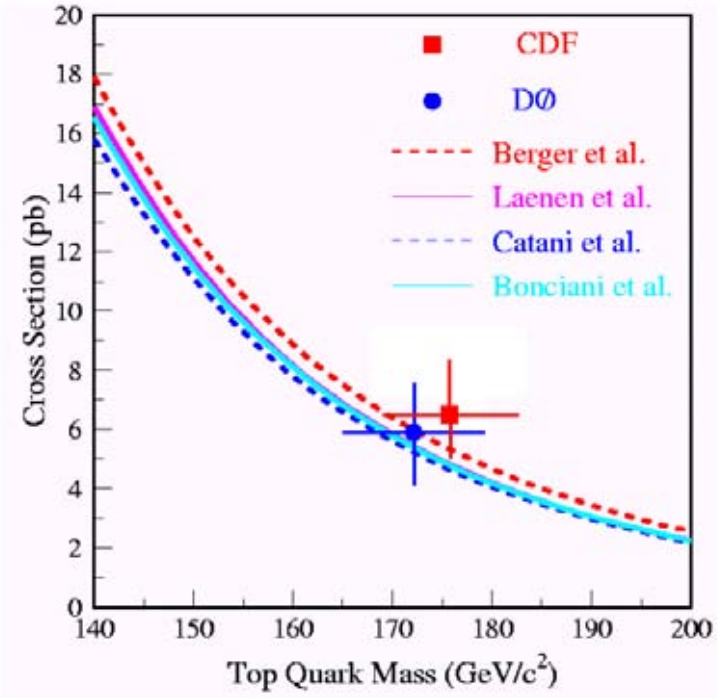

Fig. 4. Measured cross section ($\sigma_{t\bar{t}}$) for DØ and CDF (points with errors) and four theoretical NNLO calculations (lines).

with Figure 3. A true comparison of the measured cross sections is made on a plot of pair production cross section versus top mass as in Figure 4. Also shown are curves from four pertubative (NNLO) QCD calculations[21] to provide comparison to theoretical expectations (authors cited in figure).

3.3 Methods of top mass determination

Both experiments have made multiple measurements of the top quark mass through a variety of techniques and event data samples. The most straight forward of these is a two-constraint kinematic fit which reconstructs the top and antitop masses from the lepton+jet event samples.[22,23]

Eighteen quantities define the kinematics of the six particle final state of a $t\bar{t}$ decay, all of which can be measured with the exception of one; the momentum component of the neutrino along the beam axis. However, the fit can take advantage of three constraints: 1) the charged lepton and missing E_T are constrained to the mass of the W boson, 2) two jets are selected to constrain to the second W boson mass, and 3) each reconstructed W is paired with a remaining jet (which then represents the t and $\bar{t}$

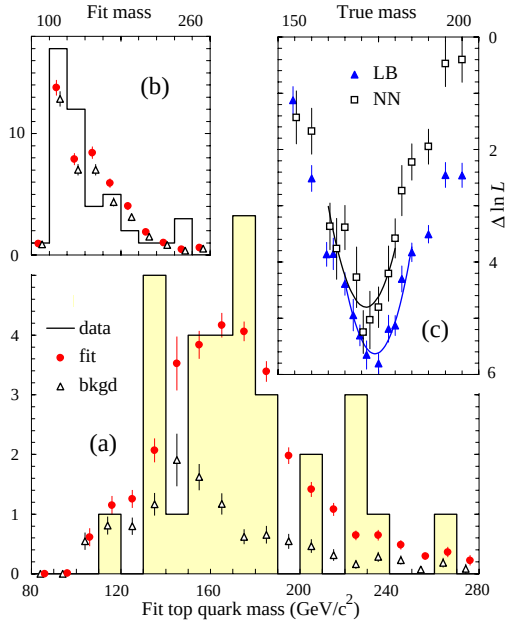

Fig. 5. The 2C, two-dimensional binned likelihood fit of the DØ lepton+jets events giving a top mass of 173.3±5.6 (stat) ±5.5 (sys) GeV/c^2

quark masses) and the final constraint is that these reconstructed t and $\bar{t}$ masses must be equal. Of course there are complications, such as extra jets from initial and final state radiation, and also without (with) b-tagging there is an up to 24 (12) fold ambiguity in the assignment of jets. The kinematic fit is performed for all permutations and the best permutations (based on χ^2) are used to specify the fitted top mass. A maximum likelihood fit to a spectrum of fitted mass values of background and signal predictions for a range of hypothesized top quark masses finally yields a measurement of m_t . The largest uncertainties are due to the jet energy scale calibrations on the Monte Carlo event generators. Figure 5 shows as a representative of this method the DØ lepton+jets mass fit result.

The second method for measuring the top quark mass is to perform a kinematic fit to the all-jets events. Here the final state is measured completely and allows a three constraint fit. However the backgrounds are very large and so far only CDF, through the use of SVX b-tags to control background, reports a measurement of m_t with these events. Here the largest errors are again from jet energy scale calibrations and background modeling.

Finally both experiments report measurements of m_t from dilepton events.[24,25] Here only the sum of the transverse momenta of the two neutrinos is measured, yet

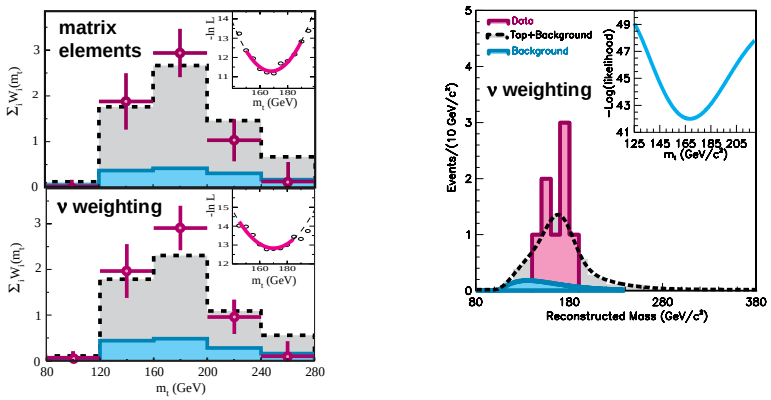

Fig. 6. Mass measurement results from the dilepton channel events for DØ (left, two methods) and CDF (right).

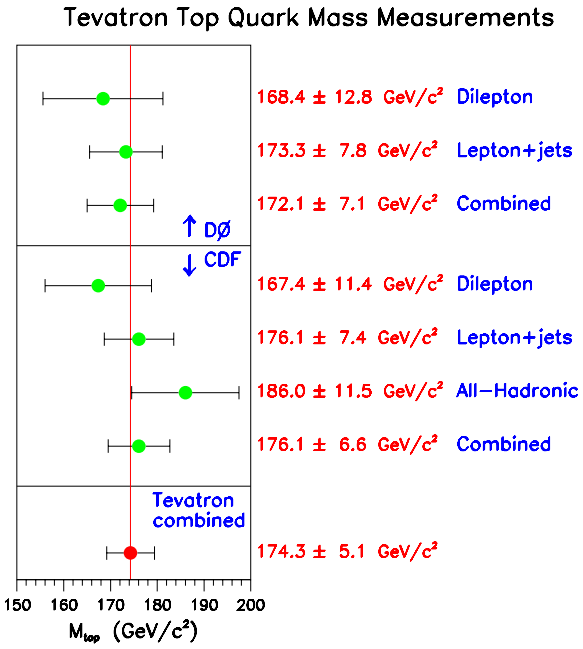

Fig. 7. Top mass measurements

there is extractable information about m_t within the event kinematics although these events are underconstrained and a kinematic fit as described above is not possible. In one analysis pioneered by DØ a dynamical likelihood method is employed where a weight function assigned to each events characterizes how likely it is that the event's kinematic variables would occur for a given range of top quark masses. These weight functions are then compared to Monte Carlo predictions to determine the most likely top mass. Figure 6 shows the results of this and another analysis from DØ and the similar analysis from CDF. With the present sample of dilepton channel events (six for DØ and eight for CDF) the statistical uncertainties are large. However this method has smaller systematic errors and will become competitive with the lepton+jets method in the Tevatron Run II despite the inherent differences in event statistics. Figure 7 summarizes and plots all five top quark mass measurements for both experiments. The results are all in good agreement within errors which further supports our claim that the signal that we see in the lepton+jets channel is indeed the same as the signal in the dilepton and all-jets channels and is that of $t\bar{t}$ decay.

3.4 The most precisely know quark mass: m_t

The CDF and DØ collaborations formed a working group to combine all the measurements of m_t to give a global Tevatron result. The systematic errors on the five mass measurements were each broken down into six components each with 22 subparts, and the correlations between the measurements were determined for each component separately. The final Tevatron Run I value of the top quark mass is: m_t = 174.3 $\pm$ 3.2 (stat) $\pm$4.0 (syst) GeV/c^2 = 174.3 $\pm$5.1 GeV/c^2. Figure 8 shows how the various measurements contribute to the central value. Most of the correlation is indirectly related to the jet multiplicity via the uncertainty on the jet energy scale calibration (the largest portion of systematic error for each).

The top quark now has the best measured mass of any quark with an uncertainty of only 2.9%. The top quark mass plays a major role in calculating predictions from the Standard Model via radiative corrections. It happens that the dominant radiative corrections to the W boson mass involve top quark and Higgs boson loops. Expressing the W boson mass as a tree-level value summed with a function of m_t and m_{Higgs}, we can constrain the mass of the Higgs boson within the framework of the Standard Model from precision measurements of m_t and m_W. Figure 9 shows the current best constraints on m_{Higgs} through a combination of the above value of m_t along with precision

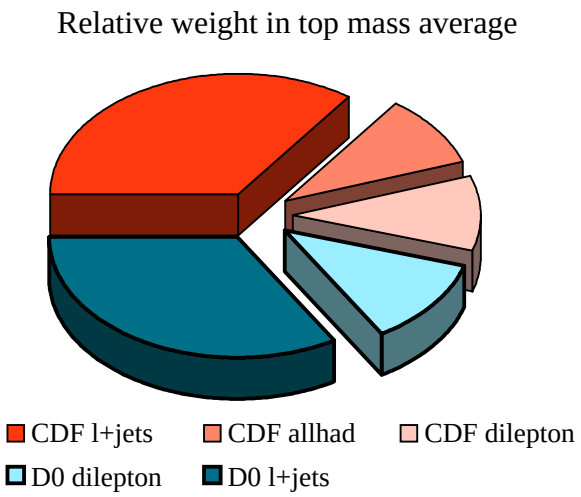

Fig. 8. The pie chart indicates the relative contribution of each measurement to the combined central value when correlations are taken into account.

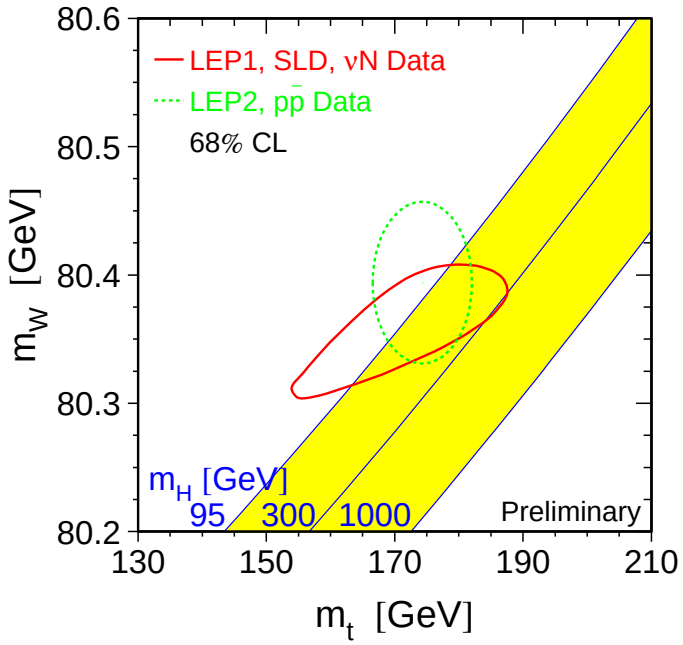

Fig. 9. Constraints on the Higgs mass in the m_W *vs.* m_t plane. The dotted ellipse is the 68% CL for Tevatron and LEP2 measurements.

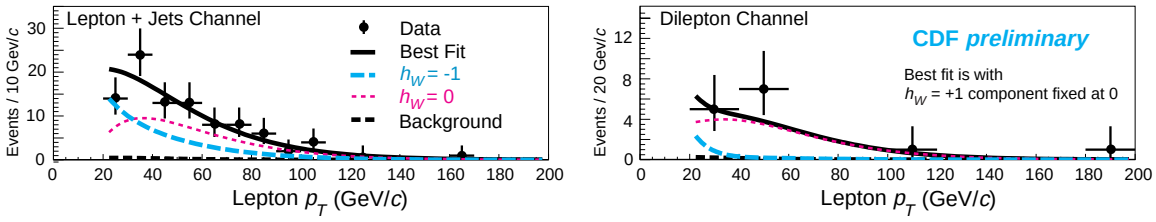

Fig. 10. Fits of W boson helicity fraction contributions to charged lepton p_T distribution in top quark decays.

measurements of electroweak parameters from around the globe.

4 Properties of $t\bar{t}$ Decay

We now turn our discussion to topics concerning the SM expectations of the decay of $t\bar{t}$ pairs. First is a description of an initial measurement of the helicity of the W in $t\bar{t}$ final states by CDF, and second we will examine a DØ analysis of spin correlations in $t\bar{t}$ decays.

4.1 Top Decay and Helicity of W Boson

As mentioned, a consequence of the top quark's extraordinarily heavy mass is that its primary decay channel is to a real W boson. Due to the V-A couplings in the electroweak sector of the SM, top can only decay to a longitudinally polarized (helicity $h_W = 0$) or left-handed ($h_W = -1$) W boson, and not to a right-handed helicity state. This well known phenomena of lepton decays has never been verified for the vector bosons themselves, until now. To leading order the decay ratio is:

$$\frac{B(t \to bW_{long})}{B(t \to bW_{left})} = \frac{1}{2}(\frac{m_t}{m_W})^2 = \frac{0.70}{0.30} = \frac{f_{long}}{f_{left}}$$

A study by the CDF collaboration uses the fact that the direction of the lepton from the W boson decay is correlated to the W boson's helicity state.[26] In the CDF analyses, a fit of the lepton p_T spectra for W decays in $t\bar{t}$ events, in both the lepton and dilepton channels, yields $f_{long} = 0.97 \pm 0.37 \pm 0.13$ (statistical and systematic uncertainties, respectively), in full agreement with the SM assuming the hypothesis of no right handed decays. The fits to lepton and dilepton top events are shown in Figure 10.

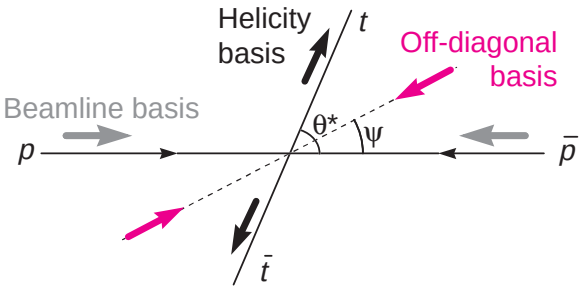

Fig. 11. Diagram of the off-diagonal basis, defined by the angle ψ relative to the beamline and the helicity basis (defined by θ_*).

4.2 W polarization and Top Pair Spin Correlation

In the Standard Model the spins of pair produced top quarks are correlated. Remarkably, the top quark lifetime ($\sim 4 \times 10^{-25}$ sec) is much shorter than the time required to hadronize, allowing information about top quark spin to be transmitted to their decay products. In this way the top's heavy mass allows a window to the spin of a bare quark!

For a polarized top quark, the angular distribution of the decay products in the top rest frame is given by:

$$\frac{1}{\Gamma}\frac{d\Gamma}{d\cos\theta} = \frac{(1+\alpha\cos\theta)}{2}$$

where $\alpha = 1$ for the charged lepton or d quark from the W decay, and $|\alpha| \leq 0.41$ for the other decay products (W, ν, b or the up quark). Unfortunately reconstructing down quarks from W boson decay is beyond current experimental analysis, so charged leptons offer the best means for extracting values of α. In addition, at the Tevatron top quarks are not polarized individually, and thus α cannot be measured in individual top decay. However, α can be determined from the correlated distribution in the decay angles θ_+ and θ_- of the t and $\bar{t}$:

$$\frac{1}{\sigma}\frac{d\sigma}{d\cos\theta_+ d\cos\theta_-} = \frac{1-\kappa\alpha_+\alpha_-\cos\theta_-\cos\theta_+}{4}$$

The value of κ depends on the axis of quantization chosen for the analysis of the decays. Note that the standard axes of the incident beam ('Gottfried-Jackson' frame) or the lines of flight of the top quarks ('helicity' frames) are not the ones preferred here. Instead Mahlon and Parke[27] have found that there is an optimal axis, or "off diagonal" basis, as defined by the transformation:

$$\tan\psi = \frac{\beta^{*2}\sin\theta^*\cos\theta^*}{1-\beta^{*2}\sin^2\theta^*}$$

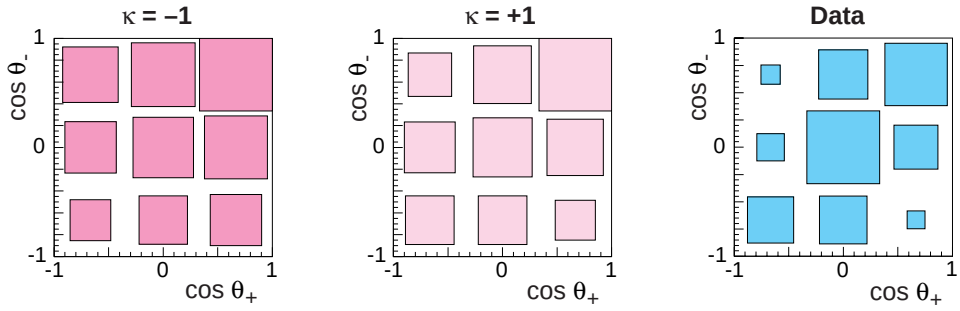

Fig. 12. Distributions for when the spins of the t and $\bar{t}$ are 100% anticorrelated, 100% correlated, and for data.

where ψ and θ^* are, respectively, the angle of the optimal axis and the angle for the line of flight of the top quarks, defined relative to the incident direction of the $\bar{p}$ in the parton-parton rest frame, and β^* refers to the velocity of the top quarks in that frame. In the off diagonal basis, the impact from opposite spin orientations of the top quarks (e.g., from gluon-gluon production) vanish to leading order in α_{strong}, providing an expected value of $\kappa \sim 0.9$. To measure the decay angles requires the full kinematic reconstruction of $t\bar{t}$ events. Unfortunately, dilepton events are kinematically underconstrained, and a special procedure was therefore developed at DØ[24] to handle the ambiguities and poor resolution brought about by the two missing neutrinos in these channels. Using the 6 dilepton $t\bar{t}$ candidates, the DØ analysis calculates all possible neutrino solutions, with smeared resolutions, and obtains a likelihood for each event permutation. These were summed for all events, and are shown in the density plot in Figure 12. A likelihood fit was then performed to signal (based on a spin-correlated $t\bar{t}$ Monte Carlo) and small sources of background, with κ as arbitrary parameter, which established that $\kappa > -0.25$ at 68% confidence.[28] This result is consistent with production through an intermediary gluon, where on the other hand a value of $\kappa \sim -1.0$ would correspond to an intermediary Higgs-like $J = 0$ boson.

5 Studies of Top Production

A priority in the search for new phenomena is to see if there are any competing or anomalous production contributions to our $t\bar{t}$ event samples. We present four analyses in this vein, including a search for single top production through electroweak processes, in which $t\bar{t}$ production is itself a major background! The topics covered in this next

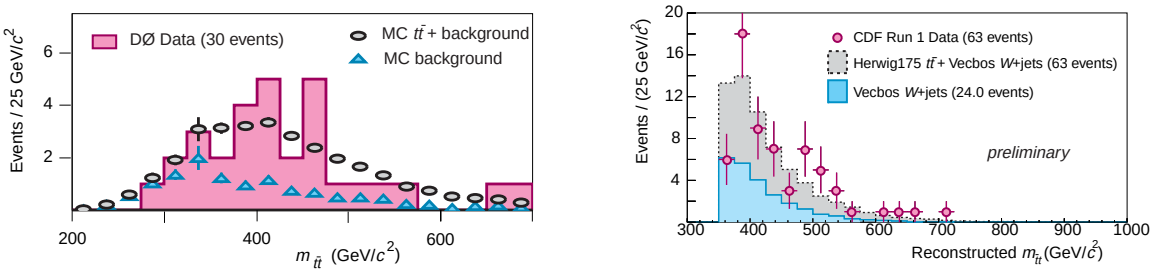

Fig. 13. Invariant mass distributions of the $t\bar{t}$ system for DØ (left) and CDF (right).

section are:

- Anomalous contributions to $t\bar{t}$ production from possible $m_{t\bar{t}}$ resonances
- Anomalous $t\bar{t}$ production and contributions to the p_T spectra of top quarks.
- Electroweak production of single top.
- Charged Higgs search through top "disappearance".

5.1 Invariant $t\bar{t}$ Mass

While the top quark lifetime is too short to permit any onium states it is still very interesting to look for possible resonances in the mass of the $t\bar{t}$ pair ($m_{t\bar{t}}$). Figure 13 contains invariant $m_{t\bar{t}}$ spectra for DØ and CDF lepton+jet events. The spectrum from the DØ events uses a 2C fit to the same events used in the mass fit. To the right of this plot is the spectrum from CDF events with an additional constraint that the top mass m_t = 175 GeV/c^2. In addition CDF applies a cut on the fit χ^2 as well as selection criteria to optimize sensitivity to new physics by reducing combinatoric backgrounds from wrong jet combinations. Neither experiment sees any significant excess with these statistics.

5.2 Transverse Momentum of Top Quarks in $t\bar{t}$ Production

Anomalous $t\bar{t}$ production through a high mass intermediate particle could also show up in the p_T spectrum of the top quark. Some extended Technicolor models predict an enhancement of the SM at high p_T . Using the measured value of m_t and event fitting techniques developed for the mass measurement, a 3C fit can be made for the p_T of the each top in lepton+jets events. CDF[30] has performed such a study and the results are shown in Figure 14 with the top quark p_T in four 75 GeV wide bins. These models predict an excess in bin 4, and the data is in excellent agreement with the SM within current statistics.

Top Quark Differential Cross Section

$$R_1 + R_2 = 0.72^{+0.13}_{-0.13}(\text{stat})^{+0.06}_{-0.06}(\text{syst})$$
$$R_4 < 0.114 \text{ at } 95\% \text{ C.L.}$$

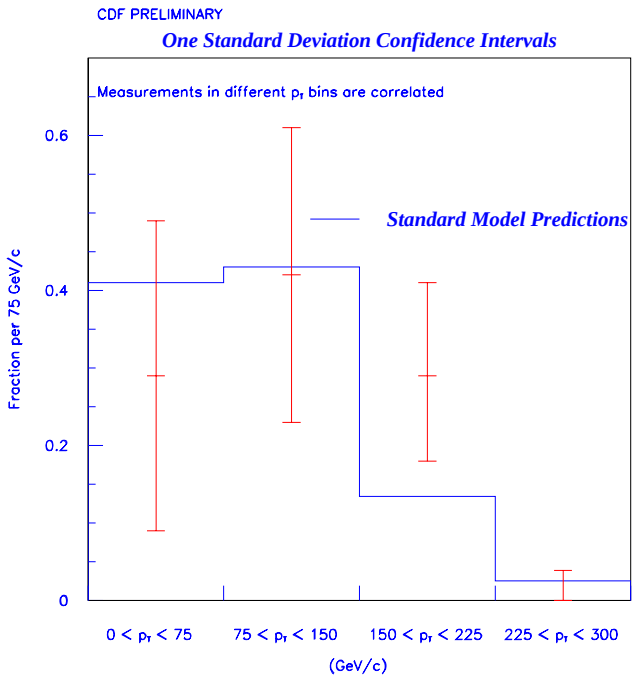

p_T Bin	Measured Fraction of Top Quarks
$0 < p_T < 75$ GeV/c	$R_1 = 0.29^{+0.18}_{-0.18}(\text{stat})^{+0.08}_{-0.08}(\text{syst})$
$75 < p_T < 150$ GeV/c	$R_2 = 0.42^{+0.18}_{-0.18}(\text{stat})^{+0.05}_{-0.07}(\text{syst})$
$150 < p_T < 225$ GeV/c	$R_3 = 0.29^{+0.12}_{-0.10}(\text{stat})^{+0.06}_{-0.05}(\text{syst})$
$225 < p_T < 300$ GeV/c	$R_4 = 0.000^{+0.035}_{-0.000}(\text{stat})^{+0.019}_{-0.000}(\text{syst})$

Fig. 14. The p_T distribution of top quarks in $t\bar{t}$ events from CDF. R_n is the fraction of events in p_T bin n.

5.3 Electroweak Production of Single Top

At the Tevatron, top quarks can also be produced singly via the electroweak interaction.[31] The electroweak production of top is predominantly through two processes involving off shell W boson exchange and the SM cross section for each is about 1pb. The tree level Feynman diagrams for the two most important processes are shown in Figure 15. CDF has performed a search for single top in 109 pb^{-1} of data. The search strategy is to look for events with an isolated high p_T electron or muon and associated significant missing E_T of a neutrino from the W decay, and exactly two jets, with one or both jets tagged as a b-quark using the displaced vertex method of b-tagging. In addition, the reconstructed invariant top quark mass must fall within $145 < m_T < 205$ GeV.

The signal from single top production is more challenging to separate from the major background of W + jets events than the signal from $t\bar{t}$ production. In fact $t\bar{t}$ production is a major background to this process. Higher background rates together with a smaller cross section prevents detection of this process with current statistics. However, CDF does set upper limits on the cross sections for these two processes. Figure 16 contains distributions of modeled background, sum of signal and background, and data, for the reconstructed top mass (for s-channel analysis) and for the quantity 'lepton charge $\times$ untagged jet pseudorapidity'(for the t-channel analysis). This second quantity takes advantage of decay kinematics in that the light quark tends to be emitted along the direction of the top quark. From likelihood fits to these distributions the following upper limits are reported by CDF[32]:

$$\sigma(p\bar{p} \to t\bar{b}, \bar{t}b) < 15.8 \text{ pb at 95\% C.L.}$$

$$\sigma(p\bar{p} \to tq\bar{b}, \bar{t}\bar{q}b) < 15.4 \text{ pb at 95\% C.L.}$$

5.4 Charged Higgs Search Through Top "Disappearance"

In supersymmetric extensions of the Standard Model the top quark has another decay option, $t \to H^+b$, in addition to the standard decay $t \to Wb$. This is allowed in the two Higgs doublet models, the phenomenology of which is characterized by two parameters: the mass of the charged Higgs boson, m_{H^+}, and the ratio of the vacuum expectation values of the two Higgs doublets, $\tan\beta$. The model predicts that when $\tan\beta$ is larger or smaller than $\tan\beta = \sqrt{m_t/m_b} \sim 6$ the decay to the charged Higgs

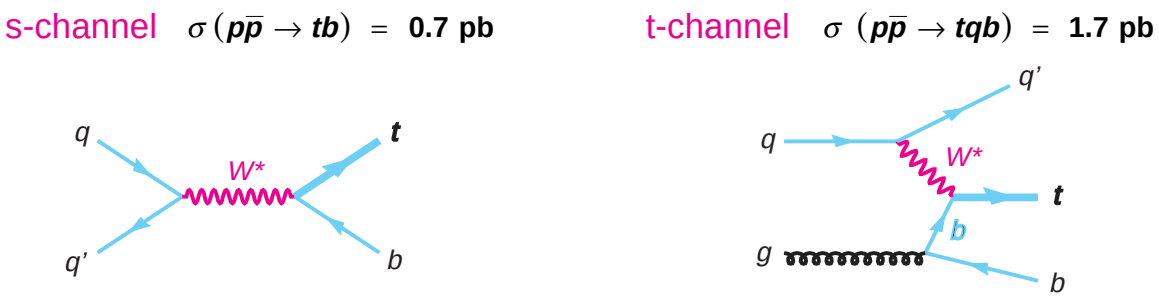

Fig. 15. Leading order Feynman diagrams for W^* single top production and W-gluon fusion at the Tevatron.

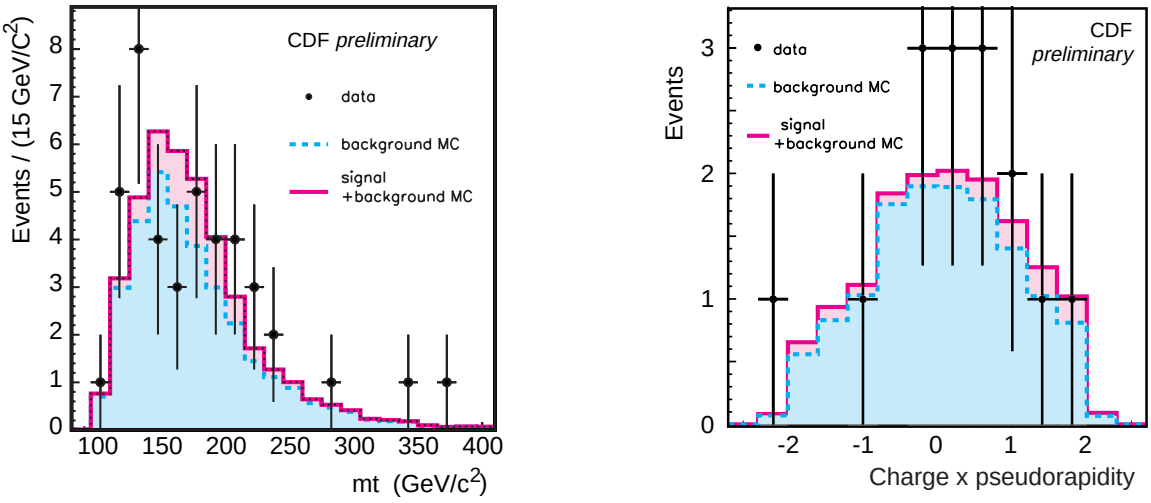

Fig. 16. The left plot is the reconstructed top mass distribution for s-channel single top production, and the right plot is the lepton charge $\times$ untagged jet pseudorapidity for t-channel single top production.

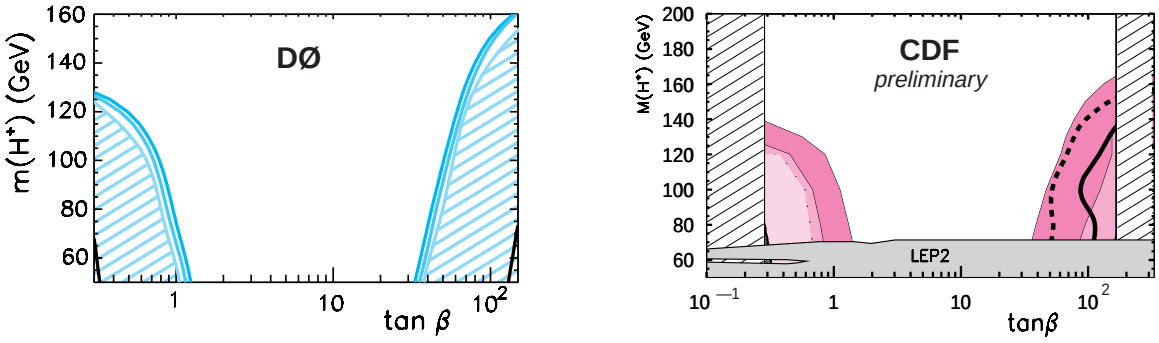

Fig. 17. Exclusion regions in the ($\tan\beta$, m_{H^+}) plane.

will dominate. At very large $\tan\beta$ the charged Higgs will decay predominantly to tau leptons ($H^+ \to \tau\nu$), and for small $\tan\beta$ the charged Higgs will decay mostly through hadronic channels ($H^+ \to c\bar{s}$ or $H^+ \to t^*\bar{b} \to Wb\bar{b}$, depending on m_{H^+}).

Both CDF[33] and DØ[34] have performed what we have termed 'disappearance' analyses in which we determine how much phase space is left for decays after all reconstructed $t \to Wb$ decays are taken into account. Here the inherent inefficiencies of our detectors for finding $t \to \tau\nu$ and $t \to c\bar{s}$ is turned to an advantage; similar decays from H^+ would also be invisible but would impact the number of top events expected by the SM in our most efficient channels. Figure 17 shows results of searches for such deficits relative to SM expectations, expressed as a limits in $\tan\beta$, m_{H^+} parameter space. The hatched regions in the DØ plot and the solid regions in the CDF plot are excluded at the 95% confidence level. The three lines at the limiting boundary of the DØ plot are for different values of the $t\bar{t}$ cross section, 5.5, 5.0 and 4.5 pb. The tightest limit on the CDF plot corresponds to 5.0 pb, and the next is 7.5 pb (close to the CDF measured value).

CDF has also performed direct searches for the top decay channel ($t \to \tau\nu$),[35] and can set direct limits on charged Higgs production at high $\tan\beta$. The solid and broken lines indicate limits set for cross sections of 5.0 and 7.5 pb. The CDF plot also indicates the $\tan\beta$ independent limit $m_{H^+} > 60$ GeV set by direct searches at LEP.

6 Conclusions

The first run of the Tevatron collider allowed the top quark to become the best measured of any of the known quarks, and we have had a successful first pass at developing the analyses to measure many properties of the top quark and its decay. Table 2 details some

of the current measurements and indicates projections for the Run II of the Tevatron based on the increased luminosity and improved detector capability. Overall the outlook for top physics at the Tevatron Run II is very bright.

Table 2. Projections for Tevatron Run II top measurements with 2 fb^{-1} of integrated luminosity.

		Precision	
Top Quark Property	Run I measurement	Run I	Run II
$\sigma_{t\bar{t}}$ (DØ)	$5.9^{+1.7}_{-1.7}$	25%	10%
$\sigma_{t\bar{t}}$ (CDF)	$6.5^{+1.7}_{-1.4}$		
m_t (DØ)	$172.1 \pm 5.2 \pm 4.9$ GeV/c^2		
m_t (CDF)	$176.1 \pm 4.2 \pm 3.1$ GeV/c^2	3.8%	1.7%
m_t (DØ + CDF)	$174.3 \pm 3.3 \pm 3.9$ GeV/c^2	2.9%	1.2%
W helicity F_{long}	$0.91 \pm 0.37 \pm 0.13$	0.4	0.09
$\sigma_{single-top}$	< 18.6 pb	-	20%
$\Gamma(t \to Wb)$	-	-	25%
$\|V_{tb}\|$	-	-	12%
BR($t \to \gamma q$) 95% CL	0.03	0.03	0.002
BR($t \to Z^0 q$) 95% CL	0.30	0.30	0.02

7 Acknowledgements

I wish to thank my colleagues on CDF and DØ for their many contributions that have provided the basis for this presentation. I am especially grateful to Ann Heinson (especially for the supply of some graphics), Tom Ferbel, Mark Kruse, John Conway, and Gordon Watts for their input and helpful comments. I thank both David Burke and Lance Dixon for the invitation and immense honor of participating in the SLAC Summer Institute 2000 and I express my appreciation to conference administrator Ellie Lwin for all her gracious help with my conference arrangements.

References

[1] S.W. Herb *et al.*, Phys. Rev. Lett. **39**, 253 (1977)

[2] G. S. Abrams *et al.*, Phys. Rev. Lett. **63**, 2447 (1989).

[3] D. Decamp *et al.* [ALEPH Collaboration], Phys. Lett. **B236**, 511 (1990). P. Abreu *et al.* [Delphi Collaboration], Phys. Lett. **B242**, 536 (1990). M. Z. Akrawy *et al.* [OPAL Collaboration], Phys. Lett. **B236**, 364 (1990). O. Adriani *et al.* [L3 Collaboration], Phys. Lett. **B313**, 326 (1993).

[4] R. Marshall, Z. Phys. **C43**, 607 (1989).

[5] V. Barger and S. Pakvasa, Phys. Lett. **B81**, 195 (1979). G. Eilam, A. Soni, G. L. Kane and N. G. Deshpande, Phys. Rev. Lett. **57**, 1106 (1986).

[6] A. Bean *et al.* [CLEO Collaboration], Phys. Rev. D **35**, 3533 (1987).

[7] D. P. Roy and S. Uma Sankar, Phys. Lett. **B243**, 296 (1990).

[8] H. Albrecht *et al.* [ARGUS Collaboration], Phys. Lett. **B324**, 249 (1994). J. Bartelt *et al.* [CLEO Collaboration], Phys. Rev. Lett. **71**, 1680 (1993).

[9] [ALEPH Collaboration], CERN-PPE-94-187 *Contributed to the 27th International Conference on High-Energy Physics - ICHEP 94, Glasgow, Scotland, UK, 20 - 27 Jul 1994*.

[10] F. Abe *et al.* [CDF Collaboration], Phys. Rev. Lett. **74**, 2626 (1995) [hep-ex/9503002].

[11] S. Abachi *et al.* [D0 Collaboration], Phys. Rev. Lett. **74**, 2632 (1995) [hep-ex/9503003].

[12] S. Abachi *et al.* [D0 Collaboration], Nucl. Instrum. Meth. **A338**, 185 (1994).

[13] F. Abe *et al.* [CDF Collaboration], Nucl. Instrum. Meth. **A271**, 387 (1988).

[14] D. Amidei *et al.* [CDF Collaboration], Nucl. Instrum. Meth. **A350**, 73 (1994).

[15] R. L. Wagner [CDF COLLABORATION Collaboration], Nucl. Instrum. Meth. **A265**, 1 (1988).

[16] S. Abachi *et al.* [D0 Collaboration], Phys. Rev. Lett. **79**, 1203 (1997) [hep-ex/9704015].

[17] F. Abe *et al.* [CDF Collaboration], Phys. Rev. Lett. **80**, 2773 (1998) [hep-ex/9710008].

[18] F. Abe *et al.* [CDF Collaboration], Phys. Rev. Lett. **79**, 3585 (1997) [hep-ex/9704007].

[19] B. Abbott *et al.* [D0 Collaboration], Phys. Rev. D **60**, 012001 (1999) [hep-ex/9808034].

[20] F. Abe *et al.* [CDF Collaboration], Phys. Rev. Lett. **79**, 1992 (1997).

[21] E. Laenen, J. Smith, and W.L. van Neerven, Phys. Lett. B **321**, 254 (1994); E.L. Berger and H. Contopanagos, Phys. Rev. D **54**, 3085 (1996); S. Catani *et al.*, Phys. Lett. B **378**, 329 (1996); R. Bonciani *et al.*, Nucl. Phys. B **529**, 424 (1998).

[22] S. Abachi *et al.* [D0 Collaboration], Phys. Rev. Lett. **79**, 1197 (1997) [hep-ex/9703008].

[23] F. Abe *et al.* [CDF Collaboration], Phys. Rev. Lett. **80**, 2767 (1998) [hep-ex/9801014].

[24] B. Abbott *et al.* [D0 Collaboration], Phys. Rev. Lett. **80**, 2063 (1998) [hep-ex/9706014].

[25] F. Abe *et al.* [CDF Collaboration], Phys. Rev. Lett. **82**, 271 (1999) [hep-ex/9810029].

[26] T. Affolder *et al.* [CDF Collaboration], Phys. Rev. Lett. **84**, 216 (2000) [hep-ex/9909042].

[27] G. Mahlon and S. Parke, Phys. Lett. **B411**, 173 (1997) [hep-ph/9706304].

[28] B. Abbott *et al.* [D0 Collaboration], Phys. Rev. Lett. **85**, 256 (2000) [hep-ex/0002058].

[29] T. Affolder *et al.* [CDF Collaboration], Phys. Rev. Lett. **85**, 2062 (2000) [hep-ex/0003005].

[30] T. Affolder *et al.* [CDF Collaboration], FERMILAB-PUB-00-101-E.

[31] T. Stelzer, Z. Sullivan and S. Willenbrock, Phys. Rev. D **58**, 094021 (1998) [hep-ph/9807340].

[32] T. Kikuchi, S. K. Wolinski, L. Demortier, S. Kim and P. Savard [CDF Collaboration], FERMILAB-CONF-00-290-E *Presented at DPF 2000, Columbus, Ohio, 9-12 Aug 2000*.

[33] F. Abe *et al.* [CDF Collaboration], Phys. Rev. Lett. **73**, 2667 (1994).

[34] B. Abbott *et al.* [D0 Collaboration], Phys. Rev. Lett. **82**, 4975 (1999) [hep-ex/9902028].

[35] F. Abe *et al.* [CDF Collaboration], Phys. Rev. D **54**, 735 (1996) [hep-ex/9601003]. T. Affolder *et al.* [CDF Collaboration], Phys. Rev. D **62**, 012004 (2000) [hep-ex/9912013].

RESULTS FROM THE K2K EXPERIMENT

Yoshinari Hayato
Institute of Particle and Nuclear Studies,
High Energy Accelerator Research Organization,
1-1 Oho, Tsukuba, Ibaraki, Japan
Representing the K2K Collaboration

ABSTRACT

The KEK to Kamioka (K2K) long baseline neutrino oscillation experiment has been successfully started since March 1999. This is the first accelerator-based long baseline neutrino oscillation experiment, and this experiment is expected to cover most of the parameter regions of neutrino oscillation which have been suggested by various atmospheric neutrino experiments. The neutrino beam is very stable, as confirmed by the secondary beam monitors and neutrino detectors located at KEK. The spectrum and profile of the neutrino beam is estimated by the newly developed pion monitor, which is one of the secondary particle monitors, and the obtained results are in good agreement with the results obtained from our Monte Carlo simulations. The accumulated number of protons on target is 2.29×10^{19} and the estimated expected number of fully contained events at Super-Kamiokande is $40.3^{+4.7}_{-4.6}$ in the case of no oscillation. The observed number of events at Super-Kamiokande is 27, which is $2\,\sigma$ off from the expected number of events.

1 Introduction

The standard model of electroweak interactions[1] is one of the most successful models in particle physics. In this model, the mass of the neutrino is defined to be zero. Therefore, it has a large impact on the standard model and requires extensions of it, if masses of neutrinos are proven to be nonzero. Since the late 1980s, some experiments on atmospheric neutrinos have reported deficits of ν_μ with energies around 1 GeV.[2–4] In 1998, the Super-Kamiokande collaboration not only confirmed a deficit of atmospheric ν_μ with high statistics, but they also reported a clear zenith angle dependence of the deficit.[5] This means that the disappearance probability of ν_μ depends on the distance between point where the neutrino was created and the detector. These experimental results are well explained by neutrino oscillation and imply that neutrinos should have non-zero masses. Therefore, it became very important to investigate the various characteristics of neutrino oscillation. For that purpose, several long baseline neutrino experiments, which use accelerators as the neutrino source, have been proposed. Among of them, the KEK to Kamioka (K2K) long baseline neutrino oscillation experiment is the first accelerator-based experiment to study the atmospheric neutrino oscillation.[6] The main purpose of this experiment is to confirm the ν_μ disappearance and to search for the ν_e appearance by neutrino oscillations. This experiment is able to cover almost all the parameter regions which are suggested by the results from atmospheric neutrino analysis. (See Fig. 1.) Because this kind of experiment will provide us with a way to study flavor mixing in the lepton sector, it is also important for the K2K experiment to establish various experimental methods of accelerator-based long baseline neutrino oscillation experiments, such as alignment, aiming of the neutrino beam, monitoring the stability of the beam, and so on.

In the first stage of the K2K experiment, the indication of neutrino oscillations is expected to be identified as a deficit of the observed number of neutrino interactions at Super-Kamiokande. Therefore, it is very important to estimate the expected number of events at Super-Kamiokande precisely. In order to estimate accurately the expected number of interactions at Super-Kamiokande, we have to understand the characteristics of the neutrino beam well. For that purpose, we have developed various kinds of primary and secondary beam monitors and neutrino detectors. In the following sections, we'll describe the beam monitors and detectors briefly and summarize the results from each detector including Super-Kamiokande.

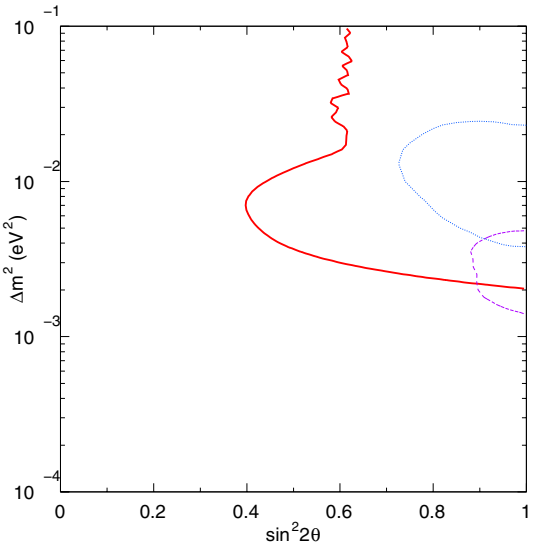

Fig. 1. Allowed parameter regions of neutrino oscillation ($\nu_\mu \rightarrow \nu_\tau$ or ν_s) and the sensitive region of the K2K experiment. The dashed (dotted) line shows the 90% C.L. allowed region obtained by the Super-Kamiokande (Kamiokande) experiment. The solid line shows the 90% C.L. sensitive region of the K2K experiment (for 10^{20} protons on target).

2 Overview of the K2K experiment

The K2K experiment is the first accelerator-based long baseline neutrino oscillation experiment. The schematic view of this experiment is shown in Fig. 2.

The neutrinos are generated and monitored at KEK in Tsukuba, travel through the Earth for 250 km, and are detected by the Super-Kamiokande detector located underground in the Kamioka mine, Gifu. The K2K neutrino beam is a horn-focused wide band beam, and is nearly pure ν_μ beam (98.2% ν_μ, 1.3% ν_e and 0.5% $\bar{\nu_\mu}$). The mean energy of the neutrino is about 1.3 GeV.[7] The oscillation probability for the two-flavor approximation can be written as follows:

$$P(\nu_\mu \rightarrow \nu_x) = \sin^2 2\theta \cdot \sin^2(1.27\Delta m^2 L/E_\nu), \tag{1}$$

where P is the oscillation probability, θ is the mixing angle, Δm^2 is the squared mass difference, L is the travel length of the neutrino (baseline distance), and E_ν is the energy of the neutrino. As described above, the baseline(L) is 250km and the mean energy of neutrinos(E_ν) is about 1.3GeV for the K2K experiment. Therefore, we can investigate the parameter regions where $\Delta m^2 \geq 2 \times 10^{-3}$ eV.

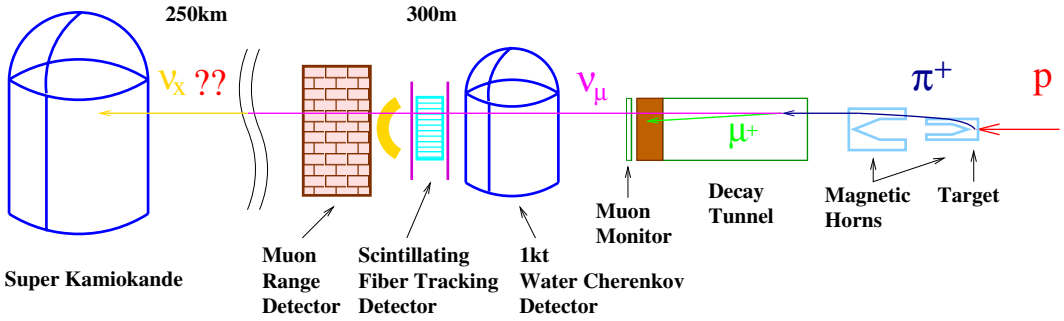

Fig. 2. Schematic view of K2K experiment. See text for detail.

The neutrino beam is generated from the decay of pions. In order to generate charged pions, we use proton Al interactions. The primary protons are extracted from the 12 GeV proton synchrotron at KEK every 2.2 sec.[8] The total width of a spill is about 1.1 μs and there are 9 bunches in a spill. The total number of protons is about 5.5×10^{12} per spill. The protons are extracted to the north direction and are bent by 90 degrees west, in which direction Super-Kamiokande detector is located. The target to generate pions is made of aluminum and its size is 30mm (25mm in June, 1999) in diameter and 660mm in length. This target is embedded in the first magnetic horn which focuses the generated positive pions and sweeps out the negative charged particles.[9] After the first horn, there is the second magnetic horn in order to make the parallel pion beam. These two horns are driven with pulsed 250 kA current (200 kA in June 1999) whose width is 2 ms. After the horns, there is a decay tunnel whose length is 200 m and which is filled with 1 atm He gas. The pions generated at the target decay into muons and neutrinos, and the muons decay into positrons and neutrinos while traveling in this tunnel. After the decay tunnel, there is a beam dump, which absorbs all the hadronic components and low energy muons. We put two muon monitors in the muon pit just after this beam dump to measure the direction of the beam by the muons which passed through the dump. Between the muon pit and the front neutrino detectors, there is 10 m of soil and all the remaining muons are absorbed. Therefore, only neutrinos reach the front neutrino detectors. We placed three different types of neutrino detectors. One is the 1 kt water Cherenkov detector. This is a miniature of Super-Kamiokande. The second one is the scintillating fiber tracking detector. This detector consists of 20 layers of scintillating fibers for particle detection, and water containers as the target material. The coverage of this detector is relatively small, 2.2 m$\times$2.2 m. However, the resolution of the vertices and particle trajectory reconstructions are much better, compared to the

other front detectors. Moreover, this detector is able to detect the tracks of low momentum charged particles, such as protons or pions, which cannot be observed by the water Cherenkov type detectors, and thus we can investigate the neutrino interactions in detail. The last detector is the muon range detector. This detector consists of 12 layers of iron absorbers and 6632 muon drift tubes. This detector covers a very large area (7.6 m$\times$7.6 m) and we can monitor the profile of the neutrinos and energy spectrum with a few days of data. By using this detector, we can confirm the stability of the neutrino beam by neutrino interactions.

As the far neutrino detector, we use the Super-Kamiokande detector. This is the world largest ring imaging water Cherenkov detector, whose fiducial volume is 22.5 kt. This detector is located at the Mozumi zinc mine near Kamioka, Japan, at a distance of 250 km from KEK. Super-Kamiokande has been running since April 1996 and neutrino interactions have been extensively studied with this detector. Therefore, it is very suitable for a long baseline experiment.

The overall alignment of the equipment is essential in a long baseline neutrino experiment.[10] In the case of the K2K experiment, the divergence of the neutrino beam at Super-Kamiokande has been estimated by Monte Carlo simulation and it was almost flat within 3 mrad. (See Fig. 3.)

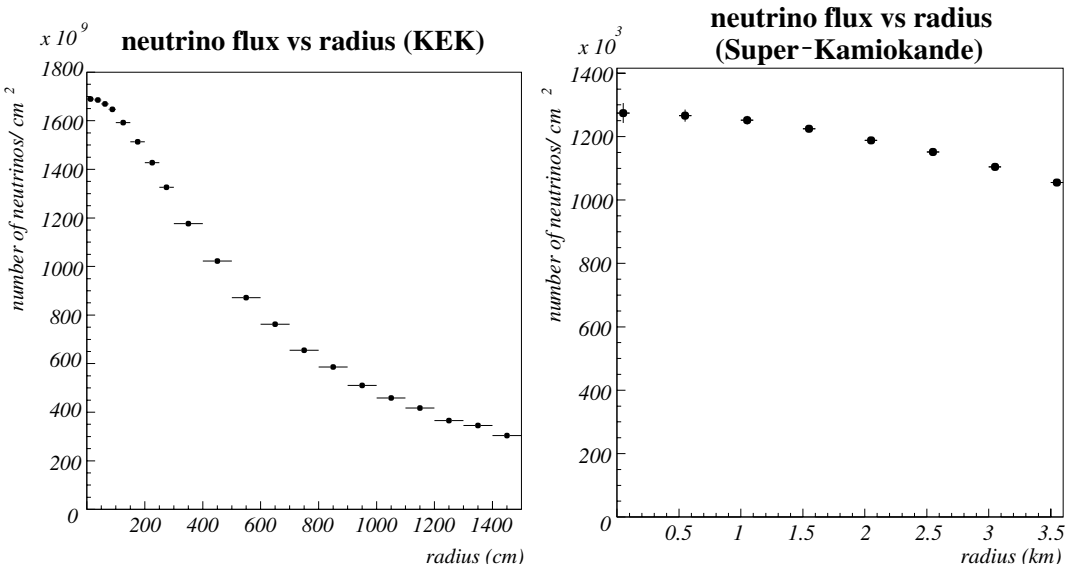

(A) (B)

Fig. 3. Neutrino profiles at (A) near detector (KEK) and (B) far detector (Kamioka). These plots are made using the K2K standard beam Monte Carlo simulation.

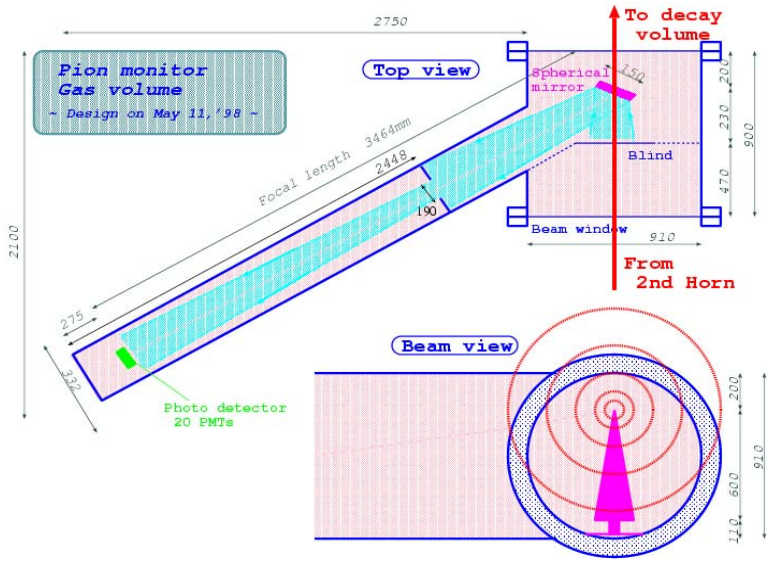

Fig. 4. Schematic view of the pion monitor. See text for detail.

Therefore, it is necessary for us to align everything much better than this tolerance. The actual alignment has been done with a GPS survey and all the equipment including target, magnetic horns, decay tunnel and all the detectors, were adjusted with an accuracy of 0.1 mrad, which is good enough for this experiment.

We started taking data in March 1999 and checked the components. The physics run started in June 1999. Since then, 2.3×10^{19} protons have been delivered on target.

3 Results from the secondary beam monitors

The secondary beam monitors[11] provide us with various important information about the neutrino beam. We use the data from the pion monitor to estimate the flux of neutrinos in KEK and at Super-Kamiokande. Muon monitors make it possible to adjust and monitor the direction of the beam spill by spill.

3.1 Pion monitor

The pion monitor is a threshold type gas Cherenkov detector and was developed to measure the energy spectrum and directional distributions of charged pions. A schematic view of the pion monitor is shown in Fig. 4. Usually, the pion monitor is located a little bit away from the beamline; we place this detector in the middle of the beamline only

when we try to take data.

Cherenkov photons are emitted from charged particles whose velocity is faster than the speed of the light in the medium. The relation between the direction of the emitted Cherenkov photon and the direction and momentum of the charged particle can be written as:

$$\cos(\theta) = \frac{1}{n\beta}\,, \qquad (2)$$
$$\beta \equiv \frac{p}{E}\,,$$

where θ is the angle between the direction of the Cherenkov photons and the direction of the charged particle, n is the refractive index of the medium, and p and E are the momentum and energy of the charged particle, respectively. If it is possible to change the refractive index of the medium in the detector, we can change the threshold momentum of the particle to be detected. We selected a Freon gas as the medium of the detector because the refractive index of the Freon gas is appropriate for our measurement and is easily controlled by changing the pressure of the gas.

Cherenkov photons emitted from the pions are reflected by the spherical mirror located at the end of the gas volume, and are detected by the Photo Multiplier Tube(PMT) array. This PMT array consists of 20 1/2 inch PMTs located on the focal plane of the spherical mirror. Because of the characteristic of a spherical mirror, the image at the focal plane reflects the incoming direction of the photons and does not depend on the position of the photons at the mirror. This means that the location of the image of the Cherenkov light observed at the focal plane corresponds to the direction of the charged particle, and the distance between the two peaks of the image corresponds to the opening angle of the Cherenkov light. The observed charge distributions of the pion monitor with various refractive indices are shown in Fig. 5. We can see clearly two peaks of Cherenkov light, and the distance between the two peaks changes according to the refractive indices. Unfortunately, we can not lower the Cherenkov threshold below $\mathrm{P}_\pi \leq 2\,\mathrm{GeV}$ because primary 12 GeV protons begin to emit Cherenkov photons in such a high refractive index region.

From these distributions, we can reconstruct the momentum and directional distributions of charged pions by fitting. Once we know the momentum and directional distributions of the pions, we can easily estimate the neutrino fluxes by assuming the decay kinematics of the pions. The obtained fluxes are shown in Fig. 6. Here the absolute normalizations of the fluxes are arbitrary. According to these results, our stan-

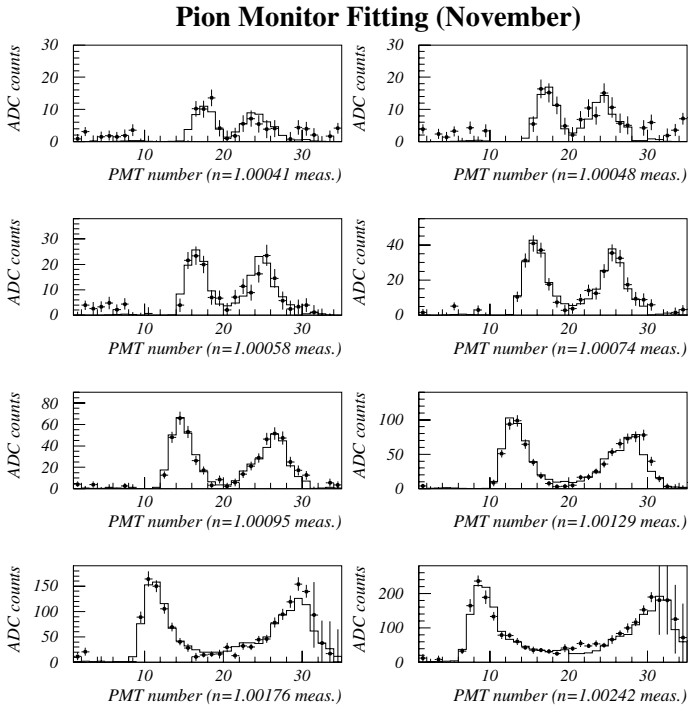

Fig. 5. Observed charge distributions from the pion monitor for different refractive indices. The circles with error bars show the data and the error bars correspond to the statistical error. The histograms show the fitted results. See text for detail.

dard beam Monte Carlo program reproduces the flux obtained from the pion monitor well. Our standard beam Monte Carlo is based on GEANT.[12] In order to simulate the primary proton interactions on aluminum, we use the parameters based on various experimental results of hadron production.[13] The other hadronic interactions are treated by GCALOR.[14]

3.2 Muon monitors

There is a muon dump after the decay tunnel. We placed two types of muon profile monitors after the muon dump: a silicon pad detector and a large area ionization chamber. (See Fig. 7.) The muon dump consists of 3.5 m of iron and 2 m of concrete. While passing through this dump, all the hadronic components are absorbed and only the high energy muons, whose momentum is more than 5.5 GeV/c at the end of decay tunnel, reach the muon monitors. The profile of these energetic muons is known to be well correlated with the profile of the neutrino beam, and there are enough muons in a spill

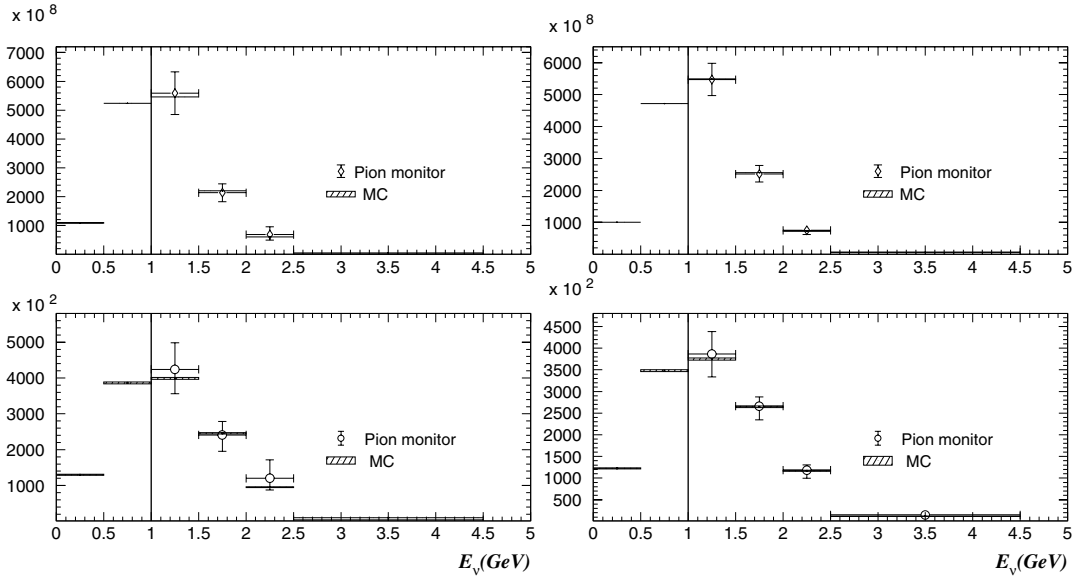

Fig. 6. Estimated neutrino spectrum for the configuration used in June '99 (A) and configuration used after Nov. '99 (B). Upper figures show the estimated flux at KEK and the lower figures show the estimated flux at Super-Kamiokande. The open circle with error bars corresponds to the results from the pion monitor; error bars include systematic errors. The hatched boxes show the Monte Carlo expectation, and the size of each box corresponds to the error.

for the profile measurement. Therefore we can adjust the direction of the beam using the observed profile of muons, and also monitor the direction of the beam spill by spill.

The ionization chamber (μ-SPIC) consists of six planes of Ar chambers, whose coverage is 2 m$\times$2 m, and the size of each chamber is 60 cm$\times$90 cm. Inside the chamber, there are two readout planes, one in the horizontal and the other in the vertical plane. Between these two readout planes, there is a high voltage plane in the middle of the two readout planes, and the distance between the central plane and one of the readout planes is 1 cm. There are 32 strips in the horizontal plane and 36 strips in the vertical plane. The width of each strip is 5cm. Each of the strip is connected to the corresponding strip in the neighboring chambers. Thus, these six chambers act as one large chamber. Fig. 8 shows the time variation of the fitted center of muons observed by this detector. It shows that the beam center is stable within 1mrad in the X and Y directions. In order to confirm the results from the ionization chamber, we prepared the other muon mon-

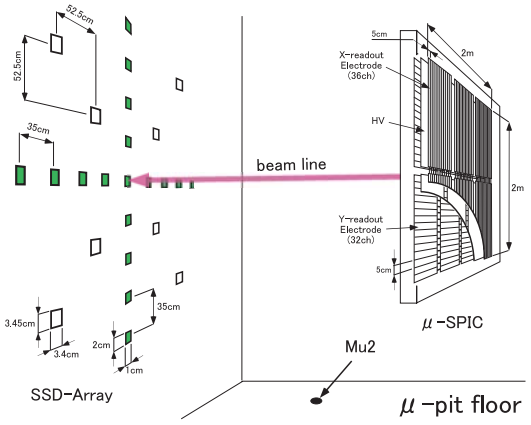

Fig. 7. Schematic view of the muon monitors. See the text for details.

itor, which has a coarse grain but is expected to be stable. We placed 26 silicon pad detectors on the wall behind the ionization chamber (SSD-Array). Seventeen of them are 10 mm×20 mm and 9 of them are 34 mm×34.5 mm. The obtained distributions are consistent with the results from ionization chamber.

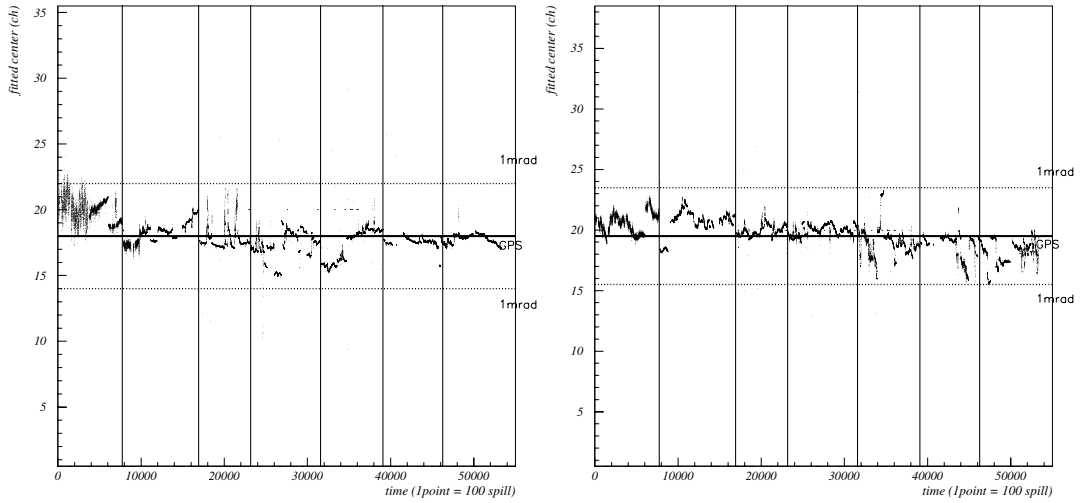

Fig. 8. Fitted center of the muons monitored by the ionization chamber in the muon pit. The variation of the center of the beam is confirmed to be less than 1 mrad.

4 Results from the neutrino detectors

In order to measure the generated neutrino fluxes and spectrums at KEK, we use three different types of neutrino detectors: water Cherenkov detector, scintillating fiber tracking detector[15] and muon range detector.[16] Each of them has different characteristics and thus we can check the consistency of our measurements, and it allows us to investigate the neutrino interactions more precisely. (See Fig. 9.)

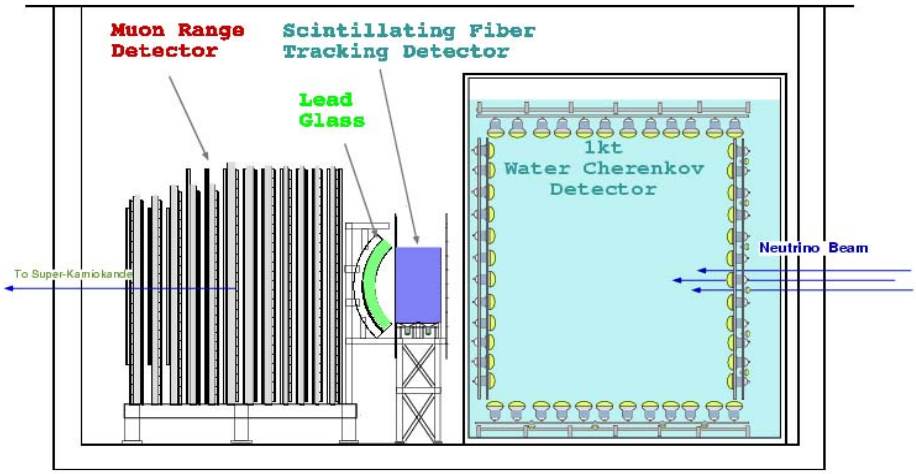

Fig. 9. Front neutrino detectors. See text for detail.

There is also a lead-glass detector to search for ν_e but this detector is not used for the ν_μ flux measurement. For the estimation of the expected number of events at Super-Kamiokande, we decided to use the results from the water Cherenkov detector as the reference value. Because these two detectors are of the same type, several systematic errors are cancelled. However, we don't have enough statistics from the water Cherenkov detector to monitor the stability of the neutrino beam in a period of only a few days. The muon range detector is suitable for this kind of monitoring. The coverage of the muon range detector is about $7\,\mathrm{m}\times 7\,\mathrm{m}$ and the fiducial mass of this detector is several times larger than that of the 1 kt water Cherenkov detector. Therefore, we can check not only the stability or time dependence of the event rate, which is directly related to the absolute flux, but also the stability of the energy spectrum of the neutrinos.

In order to estimate the detection efficiency for neutrino-induced events, contamination of the backgrounds and various systematic errors, we used Monte Carlo simulated

events. The neutrino interaction part of the simulation is basically the same which is used in Super-Kamiokande.

4.1 Muon range detector

The muon range detector consists of the drift chambers and 12 iron plates. The size of the detector is about 7.6 m in width and 7.6 m in height. There are two layers of drift chambers in both the X and Y directions, for a total of 4 layers, equipped on both sides of each iron plate. In order to get better energy resolution, the upstream 4 iron plates are 10 cm thick and the downstream 8 plates are 20 cm thick. The total thickness of iron is 2.0 m and it is possible to measure up to 2.8 GeV/c muons. We use 829 drift chamber modules, each of which has 8 independent cells. The size of each cell is 50 mm$\times$70 mm. In total, there are 6632 drift tubes and all the channels are read out by TDC modules. By using the timing information, we can reconstruct the particle trajectory precisely; the typical resolution obtained is less than 1 cm. As for the momentum reconstruction, there is no way to identify the interaction point of the neutrino in the iron plate or the stopping position of the particle. Therefore, the resolution of the reconstructed momentum of a muon is about 120 MeV.

In order to select the neutrino-induced events, we apply the following cuts after track-finding:
a) each track does not share a vertex with other tracks,
b) the tracks have to be generated within the beam spill timing,
c) both ends of the tracks have to be contained within the detector,
d) either endpoint of each track should be in one of the upstream 9 iron plates.
Criterion a) is used to avoid double-counting the number of interactions. Criterion b) is used to eliminate the cosmic-ray background events. Criterion c) is used to select the events which were generated within the detector. For the profile measurement of the neutrino interactions, we apply an additional cut, which rejects the events whose reconstructed energy is less than 0.5 GeV or greater than 2.5 GeV. These events are rejected because the acceptance of these high energy and low energy events depends on the interaction vertex, and the differences are quite large even in the fiducial volume. Typical profiles of the neutrino beam are shown in Fig. 10. The Monte Carlo prediction reproduces these profiles very well. By fitting the profile, we can monitor the time dependence of the ν_μ beam. As shown in Fig. 11-(A), the ν_μ beam is well centered and very stable within 1 mrad. We can also measure the neutrino event rate and the

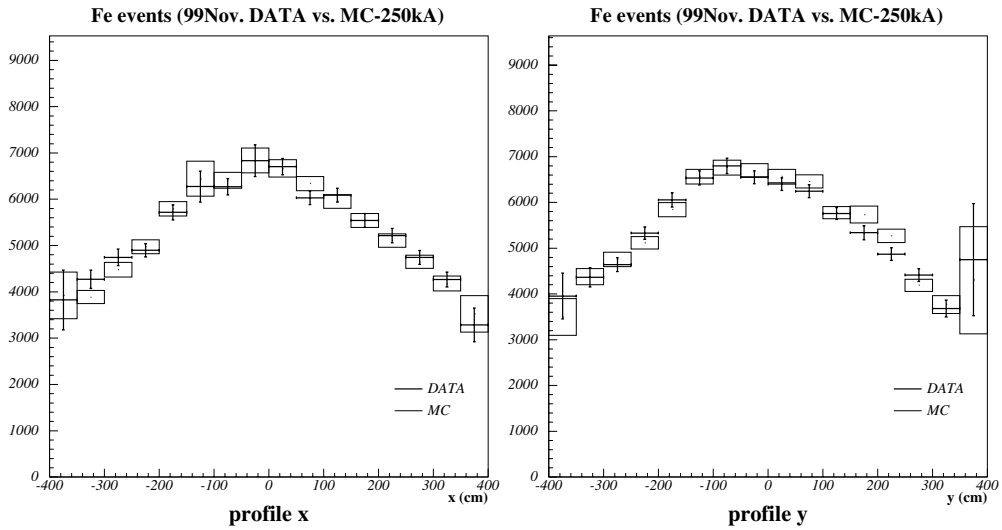

(A) (B)

Fig. 10. Typical vertex distributions of neutrino interactions (profile of neutrino beam) at the muon range detector. Fig. A (B) shows the horizontal (vertical) distribution. Each cross shows the data and error. The boxes correspond to the Monte Carlo predictions.

spectrum. For this analysis, we defined a cylindrical fiducial volume, whose radius is 3 m and the total fiducial mass is 312 tons. The typical event rate is about 0.05 events/spill, and thus we have enough events to monitor the stability on a daily basis. The time dependence of the neutrino event rate in this detector is shown in Fig. 11-(B) and it is very stable. In June '99, we used a different configuration of the target and horns, for which the event rate is slightly lower than the other periods.

It is also possible for us to measure the angular and direction distributions of the muons. These distributions are very sensitive to the neutrino spectrum. The results are shown in Fig. 12. These figures show no time dependence, and so the stability of the neutrino beam spectrum was also confirmed.

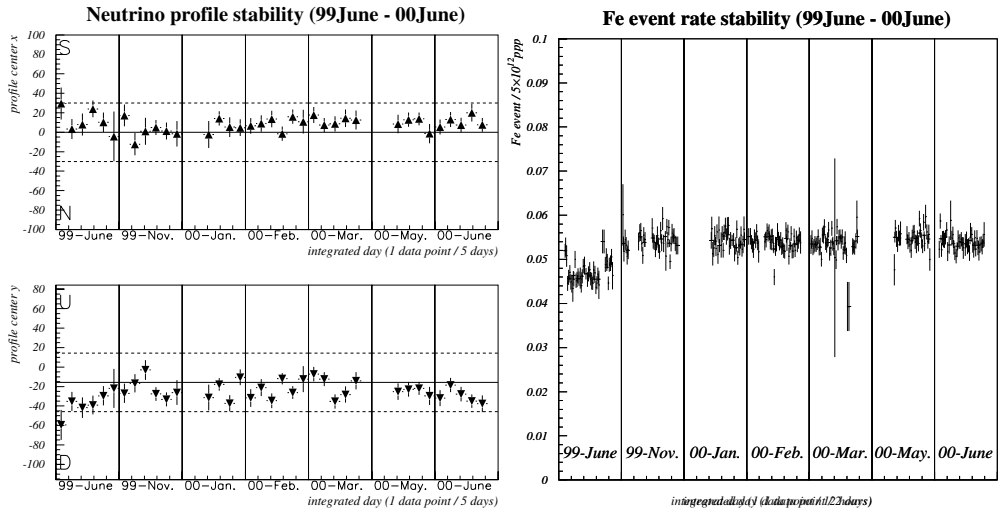

(A) (B)

Fig. 11. Time dependences of (A) the center of neutrino beam and (B) the neutrino event rate monitored by the muon range detector for all the experimental period. The upper (lower) figure of (A) shows the horizontal (vertical) distribution. The dashed lines in each figure of (A) show the position away from 1 mrad. Each error bar shows the statistical error.

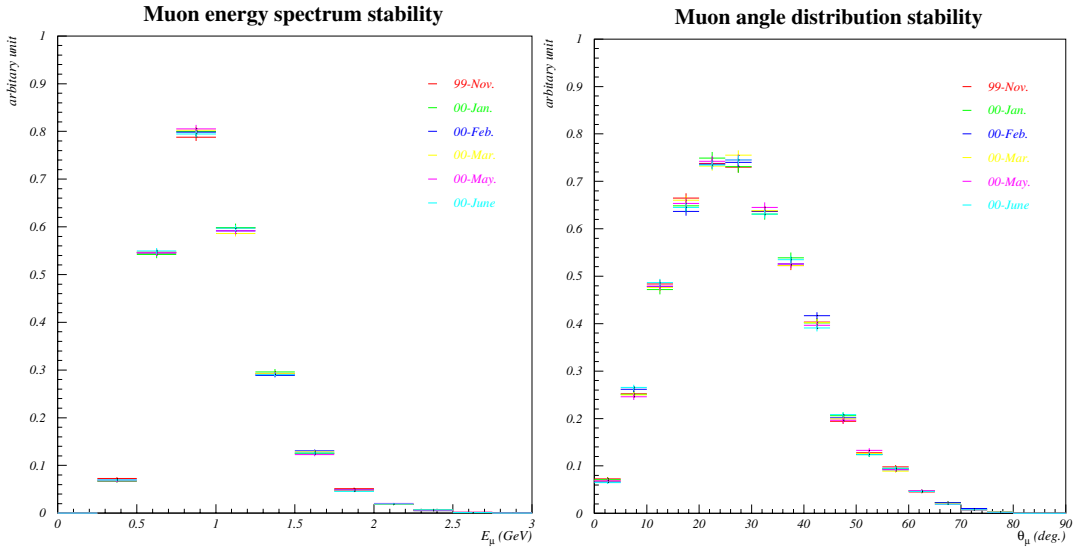

Fig. 12. Momentum and angular distributions of muons observed by the muon range detector. Each cross corresponds to one month of data.

4.2 Scintillating fiber tracking detector

The scintillating fiber tracking detector consists of 20 layers of 2.6 m×2.6 m tracking modules and 19 layers of water containers. Each tracking module consists of two scintillating fiber sheets for horizontal and vertical directions. Each scintillating fiber sheet has two layers to improve the particle detection efficiency. The diameter of the scintillating fiber is 0.7 mm and the length is 3.7 m. The water containers were made of 1.8 mm thick aluminum, and have a size of 16 cm×240 cm×6 cm. Fifteen tanks are used for one target layer. The scintillating fibers are combined and read out by 24 Image Intensifier Tubes (IITs). The IIT is an imaging detector which uses a CCD for the final readout. We have also prepared a special 8 bit depth Flash ADC (FADC) module and FIFO module to readout entire CCD images from each IIT. We can identify the individual fibers through which particles passed, and we reconstruct the tracks with this information. However, the gate width of each IIT needs to be set to more than 0.1 μsec to match the decay time of the phosphor screen. Therefore, we need trigger counters to eliminate cosmic-ray muons. For that purpose, we have also prepared two large trigger counters located both upstream and downstream of this detector. Each of the trigger counters consists of 40 scintillators and its size is 407 cm×400 cm, which is large enough to cover the entire scintillating fiber tracking detector. The size of each scintillator is 407 cm×10.5 cm×4.2 cm. For the upstream detector, we connect two scintillators with one lightguide and treat them as one large module. For the downstream counter, we need higher resolutions for both position and energy, so each scintillator is read out independently. Each of the scintillator modules is equipped with two PMTs on both sides and we can easily reconstruct the location with the obtained charge and timing information.

This time we select neutrino events which have vertices in the detector volume, and the exiting muon must generate a track in the muon range detector. With this data sample, we can check the consistency of the event rate and distributions of energy and direction of the muons by comparing the results from the two detectors, the scintillating fiber tracking detector and the muon range detector, which use different target material. The actual event selection criteria are defined as follows:

a) there is no hit in the upstream counter,

b) the track penetrates more than two layers of the tracking modules,

c) the vertex (starting point) of the track must be in the fiducial volume,

d) there must be corresponding hits in the downstream trigger counter,

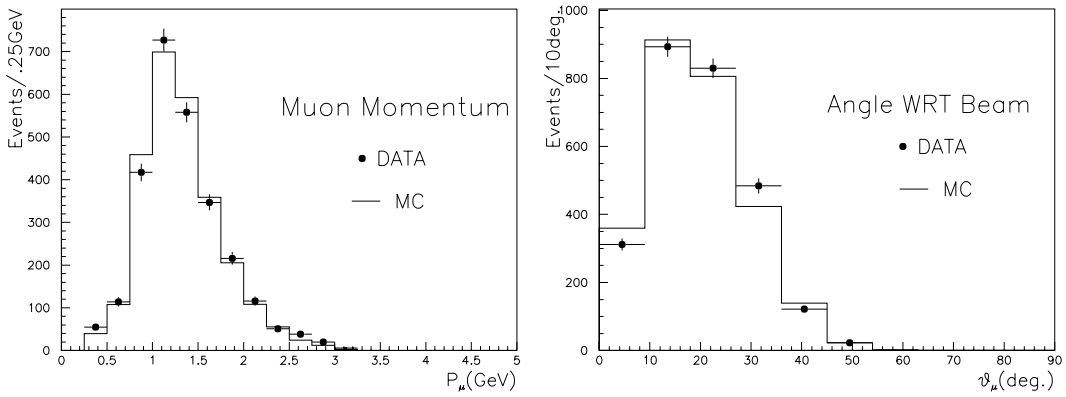

(A) (B)

Fig. 13. (A) Momentum and (B) angular distributions of muons from the scintillating fiber tracking detector. The filled circles with bars show the data. Each error bar shows statistical errors. The histograms show the Monte Carlo simulation.

e) the track found in the detector must be connected to the track in the muon range detector.

Criterion a) is used to reject the incoming cosmic ray muons. Criterion b) is used to reject noise tracks. Criterion c) is used to select the vertex-contained samples. Criteria d) and e) are used to select the tracks which have corresponding tracks in the muon range detector. After applying all these cuts, 2953 events remain. The event rate is about 8.3×10^{-4} events/spill and the expected interaction rate estimated by using the Monte Carlo is consistent with the other two detectors. The angular and momentum distributions of the muons are shown in Fig. 13. The results from the Monte Carlo reproduce the data well.

4.3 1 kt Water Cherenkov detector

The 1 kt water Cherenkov detector is a miniature of the Super-Kamiokande detector. This detector consists of a cylindrical water tank, which can hold 1 kt of pure water and 680 20 inch PMTs. Each charged particle generates one Cherenkov ring in this detector, and thus we can count the number of charged particles by counting the number of Cherenkov rings. As for the reconstruction of the direction of each particle, we can use the relation between the direction of the charged particle and the emitted Cherenkov photons. The total number of emitted Cherenkov photons is used to reconstruct the momentum of each particle, which is known to have good correlation with the neu-

trino momentum. The emission of Cherenkov photons starts from the interaction point. Therefore, it is possible to reconstruct the vertex by using the timing information. The shapes of the Cherenkov images are different for different kinds of the particles. For example, electrons and gammas, which generate electromagnetic showers, create rather diffuse Cherenkov images. By using these differences in the images, we can identify the types of particles. Therefore, we need to record both timing and charge from each PMT. For that purpose, we have developed a special electronics module, called ATM, to record this information without deadtime. In Super-Kamiokande, we have been using the same 20 inch PMT, high voltage power supply system for the PMTs, and readout electronics. Therefore, the characteristics of this equipment is well understood.

This detector generates the trigger by itself, using the number of hit PMTs within a 200 ns window, and then records the event. However, there is no earth shield for the cosmic-ray muons. Therefore, it is necessary to supply a global gate signal to avoid recording such unnecessary events. For that purpose, we prepared a global gate signal, called the spill gate, which is provided by the accelerator and whose width is adjusted based on the width of a spill. A difference from the Super-Kamiokande detector is that we also record the numbers of hit PMTs with FADC modules. This information is useful for counting the number of interactions in an event or a spill. The average number of visible interactions in a spill has been estimated, and was observed to be about 0.2. Thus about 10% of the spills have more than one interaction. Therefore, we set the threshold at 1000 photoelectrons (p.e.) to count the number of peaks in the FADC. This threshold corresponds to about 100 MeV electron equivalent energy. There are also events caused by the decay electrons from cosmic-ray muons, which stop in the detector. Some of these decay electron events, whose parent muons came into the detector just before the spill gate, cannot be eliminated only by the information from the ATM modules. Therefore, we need to use the data from the FADC to reject these events.

We apply the following criteria to select the neutrino-induced events for the estimation of the absolute neutrino flux:
a) there was no detector activity in the 1.2 μsec preceding the beam spill,
b) only one peak was recorded in the FADC,
c) the reconstructed vertex must be in the fiducial volume.
We define a cylindrical fiducial volume along the beam direction whose radius is 2 m and whose length is 4 m. Criterion a) removes events which were caused by electrons from the decay of cosmic-ray muons. Criterion b) removes events with more than

one interaction. In criterion c), we defined a rather small fiducial volume in order to remove the cosmic-ray muons and to reduce the systematic errors coming from the vertex resolution. The reconstructed vertex distributions just before criterion c) was applied are shown in Fig. 14 and agree with the Monte Carlo.

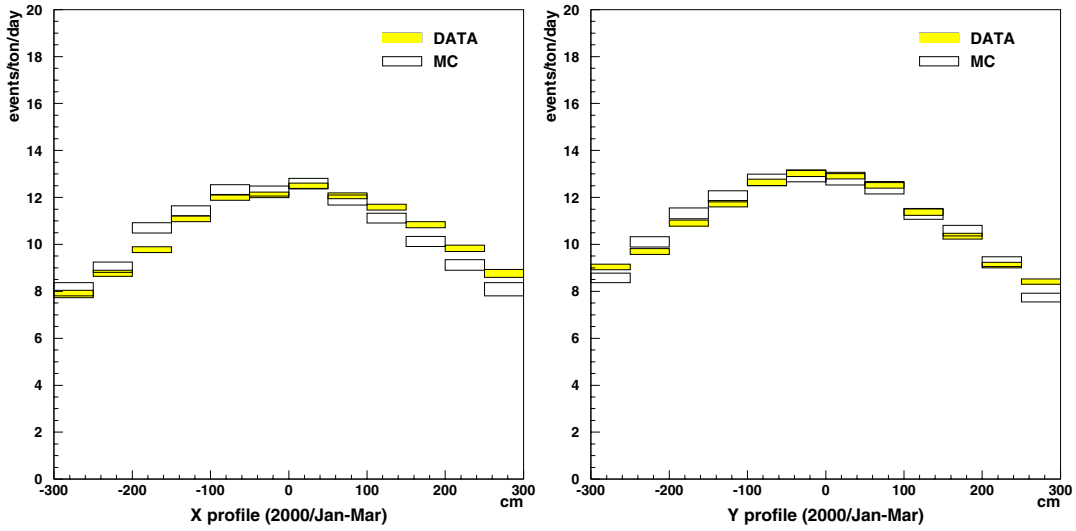

(A) (B)

Fig. 14. (A) Horizontal and (B) vertical vertex distributions of neutrino interactions in the 1 kt water Cherenkov detector. The open boxes show the data and the shaded boxes show the Monte Carlo. The vertical size of each box corresponds to the statistical error.

Fig. 15 shows the the stability of the event rate and it is very stable as expected. In June '99, the configuration of the target and horns was different, as described above, and in November '99, the detector configuration was slightly different from the other periods. Therefore, the event rate is slightly lower during these periods.

By applying all the neutrino event selection cuts to the generated Monte Carlo events, detection efficiencies were estimated to be 86% for the charged current interactions and 33% for the neutral current interactions. Combining all the interactions, the estimated detection efficiency of the 1 kt detector is 71%.

4.4 Expected number of events at Super-Kamiokande

In order to obtain the expected number of events at Super-Kamiokande, we use the following method. First, we use the Monte Carlo simulation to obtain the neutrino spectrum. The energy spectrum of this Monte Carlo has been guaranteed by the results

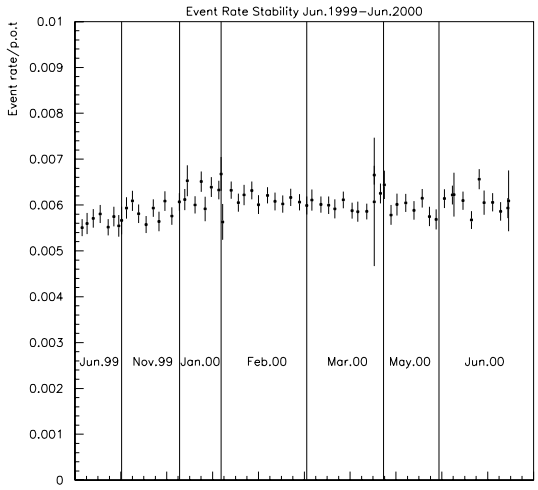

Fig. 15. Time dependence of the neutrino event rate observed at the 1 kt water Cherenkov detector. Each point represents an average of 5 days. The error bars show the statistical errors.

from the pion monitor measurement shown in Fig. 6. For the absolute normalization, we use the number of events observed in the front neutrino detectors. We have generated Monte Carlo events, passed them through the event selections, and obtained the absolute normalization factors of our neutrino fluxes by comparing the observed numbers of events from the front neutrino detectors. Then, we can calculate the expected number of events at Super-Kamiokande. The actual formula to obtain the expected number of events without oscillation is as follows:

$$N_{SK}(\text{expected}) = N_{FD} \times \frac{\eta_{SK}}{\eta_{FD}} \times \frac{M_{SK}}{M_{FD}} \times \frac{POT_{SK}}{POT_{FD}}, \quad (3)$$

$$\eta \equiv \int (\phi \times \sigma \times \epsilon)\, dE_\nu, \quad (4)$$

where N_{FD} is the observed number of neutrino events at the front detector, η_{SK}/η_{FD} is the Far-to-Near event ratio, $M_{SK}(M_{FD})$ is the fiducial mass of Super-Kamiokande (front) detector, and $POT_{SK}(POT_{FD})$ is the number of protons on target used for the analysis of Super-Kamiokande (front) detector, ϕ is the neutrino flux at each detector, σ is the neutrino cross-section, ϵ is the detection efficiency and E_ν is the energy of neutrino, respectively. The expected number of events at Super-Kamiokande, estimated by using the results from the 1 kt detector, is $40.3\ ^{+4.7}_{-4.6}$. The major sources of systematic error come from the vertex resolution and the treatment of multiple interactions in a spill. These errors will be reduced soon by refining the vertex fitter and treating the

	1kt water Cherenkov	Muon range detector	Scintillating fiber tracker
Fiducial mass (tons)	50 (H_2O)	312 (Fe)	5.9 (H_2O+Al)
Detection Efficiency	0.71	0.33	0.24
Number of observed ν events	63508	223419	2953
Expected number of events at Super-Kamiokande	$40.3^{+4.7}_{-4.6}$	$41.4^{+6.2}_{-6.4}$	$40.0^{+5.2}_{-5.5}$

Table 1. Summary of expected number of events at Super-Kamiokande

events with multiple interactions more precisely. The systematic error coming from the extrapolation of the neutrino flux from the near measurement to Super-Kamiokande is estimated to be 7%. This error comes from the uncertainty in the measurement of the pion monitor and the Monte Carlo uncertainty for low energy neutrinos. The systematic error from the measurements at Super-Kamiokande is estimated to be 2%, which comes mainly from the uncertainty of the vertex fitting and the fiducial volume cut. The expected numbers of events obtained from the other two near detectors are also summarized in Table 1. All the numbers are consistent within errors.

4.5 Super-Kamiokande

The Super-Kamiokande detector is the world largest ring imaging water Cherenkov detector. It is located 1000 m (2700 m water equivalent) below the peak of Mt. Ikenoyama in the Mozumi zinc mine near Kamioka, Japan. Fifty kilotons of ultra pure water are held within a stainless steel tank of height 41.4 m and diameter 39.3 m. The tank is optically separated into two regions, the inner and anti-detectors, by a PMT support structure covered with a white reflector sheet (Tyvek), and a black sheet. The inner detector has a height of 36.2 m and a diameter of 33.8 m. The anti-detector completely surrounds the inner detector and is used to identify incoming and outgoing particles. On the wall of the inner detector, there are 11,146 50 cm inward-facing PMTs, which cover 40% of the surface. The anti-detector is lined with 1,885 20 cm PMTs equipped with 60×60 cm wavelength-shifter plates to increase the collection efficiency for Cherenkov photons.

In order to select the events at Super-Kamiokande which were generated by the neutrinos from KEK, we use the timing information provided by the GPS system.[17] At the KEK site, we record the absolute timing information of each spill (T(KEK)).

Also we record the timing information for all the events in Super-Kamiokande (T(SK)). Then, we calculate the time differences between the beam spill timing and the trigger timing of the events in Super-Kamiokande. If the neutrino-induced events have a timing difference which is consistent with the time of flight from KEK to Super-Kamiokande (T(TOF)), those events are defined to be events generated by the neutrinos from KEK. The two GPS systems, one placed in KEK and the other located at the Kamiokande site, have been checked with an atomic clock, and the absolute timing difference of these two clocks is obtained to be less than ± 100 ns. Therefore, we can set a very narrow timing window. Basically there are no background events to search for the neutrino interactions in Super-Kamiokande, and thus we don't have to worry about the background other than atmospheric neutrino events. In Super-Kamiokande, about 10 atmospheric neutrino events are detected every day. On the other hand, the protons are extracted about 40,000 times per day and we open only 1.4 μs as spill gate for each spill. From there numbers we can easily estimate the probability to misidentify an atmospheric neutrino event as a neutrino beam event, and the probability is less than 1×10^{-5}. Therefore, we can safely assume that the events within the gate are generated by the neutrinos from KEK.

The actual criteria to select the neutrino events at Super-Kamiokande are defined as follows:

a) the timing of the event is consistent with the beam,

-0.1 $\leq \Delta$T ($\equiv$ T(SK)-T(KEK)-T(TOF)) $\leq$ 1.3 μs,

b) there should be no events within 30 μs before the event,

c) the number of photoelectrons in a 300 ns window must be greater than 200,

d) the maximum charge of a PMT in the event must be smaller than 200 p.e.,

e) the number of hit PMTs of the largest cluster in the outer detector should be less than 10,

f) the reconstructed vertex must be in the fiducial volume.

Criterion a) is used to select events which could be generated by the neutrino from KEK. Criterion b) is used to remove events generated by decay-electron s from incoming cosmic-ray muons. Criterion c) is used to remove low energy events. Criterion d) is used to eliminate events in which a particle escaped from the inner detector. Criterion e) is used to reject entering cosmic-ray muons. We have generated Monte Carlo events to estimate the detection efficiencies. The detection efficiencies for charged and neutral current interactions are estimated to be 93% and 42%, respectively, and the overall detection efficiency is estimated to be 79%. Figure 16 shows the distributions of ΔT.

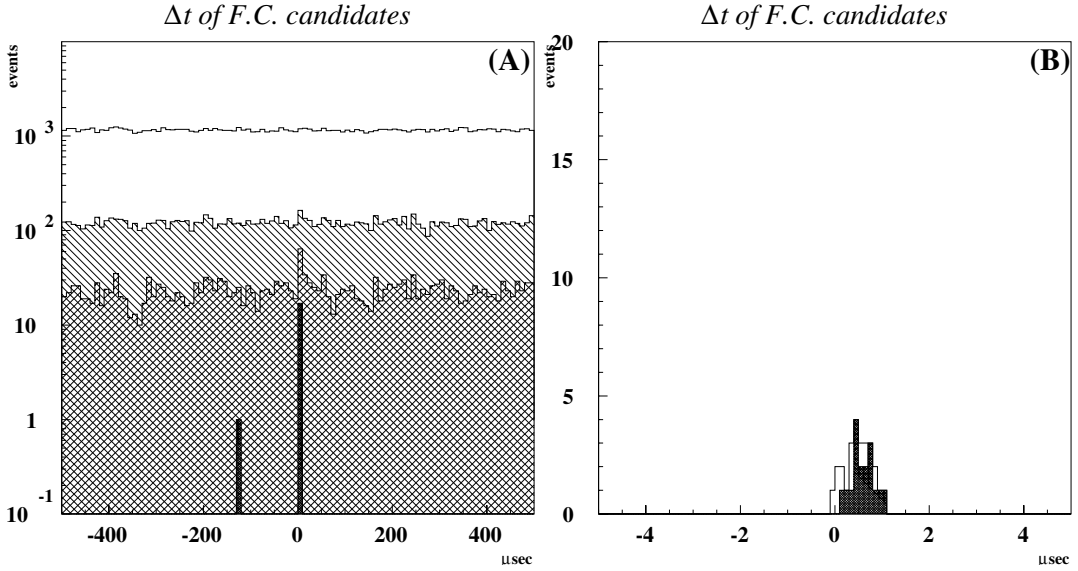

Fig. 16. ΔT ($\equiv T(SK) - T(KEK) - TOF$) distributions. (A) ΔT distributions for ± 500 μs window. The clear histogram shows the events after the decay-electron cut (criterion b). The hatched histogram shows the events after the HE trigger cut. The shaded histogram shows the events after imposing criterion d. The filled histogram shows the events after the fully-contained cut (criterion e) and the fiducial volume cut. (B) ΔT distributions for ± 5 μs window. The clear histogram shows all the fully contained events. The filled area corresponds to the fully contained events in the fiducial volume.

In figure 16-(A), we used a rather loose timing cut instead of criterion a). After applying the fiducial volume cuts, there is a clear peak observed around 0 to 1 μs as shown in Figure 16-(B).

There are 27 events observed after applying the 22.5 kt fiducial volume cut, which is the same criterion as for the atmospheric neutrino analysis in Super-Kamiokande. The number of background events is estimated to be less than 10^{-3} events. The expected number of events was 40.3 and the deficit from the expected value is at the 2 sigma level. The detailed numbers of events are summarized in Table 2.

Figure 17 shows various distributions of the observed events. The particle direction of 1-ring μ-like events shown in Fig. 17-(B) seems to have a good correlation with the direction of the neutrino from KEK, as expected. However, the statistics are so low that it is impossible to say something conclusive.

# of observed events and expected events			1999/06-2000/06		
			$\Delta m^2(\times 10^{-3} eV^2)$		
	Obs.	Exp.	3	5	7
FC 22.5kt	27	$40.3\ ^{+4.7}_{-4.6}$	$26.6\ ^{+3.4}_{-3.3}$	$17.8\ ^{+2.3}_{-2.2}$	$14.9\ ^{+1.9}_{-1.9}$
1-ring	15	24.3±3.6	14.4±2.3	9.4±1.5	8.6±1.4
μ-like	14	21.9±3.5	12.4±2.1	7.5±1.3	6.8±1.2
e-like	1	2.4±0.5	2.1±0.4	1.9±0.4	1.8±0.4
multi ring	12	16.0±2.7	12.2±2.1	8.4±1.5	6.3±1.1
out-of-FV	16	17.2	11.2	7.6	6.7

Table 2. Observed and expected number of events.

5 Summary

The K2K experiment, which is the first accelerator-based long baseline neutrino oscillation experiment, was successfully started in March 1999. All the equipment has been aligned to an accuracy of 0.1 mrad, which is sufficient for this experiment. The accumulated number of protons delivered on target is 2.29×10^{19}. The beam has been monitored spill by spill by the muon monitors and is well controlled and the direction of the beam is well centered within 1 mrad for both vertical and horizontal directions throughout the experimental period. The pion monitor also works well and we obtained the distributions of momentum and direction of pions just after the target. The neutrino fluxes at both near and far sites, obtained from the pion monitor, are well reproduced by our Monte Carlo simulation. Also, the neutrino detectors at the near site have been working fine. We have monitored the profile and the direction of the neutrino beam with the muon range detector. The time variation of the spectrum of the neutrino beam has also been monitored and it was found to be stable. The expected number of events at Super-Kamiokande was estimated by using the results from the 1 kt water Cherenkov detector, and it was $40.3^{+4.7}-4.6$. The expected numbers of events at Super-Kamiokande are also calculated based on the results from the other two detec-

tors, the muon range detector and the scintillating fiber tracking detector. As a result, all the numbers are consistent within the errors. We have observed 27 events at Super-Kamiokande, which is 2 sigma off from the expected number of events. It is planned to run for few more years and the total number of protons on target will reach 1.0×10^{20}, which is 5 times larger than the current statistics.

We gratefully acknowledge the cooperation of the Kamioka Mining and Smelting Company. This work has been supported by the Ministry of Education, Science, Sports and Culture, Government of Japan, US Department of Energy and the Korean Ministry of Science.

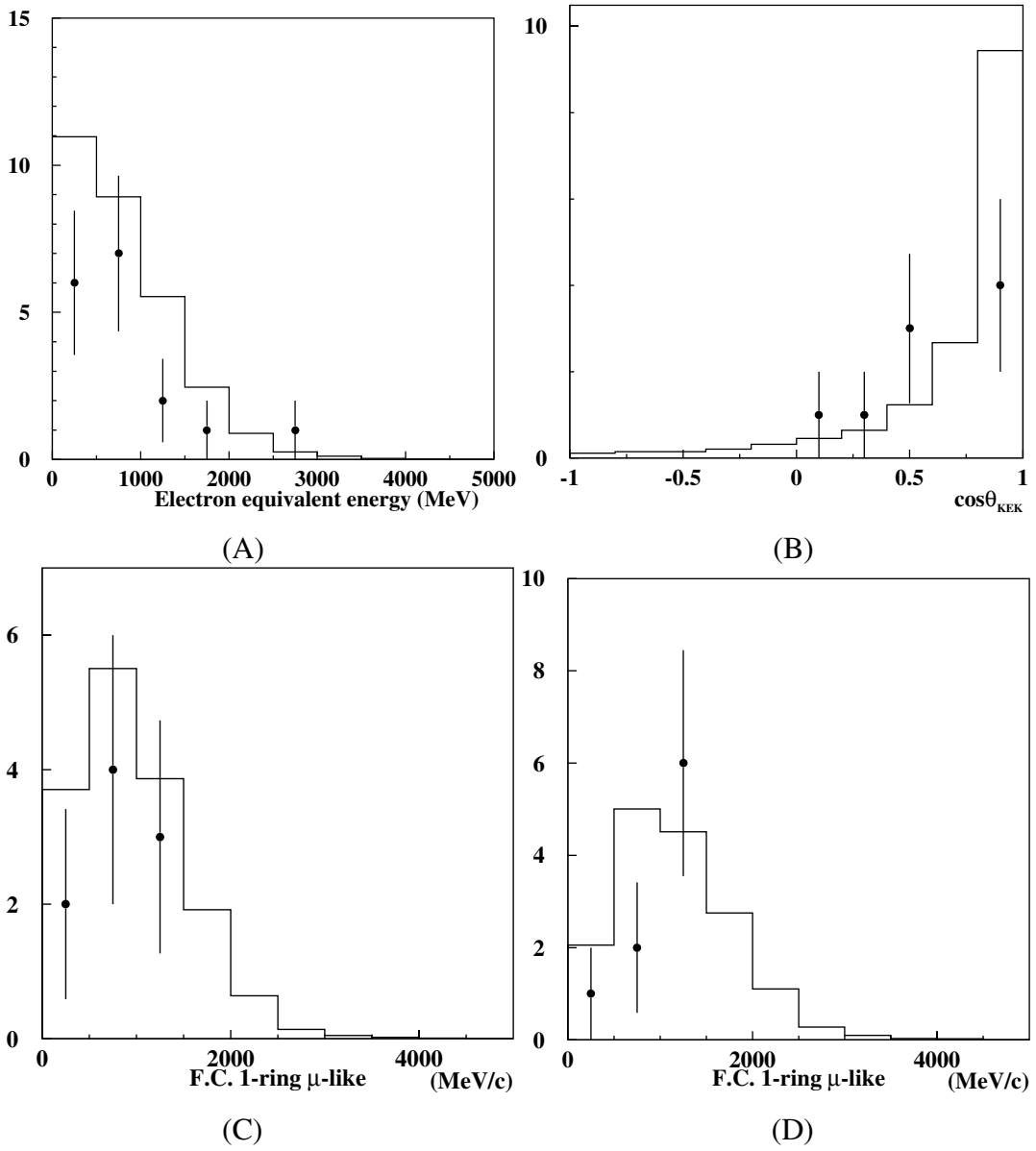

Fig. 17. Various distributions of K2K neutrino events observed at Super-Kamiokande. (A) Electron equivalent energy of all the fully contained events. (B) Opening angle between the direction of the neutrino and the observed muon. (C) Reconstructed momentum of the muon. (D) Reconstructed energy of ν assuming quasi-elastic scattering. We used the fully contained 1-ring μ-like events for figures (B) to (D). The open circles show the data and each error bar shows the statistical error. The solid histograms show the expectation assuming that there is no oscillation.

References

[1] S. Glashow, Nucl. Phys. **22**, 59 (1961);
S. Weinberg, Phys. Rev. Lett. **19**, 1264 (1967);
A. Salam, Elementary Particle Physics, ed. by N. Svartholm, Stockholm, Almquist and Wiksell (1968).

[2] K.S. Hirata *et al.*, Phys. Lett. **B205**, 416 (1988);
K.S. Hirata *et al.*, Phys.Lett. **B280**, 146 (1992);
Y. Fukuda *et al.*, Phys. Lett. **B335**, 237 (1994).

[3] D. Casper *et al.*, Phys. Rev. Lett. **66**, 2561 (1991);
R. Becker-Szendy *et al.*, Phys. Rev. **D46**, 3720 (1992).

[4] W.W.M. Allison *et al.*, Phys. Lett. **B391**, 491 (1997);
W.W.M. Allison *et al.*, Phys. Lett. **B449**, 137 (1999).

[5] Y. Fukuda *et al.*, Phys. Lett. **B433**, 9 (1998);
Y. Fukuda *et al.*, Phys. Lett. **B436**, 33 (1998);
Y. Fukuda *et al.*, Phys. Rev. Lett. **81**, 1562 (1998).

[6] K. Nishikawa, Nucl. Phys. B. (Proc. Suppl.) **77**, 198 (1999).

[7] M. Ieiri *et al.*, Proc. 1st Asian Pacific Accelerator Conference, 579 (1998).

[8] H. Sato, Proc. Particle Accelerator Conference (1999);
K. Takayama, ICFA Beam Dynamics Newsletter No. 20 (1999).

[9] Y. Yamanoi *et al.*, Proc. 15th International Conference on Magnet Technology (1997);
Y. Yamanoi *et al.*, IEEE Transactions on Applied Superconductivity **10**, 252 (2000);
Y. Suzuki *et al.*, Proc. International Conference on Accelerator and Large Experimental Physics Control Systems (ICALEPCS) (1997);
Y. Suzuki *et al.*, Proc. of ICALEPCS (1999).

[10] H. Noumi *et al.*, NIM **A398**, 399 (1997).

[11] T. Maruyama, Ph.D. Thesis, Tohoku University (2000).

[12] R. Brun *et al.*, CERN DD/EE/84-1 (1987).

[13] J.R. Sanford and C.L. Wang, BNL AGS internal reports No. BNL11299 and No. BNL11479 (1967);

C.L. Wang, Phys. Rev. Lett. **25**, 1068 (1970);
Y. Cho *et al.*, Phys. Rev. **D4**, 1967 (1971);
J.G. Asbury *et al.*, Phys. Rev. **178**, 2086 (1969);
G.J. Marmer *et al.*, Phys. Rev. **179**, 1294 (1969);
G.J. Marmer and D.E. Lundquist, Phys. Rev. **D3**, 1089 (1971);
J.V. Allaby *et al.*, CERN-TH-70-12 (1970).

[14] T.A. Gabriel *et al.*, ORNL/TM-11185;
C. Zeitnitz and T.A. Gabriel, NIM **A349**, 106 (1994).

[15] A. Suzuki *et al.*, NIM **A453**, 165 (2000).

[16] K2K collaboration, to be published.

[17] H.G. Berns and R.J. Wilkes, IEEE NS **47**, 340 (2000).

A STUDY OF CP-VIOLATION IN B^0 DECAYS

Nobu Katayama*
Institute of Particle and Nuclear Studies
High Energy Accelerator Research Organization
Oho 1–1, Tsukuba-shi, 305–0801, Japan

Representing the Belle Collaboration

ABSTRACT

We present a preliminary measurement of time-dependent CP asymmetries in B^0 decays using the Belle detector at the KEKB asymmetric e^+e^- collider. The data sample consists of $6.2\,\mathrm{fb}^{-1}$ collected at the $\Upsilon(4S)$ resonance. One of the neutral B mesons is fully reconstructed via its decay to a CP eigenstate. The flavor of the other B meson is tagged mainly with the charge of identified leptons and kaons. The time interval between the two decays is determined from the distance between the decay vertices. A maximum likelihood method is used to extract $\sin 2\phi_1$ from the asymmetry in the time interval distribution. We present a preliminary result of $\sin 2\phi_1 = 0.45^{+0.43}_{-0.44}(stat)^{+0.07}_{-0.09}(syst)$.

*E-mail address:nobu.katayama@kek.jp

1 Introduction

The CP violating effects have been observed in K_L decay.[1] Kobayashi and Maskawa proposed an elegant explanation of these effects in the three-generation Standard Model.[2] In their model, CP violation is a consequence of the complex phases in the quark mixing matrix,

$$\begin{pmatrix} V_{ud} & V_{us} & V_{ub} \\ V_{cd} & V_{cs} & V_{cb} \\ V_{td} & V_{ts} & V_{tb} \end{pmatrix}$$

The nontrivial complex phases are conventionally assigned to the furthest off-diagonal elements V_{ub} and V_{td}. Sanda and Carter pointed out that the KM model contained the possibility of rather sizable CP violating asymmetries in certain decay modes of the B mesons.[3]

Unitarity of the KM matrix implies that $\sum_i V_{ij}V_{ik}^* = \delta_{jk}$, which gives the following relation involving V_{ub} and V_{td}:

$$V_{td}V_{tb}^* + V_{cd}V_{cb}^* + V_{ud}V_{ub}^* = 0.$$

This relation can be expressed as a closed triangle in the complex plane. The three interior angles of this triangle (the Unitarity Triangle) are defined as:

$$\phi_1 \equiv \arg\frac{V_{cd}V_{cb}^*}{V_{td}V_{tb}^*}, \qquad \phi_2 \equiv \arg\frac{V_{ud}V_{ub}^*}{V_{td}V_{tb}^*}, \qquad \phi_3 \equiv \arg\frac{V_{cd}V_{cb}^*}{V_{ud}V_{ub}^*}.$$

In e^+e^- storage rings operating at the $\Upsilon(4S)$ resonance, a $B^0\bar{B}^0$ pair produced in a decay of the $\Upsilon(4S)$ remains in a coherent P-wave state until one of the B mesons decays. In this state, when a neutral B meson decays into a CP eigenstate f, there is an interference between two amplitudes, $A(B^0 \to f)$ and $A(B^0 \to \bar{B}^0 \to f)$, which gives a time-dependent CP asymmetry shown by

$$A_{CP}(\Delta t) = \frac{R(B^0 \to f;\ \Delta t) - R(\bar{B}^0 \to f;\ \Delta t)}{R(B^0 \to f;\ \Delta t) + R(\bar{B}^0 \to f;\ \Delta t)} = \eta_f \sin 2\phi_{CP} \sin(\Delta m_d \Delta t),$$

where η_f is the CP eigenvalue of f, Δm_d is the mass difference between the two B^0 mass eigenstates and Δt is the proper time difference between two B meson decays, *i.e.* $\Delta t = t_2 - t_1$, where t_1 and t_2 are the proper time for the B^0 and $\bar{B}^0$ decays, respectively. The angle ϕ_{CP} is the phase difference between the two interfering amplitudes, which is directly related to the interior angles of

the unitarity triangle. It can be shown that ϕ_{CP} is equal to ϕ_1 when $J/\psi K_S$, or another decay mode that arises from $b \to c\bar{c}s$, is used as the CP eigenstate f. This asymmetry vanishes in the time integrated rate. This is the motivation for the asymmetric beam energies in the B factories.[4]

At an asymmetric collider, Δt can be deduced from the distance, Δz between the two B^0 decay vertices along the axis of the boost, $\Delta t \approx \Delta z/(c\beta\gamma)$, where $\beta\gamma$ is the Lorentz boost factor from the asymmetric beam energies. The CP asymmetry is thus observed as an asymmetry in the distribution of the difference between the proper decay distances of the two B mesons produced in the decay of $\Upsilon(4S)$, one B decaying to the CP eigenstate and another to any final state with its flavor tagged.

2 KEKB and Belle

2.1 The KEKB asymmetric e^+e^- collider

KEKB[5] is an asymmetric e^+e^- collider of 3 km circumference, consisting of 8 GeV e^- and 3.5 GeV e^+ storage rings and an injection linear accelerator for them. The collider has one interaction point (IP) where the e^+ and e^- beams collide with a finite crossing angle of 22 mrad. The instantaneous luminosity of the KEKB collider reached $2.04\times10^{33}/\mathrm{cm}^2/\mathrm{sec}$ in July 2000. At KEKB, the average boost of the $\Upsilon(4S)$ and its daughter B mesons is $\beta\gamma \approx 0.425$ in the laboratory frame. The average distance of the two decay vertices of the B mesons is approximately 200μm.

2.2 The Belle detector

The Belle experiment at KEKB has recently completed a successful first year of operation. The Belle detector collected a total integrated luminosity of $6.8\,\mathrm{fb}^{-1}$, of which $6.2\,\mathrm{fb}^{-1}$ are taken on the $\Upsilon(4S)$ resonance and $0.6\,\mathrm{fb}^{-1}$ at 60 MeV below the resonance. A detailed description of the Belle detector can be found elsewhere.[6]

2.2.1 Charged particle tracking system

Charged particles are detected and their momenta measured by a three-layer, double sided silicon vertex detector (SVD) and a fifty layer small-cell cylindrical

drift chamber (CDC). Eighteen layers of the CDC are inclined at small angle in order to provide three-dimensional reconstruction of charged particle trajectories. The CDC is operated with a $He(50\%)+C_2H_6(50\%)$ mixture to ensure a good momentum resolution in particular for low momentum particles. The CDC covers the polar angle region between 17 and 150 degrees in the laboratory frame, where polar angle is measured with respect to the opposite direction of the positron beam. The CDC also provides the measurement of energy loss for charged particles with a resolution of $\sigma(dE/dx)= 6.9\%$. The vertex measurement is provided by the SVD. The double-sided silicon strip detectors (DSSD) are arranged in barrel configuration and cover 86% of solid angle. The three layers are at radii of 3.0, 4.5 and 6.0 cm, respectively. Each DSSD consists of 1280 ϕ strips with 25μm pitch, and 640 z strips with 84μm pitch. The resolutions of the impact parameters in the plane transverse to the beam axis (xy plane) and along the beam axis (z axis) are measured to be σ_{xy}=21$\oplus$69/($p\beta\sin^{3/2}\theta$)μm and σ_z=41$\oplus$48/($p\beta\sin^{5/2}\theta$)μm, respectively, where p is momentum of the particle measured in GeV/c and θ is the polar angle of the direction of the particle. The transverse momentum resolution is $\sigma_{p_t}/p_t = 0.0019\,p_t \oplus 0.0034$ where p_t is measured in GeV/c. The beampipe is made of double-wall beryllium of 2.3 cm radius and 1 mm thick. The tracking system is situated in a 1.5 T solenoidal magnetic field.

2.2.2 Kaon identification system

The charged kaon identification is provided by the dE/dx measurements in the CDC, aerogel Cherenkov counters (ACC) and time-of-flight scintillation counters (TOF). The ACC consists of 1188 aerogel blocks with the refractive indices between 1.01 and 1.03 depending on the polar angle. The Cherenkov light is detected by fine-mesh photomultipliers directly attached to the aerogel blocks. The effective number of photoelectrons is approximately 6 for $\beta = 1$ particles. The TOF consists of 128 plastic scintillators viewed by fine-mesh photomultipliers on both ends. The time resolution is 95 psec (rms), which provides $\pi^{\pm}/K^{\pm}$ separation up to 1.2 GeV.

The charged kaon identification probabilities are calculated from the combined response of the three systems. The efficiency for $K^{\pm}$ is $\approx$80% while the charged pion fake rate as kaon is $\approx$10% for momentum up to 3.5 GeV/c.

2.2.3 Photon detection system

The electromagnetic calorimetry (ECL) is provided by an array of 8736 CsI(Tl) crystals of 16.1 radiation lengths. The ECL covers the same angular region as the CDC. The photon energy resolution is measured, in a beam test, to be $\sigma_E/E = (1.3 \oplus 0.07/E \oplus 0.8/E^{1/4})\%$, where E is measured in GeV. Neutral pions are detected via their decay to $\gamma\gamma$. The π^0 mass resolution varies slowly with their energy, averaging $\sigma_{m_{\pi^0}}$ of 4.9 MeV/c^2. With a $\pm 3\sigma$ mass selection requirement, the overall detection efficiency, including geometric acceptance, for π^0s in the $B\bar{B}$ events is 40%.

2.2.4 Lepton identification system

Electron identification is based on the dE/dx measurements in the CDC, the response of the ACC, and the position, shape and energy deposit of CsI clusters that have been associated with the electron trajectory in the charged particle tracking system (CDC and SVD). Likelihood functions as electrons and non-electrons are constructed to discriminate between them. This is above 90% efficient for electrons and has a $\approx$0.5% fake probability for charged hadrons with momenta above 1 GeV/c.

In the return yoke of the solenoidal magnetic field are instrumented 14 layers of resistive plate counters (KLM) between 4.7 cm-thick iron plates. The KLM detects muons and K_Ls in the angular region of $20^\circ < \theta < 155^\circ$. The overall muon identification efficiency is above 90% for muons with momentum above 1.0 GeV/c with a pion fake probability of 4%.

2.2.5 K_L detection

K_L mesons are identified by the presence of energy deposits originating from hadronic interactions of the K_L in the CsI and/or iron. If there are CsI clusters associated with a candidate K_L, its direction is determined from the energy-weighted center of gravity of the energy deposit of the CsI counter alone. Otherwise, the direction is determined from the average position of the associated KLM hits. The angular resolution of the K_L direction is estimated to be $\approx 1.5^\circ$ and $\approx 3^\circ$ with and without associated CsI clusters, respectively.

2.3 Hadronic event selection

The hadronic events are selected by requiring:

- At least three "good" charged tracks be coming from the IP; where a "good" track has a minimum transverse momentum of 0.1 GeV/c and originates within 2.0 cm and 4.0 cm of the average IP in the xy plane and along the z axis.
- At least two "good" neutral clusters be observed in the barrel region of the calorimeter, where a "good" cluster is detected in the good acceptance region with an energy deposit greater than 0.1 GeV, and no charged tracks are associated with the cluster.
- A sum of all cluster energies, after a boost back into to the center-of-mass frame, and assuming they are deposited by massless particles, to be between 10% and 80% of the center-of-mass energy.
- The total visible energy, computed as the sum of the "good" tracks assuming pions and the "good" clusters in the center-of-mass frame, exceeds 20% of the center-of-mass energy.
- The absolute value of the momentum balance in z, calculated in the center-of-mass frame, to be less than 50% of the center-of-mass energy.
- The event vertex reconstructed from the "good" tracks, to be within 1.5 cm and 3.5 cm of the IP in the xy plane and along the z axis, respectively.

From Monte Carlo simulation studies, the efficiency to retain $B\bar{B}$ events is estimated to be 92.5%. For $B \to J/\psi X$ events, the efficiency is estimated to be 99.4%.

We applied slightly tighter selection criteria for the data in the earlier part of the data taking period. The tighter set of cuts gives a few percent lower efficiency for the J/ψ events.

Events passing the hadronic event selection criteria and satisfying $H_2/H_0 \leq 0.5$, where H_2 and H_0 are the second and 0-th Fox-Wolfram moments, are used in the subsequent analysis.

3 Analysis Procedures

The measurement of the CP violation asymmetry has four major steps: (1) selection of the decay of one of the neutral B mesons into a CP eigenstate, (2) determination of the flavor of the other B meson, (3) measurement of the distance Δz between the two B^0 decay vertices, and (4) extraction of the amplitude of the CP asymmetry and the value of $\sin 2\phi_1$ using an unbinned maximum likelihood fit.

We would like to determine, whenever possible, resolutions, efficiencies and wrong-tag fractions from the data. The measurements of B lifetimes and the neutral B meson mixing parameter have been made and are discussed in the following sections, as they have the same above-described steps in the analyses.

3.1 Reconstruction of the CP eigenstates

We reconstruct B^0 decays to the following CP eigenstates; $J/\psi K_S, \psi(2S)K_S, \chi_{c1}K_S$ for $CP = -1$ states and $J/\psi\pi^0, J/\psi K_L$ for $CP = +1$ states.

3.1.1 Selection of J/ψ, $\psi(2S)$, χ_{c1} and K_S

The J/ψ and $\psi(2S)$ mesons are reconstructed via their decays to $\mu^+\mu^-$ and e^+e^-. For the $J/\psi \to \mu^+\mu^-$ candidates, at least one track is positively identified as a muon by the KLM and the other is either positively identified as a muon or has a CsI energy deposit that is consistent with that of a minimum ionizing particle. For the $J/\psi \to e^+e^-$ candidates, at least one track is positively identified as an electron and the other track has an energy deposit in the CDC dE/dx system or the CsI calorimetry system that is consistent with that of an electron. For the dielectron candidates, we correct for final state radiation or Bremsstrahlung in the inner parts the detector by including the four-momentum of every photon detected within 0.05 radian of the original electron in the invariant mass calculation. The invariant mass distributions for the $J/\psi \to \mu^+\mu^-$ candidates, the $J/\psi \to e^+e^-$ candidates, and the $\psi(2S) \to \mu^+\mu^-, e^+e^-$ candidates are shown in Figures 1(a), (b) and (c), respectively. The $\psi(2S)$ is also reconstructed via its decay to $J/\psi\pi^+\pi^-, J/\psi \to \mu^+\mu^-, e^+e^-$ and the χ_{c1} via the mode $J/\psi\gamma$. Figures 2(a) and (b) show the mass difference distributions, $M_{\ell^+\ell^-\pi^+\pi^-} - M_{\ell^+\ell^-}$ and $M_{\ell^+\ell^-\gamma} - M_{\ell^+\ell^-}$.

For the $K_S \to \pi^+\pi^-$ candidates, the oppositely charged track pairs are required

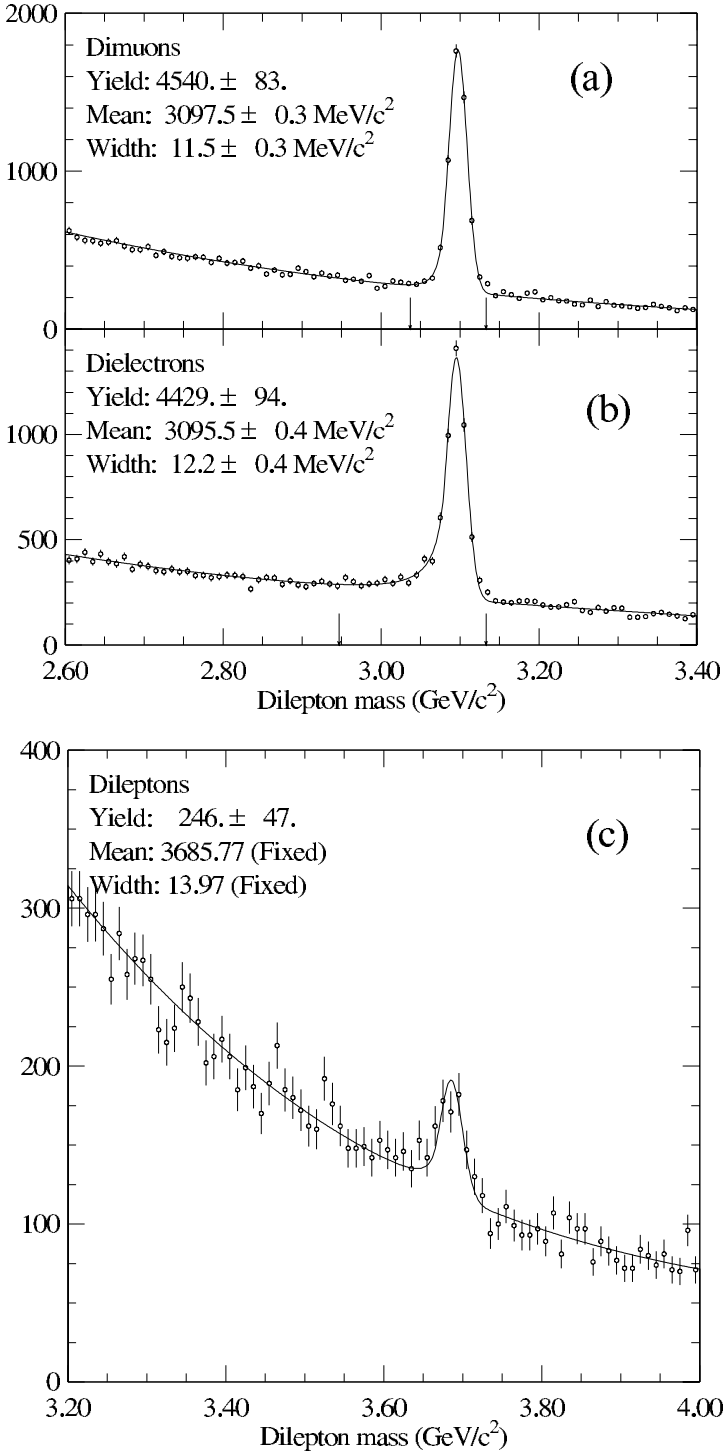

Fig. 1. The invariant mass distributions for (a) $J/\psi \to \mu^+\mu^-$, (b) $J/\psi \to e^+e^-$ and (c) $\psi(2S) \to \mu^+\mu^-$ and e^+e^-.

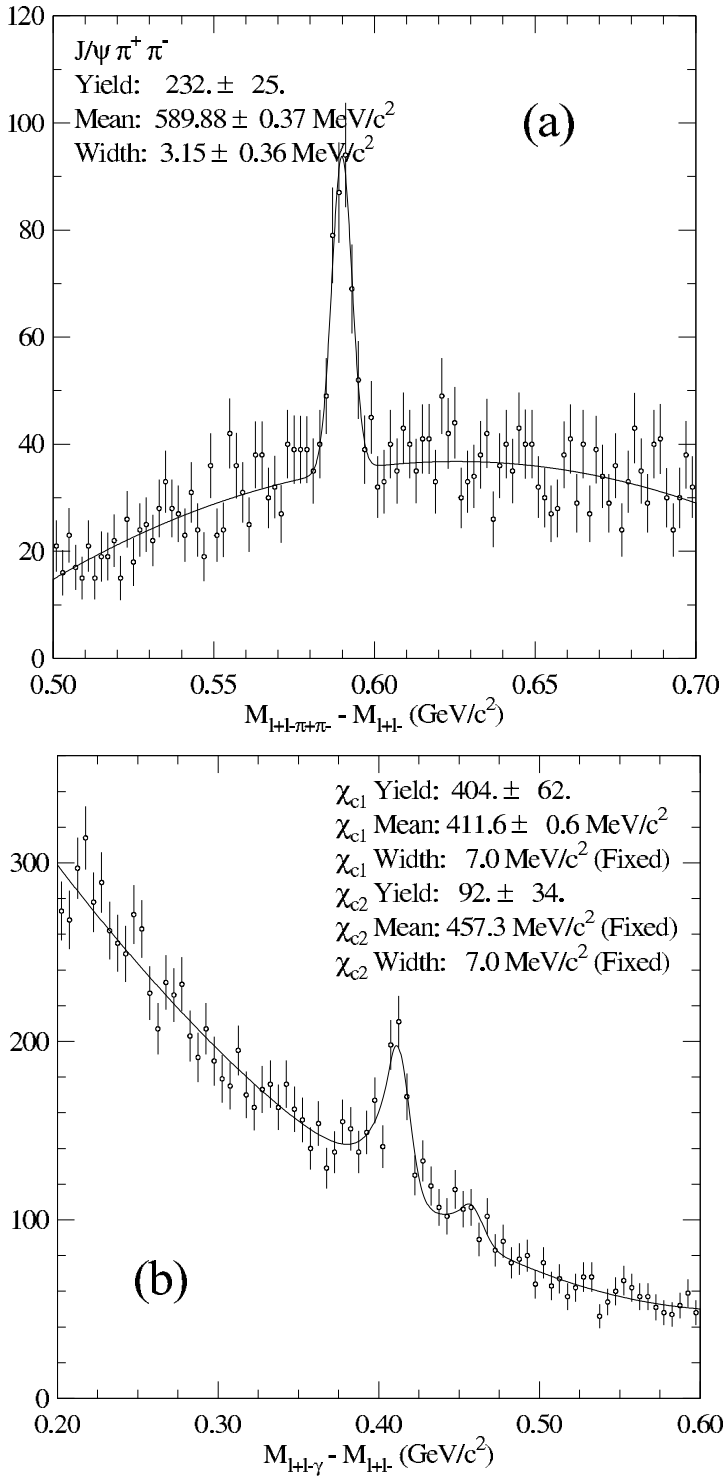

Fig. 2. The invariant mass difference distributions for (a) $M_{\ell^+\ell^-\pi^+\pi^-} - M_{\ell^+\ell^-}$ and (b) $M_{\ell^+\ell^-\gamma} - M_{\ell^+\ell^-}$.

to have an invariant mass between 482 and 514 MeV/c^2, which corresponds to $\pm 3\sigma$ around the K_S mass peak. The $K_S \to \pi^0\pi^0$ decay candidates are also used for reconstructing the $J/\psi K_S$ decay channel. The K_S are selected among photons with a minimum energy of 50 MeV and 200 MeV in the barrel and end-cap regions, respectively, by requiring, assuming that the K_S decayed at the IP, (a) a minimum π^0 momentum of 100 MeV/c, (b) $118 < M_{\gamma\gamma} < 150$ MeV/c^2, and (c) $300 < M_{\pi^0\pi^0} < 1000$ MeV/c^2. For each candidate, we determine the most probable K_S decay point by minimizing the sum of the χ^2 values from constraining each photon pair to π^0 invariant mass, while varying the K_S decay point along the K_S flight direction that is defined by the sum of four photon momenta and the IP. We then recalculate the invariant masses of the photon pairs and the π^0 and require the recalculated K_S mass to be in between 470 and 520 MeV/c^2. For the $J/\psi\pi^0$ decay mode, the π^0 candidates are selected from photons with minimum energy of 100 MeV.

3.1.2 Selection of the B candidates

To identify reconstructed B meson decays we use the beam-constrained mass, $M_{beam} \equiv \sqrt{E^2_{beam} - p^2_B}$ and the energy difference $\Delta E \equiv E_B - E_{beam}$, where E_{beam} is half of the center-of-mass energy and p_B and E_B are the B candidate's absolute three-momentum and energy calculated in the center-of-mass system. Figure 3 shows the M_{beam} distribution of the combined $B \to J/\psi K_S, K_S \to \pi^+\pi^-$; $J/\psi K_S, K_S \to \pi^0\pi^0$; $\psi(2S)K_S, K_S \to \pi^+\pi^-$; $\chi_{C1}K_S, K_S \to \pi^+\pi^-$; and $J/\psi\pi^0$ decay candidates, with a $\pm 3.5\sigma$ cut on $|\Delta E|$. The actual value of the cut varies with the decay mode; ± 40 MeV for modes with $K_S \to \pi^+\pi^-$ and ± 100 MeV for modes containing π^0s. All B meson candidates within 10 MeV from the mean of M_{beam} are considered as signal. Table 1 lists the number of signal B mesons, and the backgrounds which are estimated using the events lying outside of the signal region and from the full Monte Carlo simulation results.

3.1.3 Selection of $J/\psi K_L$

The $B^0 \to J/\psi K_L$ candidates are selected by requiring the J/ψ candidate momentum and the K_L direction to be consistent with the $B^0 \to J/\psi K_L$ two body decay hypothesis. After requiring the J/ψ momentum to be between 1.42 and 2.0 GeV/c in the center-of-mass frame, we calculate the momentum of the B

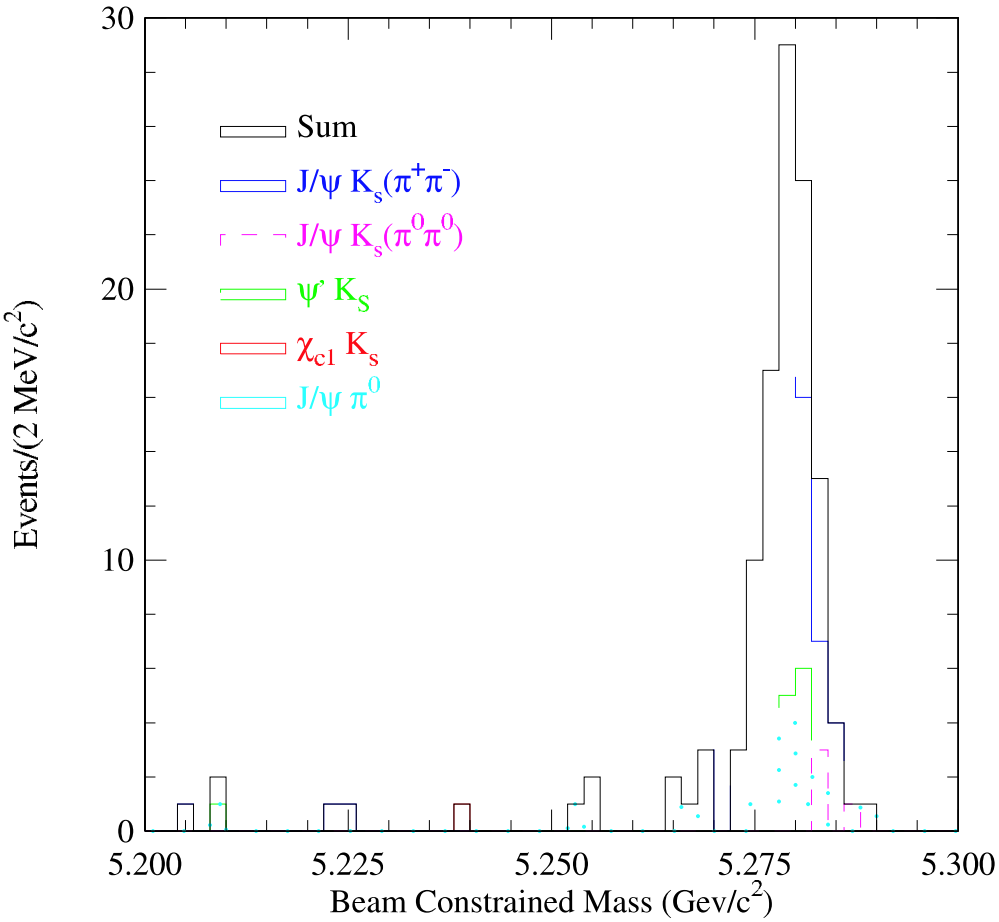

Fig. 3. The beam constrained mass distribution of the combined $B \to J/\psi K_S(\pi^+\pi^-), J/\psi K_S(\pi^0\pi^0), \psi(2S)K_S(\pi^+\pi^-), \chi_{C1}K_S(\pi^+\pi^-)$, and $J/\psi\pi^0$ decay candidates with a $\pm 3.5\sigma$ cut on $|\Delta E|$.

Table 1. Summary of the reconstructed CP eigenstates

Mode	N_{events}	$N_{background}$
$B \to J/\psi K_S,\ K_S \to \pi^+\pi^-$	70	3.4
$B \to J/\psi K_S,\ K_S \to \pi^0\pi^0$	4	0.3
$B \to \psi(2S)K_S,\ K_S \to \pi^+\pi^-,\ \psi(2S) \to \ell^+\ell^-$	5	0.2
$B \to \psi(2S)K_S,\ K_S \to \pi^+\pi^-,\ \psi(2S) \to J/\psi\pi^+\pi^-$	8	0.6
$B \to \chi_{C1}K_S,\ K_S \to \pi^+\pi^-$	5	0.75
$B \to J/\psi\pi^0$	10	1
Total	102	6.25

meson, p_B^*, using the K_L direction and the B meson mass. Figure 4 shows the p_B^* distribution. The p_B^* should be about 0.34 GeV/c for a true $B^0 \to J/\psi K_L$ candidate. Also shown are expected distributions of signal and background derived from the full Monte Carlo simulation studies. The background is found to be dominated by $B^0 \to J/\psi X$ events including $B^0 \to J/\psi K^{*0}, K^{*0} \to K_L\pi^0$ and $B^0 \to J/\psi$ non-resonant $K_L\pi^0$, which are a mixture of $CP = +1$ and $CP = -1$ eigenstates. There are 102 $J/\psi K_L$ candidates in the signal region, which is defined as $0.2 < p_B^* < 0.45\,\mathrm{GeV/c}$. By fitting the data with the expected signal and background shapes, we estimate that there are 48 background events in the signal region, of which 8 events are from $B^0 \to J/\psi K^{*0}, K^{*0} \to K_L\pi^0$ and $B^0 \to J/\psi+$ non-resonant $K_L\pi^0$.

3.2 Flavor tagging

Each event with a CP eigenstate decay candidate is classified as a B^0 or $\bar{B}^0$ tag if the rest of the event contains a signature that is specific to B^0 or $\bar{B}^0$ decays. The rest of the event is defined as the event with the daughter charged and neutral tracks of the CP eigenstate decay candidate removed.

For the tagging methods, we use the sign of the primary lepton in semi-leptonic B^0 decay, and the kaon charge which is the signature of a cascade decay $b \to c \to s$. We define the charged and neutral tracks used in reconstruction of the CP eigenstate decay mode as "CP-side" tracks, and the rest of the tracks as "tag-side" tracks. We assign the B-flavor for the tag-side B-meson (B_{tag}) using the following criteria:

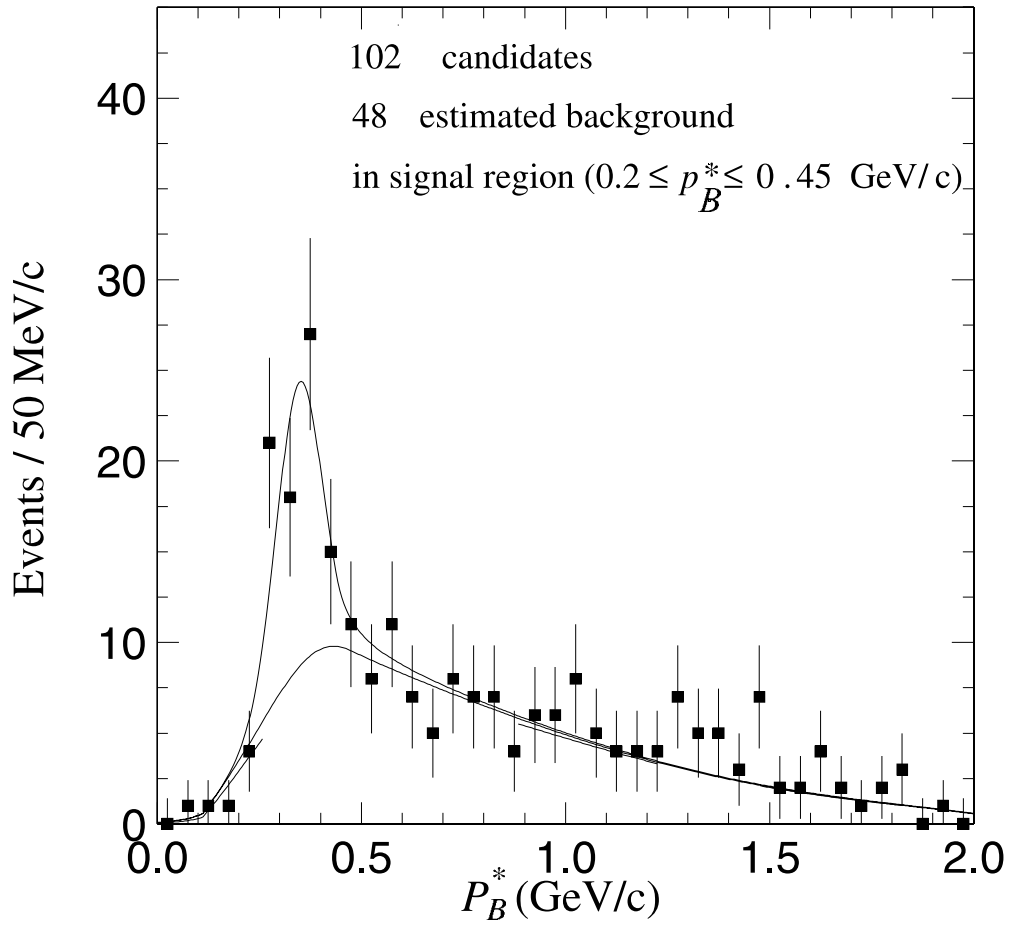

Fig. 4. The p^*_B distribution for $J/\psi K_L$ candidates with the results of the fit. The upper solid line is a sum of the signal and backgrounds. The total background (lower solid line) is divided into those coming from $J/\psi K^{*0}$, $K^{*0} \to K_L\pi^0$ and $J/\psi + \mathrm{non-resonant}\ K_L\pi^0$, and those coming from all other sources (below the dotted line).

1. High momentum lepton: If B_{tag} contains a high momentum lepton ($p^*_{lepton} >$ 1.1 GeV/c for both electrons and muons) which comes from the semileptonic decay of $B_{\rm tag}$. $B_{\rm tag} = B^0$ for ℓ^+ and $B_{\rm tag} = \bar{B}^0$ for ℓ^- are assigned. We first test whether the event contains an electron. If the event fails the test then we test whether it contains a muon. No flavor is assigned when two or more high momentum electrons or muons satisfy the criteria.

2. Charged kaon: If B_{tag} does not contain any high momentum lepton, the sum of the charges of all identified kaons in B_{tag}, Q_K is computed. $B_{\rm tag} = B^0$ for $Q_K > 0$ and $B_{\rm tag} = \bar{B}^0$ for $Q_K < 0$ are assigned.

For the above flavor tagging methods, we use the tag-side tracks satisfying $|dr| < 3$cm and $|dz| < 4$cm. We require the lepton identification probability be greater than 0.5 for electrons and 0.8 for muons, where the probabilities for electron and muon identification are calculated as mentioned previously. For charged kaons, we require the particle identification probability ratio be greater than 0.9 for K/π, less than 0.6 for e/K, and less than 0.7 for p/K.

The efficiency and wrong-tag fraction are measured using exclusively reconstructed $B \to D^{(*)}\ell\nu$ events from the same data sample. Here, we define

- Tagging efficiency: $\epsilon_{tag} = N_{tag}/N_{rec}$, where N_{rec} and N_{tag} are number of reconstructed and tagged CP events, respectively.
- Wrong-tag fraction: ω = (number of wrongly tagged events)/(total number of tagged events)

3.2.1 Measurement of wrong-tag fraction from B^0 mixing

Taking into account the wrong-tag farction, the time evolution of the opposite flavor (OF) and same flavor (SF) neutral B-meson pair is given as

$$\begin{aligned} \mathcal{P}_{OF}(\Delta t) &\propto 1 + (1-2\omega)\cos(\Delta m_d \Delta t), \\ \mathcal{P}_{SF}(\Delta t) &\propto 1 - (1-2\omega)\cos(\Delta m_d \Delta t). \end{aligned}$$

The wrong-tag fraction determines the oscillation amplitude of the OF-SF asymmetry,

$$A_{mix} = \frac{\mathcal{P}_{OF} - \mathcal{P}_{SF}}{\mathcal{P}_{OF} + \mathcal{P}_{SF}} = (1-2\omega)\cos(\Delta m_d \Delta t).$$

We fit the time evolution of the OF and SF events simultaneously and measure the wrong-tag fraction.

We use the following decay modes:

- $B^0 \to D^{*-}\ell^+\nu$, $D^{*-} \to \bar{D}^0\pi^-$
  - $\bar{D}^0 \to K^+\pi^-$
  - $\bar{D}^0 \to K^+\pi^-\pi^0$
  - $\bar{D}^0 \to K^+\pi^+\pi^-\pi^-$
- $B^0 \to D^-\ell^+\nu$, $D^- \to K^+\pi^-\pi^-$

The vertex position of the $D^{(*)}\ell\nu$ is determined in the following way. First, we fit the D meson vertex using the K and π tracks, where the $K\,\pi$ invariant mass is constrained to the world average D mass. For the $K\pi\pi^0$ mode, the D mass constraint is not used. Then, the ℓ and D tracks are fit to form the B vertex. The slow pion track from the D^* is not used in the fit, as it does not help to improve the B vertex resolution.

We apply the flavor tagging methods described above to the tag-side, treating the tracks used in the reconstruction of the $D^{(*)}\ell\nu$ decay as the CP-side tracks. To reconstruct the tag-side vertex position of the mixing events, we use the same method as in an analysis to be described in detail later.

We measure the wrong-tag fraction together with the mixing parameter Δm_d by fitting the Δz distribution of the SF and OF events. Figure 5 shows the OF–SF asymmetries as a function of Δt for tagged $D^{*\mp}\ell^\pm\nu$ and $D^{\mp}\ell^\pm\nu$ events together with the results of the fit.

The results of the fit are

$$\begin{aligned} \Delta m_d &= 0.488 \pm 0.026\,\mathrm{ps}^{-1}, \\ \omega_{lepton} &= 0.071 \pm 0.019(stat), \\ \omega_K &= 0.199 \pm 0.021(stat). \end{aligned}$$

Using the same $D^{(*)}\ell\nu$ sample, the tagging efficiencies are also determined.

$$\begin{aligned} \epsilon_{lepton} &= 0.142 \pm 0.005(stat) \pm 0.020(sys), \\ \epsilon_K &= 0.279 \pm 0.007(stat) \pm 0.041(sys). \end{aligned}$$

We estimate the systematic errors of the ω's due to uncertainties in the response function, backgrounds, and Monte Carlo parameters used in the fit. The total

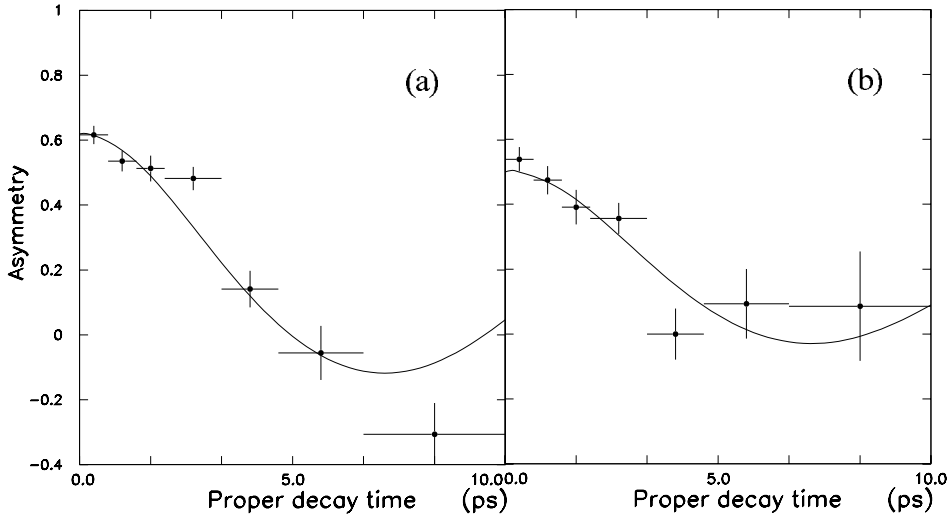

Fig. 5. The $B^0 - \bar{B}^0$ mixing asymmetry as a function of the proper time interval Δt between the two neutral B meson decays, (a) for $D^*\ell$, (b) for $D^+\ell$ decays. Also shown are the results of the fit.

systematic error from these sources are ± 0.018 and ± 0.032 for ω_{lepton} and ω_K, respectively.

The wrong-tag fraction is also measured using the time-integrated number of the OF and SF events in the $D^{(*)\mp}\ell^{\pm}\nu$ sample. Taking into account the B^0-$\bar{B}^0$ mixing effect, ω is determined by the equations

$$\omega = \frac{\chi_{obs} - \chi_d}{1 - 2\chi_d}, \qquad \chi_d = \frac{\tau_{B^0}^2 \Delta m_d^2}{2(1 + \tau_{B^0}^2 \Delta m_d^2)}.$$

where $\chi_{obs} = N_{SF}/(N_{OF} + N_{SF})$. Using $\chi_d = 0.172 \pm 0.010$, we find that both results are consistent within errors.

As a further systematic check, we obtain the wrong-tag fractions in the $B^{\pm} \to J/\psi K^{\pm}$ events. Since $B^{\pm}$ does not mix and the $B^{\pm} \to J/\psi K^{\pm}$ sample is almost free from background, we can measure the wrong-tag fractions with small systematic errors. On the other hand, ω's for $B^{\pm}$ can be different from those of B^0 because the decay modes are different. For example, D^0 and $D^{\pm}$ inclusive production fractions are different. Monte Carlo simulation studies show ω's of $B^{\pm}$ are 2 to 3% smaller than those of B^0. We measure $\omega^{\pm}_{lepton} = 0.026 \pm 0.025(stat)$ and $\omega^{\pm}_K = 0.129 \pm 0.036(stat)$. We observe a larger difference between B^0 and $B^{\pm}$ ωs than that from the Monte Carlo simulation studies.

Based on the above studies, we conservatively take the difference between the measured ω's for B^0 and $B^\pm$ as the systematic errors on the ω's, and use in the following analysis:

$$\begin{aligned} \omega_{\ell epton} &= 0.071 \pm 0.045(total), \\ \omega_K &= 0.199 \pm 0.070(total). \end{aligned}$$

The results are summarized in Table 2 for the data and in Table 3 for the Monte Carlo simulation results.

Table 2. Summary of the tagging efficiencies (ϵ_{tag}), wrong-tag fractions (ω_{tag}), and effective tagging efficiencies (ϵ_{eff}) for the data.

	mode	ϵ_{tag} (data)	ω_{tag} (data)	ϵ_{eff} (data)
B^0	lepton	0.142 ± 0.021	0.071 ± 0.045	0.105 ± 0.027
	kaon	0.279 ± 0.042	0.199 ± 0.070	0.101 ± 0.049
	Total	0.421 ± 0.047	0.150 ± 0.051	0.206 ± 0.056
$B^\pm$	lepton	0.127 ± 0.019	0.026 ± 0.025	0.114 ± 0.021
	kaon	0.282 ± 0.026	0.129 ± 0.036	0.155 ± 0.033
	Total	0.409 ± 0.032	0.095 ± 0.033	0.269 ± 0.039

Table 3. Summary of the tagging efficiencies (ϵ_{tag}), wrong-tag fractions (ω_{tag}), and effective tagging efficiencies (ϵ_{eff}) from the Monte Carlo simulation studies.

	mode	ϵ_{tag} (MC)	ω_{tag} (MC)	ϵ_{eff} (MC)
B^0	lepton	0.123	0.088	0.084
	kaon	0.275	0.161	0.127
	Total	0.398	0.138	0.201
$B^\pm$	lepton	0.124	0.088	0.084
	kaon	0.291	0.126	0.162
	Total	0.414	0.108	0.246

In addition to the above tagging methods we also use the following tagging methods; (3) Mid-momentum lepton: If the event contains an identified lepton in the momentum range $0.6 < p^*_\ell < 1.1$ GeV/c, we use the missing momentum as an

approximation of the ν momentum. If $|\mathbf{p}^*_\ell + \mathbf{p}^*_\nu| > 2.0$ GeV/c, we assume the event contains a $b \to c\ell\nu$ decay and assign its flavor based on the charge of the lepton as in the high momentum lepton method. (4) Soft pion: If the event contains a low momentum ($p^* < 200$MeV/c) charged track consistent with being a π from the $\bar{B}^0 \to D^{*+}$X, $D^{*+} \to D^0\pi^+$ decay chain, we assign the flavor of the event as $B^0(\bar{B}^0)$ for π^- (π^+). The effective tagging efficiency of the mid-momentum lepton (soft pion) method is estimated to be 0.50% (0.71%) from the Monte Carlo simulation studies and the wrong-tag fraction, 29% (34%).

The total effective tagging efficiency is estimated to be 21.8 $\pm$5.6%.

We find a total of 98 tagged events, of which 14 events were tagged by the high momentum e tag, 12 by high momentum μ, 48 by $K^\pm$, 3 by medium momentum e, 3 by medium momentum μ, and 18 by soft π. Table 4 summarizes the tagged events with reconstructed B candidates in various CP eigenstates.

Table 4. Summary of the tagged events with reconstructed CP eigenstates

Mode	N_{events}
$B \to J/\psi K_S, K_S \to \pi^+\pi^-$	40
$B \to J/\psi K_S, K_S \to \pi^0\pi^0$	4
$B \to \psi(2S)K_S, K_S \to \pi^+\pi^-, \psi(2S) \to \ell^+\ell^-$	2
$B \to \psi(2S)K_S, K_S \to \pi^+\pi^-, \psi(2S) \to J/\psi\pi^+\pi^-$	3
$B \to \chi_{C1}K_S, K_S \to \pi^+\pi^-$	3
$B \to J/\psi\pi^0$	4
$B \to J/\psi K_L$	42
Total	98

3.3 Vertexing

The proper time difference, Δt, is given by $\Delta t \simeq \Delta z/(c\beta\gamma)$ and Δz is the distance between the decay vertices of the two B mesons along the boost axis. The vertices for the CP-side are reconstructed from the leptons from the J/ψ, using the constraint that the tracks are coming from the IP profile smeared with finite B flight length in the r-ϕ plane. We use leptons only if there are sufficient numbers of SVD hits associated using the Kalman filtering technique; *i.e.* with both z and r-ϕ hits in at least one layer and with two or more z hits in total. The IP

profile is calculated offline for every accelerator fill using hadronic events. The typical size of the IP profile is 100μm in the horizontal direction (x), 5μm in the vertical direction (y) and 3000μm in z. Because of the flat nature of the beam profile, the size in y is determined from the average luminosity, the beam current and the width of the measured vertex distribution in the x-coordinate. The efficiency of the vertex reconstruction is estimated to be 96% with $B^{\pm} \to J/\psi K^{\pm}$ and $B^0 \to J/\psi K^{*0}(\to K^{\pm}\pi^{\mp})$ events. The measured reconstruction efficiency is consistent with the expectation from the SVD acceptance and hit-matching efficiency.

The algorithm for tag-side vertex reconstruction is carefully chosen to minimize effects from long-lived particles, secondary vertices from charmed hadrons and poorly-reconstructed tracks. Among charged tracks remaining after the reconstruction of the CP-side, we use tracks with SVD hits (the same condition as that for the CP side) with an impact parameter with respect to the IP center of less than 1 mm in the r-ϕ plane, and less than 2 mm from the CP-side vertex in z. Tracks are also removed if they form a K_S candidate satisfying the K_S selection criteria and $|M_{K_S} - M_{\pi^+\pi^-}| < 15\,\mathrm{MeV}/c^2$; or if the track has a large tracking error in the z direction ($\sigma_z > 0.5\,\mathrm{mm}$); or if the distance between the track and the reconstructed CP-side vertex is too large ($\delta z > 1.8\,\mathrm{mm}$ or $\delta r > 0.5\,\mathrm{mm}$). The remaining tracks are used to reconstruct the tag-side vertex with the IP constraint. The track with the largest χ^2 is removed from the fit if the reduced χ^2 (χ^2/ndf, where ndf is the number of degrees of freedom) of the vertex fit is greater than 20. In the case that such a track is the lepton which is used to tag the flavor of the event, however, we keep the lepton and remove the track with the second largest χ^2. This procedure is iterated until the reduced χ^2 becomes less than 20. If the number of remaining tracks becomes one, we impose a tighter requirement to ensure the quality of the vertex fitted with one track and the IP constraint; *i.e.* χ^2/ndf less than 6 and the momentum of the track greater than $0.6\,\mathrm{GeV}/c$. The reconstruction efficiency is measured to be 96% using $B^{\pm} \to J/\psi K^{\pm}$ and $B^0 \to J/\psi K^*(\to K^{\pm}\pi^{\mp})$ events.

3.3.1 Resolution function

The resolution function, $R_{sig}(\Delta t)$ is parameterized as the sum of two Gaussians:

$$R_{sig}(\Delta t) = (1-f_{tail})\frac{1}{\sqrt{2\pi}\sigma_{\Delta t}}e^{-\frac{(\Delta t-\mu_{\Delta t})^2}{2\sigma^2_{\Delta t}}} + f_{tail}\frac{1}{\sqrt{2\pi}\sigma^{\Delta t}_{tail}}e^{-\frac{(\Delta t-\mu^{\Delta t}_{tail})^2}{2(\sigma^{\Delta t}_{tail})^2}},$$

where f_{tail} is the fraction of the tail part of the resolution function, and $\sigma_{\Delta t}$, $\sigma^{\Delta t}_{tail}$, $\mu_{\Delta t}$ and $\mu^{\Delta t}_{tail}$ are the proper time difference resolutions and the shift in the mean value of the proper time difference for the main part and the tail part of the resolution function, respectively. f_{tail} is determined to be 0.04 ± 0.04 in the lifetime measurement using the $B \to \bar{D}^*\ell^+\nu$ sample with the same resolution function. $\mu_{\Delta t}$ and $\mu^{\Delta t}_{tail}$ originate from the shift in the mean value of the Δz measurement and are discussed below.

The proper time difference resolution, $\sigma_{\Delta t}$ (and $\sigma^{\Delta t}_{tail}$) is calculated event by event and is a convolution of the Δz resolution, $\sigma_{\Delta z}$, and the error due to the kinematic approximation ($\Delta t \approx \frac{\Delta z}{c(\beta\gamma)}$, $(\beta\gamma) = \frac{p_z(\Upsilon)}{m(\Upsilon)}$), σ_K:

$$\sigma_{\Delta t} = \sqrt{(\frac{\sigma_{\Delta z}}{c(\beta\gamma)})^2 + \sigma_K^2},$$
$$\sigma^{\Delta t}_{tail} = \sqrt{(\frac{\sigma^{\Delta z}_{tail}}{c(\beta\gamma)})^2 + (\sigma^K_{tail})^2}.$$

The σ_K and σ^K_{tail} are determined to be $\sigma_K = 0.30 \pm 0.03$ ps and $\sigma^K_{tail} = 0.0^{+0.4}_{-0.0}$ ps from the Monte Carlo simulation studies as they are independent of the detector performance.

The Δz resolution $\sigma_{\Delta z}$ ($\sigma^{\Delta z}_{tail}$) is calculated from the vertex resolutions of the two B mesons, σ_z^{CP} and σ_z^{tag}:

$$\sigma^2_{\Delta z} = S^2_{det}(\sigma_z^{CP})^2 + (S^2_{det} + S^2_{charm})(\sigma_z^{tag})^2$$
$$(\sigma^{\Delta z}_{tail})^2 = (S^{det}_{tail})^2(\sigma_z^{CP})^2 + \{(S^{det}_{tail})^2 + (S^{charm}_{tail})^2\}(\sigma_z^{tag})^2$$

where S_{charm} and S^{charm}_{tail} are scaling factors for the degradation of the vertex resolution of the tagging side B meson due to contamination of the charm daughters, and S_{det} and S^{det}_{tail} are the global scaling factors due to the systematic uncertainties in the vertex resolutions (σ_z^{CP} and σ_z^{tag}) computed from the track helix errors in the vertex fits. We find the S_{charm} and S^{charm}_{tail} to be $S_{charm} = 0.42^{+0.08}_{-0.09}$ and

$S_{tail}^{charm} = 0.0^{+1.1}_{-0.0}$ from the Monte Carlo simulation studies. The S_{det} and S_{tail}^{det} must be determined from the data as they depend on the detector performance. S_{det} is determined using a $D^0 \to K^-\pi^+$ sample. The production vertex of the the D^0 is measured using the primary tracks in the same hemisphere as the D^0 candidate with the IP constraint. The distance between the D^0 decay vertex and the production vertex in the z direction is fit using the same resolution function and known D^0 lifetime to obtain S_{det}. We find $S_{det} = 1.00 \pm 0.03$ for the data and $S_{det} = 1.23 \pm 0.02$ from the Monte Carlo simulation studies of the D^0 sample. As we find $S_{det} = 1.16 \pm 0.03$ for $B \to J/\psi K$ Monte Carlo sample, we scale the S_{det} to be $S_{det} = (1.00 \pm 0.03) \cdot (1.16 \pm 0.03)/(1.23 \pm 0.02) = 0.94 \pm 0.04$. S_{tail}^{det} is determined to be 2.4 ± 0.6 in the measurement of the B lifetime using the $B \to \bar{D}^* \ell^+ \nu$ sample.

A small fraction of events have large reduced χ^2s. We find that the errors of the vertices computed from the errors of the track helix parameters in the vertex fits underestimate the vertex resolution and in fact, that the vertices with large χ^2s have worse resolution than those estimated. In order to take into account this effect, we introduce the effective vertex resolutions $\tilde{\sigma}_z^{CP}$ and $\tilde{\sigma}_z^{tag}$ when χ^2/ndf is greater than 3:

$$\begin{aligned}
(\tilde{\sigma}_z^{CP})^2 &\equiv [1 + \alpha_{CP}\{(\chi^2/ndf)_{CP} - 3\}](\sigma_z^{CP})^2 : \ (\chi^2/ndf)_{CP} > 3, \\
(\tilde{\sigma}_z^{tag})^2 &\equiv [1 + \alpha_{tag}\{(\chi^2/ndf)_{tag} - 3\}](\sigma_z^{tag})^2 : \ (\chi^2/ndf)_{tag} > 3,
\end{aligned}$$

where $(\chi^2/ndf)_{CP}$ and $(\chi^2/ndf)_{tag}$ are the reduced χ^2 of the vertex fits for the CP- and tag-side B decay vertices, respectively.

As mentioned above, $\mu_{\Delta t}$ (and $\mu_{tail}^{\Delta t}$) originates from the shift of the mean of the Δz measurements, $\mu_{\Delta z}$ (and $\mu_{tail}^{\Delta z}$):

$$\begin{aligned}
\mu_{\Delta t} &\equiv \frac{\mu_{\Delta z}}{c(\beta\gamma)}, \\
\mu_{tail}^{\Delta t} &\equiv \frac{\mu_{tail}^{\Delta z}}{c(\beta\gamma)}.
\end{aligned}$$

This shift of the Δz, $\mu_{\Delta z}$ and $\mu_{tail}^{\Delta z}$, is caused by the contamination of the charm daughters in the vertex reconstruction of the tagging side B meson and is correlated with the σ_z^{tag}:

$$\begin{aligned}
\mu_{\Delta z}(\sigma_z^{tag}) &= \mu_0 + \alpha_\mu \sigma_z^{tag}, \\
\mu_{tail}^{\Delta z}(\sigma_z^{tag}) &= \mu_{tail}^0 + \alpha_{tail}^\mu \sigma_z^{tag}.
\end{aligned}$$

The μ_0 and α_μ are determined to be $\mu_0 = -6 \pm 4$ μm and $\alpha_\mu = -0.17 \pm 0.06$ using the Monte Carlo simulation. Since α^{μ}_{tail} is found to be consistent with zero, $\mu^{\Delta z}_{tail}$ is fixed at the value -160 μm determined from the Monte Carlo simulation studies.

Figure 6 shows the sum of event-by-event resolution functions described above, over 300 $B^{\pm} \to J/\psi K^{\pm}$ events. The width of this distribution is dominated by the main Gaussian ($1 - f_{tail} = 0.96 \pm 0.04$); we find $\bar{\sigma} \approx 1.11$ ps, $\bar{\sigma}_{tail} \approx 2.24$ ps and $\bar{\mu} = -0.19$ ps, where "$\bar{\ }$" indicates the average over all events. The μ_{tail} is fixed to -1.25 ps based on the Monte Carlo simulation studies.

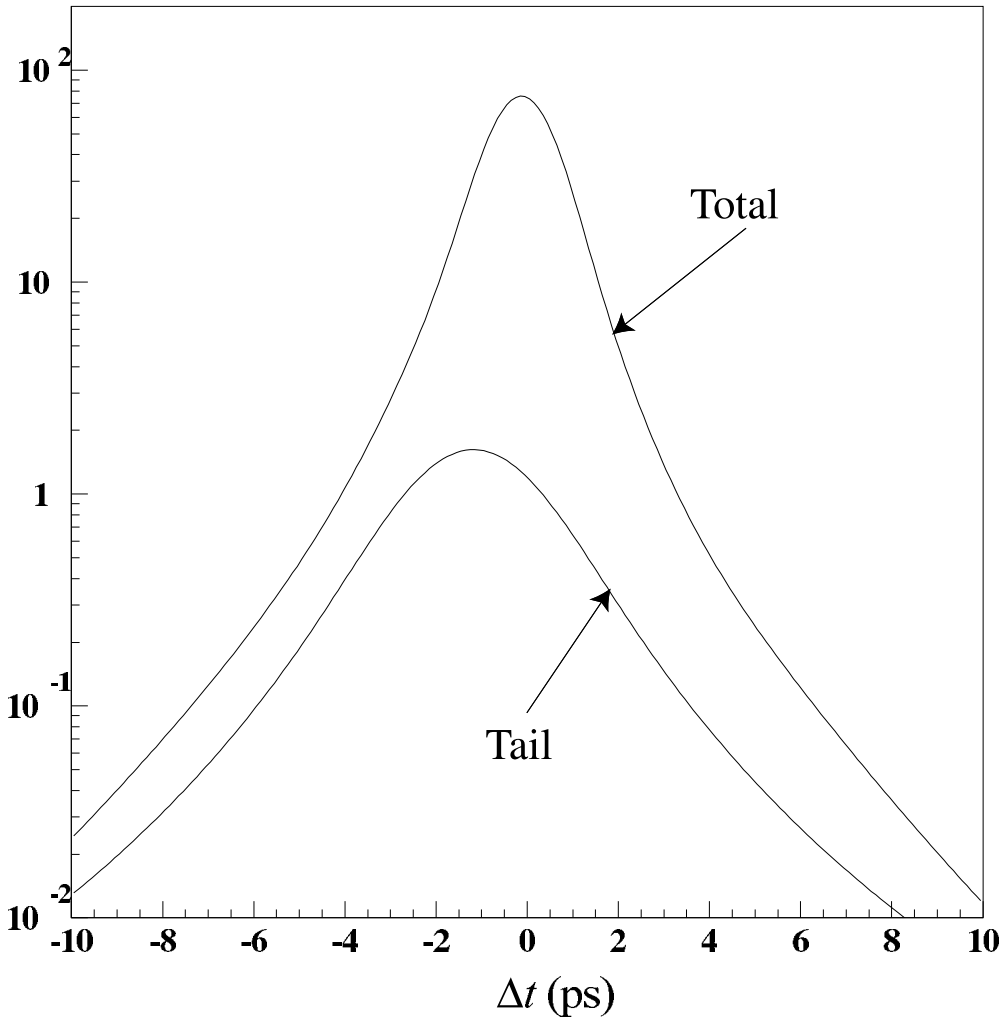

Fig. 6. The sum of event-by-event resolution functions of over 300 $B^{\pm} \to J/\psi K^{\pm}$ events, showing the average shape of the resolution function.

3.3.2 Measurements of B lifetimes

Using the vertex reconstruction algorithm and the resolution function described in the previous sections, we measure lifetimes of neutral and charged B mesons. Figures 7 and 8 show Δt distributions of decay modes that involve J/ψ with the result of the fit. Table 5 summarizes the results. The results for different decay modes of the B are consistent with each other and are in good agreement with the world average.

Table 5. Summary of B meson lifetime measurements

Decay mode	Lifetime (ps)
$\bar{B}^0 \to D^{*+}\ell^-\nu$	$1.50 \pm 0.06^{+0.06}_{-0.04}$
$\bar{B}^0 \to D^{*+}\pi^-$	$1.55^{+0.18}_{-0.17}{}^{+0.10}_{-0.07}$
$\bar{B}^0 \to D^{+}\pi^-$	$1.41^{+0.13}_{-0.12} \pm 0.07$
$\bar{B}^0 \to J/\psi \bar{K}^{*0}$	$1.56^{+0.22}_{-0.19}{}^{+0.09}_{-0.15}$
Combined	$1.50 \pm 0.05 \pm 0.07$
$\bar{B}^0 \to J/\psi K_S$	$1.54^{+0.28}_{-0.24}{}^{+0.11}_{-0.19}$
$\bar{B}^0 \to J/\psi K_L$	$1.28^{+0.36}_{-0.35}$
$B^- \to D^{*0}\ell^-\nu$	$1.54 \pm 0.10^{+0.14}_{-0.07}$
$B^- \to D^{0}\pi^-$	$1.73 \pm 0.10 \pm 0.09$
$B^- \to J/\psi K^-$	$1.87^{+0.13}_{-0.12}{}^{+0.07}_{-0.14}$
Combined	$1.70 \pm 0.06^{+0.11}_{-0.10}$

3.4 Maximum likelihood

An unbinned maximum likelihood method is used to extract the best value for $\sin 2\phi_1$. The probability density function expected for the signal distribution with a CP eigenvalue of η_f is given by:

$$Sig(\Delta t, \eta_f, q) = \frac{1}{\tau_{B^0}} \exp(-|\Delta t|/\tau_{B^0}) \times (1 - q(1-2\omega)\eta_f \sin 2\phi_1 \sin(\Delta m_d \Delta t))$$

where $q = 1(-1)$ if the tag is $B^0(\bar{B}^0)$ and ω depends on the flavor tagging method as given in the previous section. The values of τ_{B^0} and Δm_d are fixed to the world averages,1.548 ± 0.032 ps and 0.472 ± 0.017 ps^{-1}, respectively. By investigating events in background dominated regions (the side bands in the ΔE and

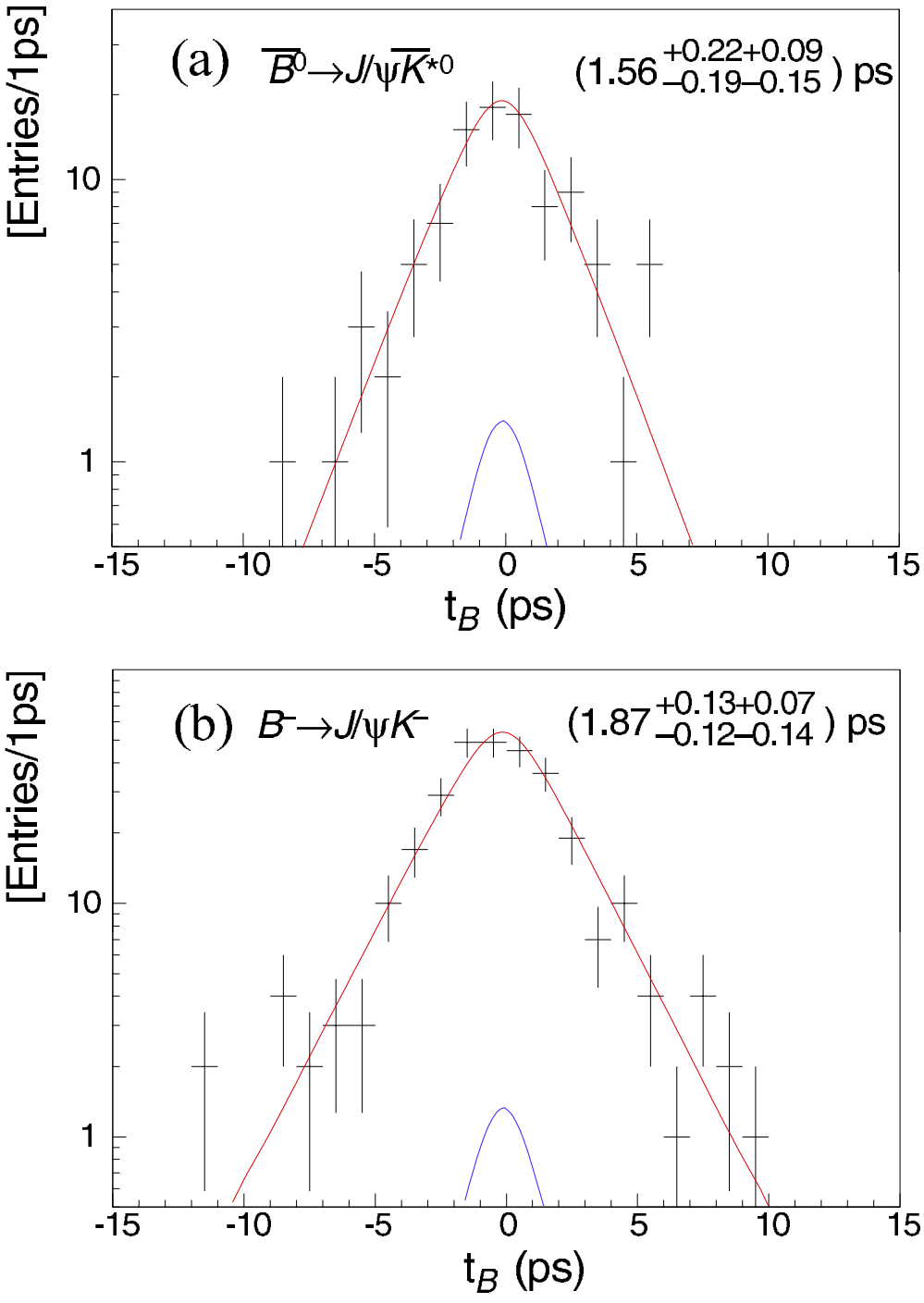

Fig. 7. Δt distributions and the results of the fit for (a) $\bar{B}^0 \to J/\psi \bar{K}^{*0}$, (b) $B^- \to J/\psi K^-$. The lower solid curve represents the background distribution.

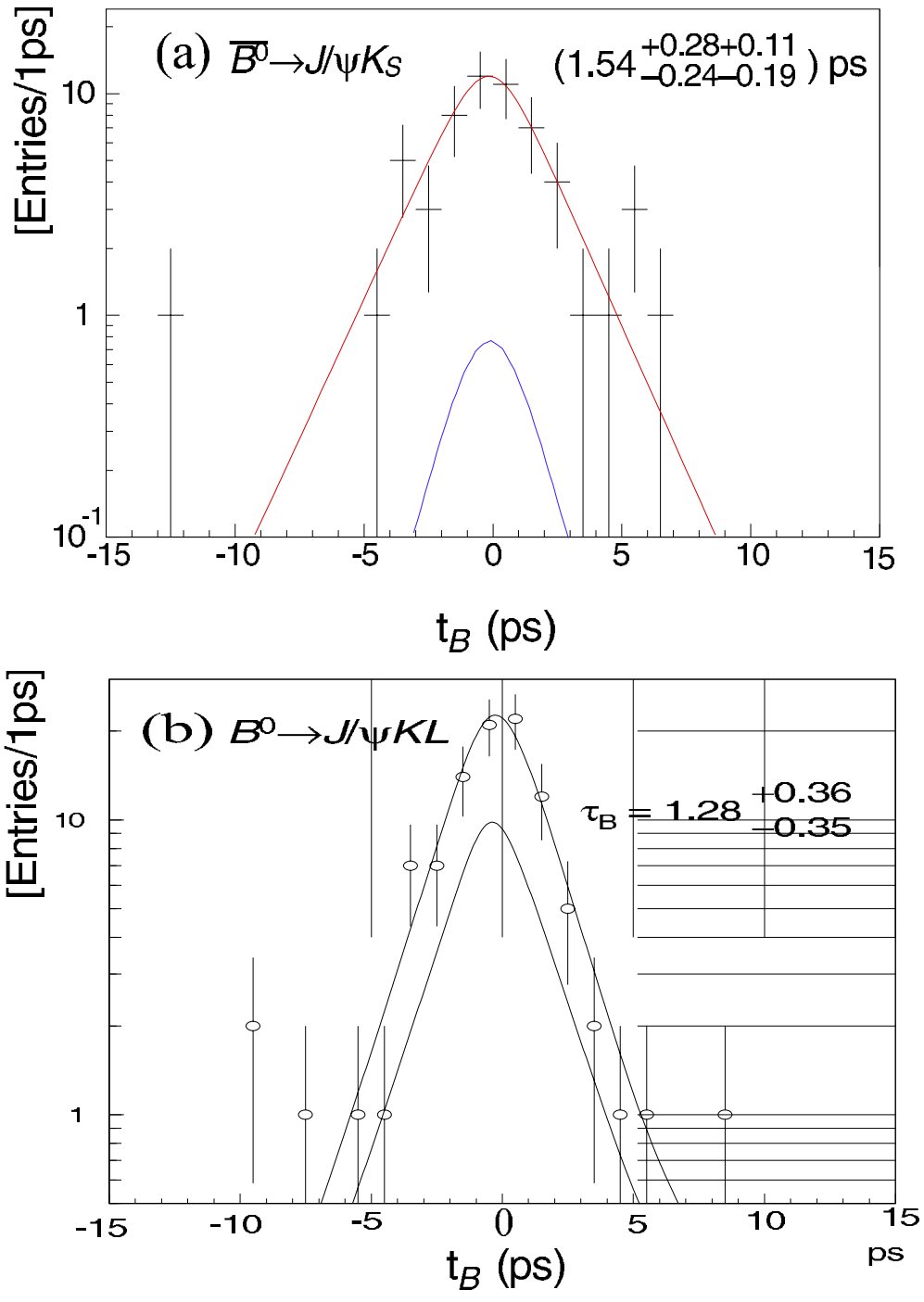

Fig. 8. Δt distributions and the results of the fit for (a) $\bar{B}^0 \to J/\psi K_S$, (b) $\bar{B}^0 \to J/\psi K_L$. The lower solid curve represents the background distribution.

M_{beam} two dimensional plots), we find that the probability density function for the background events is consistent with

$$Bkg(\Delta t) = \frac{1}{2\tau_{bkg}} \exp(-|\Delta t|/\tau_{bkg})$$

where $\tau_{bkg} = 0.73 \pm 0.12$ ps, except for the case of $B^0 \to J/\psi K_L$ candidates. The likelihood of an event, i, is calculated as:

$$\rho_i = p_{sig} \int_{-\infty}^{+\infty} Sig(s, \eta_f, q) R(\Delta t - s) ds + (1 - p_{sig}) \int_{-\infty}^{+\infty} Bkg(s, \eta_f, q) R(\Delta t - s) ds$$

where p_{sig} is the probability for the event being a signal, and $R(\Delta t)$ is the resolution function described in the previous section. The log-likelihood, $-\sum_i ln\rho_i$ is calculated by summing over all candidate events. The most probable $\sin 2\phi_1$ value is found by scanning over $\sin 2\phi_1$ values to minimize the log likelihood function.

We perform a simultaneous fit to $CP = -1$ and $CP = +1$ candidate events to extract the $\sin 2\phi_1$ value. Figure 9(a) shows the log-likelihood as a function of $\sin 2\phi_1$ for a total of 98 $CP = -1$ and $CP = +1$ candidate events. The log-likelihood for $CP = -1$ and $CP = +1$ events are shown separately. We find $\sin 2\phi_1 = 0.45^{+0.43}_{-0.44}$. To display the results of the fit, $dN/d(\Delta t)$ for $q = +1$ and $dN/d(-\Delta t)$ for $q = -1$ for $\eta_f = -1$ and $dN/d(-\Delta t)$ for $q = +1$ and $dN/d(\Delta t)$ for $q = -1$ for $\eta_f = +1$ are combined so that the distribution becomes approximately proportional to $\exp(-|\Delta t|/\tau_{B^0})(1 + (1 - 2\omega) \sin 2\phi_1 \sin(\Delta m_d \Delta t))$, as shown in Figure 9(b).

The results of the fit to the tagged events of various CP modes are summarized in Table 6. To display the fitted results, the $dN/d\Delta t$ distribution for $q = +1$ events and $dN/d(-\Delta t)$, $q = -1$ are added. Figure 10(a) and (b) show the results for only $J/\psi K_S, K_S \to \pi^+\pi^-$ events and for all $CP = -1$ events combined. Figure 11 shows the results for $CP = +1$ events, *i.e.* $J/\psi K_L$ and $J/\psi \pi^0$. In fitting to $J/\psi K_L$ candidate events, the background due to $J/\psi K_L \pi^0$, which amounts to $\approx$ 17% of the total background, is taken to be a mixture of $CP = -1(73\%)$ and $CP = +1(27\%)$ states, based on the results of a $B \to J/\psi K_S \pi^0$ analysis. A fit to 52 events in the $J/\psi K_L$ sideband ($1.0 > p_B^* > 2.0$ GeV/c region), where the non-CP $J/\psi X$ events dominate, gives the result, $\sin 2\phi_1 = 0.02^{+0.48}_{-0.49}$, consistent with null asymmetry.

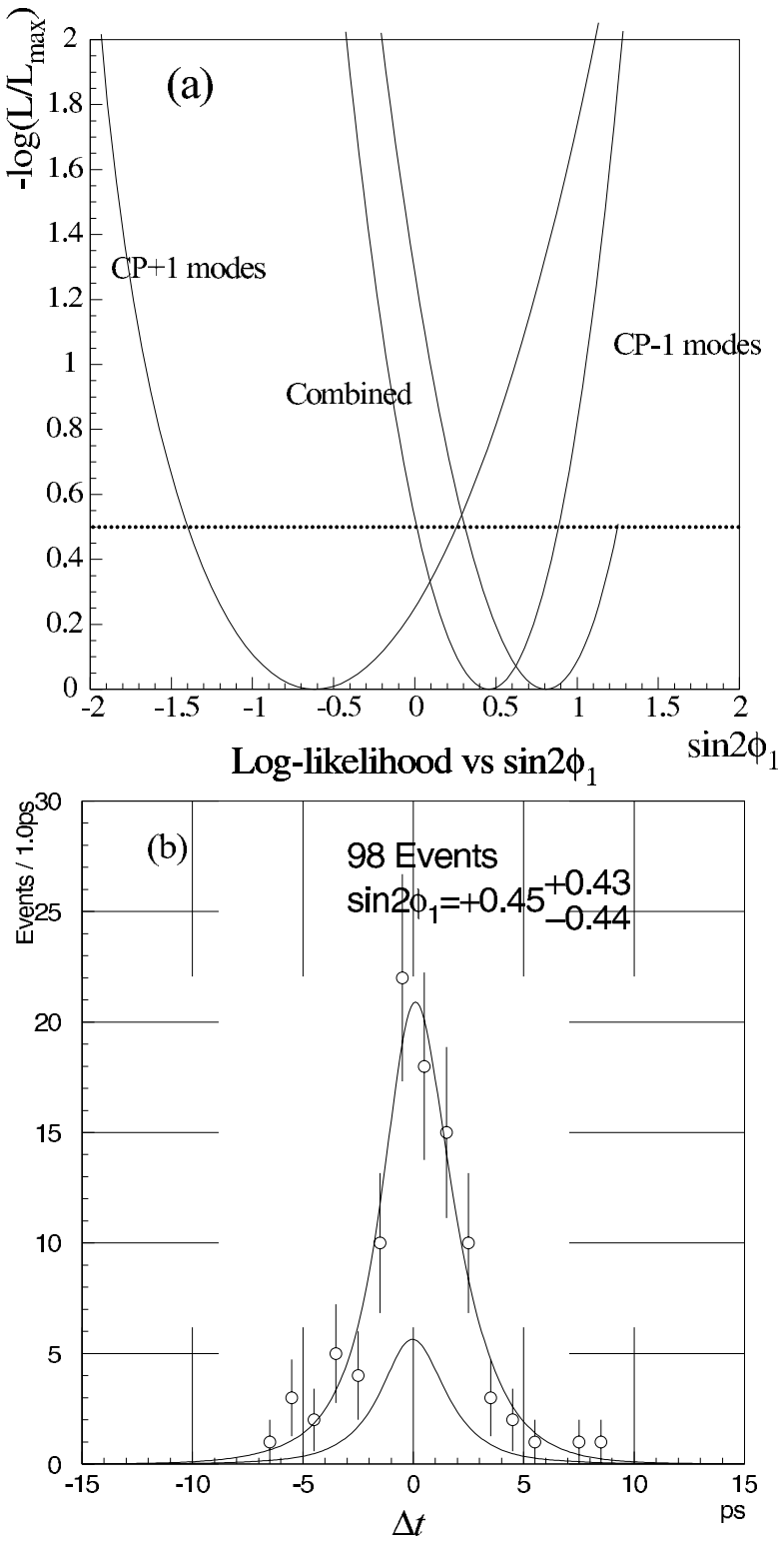

Fig. 9. (a) The log likelihood as a function of $\sin 2\phi_1$. (b) a sum of $dN/d(\Delta t)$ for $q = +1$ and $dN/d(-\Delta t)$ for $q = -1$ for $\eta_f = -1$ and $dN/d(-\Delta t)$ for $q = +1$ and $dN/d(\Delta t)$ for $q = -1$ for $\eta_f = +1$ events with the result of the fit. The lower solid curve represents the background distribution.

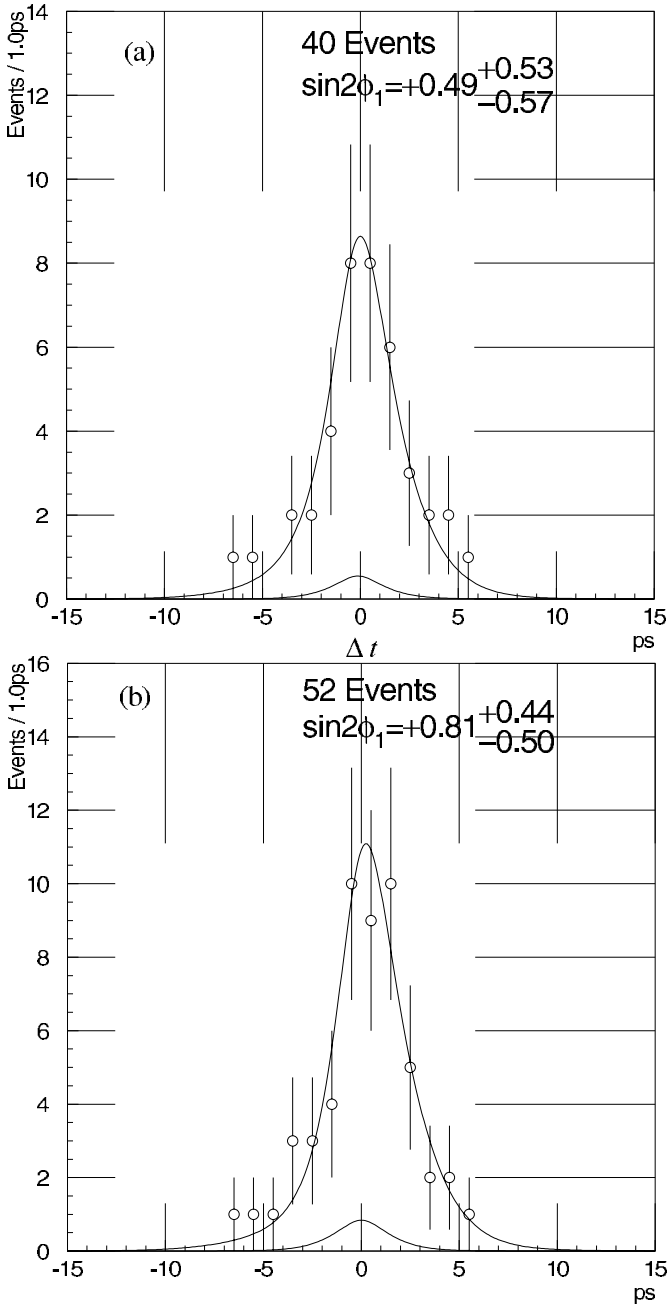

Fig. 10. Sum of $dN/d(\Delta t)$ for $q = +1$ and $dN/d(-\Delta t)$ for $q = -1$ for $\eta_f = -1$ events with the results of the fit for (a) $B^0 \to J/\psi K_S$, $K_S \to \pi^+\pi^-$ mode and (b) all $CP = -1$ modes combined. The lower solid curves represent the background distribution.

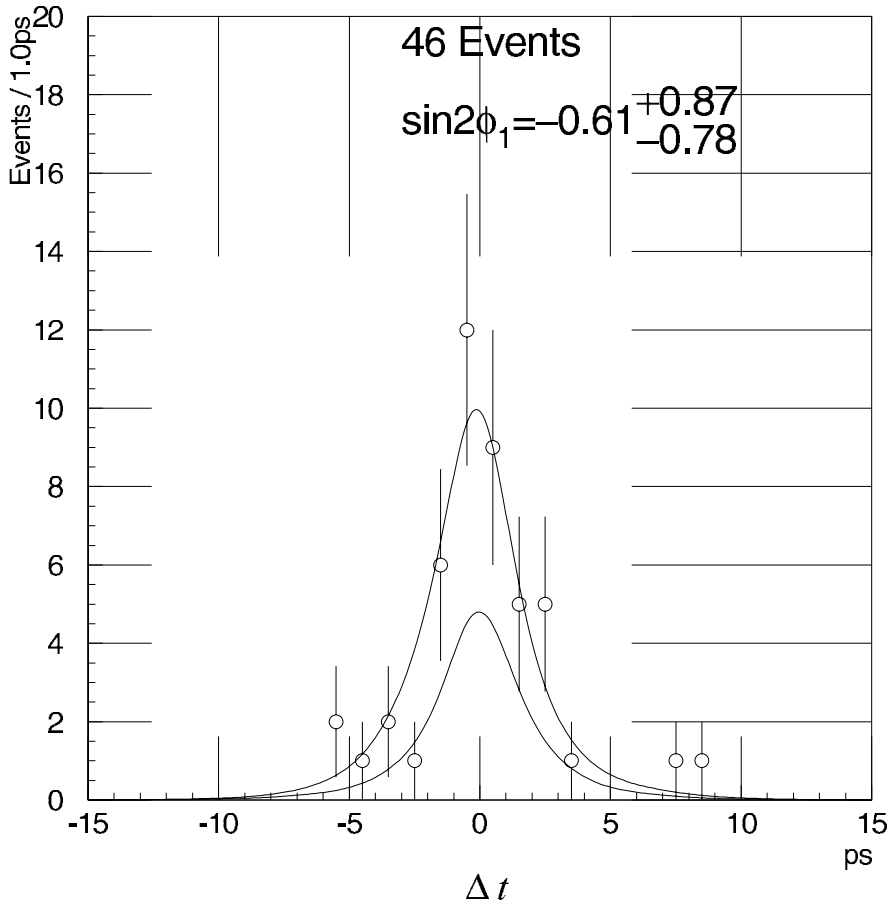

Fig. 11. Sum of $dN/d(\Delta t)$ for $q = +1$ and $dN/d(-\Delta t)$ for $q = -1$ for $\eta_f = -1$ events with the results of the fit for all $CP = +1$ modes combined. The lower solid curves represent the background distribution.

Table 6. Summary of CP fits to tagged CP events.

Category	$\sin 2\phi_1$
$J/\psi K_S, K_S \to \pi^+\pi^-$	$0.49^{+0.53}_{-0.57}$
All $CP = -1$ modes combined	$0.81^{+0.44}_{-0.50}$
All $CP = +1$ modes combined	$-0.61^{+0.87}_{-0.78}$
All modes combined	$0.45^{+0.43}_{-0.45}$

3.4.1 Systematic checks

To test for possible bias in the analysis, we apply the same analysis procedure including tagging, vertexing and log-likelihood fitting to control data samples with null intrinsic CP asymmetry; $B^0 \to J/\psi K^{*0}, K^{*0} \to K^+\pi^-$, $B^- \to J/\psi K^-$, $B^- \to D^0\pi^-$, and $B^0 \to D^{*-}\ell^+\nu$ decays. Figures 12 and 13 show the Δt distributions for $B^0 \to J/\psi K^{*0}, K^{*0} \to K^+\pi^-$, $B^- \to J/\psi K^-$, and $B^- \to D^0\pi^-$ events. The results of the fit for these samples are given in Table 7. All results are consistent with the null asymmetry.

Table 7. Summary of CP fits to control samples.

Category	Fit results
$\bar{B}^0 \to J/\psi \bar{K}^{*0}, \bar{K}^{*0} \to K^-\pi^+$	$-0.09^{+0.49}_{-0.46}$
$B^- \to J/\psi K^-$	$0.22^{+0.23}_{-0.24}$
$B^- \to D^0\pi^-$	-0.10 ± 0.17
$\bar{B}^0 \to D^{*+}\ell^-\bar{\nu}$	0.09 ± 0.18

We generate 1000 toy Monte Carlo experiments with the same number of tagged CP events, having the same composition of the tags and the same resolutions as in the CP data sample, for an input value of $\sin 2\phi_1 = 0.45$. Figure 14(a) and (b) show the distributions of the central $\sin 2\phi_1$ value and the statistical errors, the + side and − side separately. We find that the probability of obtaining a value of the statistical error greater than the values observed is $\approx 5\%$.

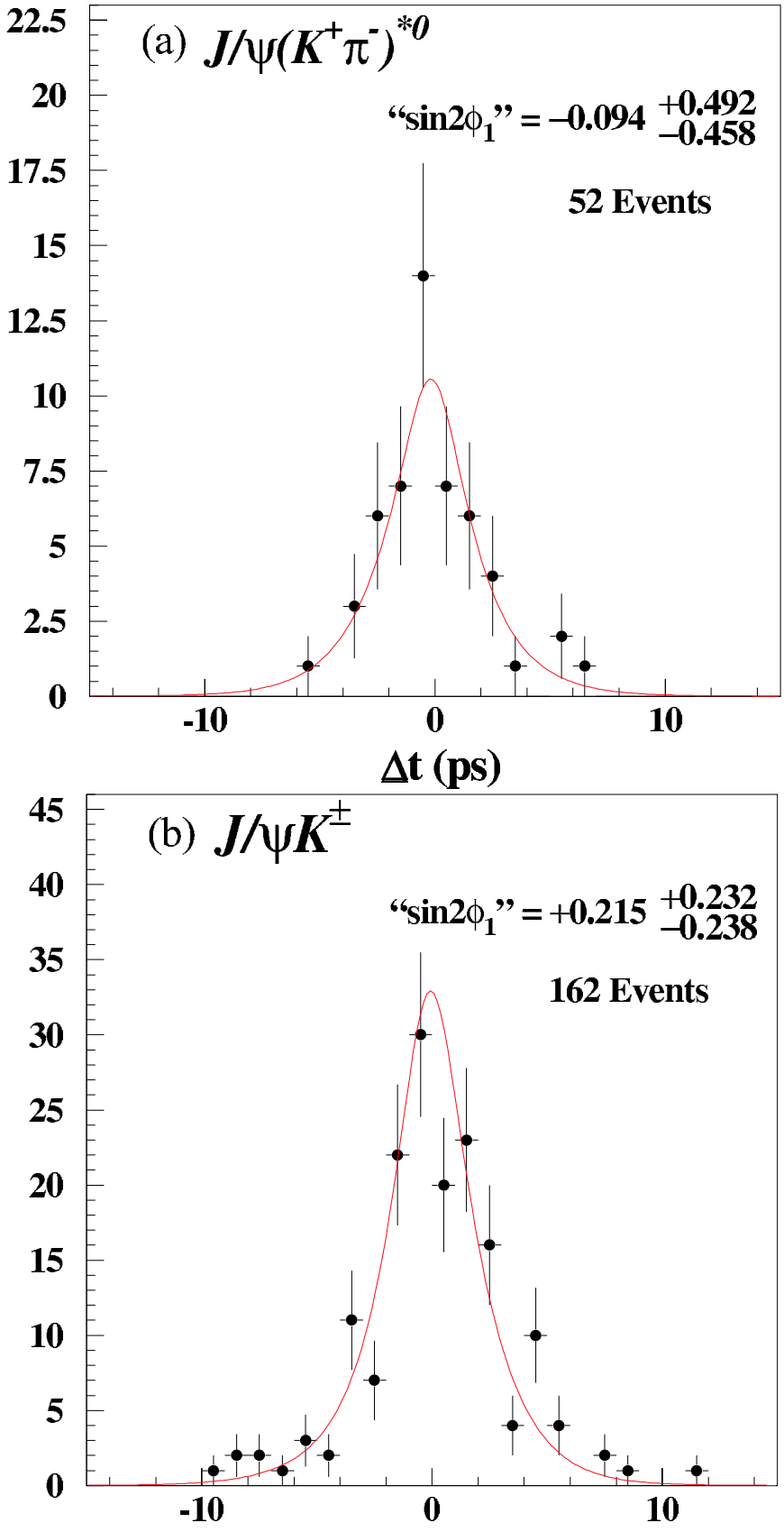

Fig. 12. Δt distributions for (a) $B^0 \to J/\psi K^{*0}$, $K^{*0} \to K^+\pi^-$ and (b) $B^- \to J/\psi K^-$ events.

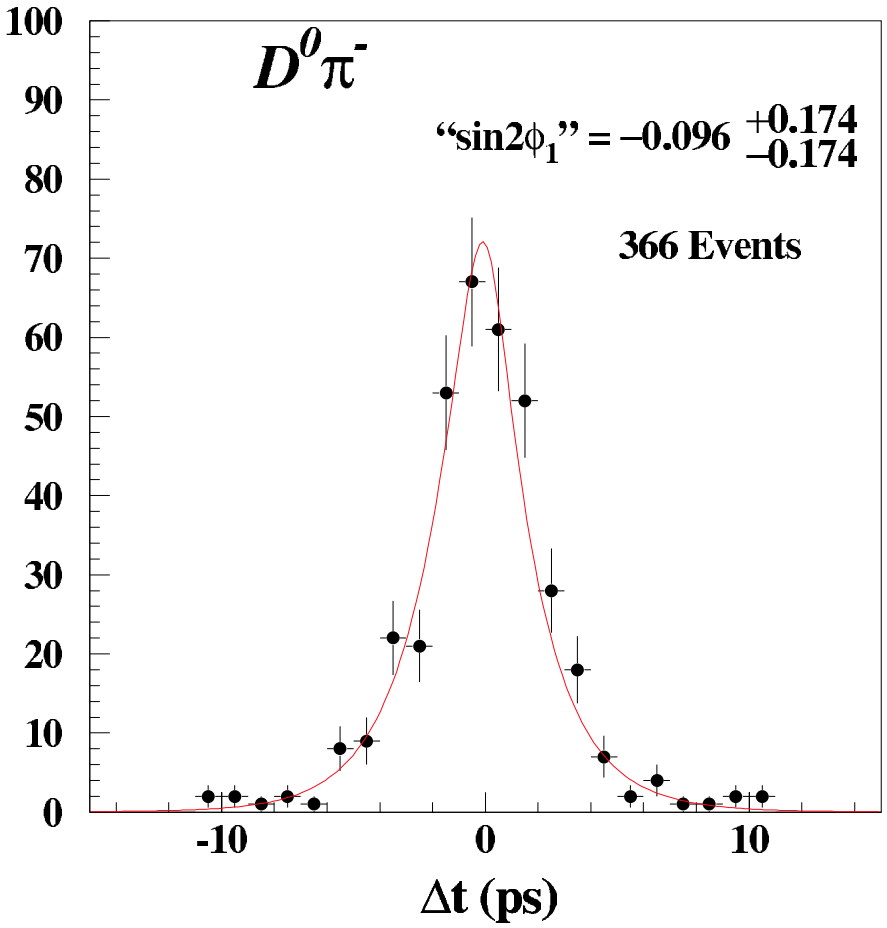

Fig. 13. Δt distributions for $B^- \to D^0\pi^-$ events.

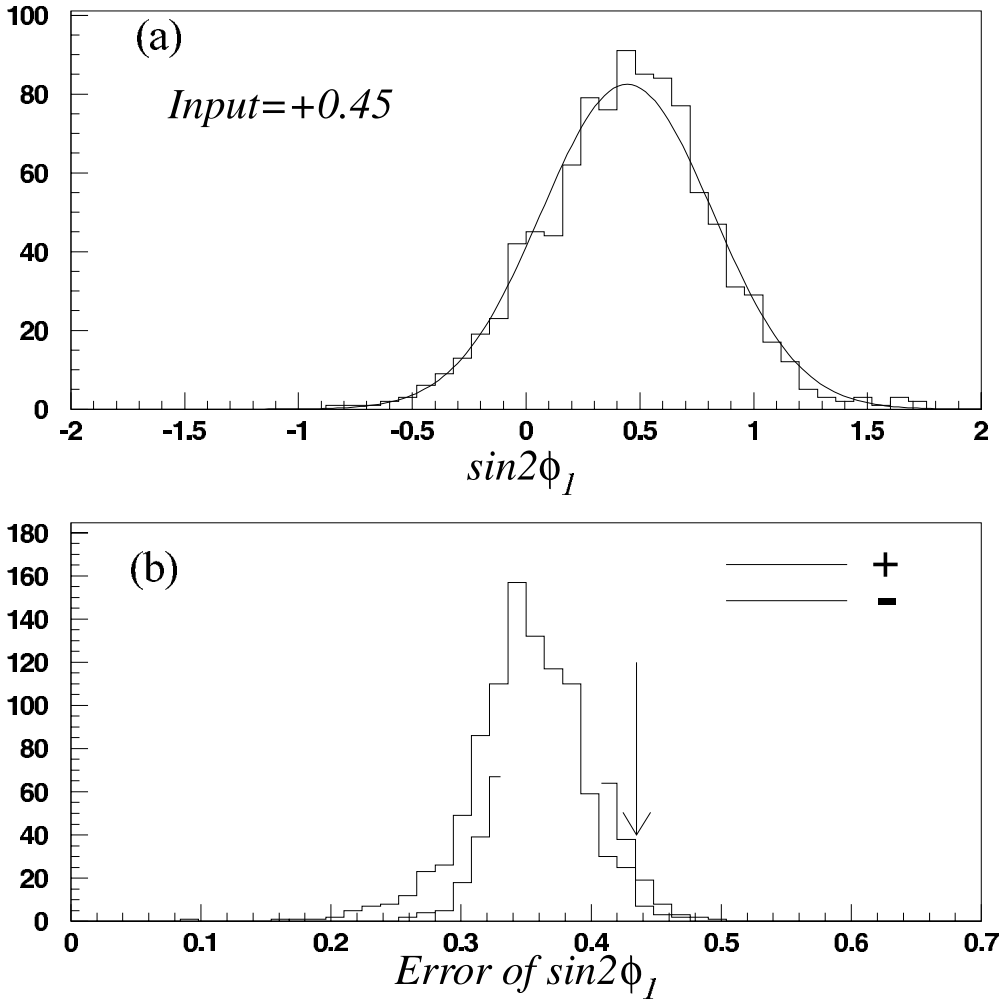

Fig. 14. Results of 1000 toy Monte Carlo experiments generated for $\sin 2\phi_1 = 0.45$. (a) the distribution of the fitted values of $\sin 2\phi_1$ is shown as the histogram with a fit to a Gaussian. (b) the distribution of the fitted errors on the + side and − side are shown separately.

3.4.2 Systematic errors

Table 8 summarizes the systematic errors. The largest source of systematic errors is the uncertainty in the wrong-tag fraction determination. The effect of this error is studied by varying the value of ω individually for each tagging method. The effect due to uncertainty in Δt resolutions for both signal and background is studied by varying parameters in the resolution function, $R(\Delta t)$. Also included are the effects due to uncertainties in the estimates of the background fraction, in the world average τ_{B^0} and Δm_d values. An imperfect knowledge of the event by event interaction point could cause a systematic error in $\sin 2\phi_1$ due to the vertex reconstruction. This effect is studied by repeating the entire fitting procedure by varying the IP envelope by $\pm 1\sigma$ in all three dimensions. The total systematic error of $\sin 2\phi_1$ is found to be $+0.07$ and -0.09.

Table 8. List of systematic errors of $\sin 2\phi_1$

Source	$\sigma(+$ side)	$\sigma(-$ side)
Wrong-tag	0.050	0.066
$R(\Delta t)$	0.026	0.025
Background shape	0.029	0.042
Background fraction	0.029	0.032
$\tau_{B^0}, \Delta m_d$	0.005	0.005
IP profile	0.004	0.000
Total	0.07	0.09

4 Conclusions

Using 98 flavor tagged events, we made a preliminary measurement of the time-dependent CP asymmetry in B^0 decays into CP eigenstates: $J/\psi K_S, K_S \to \pi^+\pi^-$ and $K_S \to \pi^0\pi^0$; $\psi(2S)K_S, K_S \to \pi^+\pi^-$; $\chi_{c1}K_S, K_S \to \pi^+\pi^-$; $J/\psi\pi^0$; and $J/\psi K_L$. We find $\sin 2\phi_1 = 0.45^{+0.43}_{-0.44}(stat)^{+0.07}_{-0.09}(syst)$.

Figure 15 shows the constraint on the angle ϕ_1 corresponding to this measurement, $\sin 2\phi_1 = 0.45^{+0.44}_{-0.45}$, together with the constraints derived from other measurements. While the current statistical uncertainty of our measurement does

not allow anything conclusive, the result is consistent with the Standard Model prediction.

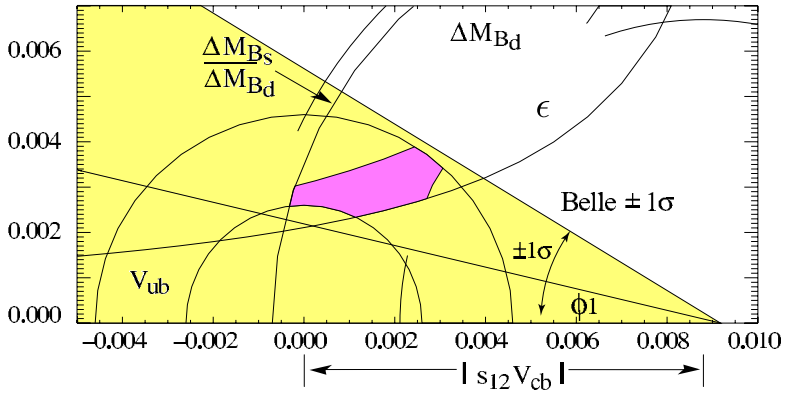

Fig. 15. Constraint on the angle ϕ_1 corresponding to this measurement $\pm 1\sigma$, $\sin 2\phi_1 = 0.45^{+0.44}_{-0.45}$. This figure was made from Fig. 11.2 of Ref. [7] .

5 Acknowledgments

We gratefully acknowledge the efforts of the KEKB group in providing us with excellent luminosity and running conditions and the help with our computing and network systems provided by members of the KEK computing research center. We thank the staffs of KEK and collaborating institutions for their contributions to this work, and acknowledge support from the Ministry of Education, Science, Sports and Culture of Japan and the Japan Society for the Promotion of Science; the Australian Research Council and the Australian Department of Industry, Science and Resources; the Department of Science and Technology of India; the BK21 program of the Ministry of Education of Korea and the Basic Science program of the Korea Science and Engineering Foundation; the Polish State Committee for Scientific Research under contract No.2P03B 17017; the Ministry of Science and Technology of Russian Federation; the National Science Council and the Ministry of Education of Taiwan; the Japan-Taiwan Cooperative Program of the Interchange Association; and the U.S. Department of Energy.

References

[1] J.H. Christenson et al., Phys Rev. Lett. **13**, 138 (1964).

[2] M. Kobayashi and T. Maskawa, Prog. Theo. Phys. **49**, 652 (1973).

[3] A. Carter and A.I. Sanda, Phys. Rev. Lett. **45**, 952 (1980);
A. Carter and A.I. Sanda, Phys. Rev. **D23**, 1567 (1981);
I.I. Bigi and A.I. Sanda, Nucl. Phys. **B193**, 851 (1981).

[4] P. Oddone, in Proceedings of *the UCLA Workshop: Linear Collider $B\overline{B}$ Factory Conceptual Design*, D. Stork, ed., World Scientific, p. 243 (1987).

[5] "KEKB B-Factory Design Report", KEK Report 95-7 (1995);
K. Akai, et al., "COMMISSIONING OF THE KEKB B-FACTORY", WEAR4, Proc. 1999 Particle Accelerator Conference, New York (1999);
K. Akai, et al., "COMMISSIONING OF THE KEKB B-FACTORY", Proc. Intl. Workshop on e^+e^- Factories, Tsukuba, Japan, edited by K. Akai and E. Kikutani (1999);
H. Fukuma, et al., "OBSERVATION OF VERTICAL BEAM BLOW-UP IN KEKB LOW ENERGY RING", Proc. 2000 European Particle Accelerator Conference, Vienna (2000);
Y. Funakoshi, et al., "KEKB PERFORMANCE", Proc. 2000 European Particle Accelerator Conference, Vienna (2000).

[6] Belle Collaboration, *The Belle Detector*, Submitted to Nucl. Instrum. Methods (2000).

[7] Particle Data Group, D.E. Groom, et al., Eur. Phys. J. **C15**, 1 (2000).

FIRST OBSERVATIONS OF NEUTRINOS WITH THE SUDBURY NEUTRINO OBSERVATORY

Ilan Levine*
Department of Physics
Carleton University, Ottawa, Ontario, Canada

Representing the Sudbury Neutrino Observatory (SNO) Collaboration

ABSTRACT

The first neutrino observations from the Sudbury Neutrino Observatory are presented from preliminary analyses. Based on energy, direction and location, the data in the region of interest appear to be dominated by ^8B solar neutrinos, detected by the charged current reaction on deuterium and elastic scattering from electrons, with very little background. Measurements of radioactive backgrounds indicate that the measurement of all active neutrino types via the neutral current reaction on deuterium will be possible with small systematic uncertainties. Quantitative results for the fluxes observed with these reactions will be provided when further calibrations have been completed.

1 Introduction

This paper presents the first neutrino observations from the Sudbury Neutrino Observatory[1] (SNO), a 1000 tonne heavy-water-based Cerenkov detector situated 2 km underground in INCO's Creighton mine near Sudbury, Ontario, Canada. The SNO detector has been filled with water since May, 1999. After a commissioning period, the detector parameters were fixed at the start of November 1999 and neutrino data acquisition and associated calibrations have been taking place almost continuously since then. In this initial phase of the project, the detector is filled with pure heavy water. Neutrinos from ^{8}B decay in the sun are observed from Cerenkov processes following these reactions:
1. The Charged Current (CC) reaction, specific to electron neutrinos:

$$d + \nu_e \rightarrow p + p + e^- \tag{1}$$

This reaction has a Q value of -1.4 MeV and the electron energy is strongly correlated with the neutrino energy, providing very good sensitivity to spectral distortions.
2. Neutral Current (NC) reaction, equally sensitive to all non-sterile neutrino types:

$$\nu_x + d \rightarrow n + p + \nu_x \tag{2}$$

This reaction has a threshold of 2.2 MeV and is observed through the detection of neutrons by three different techniques in separate phases of the experiment.
3. Elastic Scattering (ES) reaction:

$$\nu_x + e^- \rightarrow e^- + \nu_x \tag{3}$$

This reaction has a substantially lower cross section than the other two and is predominantly sensitive to electron neutrinos; they have about six times greater cross-section than μ or τ neutrinos.

The reaction:

$$\bar{\nu}_e + d \rightarrow n + n + e^+ \tag{4}$$

also provides a unique signature for anti-electron neutrinos from various possible sources. The SNO experimental plan calls for three phases of about one year each wherein different techniques will be employed for the detection of neutrons from the NC reaction. During the first phase, with pure heavy water, neutrons are observed through the Cerenkov light produced when neutrons are captured in deuterium, producing 6.25

MeV gammas. In this phase, the capture probability for such neutrons is about 25% and the Cerenkov light is relatively close to the threshold of about 5 MeV electron energy, imposed by radioactivity in the detector. (Figure 1.) For the second phase, about 2.5 tonnes of NaCl will be added to the heavy water and neutron detection will be enhanced through capture on Cl, with about 8.6 MeV gamma energy release and about 83% capture efficiency. (See Figure 1.) For the third phase, the salt will be removed and an array of ^{3}He- filled proportional counters will be installed to provide direct detection of neutrons with a capture efficiency of about 45%.

2 Physics Objectives

The main physics goals for the Observatory are observations of:
- Solar Neutrinos
- Atmospheric Neutrinos
- Supernova Neutrinos
- Cosmic Ray Muons
- Anti-electron neutrinos from various processes including transformations of solar neutrinos or relic supernova neutrinos.

For Solar Neutrinos, the combination of three detection reactions provides several sensitive ways to seek evidence for neutrino flavor change without relying on calculations of initial fluxes from solar models. The ratio of neutrino fluxes above a threshold, as observed by the CC and NC reactions, provides a very sensitive way to observe transformations to active neutrinos.

The ratio of CC/NC can be observed during all three phases of operation. The sensitivity to the NC reaction is limited during the first phase, but there will be excellent sensitivity with different systematic uncertainties during the other two phases. The ratio of fluxes detected by the CC and ES reaction has a smaller dependence on flavor change to active species through the sensitivity to μ and τ neutrinos in the ES cross section. Events from the CC and ES reactions can be distinguished through the very different directional response. The ES reaction is strongly peaked away from the Sun, whereas the CC reaction has a form of approximately $1 - \frac{1}{3}\ \cos\theta_{sun}$, with about a factor of two difference in rate between forward and backward directions relative to the Sun. The angular resolution of the detector is better than 25 degrees. The NC rate may be determined during the pure D_2O phase partly through a distinctive variation

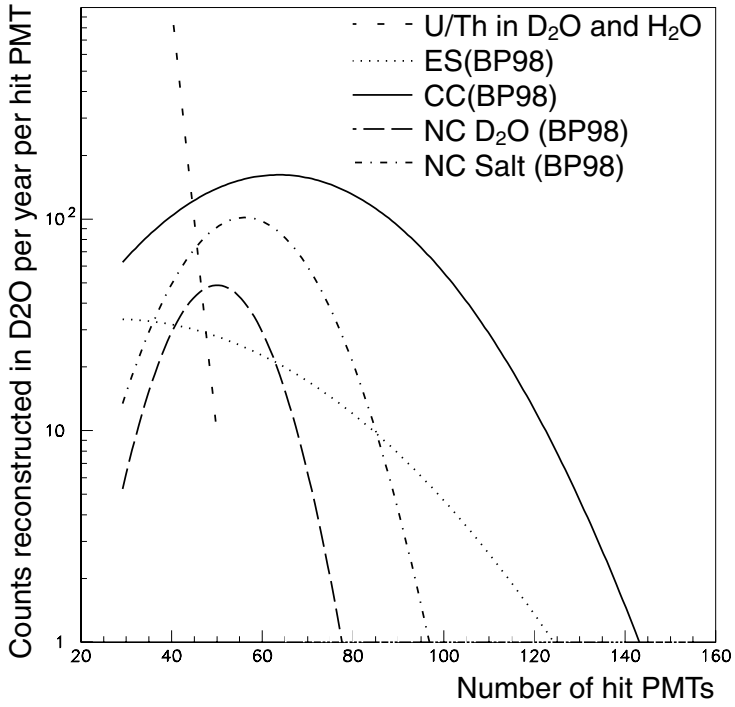

Fig. 1. Simulations of spectra obtained from the three detection reactions (CC,ES,NC)for neutrino fluxes as calculated[2] by BP98. Spectra from the NC reaction are shown for pure heavy water and with added salt. The expected counting rate from U and Th radioactivity in the water is also shown. An MeV of electron energy corresponds to about 9 photomultipliers (PMT's) hit.

as a function of radius. However, the definition of the number of events observed with this reaction is clearly enhanced by the addition of salt (see Figure 1), and will be determined independently of the Cerenkov signals when the ^{3}He-filled proportional counters are installed. The observed spectrum for the CC reaction is a very sensitive indicator of distortions caused by the MSW effect[3] because the energy of outgoing electrons is strongly correlated with the incoming neutrino energy, and the detector energy resolution is better than 20% for the range of interest. With the relatively high statistical accuracy indicated by Figure 1, the SNO detector will also provide sensitive measurements of the solar neutrino flux as a function of zenith angle to search for MSW regeneration in the Earth. Correlations between flux, energy spectrum, zenith angle and time of year will also be studied. With the variety of reactions to be studied, the SNO

detector can explore oscillations via the MSW effect or vacuum oscillation processes, over the full range of parameters consistent with previous experiments. It could provide clear evidence for electron neutrino flavor change, including transformations to either active or sterile types.

3 Detector Performance

The SNO detector consists of 1000 tonnes of pure D_2O contained within an acrylic vessel (12 m diameter, 5 cm thick), viewed by 9438 PMT's mounted on a geodesic structure 18 m in diameter, all contained within a polyurethane-coated (to suppress the ingress of radon from radioactivity in the rock) barrel-shaped cavity (22m diameter by 34 m high). The cavity volume outside the acrylic vessel (AV) is filled with purified H_2O. There are 91 PMT's looking outward from the geodesic structure, viewing the outer H_2O volume. Above both the D_2O and H_2O are small vapor spaces. These are filled with vapor boiled from a 1000 liter liquid nitrogen dewar to protect the fiducial volume of the detector from radon in laboratory air.

The SNO detector has been full of water since May, 1999. During the period until November, 1999, detailed commissioning tests and calibrations were performed. There has been no substantial problem from electrical breakdown of high voltage connectors submerged in light water since nitrogen was added to the degassed water. During the period before November, a variety of adjustments were made to improve the light sensitivity by about 25% and to reduce the trigger threshold to about 2 MeV. Four additional PMT's were installed in the neck of the acrylic vessel to provide a clear indication of instrumental light emitted in this region, probably from static discharges of insulating materials. ^{222}Rn in the gas space above the heavy water was reduced to acceptable levels by introducing an active flush of the vapor space with boil-off gas from the liquid nitrogen dewar.

As of November, 1999, the desired detector specifications had been met, the detector parameters were frozen and production data accumulation was started, interspersed with a variety of calibration measurements. The detector performance has been very good, with more than 98.5% of all channels operational; a total event rate of less than 5 Hz above a threshold of about 20 hit PMT's; PMT individual noise rates of less than 500 Hz for a threshold of about 0.3 photoelectrons, providing fewer than 2 noise hits per event.

4 Calibration

Detector calibration is being carried out with a variety of techniques and sources. Electronic calibrations of pedestals, slopes and timing are performed regularly with pulsers. The 600,000 electronic constants are very stable. Optical properties of the detector have been studied using a diffusing ball (Laserball), receiving light from a pulsed laser system providing wavelengths between 337 and 700 nm with variable intensity at repetition rates from near 0 to 45 Hz. This source and other calibration sources are moved within the D_2O volume using a manipulator system capable of positioning them to better than 5 cm. Positions in the H_2O volume between the D_2O and the PMT's are also accessible along vertical paths from above. A nearly mono-energetic ^{16}N gamma ray source has also been deployed.

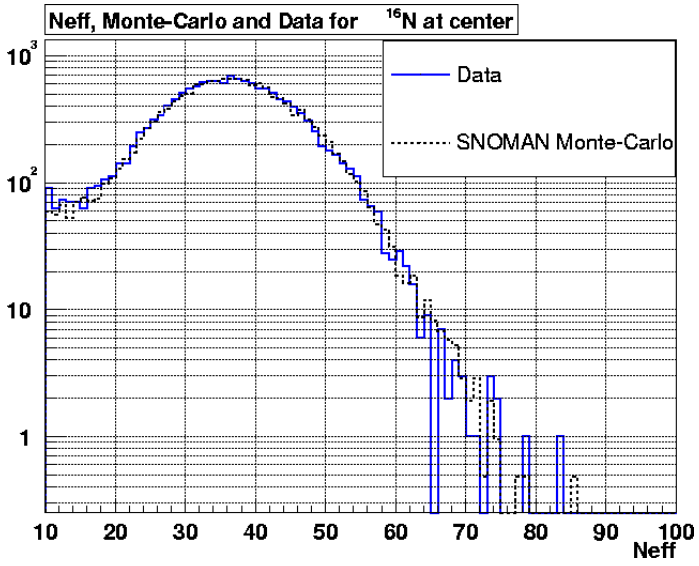

Fig. 2. Data from the ^{16}N source compared with Monte Carlo simulation. Neff is the number of PMTs hit by prompt light less the average number of noise hits.

Figure 2 shows a spectrum from the ^{16}N source compared with a Monte Carlo simulation, using optical parameters extracted from a preliminary analysis of the laserball data. A single constant corresponding to the average quantum efficiency of the PMT's has been adjusted to match the centroid of these spectra. A further comparison of centroids for over 20 other locations throughout the D_2O volume showed less than 2% difference between the data and the simulation at any point. An acrylic- encapsulated

^{242}Cf fission neutron source has also been deployed to study the neutron response of the detector. Starting in late October of 2000, a triggered source for the ^{232}Th and ^{238}U chains producing 2.6 and 2.4 MeV gammas was deployed and commisioned. This source will be used to calibrate the response of the detector to radioactive contaminants in the water and other detector materials.

Other sources being prepared include a 19.8 MeV gamma source produced by the (p,t) reaction and a source of ^{8}Li, emitting betas up to 13 MeV. The short-lived ^{16}N and ^{8}Li activities are produced by a pulsed neutron generator located near the SNO detector and are transported via capillary tubing to decay chambers within the detector volume.

5 Observations To Date

In addition to Cerenkov light produced by neutrinos and radioactivity, there can be other sources of "instrumental light" arising from parts of the detector. For example, it is well known that PMT's can occasionally emit light, perhaps through internal electrical discharges. Light from these sources has very different characteristics from the typical patterns observed for Cerenkov light at solar neutrino energies. The light from a flashing PMT shows an early trigger for the flashing PMT, followed by light observed across the detector, at least 70 ns later. For SNO, six or more electronic channels surrounding the flashing PMT typically show pickup signals, distinguishing the events further from Cerenkov events.

Figure 3 shows the raw spectrum of events (solid line) observed with the detector for a fraction of the data obtained since the start of data taking in November, 1999. The events are plotted against NHIT, the number of PMT's contained in a 400 ns second window surrounding the detector trigger (more than about 20 PMT's hit within a 100 ns window). NHIT is approximately proportional to the electron energy for a Cerenkov event, with about 9 NHIT corresponding to 1 MeV. Only a fraction of the data have been shown, as the remainder are being saved for a comparison after the cuts have been fully defined.

The dashed line shows the residual data after cuts have been imposed to remove events that show characteristics matching the Flashing PMT's. The dotted line shows the residual data after further cuts are imposed to remove another class of events associated with bursts of light from the neck region of the detector. These events may arise from static discharges of insulating materials. Four additional PMT's were installed in

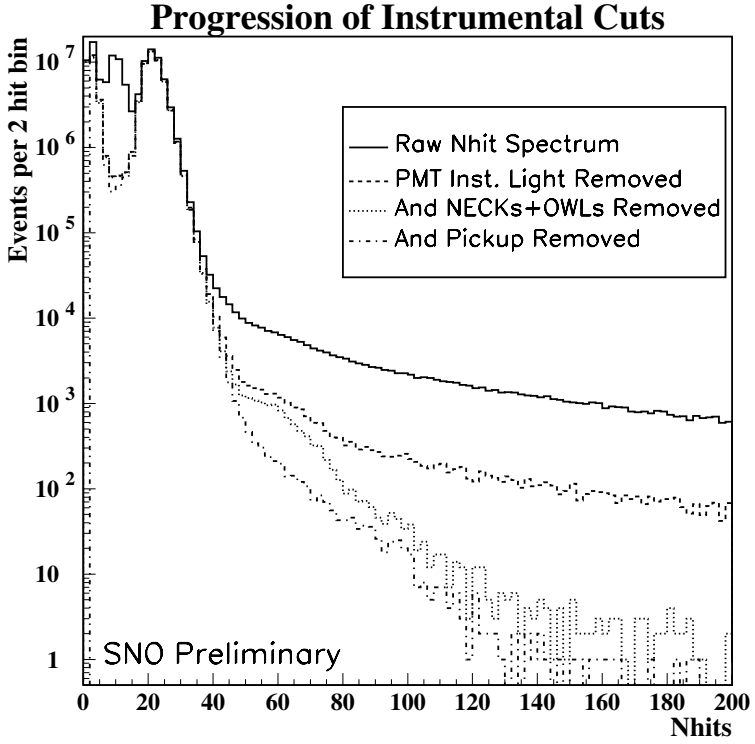

Fig. 3. Progression of instrumental cuts.

this region in September, 1999. They clearly observe these events and are very insensitive to light generated in the detector itself, as determined from the calibration sources. The dot and dash line shows the residual events after the imposition of further cuts which eliminate events that show characteristics of pickup in the electronic systems.

Two separate groups within the SNO Collaboration developed a series of cuts to eliminate these instrumental light sources and their results for the residual spectrum were virtually identical, lending confidence in the robustness with which these events can be distinguished from neutrinos. To ensure that these cuts do not remove a significant number of neutrino events, the fraction of signal loss was tested with the ^{16}N source. The results are shown in Figure 4, indicating very low loss of signal in the region tested.

Following these cuts, algorithms based on timing and spatial information were used to reconstruct the position and direction of the events. Figure 5 shows the resulting spectrum for a large fiducial volume.

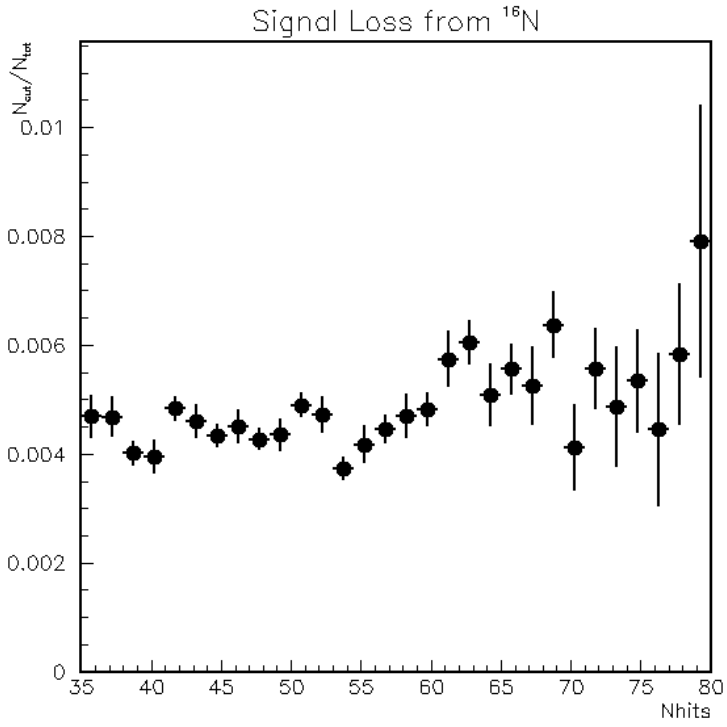

Fig. 4. Signal loss as measured with ^{16}N.

Superimposed on the data is the simulated spectrum for the CC reaction in Figure 1, scaled to the data. As the calibrations are not yet complete, the SNO collaboration has chosen not to quote a number for the flux of electron neutrinos measured by the CC reaction on deuterium. However, it should be apparent from the figure that the spectrum is well defined so that an accurate measurement will be obtained when further calibrations have been completed.

Figure 6 shows events as a function of the direction to the sun for a lower energy threshold and a larger fiducial volume. Even with somewhat more radioactive background included by these parameter choices, the peak at $\cos\theta_{sun} = 1$ from the ES reaction is apparent.

Figure 7 shows the distribution of events as a function of (radius/600cm)^3, for a high-energy threshold. The radius of the AV is 600 cm, so the heavy water volume corresponds to values less than 1. It is apparent that there is a clear excess of events in this region, indicating the substantial contribution from the CC reaction on deuterium.

Figure 8 shows the distribution of events with a high energy threshold for a region in the light water outside the AV. Events have been selected to remove inward-coming

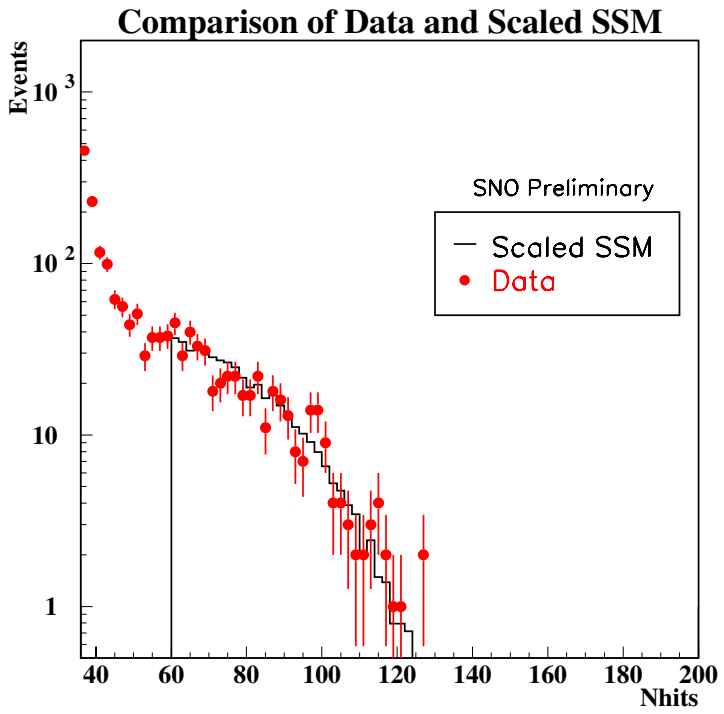

Fig. 5. Distribution of events versus number of hit PMTs.

gamma rays. The peak from ES events is apparent with a relatively small background.

6 Radioactive Backgrounds

Radioactive backgrounds that contribute to the Cerenkov light in the detector arise from the decay chains of ^{238}U and ^{232}Th impurities in the water and other detector materials. At low energies, the dominant contributions come from impurities in the water. These contributions can be measured through the radioassay of the light and heavy water. They can also be measured independently through observation of the low energy region of the Cerenkov spectrum for events reconstructing in the water regions. Sensitive techniques have been developed for radioassay of ^{224}Ra, ^{226}Ra and ^{222}Rn in the water. The measurements for Ra are performed by extracting the Ra on beads coated with manganese oxide or on ultrafiltration membranes coated with hydrous titanium oxide. After sampling hundreds of tonnes of water, these materials are measured for radioactive decay of the Ra with techniques sensitive to tens of atoms. (See reference 1 for

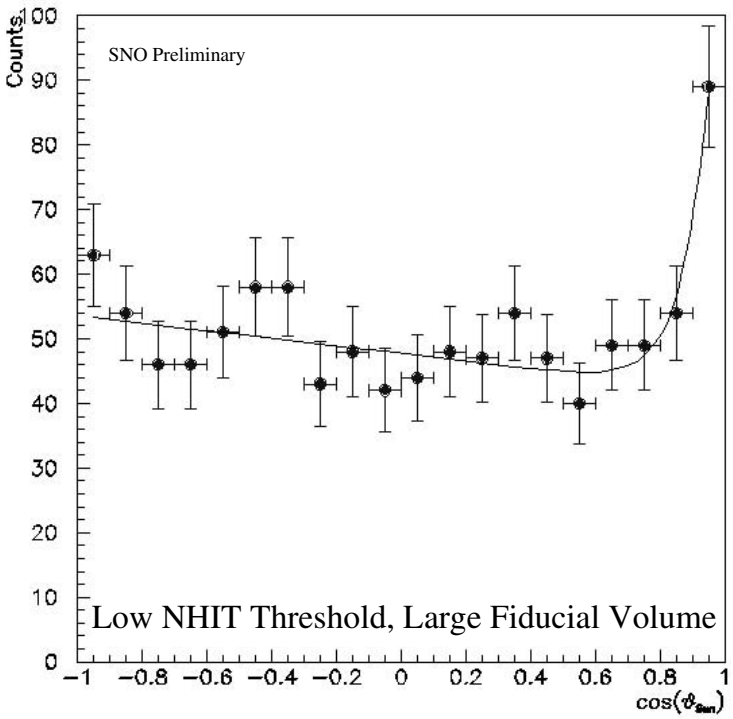

Fig. 6. Distribution of events versus cosθ_{sun}.

more details.) The ^{222}Rn is measured by degassing 50 or more tonnes of water and collecting the Rn gas with liquid nitrogen-cooled traps. The collected gas is then counted with ZnS coated scintillation cells (Lucas cells) to observe the alpha decays. These techniques have been employed to make very sensitive measurements of the water, as shown in Figures 9 and 10.

The Cerenkov light generated by the Th and U radioactivity can be observed at low energies as illustrated in figure 1 and observed in figures 3 and 5. As the decay products and sequence are different for the two chains it is also possible to use pattern recognition to obtain a statistical separation of the contributions from the two chains. Future calibrations will include the use of proportional counters containing Th and U chain sources to provide triggered events to calibrate the detector response in this region. However, the data to date, with large calibration uncertainties, do agree with the radioassay measurements. The light water in the SNO detector is designed to attenuate higher energy gamma rays (fission and alpha-induced) from radioactivity in the cavity walls and the PMT support structure. High-energy events reconstructed in the

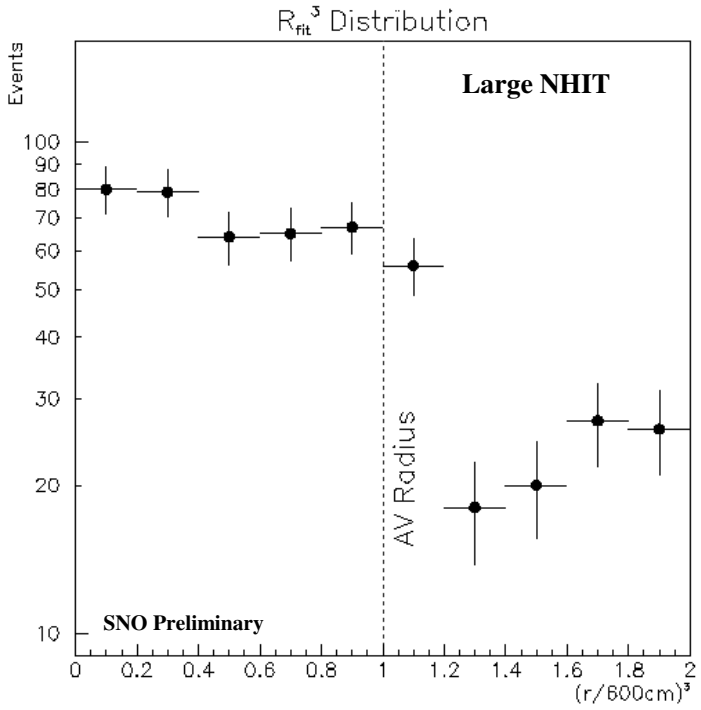

Fig. 7. Distribution of events versus radius cubed.

light water volume outside the AV are found to be predominantly inward going and the numbers decrease rapidly as a function of radius. Using calibration data from the ^{16}N source positioned near the PMT's, extrapolations of the number of high energy gammas interacting within the D_2O volume indicate that fewer than a few percent of the events above NHIT = 60 in Figure 5 arise from external high energy gammas. In addition to the contributions to Cerenkov light, the presence of Th and U chain elements can produce a background for the NC reaction through the photodisintegration of deuterium by 2.6 MeV gammas from the Th chain and 2.4 MeV gammas from the U chain. The horizontal lines in Figure 10 individually represent contributions to the neutron background in the detector from photodisintegration equivalent to 5% of the signal expected for the NC reaction for the neutrino flux[2] of BP98. As is apparent from the figure, these goals have been met for the U chain and are met within a factor of two for the Th chain.

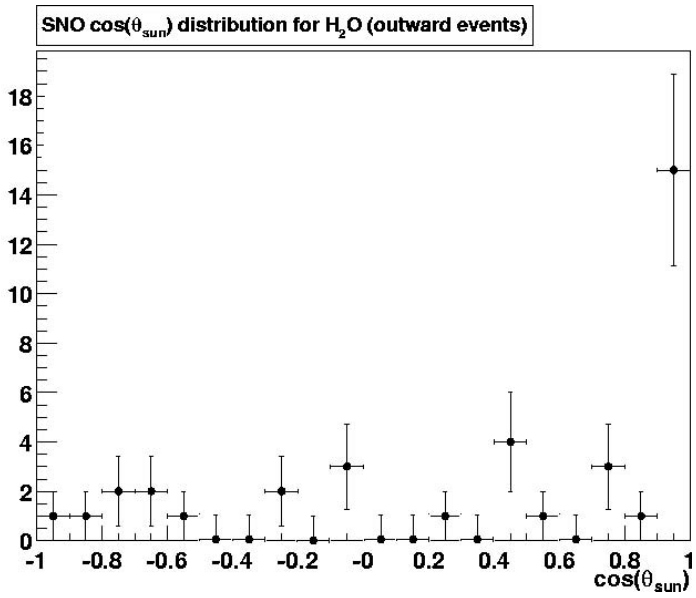

Fig. 8. Distribution of events in H_2O versus $\cos\theta_{sun}$.

7 Conclusions

Based on energy, direction and location information, the data in the regions of interest in Figures 5 to 8 appear to be dominated by ^{8}B solar neutrino events observed with the CC and ES reactions, with very little background. This implies that measurements during the pure heavy water phase will provide an accurate measurement of the electron neutrino flux via the CC reaction after completion of further calibrations. The measurements of radioactivity imply that the NC measurements can be made with only a small uncertainty from the radioactive background.

8 Acknowledgments

This research has been financially supported in Canada by the Natural Sciences and Engineering Research Council, Industry Canada, National Research Council of Canada, Northern Ontario Heritage Fund Corporation and the Province of Ontario, in the United States by the Department of Energy, and in the United Kingdom by the Science and Engineering Research Council and the Particle Physics and Astronomy Research Council. Further support was provided by INCO, Atomic Energy of Canada Limited (AECL),

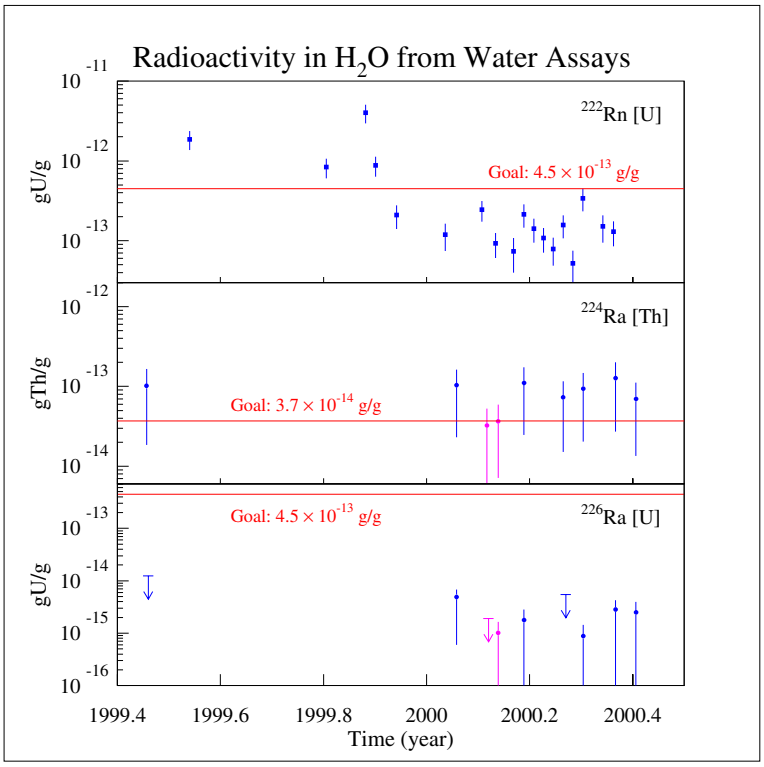

Fig. 9. Measurements of Radium from the Th and U chains and Radon from the U chain in H_2O.

Agra-Monenco, Canatom, Canadian Microelectronics Corporation and Northern Telecom. The heavy water has been loaned by AECL with the cooperation of Ontario Hydro. The provision of INCO of an underground site is greatly appreciated.

References

[1] J. Boger et al, Nucl. Instrum. Meth. A449 (2000) 172.

[2] J.N. Bahcall, S. Basu and M. H. Pinsonneault, Phys. Lett. B433 (1998) 1.

[3] L. Wolfenstein, Phys. Rev. D17 (1978) 2369; S.P. Mikheyev and A.Y. Smirnov, Sov. Jour. Nucl. Phys. 42 (1985) 913.

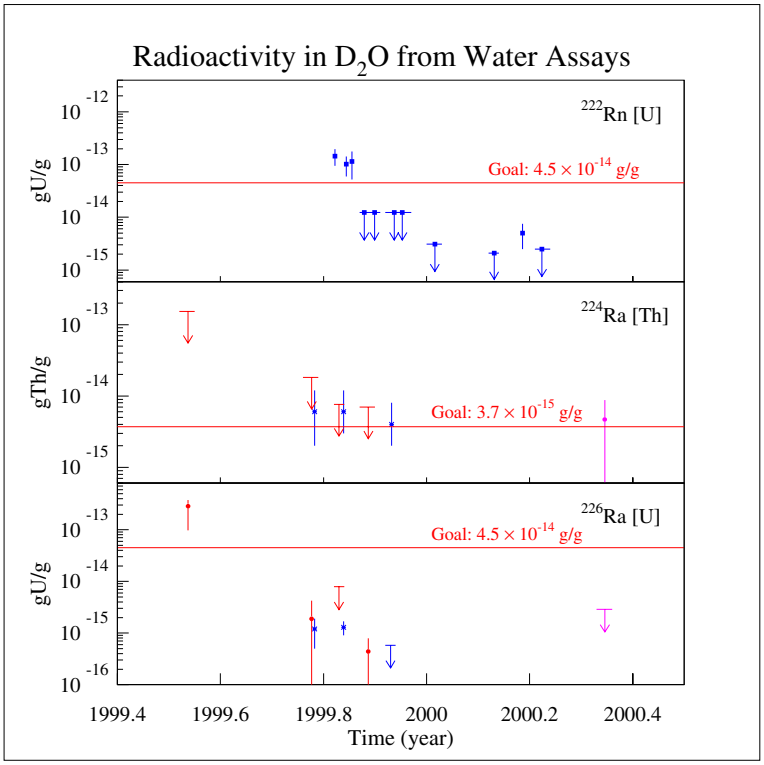

Fig. 10. Measurements of Radium from the Th and U chains and Radon from the U chain in D_2O.

THE SEARCH FOR NEW PARTICLES AT LEP

Chiara Mariotti
CERN, Geneva, Switzerland *

ABSTRACT

LEP is a fantastic machine to search for new particles because of the very simple initial and final state. In these days LEP has the leading role in all of the searches: Higgs, supersymmetric particles, Technicolor, LeptoQuarks, excited fermions, extra dimensions, and many others.

Particular attention will be given to the Higgs bosons search: production and decay in various models will be reviewed and the results presented. In particular the phenomenology of the Higgs bosons in the Standard Model, the Minimal Supersymmetric Standard Model and more exotic extensions of the standard model will be detailed. The potential for discovery at the end of LEP and for future colliders will be discussed.

In the supersymmetry (SUSY) domain the main results will be review: the limits on the chargino mass and on the lightest supersymmetric particle.

Results of the searches for LeptoQuark, FCNC processes, Technicolor particles, excited leptons and extra dimensions will be summarised.

All the results are as of summer 2000.

*On leave of absence from INFN-Torino, Italy

1 Introduction

From 1995 LEP started to run at centre of mass energies higher than the Z mass. From $\mathrm{E_{cm}}$=130 GeV in Autumn 1995, LEP gradually increased the centre of mass energy, reaching $\mathrm{E_{cm}}\sim$ 209 GeV in the year 2000.

In Table 1 the centre of mass energies and the luminosity collected by each of the 4 experiments are shown. More than 2 fb^{-1} at $\mathrm{E_{cm}}$ larger than 180 GeV have been collected.

year	89-95	95		96		97	98	99				2000
$\mathrm{E_{cm}}$(GeV)	91	130	136	161	172	183	189	192	196	200	202	204-209
Lum(pb^{-1})	175	2.5	2.5	11	11	55	160	30	80	80	40	>220

Table 1. *LEP Centre of Mass Energies and Average Luminosity per Experiment*

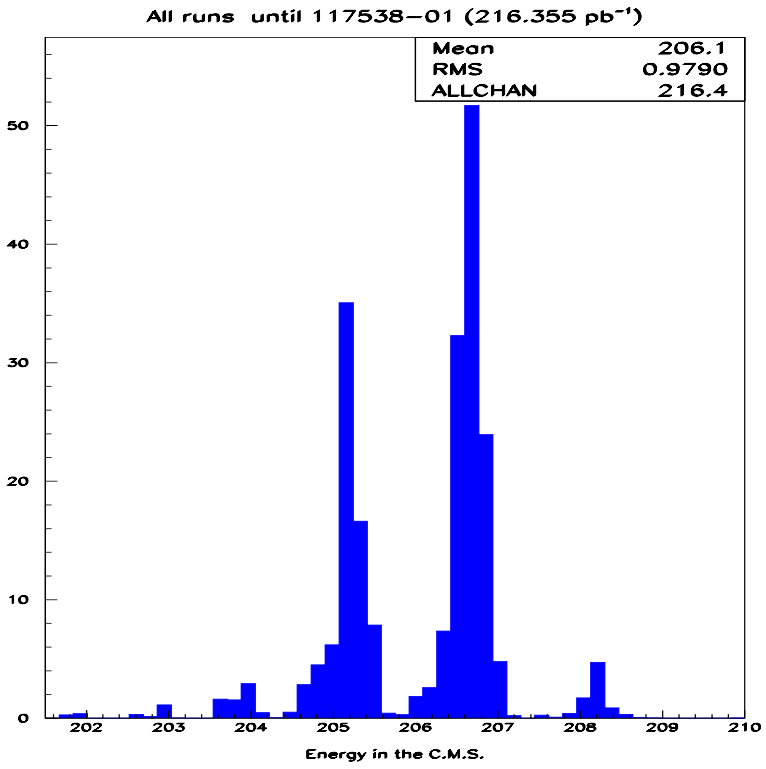

Fig. 1. *Luminosity delivered per experiment as a function of* $\mathrm{E_{cm}}$.

In the year 2000 the running mode of the machine changed in order to exploit the full potential of the machine and reach the maximum energy and luminosity. Instead

of running at a fixed $\mathrm{E_{cm}}$, the energy of the beam is increased during a fill when the luminosity starts to decrease. In this way the machine is always at its cryogenic limit. In Figure 1 the luminosity as a function of the centre of mass energy is shown for the 2000 run (as of the end of October). LEP delivered to each experiment $\sim$10 pb^{-1} at $\mathrm{E_{cm}}$>208 GeV and more than 220 pb^{-1}at $\mathrm{E_{cm}}$>200 GeV.

With increasing energy the phase space available to produce new particles increases. At LEP we try to look everywhere and consider all the models, we investigate each channel and each fluctuation. In direct searches the signal is looked for in the framework of a theoretical model or as an excess in any final state topology. Indirect searches instead take the Standard Model as the null hypothesis and look for any possible deviations.

The four experiments then combined their results in order to increase the kinematical range accessible and to smooth eventual statistical fluctuations.

One of the main physics goal of the four LEP experiments was the search for the Higgs boson. The Higgs boson mass is not predicted by the Standard Model (SM) and as of today only limits from the precise electroweak measurements could be inferred. Results on SM Higgs, MSSM and 2HDM Higgs bosons, and on anomalous couplings will be reviewed and the situation at the end of LEP will be discussed.

In the supersymmetry (SUSY) domain various messenger interactions are investigated by which the symmetry breaking is transmitted from the hidden sector to the "particle" world. The main results will be review: the limits on the mass of the particle with the highest cross section (the chargino) and on the lightest supersymmetric particles will be given.

Finally some other searches like the searches for excited leptons, LeptoQuark, Technicolor particles and single top production will be reviewed.

2 The Standard Model Higgs

The Standard Model has been tested by the experiments at LEP, SLC and Tevatron accelerators to a per mil precision. In the data no significant evidence for departure from the SM has been observed,[1] as shown in Figure 2. This tells us that the theory (SU(2)$\times$SU(1)) describes at the per mil level the coupling of quarks and leptons to photons, Z and W bosons, and (to less accuracy) the triple gauge vertices, or in other words that the gauge symmetry is indeed exact.

Yet, the particles have mass and are not degenerate in mass: this implies that the

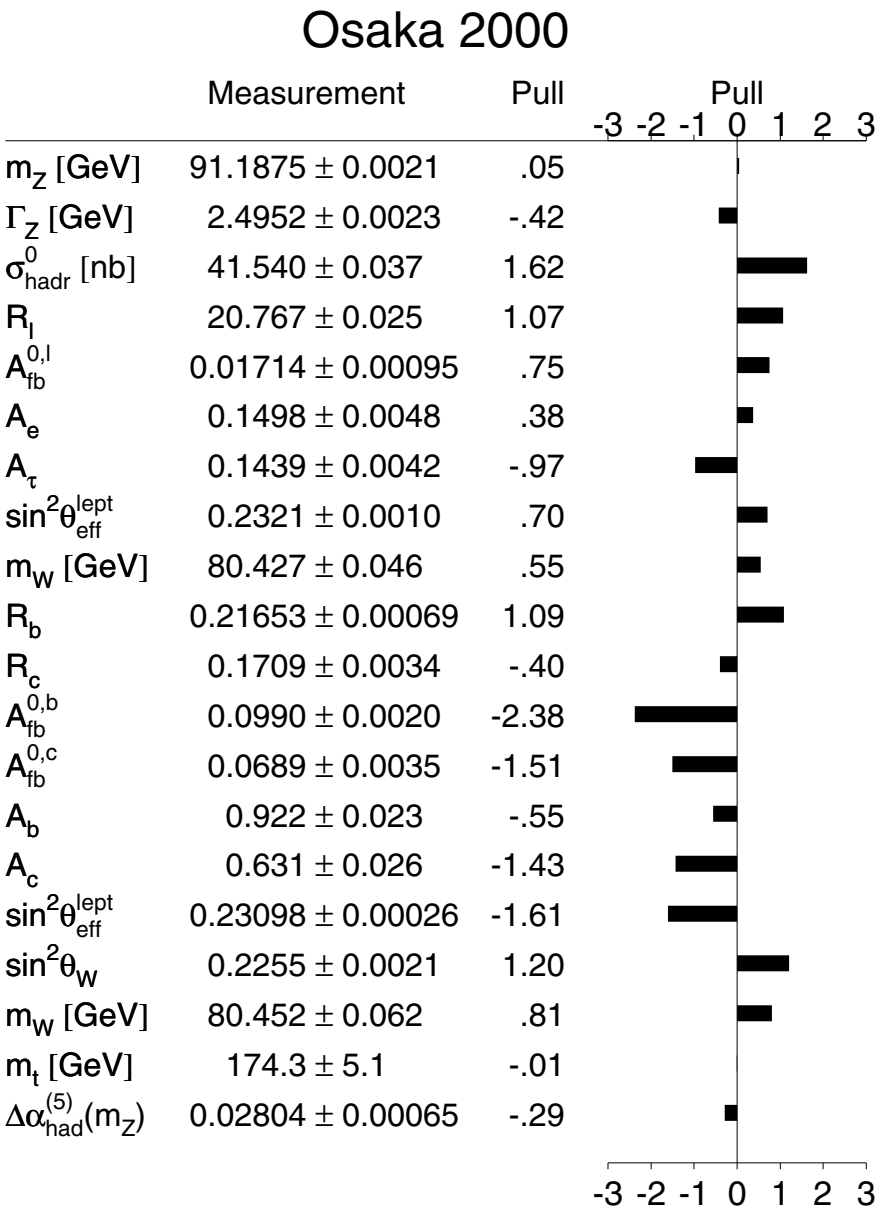

Fig. 2. *Summary of the measurements of the Standard Model parameters from LEP, SLD and $p\bar{p}$ and νN experiments.*

symmetry is broken in the masses. The mechanism that describes the spontaneous breaking of the symmetry is the Higgs mechanism.[2] While the existence of the Higgs boson is well supported by the data on radiative corrections,[1] the value of its mass is not predicted by the theory and only weak limits come from the experiments. In Figure 3 the theoretical bounds on the Higgs mass are shown as a function of Λ, the scale at which new physics can occur. These bounds are derived from general considerations: the lower bound arises from the requirement of vacuum stability after the inclusion of radiative corrections, while the upper bound is a consequence of the requirement that the Higgs quartic coupling does not leave the perturbative domain up to the scale Λ. This means that if we assume the SM to be valid up to the Planck scale the Higgs boson mass should be between 130 $\mathrm{GeV/c^2}$ < m(H) < 180 $\mathrm{GeV/c^2}$.

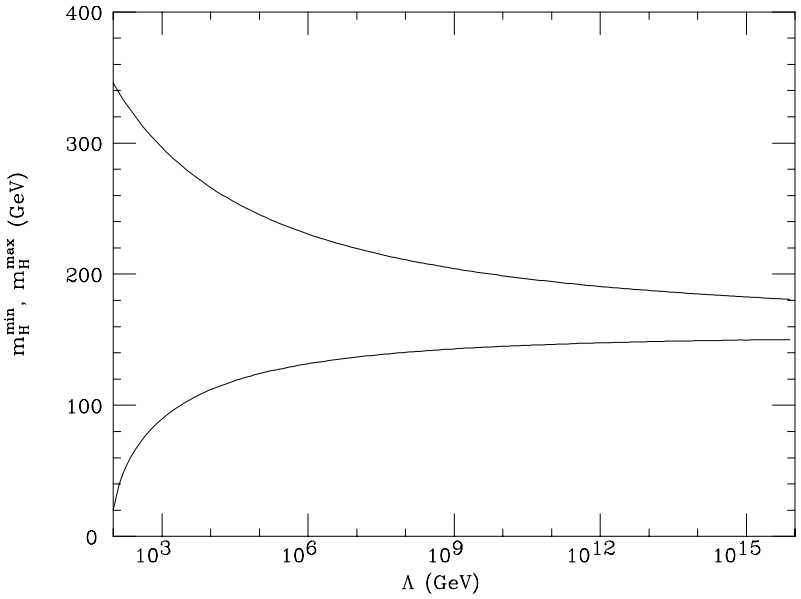

Fig. 3. *Theoretical upper and lower bounds on the Higgs mass.*

As of the Osaka conference of 2000 the experiments could set the following limits: from a fit to all the electroweak observables[1] the most probable value is m(H)=62^{+53}_{-30} $\mathrm{GeV/c^2}$, implying an upper limit at 95% CL of m(H)$\leq$ 170 $\mathrm{GeV/c^2}$ as shown in Figure 4. In a completely independent way the direct search could set a lower limit of 113.3 $\mathrm{GeV/c^2}$ at 95% CL.[3]

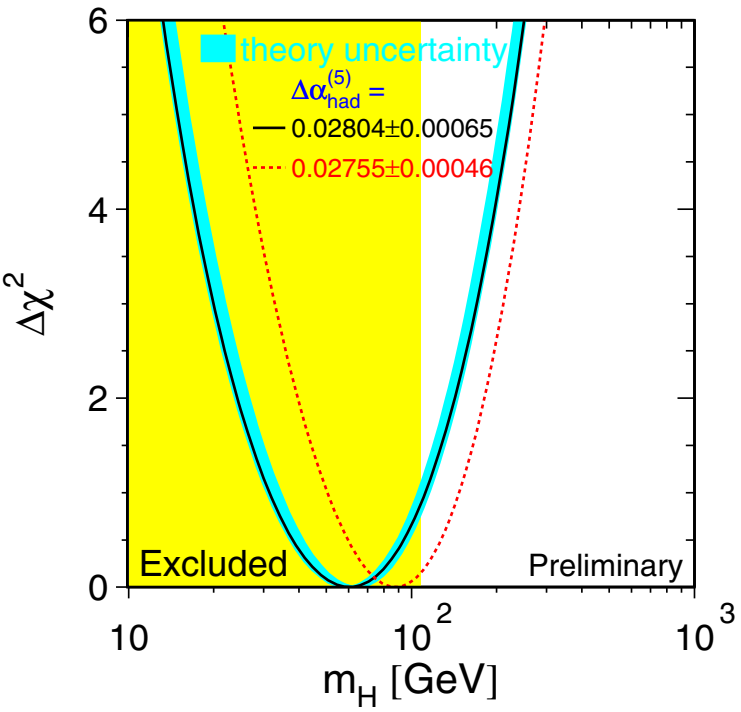

Fig. 4. $\Delta\chi^2 = \chi^2 - \chi^2_{min}$ $m_{\rm H}$*curve. The line is the result of the fit using all data*[1]*; the band represents an estimate of the theoretical error due to missing higher order corrections. The vertical band shows the 95% CL exclusion limit on* $m_{\rm H}$ *from the direct search. The dashed curve is the result obtained using the evaluation of* $\Delta\alpha^5_{\rm had}(m_{\rm Z}{}^2)$ *from Ref. 4.*

2.1 Higgs Production Cross Sections

At LEP the Higgs is expected to be produced mainly via the Higgstrahlung process $\rm e^+e^- \rightarrow$ HZ, plus a small contribution from the WW-fusion process (shown in Figure 5). The two diagrams interfere positively. The contribution from the ZZ-fusion process is an order of magnitude smaller than the WW-fusion process and therefore is not considered in the analyses. The Higgstrahlung mechanism dominates for m(H)$\leq \sqrt{s}-$m(Z) (the so-called Higgstrahlung wall) while the WW-fusion mechanism is our only possibility to go beyond. Figure 6 show the various contributions to the cross section as a function of the Higgs mass for a centre of mass energy of 206 GeV.

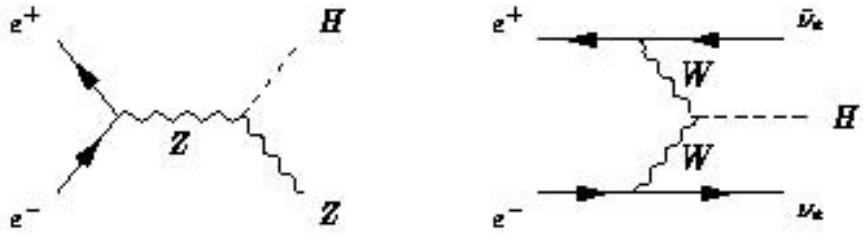

Fig. 5. *The two main diagrams describing the Higgs production at LEP: the Higgstrahlung process and the WW-fusion process.*

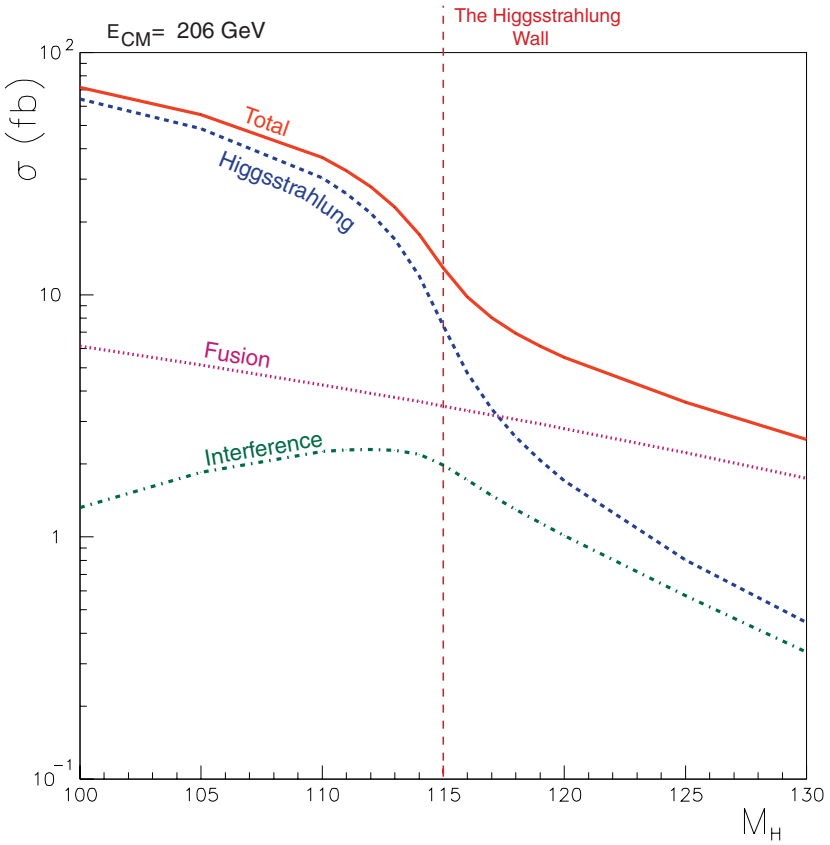

Fig. 6. *The cross section for Higgs production at* $\mathrm{E_{cm}}$*=206 GeV as a function of the Higgs mass for the different production processes.*

2.2 Final State Topologies at LEP

For masses accessible at LEP the Higgs decays predominantly into b quarks (BR(H $\rightarrow \mathrm{b\bar{b}}$) $\sim 85\%$) and $\tau^+\tau^-$pairs (BR(H $\rightarrow \tau^+\tau^-$) $\sim 8\%$). These values are approximately constant for Higgs masses that can be produced at LEP. Thus the Higgs search is typically divided into channels with topologically distinct final states characterised by the decays of the Z as: 4-jets (HZ $\rightarrow \mathrm{b\bar{b}q\bar{q}}$) $\sim 60\%$ of the time, 2-jets and missing energy (HZ $\rightarrow \mathrm{b\bar{b}}\nu\bar{\nu}$) 19% of the time; leptonic (HZ $\rightarrow \mathrm{b\bar{b}e^+e^-}$and $\mathrm{b\bar{b}}\mu^+\mu^-$) and taus (HZ $\rightarrow \mathrm{b\bar{b}}\tau^+\tau^-$and $\tau^+\tau^-\mathrm{b\bar{b}}$) 9% of the time.

The dominant backgrounds are the Standard Model processes with WW, ZZ, $\mathrm{q\bar{q}}(n\gamma)$ and $\mathrm{q\bar{q}}(gluons)$.[5]

2.3 The Fundamental Tools

The identification of a jet coming from a b-quark is the fundamental tool to search for a Higgs boson. The characteristics of hadrons with b-quarks (i.e. an average lifetime of 1.564$\pm$0.014 ps and a mass of 4.5 $\mathrm{GeV/c^2}$) imply that b-hadrons produced at LEP will fly for few millimetres and the decay products will have large transverse momentum ($\mathrm{p_T}$) and large impact parameters when compared to mesons from light quarks. These features, combined with other characteristics of the secondary vertices, or the lepton $\mathrm{p_T}$, or the rapidity of the tracks using likelihood techniques or Neural Networks, allowed one to reach very high discrimination, as shown for example in Figure 7 (where for a Higgs efficiency of 60% the WW background is suppressed to the 1% level). In parallel it is essential to have a good agreement between data and simulation, as shown in Figure 8.

In the search for the Higgs boson it is fundamental to reach high accuracy in the measurement of the energy deposited in the detector (especially for final states with neutrinos), and to be able to reconstruct the invariant mass of di-jets with 2-3 GeV precision in order to distinguish the various particles produced.

The experiments[6] use different neural network or likelihood techniques to combine the properties of the events (like b-quark tagging, kinematical or topological informations) into a discriminant variable that allows them to reach a high Higgs signal efficiency and high background rejection. The discriminant variable is then combined with the mass information of the candidates to give each candidate event a weight, expressing its significance with respect to a given Higgs mass hypothesis.

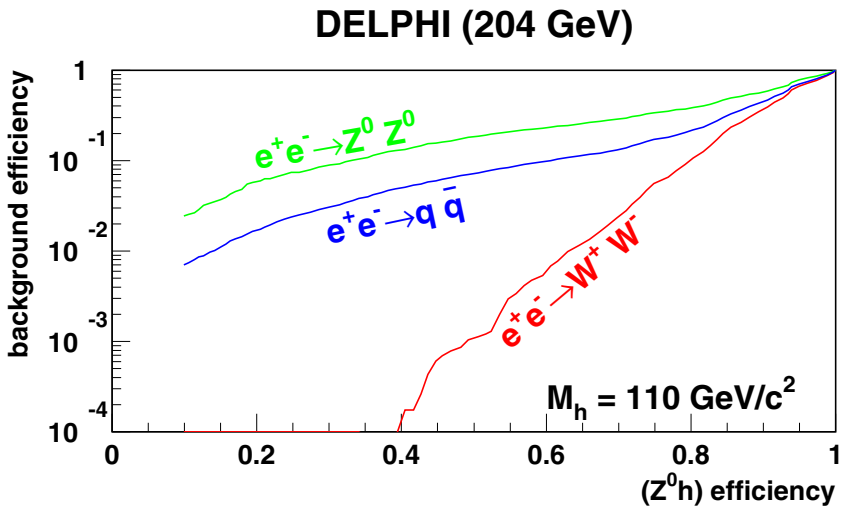

Fig. 7. *The number of background events versus the SM Higgs efficiency (as an example for the DELPHI experiment).*

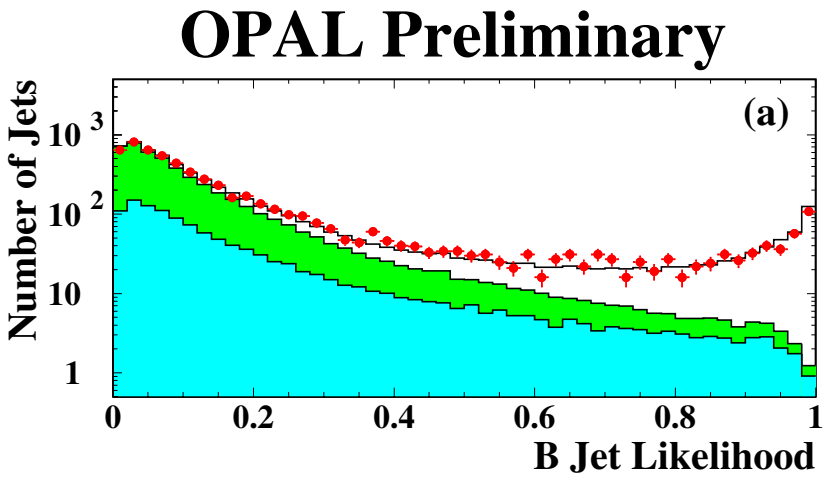

Fig. 8. *Agreement between data and simulation in the b-tagging algorithm output for Zγ events (as an example for the OPAL experiment).*

2.4 Problems for each of the topologies

The 4-jet channel: One of the biggest difficulties in this channel is the pairing of the jets. In a genuine 4-jet event there are 3 possible di-jet combinations, while in a 5-jet event there are 10 combinations. Different solutions using more than one criteria are pursued by the different experiments: forcing one of the di-jets to the Z boson; pairing jets with the highest b-tag probability as the ones coming from the Higgs; making all the possible combinations with the WW, ZZ and HZ hypotheses and looking at the minimal χ^2 of the fit; checking the spin of the boson with the jet decay angles. The irreducible background in this channel comes from ZZ and WW production having done the wrong pairing, and from the so-called QCD events, i.e. the $\mathrm{q\bar{q}gg}$ final state. As an example in Figure 9 the 3 possible pairings of a 4-jet b-tagged event from DELPHI at $\mathrm{E_{cm}}$=200 GeV are shown. The "ideogram" plot[7] shows the goodness of the fit for each of the two di-jet masses hypotheses. The dimensions of the circles (standard deviation contours) show that some jet-pairings are more probable than others. In this case the HZ hypothesis (for a Higgs of mass 105 GeV) is more likely than the ZZ hypothesis.

The leptonic channel is the cleanest of the topologies since it is almost background-free. It is the "golden candidate" that every experiment dreams of. Indeed it is possible to fake a high mass candidate in this channel if a photon from initial state radiation or a photon emitted from one of the leptons is associated to one of the jets, artificially increasing the di-jet Higgs mass.

The missing energy channel is probably the most difficult one because of the high background contamination and the poor di-jet mass resolution. In order to increase the mass resolution the missing mass is forced to be that of the Z. By doing so part of the background is also pushed to the kinematic limit: M(jj)=$\mathrm{E_{cm}}$-M(Z). In particular the double radiative return events to the Z ($\mathrm{Z}\gamma\gamma$) become the biggest danger, because the cross section is not known with high accuracy. In these events[8] two photons are emitted back to back and the Z is produced at rest. The events are characterised by E($\gamma\gamma$)=$\mathrm{E_{cm}}$-M(Z). If the photons are lost in the beam pipe and the missing mass is forced to be equal to the Z, the visible mass is pushed to the kinematical limit.

2.5 The Results

The results from the four collaborations for the data collected in 2000 are summarised in Table 2. The large spread in the numbers of selected candidates reflects substantial differences in the selection methods and optimisation procedures.

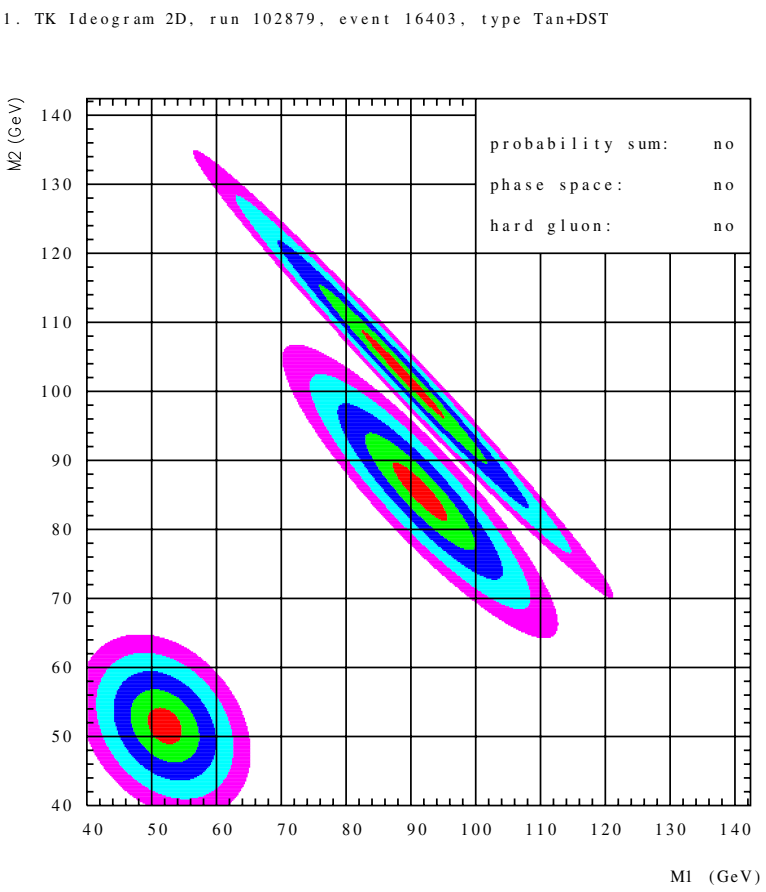

Fig. 9. *The mass of one di-jet versus the mass of the other di-jet for 3 possible pairings of a 4-jet b-tagged event from DELPHI at* $\mathrm{E_{cm}}$*=200 GeV.*

Experiment:	ALEPH	DELPHI	L3	OPAL
Total: Integrated luminosity (pb^{-1}):	94.2	96.1	81.8-84.7	80.0
Backg. predicted / Evts. observed				
Four-jet:	20.2/18	76.4/87	15.0/11	8.9/7
Missing-energy:	17.0/19	42.8/39	5.3/5	13.6/6
Leptonic (e, μ):	12.9/9	9.5/5	1.0/1	3.0/8
Tau channels:	5.9/7	3.2/3	0.69/1	1.3/0
Events in all channels	56.1/53	131.9/134	22.1/18	26.8/21
Limit ($\mathrm{GeV/c^2}$) exp. (median) at 95% CL:	112.0	109.2	108.0	109.5
Limit ($\mathrm{GeV/c^2}$) observed at 95% CL:	110.8	109.0	107.5	109.5

Table 2. *Information on the searches of the LEP experiments for the SM Higgs boson for* $\mathrm{E_{cm}}$*= 200−209 GeV (year 2000 data). In the L3 analysis the event selection depends on the Higgs boson mass hypothesis (here* m_{H}*=110* $\mathrm{GeV/c^2}$*).*

The statistical procedure adopted for the combination of the data, and the precise definition of the confidence levels CL_b, CL_{s+b} and CL_s with which the search results are expressed, are stated in Ref. 3. The main sources of systematic errors affecting the signal and background rate predictions are included, taking into account correlations between search channels, LEP energies and individual experiments. In the procedure used to determine the limits, the treatment of candidate events depends on the values of reconstructed quantities, such as b-tag significances and reconstructed invariant masses. An excess or deficit of candidates may occur in a region of high background and low signal, hence the total count does not indicate whether the actual limit ought to be stronger or weaker than the expectation.

The compatibility of the result with the background hypothesis is given by $1-CL_b$, which is plotted as a function of m_{H} in Figure 10. Values of $1-CL_b$ below 5.7×10^{-7}, indicated by the horizontal full line, corresponding to a 5 standard deviation fluctuation of the background, are considered to be in the discovery region. The dotted line shows the expectation in the presence of a signal of true mass m_{H}; its crossing with the 5σ line at 109.5 $\mathrm{GeV/c^2}$ indicates the range of sensitivity of the presently available data to a discovery. It is not enough just to read off the value of $1-CL_b$ at the value of m_{H} for which $-2\ln(Q)$ has its minimum to claim observation of a signal, because this only gives the probability that the background fluctuated at precisely that mass, while in principle it could have fluctuated anywhere in the mass region considered. This mass region is chosen to include values of m_{H} not strongly excluded by previous searches and for which the present searches have sensitivity. An estimate based on Monte Carlo studies shows that $1-CL_b$ must be multiplied by a factor of four in the present case, corresponding roughly to the width of the mass search region divided by the typical mass resolution.

A 95% confidence level lower limit on the Higgs mass may be set by identifying the mass region where $CL_s<0.05$, as shown in Figure 11. The median limit expected in the absence of a signal is 113.4 $\mathrm{GeV/c^2}$, and the limit observed by combining the LEP data is 113.3 $\mathrm{GeV/c^2}$. The inclusion of systematic errors, together with their correlations, has decreased the limits by approximately 100 MeV/c^2.

Figure 12 shows the distribution of reconstructed Higgs masses for a subset of the events in Table 2. The corresponding background from SM processes and the signal expected from a SM Higgs boson of 110 $\mathrm{GeV/c^2}$ mass are also shown. The figure has been obtained requiring that the contributions from the four experiments (selecting the most signal-like set of events) be roughly equal. Since all events enter with

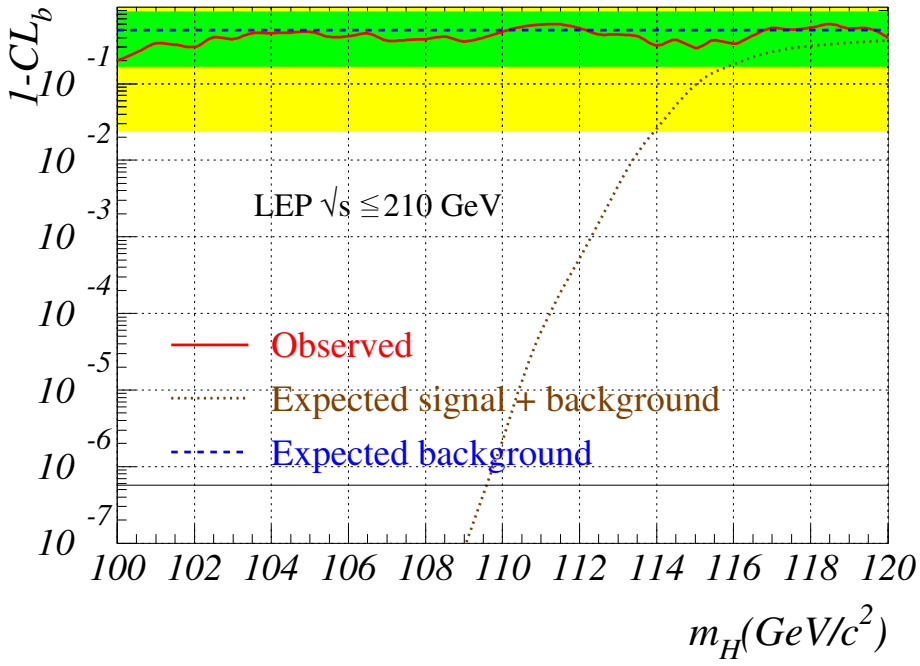

Fig. 10. *The confidence level* $1-CL_b$ *as a function of* m_{H}. *The straight dashed line at 50% and the shaded bands represent the median result and the* $\pm 1\sigma$ *and* $\pm 2\sigma$ *probability bands expected in the absence of a signal. The solid curve is the observed result and the dotted curve shows the median result expected for a signal when tested at the "true" mass. The horizontal line at* 5.7×10^{-7} *indicates the level for a* 5σ *discovery.*

equal weight, such a distribution does not reflect for example differences in mass resolutions, signal sensitivities and background rates, which characterise the various search channels and individual experiments.

3 The Minimal Supersymmetric Standard Model Higgs

There are conceptual problems in the Standard Model that are solved by its supersymmetric extension: the extrapolation of the SM at very high energy, the unification of the couplings, the hierarchy problems, the dark matter.[9]

In the Minimal Supersymmetric extension of the Standard Model (MSSM) the symmetry is "softly" broken in a hidden sector,[9] that communicates with the visible sector via gravity (SUGRA model) or via gauge bosons (GMSB model). The MSSM predictions tend to reproduce the result of the SM with a light Higgs of mass less than 130 $\mathrm{GeV/c^2}$ as shown in Figure 13[5] and Figure 14.[10]

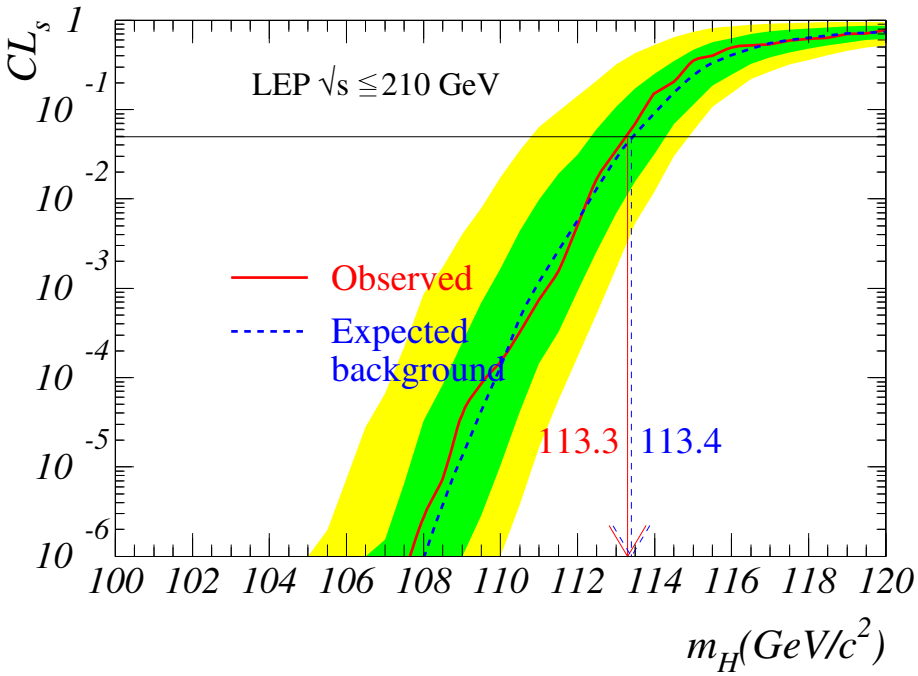

Fig. 11. *The confidence level CL_s for the signal hypothesis versus m_{H}. The solid curve is the observed result, the dashed curve the median result expected in the absence of a signal. The shaded areas represent the symmetric 1σ and 2σ probability bands of CL_s in the absence of a signal. The intersections of the curves with the horizontal line at $CL_s = 0.05$ give the mass limits at the 95% confidence level.*

In the MSSM there are two fundamental Higgs field doublets, and the Higgs sector comprises five physical states: two CP-even neutral Higgs bosons, h and H ($m_{\mathrm{h}}<m_{\mathrm{H}}$), one CP-odd neutral Higgs boson, A, and a pair of charged Higgs bosons, H^+ and H^-. At LEP energies the h and A particles are expected to be produced mainly via the Higgs-stralung process $\mathrm{e}^+\mathrm{e}^- \rightarrow \mathrm{hZ}$ (analogous to the main SM production process) or the pair production process $\mathrm{e}^+\mathrm{e}^- \rightarrow \mathrm{hA}$. The two processes are complementary: the cross-section of the first is proportional to $\sin^2(\beta-\alpha)$ and that of the second proportional to $\cos^2(\beta-\alpha)$ ($\tan\beta$ is the ratio of the vacuum expectation values of the two Higgs field doublets and α is a mixing angle in the CP-even Higgs sector).

3.1 Results

The combined data of the four LEP experiments are interpreted here within the framework of a 'constrained' MSSM where universal values M_{SUSY} and M_2 are assumed

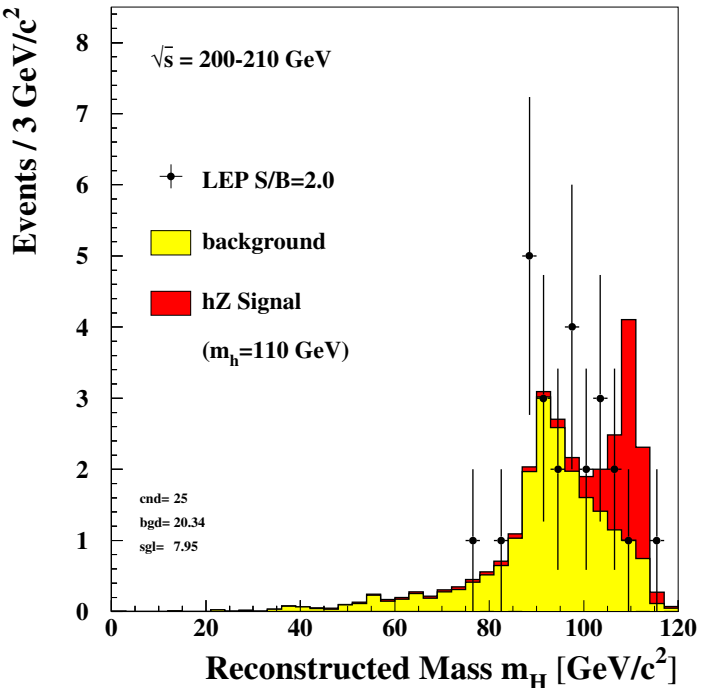

Fig. 12. *LEP-combined distribution of the reconstructed SM Higgs boson mass in searches conducted at $\sqrt{s}$ between 200 and 209 GeV. The events satisfy the condition S/B>2, where the S/B cut applies to the region m>105* $\mathrm{GeV/c^2}$ *and for* m_{H}*=110* $\mathrm{GeV/c^2}$*. The figure displays the data (dots with error bars), the predicted SM background (shaded histogram) and the prediction for a Higgs boson of 110* $\mathrm{GeV/c^2}$ *mass (dashed histogram). The number of data events selected for this figure is 25 while 20.34 are expected from SM background processes. A signal at 110* $\mathrm{GeV/c^2}$ *mass would contribute with 7.95 events.*

for the SUSY breaking sfermion and gaugino masses, respectively, at the electroweak scale. Combined search results are given for two new 'benchmark' MSSM parameter scans.[11] The first benchmark corresponds to *no-mixing* in the scalar-top sector; the second to large mixing and other parameters tuned to allow maximal values for m_{h} for each value of $\tan\beta$ (m_{h}*-max* hereafter). In both benchmark scans the top mass, which has an impact on the results via radiative corrections, is fixed to the experimental[12] central value of m_{t}=174.3 $\mathrm{GeV/c^2}$, and to two alternative values where the central value is decreased and increased by the current experimental error of 5.1 $\mathrm{GeV/c^2}$. In each case, the exclusion limits obtained are valid for m_{t} less than or equal to the chosen value.

The individual searches of the four LEP collaborations for the processes $\mathrm{e^+e^-}\rightarrow \mathrm{hZ}$

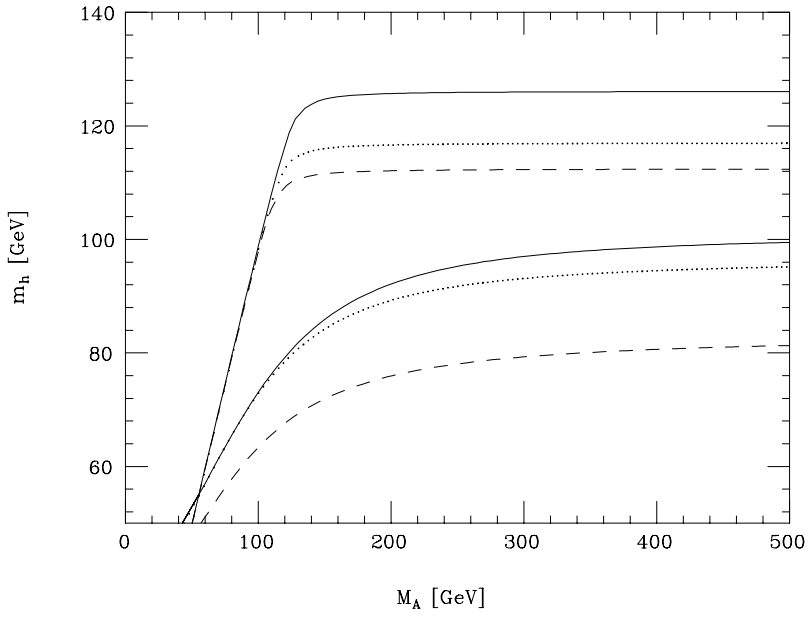

Fig. 13. *Lightest neutral Higgs h in the MSUGRA model as a function of* m_A *for zero mixing (dashed line), for intermediate mixing (dotted line) and for maximal mixing in stop sector (solid line); for two values of tan*β*=1.6 (lower set), 15 (upper set).*

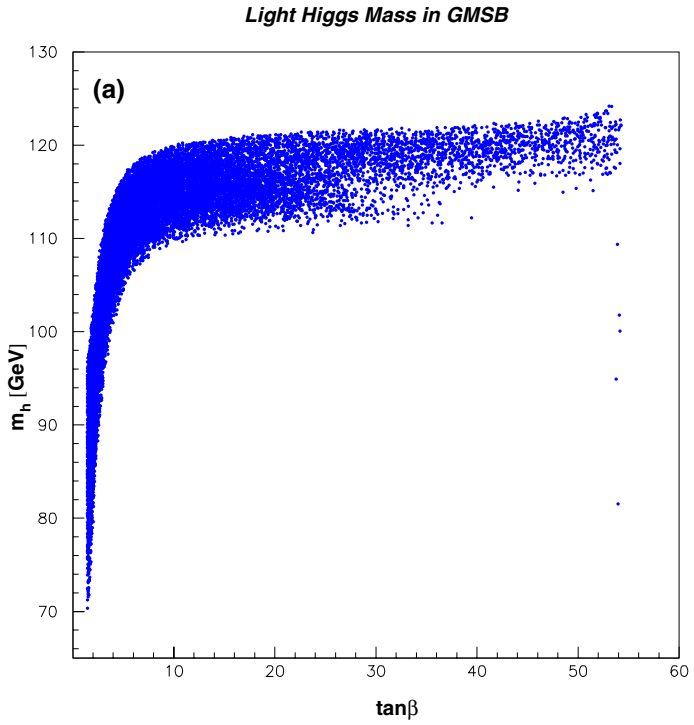

Fig. 14. *Scatter plot for the light scalar Higgs boson as a function of tan*β *for the GMSB model.*

and $e^+e^- \to hA$, which include the data taken at $\sqrt{s}$ from 200 to 209 GeV, are described in Ref. 6. For the process $e^+e^- \to hZ$, the searches for the SM Higgs boson are interpreted in the MSSM while taking into account the reduced cross-section due to the factor $\sin^2(\beta - \alpha)$ and the predicted variations of the decay branching ratios of the h boson in the scans. For the process $e^+e^- \to hA$, the most relevant final states are $b\bar{b}b\bar{b}$, $\tau^+\tau^- b\bar{b}$ and $b\bar{b}\tau^+\tau^-$.

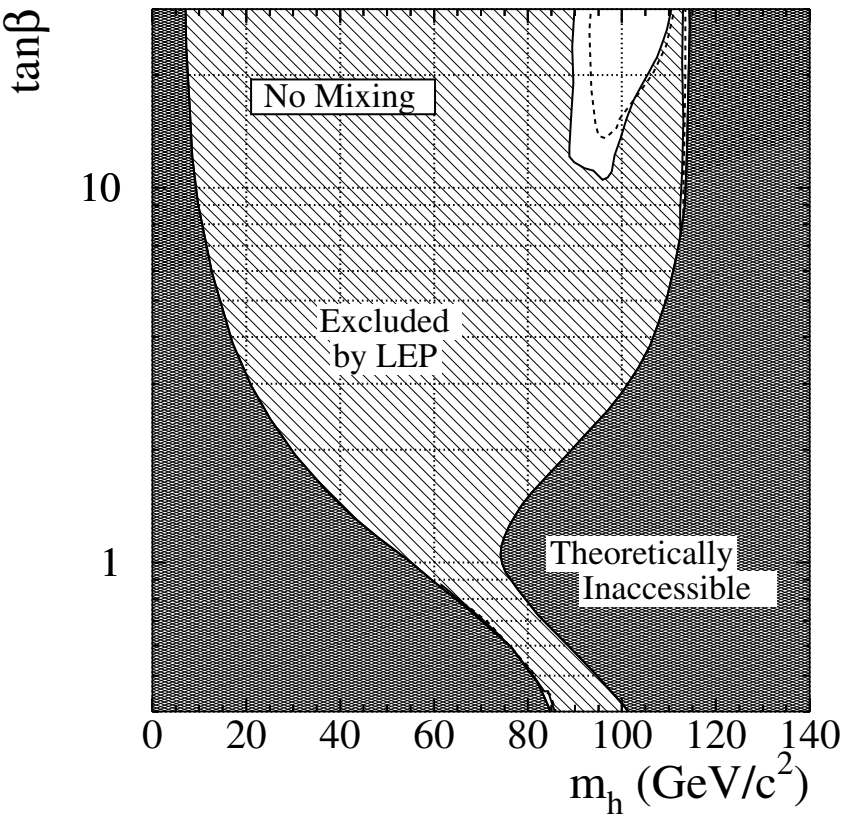

Fig. 15. *The 95% CL bounds on m_h, m_A and $\tan\beta$, for the no-mixing benchmark, from combining the data of the four LEP experiments at 200 to 209 GeV with earlier data taken at lower energies. The full lines represent the actual observation and the dashed lines the median limits expected on the basis of 'background only' Monte Carlo experiments.*

The results are shown in Figures 15 and 16, for the *no-mixing* and m_h*-max* benchmarks. The limits are presented for $\tan\beta$>0.4 and in one parameter projection, (m_h, $\tan\beta$). Boundaries obtained from the data and the ones expected on the basis of background Monte Carlo experiments are shown.

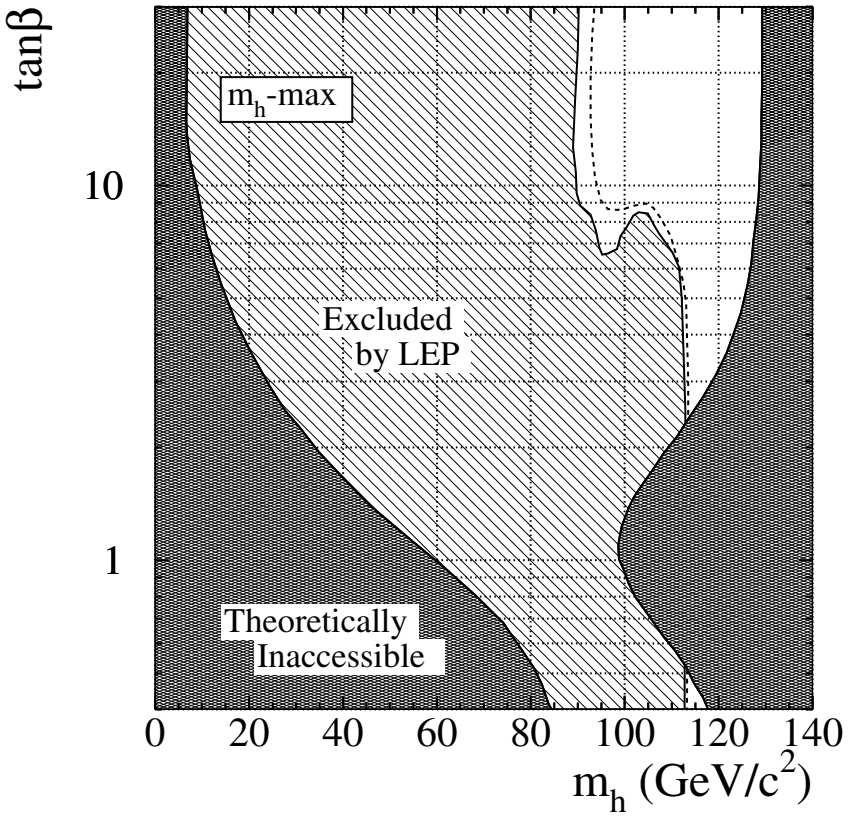

Fig. 16. *The 95% CL bounds on $m_{\rm h}$, $m_{\rm A}$ and $\tan\beta$, for the $m_{\rm h}$-max benchmark, from combining the data of the four LEP experiments at 200 to 209 GeV with earlier data taken at lower energies. The full lines represent the actual observation and the dashed lines the median limits expected on the basis of 'background only' Monte Carlo experiments.*

	no-mixing	m_{h}-max
Limits for m_{h} ($\mathrm{GeV/c^2}$)		
expected (median) :	92.4	92.2
observed :	90.4	90.5
Limits for m_{A} ($\mathrm{GeV/c^2}$)		
expected (median):	92.9	92.8
observed :	90.5	90.5
Exclusion in $\tan\beta$		
expected (median):	0.8-8.6	0.5-2.3
observed :	0.9-7.7	0.5-2.3

Table 3. *Combined 95% CL MSSM limits for m_{h} and m_{A} (valid for $\tan\beta > 0.4$) and excluded ranges in $\tan\beta$, for the two benchmark scenarios, and for top masses less than 174.3 $\mathrm{GeV/c^2}$. The quoted limits were obtained including systematic errors and their correlations.*

The mass limits obtained for the two benchmark scans are presented in Table 3.

4 The Charged Higgs Boson Search

At LEP2 energies charged Higgs bosons are expected to be produced mainly through the process $\mathrm{e^+e^-}\to\mathrm{H^+H^-}$. In the MSSM and at tree-level the $\mathrm{H^\pm}$ is constrained to be heavier than the $\mathrm{W^\pm}$ bosons but loop corrections drive the mass to lower values for some values of the MSSM parameters. Since the sensitivity of current searches is limited to the range below m_{W} due to the background from $\mathrm{e^+e^-}\to\mathrm{W^+W^-}$, a signal for $\mathrm{H^+H^-}$ would indicate either new physics beyond the MSSM or place very stringent constraints on the MSSM parameter values. The present searches for charged Higgs bosons are placed in the general context of 2 Higgs Doublet Models (2HDM) where the mass is not constrained. The searches are carried out under the assumption that the two decays $\mathrm{H^+}\to\mathrm{c\bar{s}}$ and $\mathrm{H^+}\to\tau^+\nu_\tau$ exhaust the $\mathrm{H^+}$ decay width; however, the relative branching ratio is not predicted. Thus, the searches encompass the following $\mathrm{H^+H^-}$ final states: $(\mathrm{c\bar{s}})(\mathrm{\bar{c}s})$, $(\tau^+\nu_\tau)(\tau^-\bar{\nu}_\tau)$ and the mixed modes $(\mathrm{c\bar{s}})(\tau^-\bar{\nu}_\tau)$, $(\mathrm{\bar{c}s})(\tau^+\nu_\tau)$. The combined search results are presented as a function of the branching ratio $\mathrm{B}(\mathrm{H^+}\to\tau^+\nu_\tau)$.

In the search for the $\mathrm{H^\pm}$ c-quark and s-quark tags, plus the polar angles of the jets to identify the spin of the boson, are used to reject the dominant $\mathrm{W^\pm}$ background, while

	Mass limit in $\mathrm{GeV/c^2}$
B($\mathrm{H^+}\to\tau^+\nu_\tau$)=0	
Limit expected (median) :	79.7
Limit observed :	80.8,"islands"
B($\mathrm{H^+}\to\tau^+\nu_\tau$)=1	
Limit expected (median) :	90.5
Limit observed :	87.7
Any B($\mathrm{H^+}\to\tau^+\nu_\tau$)	
Limit expected (median):	78.5
Limit observed :	77.4

Table 4. *The combined 95% CL lower bounds for the mass of the charged Higgs boson, expected and observed, for fixed and arbitrary values of the branching ratio B($\mathrm{H^+}\to\tau^+\nu_\tau$).*

shape variables and acoplanarity are used to reject the QCD background.[13]

The expected and observed mass limits are shown in Figure 17. The combined 95% CL bounds are listed in Table 4 for B($\mathrm{H^+}\to\tau^+\nu_\tau$)=0, 1, and for arbitrary values of the branching ratio.

5 The Invisible Higgs

The Higgs boson decays into the heaviest kinematically accessible particle. In the MSSM it can decay into invisible super-particles, like the lightest neutralino χ_1^0: h $\to \chi_1^0\chi_1^0$. If the χ_1^0 is purely photino then this process is suppressed and h $\to\chi_2^0\chi_1^0$ with $\chi_2^0 \to \chi_1^0$ Z/γ^*. The final state is characterised by the 2 leptons or the two jets from the Z decay and missing energy and momentum carried away by the neutralinos. The analysis is then similar to the search for the SM Higgs, in the H$\nu\bar{\nu}$ final state, but there is no need for the b-tag. The main backgrounds are $\mathrm{q\bar{q}}(\gamma)$, single W production and WW production for the final state Z $\to l\bar{l}$. The consistency of the combined data with the background expectation can be seen in Figure 18. There is an extreme minimum of $1-\mathrm{CL}_b$ of 0.018 at 110.2 $\mathrm{GeV/c^2}$. There is also a maximum of 0.986 at 83 $\mathrm{GeV/c^2}$, corresponding to a deficit of candidates. Each of these deviations is a little over two sigma. The observed limit is $m_\mathrm{H}>$ 107.6 $\mathrm{GeV/c^2}$ (expected limit is $m_\mathrm{H}>$ 109.9 $\mathrm{GeV/c^2}$) for $\mathrm{E_{cm}}$=200-209 GeV, for only 3 experiments combined together.

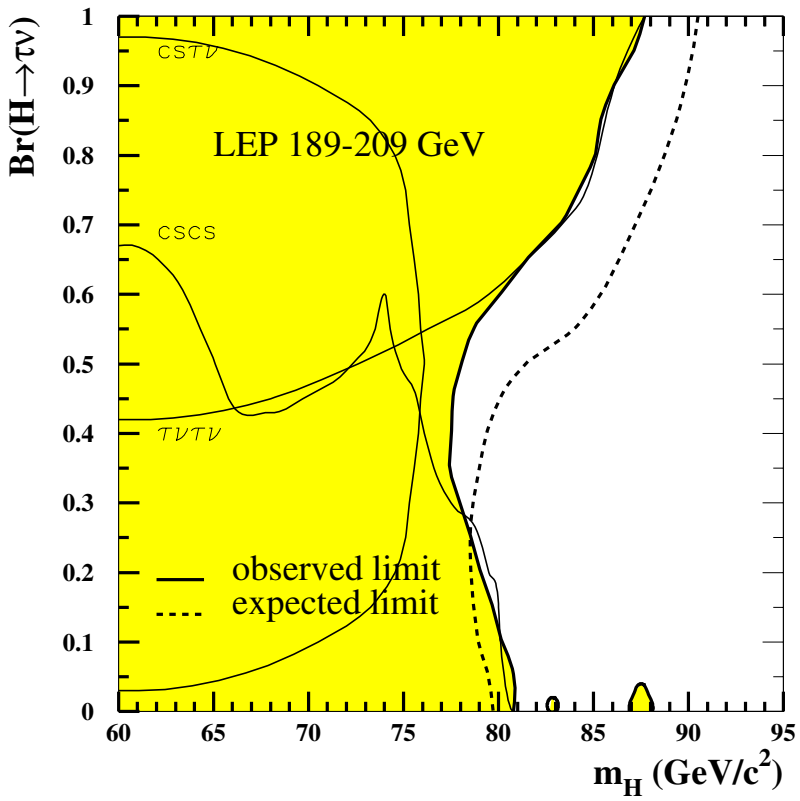

Fig. 17. *The 95% CL bounds on $m_{\mathrm{H}^{\pm}}$ as a function of the branching ratio B($\mathrm{H}^{+}\to\tau^{+}\nu_{\tau}$), combining the data collected by the four LEP experiments at energies up to 209 GeV. The median expected exclusion limits are indicated by the dashed line and the observed limits by the heavy full line. The light full lines show the observed limits channel by channel.*

6 Non Fermionic Higgs couplings

Anomalous coupling. In the SM the anomalous coupling $\mathrm{e}^{+}\mathrm{e}^{-}\to\mathrm{H}\gamma$ has a very small cross section, but it would be the ideal channel to reach $m_{\mathrm{H}}\leq\mathrm{E}_{\mathrm{cm}}$. In a more general 2 Higgs Doublet Model (of which the MSSM is a particular case) it can be enhanced. At LEP the following final states are studied: $\mathrm{e}^{+}\mathrm{e}^{-}\to\mathrm{H}\gamma\to\gamma\gamma\gamma$, $\mathrm{b\bar{b}}\gamma$, $\mathrm{e}^{+}\mathrm{e}^{-}\to\mathrm{HZ}\to\gamma\gamma\nu\bar{\nu}$, $\mathrm{e}^{+}\mathrm{e}^{-}\to\mathrm{HZ}/\gamma^{*}\to\gamma\gamma\mathrm{q\bar{q}}$. No signal has been found at LEP in 2000 data.

Fermiophobic decays. In both the SM and in the 2HDM the Higgs can decay into photons via quark or W boson loop. While in the SM the rate is too small to be observed at LEP, in the 2HDM there is a value of the parameter α that can cause

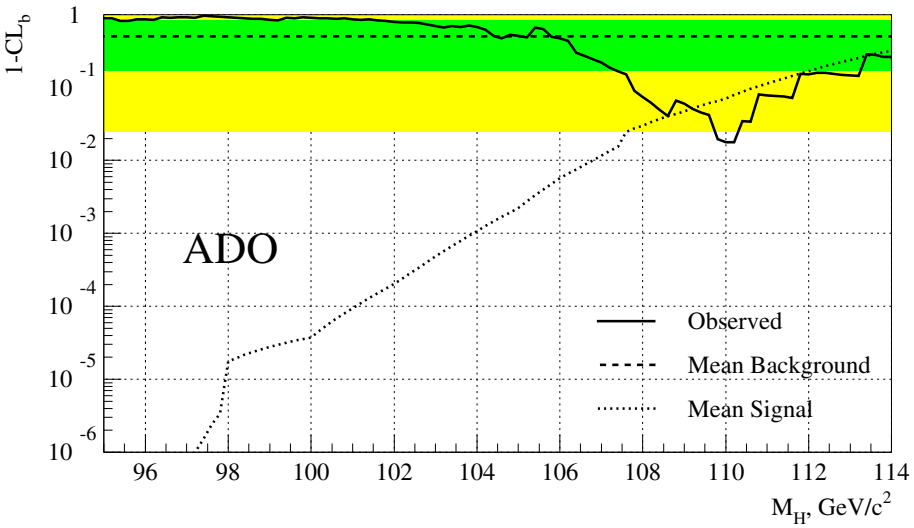

Fig. 18. *The value of $1-CL_b$ for the A,D,O combined data in the h $\rightarrow\chi_1^0\chi_1^0$ search. The step nature of the results comes because ALEPH used a sliding window (in test mass) analysis and reports relevant candidates in the a discretised way. There is a "knee" in the curve of signal expectations; below 98* $\mathrm{GeV/c^2}$ *the ALEPH results from lower energies contribute.*

the h to couple only to bosons. The final state can be very simple, i.e. 2 photons only and missing energy from the process $\mathrm{e^+e^-}\rightarrow$hZ $\rightarrow\gamma\gamma\nu\bar{\nu}$, or more complex in the case of associated production of hA: $\mathrm{e^+e^-}\rightarrow$hA $\rightarrow\gamma\gamma$A $\rightarrow\gamma\gamma\mathrm{b\bar{b}}$, $\mathrm{e^+e^-}\rightarrow$hA $\rightarrow$AAA $\rightarrow\gamma\gamma\gamma\gamma\nu\bar{\nu}$, $\gamma\gamma\gamma\gamma\mathrm{b\bar{b}}$.[14]

The four LEP experiments combine the results only for events with two energetic and isolated photons. In addition, the Z decay products are either classified, or, in the case of Z $\rightarrow\nu\bar{\nu}$, acoplanarity in the photons is required. The analysis procedures of the four LEP experiments producing the inputs for the present combination are described in individual documents.[15]

As a benchmark for exclusion of Higgs bosons in fermiophobic models, we consider an h produced in $\mathrm{e^+e^-}\rightarrow$hZ with the Standard Model production cross section and with the partial width for h $\rightarrow\gamma\gamma$ given by the SM,[16] but with the di-fermion partial width set to zero. Figure 19 shows the combined data for the 4 LEP experiments, together with the expected signal of a fermiophobic Higgs of mass 100 $\mathrm{GeV/c^2}$. The 95% confidence level upper limit for BR(h$\rightarrow\gamma\gamma$) incorporating all the combined ADLO data is shown in Figure 20. A lower mass limit for fermiophobic Higgs boson is obtained where the limit curve crosses the $\mathrm{B}_{\gamma\gamma}(m_{\mathrm{h}})$ curve; for the combined ADLO data this limit is 106.4 $\mathrm{GeV/c^2}$.

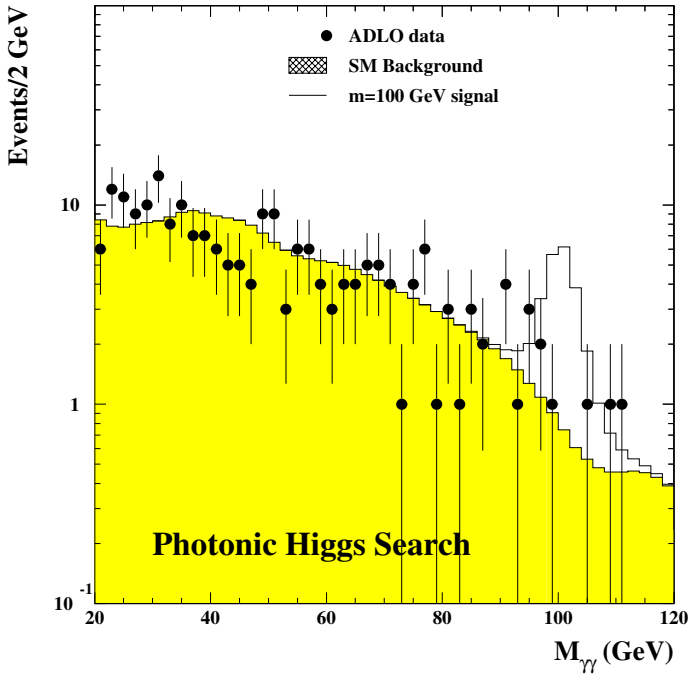

Fig. 19. *Distribution of the di-photon mass in the h* $\rightarrow\gamma\gamma$ *search. All the search channels are included. The white histogram is the benchmark signal for* m_{h}*= 100* $\mathrm{GeV/c^2}$.

7 The end of LEP

The year 2000 is scheduled to be the last year of LEP. In the first period of the year the maximum of the luminosity was collected at $\mathrm{E_{cm}}\sim$205 GeV, while in the second part of the year it was at $\mathrm{E_{cm}}\sim$206.7 GeV. About 10 pb^{-1} has been collected at $\mathrm{E_{cm}}\sim$208.1 GeV so far. With increasing energy and luminosity the Higgs reach of LEP increases day by day. At the end of the year 2000 the SM Higgs will be observed if $m_{\mathrm{H}}\leq$115 $\mathrm{GeV/c^2}$. At LEP the experiments are still working to see if 1 or 2 $\mathrm{GeV/c^2}$ can be gained in the final Higgs mass reach if the signal over background ratio of the analysis can be further improved optimising the search for a 115 $\mathrm{GeV/c^2}$ mass Higgs and going towards a "background-free" analysis (keeping in mind that 1 event for 0 expected is a discovery!). For example, for a Higgs of 115 $\mathrm{GeV/c^2}$ we expect for all the 4 experiments, integrating over all the channels and over data from 1998 to the end of 2000, a total of 20 events for 100% efficiency. Considering an average efficiency of 30% we need no more than 3 events of background in all LEP! It is also clear that only the 4 experiments together can hope to make it.

If the Higgs is discovered at LEP then future experiments will determine its nature

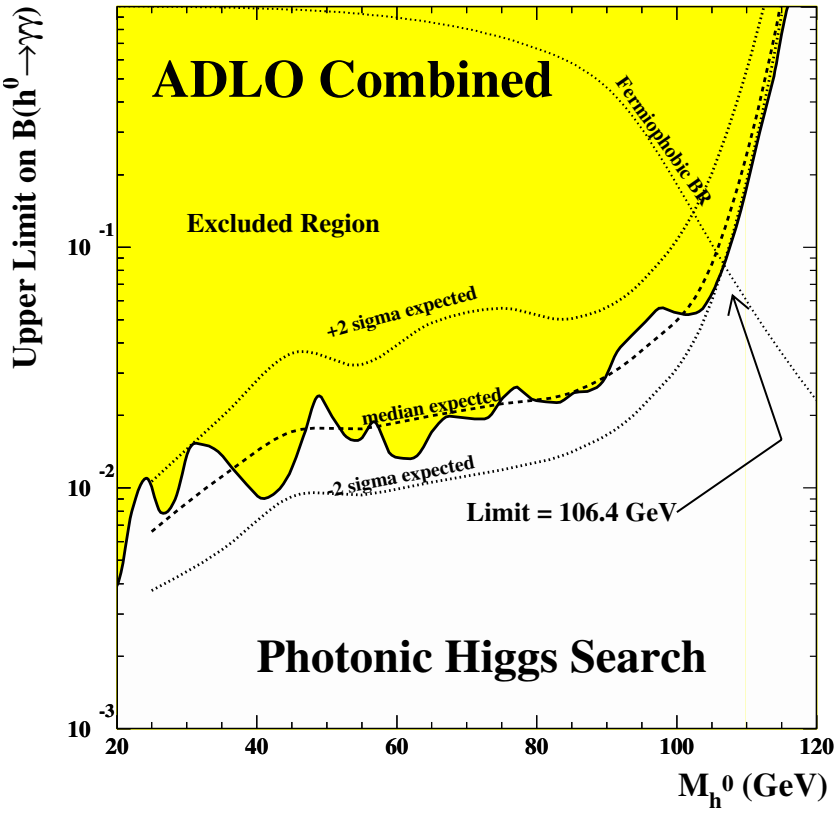

Fig. 20. *98% CL level upper limit on the di-photon branching fraction for a SM Higgs boson production rate. The shaded area is excluded. The dashed line is the predicted benchmark di-photon branching fraction assuming B($h \to f\bar{f}$)=0. The intersection of the dotted line with the exclusion curve gives a lower limit of 106.4* $\mathrm{GeV/c^2}$ *for a fermiophobic Higgs model. Also shown (dotted lines) are the median expected limit and the 95% CL zone for the expected limit.*

(SM, MSSM...). If it is not discovered at LEP, i.e. its mass is heavier than 115 $\mathrm{GeV/c^2}$, then a very small region is left for the MSUGRA and GMSB scenarios. For a top mass of $\sim$175 $\mathrm{GeV/c^2}$ and for large tan(β) the lightest Higgs h is predicted to be lighter than 125-130 $\mathrm{GeV/c^2}$. This also means that 7 GeV more to LEP would have allowed the machine to cover the entire MSSM plane!

8 After LEP: Tevatron and LHC

The experiments at the Tevatron will soon start to take data again with upgraded detectors. At a $\mathrm{p\bar{p}}$ collider the Higgs is produced mainly via gluon-gluon fusion or together with a W or a Z ($\mathrm{q\bar{q}}\rightarrow$W*(Z*) $\rightarrow$HW(Z)). The first process has a higher cross section, but the second one has a clearer signature. Studies[17] have shown that assuming 10% resolution on M($\mathrm{b\bar{b}}$), and a 30% improvement in the S/B with respect to the actual analyses combining all the channels and the two experiments, they can exclude at 95% CL a Higgs of mass $\leq$114 $\mathrm{GeV/c^2}$ with 2 fb^{-1} of luminosity. With about 30 fb^{-1} they can cover all the masses up to $\sim$180 $\mathrm{GeV/c^2}$, as shown in Figure 21.

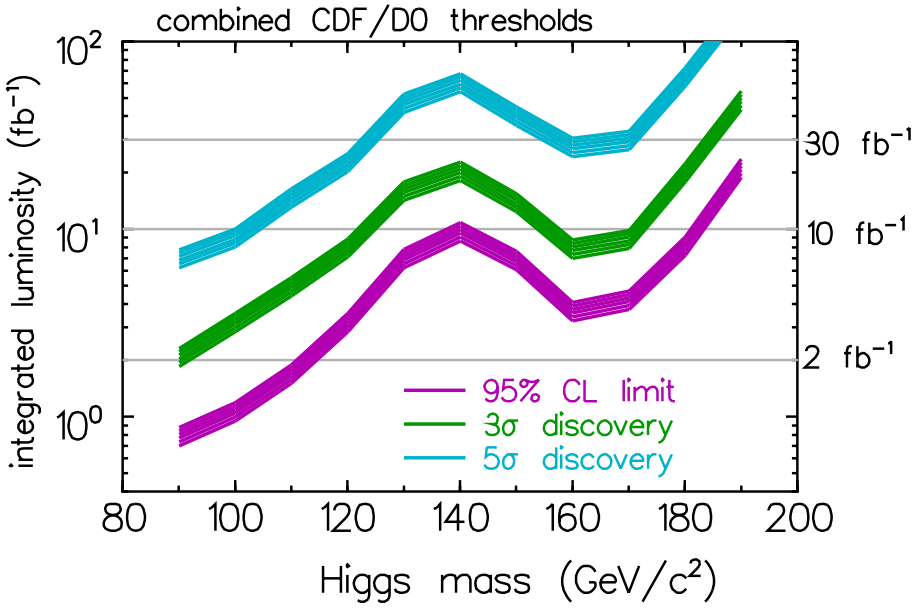

Fig. 21. *Minimum luminosity needed at the Tevatron to exclude (bottom curve), or discover (top curve) a SM Higgs boson at* $\mathrm{E_{cm}}$*= 2 TeV.*

The experiments at the LHC pp collider will start to take data in 2005. integrating 10 fb^{-1} per year for the first 3 years. In Figure 22 the signal significance versus the

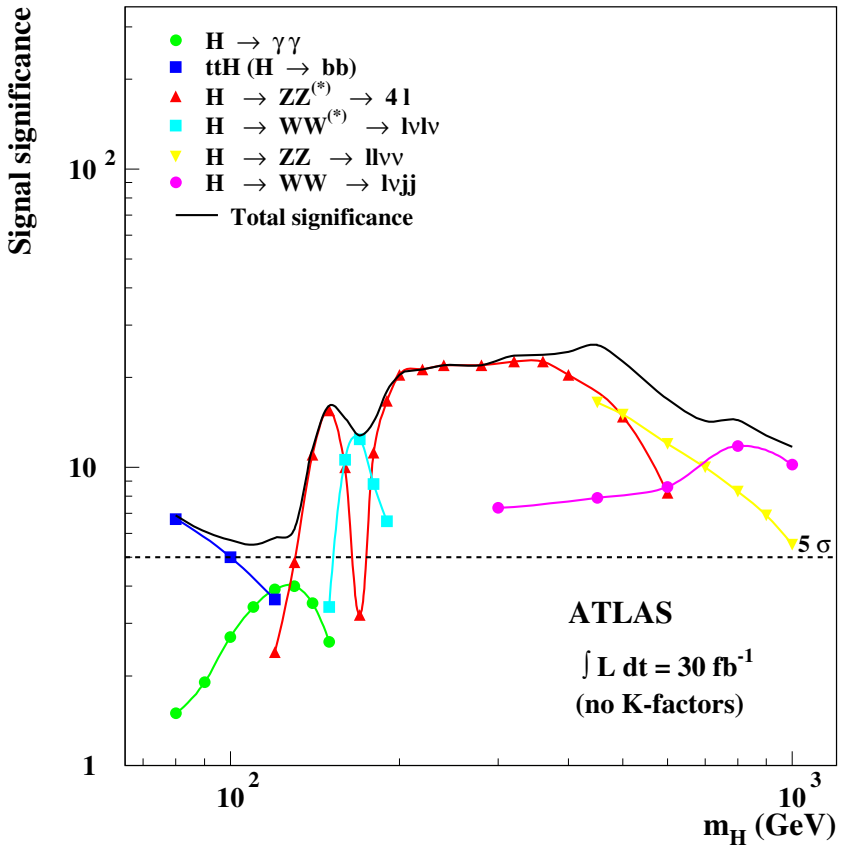

Fig. 22. *Individual channels and combined statistical significance for a discovery in ATLAS as a function of* m_{H} *for a total integrated luminosity of 30 fb*-1

Higgs mass is shown for one of the experiments (ATLAS)[18] for every final state and for their combination after the first 30 fb^{-1}. If the Higgs is discovered before then, LHC will measure its characteristics: the mass with a 0.1-1% accuracy, the coupling and branching ratios with $\sim$20% accuracy, and it will determine its nature (SM or MSSM).

9 The search for supersymmetric particles

In models invoking supersymmetry (SUSY) each elementary particle is accompanied by a supersymmetric partner whose spin differs by half a unit. SUSY models require a minimum of 2 Higgs doublets to generate the masses of the bosons and fermions. The super-partners of the gauge bosons are fermions called gauginos, the ones of the gluons are the gluinos and the ones of the Higgs fields are the Higgsinos. The super-partners of the fermions are the sfermions (f_R and f_L) with zero spin.

If there are 2 Higgs doublets, the fields of the fermionic partners of the $W^{\pm}$ and of the charged Higgs $H^{\pm}$ mix to form two mass eigenstates, the charginos $\chi^{\pm}_{1,2}$. The partners of the photon, of the Z and of the neutral Higgs bosons mix to form four eigenstates, the neutralinos $\chi^0_{1,2,3,4}$, where the χ^0_1 is often assumed to be the lightest SUSY particle (LSP).

Particles and s-particles are characterised by a quantum number: the R-parity (defined as R=$(-1)^{3(B-L)+2S}$). The particles have positive R-parity while s-particles have negative. If R-parity conservation is assumed SUSY particles can only be produced in pairs and the LSP cannot decay.

In the Minimal Supersymmetric Model (MSSM) there are 124 parameters,[9] 2 Higgs doublets and R-parity is conserved. These parameters are reduced to 5 at the GUT scale: $m_{1/2}$ (=M_1=M_2=M_3) the masses of the gauginos, m_0 the masses of the s-fermions, μ the mass coupling strength between the 2 Higgs super-fields, tanβ the ratio of the vacuum expectations of the 2 Higgs fields that couple respectively to up and down quarks, A_t the trilinear stop-Higgs coupling. Most of LEP results are interpreted within this model. If, on top of the above GUT scale constraints, one also requires that the Higgs mass will be universal, $m_H^2 = m_0^2 + \mu^2$, the number of parameters is further constrained, the sign of μ is determined and one ends up with the mSUGRA model with 5 parameters, m_0, $m_{1/2}$, A_t, tanβ and $sign(\mu)$.

In SUSY the breaking of the symmetry occurs in a hidden sector, which then communicates it to the visible sector of the particles via *messengers*. In mSUGRA the messengers are the gravity forces, the scale is broken at $\sqrt{F} = 10^{10}$ GeV and the

Lightest Supersymmetric Particle (LSP) is the neutralino χ_1^0.

In another SUSY scenario, the Gauge Mediated Susy Breaking model (GMSB), the messengers are the gauge forces and the symmetry is broken at a much lower scale $\sqrt{F} = 10^2 - 10^4$ TeV. The LSP is the gravitino.

9.1 The MSSM topologies

If R-parity is conserved the s-particles are produced in pairs and the LSP is stable. This means that at LEP the final state of an event with super-particles will be characterised by 2 acoplanar objects (2 leptons, or 2 jets or 2 photons) and missing energy from the two undetected neutralinos. The topology will also then depend of the difference in mass between the s-particle produced and the LSP $\Delta M = M(\tilde{s}) - M(\chi^0)$.

Recently a particular MSSM case has been explored: the LSP being the gluino $\tilde{g}$ instead of the neutralino. The gluino hadronises in R hadrons ($R^{\pm}$, R^0) so there will be no missing energy signature, but instead the presence of R hadrons.[19]

9.2 The search for the Chargino

The charginos are pair produced at LEP either in the s-channel or in the t-channel via the exchange of a sneutrino. The cross section of this process in generally very high, so the chargino is likely to be the first sparticle detected at LEP. In the case where the charginos are gaugino-like ($\mu \gg M_2$) and the sneutrinos are light (small m_0), there is a destructive interference between the two processes which reduces the cross section and thus the search sensitivity. The decrease in sensitivity also occurs when the difference in mass between the chargino and the neutralino is quite small (a few hundred MeV). The decay of the chargino into a neutralino is via a $W^{(*)}$, so the final state will be characterised by the decays of the 2 $W^{(*)}$ and the missing energy carried away by the 2 undetectable χ_1^0. About 5-10 pb^{-1} per experiment are sufficient to reach masses close to the kinematic limit in most of the parameter space. In Figure 23 the combined LEP limit on the chargino mass for $\mathrm{E_{cm}} > 206.5$ GeV is shown as a function of the sneutrino mass (plot on the left), and for the DELPHI experiment as a function of mass difference ($\Delta M = M(\tilde{s}) - M(\chi^0)$) for $\mathrm{E_{cm}}$=205.3 GeV (plot on the right).

At the end of LEP the limit on the chargino mass will be (unless it is found!) ${\mathrm{E_{cm}}}^{max}/2$ for most of the parameter space.

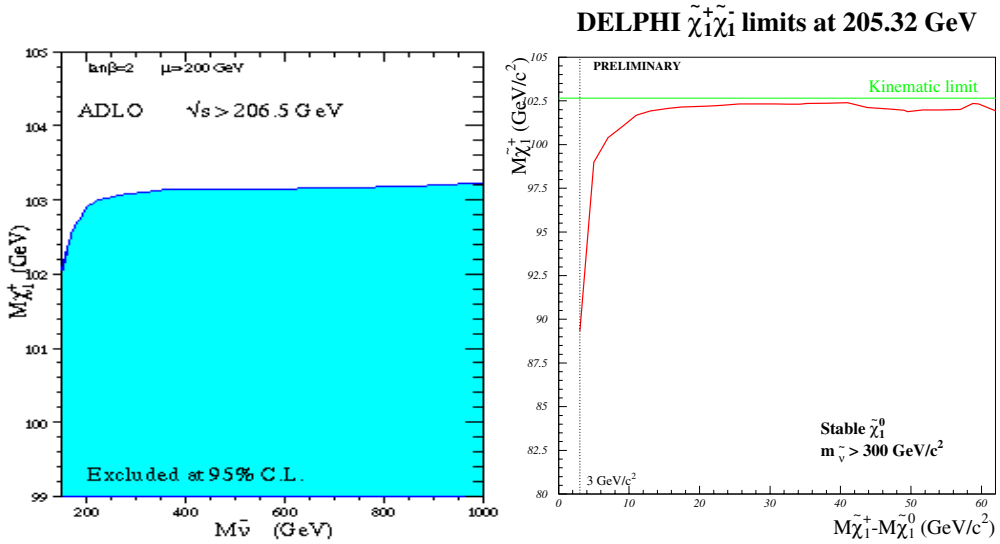

Fig. 23. *Left: The chargino mass limit as a function of the sneutrino mass for the four experiments combined together and for* $\mathrm{E_{cm}}$*>206.5 GeV. Right: The chargino mass limit as a function of the* ΔM *value under the assumption of a heavy sneutrino. The limit applies to the case of a stable* χ_1^0*. The straight horizontal line shows the kinematic limit.*

9.3 The search for the stau

It is likely, due to potentially large mixing parameters, that the lightest slepton is the stau. At LEP a pair of $\tilde{\tau}_R$, or of $\tilde{\tau}_L$, is produced via s-channel process. The main decay mode is $\tilde{\tau} \rightarrow \tau\chi_1^0$, i.e. a final state characterised by 2 acoplanar τ's and missing energy, for a total of 2 LSP and 4 neutrinos escaping detection. The efficiency is strongly dependent on the visible energy, i.e. on $\Delta M = M(\tilde{s}) - M(\chi^0)$. In the 1998 and 1999 data there was an excess observed by the 4 experiments (as shown in Figure 24), compatible with a M($\tilde{\tau}$)=85 $\mathrm{GeV/c^2}$ and M(χ_1^0)=22 $\mathrm{GeV/c^2}$. The systematic error on this measurement is estimated to be of the order of 4%, for an excess of the order of 20%, where the main background is coming by 80% from the WW final state and 20% from $\gamma\gamma$ pprocesses.

In the 2000 data and with a luminosity of about 85 $\mathrm{pb^{-1}}$ per experiment the excess was not confirmed (while for a given $\tilde{\tau}$ and χ_1^0 mass the cross section was supposed to be higher at the higher energies of the 2000 run) and the data agreed perfectly with the expectation from background only (49 events were observed in data while 51.6 were expected for the 4 experiments). Limits are then computed as shown in Figure 25.

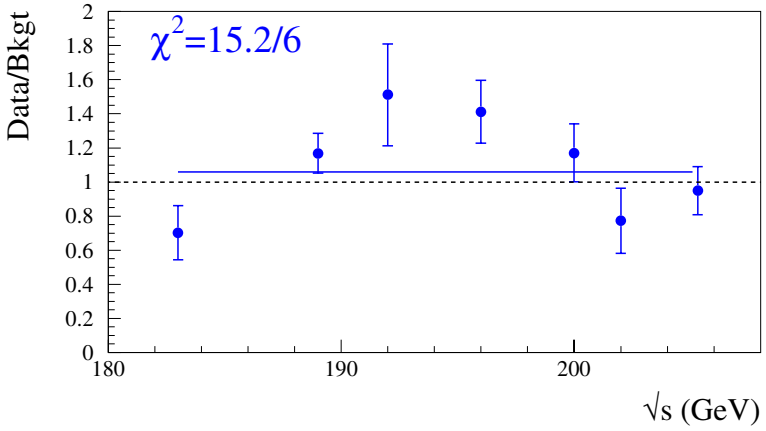

Fig. 24. *The ratio of data over background only simulation in the combined LEP $\tilde{\tau}$ analyses as a function of* $\mathrm{E_{cm}}$. *The full line is the average value.*

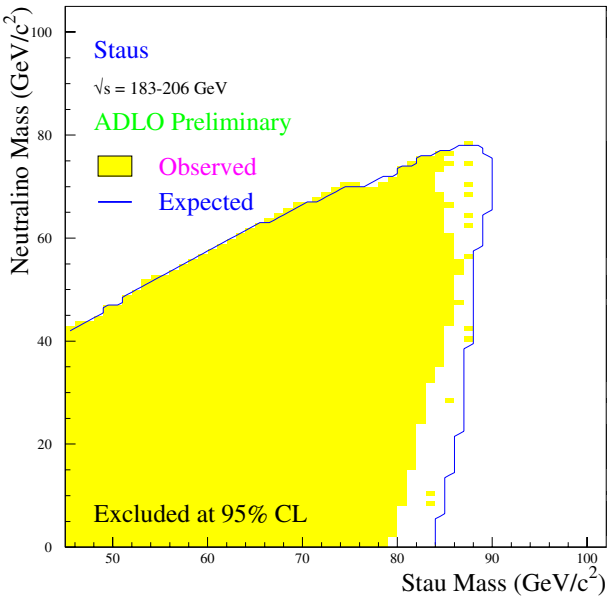

Fig. 25. *Exclusion limit at 90% CL for $\tilde{\tau}$. The line represents the expected limit from the combination of the 4 LEP experiments in the hypothesis of background only. The shaded area is the excluded region obtained from the combination of the 4 LEP experiments.*

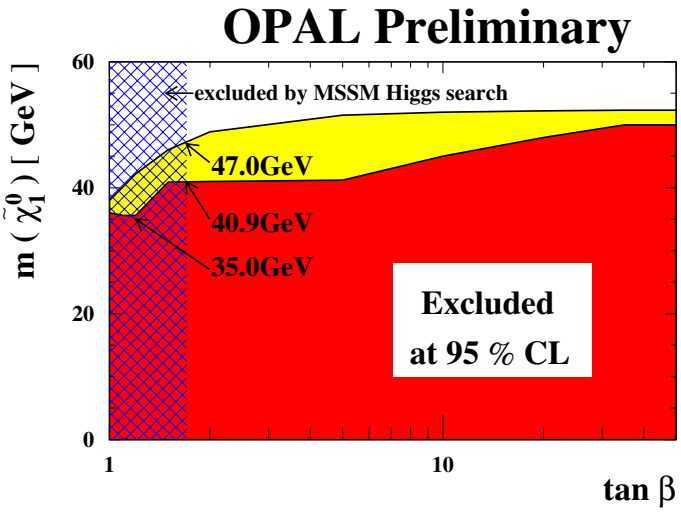

Fig. 26. *The 95% CL mass limit on the lightest neutralino χ_1^0 as a function of tanβ. The exclusion region for $m_0 \geq 500$ GeV is shown by the lighter area and the exclusion valid for all m_0 values by the darker area. The hatched area shows the region in tanβ excluded by the MSSM Higgs search.*

9.4 Limit on the LSP

The results of the search for the Lightest Supersymmetric Particle will be one of the important milestones of LEP. SUSY models with R-parity conservation predict the existence of cold dark matter (CDM) in the universe, i.e. the relic LSP remaining from the Big Bang. Thus the importance of a discovery or even setting limits on this particle. At LEP no evidence of neutralino production has been seen and limits can be set as a function of the SUSY parameters. Combining the direct search for the neutralino with the searches for charginos and sleptons and by scanning the MSSM parameter space the lower bound for M(LSP) is set to 36-38 $\mathrm{GeV/c^2}$ by each experiment. Limits around 46-48 $\mathrm{GeV/c^2}$ are obtained if constraints on tanβ from MSSM Higgs searches are also used (see section 3.1), as shown in Figure 26 for the OPAL experiment.[20] The four LEP experiments' results on the LSP will be combined at the end of this year.

9.5 The GMSB scenario and the photons only final state

In the GMSB scenario the lightest supersymmetric particle is the gravitino. The phenomenology is then determined by the nature of the next to lightest supersymmetric

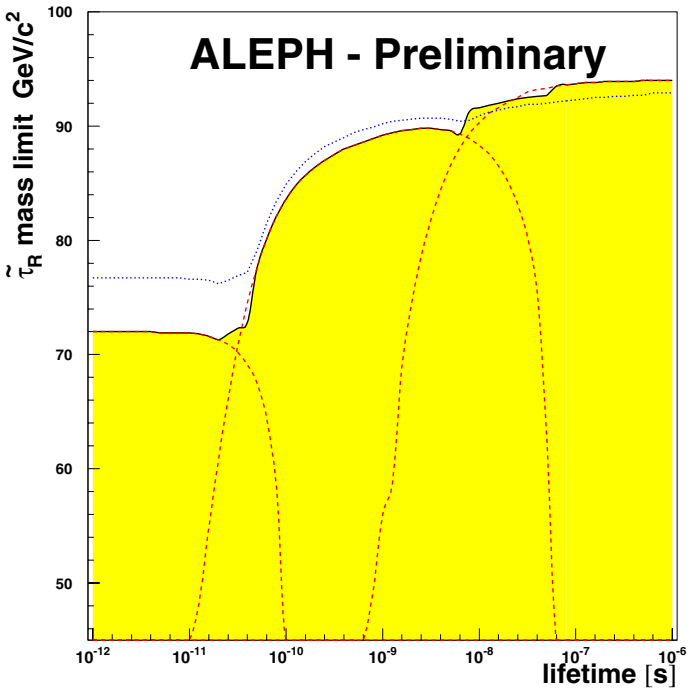

Fig. 27. *Lower bound for the stau NLSP mass in GMSB as a function of its lifetime, for the ALEPH experiment*

particle (NLSP), which could be the χ_1^0 or the $\tilde{\tau}_R$. The final state should thus contain isolated photons or $\tau^{\pm}$ leptons from the NLSP decays: $\chi_1^0 \rightarrow \gamma\tilde{\mathrm{G}}$ or $\tilde{\tau}_R \rightarrow \tau^{\pm}\tilde{\mathrm{G}}$. This is a clear supplementary signature for the search for GMSB processes. The NLSP lifetime is not defined in GMSB. If it is very short ($c\tau \ll L_{det}$) the final state will be characterised by two acoplanar photons or two acoplanar leptons; if $c\tau \approx L_{det}$ there will be non-pointing photons towards the beam spot or "kinks" (i.e. non-pointing tracks); if $c\tau \gg L_{det}$ then it will be an invisible final state in the case of LSP being the χ_1^0 or there will be the presence of heavy stable particles. The current NLSP limits,[21] independent of the lifetime, are m(χ_1^0)$>$ 95 $\mathrm{GeV/c^2}$, m($\tilde{\tau}$)$>$75 $\mathrm{GeV/c^2}$ (see for example Figure 27 for the ALEPH result). The two photons mass plot for the all-LEP data in Figure 28 shows a good agreement between the data and the SM expectation, and no hint of a new signal.

9.6 R-parity violation

If R-parity is not conserved, then

a) the LSP is not stable any longer and the s-particles decay into SM ones. The clean

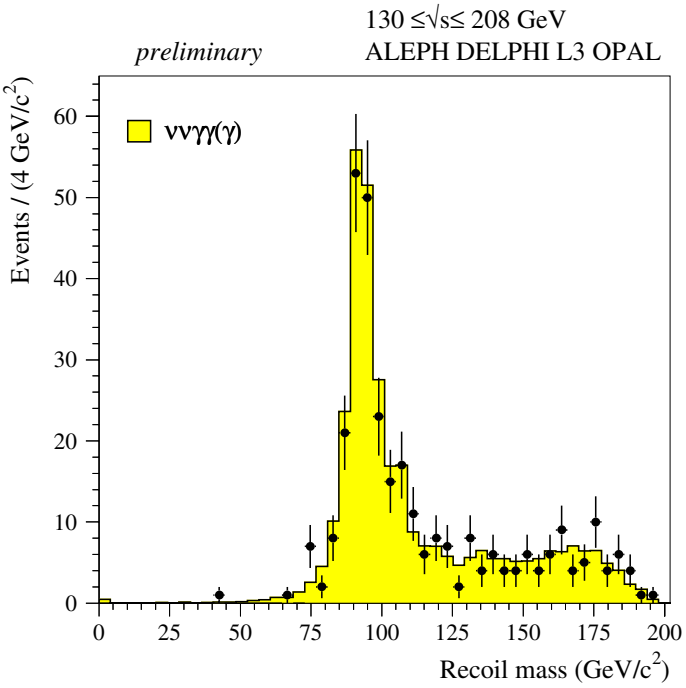

Fig. 28. *The recoil mass for final states with two acoplanar photons only, for the LEP data integrated over the full LEP2 statistics.*

missing energy signature is lost.

b) single s-particles production is possible, and s-particle exchange in the s- or t-channel contributes to SM processes.

R-parity violation predicts 45 new couplings with baryon- and/or lepton-number violation: λ_{ijk}, λ'_{ijk}, λ''_{ijk}. The proton lifetime and low-energy data impose severe constraints on these couplings, but LEP data can test even smaller values.

A LSP sfermion would decay directly into fermions ($\tilde{\mathrm{f}} \rightarrow \mathrm{ff'}$). If the LSP is the χ_1^0 then the decay into fermions is indirect: $\tilde{\mathrm{f}} \rightarrow \mathrm{f}\chi_1^0 \rightarrow \mathrm{ff'f''}$. The final state is then characterised by a large number of leptons or jets due to the LSP decay. At LEP most of these final states have been studied, but with the assumption that only one of the λ couplings is nonzero at a time. Limits on gauginos in this scenarios are very similar to those obtained in the R-parity conserving case.

R-parity violation also predicts the lepton-number violating s-channel process $\mathrm{e^+e^-} \rightarrow \tilde{\nu}$. Anomalies in the distributions of $\mathrm{e^+e^-} \rightarrow \tilde{\nu} \rightarrow \mathrm{e^+e^-}$, $\mu^+\mu^-$ and $\tau^+\tau^-$ have been searched for at LEP.[22] No signal of new physics has been found in these channels.

R-parity may also be broken spontaneously in the third generation via the bilin-

ear Higgs term $\epsilon L H_u$ in the Lagrangian (generated by a vacuum expectation of the right-handed sneutrino). The resulting massless Majoron J has been searched for by DELPHI[23] in the process $\chi^{\pm}_{1,2} \to \tau^{\pm}$J, and large domains of m($\chi^{\pm}_{1,2}$) have been excluded.

10 Search for LeptoQuarks

LeptoQuarks (LQ) are coloured objects that carry both lepton L and baryon B quantum numbers and interact directly with SM fermions. There are 18 different LQ, 9 scalar (spin S=0) and 9 vector (S=0). Their decay is LQ $\to$l$^{\pm}$q, νq. At the Tevatron and at Hera the lower bound on the LQ mass has been set around 250 $\mathrm{GeV/c^2}$ (for S=0) and 340 $\mathrm{GeV/c^2}$ (for S=1). At LEP the first generation of LQ can also be produced. The LQ can be directly produced in pairs (in a s-channel process) if their mass is M(LQ)$<$ $\mathrm{E_{cm}}$/2 or singly (the positron emits a photon that goes into a $\mathrm{q\bar{q}}$ pair, then one of the quarks couples to the electron to form a LQ) reaching M(LQ)$<$ $\mathrm{E_{cm}}$. The indirect production (i.e. $\mathrm{e^+e^-} \to$LQ $\to$ql) can instead reach higher masses and, depending on the final state, L3 and ALEPH set limits ranging from 100 to 400 $\mathrm{GeV/c^2}$.

11 Search for single top production

The single production of the top quark by the process $\mathrm{e^+e^-} \to t\bar{c}$ or $t\bar{u}$ became kinematically possible with LEP2 energies larger than 180 GeV. Flavour Changing Neutral Currents (FCNC) are known to be absent at tree level in the Standard Model (the cross section is very low, $\sim 10^{-9}$ fb), but can naturally appear at the one-loop level due to CKM mixing. Many extended models[24] give rise to detectable FCNC amplitudes already at tree level. The detection of a single top would be a sign of an anomalously large tcZ or $tc\gamma$ coupling (k_Z, k_γ). The searches at LEP have been combined,[25] giving rise to upper bounds in the plane of the couplings (see the upper plot of Figure 29), improving slightly on previous limits from CDF. Alternatively, limits on the BR(t $\to$cZ+uZ) can be set, as shown in the bottom plot of Figure 29 for LEP and CDF.

12 Technicolor

Technicolor (TC) models provide an alternative way to the Higgs mechanism to give mass to the particles by assuming a new very strong interaction ($\Lambda_{TC} \gg \Lambda_{QCD}$). The

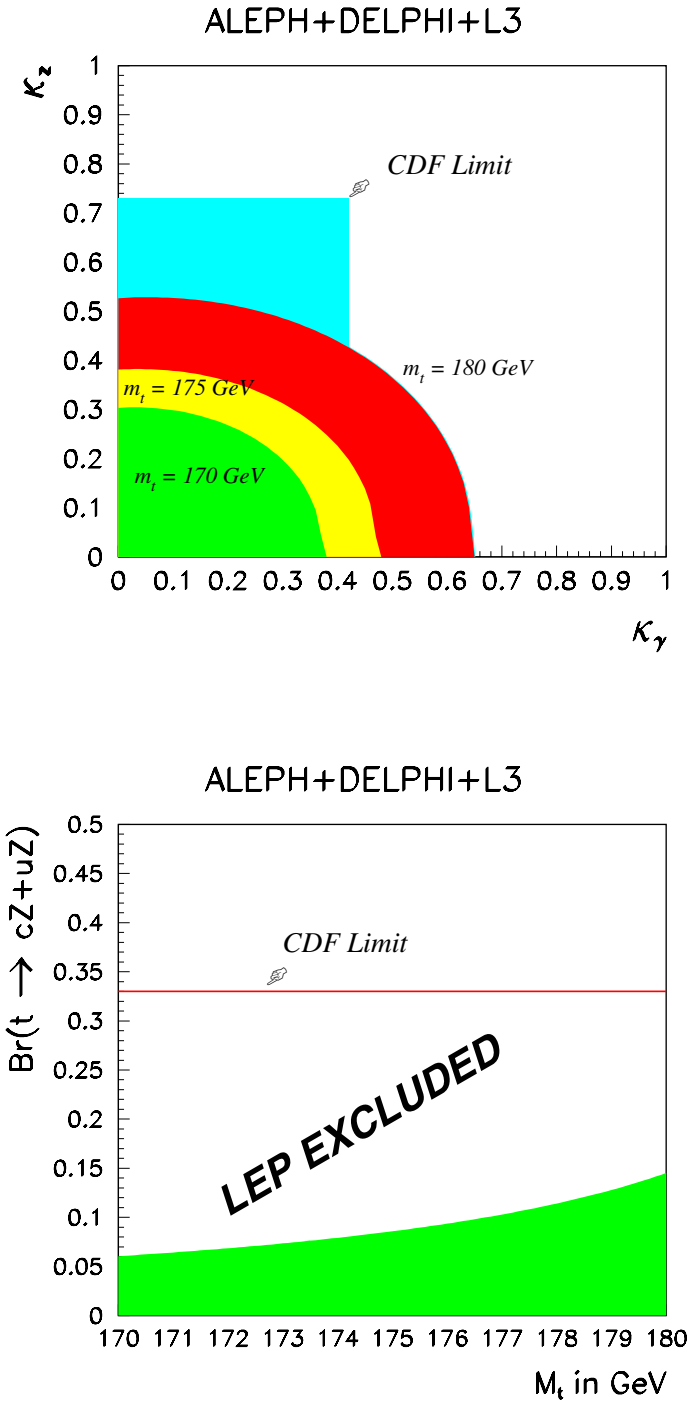

Fig. 29. *Top: Exclusion in the plain of couplings (k_Z, k_γ) for various top quark masses from the LEP combined data and from CDF. Bottom: Excluded values (at 95%CL) for the BR(t →cZ+uZ) from the LEP combined data and from CDF. The shaded area is the region not excluded.*

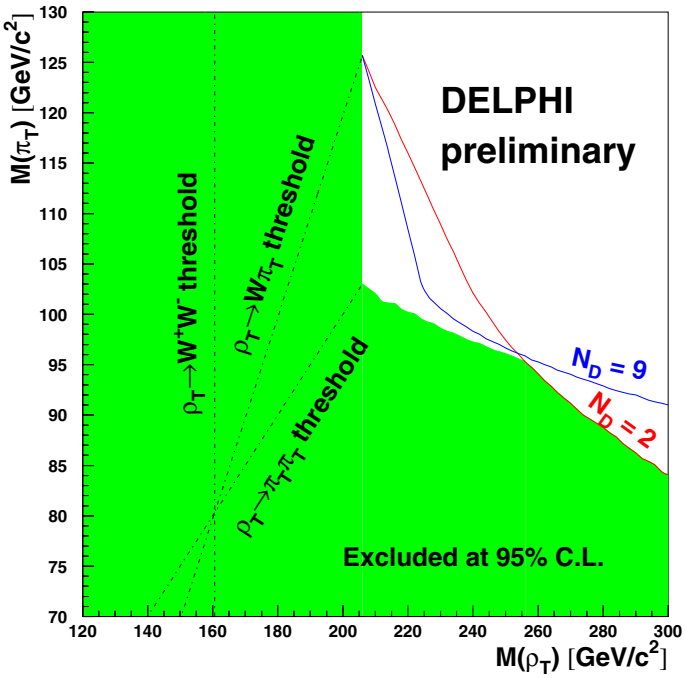

Fig. 30. *The region in the (M_{ρ_T} - M_{π_T}) plane (filled area) excluded at 95% C.L. for any value of W_L - π_T mixing for the DELPHI experiment with 2000 data.*

"standard" TC with a QCD-like running of Λ_{TC} is ruled out by precision measurements, but an extension of this model with a "slower" running (the "walking Technicolor" model) predicts light bound states of TC particles accessible at LEP. The parameters of the model are the mass of the Technipion π_T, the mass of the Technirho ρ_T, the number of doublets (up to 9, while in the original model it was 2) and the mixing between the π_T and the longitudinal component of the W, W_L. LEP data has been analysed in the framework of this model by L3 (for $\mathrm{E_{cm}}$=189 GeV)[26] and by DELPHI (for $\mathrm{E_{cm}}$=189-210 GeV)[27,28].

For the case in which $\mathrm{M}(\rho_T) < \mathrm{E_{cm}}$ the following channel can be studied: $\mathrm{e^+e^-} \to \rho_T \to \mathrm{W^+W^-}$, $f\bar{f}$(g), $\pi_T\gamma$. The expected cross section for $\rho_T \to$ WW is $\approx$ 3 pb. The precision on the WW cross section is of the order of 0.5 pb and the measurement is in good agreement with the SM expectation, leaving no room for the ρ_T to be lighter than $\mathrm{E_{cm}}$. As well from the direct search in $\mu^+\mu^-\gamma$ or $\pi_T\gamma$ spectra there is no indication of a resonant production. From these measurements a lower bound of $\mathrm{M}(\rho_T) < \mathrm{E_{cm}}$ can be set as shown in Figure 30 for the DELPHI 2000 data.

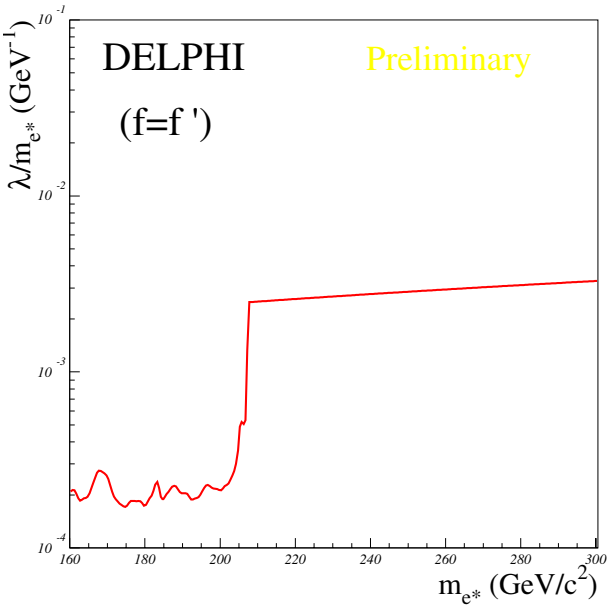

Fig. 31. *Upper bounds on the ratio λ/m_{e^*} combining direct and indirect limits, by DELPHI.*

Independent of the value of M(ρ_T) (i.e. also for M(ρ_T) $>$ $\mathrm{E_{cm}}$) the following processes can be studied: $\mathrm{e^+e^-}\to\rho_T\to\pi_T\pi_T$, $\pi_T\mathrm{W}_L$ where $\pi_T\to$bc. Since no signal has been found at LEP during the first half of this year (nor in the previous year) a lower bound on the mass of the π_T as a function of the ρ_T mass and the number of doublets can be set as shown in Figure 30.

13 Excited lepton

Excited leptons would be a clear signal for substructure. They can be produce in pairs, or singly in the s- or t-channel, with the subsequent decay l* $\to$l(γ/Z), $\nu^*\to\nu(\gamma/\mathrm{Z})$,[28].[6]

The current emphasis is on the production of a single excited lepton with mass close to $\mathrm{E_{cm}}$. The new interaction is characterised by a compositness scale Λ, by charged- and neutral-current couplings f and f' which control the rate of the radiative and weak decays (e* $\to$eγ/Z/W, $\nu^*\to$eW, e* $\to\nu$W, $\nu^*\to\nu\gamma$/Z). Upper bounds for $\lambda/m_{e^*} = f/\Lambda\sqrt{2}$ are obtained, see Figure 31. In the figure direct and indirect limits (from the process $\mathrm{e^+e^-}\to\gamma\gamma$ in a t-channel process where an l* is exchanged) have been combined.

A nice candidate for excited lepton production has been observed at LEP by L3 ($\mathrm{e^+e^-}\to\mathrm{e}\gamma\nu\mathrm{W}\to\mathrm{e}\gamma\nu\mu\nu$) and DELPHI ($\mathrm{e^+e^-}\to\mu\mu^*\to\mu\mu\gamma$). These events are also compatible with being produced by SM processes.

14 Extra dimensions

New models of low scale quantum gravity in extra dimensions predict the gauge and gravitational forces to unify at a mass scale smaller than M_{Planck}.[29] These theories solve the "scale-hierarchy problem" of the SM without introducing SUSY or compositness. The gravitational coupling could become of the same order of the gauge ones already at a weak scale if our 4-dimensional world would be inside a N-dimensional world where only gravitons G can roam. If N=4+δ and the extra dimensions δ have dimension R, then $M^2_{Planck} = R^{\delta} M^{\delta+2}$.

Models with $\delta = 1$ have already been excluded by test of the gravitational force ($R \sim 10^{13}$ cm) and astronomical observations. $\delta \geq 2$ is tested at LEP either by searching for the graviton G in the reaction $e^+e^- \rightarrow \gamma G$ and $e^+e^- \rightarrow ZG$ or in an indirect way via virtual effects on $e^+e^- \rightarrow f\bar{f}\ \gamma\gamma$, WW and ZZ distributions. Lower bounds on M of 1-1.3 TeV, 0.7-0.8 TeV, $\sim$0.5 TeV are obtained respectively for δ=2, 4 and 6. Thus current results from e^+e^-collisions do not favour low-scale quantum gravity with a scale close to the electroweak scale.

15 Summary and Conclusions

LEP is a unique machine to study new physics and to search for new particles. Many theories and models have been studied by the LEP experiments and strong constraints have been set on their parameters.

With the data taken until summer 2000 the four collaborations exclude a Standard Model Higgs lighter than 113.3 $\mathrm{GeV/c^2}$ at 95% CL. At the end of data taking in 2000 LEP will be able to exclude or observe with a 3σ significance a Higgs with a mass of $\sim$115 $\mathrm{GeV/c^2}$. For the lack of just a few GeV, LEP will not able to cover the MSSM plane entirely, although strong constraints have been put up to now: m_{h}, $m_{\mathrm{A}} \geq$ 90.5 $\mathrm{GeV/c^2}$, tan(β)>2.3 or tan(β)>0.9, $m_{\mathrm{H}^{\pm}}$>77.4 $\mathrm{GeV/c^2}$.

From the SUSY world there is no evidence of a supersymmetric particle and a lower bound on the chargino mass can be set at 104 $\mathrm{GeV/c^2}$ in most of the MSSM parameter space, and for the LSP mass at 46-48 $\mathrm{GeV/c^2}$ when including the results from the Higgs search.

No other anomaly has been found up to now in the framework of any other model and no deviation from the SM prediction has been observed.

In these days LEP is still running very well and at very high energies ($\mathrm{E_{cm}}$=206.7

GeV and 208.1 GeV) so let's wait for these last exciting days!

References

[1] The LEP and SLD Electroweak Working Group: results of Summer 2000, presented by B. Pietrzyk at ICHEP 2000, Osaka Japan.

[2] See for example: S. Weinberg, *The quantum theory of Fields*, Vol. II, Cambridge University Press (1996) and references therein.

[3] ALEPH, DELPHI, L3 and OPAL Collab., The LEP working group for Higgs boson searches, *Searches for Higgs bosons: Preliminary combined results using LEP data collected at energies up to 209 GeV*, DELPHI 2000-148 CONF 447.

[4] M. Davier and A. Höcker, Phys. Lett. **B419** (1998), 419.

[5] *Physics at LEP2*, CERN 96-01.

[6] ALEPH Collab., *Search for the neutral Higgs bosonos in* $\mathrm{e^+e^-}$ *collisions at energies up to* $\sqrt{s}$ *= 206 GeV*, ALEPH 2000-064 CONF 2000-042;
DELPHI Collab., *Searches for Neutral Higgs Bosons at LEP in the year 2000*, DELPHI-2000-077 CONF 376;
L3 Collab., *Preliminary results on new particle searches obtained from data collected during the year 2000*, L3 note 2601, July 25, 2000;
OPAL Collab., *Search for Higgs Bosons in* $\mathrm{e^+e^-}$ *Collisions at the Highest LEP Energies*, OPAL Physics Note PN450, July 21, 2000.

[7] N. Kjaer, M. Mulders, *The ideogram technique for LEP2 analysis*, DELPHI note 97-55 PHYS 705.

[8] DELPHI Collab., *Symmetric double radiative return with* $Z\rightarrow\mathrm{q\bar{q}}$, DELPHI 2000-132 OSAKA CONF 431

[9] H.P. Nilles, Phys. Rept. **110** (1984), 1.

[10] Ambrosanio et al., *Aspects of GMSB Phenomenology at TeV Colliders*, hep-ph/0002191.

[11] M. Carena, S. Heinemeyer, C.E.M. Wagner and G. Weiglein, *Suggestions for Improved Benchmark Scenarios for Higgs-Boson Searches at LEP2*, CERN-TH/99-374, DESY 99-186, hep-ph/9912223.

[12] W.-M. Yao, *Standard Model Higgs and Top Mass Measurements at the Tevatron*, FERMILAB-CONF-99/100-E.

[13] ALEPH Collab., *Search for charged Higgs bosons in* e^+e^- *collisions at energies from* $\sqrt{s}$*= 192 GeV to 202 GeV*, ALEPH 2000-011 CONF 2000-008;
DELPHI Collab., *Search for Charged Higgs Bosons in* e^+e^- *collisions at* $\sqrt{s}$*= 183 - 202 GeV*, DELPHI-2000-029 CONF 348;
L3 Collab., *Search for Charged Higgs Bosons in* e^+e^- *Collisions at Centre of Mass Energies between 192 and 202 GeV*, L3 Note 2510 (March 7, 2000)
OPAL Collab., *Search for Higgs Bosons in* e^+e^- *Collisions at* $\sqrt{s}$*=192-202 GeV*, OPAL Physics Note PN421, November 8, 1999.

[14] DELPHI Collab., *Update on the search for non-fermionic neutral Higgs couplings at LEP 2*, DELPHI 2000-082 CONF 381;
L3 Collab., *Search for anomalous couplings in Higgs production at LEP*, L3 note 2558;
OPAL Collab., *Search for Higgs Bosons Decaying into Photons in* e^+e^- *Collisions at* $\sqrt{s}$ *up to 202 GeV*, OPAL PN450.

[15] ALEPH Collab., *Search for a Higgs boson decaying to gamma gamma in* e^+e^- *collisions at centre of mass energies from 88 GeV up to 202 GeV*, CERN-EP/2000-083;
DELPHI Collab., *Preliminary results from searches for invisibly decaying Higgs bosons*, DELPHI note 2000-078 CONF 377;
L3 Collab., *Search for the Higgs Boson Decaying into Two Photons in* e^+e^- *Interactions at center-of-mass energies up to 202 GeV at LEP*, L3 note 2580;
OPAL Collab., *Search for Higgs Bosons Decaying into Photons in* e^+e^- *Collisions at* $\sqrt{s}$ *up to 202 GeV*, OPAL PN450.

[16] A. Djouadi, J. Kalinowski and M. Spira, Comp. Phys. Comm. **108** (1998) 56.

[17] CDF and D0 Collab., *Physics at Run II Workshop - Higgs Bosons*, 25-June-2000.

[18] ATLAS Detector and Physics Performance Technical Design Report LHCC 99-14/15.

[19] DELPHI Collab., *Gluino search from stop decay*, DELPHI 2000-086 CONF 38.

[20] OPAL Collab., *New Particle Searches in* e^+e^- *Collisions at the Highest LEP Energies*, OPAL PN435.

[21] V. Hedberg, *Photonic and gravitino searches at LEP*, proceedings of ICHEP-2000 (Osaka).

[22] I. Fleck, *R-parity violation searches at LEP* , proceedings of ICHEP-2000 (Osaka).

[23] DELPHI Collab., DELPHI 2000-082 CONF 342.

[24] G.M. Divitiis, R. Petronzio, and L. Silvestrini, hep-ph/9704244 (1997);
D. Atwood, L. Reina, and A. Soni, SLAC-PUB-95-6927 (1995);
B.A. Arbuzov and M.Yu. Osipov, hep-ph/9802392 (1998).

[25] V. Obraztsov, *Single top searches at LEP*, proceedings of ICHEP-2000 (Osaka).

[26] L3 Collab., *Search for Technicolour production at LEP*, L3 note 2428.

[27] DELPHI Collab., *Search for Technicolor with DELPHI*, DELPHI 2000-074 CONF 373.

[28] DELPHI Collab., *Update of results on exotic and supersymmetric particle searches with recent LEP 2 data from 2000*, DELPHI 2000-088 CONF 387.

[29] See for example: Raman Sundrum, proceedings of this conference.

ELECTROWEAK AND B PHYSICS RESULTS FROM THE FERMILAB TEVATRON COLLIDER

Kevin T. Pitts*
University of Illinois, Department of Physics
1110 West Green Street, Urbana, IL 61801-3080, USA
E-mail: kpitts@uiuc.edu

Representing the CDF and DØ Collaborations

ABSTRACT

This writeup is an introduction to some of the experimental issues involved in performing electroweak and b physics measurements at the Fermilab Tevatron. In the electroweak sector, we discuss W and Z boson cross section measurements as well as the measurement of the mass of the W boson. For b physics, we discuss measurements of $B^0/\overline{B^0}$ mixing and CP violation. This paper is geared towards nonexperts who are interested in understanding some of the issues and motivations for these measurements and how the measurements are carried out.

*Work supported by the Department of Energy, Contract DE-FG02-91ER40677.

1 Introduction

The Fermilab Tevatron collider is currently between data runs. The period from 1992-1996, known as Tevatron Run 1, saw both the CDF and DØ experiments accumulate approximately $110\,\mathrm{pb}^{-1}$ of integrated luminosity. These data sets have yielded a large number of results and publications on topics ranging from the discovery of the top quark to precise measurements of the mass of the W boson; from measurements of jet production at the highest energies ever observed to searches for physics beyond the Standard Model.

This talk and subsequent paper focus on two aspects of the Tevatron program: electroweak physics and the physics of hadrons containing the bottom quark. Each of these topics is quite rich in its own right. It is not possible to do justice to either of these topics in the space provided.

Also, there are a large number of sources for summaries of recent results. For example, many conference proceedings and summaries are easily accessible to determine the most up-to-date measurements of the mass of the W boson. Instead of trying to summarize a boat-load of Tevatron measurements here, I will attempt to describe a few measurements in an introductory manner. The goal of this paper is to explain some of the methods and considerations for these measurements. This paper therefore is geared more towards students and non-experts. The goal here is not to comprehensively present the results, but to discuss how the results are obtained and what the important elements are in these measurements.

After a brief discussion of the Tevatron collider and the two collider experiments, we will discuss electroweak and b physics at the Tevatron.

2 The Tevatron Collider

The Fermilab Tevatron collides protons (p) and antiprotons ($\overline{p}$) at very high energy. In past runs, the $p\overline{p}$ center of mass energy was $\sqrt{s} = 1.8\,\mathrm{TeV}$. It will be increased in the future to $2\,\mathrm{TeV}$.* Until the Large Hadron Collider begins operation at CERN late in this decade, the Tevatron will be the highest energy accelerator in the world. The high energy, combined with a very high interaction rate, provides many opportunities for unique and interesting measurements.

*For the upcoming Tevatron run, the center of mass energy will be $\sqrt{s} = 1.96\,\mathrm{TeV}$. Running the machine at slightly below 2 TeV drastically improves the reliability of the superconducting magnets.

Table 1. Some highlights in the history of the Fermilab Tevatron. This table lists primarily milestones associated with the collider program. In addition, there have been several Tevatron fixed-target runs, producing a wealth of physics results.

1969	ground breaking for National Accelerator Laboratory "Main Ring"
1972	200 GeV beam in the Main Ring
1983	first beam in the "Energy Doubler" $\Rightarrow$ "Tevatron"
1985	CDF observes first $p\overline{p}$ collisions
1988-89	Run 0, CDF collects $\sim$3 pb^{-1}
1992-93	Run 1A, CDF and DØ collect $\sim$20 pb^{-1}
1994-95	Run 1B, CDF and DØ collect $\sim$90 pb^{-1}
2001-02	Run 2 with new Main Injector and Recycler,
	upgraded CDF and DØ expect 2000 pb^{-1}=2 fb^{-1}
2003-	Run 3, 15-30 fb^{-1}

The Tevatron has a history that goes back over 20 years. Table 1 lists a few of the highlights. The original Fermilab accelerator, the "Main Ring", was finally decommissioned in 1998 after more than 25 years of operation. In collider mode, the Main Ring served as an injector for the Tevatron. The Main Ring and Tevatron resided in the same tunnel of circumference of ~ 4 miles. The Tevatron now resides alone in this tunnel.

The Tevatron consists of approximately 1000 superconducting magnets. Dipole magnets are $\sim 7\,\mathrm{m}$ in length, cooled by liquid helium to a temperature of $3.6\,\mathrm{K}$ and typically carry currents of over $4000\,\mathrm{Amps}$. Protons and anti-protons are injected into the Tevatron at an energy of $150\,\mathrm{GeV}$, then their energy is raised to the nominal energy which was $900\,\mathrm{GeV}$ per beam in the past and will be $980\,\mathrm{GeV}$ per beam for the upcoming run. During the period known as Run 1B, the Tevatron routinely achieved[1] a luminosity that was more than 20 times the original design luminosity of $10^{30}\,\mathrm{cm}^{-2}\mathrm{s}^{-1}$.

The major upgrade in recent years has been the construction of the Main Injector which replaces the Main Ring. The Main Injector, along with another new accelerator component, the Recycler, will allow for much higher proton and antiproton intensities, and therefore higher luminosity than previously achievable. The anticipated Tevatron luminosity in the upcoming run will be a factor of 200 beyond the original design luminosity for the Tevatron.

The CDF and DØ results presented here are from the $110\,\mathrm{pb}^{-1}$ of integrated lu-

minosity collected in the period of 1992-1996. The expectations for Run II are for a 20-fold increase in the data sample by 2003 ($2\,\mathrm{fb}^{-1}$). Beyond Run II, the goal is to increase the data sample by an additional factor of 10 (15–$30\,\mathrm{fb}^{-1}$) by the time that the LHC begins producing results.

3 CDF and DØ

The CDF and DØ detectors are both axially symmetric detectors that cover about 98% of the full 4π solid angle around the proton-antiproton interaction point. The experiments utilize similar strategies for measuring the interactions. Near the interaction region, tracking systems accurately measure the trajectory of charged particles. Outside the tracking region, calorimeters surround the interaction region to measure the energy of both the charged and neutral particles. Behind the calorimeters are muon detectors, that measure the deeply penetrating muons. Both experiments have fast trigger and readout electronics to acquire data at high rates. Additional details about the experiments can be found elsewhere.[2,3]

The strengths of the detectors are somewhat complementary to one another. The DØ detector features a uranium liquid-argon calorimeter that has very good energy resolution for electron, photon and hadronic jet energy measurements. The CDF detector features a $1.4\,\mathrm{T}$ solenoid surrounding a silicon microvertex detector and gas-wire drift chamber. These properties, combined with muon detectors and calorimeters, allow for excellent muon and electron identification, as well as precise tracking and vertex detection for B physics.

4 Electroweak Results

Although many precise electroweak measurements have been performed at and above the Z^0 resonance at LEP and SLC, the Tevatron provides some unique and complementary measurements of electroweak phenomena. Some of these measurements include W and Z production cross sections; gauge boson couplings (WW,$W\gamma$,WZ,$Z\gamma$,ZZ); and properties of the W boson (mass, width, asymmetries).

For the most part, both W and Z bosons are observed in hadron collisions through leptonic decays to electrons and muons, such as $W^+ \to e^+\bar{\nu}_e$ and $Z^0 \to \mu^+\mu^-$. The branching ratios for the leptonic decays of the W and Z are significantly smaller than

the branching ratios for hadronic decays. There are about 3.2 hadronic W decays for every W decay to e or μ and about 10 hadronic Z decays for every Z decay to e^+e^- or $\mu^+\mu^-$. Unfortunately, the dijet background from processes like $qg \to qg$ and $gg \to q\overline{q}/gg$ (in addition to higher order processes) totally swamp the signal from $Z^0 \to q\overline{q}$ and $W^+ \to q\overline{q}'$.[†]

4.1 W and Z Production

The rate of production of W and Z bosons is an interesting test of the theories of both electroweak and strong interactions. The actual production rates are determined by factors that include the gauge boson couplings to fermions (EW) and the parton distribution functions and higher order corrections (QCD).

As an example analysis, we will discuss the measurement of the Z production cross-section from the $Z^0 \to e^+e^-$ mode. The total number of events we observe will be:

$$N = \mathcal{L}_{int} \cdot \sigma_Z \cdot Br(Z^0 \to e^+e^-) \cdot \epsilon_{ee}\,, \tag{1}$$

where $\mathcal{L}$ is the instantaneous luminosity, $\mathcal{L}_{int} = \int \mathcal{L}dt$ is the integrated luminosity, $\sigma_Z = \sigma(p\overline{p} \to Z^0X)$ is the Z boson production cross section, $Br(Z^0 \to e^+e^-)$ is the branching ratio for $Z^0 \to e^+e^-$, and ϵ_{ee} is the efficiency for observing this decay mode. We have made the simplifying assumption that there are no background events in our signal sample. Let's take each term in turn:

- $\mathcal{L}_{int} = \int \mathcal{L}dt$: the integrated luminosity is measured in units of cm^{-2} and is a measure of the total number of $p\overline{p}$ interactions. The instantaneous luminosity is measured in units of $\mathrm{cm}^{-2}\mathrm{s}^{-1}$. In this case, "integrated" refers to the total time the detector was ready and able to measure $p\overline{p}$ interactions.[‡]
- $\sigma_Z = \sigma(p\overline{p} \to Z^0X)$: cross sections are measured in units of cm^2 and are often quoted in units of "barns", where $1\mathrm{b} = 10^{-24}\mathrm{cm}^2$. Typical electroweak cross sections measured at the Tevatron are in nanobarns ($\mathrm{nb} = 10^{-9}\mathrm{b}$) or picobarns ($\mathrm{pb} = 10^{-12}\mathrm{b}$). The **total** cross section for $p\overline{p}$ at the Tevatron is about $70\,\mathrm{mb} =$

[†] There are special cases where hadronic decays of heavy gauge bosons have been observed: hadronic W boson decays have been observed in top quark decays, and a $Z^0 \to b\overline{b}$ signal has been observed by CDF. Also, both experiments have observed W and Z decays to τ leptons.

[‡] We refer to the detector as "live" when it is ready and available to record data. If the detector is off or busy processing another event, it is not available or able to record additional data. This is known as "dead-time".

70×10^{-3}b. The cross section listed here is for any and all types of Z boson production. The "X" includes the remaining fragments of the initial p and $\overline{p}$, in addition to allowing for additional final state particles.

- $Br(Z^0 \to e^+e^-)$: The branching ratio is the fraction of Z^0 bosons that decay to a specific final state, e^+e^- in this example.[§]
- ϵ_{ee}: Of the Z^0 bosons that are produced and decay to e^+e^-, not all of them are detected or accepted into the final event sample. Some of the events are beyond the region of space the detector covers, in addition to the fact that the detector is not 100% efficient for detecting any signature.

Our ultimate goal is to extract σ_Z. Rearranging Equation 1, we have:

$$\sigma_Z = \frac{N}{\mathcal{L}_{int} \cdot Br(Z^0 \to e^+e^-) \cdot \epsilon_{ee}}. \tag{2}$$

From the data, we can count the number of signal events, N. To extract a cross section, we need to know the terms in the denominator as well:

- The luminosity is measured by looking at the total rate for $p\overline{p} \to p\overline{p}X$ in a specific and well-defined detector region. This rate is measured as a function of time and then integrated over the time the detector is live. The equation $N = \mathcal{L}\sigma$ is used again, in this case we already know the total $p\overline{p}$ cross section(σ), so we can use this equation to extract $\mathcal{L}$. At e^+e^- machines, the measurement of the luminosity is quite precise, with a relative error of 1% or less. For hadron machines, that level of precision is not possible. Typical relative uncertainties on the luminosity are 5-8%.[4]
- The branching ratio for $Z^0 \to e^+e^-$ is measured quite precisely by the LEP and SLC experiments. The world average value is used as an input here. The uncertainty on that value is incorporated into the ultimate uncertainty on the cross section.
- The efficiency for a final state like this is measured by a combination of simulation and control data samples. Primarily, data samples are used that are well understood. For example, Z^0 decays ($Z^0 \to e^+e^-$ and $Z^0 \to \mu^+\mu^-$) provide an excellent sample of electrons and muons for detector calibration. The high invariant mass of the lepton pair is a powerful handle to reject background.

[§]The branching ratio is the fraction of times that a particle will decay into a specific final state. More concisely, the branching ratio is $Br(Z^0 \to e^+e^-) = \Gamma(Z^0 \to e^+e^-)/\Gamma(Z^0 \to \text{all})$, where $\Gamma(Z^0 \to e^+e^-)$ is the partial width for Z^0 decaying to e^+e^- and $\Gamma(Z^0 \to \text{all})$ is the total Z^0 width.

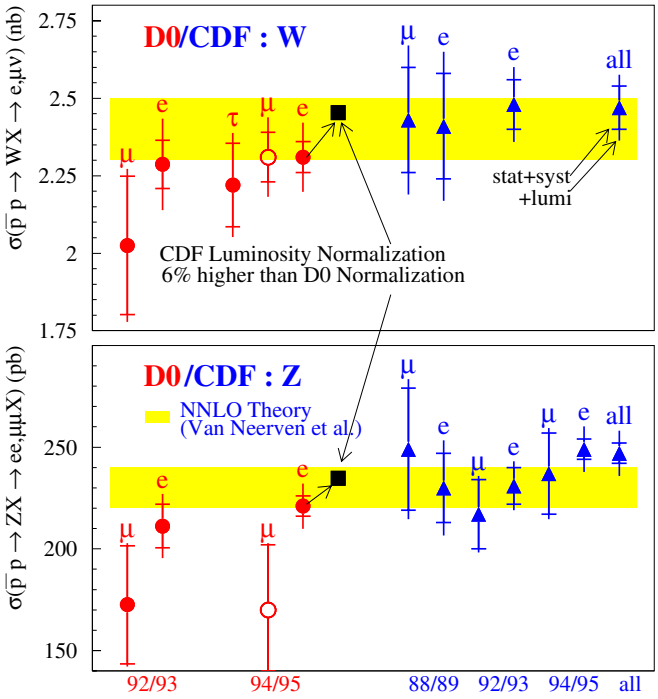

Fig. 1. Summary of DØ and CDF W and Z boson cross section measurements. The solid bands indicate the theoretical prediction. The circular points are the DØ results; the triangles are the CDF results. The two experiments use a different luminosity normalization.

Putting all of these factors together, it is possible to measure the total cross sections for $p\overline{p} \rightarrow WX$ and $p\overline{p} \rightarrow ZX$. These measurements are performed independently in both electron and muon modes. However, after the corrections for the efficiencies of each mode, the measurements should (and do) yield consistent measured values for the production cross section.

The results from DØ and CDF are represented in Fig. 1. The top plot is for W production, the bottom plot for Z production. The shaded region is the theoretical cross section. On both plots, the circular points are the DØ measurements, the triangles the CDF measurements. Part of the difference in the results from the two experiments arises from a different calculation of $\mathcal{L}_{int}$. If a common calculation were used, the DØ numbers would be 6% larger than those presented. This shows that in fact the integrated luminosity is the largest systematic uncertainty on the cross sections. Details of these analyses may be found in the literature.[5,6]

4.2 $\mathcal{R}$ and the W Width

One way to make the measurement more sensitive to the electroweak aspects of the W and Z production processes is to measure the cross section ratio. This ratio is often referred to as "$\mathcal{R}$", and defined as:

$$\mathcal{R} \equiv \frac{\sigma(W)}{\sigma(Z)} \cdot \frac{Br(W \to \ell\nu)}{Br(Z \to \ell\ell)} .$$

In taking the ratio of cross sections, the integrated luminosity ($\mathcal{L}_{int}$) term and its uncertainty cancel. Other experimental and theoretical uncertainties cancel as well, making the measurement of $\mathcal{R}$ a more stringent test of the Standard Model. As we can see from Fig. 1, the ratio is about equal to 10. This is confirmed by the results shown in Table 2. The DØ result is for the electron final state[7]; the CDF result is for the electron

Table 2. Summary of Tevatron measurements of $\mathcal{R}$, where $\mathcal{R} \equiv \frac{\sigma(W)}{\sigma(Z)} \cdot \frac{Br(W\to\ell\nu)}{Br(Z\to\ell\ell)}$.

	measured value of $\mathcal{R}$
DØ	$10.43 \pm 0.15(\text{stat.}) \pm 0.20(\text{syst.}) \pm 0.10(\text{theory})$
CDF	$10.38 \pm 0.14(\text{stat.}) \pm 0.17(\text{syst.})$

and muon final states.[8] For the CDF result, the theoretical uncertainty is contained in the systematic uncertainty.

We can take this result one step further. The measured quantity is $\mathcal{R}$. Theoretically, the cross section ratio $\sigma(W)/\sigma(Z)$ is calculated with good precision. This can be understood by noting that the primary production of Z bosons at the Tevatron arise from the reactions: $u\overline{u} \to Z^0$ and $d\overline{d} \to Z^0$, where the up and down quarks (and antiquarks) can be valence or sea quarks in the proton. An example of valence-valence production is shown in Fig. 2. For W production, the primary contributions are $u\overline{d} \to W^+$ and $\overline{u}d \to W^-$. These reactions look quite similar to the Z production mechanisms where a u quark is replaced with a d quark (or vice-versa). An example of valence-valence W^+ production is also shown in Fig. 2.

Although both Z^0 and $W^\pm$ are produced through quark-antiquark annihilation, the dominant contribution is not from the valence-valence diagrams shown in Fig. 2. The typical $q\overline{q}$ interaction energy for heavy boson production is the mass of the boson: $\sqrt{\hat{s}} \sim M_{Z,W}$. Since the heavy boson mass $M_{Z,W} \sim 100\,\text{GeV} = 0.1\,\text{TeV}$ and the $p\overline{p}$ center of mass energy is $\sqrt{s} \sim 2\,\text{TeV}$, the process requires the $q\overline{q}$ center of mass energy

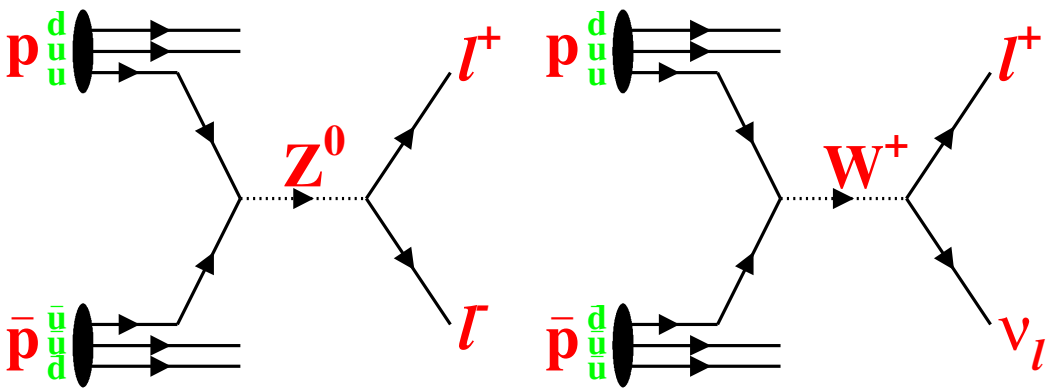

Fig. 2. Example Z and W production diagrams in high energy $p\overline{p}$ collisions. These figures show valence-valence production, which in fact is not dominant at Tevatron energies. The dominant production mechanism is quark-antiquark annihilation, where one quark(antiquark) is a valence quark and the other antiquark(quark) is a sea quark.

to be only $\sqrt{\hat{s}}/\sqrt{s} \simeq 5\%$ of the $p\overline{p}$ center of mass energy. In other words, if a quark and antiquark are each carrying 5% of the proton (and antiproton) momentum, then there is sufficient collision energy to produce a heavy boson.

Both valence and sea quarks have a good probability for carrying a sufficient fraction of the proton's energy to produce a gauge boson. In fact, the dominant production mechanism at the Tevatron is annihilation where the quark(antiquark) is a valence quark and the antiquark(quark) is a sea quark. The valence-sea production mechanism is about 4 times larger than the valence-valence and sea-sea production mechanisms. It is coincidental that the valence-valence and sea-sea mechanisms are about equal at this energy. At higher energies, the sea-sea mechanism dominates; at lower energies, the valence-valence mechanism dominates.[9]

The theoretical predictions for the production cross sections of Z and W bosons are not known to high precision. Strong interaction effects, such as the parton distribution functions and higher order diagrams lead to theoretical uncertainty. The ratio of cross sections is well calculated, however, because going from Z production to W^+ production amounts to replacing an $\overline{u}$ with a $\overline{d}$. In addition, the gauge boson couplings to fermions are well measured. Combining these points makes the ratio of cross sections a much better determined quantity than the individual cross sections.

Additionally, the branching ratio for $Z^0 \to \ell^+\ell^-$ is well measured at LEP. Using

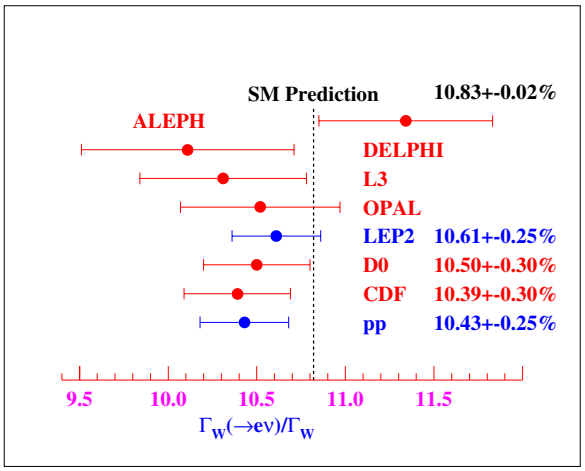

Fig. 3. Measurements of the branching ratio for $W \to e\nu_e$. The Tevatron results come from a measurement of $\mathcal{R}$ combined with the LEP measurement of $Br(Z^0 \to e^+e^-)$ and a theoretical calculation of $\sigma(W)/\sigma(Z)$.

our measured value of $\mathcal{R}$, inputting the theoretical value for $\sigma(W)/\sigma(Z)$ and using the LEP value for $Br(Z^0 \to \ell^+\ell^-)$, we can extract the branching ratio for $W \to \ell\nu$. This is shown in Fig. 3. The Tevatron results have similar uncertainties to the results from LEP2. As the uncertainties are reduced, this measurement will continue to be an important test of the Standard Model.

4.3 W mass

The electroweak couplings and boson masses within the Standard Model may be completely specified by three parameters. Typically, those parameters are chosen to be M_Z (the mass of the Z^0 boson), G_F (the Fermi constant), and α_{QED} (the electromagnetic coupling constant). These three parameters are not required to be the inputs, though. For example, we could choose to use the charge of the electron (e), the weak mixing angle ($\sin^2\theta_W$) and the mass of the W boson (M_W) as our inputs. At tree level (no radiative corrections, also known as Born level), any set of three parameters is sufficient to calculate the remaining quantities. The three chosen: M_Z, G_F and α_{QED} are the ones measured experimentally with the highest precision.

Therefore, at Born level, these three parameters are sufficient to exactly determine the mass of the W boson. The true W mass depends additionally on radiative corrections, the most important of which involve the top quark and the Higgs boson. Radiative

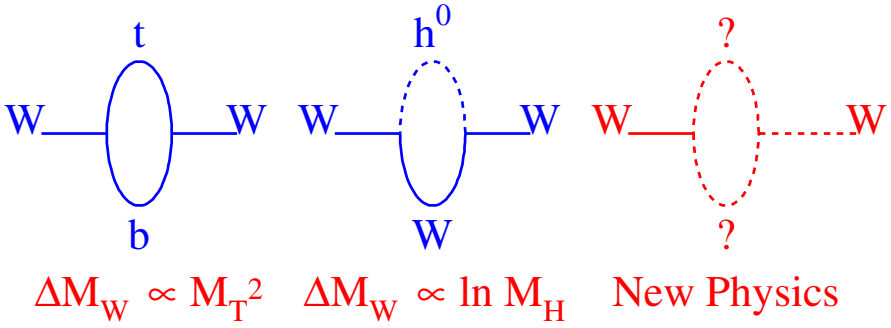

Fig. 4. Loop contributions to the W mass. The ΔM_W denotes the shift in W mass from the Born level value. The dependence upon the top quark mass is more dramatic than the dependence on the Higgs mass. New physics can appear in these loop corrections as well.

corrections involving fermion or boson loops grow with the mass of the particle in the loop. This is why the top quark and Higgs boson masses are the most important corrections to the W mass. These loop diagrams are shown graphically in Fig. 4.

The W mass can be calculated with a high degree of precision and therefore simply measuring the W mass provides a test of the Standard Model. Since there is additional uncertainty on the W mass due to the unknown mass of the Higgs boson (or perhaps it doesn't exist in the Standard Model form) the simple test of comparing the measured W mass value to the prediction is not a high precision test. It is an important test, though, because deviations from the Standard Model predicted W mass can arise through other non-Standard Model particles affecting the W mass through loops.

In addition, when combined with the measured value for the top quark mass (M_t), we can constrain the Higgs mass. In saying that we can constrain the Higgs mass, this is implicitly assuming a Standard Model Higgs boson. This can be seen graphically in Fig. 5, where electroweak results are plotted in the M_W,M_t plane. The contour marked "Tevatron" shows the directly measured values for M_W and M_t. The bands are contours of Standard Model calculations for M_W versus M_t for different masses of the Higgs boson. The current Tevatron region is consistent with the Standard Model and prefers a light Higgs boson.

Another way the W mass tests the Standard Model is through self-consistency with other Standard Model measurements. For example, the LEP1, SLD, νN data contour in Fig. 5 arises from taking the electroweak measurements of $\sin^2\theta_W^{eff}$, Z boson param-

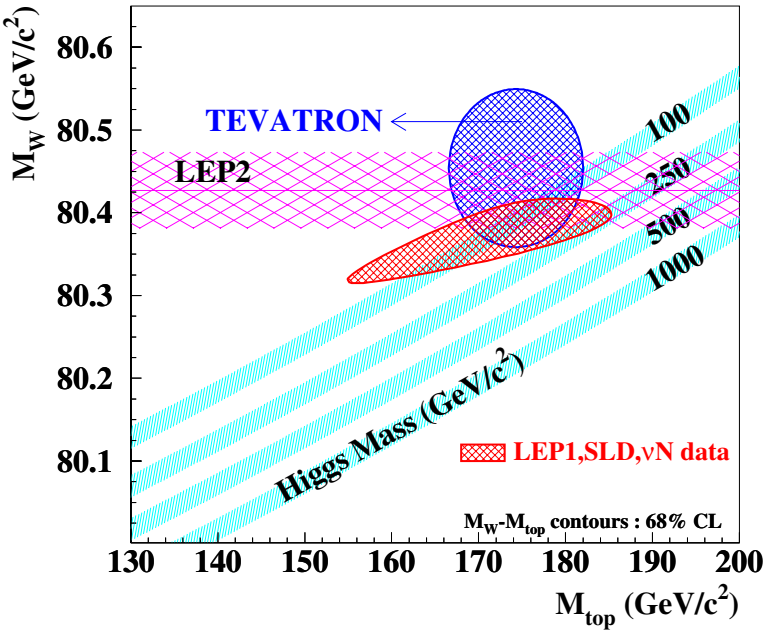

Fig. 5. A summary of precision electroweak measurements. The Tevatron contour is from direct measurements of M_W and M_t. The horizontal band is the direct measurement of M_W from LEP2. The oval contour arises from precision electroweak measurements of $\sin^2\theta_W^{eff}$, and Z couplings and asymmetries translated into the M_W, M_t plane. The bands are Standard Model contours for various values of the Higgs mass, M_H. It is clear that the experimental results are consistent with one another and currently favor a light Higgs boson.

eters and couplings and translating them into the M_W,M_t plane. Right now, the three contours: M_W,M_t from the Tevatron; M_W from LEP2; and the LEP, SLD, νN contour are all consistent with one another and tend to favor a light Higgs mass. It is conceivable that the contours could all be consistent with the Standard Model yet inconsistent with one another. An inconsistency of this type would indicate non-Standard Model physics.

The smaller the contours, the more stringent the constraints on the Higgs boson mass and the Standard Model tests. The goal of current and future experiments is to measure electroweak parameters as precisely as possible to further constrain and test the Standard Model. Currently, the crucial aspects of these measurements are the top quark mass and the mass of the W boson.

4.3.1 The Measurement of M_W

As stated previously, the dominant mechanism for W boson production is quark-antiquark annihilation ($q\overline{q}' \rightarrow W^{\pm}$). The center of mass energy for this interaction, $\sqrt{\hat{s}}$ is much less than the $p\overline{p}$ center of mass energy of $\sqrt{s} = 1.8\ \mathrm{TeV}$. This production mechanism leads to two important consequences:

1. The energies of the annihilating quark and antiquark are not equal, meaning the W will be produced with a momentum component along the beam line (p_z^W). Another way to put this is to say that center-of-mass of the parton-parton collision is moving in the lab frame. The momentum of the partons transverse to the beam direction is effectively zero, so this center-of-mass motion is along the beam direction.
2. Since the remnants of the p and $\overline{p}$ carry a large amount of energy in the far forward direction (along the beam line) it is not possible to accurately measure the $\hat{s}$ of the interaction. Therefore the initial p_z of the W is not known.

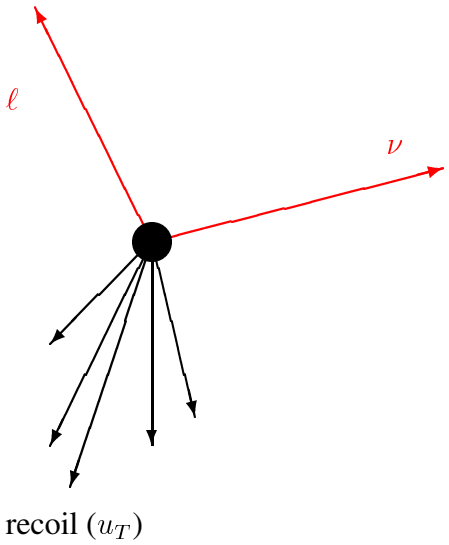

Fig. 6. A cartoon of a $W \rightarrow \ell\nu_\ell$ decay. The lepton is measured directly. The transverse momentum of the neutrino is inferred by the recoil energy (u_T).

Because of these points, it is not possible to measure the mass of the W boson based upon the collision energy, $\sqrt{\hat{s}}$. We must measure the W mass by reconstructing the decay products.

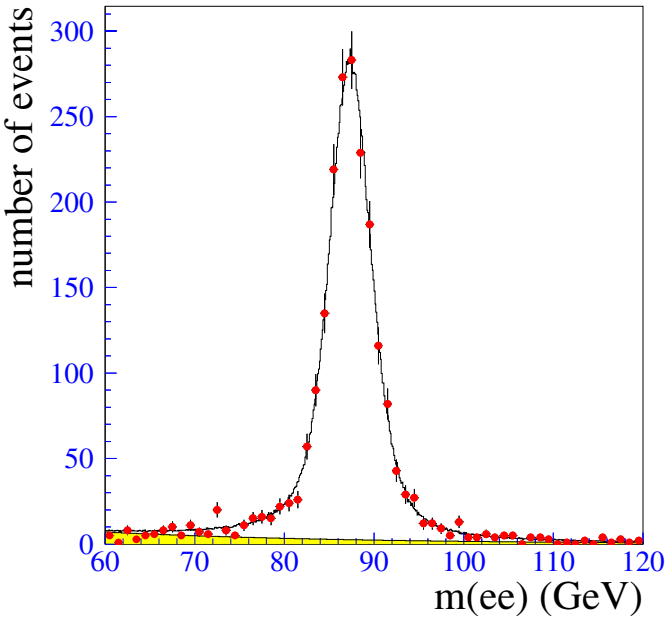

Fig. 7. The Z^0 mass as reconstructed in the mode $Z^0 \to e^+e^-$ by the DØ detector. The shaded region at the bottom of the plot is the background contribution. The peak does not fall exactly on the true value of M_Z because not all of the energy corrections have been applied to the data.

Recall that we are dealing with $W \to e\nu_e$ and $W \to \mu\nu_\mu$ modes. The quantities associated with these decays that we can directly measure are:

- The momentum of the muon, $\vec{p}_\ell$.
- The recoil energy, $\vec{u}$.

The lepton momentum can be measured in three dimensions. The recoil energy can be measured in three dimensions, but since we do not know the initial p_Z of the center of mass, the z component of $\vec{u}$ and $\vec{p}_\ell$ are of no use to us. Since we know that (to very good approximation) $p_x^W + u_x = p_y^W + u_y = 0$, we can implement conservation of momentum in the transverse (x, y) plane and infer the transverse momentum of the neutrino. Since we do not know p_z^W, we can not infer the p_z^ν from momentum conservation. Even with three-dimensional measurements of $\vec{u}$ and $\vec{p}_\ell$, it is not possible to unambiguously determine the neutrino momentum in three dimensions. If it were possible to determine $\vec{p}_\nu$, then we could simply calculate the invariant mass of the ℓ-ν_ℓ and measure the W mass from the resonance.

The case of Z production as discussed above is quite similar to W production. The difference, however, is that the Z can decay to two charged leptons that we can measure in the detector. Figure 7 shows the reconstructed Z mass in the mode $Z^0 \to e^+e^-$ from the DØ detector. The Z peak is clear and well-resolved, with small backgrounds.

In the case of the W mass, the information we have is the momentum of the lepton $\vec{p}^{\,\ell}$ and the transverse momentum of the neutrino, $\vec{p}_T^{\,\nu}$, which was inferred from the transverse momentum of the lepton and the transverse recoil energy ($\vec{u}_T$).

From the transverse momenta of the lepton and the neutrino, we can calculate a quantity known as the "transverse mass":

$$M_T^W = \sqrt{2p_T^\ell p_T^\nu (1 - \cos\Delta\phi_{\ell,\nu})},$$

where p_T^ℓ and p_T^ν are the magnitudes of the lepton and neutrino transverse momenta and $\Delta\phi_{\ell,\nu}$ is the opening angle between the lepton and neutrino in the x, y plane.

The transverse mass equation may look familiar. If we have two particles where we have measured the momenta in 3 dimensions with momenta $\vec{p}_1$ and $\vec{p}_2$, then the invariant mass of those two particles, in the approximation that the particles are massless, is:

$$M_{1,2} = \sqrt{2p_1p_2(1 - \cos\alpha)},$$

where α is the opening angle (in 3-dimensions) between the two particles.

By comparing the two equations, we can see that the term "transverse mass" is accurate in that the calculation is identical to the invariant mass except only the transverse quantities are used. If the W boson has $p_Z^W = 0$, and decays in the transverse plane, then the transverse mass is exactly the invariant mass. If the W boson has $|p_z^W| > 0$, then the transverse mass is less than the invariant mass. A W boson transverse mass distribution is shown in Fig. 8.

Although not quite as clean as a full invariant mass, the transverse mass distribution quite clearly contains information about the W mass. By fitting this distribution, it is possible to extract a precise measurement of the W mass. There are three basic ingredients that determine the shape of the transverse mass distribution:

- W boson production and decay.
- p_T^ℓ measurement.
- $u_T \Rightarrow p_T^\nu$ measurement.

Each of these items will be discussed in detail below. All of the details are ultimately combined into a fast Monte Carlo simulation that is able to generate transverse mass

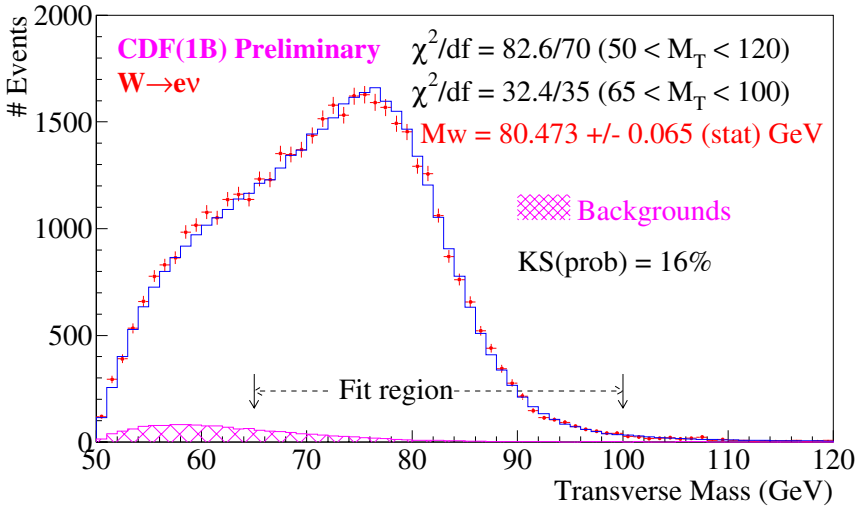

Fig. 8. The W transverse mass in the mode $W \to e\nu_e$ as measured by CDF. The points are the data, the histogram is the fit. The hatched region shows the background contribution.

spectra corresponding to various values of the W mass. The measured transverse mass distribution is then fit to the generated spectra and the W mass is extracted from this fit.

In the following subsections, we discuss each of the elements required for precise W mass determination.

4.3.2 W boson production and decay

Modeling of the W boson production and decay includes the Breit-Wigner lineshape, parton distribution functions, the momentum spectrum of the W boson, the recoiling system and radiative corrections. The intrinsic width of the W boson is about $2.1\,\mathrm{GeV/c^2}$, which must be included in the fit. The parton distribution functions (PDF) are representations of the distributions of valence quarks, sea quarks and gluons in the proton. The probability for specific processes as a function of $\hat{s}$ depend upon these distributions. Related to the PDFs and the production diagrams is the momentum distribution of the produced W bosons. The model of the recoil system must be accurate. Higher order QED diagrams, such as $W \to \ell\nu\gamma$, are also included in the modeling.

4.3.3 p_T^ℓ measurement

This aspect is quite crucial in the W mass determination. For muons, the transverse momentum is measured by the track curvature in the magnetic field. For electrons, it is more accurate to measure the energy (and infer the momentum) in the calorimeter because the resolution is better and bremsstrahlung tends to bias the tracking measurement of the curvature.

The energy scale is crucial. If we measure a muon with a transverse momentum of $30\ \mathrm{GeV/c}$, is the true momentum $30\ \mathrm{GeV/c}$? Is it $29.9\ \mathrm{GeV/c}$? Is it $30.1\ \mathrm{GeV/c}$? Also, the resolution is important to understand. For a measured momentum of $30\ \mathrm{GeV/c}$, we also need to know the uncertainty on that value, because it will smear out the transverse mass distribution. In reality, the resolution is a rather small effect, much smaller than the overall momentum scale.

To set the momentum/energy scale, we use "calibration" samples. The J/ψ, Υ and Z^0 masses are all known very precisely based upon measurements from other experiments. We can measure these masses using $\mu^+\mu^-$ and e^+e^- final states to calibrate our momentum scale. If a muon measured with $p_T = 29.9\ \mathrm{GeV/c}$ is truly a muon with $p_T = 30.0\ \mathrm{GeV/c}$, then we will measure an incorrect Z^0 mass. This scale can be noted and ultimately corrected.

The Z^0 is particularly important for the W mass measurement because both its mass and the production mechanism are very similar to that of the W. They are not identical, though, because the Z^0 is $10.7\ \mathrm{GeV/c^2}$ more massive than the W. Also, due to coupling and helicity considerations, the decay distributions are not identical between the two. They are quite close, however, and the Z^0 provides a crucial calibration point. The limiting factor then arises from the number of Z^0 decays available. As noted earlier, the ratio of observed leptonic W decays to Z decays ($\mathcal{R}$) is about 10:1. In some cases, the limiting factor on the systematic uncertainty arises from the statistics of the Z samples.

4.3.4 $u_T \Rightarrow p_T^\nu$ measurement

The recoil energy is required to infer the transverse momentum of the neutrino. Since the recoil energy is largely hadronic and contains both charged and neutral components, it must be measured with the calorimeter. All of the charged and neutral energy recoiling against the W is included in the measurement, so all sources of calorimetric energy must be included in the model. The recoil distribution is affected by the collider environment, the resolution of the calorimeter, the coverage of the calorimeter and the

ability to separate u_T from p_T^ℓ. At typical Tevatron luminosities, there are more than one, sometimes as many as six $p\overline{p}$ interactions per beam crossing. Most of these are inelastic events that have low transverse momentum. However, there is no way to directly separate out the contributions from other interactions from the contributions of the W recoil. Instead, this must be modeled and the background level subtracted on an average basis. Uncertainty in this background subtraction leads to uncertainty in M_W.

The hadronic energy resolution of the calorimeter is much larger (*i.e.*, worse) than the resolution on the lepton energy. Therefore, the resolution on the neutrino p_T is determined by the hadronic energy resolution. The smaller this resolution, the less smeared the transverse mass distribution.

The coverage of the calorimeter must be understood, also, because some of the recoil can be carried away at very small angles to the beamline, where there is no instrumentation.

Finally, the recoil measurement is a sum of all calorimeter energy except the energy of the lepton. In the case of the muon channel, it is pretty straightforward to subtract the contribution from the muon. For the electron, some of the recoil energy is included in the electron energy cluster in the calorimeter simply because the recoil and electron energy "overlap". This affects both the electron energy measurement and the u_T measurement and therefore we must correct for that effect.

4.3.5 W Mass Summary

Each of these pieces needs to be fully and accurately modeled in order to understand how they effect the transverse mass distribution. There are many important aspects to this analysis, but the most important is the lepton energy scale. A great deal of work has gone into calibrating, checking and understanding the lepton energy scale. Details of the DØ and CDF W mass measurements may be found in Refs. 10,11. A recent compilation of the world's W mass measurements may be found in Ref. 12. The results for M_W from DØ and CDF are plotted, along with those from LEP II and UA2, in Fig. 9.

4.3.6 The Future

In addition to the Tevatron upgrades for Run II, the DØ and CDF collaborations are significantly upgrading their detectors.[13,14] Figure 11 shows how the uncertainty on the W mass has progressed over time. Since $N \propto \mathcal{L}_{int}$, the horizontal axis, plotted

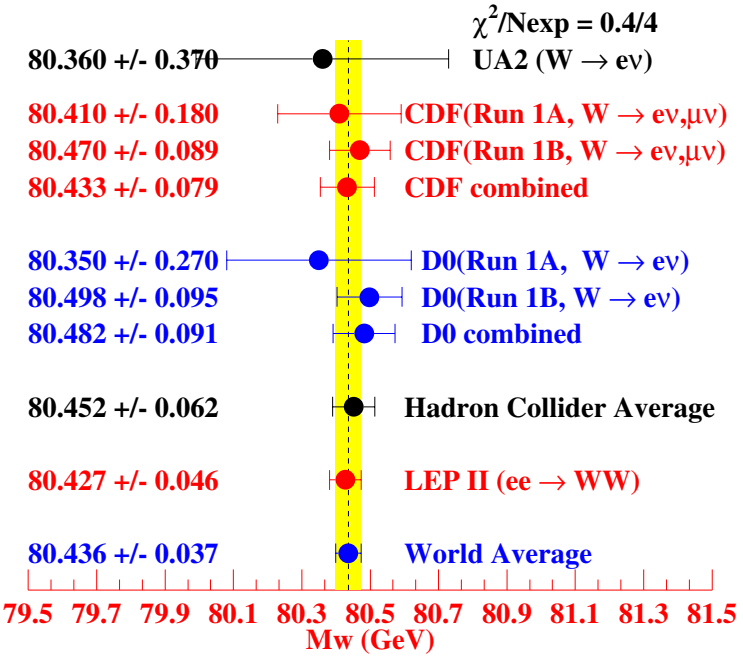

Fig. 9. Summary of direct measurements of the W mass. The LEP II point is the combination of four experiments, while the CDF and DØ results are shown separately. The world average uncertainty is $37\,\mathrm{MeV}$.

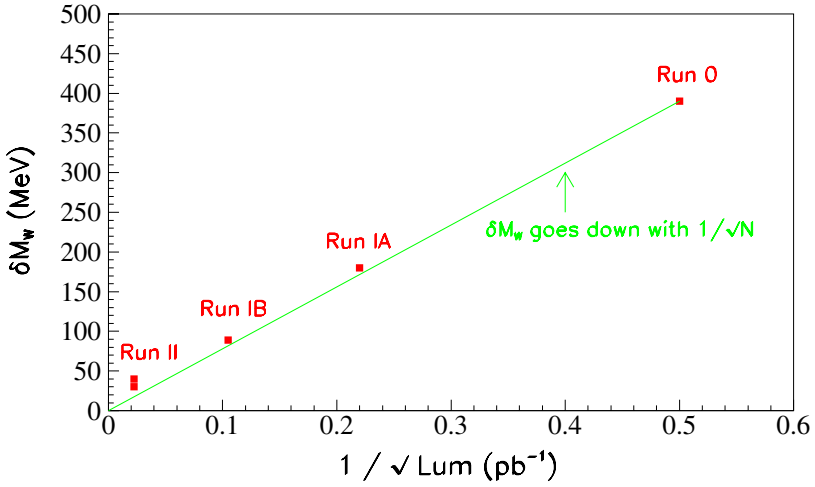

Fig. 10. The W mass uncertainty as a function of data size. Both the statistical and systematic errors have continually fallen linearly as $1/\sqrt{N}$. This trend will continue in the future, although the ultimate Run II sensitivity will deviate from the line.

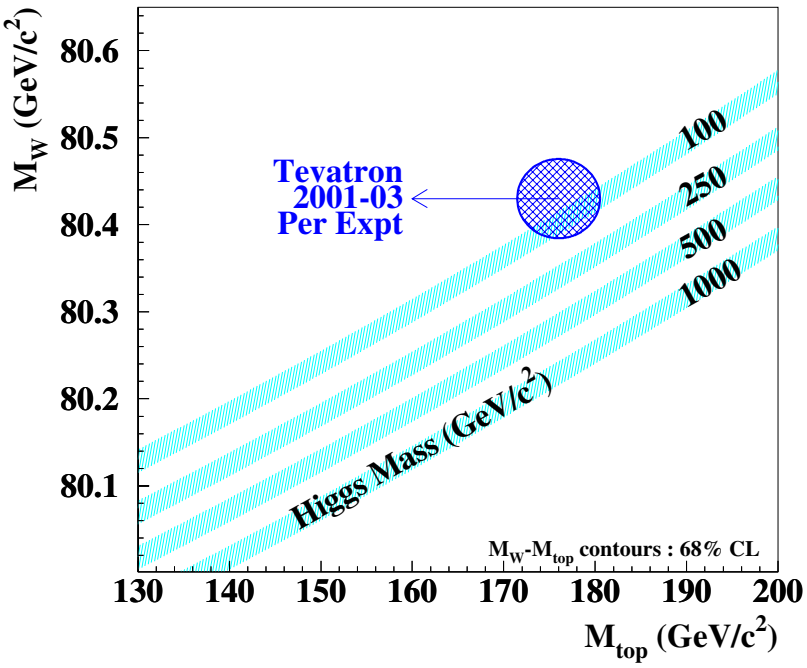

Fig. 11. The M_W versus M_t plot at the end of Run II. The central value is plotted as it currently stands. For Run II, we anticipate $\delta M_W \sim 30\ \mathrm{MeV}$ and $\delta M_t \sim 3\ \mathrm{GeV}$. These results will further test and constrain the Standard Model.

as $\sqrt{\mathcal{L}_{int}}$ is equivalent to $\sqrt{N_W}$, with N_W being the number of identified W boson decays. So far, the uncertainty on the W mass has fallen linearly with $1/\sqrt{N_W}$. We expect the statistical uncertainty to fall as $1/\sqrt{N_W}$. The recent measurements of M_W are not dominated by the statistical uncertainty, however. To maintain the $1/\sqrt{N_W}$ behavior of the total error, both the systematic and statistical uncertainties must fall as the statistics increase. This can be understood from the fact that many of the systematic uncertainties are limited by the statistics of the control samples, such as $Z^0 \to \ell^+\ell^-$. As those samples grow, the systematic uncertainties fall.

Tevatron Run II is projected to move slightly away from the strict $1/\sqrt{N_W}$ behavior as some of the systematic uncertainties become limited by factors other than the statistics of the control samples. Nevertheless, the uncertainty is expected to be significantly reduced. The combined W mass uncertainty from DØ and CDF is expected to be between 20 and $40\ \mathrm{MeV/c^2}$ in Run II.

At the same time, the uncertainty on the top quark mass will also be reduced. Figure 11 also shows what the M_W, M_t plot could look like by about 2003. For this plot, we assume that the central measured value is the same as it is currently, simply to

demonstrate how the uncertainty contours will look at that time. This compares quite favorably to the current version of this plot, shown previously in Fig. 5.

5 B Physics Results

Since the first observation of a violation of charge-conjugation parity (CP) invariance in the neutral kaon system in 1964,[15] there has been an ongoing effort to further understand the nature of the phenomenon. To date, violation of CP symmetry has not been directly observed anywhere other than the neutral kaon system. Within the framework of the Standard Model, CP violation arises from a complex phase in the Cabibbo-Kobayashi-Maskawa (CKM) quark mixing matrix,[16] although the physics responsible for the origin of this phase is not understood. The goal of current and future measurements in the K and B meson systems is to continue to improve the constraints upon the mixing matrix and further test the Standard Model. Inconsistencies would point towards physics beyond the Standard Model.

In recent years, the importance and experimental advantages of the B system have been emphasized.[17] The long lifetime of the b quark, the large top quark mass and the observation of $B^0/\overline{B^0}$ mixing with a long oscillation time all conspire to make the B system fruitful in the study of the CKM matrix. Three e^+e^- B-factories running on the Υ(4s) resonance, in addition to experiments at HERA and the Tevatron, indicate the current level of interest and knowledge to be gained by detailed study of the B hadron decays.

This section is an introduction to CP violation in the B system, with a focus on experimental issues. After a some notational definitions, I will give a brief overview of the CKM matrix and $B^0/\overline{B^0}$ mixing. Following that, I will discuss experimental elements of flavor tagging, which is a crucial component in mixing and CP asymmetry measurements. Our discussion of CP violation in the B system will be presented in the framework of the specific example of the measurement of $\sin 2\beta$ using $B^0/\overline{B^0} \to J/\psi K^0_S$ decays by the CDF Collaboration. Finally, I will briefly survey future measurements.

5.1 Notation

There are enough B's and b's associated with this topic that it is worthwhile to specifically spell out our notation. First of all, we will refer to bottom (antibottom) quarks using small letters: b ($\overline{b}$). When we are referring to generic hadrons containing a bottom

quark (*e.g.* $|b\overline{q}\rangle$, where q is any quark type), we will use a capital B with no specific subscripts or superscripts.

In the cases where we are referring to specific bottom mesons or baryons, we will us the notation listed in Table 3. Neutral B mesons follow the convention of the neutral kaon system, where $K^0 = |\overline{s}d\rangle$ and $\overline{K^0} = |s\overline{d}\rangle$.

Table 3. B mesons and baryons. This is an incomplete list, as there are excited states of the mesons and baryons (*e.g.* B^{*0}). Also, a large number of B-baryon states are not listed (*e.g.* $\Sigma_b^- = |ddb\rangle$).

name	$\overline{b}$ hadron	b hadron
charged B meson	$B^+ = \|\overline{b}u\rangle$	$B^- = \|b\overline{u}\rangle$
neutral B meson	$B^0 = \|\overline{b}d\rangle$	$\overline{B^0} = \|b\overline{d}\rangle$
B_s (B-sub-s) meson	$B_s^0 = \|\overline{b}s\rangle$	$\overline{B_s^0} = \|b\overline{s}\rangle$
B_c (B-sub-c) meson	$B_c^+ = \|\overline{b}c\rangle$	$B_c^- = \|b\overline{c}\rangle$
Λ_b (Lambda-b)	$\overline{\Lambda_b} = \|\overline{u}\overline{d}\overline{b}\rangle$	$\Lambda_b = \|udb\rangle$
Υ (Upsilon)	$\Upsilon = \|\overline{b}b\rangle$	

5.2 Overview: the Cabibbo-Kobayashi-Maskawa Matrix

Within the framework of the Standard Model, CP nonconservation arises through a non-trivial phase in the Cabibbo-Kobayashi-Maskawa (CKM) quark mixing matrix.[16] The CKM matrix V is the unitary matrix that transforms the mass eigenstates into the weak eigenstates:

$$V = \begin{pmatrix} V_{ud} & V_{us} & V_{ub} \\ V_{cd} & V_{cs} & V_{cb} \\ V_{td} & V_{ts} & V_{tb} \end{pmatrix} \tag{3}$$

$$\simeq \begin{pmatrix} 1-\frac{\lambda^2}{2} & \lambda & A\lambda^3(\rho-i\eta) \\ -\lambda & 1-\frac{\lambda^2}{2} & A\lambda^2 \\ A\lambda^3(1-\rho-i\eta) & -A\lambda^2 & 1 \end{pmatrix} + \mathcal{O}(\lambda^4). \tag{4}$$

The second matrix is a useful phenomenological parameterization of the quark mixing matrix suggested by Wolfenstein,[18] in which λ is the sine of the Cabibbo angle, $\lambda = \sin\theta_C \simeq 0.22$. The CKM matrix is an arbitrary three-dimensional rotation matrix. The only requirement *a priori* is that it be unitary — the elements can take on any value

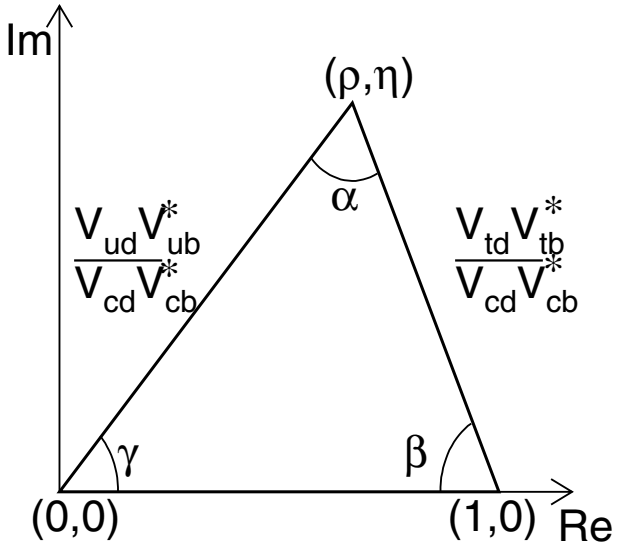

Fig. 12. The unitarity triangle. The horizontal axis is the real axis; the vertical axis is the imaginary axis. The apex of the triangle is (ρ, η).

so long as unitarity is preserved. The Wolfenstein parameterization arose based upon experimental results indicating that the matrix is nearly diagonal. Using experimental results on V_{us} and V_{cb} along with the unitarity requirement, Wolfenstein proposed the commonly-seen expansion shown here.

The condition of unitarity, $V^\dagger V = 1$, yields several relations, the most important of which is a relation between the first and third columns of the matrix, given by:

$$V_{ub}^* V_{ud} + V_{cb}^* V_{cd} + V_{tb}^* V_{td} = 0. \tag{5}$$

This relation, after division by $V_{cb}^* V_{cd}$, is displayed graphically in Fig. 12 as a triangle in the complex (ρ-η) plane, and is known as the unitarity triangle.[19] CP violation in the Standard Model manifests itself as a nonzero value of η, the height of the triangle, which indicates the presence of an imaginary CKM component.

The "unitarity triangle" is simply a graph of a single point in the complex plane: (ρ, η). We use the triangle to show how these two numbers are related to the CKM elements. Different experimental measurements are sensitive to different aspects of the unitarity triangle, *i.e.* they are sensitive to different combinations of ρ and η.

Six unique triangles can be constructed from unitary relations (six more are complex conjugates of the first six). The one shown here is the most useful because all of the sides are of $\mathcal{O}(\lambda)$, insuring that none of the three interior angles is near 0° or 180°. The

other triangles are "squashed", having one side $\mathcal{O}(\lambda^2)$ or $\mathcal{O}(\lambda^3)$ smaller than the other two sides.

The goal of current and future experiments in the K and B system is to measure as many aspects of the triangle as possible in as many ways as possible. Inconsistencies in these measurements will point to physics beyond the Standard Model and hopefully give us some indication from where these "fundamental constants" arise.

Based upon current measurements in the K and B system, such as $B^0/\overline{B^0}$ mixing, $K \to \pi^{\pm}\ell^{\mp}\nu$, $b \to u$ decays and $b \to c$ decays, the CKM solution indicates that the CP violating phase is large. The fact that CP violation in the K system is small, $\mathcal{O}(0.1\%)$, arises from the fact that the magnitude of the matrix element V_{td} is rather small. An alternate solution would be if the CP violating phase were to be small and the magnitude of V_{td} larger. Direct measurements of CP violation in the B system will permit clear distinction between the two cases.[20]

5.3 $B^0/\overline{B^0}$ Mixing

Mixing occurs in the neutral K and B systems because the electroweak eigenstates and the strong interaction eigenstates are not the same. If we start with a B^0 meson, then the probability that we will see a $B^0(\overline{B^0})$ at a given time, t, is

$$P(B^0(t)) = \frac{1}{2\tau}e^{-\frac{t}{\tau}}(1+\cos(\Delta m_d t)),$$

$$P(\overline{B^0}(t)) = \frac{1}{2\tau}e^{-\frac{t}{\tau}}(1-\cos(\Delta m_d t)), \tag{6}$$

where τ is the B^0 lifetime and $\Delta m_d = m_H - m_L$,[¶] where m_H and m_L are the masses of the heavy and light weak eigenstates of the mesons. The mass difference Δm_d in the $B^0/\overline{B^0}$ system is relatively small, therefore the mixing frequency is rather low. In units where $\hbar = c = 1$, the mass difference is presented in units of ps^{-1}. The current world average for Δm_d is[21] $0.487 \pm 0.014\,\mathrm{ps}^{-1}$. With this mass difference, the oscillation period for $B^0/\overline{B^0}$ is close to nine B lifetimes.

Mixing is shown graphically in Fig. 13. When we begin with a beam of B^0 mesons, they disappear at a rate faster then $e^{-t/\tau}$, because some B^0 mesons are decaying and some are oscillating into $\overline{B^0}$ mesons. The sum of B^0 plus $\overline{B^0}$ decays at a rate $e^{-t/\tau}$.

[¶]The subscript d on Δm_d refers to the down quark in the neutral B meson. This is to distinguish from the $B_s^0/\overline{B_s^0}$ mass difference, which is written as Δm_s with the subscript s referring to the strange quark.

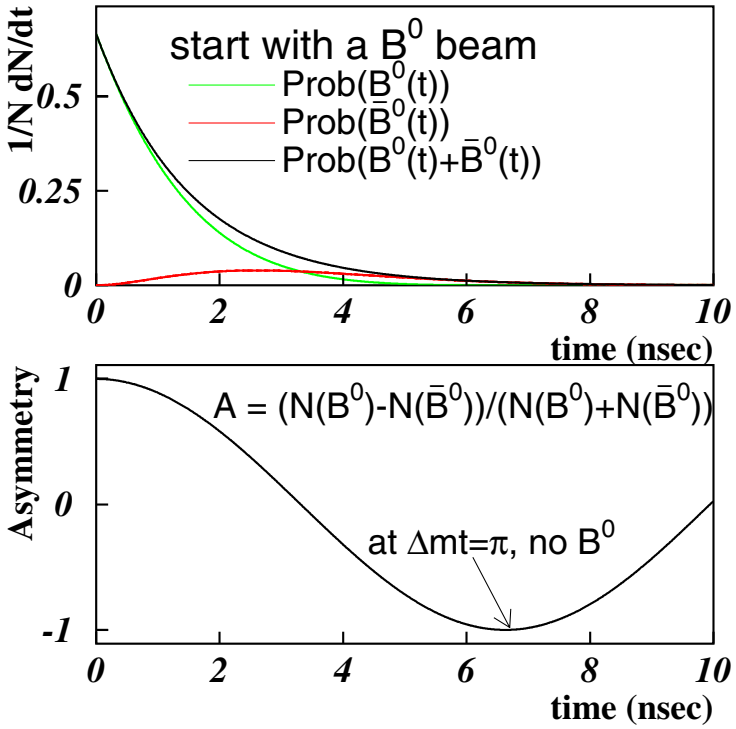

Fig. 13. $B^0/\overline{B^0}$ mixing. The top plot shows the probability functions for both B^0 and $\overline{B^0}$ as a function of time. At $t = 0$, we have 100% B^0. As time increases, the mesons decay away exponentially $\propto e^{-t/\tau}$, but some of the B^0 mesons become $\overline{B^0}$ mesons. The bottom plot shows the asymmetry so that the exponential effect has been removed. At $\Delta m_d t = \pi$ ($\Rightarrow t \simeq 4.4\tau \simeq 6.8\,\text{ps}$, because the B^0 lifetime is $\tau = 1.56\,\text{ps}$.), **all of the remaining mesons are $\overline{B^0}$!**

Mixing in the neutral B system is a second order $\Delta B = 2$ transition[‖] that proceeds through "box" diagrams shown in Fig. 14. All up-type quarks (u, c and t) are eligible to run around in the box, but the heavy top quark dominates because the amplitude is proportional to the mass of the fermion. As a consequence of this, there are two top-W-$down$ vertices (V_{td}) in the dominant box diagram. This will play a role in CP violation, as we will discuss below.

The Feynman diagrams for $B_s^0/\overline{B_s^0}$ look quite similar with the exception that the

[‖]The B used here refers to the "bottomness" quantum number. Since the box diagram is responsible for annihilating a $\overline{b}$ and producing a b (or vice versa) the change in the bottomness quantum number is $\Delta B = 2$.

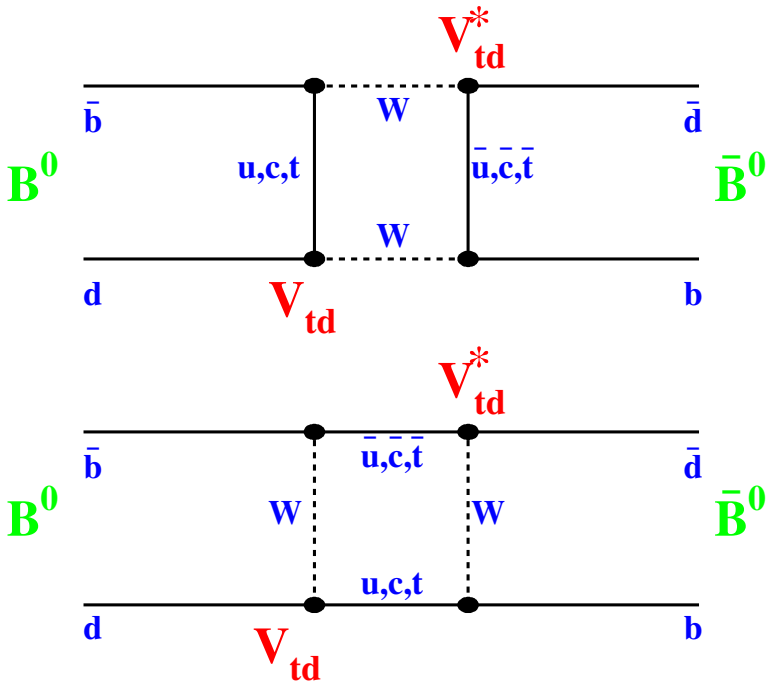

Fig. 14. $B^0/\overline{B^0}$ mixing diagrams. The diagrams shown are for B^0 oscillating into $\overline{B^0}$. The charge-conjugate process ($\overline{B^0}$ oscillating into B^0) takes place as well. The top quark dominates these 2^{nd} order weak transitions, which is why V_{td} (and not V_{ud} or V_{cd}) is shown at the vertices.

top-W-down vertices (V_{td}) are replaced by the *top-W-strange* (V_{ts}) vertices. Since $|V_{ts}| > |V_{td}|$, the B_s system oscillates much faster than does the B_d system. Put another way, Δm_s is much larger than Δm_d. The B_s oscillates so quickly that the oscillation period is smaller than the experimental resolution on the decay time of the B_s. In other words, we can identify and distinguish between B_s^0 and $\overline{B_s^0}$ mesons at the time of decay, but the resolution of the decay time is not yet good enough to resolve the oscillations. The current experimental bound is $\Delta m_s > 14\,\mathrm{ps}^{-1}$, which means that the B_s fully mixes in less than 0.17 lifetimes!

5.4 Flavor Tagging

To measure time-dependent mixing, it is necessary to know what the flavor of the meson was at the time of production and at the time of decay. For example, an "unmixed" event would be an event where a neutral B meson was produced as a B^0 and decayed as a B^0. A "mixed" event would be one where a neutral B meson was produced as a B^0 but

decayed as a $\overline{B^0}$. Typically, mixing results are plotted (bottom plot of Fig. 13) as an asymmetry: $\mathcal{A} = (N_{unmixed} - N_{mixed})/(N_{unmixed} + N_{mixed})$. This has the advantage of removing the exponential term from the decay probabilities. Once plotted in this way, the functional form of the mixing is $\mathcal{A} = \cos \Delta m_d t$.[**]

Experimentally, the determination of the flavor of the B meson at the time of production and/or the time of decay is referred to as "flavor tagging". Flavor tagging is an inexact science. The B mesons have numerous decay modes, thanks in large part to the large phase space for production of light hadrons in the dominant $B \to D \to X_s$ decay, where D and X_s represent generic charmed and strange hadrons respectively. There is very low efficiency for fully reconstructing B states. Therefore more inclusive techniques must be used to attempt to identify flavor.

Since flavor tagging is imprecise, it is crucial that we measure our success/failure rate. There are two parameters required to describe flavor tagging. The first is known as the tagging efficiency, ϵ, which is simply the fraction of events that are tagged. For example, if we are only able to identify a lepton on 10% of all of the events in our sample, then the lepton tagging efficiency is 10%. We can not distinguish a B^0 from a $\overline{B^0}$ in the other 90% of the events because there was no lepton found to identify the flavor.

The second parameter is associated with how often the identified flavor is correct. A "mistag" is an event where the flavor was classified incorrectly. A mistag rate (w) of 40% is not unusual; while a mistag rate of 50% would mean that no flavor information is available – equivalent to flipping a coin. Another way to classify the success rate is through a variable called the "dilution" ($\mathcal{D}$), defined as

$$\mathcal{D} = \frac{N_{right} - N_{wrong}}{N_{right} + N_{wrong}} = 1 - 2w, \tag{7}$$

where $N_{right}(N_{wrong})$ are the number of events tagged correctly (incorrectly). The term is dubbed "dilution" because it dilutes the true asymmetry:

$$\mathcal{A}_{observed} = \mathcal{D}\mathcal{A}_{true}, \tag{8}$$

where $\mathcal{A}_{observed}$ is the experimentally measured asymmetry and $\mathcal{A}_{true}$ is the measurement of the real asymmetry we are trying to uncover.[††]

[**] Another common way to display mixing data is of the form $\mathcal{A} = N_{mixed}/(N_{unmixed} + N_{mixed})$ which then takes the functional form $\mathcal{A} = \frac{1}{2}(1 - \cos \Delta m_d t)$.

[††] The choice of the term "dilution" here is unfortunate, since in this case a high dilution is good and a

Table 4. Methods of flavor tagging. These methods can be used in mixing analyses as well as CP asymmetry measurements. In the case of CP asymmetry measurements, the initial state flavor is the one of interest, as will be shown later.

method	initial/final state tag
exclusive reconstruction	final
partial reconstruction	final
lepton tagging	initial/final
jet charge tagging	initial
same side tagging	initial

In the following subsections we discuss some commonly used flavor tagging techniques. The methods outlined below are all utilized in mixing analyses. However, it is the initial state flavor tag that is important for CP asymmetry measurements. The methods discussed here are summarized in Table 4.

5.4.1 Full/Partial Reconstruction

The flavor of the B meson at the time of decay can be determined from the decay products. An example of this is $B^0 \to D^-\pi^+$, with $D^- \to K^+\pi^-\pi^-$. This all-charged final state is an unambiguous signature of a B^0 meson at the time of decay. The drawback of the full reconstruction technique is that both the branching ratios to specific final states and reconstruction efficiencies are low.

To improve upon this, we can relax by performing a "partial" reconstruction. An example of this relating to the example above is to reconstruct $B^0 \to D^-X$, with $D^- \to K^+\pi^-\pi^-$. In this case, the X would include the state listed above, but would include all other decays of this type (*e.g.* $B^0 \to D^-\pi^+\pi^0$.) Partial reconstruction is not as clean as full reconstruction — it is also possible to have $\overline{B^0} \to D^-X$, $B^+ \to D^-X$, $B_s^0 \to D^-X$ in addition to direct charm production, where $\overline{c} \to D^-$. Therefore the reconstruction of a D^- meson is not an unambiguous signature for a B^0 meson. These other contributions must be accounted for in the extraction of Δm_d.

low dilution is bad. The definition comes about because the factor $\mathcal{D} = 1 - 2w$ "dilutes" the measured asymmetry. If our flavor tagging algorithm were perfect (no mistags) then we would have $\mathcal{D} = 1$, the highest possible dilution.

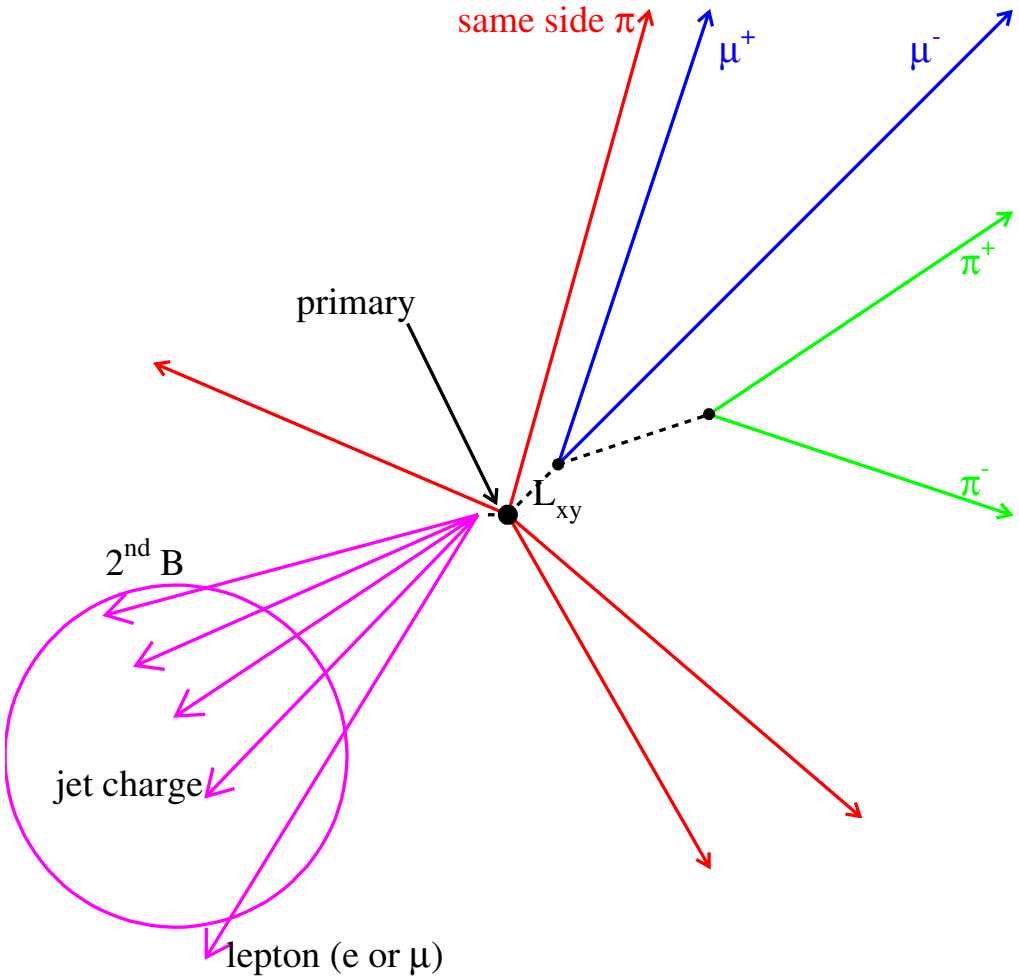

Fig. 15. Initial state flavor tags. This example shows a reconstructed $J/\psi K^0_S$ final state. The other information in the event is used to identify the flavor of the B^0 or $\overline{B^0}$ at the time of production.

5.4.2 Initial State Tagging

It is not possible to measure the flavor of a neutral B meson at the time of production using full or partial reconstruction, because the decay only reflects the flavor of the final state. To perform initial state flavor tagging, two types of methods are employed. The first technique, known as opposite-side tagging, involves looking at the other B hadron in the event. The second technique, known as same-side tagging, involves looking at the local correlation of charged tracks near the B.

In the case of opposite-side tagging, we are taking advantage of the fact that b and $\overline{b}$ are produced in pairs. If we determine the flavor of one B hadron, we can infer the

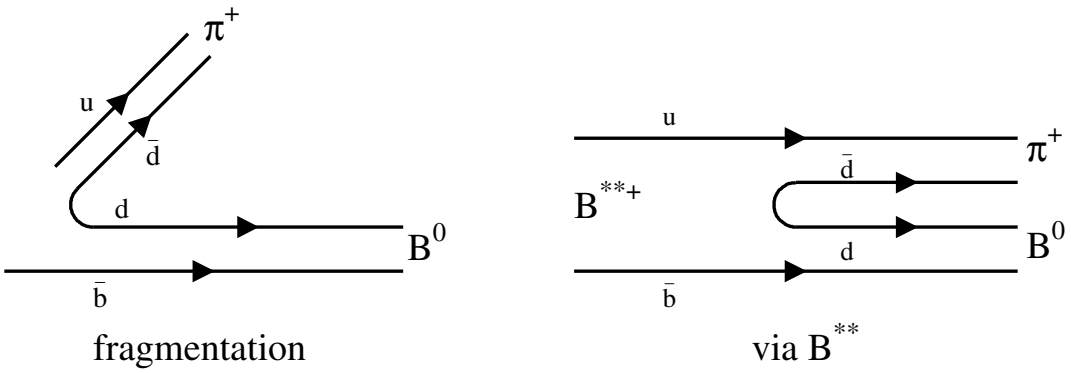

Fig. 16. Same-side flavor tagging. In both cases shown above, a $\overline{b}$ quark is produced and ultimately ends up as a B^0 meson. In the left diagram, the $\overline{b}$ quark has grabbed a d quark from the vacuum. The remaining d quark has paired with a $\overline{u}$ quark to make a π^+. In the right diagram, the $\overline{b}$ quark grabs a u quark to produce a radially-excited B^{**+} state. The B^{**+} then decays to a $B^0\pi^+$. In both cases, the π^+ is associated with a B^0 meson and a π^- would be associated with a $\overline{B^0}$ meson. No information about the other B hadron in the event is required.

flavor of the other B hadron. This is not perfect, of course, because in addition to the complications mentioned above, the opposite-side B hadron may have been a B^0 or B_s^0 and mixed.

Three types of opposite-side tagging are commonly used:

- **lepton tagging:** identify $B \to \ell\nu X$. The lepton carries the charge of the b.
- **kaon tagging:** identify $B \to D \to K$ ($b \to c \to s$). The strange particle carries the charge of the b.
- **jet charge tagging:** identify a "jet" associated with $B \to X$ and perform a momentum weighted charge sum. On average, the net charge of the jet will reflect the charge of the b.

Each of the methods has different experimental requirements and therefore different sets of positive and negative aspects. For example, with lepton tagging, the branching ratio and efficiency are rather low. In addition, there are mistags that come from $b \to c \to \ell$. On the other hand, lepton tags tend to have high dilution (=large $\mathcal{D}$). For jet charge tagging, the dilution is lower (=small $\mathcal{D}$), but we are more likely to find a jet, which means a higher tagging efficiency.

By contrast, same-side tagging makes no requirement on the second B hadron in the event. It instead takes advantage of the effects associated with hadronization. When a $\overline{b}$ quark becomes a B^0 meson, it must pair up with a d quark. Since quark pairs pop-up from the vacuum, there is a $\overline{d}$ quark associated with the d quark. Now if the $\overline{d}$ quark grabs a u quark, then there is a π^+ associated with the B^0. This is shown in Fig. 16. An alternative path to the same correlation is through the production of a B^{**} state. In either case, the correlation is: $B^0\pi^+$ and $\overline{B^0}\pi^-$. In our example above, if the $\overline{d}$ grabs a d quark, then we have a π^0, in which case the first-order correlation is lost.

The same-side technique has the advantage of not relying on the second B hadron in the event. The disadvantage is that, depending upon the hadronization process for a given event, the measured correlation may be absent or may be of the wrong sign. For example, the correlation would not be measurable if the mesons from the fragmentation chain were neutral. If the up quark in Fig. 16 were replaced by a down quark, then the associated meson would be a π^0. Likewise, wrong-sign correlations are present: if the up quark in Fig. 16 were replaced with a strange quark, then a K^{*0} would be produced, with $K^{*0} \to K^-\pi^+$. If the K^- is selected as the tagging track, then the wrong-sign is measured. This type of mistag can be reduced through the use of particle identification to separate charged kaons, pions and protons.

As will be seen below, initial state flavor tagging is a crucial aspect in measuring CP asymmetries in the B system. In the analysis we will discuss here, three of the four initial state tagging methods are used: lepton tagging, jet-charge tagging and same-side tagging.

5.5 CP Violation Via Mixing

For Standard Model CP violation to occur, we need an interference to expose the complex CKM phase. The CP violating phase in V_{td} can manifest itself through the $\Delta B = 2$ box diagrams responsible for $B^0/\overline{B^0}$ mixing. In the Standard Model, the decay mode $B^0/\overline{B^0} \to J/\psi K^0_S$ is expected to exhibit mixing-induced CP violation. This final state can be accessed by both B^0 and $\overline{B^0}$. CP violation in this case would manifest itself as:

$$\frac{dN}{dt}(B^0 \to J/\psi K^0_S) \neq \frac{dN}{dt}(\overline{B^0} \to J/\psi K^0_S), \tag{9}$$

where $J/\psi = |c\overline{c}\rangle$, $K^0_S = \frac{1}{\sqrt{2}}(|d\overline{s}\rangle + |s\overline{d}\rangle)$ and the final state, $J/\psi K^0_S$, is a CP eigenstate:

$$CP|J/\psi K^0_S\rangle = -|J/\psi K^0_S\rangle. \tag{10}$$

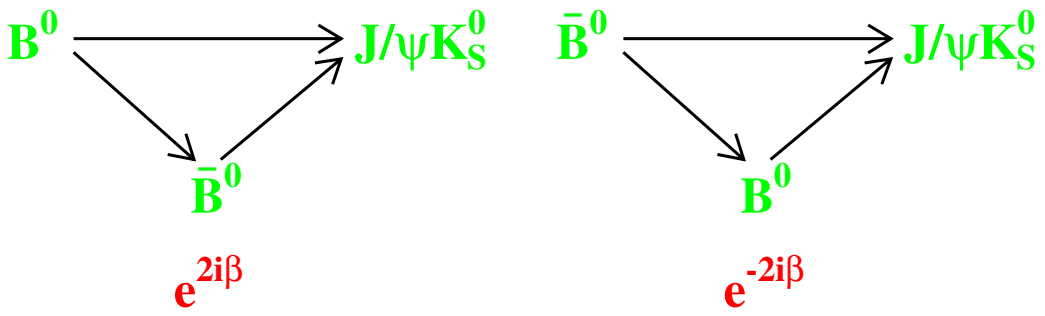

Fig. 17. CP violation via mixing. Since both B^0 and $\overline{B^0}$ can decay to the CP eigenstate $J/\psi K^0_S$, we have an interference between the mixed and unmixed decays. For example, if a meson is produced as a B^0 (shown on the left) and ultimately decays into $J/\psi K^0_S$, it could have decayed as a B^0 or mixed into a $\overline{B^0}$ before decaying. The process shown on the right is for an initial state $\overline{B^0}$. The interference exposes the phase in the CKM matrix element V_{td}, giving rise to CP violation in the Standard Model.

In the CKM framework, CP violation occurs in this mode because the mixed decay and direct decay interfere with one another. This is shown in Fig. 17. An initial state B^0 can decay directly to $J/\psi K^0_S$, or it can mix into a $\overline{B^0}$ and then decay to $J/\psi K^0_S$. The interference between those two paths exposes the complex phase in the CKM matrix element V_{td}.

When we produce a $\overline{B^0}$ at $t = 0$:

$$\frac{dN}{dt}(\overline{B^0} \to J/\psi K^0_s) \propto e^{-t/\tau}(1 + \sin 2\beta \sin \Delta m_d t). \tag{11}$$

If we produce a B^0 at $t = 0$:

$$\frac{dN}{dt}(B^0 \to J/\psi K^0_s) \propto e^{-t/\tau}(1 - \sin 2\beta \sin \Delta m_d t). \tag{12}$$

Forming the asymmetry:

$$\begin{aligned} A_{CP}(t) &= \frac{\frac{dN}{dt}(\overline{B^0} \to J/\psi K^0_S) - \frac{dN}{dt}(B^0 \to J/\psi K^0_S)}{\frac{dN}{dt}(\overline{B^0} \to J/\psi K^0_S) + \frac{dN}{dt}(B^0 \to J/\psi K^0_S)} \\ &= \sin 2\beta \ \sin(\Delta m_d t). \end{aligned} \tag{13}$$

This is the time-dependent equation for the CP asymmetry in this mode. The asymmetry as a function of proper time oscillates with a frequency of Δm_d. The amplitude of the oscillation is $\sin 2\beta$, where β is the angle of the unitarity triangle shown earlier.

We can also perform the time-integral of equation 13:

$$\begin{aligned} A_{CP} &= \frac{\int \frac{dN}{dt}(\overline{B}^0 \to \psi K_S^0)dt - \int \frac{dN}{dt}(B^0 \to \psi K_S^0)dt}{\int \frac{dN}{dt}(\overline{B}^0 \to \psi K_S^0)dt + \int \frac{dN}{dt}(B^0 \to \psi K_S^0)dt} \\ &= \frac{N(\overline{B}^0 \to \psi K_S^0) - N(B^0 \to \psi K_S^0)}{N(\overline{B}^0 \to \psi K_S^0) + N(B^0 \to \psi K_S^0)} \end{aligned} \tag{14}$$

Integrating equations 11 and 12 and substituting them into equation 14, we get:

$$A_{CP} = \frac{\Delta m_d \tau_B}{1 + (\Delta m_d \tau_B)^2} \cdot \sin 2\beta \tag{15}$$

$$A_{CP} \simeq 0.47 \sin 2\beta \tag{16}$$

This shows that we do not need to measure the proper time of the events. Integrating over all lifetimes still yields an asymmetry, although information is lost in going from the time dependent to the time-integrated asymmetry. The above formalism is true when the B^0 and $\overline{B^0}$ are produced in an incoherent state, as they are in high energy hadron collisions. At the $\Upsilon(4s)$, the B^0 and $\overline{B^0}$ are produced in a coherent state and the time-integrated asymmetry vanishes.[22]

5.6 Experimental Issues

The bottom line when it comes to CP violation in the B system is that you need to tell the difference between B^0 mesons and $\overline{B^0}$ mesons at the time of production. After identifying a sample of signal events, flavor tagging is the most important aspect of analyses of CP violation.

In the case of the $J/\psi K_S^0$ final state, we have no way of knowing whether the meson was a B^0 or $\overline{B^0}$ as it decayed, nor do we need to know. The difference we are attempting to measure is the decay rate difference for mesons that were **produced** as B^0 or $\overline{B^0}$. In this case, we are tagging the flavor of the B meson when it was produced.

The analysis we are going to discuss here is a measurement of the CP asymmetry in $B^0/\overline{B^0} \to J/\psi K_S^0$ from the CDF experiment. Before discussing that measurement, we begin by presenting some of the unique aspects to b physics in the hadron collider environment.

5.6.1 B Production and Reconstruction

First of all, the $b\overline{b}$ cross section is enormous, $\mathcal{O}(100\mu b)$, which means at typical operating luminosities, 1000 $b\overline{b}$ pairs are produced every second! The $b\overline{b}$ quarks are produced

by the strong interaction, which preserves "bottomness"; therefore they are always produced in pairs. The transverse momentum (p_T) spectrum for the produced B hadrons is falling very rapidly, which means that most of the B hadrons have very low transverse momentum. For the sample of $B \to J/\psi K^0_S$ decays we are discussing here, the average p_T of the B meson is about $10\,\mathrm{GeV/c}$. The fact that the B hadrons have low transverse momentum does not mean that they have low total momentum. Quite frequently, the B mesons have very large longitudinal momentum (longitudinal being the component along the beam axis.) These B hadrons are boosted along the beam axis and are consequently outside the acceptance of the detector.

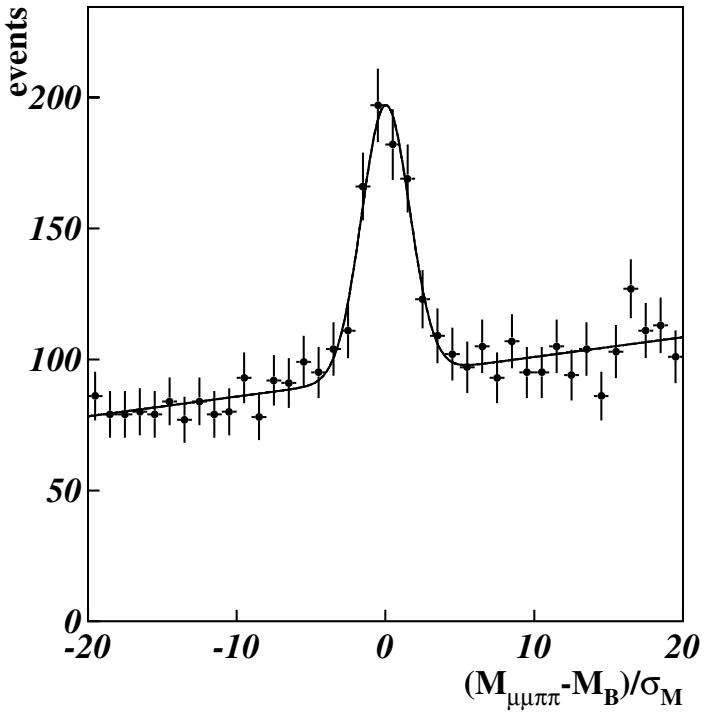

Fig. 18. $B^0/\overline{B^0} \to J/\psi K^0_S$ event yield after the selection criteria discussed in the text have been applied. The data is plotted in units of "normalized mass": $m_{norm} = (M_{fit} - M_B)/\sigma_{fit}$, where M_{fit} and σ_{fit} are the four-track fitted mass and uncertainty, respectively, and M_B is the world average B^0 mass. Signal events show up with M_{norm} near zero, while combinatoric background shows up uniformly across the plot.

For $b\overline{b}$ production, like W production discussed previously, the center of mass of the parton-parton collision is not at rest in the lab frame. Even in the cases where one

B hadron is reconstructed (fully or partially) within the detector, the second B hadron may be outside the detector acceptance.

To identify the B mesons, we must first trigger the detector readout. Even though the $b\bar{b}$ production rate is large, it is about 1000 times below the generic inelastic scattering rate. In the trigger, we attempt to identify leptons: electrons and muons. In this analysis, we look for two muons, indicating that we may have had a $J/\psi \rightarrow \mu^+\mu^-$ decay.*

Once we have the data on tape, we can attempt to fully reconstruct the $B^0/\overline{B^0} \rightarrow J/\psi K^0_S$ final state. The event topology that we are describing here can be seen in Fig. 15. To reconstruct $B \rightarrow J/\psi K^0_S$, we again look for $J/\psi \rightarrow \mu^+\mu^-$, this time with criteria more stringent than those imposed by the trigger. Once we find a dimuon pair with invariant mass consistent with the J/ψ mass, we then look for the decay $K^0_S \rightarrow \pi^+\pi^-$. At this point, we require the dipion mass to be consistent with a K^0_S mass, and we also take advantage of the fact that the K^0_S lives a macroscopic distance in the lab frame. Once we have both a J/ψ and K^0_S candidate, we put them all together to see if they were consistent with the decay $B^0/\overline{B^0} \rightarrow J/\psi K^0_S$. For example, the momentum of the K^0_S must point back to the B decay vertex, and the B must point back to the primary (collision) vertex. After all of these selection criteria, we have a sample of 400 signal events with a signal to noise of about 0.7-to-1, as shown in Fig. 18.

5.6.2 Flavor Tagging and Asymmetry Measurement

Now that we have a sample of signal events (intermixed with background), we must attempt to identify the flavor of the B^0 or $\overline{B^0}$ at the time of production using the flavor tagging techniques outlined above. For this analysis, we use three techniques: same-side tagging, lepton tagging and jet charge tagging. The lepton and jet charge flavor tags are looking at information from the other B hadron in the event to infer the flavor of the B we reconstructed. Table 5 summarizes the flavor tagging efficiency and dilution for each of the algorithms.

With the sample of events, the proper decay time and the measured flavor for each

*It is difficult to trigger on the decay $J/\psi \rightarrow e^+e^-$ at a hadron collider. The distinct aspect of electrons is their energy deposition profile in the calorimeter. For low p_T electrons from J/ψ decays ($p_T < 10\,\mathrm{GeV/c}$), there is sufficient overlap from other particles to cause high trigger rates and low signal-to-noise.

Table 5. Summary of tagging algorithms performance. All numbers listed are in percent. The efficiencies are obtained from the $B \to J/\psi K^0_S$ sample. The dilution information is derived from the $B^\pm \to J/\psi K^\pm$ sample.

tag side	tag type	efficiency (ϵ)	dilution ($\mathcal{D}$)	$\epsilon\mathcal{D}^2$
same-side	same-side	73.6 ± 3.8	16.9 ± 2.2	2.1 ± 0.5
opposite-side	soft lepton	5.6 ± 1.8	62.5 ± 14.6	2.2 ± 1.0
	jet charge	40.2 ± 3.9	23.5 ± 6.9	2.2 ± 1.3

event, we are ready to proceed. In practice, we are measuring $\mathcal{A}(t)$:

$$\mathcal{A}(t) = \frac{1}{\mathcal{D}}\left(\frac{N_- - N_+}{N_- + N_+}\right) = \frac{1}{\mathcal{D}} A_{raw}(t), \tag{17}$$

where $N_-(N_+)$ are the number of negative (positive) tags. A negative tag indicates a $\overline{B^0}$, while a positive tag indicates a B^0. We do not write $\overline{B^0}$ and B^0 in the equation, though, because not every negative tag is truly a $\overline{B^0}$.

We arrive at the quantity $\mathcal{A}_{raw}$ using the $J/\psi K^0_S$ data, but to get to the measured asymmetry, we must also know $\mathcal{D}$. We can measure $\mathcal{D}$ using control samples and Monte Carlo, but it can not be extracted from the $J/\psi K^0_S$ data. Since typical dilutions are about 20%, that means that the raw asymmetry is 1/5 the size of the measured asymmetry. The higher the dilution (the more effective the flavor tagging method) the closer the raw asymmetry is to the measured asymmetry. We can classify the statistical uncertainty on the asymmetry as:

$$(\delta\mathcal{A})^2 = (\delta\mathcal{A}_{raw}/\mathcal{D})^2 + (\mathcal{A}_{raw}/\mathcal{D})^2(\delta\mathcal{D}/\mathcal{D})^2, \tag{18}$$

where $\delta\mathcal{D}$ is the uncertainty on the dilution and $\delta\mathcal{A}_{raw}$ is the statistical uncertainty on the raw asymmetry. Ignoring (for the moment) the presence of background in our sample, $(\delta\mathcal{A}_{raw})_{stat} = 1/\sqrt{N_{tagged}} = 1/\sqrt{\epsilon N_{sig}}$, where ϵ is the flavor tagging efficiency discussed previously and N_{sig} is the number of signal events. More realistically, we cannot neglect the presence of background, and the statistical uncertainty on the measured asymmetry is: $(\delta\mathcal{A}_{raw})_{stat} = \frac{1}{\sqrt{\epsilon N_{sig}}}\sqrt{\frac{N_{sig}+B}{N_{sig}}}$. The first term in Equation 18 is the "statistical" uncertainty on the asymmetry and is of the form: $\delta\mathcal{A} = 1/\sqrt{\epsilon\mathcal{D}^2 N_{sig}}$. Not only does the dilution factor degrade the raw asymmetry, it also inflates the statistical error. Think of it this way: we have events that we are putting into two bins — a B^0 bin and a $\overline{B^0}$ bin. When we tag an event incorrectly (mistag), we take it out of one

bin and put it into the other bin. Not only do we have one less event in the correct bin, we have one more event in the incorrect bin! This hurts our measurement more than had we simply removed the event from the correct bin and thrown it away.

In reality, there are several complications to this measurement:

- Our data sample has both signal and background events in it. For an event in the signal region, we don't know *a priori* if it is signal or background.
- We are using multiple flavor tagging algorithms. Each algorithm has a different $\mathcal{D}$ associated with it. Some events are tagged by more than one algorithm, and those two tags may agree or disagree.
- Due to experimental acceptance, not every event in our sample has a precisely determined proper decay time.
- Due to experimental acceptance, the efficiencies for positive and negative tracks are not identical (although the correction factor is tiny).

We handle these effects with a maximum likelihood fit that accounts for the probability that any given event is signal versus background and tagged correctly versus incorrectly. In doing so, we not only account for the multiple flavor tagging algorithms and the background in our data, but the correlations between all of these elements is handled as well.[23]

5.6.3 Results

The final result of our analysis is show in Fig. 19. The points are the $J/\psi K^0_S$ data, after having subtracted out the contribution from the background. The data has also been corrected for the flavor tagging dilutions. The solid curve is the fit to the data of the functional form: $\mathcal{A}_{CP} = \sin 2\beta \sin \Delta m_d t$, with Δm_d constrained to the world average value. The amplitude of the oscillation is $\sin 2\beta$. The single point to the right shows all events that do not have a precisely measured lifetime. As shown earlier, the time-integrated asymmetry is nonzero, therefore these events are quite useful in extracting $\sin 2\beta$.

The result of this analysis is:

$$\sin 2\beta = 0.79 \, ^{+0.41}_{-0.44} \, (\text{stat.} + \text{syst.}).$$

This is consistent with the expectation of $\sin 2\beta = 0.75$ based upon indirect fits to other data. This result rules out $\sin 2\beta = 0$ at the 93% confidence level, not sufficient to claim

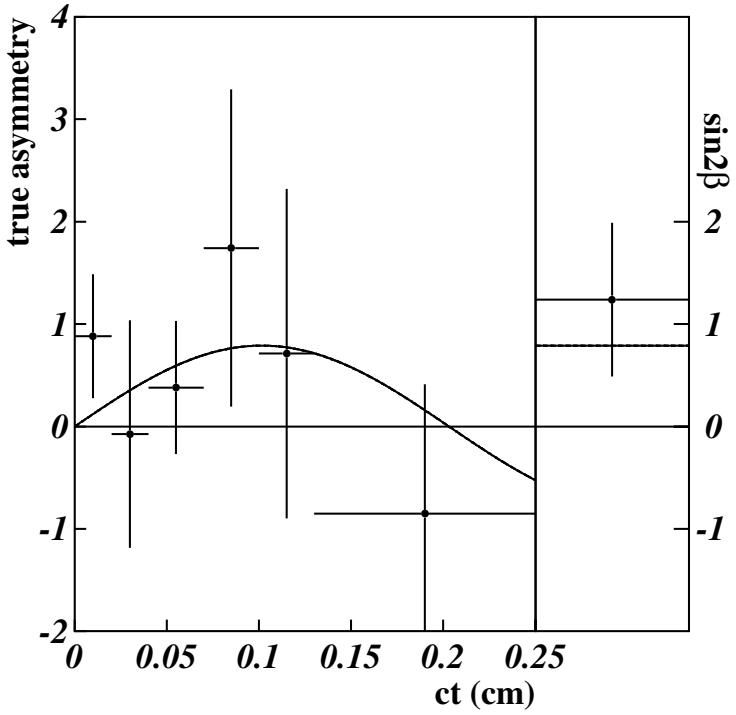

Fig. 19. The true asymmetry ($\mathcal{A}_C P(t) = \sin 2\beta \sin \Delta m_d t$) as a function of lifetime for $B \to J/\psi K^0_S$ events. The data points are sideband-subtracted and have been combined according to the effective dilution for single and double-tags. The events shown in the rightmost point are those that do not have precision lifetime information.

observation of CP violation in the B system. On the other hand, this is the best direct evidence to date for CP violation in the B system. When broken down into statistical and systematic components, the uncertainty is $\delta(\sin 2\beta) = \pm 0.39(\mathrm{stat.}) \pm 0.16(\mathrm{syst.})$. The total uncertainty is dominated by the statistics of the sample and efficacy of the flavor tagging. The systematic uncertainty arises from the uncertainty in the dilution measurements ($\delta\mathcal{D}$.) However, the uncertainties on the dilution measurements are actually limited by the size of the data samples used to measure the dilutions. In other words, the **systematic** uncertainty on $\sin 2\beta$ is really a **statistical** uncertainty on the $\mathcal{D}$'s. As more data is accumulated in the future, both the statistical and systematic uncertainty in $\sin 2\beta$ will decrease as $1/\sqrt{N}$.

Figure 20 shows the contours which result from global fits to measured data in the B and K system.[24,25] The dashed lines originating at (1,0) are the two solutions for

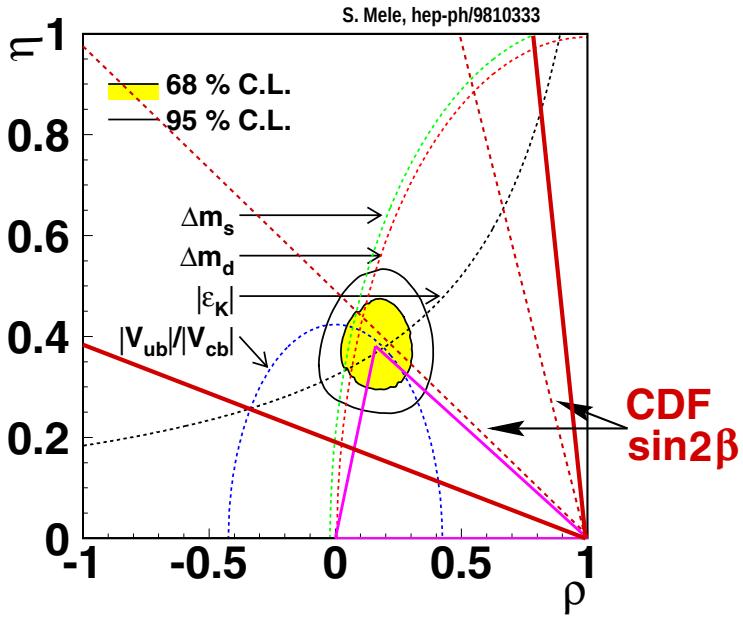

Fig. 20. The experimental determination of ρ and η. The curves are based upon experimental measurements of V_{ub}, ϵ_K, B_d^0 and B_s^0 mixing. The contours are the result of the global fit to the data.[25] The dashed lines originating at (1,0) are the two solutions for β corresponding to $\sin 2\beta = 0.79$. The solid lines are the 1σ contours for this result.

β corresponding to $\sin 2\beta = 0.79$. The solid lines are the 1σ contours for this result. Clearly the result shown here is in good agreement with expectations.

The uncertainty on the $\sin 2\beta$ result presented here is comparable to the uncertainties from recent measurements by the Belle and Babar collaborations.[22,26] While none of the measurements have the precision yet to stringently test the Standard Model, the fact that this measurement can be made in two very different ways is interesting. The hadron collider environment has an enormous $b\overline{b}$ cross section, but backgrounds make flavor tagging difficult. In the e^+e^- environment, the production cross section is much smaller, but the environment lends itself more favorably to flavor tagging. These facts make the measurements performed in the different environments complementary to one another.

5.7 The Future

The Fermilab Tevatron is scheduled to run again in 2001. Both CDF[14] and DØ[13] detectors are undergoing massive upgrades in order to handle more than a factor of 20 increase in data. In addition, e^+e^- B-factories at Cornell (CLEO-III),[27] KEK (Belle)[28] and SLAC (BaBar)[29] are all currently taking data. Finally, HERA-B,[30] a dedicated B experiment at DESY, also will begin taking data in 2001.

On the timescale of 2003-2004, there could be as many as 5 different measurements of $\sin 2\beta$, all of them with an uncertainty of $\delta(\sin 2\beta) \lesssim 0.1$. Putting these together would yield a world average measurement with an uncertainty of $\delta(\sin 2\beta) \lesssim 0.05$. Although this alone will provide an impressive constraint upon the unitarity triangle, it will not be sufficient to thoroughly test the Standard Model for self-consistency. On the same timescale, improvements are required in the lengths of the sides of the triangle, as well as other measurements of the angles. Finally, there are measurements of other quantities that are not easily related to the unitarity triangle that are important tests of the Standard Model.

The following is a list of some of the measurements that will be undertaken and/or improved-upon in the coming years (*this is an incomplete list*):

- CP asymmetries in other modes: *e.g.*
  - $B^0/\overline{B^0} \to \pi^+\pi^-$;
  - $B_s^0/\overline{B_s^0} \to J/\psi\,\phi$;
  - $B_s^0/\overline{B_s^0} \to K^+K^-$;
  - $B_s^0/\overline{B_s^0} \to D_s^\pm K^\mp$;
  - $B^0/\overline{B^0} \to D^+D^-$.
- $B_s^0/\overline{B_s^0}$ mixing.
- rare B decays: *e.g.* $B^\pm \to \mu^+\mu^- K^\pm$; $B^0 \to \mu^+\mu^-$.
- radiative B decays: *e.g.* $B^0 \to K^*\gamma$; $B_s^0 \to \phi\gamma$.
- improved measurements of V_{ub}: *e.g.* $B \to \pi\pi$; $B \to \rho\ell\nu$.
- mass and lifetime of the B_c meson.
- mass and lifetimes of the B baryons: *e.g.* $\Lambda_b = |udb\rangle$.

It will take many years and a body of measurements to gain further insights into the mechanisms behind the CKM matrix and CP violation.

Advances in kaon physics over the last 40 years and advances in B physics in the last 25 years have put us on track to carry out these measurements in the very near future. These measurements will hopefully bring us to a more fundamental understanding to the mechanism behind CP violation.

Acknowledgments

I would like to thank David Burke, Lance Dixon, Charles Prescott and the organizers of the 2000 SLAC Summer Institute. I would also like to thank and acknowledge the collaborators of the CDF and DØ experiments, as well as the Fermilab accelerator division. This work is supported by the U.S. Department of Energy Grant Number DE-FG02-91ER40677.

References

[1] http://www-bd.fnal.gov/runII/index.html

[2] The CDF Collaboration (F. Abe *et al.*), Nucl. Instr. & Meth **A271**, 387 (1988); http://www-cdf.fnal.gov/

[3] The DØ Collaboration (S. Abachi *et al.*), Nucl. Instr. & Meth **A338**, 185 (1994); http://www-d0.fnal.gov/

[4] D. Cronin-Hennessy, A. Beretvas and P. Derwent, Nucl. Instr. & Meth **A443**, 37 (2000);

[5] The CDF Collaboration (T. Affolder *et al.*), Phys. Rev. Lett. **84**, 845 (2000); the CDF Collaboration (F. Abe *et al.*), Phys. Rev. **D59**, 052002 (1999).

[6] The DØ Collaboration (B. Abbott *et al.*), Phys. Rev. **D60**, 052003 (1999).

[7] The DØ Collaboration (B. Abbott *et al.*), Phys. Rev. **D61**, 072001 (2000).

[8] The CDF Collaboration (F. Abe *et al.*), Phys. Rev. **D52**, 2624 (1995).

[9] E. Berger, F. Halzen, C.S. Kim and S. Willenbrock, Phys. Rev. **D40**, 83 (1989).

[10] The DØ Collaboration (B. Abbott *et al.*), Phys. Rev. **D58**, 092003 (1998); the DØ Collaboration (B. Abbott *et al.*), Phys. Rev. **D62**, 092006 (2000).

[11] The CDF Collaboration (T. Affolder *et al.*), FERMILAB-PUB-00-158-E (2000), submitted to Phys. Rev. **D** [hep-ex/0007044].

[12] The LEP Electroweak Working Group, http://lepewwg.web.cern.ch/LEPEWWG/

[13] The DØ Collaboration, FERMILAB-Pub-96/357-E (1996).

[14] The CDF-II Collaboration, FERMILAB-Pub-96/390-E (1996); the CDF-II Collaboration Fermilab-Proposal-909 (1998).

[15] J.H. Christenson *et al.*, Phys. Rev. Lett. **13**, 138 (1964).

[16] N. Cabibbo, Phys. Rev. Lett. **10**, 531 (1963); M. Kobayashi and T. Maskawa, Prog. Theor. Phys. **49**, 652 (1973).

[17] A.B. Carter and A.I. Sanda, Phys. Rev. Lett. **45**, 952 (1980); Phys. Rev. D **23**, 1567 (1981); I.I. Bigi and A.I. Sanda, Nucl. Phys. **B193**, 85 (1981); Nucl. Phys. **B281**, 41 (1987).

[18] L. Wolfenstein, Phys. Rev. Lett. **51**, 1945 (1983).

[19] L.-L. Chau and W.-Y. Keung, Phys. Rev. Lett. **53**, 1802 (1984); C. Jarlskog and R. Stora, Phys. Lett. B **208**, 268 (1988); J.D. Bjorken, Phys. Rev. D **39**, 1396 (1989).

[20] Y. Nir, lectures at SSI 99, IASSNS-HEP-99-96 (1999), hep-ph/9911321.

[21] Particle Data Group (C. Caso *et al.*), Eur. Phys. J. C **3**, 1 (1998); LEP B Oscillations Working Group, http://lepbosc.web.cern.ch/LEPBOSC/

[22] C. Hearty, these proceedings.

[23] CDF Collaboration (T. Affolder *et al.*), Phys. Rev. D **61**:072005 (2000).

[24] S. Herrlich and U. Nierste, Phys. Rev. D **52**, 6505 (1995); A. Ali and D. London, Nucl. Phys. B (Proc. Suppl.) **54A**, 297 (1997); P. Paganini *et al.*, Phys. Scr. **58**, 556 (1998).

[25] S. Mele, Phys. Rev. D **59**, 113011 (1999).

[26] N. Katayama, these proceedings.

[27] CLEO-III Collaboration, CLNS 94/1277 (1994).

[28] BELLE Collaboration, KEK Report 95-1 (1995).

[29] BaBar Collaboration, SLAC-Report-95-457 (1995).

[30] HERA-B Collaboration, DESY-PRC 95/01 (1995).

THE DONUT EXPERIMENT: FIRST DIRECT EVIDENCE OF ν_τ

Regina Rameika
Fermi National Accelerator Laboratory
Batavia, IL 60510

Representing the DONUT Collaboration*

ABSTRACT

The DONUT experiment was designed to directly observe the charged-current interactions of the tau-neutrino. An 800 GeV proton beam from the Fermilab Tevatron is used to create a prompt neutrino beam, predicted to have a 5% tau neutrino component. Tau neutrino interactions are identified by observing the τ lepton produced in the charged current interaction $\nu_\tau + N \rightarrow \tau + X$. The experiment locates and identifies τ lepton decays using an emulsion target and spectrometer. An overview of the experiment and analysis methods is presented. The results from an analysis of 203 neutrino interactions are also presented. A decay search on these events has found evidence of four tau neutrino interactions with an estimated background of 0.42 events. This number is consistent with the Standard Model expectation.

*DONUT is an acronym standing for Direct Observation of Nu Tau. The DONUT Collaboration is composed of 56 physicists from 13 institutions in the U.S., Japan, Korea and Greece.

1 Introduction

The discovery of the τ lepton in 1975[1] led to the assumption that the ν_τ exists as the Standard Model third generation neutrino. Since then there has been compelling evidence that it participates normally in electroweak interactions.[2,3] Recent results from the Super-K experiment postulate that the observed deficit of ν_μ atmospheric neutrinos is explained by the oscillation of $\nu_\mu \rightarrow \nu_\tau$.[4] However, its interactions with matter have not been directly observed in the same manner as the interactions of ν_e or ν_μ.[5,6]

Observation of a ν_τ interaction is made by observing the τ lepton produced in the charged current interaction $\nu_\tau + N \rightarrow \tau + X$, and the subsequent decay of the τ in an active target. The τ lepton has a $c\tau$ of 0.087 cm and therefore will decay within a distance of $\sim$ 5mm. Eighty-six per cent of the τ decays have only one charged track (a "kink" decay). This implies that a very high spatial resolution on tracks near the vertex is required.

In the early 1980's two proposals to produce and observe ν_τ interactions were approved to run at the Fermilab Tevatron.[7,8] The proposals were expensive and concerns about event yields and detector resolution led to the cancellation of the experiments before they were constructed. Ten years later, as a first step in the development of the Fermilab neutrino oscillation program, the DONUT experiment was proposed and approved.[9]

Nuclear emulsion was chosen as the neutrino interaction target since it provides the very high spatial resolution necessary to resolve τ decays, as well as sufficient mass to produce a reasonable event rate. The ν_τ interaction candidates are recognized by the topology of the tracks associated with the neutrino interaction vertex. The primary characteristics of the decay which can be measured with an emulsion target are the direction of the τ with respect to the incoming neutrino, the decay length of the τ, the angle(s) between the tau and its daughter(s), and the momentum of the daughter(s).

2 The Experimental Setup

2.1 Prompt Neutrino Beam

The primary source of the ν_τ is the leptonic decay of the D_S meson into a τ and $\bar{\nu}_\tau$. The τ subsequently decays yielding another ν_τ. The charmed mesons are produced in the interactions of 800 GeV protons from the Fermilab Tevatron in a tungsten beam dump.

Production of ν_τ from other sources such as charged D decays, secondary interactions of the D_S in the dump, and B meson to τ decay contributes an additional 14% to the total ν_τ flux. The proton intensity was typically 8×10^{12} protons per 20 second spill. The unwanted products of the high energy proton interactions were reduced to tolerable levels by shielding the emulsion with active magnetic shields and passive iron shielding. The large flux of muons that is created in the dump is swept to either side of the emulsion targets by the magnets and the rate of muons in the target area was measured to be 2×10^4 per spill.

Eighty five per cent of all the neutrinos at the emulsion targets originate in the leptonic or semi-leptonic decays of charmed mesons. Thus, the beam consists of approximately equal numbers of ν_μ and ν_e as well as an equal number of ν and $\bar{\nu}$. Neutrinos from π decays are calculated to account for $\sim$23% of the total number of observed interactions. The mean energy of the neutrinos (uninteracted) is estimated to be 54 GeV for ν_e and ν_μ and 56 GeV for ν_τ. The interaction rate of ν_τ relative to the total interaction rate is calculated to be $5 \pm 1\%$. The largest uncertainty in this number originates in an uncertainty of $\pm$20% in the D_S production rate and $\pm$15% in f_{D_S}, which controls the branching ratio of $D_S \to \tau\bar{\nu}_\tau$

2.2 Hybrid Emulsion Spectrometer

Emulsion is an "active" target since it records all the tracks that are produced at the interaction vertex. However, it is passive in the sense that it has no electronic output indicating when an interaction has occurred. It simply integrates all tracks that are produced in it or pass through it during the time in which it is exposed to the beam. In order to untangle interesting interactions from the background, an electronic spectrometer is used to trigger a data acquisition system which records the signals from the particles that emerge from the emulsion targets. The electronic spectrometer in conjunction with the emulsion target is called a hybrid emulsion spectrometer (HES). This technique for detecting rare, short lived particles has been used in a number of previous experiments.[2,10,11]

2.2.1 Electronic Spectrometer

A conventional spectrometer provides the event trigger, tracking to locate the primary vertex, momentum measurement and lepton identification. It consists of a charged particle veto wall, trigger counters, 44 planes of 0.5mm diameter scintillating fiber

tracker (SFT), 38 drift chamber planes, an analysis magnet, a lead glass electromagnetic calorimeter and a muon tagging system.

The spectrometer readout was initiated by a fast trigger formed from signals from three planes of scintillator hodoscopes placed in the target region. The trigger logic required that more than one charged track passed through the target region, and no signal from the upstream veto wall. Muons were identified with an array of proportional tubes between 3 walls of iron (from upstream) 0.6 m, 1m, and 1m thick. Electrons were tagged either by a lead glass calorimeter, shower development in the SF, or pair production in the emulsion.

Tracks in the scintillating fibers were linked to those in drift chambers upstream and downstream of the 1.85 m $\times$ 1.45 m aperture magnet with a strength of 0.76 T-m. The detector tracking accuracy increased from downstream to upstream. The drift chambers had a resolution of $\sim$300μm, whereas the resolution of the scintillating fibers was $\sim$100μm. The reconstructed tracks were used to predict the location of an interaction in the emulsion targets to $\sim$1mm accuracy.

A plan view of the experimental apparatus is shown in figure 1.

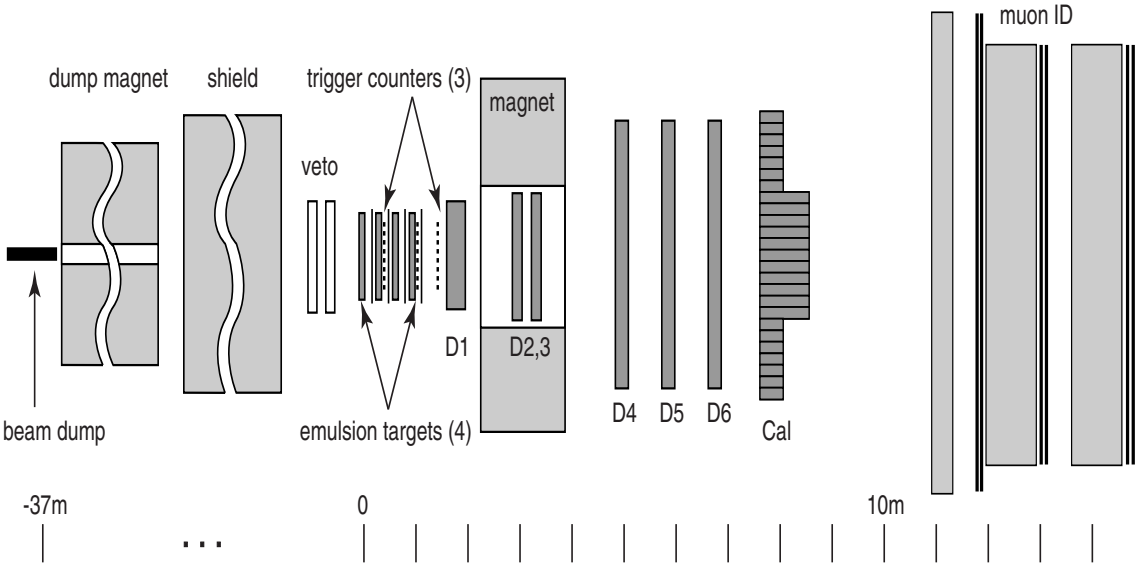

Fig. 1. Experimental beam and spectrometer. At the left, 800 GeV protons were incident on the beam dump, which was 36.5m from the first emulsion target. Muon identification was done by range in the system at the right (downstream).

2.2.2 Emulsion Targets

The target station, located 36 m from the dump, was composed of four emulsion modules placed one behind the other on a precision stand. Each module was made from emulsion sheets, 50 cm$\times$50 cm in area, oriented perpendicular to the ν beam. The emulsion modules and arrangement of SFT planes is illustrated in figure 2.

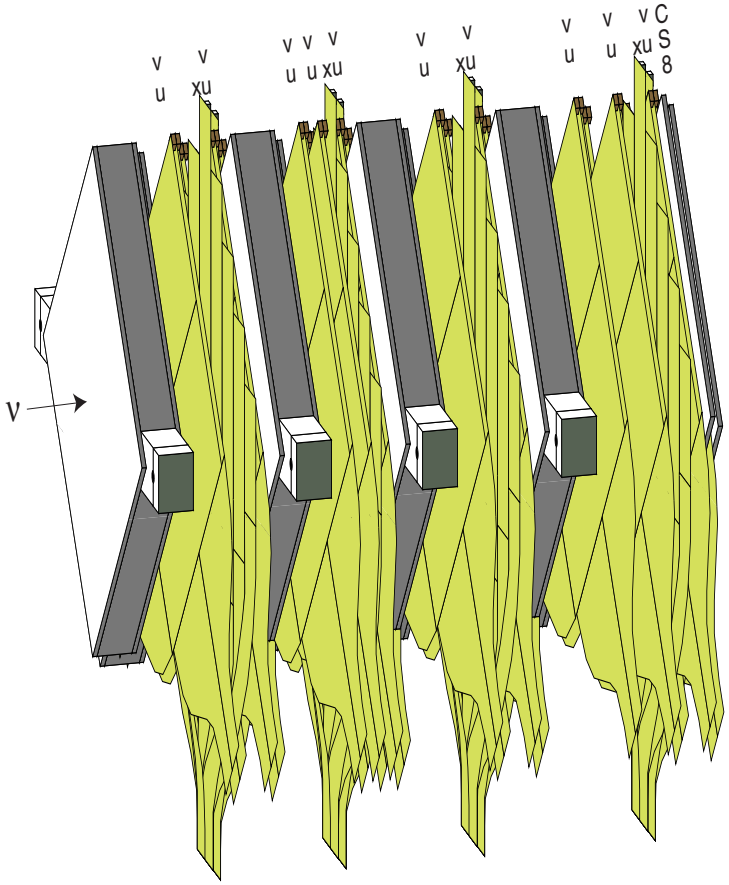

Fig. 2. Emulsion target and scintillating fiber tracker configuration. The fiber planes are arranged in three views, (u,v,x). The six image intensifiers and readout CCD cameras are not shown.

The emulsion used for the DONUT experiment was Fuji ET7C. A typical grain size in this emulsion was $0.07\pm0.02\mu$m. A minimum ionizing track would then form 29 ± 2 grains per 100μm. Thus, the information capacity of an emulsion detector is staggering. After exposure the DONUT emulsion modules literally held terabytes of data!

Three types of emulsion modules were used as neutrino targets. The first type of

emulsion target (called *bulk*) was constructed from 88 sheets with 330μm thick emulsion layers on both sides of a 90 μm thick plastic base. The nuclear emulsion comprised 96% of the total mass (50kg) and had a thickness of 2 radiation lengths and 0.17 interaction lengths. The second type (called *ECC*) had 48 alternating sheets of 1mm thick stainless steel and emulsion. The emulsion sheets had 100 μm emulsion layers on each side of a 200 μm thick plastic base. The mass of the emulsion in the *ECC* target was just 8% of the total (97 kg), so that the neutrino interactions most likely occured in the steel plates. This type of target was 3.0 radiation lengths and 0.29 interaction lengths. The third type (*ECC/bulk*) was a hybrid target, where the downstream part was 50 sheets of bulk-type, and upstream part was a variation of the *ECC* design, such that the thickness of the plastic base was increased to 800 μm. The mass of the emulsion for the *ECC/bulk* target was 44% of the total (67 kg). Each *ECC/bulk* target had a thickness of 2.5 radiation lengths and 0.24 interaction lengths. A schematic drawing of an *ECC* and a *Bulk* sheet are shown in figure 3.

In the course of the experiment a total of seven targets were exposed: five were *ECC/bulk*, two were *ECC*, and one *bulk*.

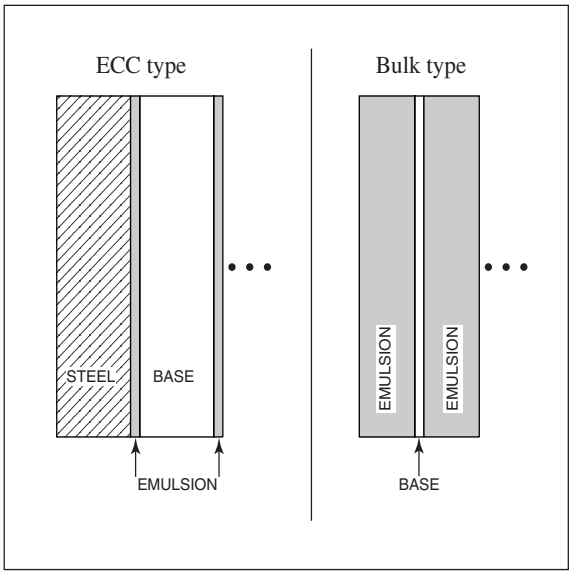

Fig. 3. Two configurations of emulsion sheets used in constructing the target modules

3 The Data Set

Data was taken between April 1997 and September 1997. During that time the emulsion modules were exposed to a total of 4.6×10^{17} protons on target. A total of 6.6×10^{6} triggers were recorded. After live-time correction the effective proton intensity was 3.54×10^{17}. For this number of protons on target the expected number of neutrino interactions of all types is $\sim$1100$\pm$300.

A trigger was selected as an interaction candidate by requiring that a vertex position predicted from SFT tracks be within an emulsion target. In addition, the event trigger timing between two counters was required to be within 10ns, and show no evidence of nearby showering from muon interactions. Remaining events with a visible energy more than 2 GeV and a vertex in the emulsion volume were classified as neutrino interaction candidates. The number of interaction vertices predicted with the spectrometer is 901, and after all fiducial cuts are made this is reduced to 699 events. In 451 of the 699, the primary vertex location was attempted and 264 were found. As of the Spring 2000, 203 events were selected for a complete systematic decay search for tau kinks. The selection of the data set is summarized in Table 1.

Selection	Number of Events
Triggers	6.6 $\times 10^{6}$
Predicted vertices from spectrometer	901
Vertices in fiducial volume	699
Digited emulsion data taken	511
Vertex location attempted	451
Vertex located	264
Sytematic decay search	203

Table 1. The Data Set (Spring/Summer 2000)

The distribution of vertices as a function of z is shown in figure 4. The distribution across the face of the targets is shown in figure 5. A typical ν_μ charged current event is shown in figure 6 and a typical ν_e charged current interaction is shown in figure 7.

In the set of 203 events, there are 71 events with an identified muon from the primary vertex. After correcting for the acceptance and the efficiency of the muon detectors, the number of ν_μ charged current interactions is 86 ± 12. The measured energy distribution in the calorimeter is used to separate the ν_e charged current events from ν_μ

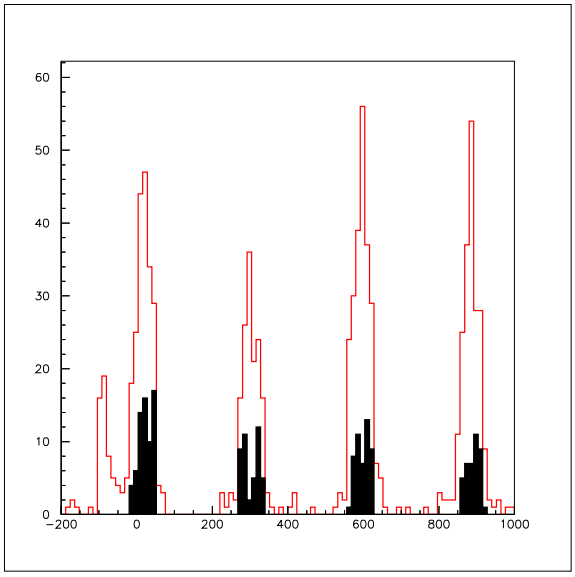

Fig. 4. Distribution of predicted (line) and located vertices (fill). The spike upstream of the first module is produced by neutrino interactions occurring in the upstream veto wall and a lead sheet surrounding the emulsion targets.

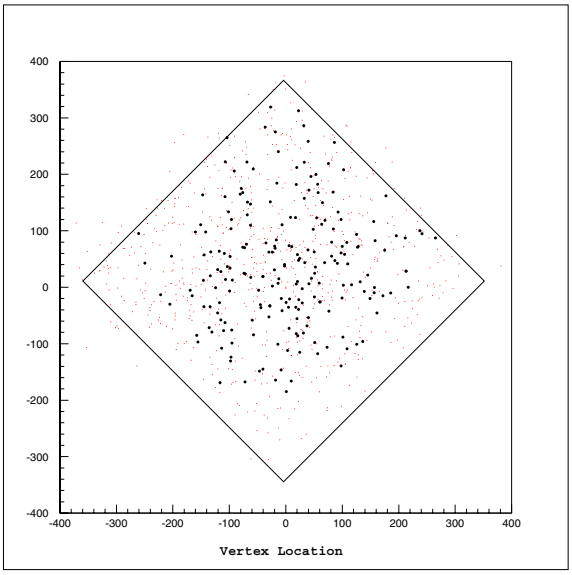

Fig. 5. Distribution of predicted (light) and located vertices (dark).

and neutral current interactions containing electrons. The result obtained is 61 ± 14 ν_e charged current interactions. From the ν_μ charged current event spectrum, an estimated 23% of the total number of interactions were ν_μ interactions from π and K decays in the dump, rather than from charm decays. Since the ν_τ rate is predicted to be $\sim$5% of the total number of interactions, 10 ± 3 ν_τ interactions (before kink finding efficiency) are expected in the "203" data set.

4 Emulsion Analysis

Following the DONUT data-taking phase the emulsion sheets were shipped back to Japan for development and analysis. The use of automated scanning stations, pioneered at Nagoya University, has brought emulsion analysis into the digital era. The data recorded in the emulsion is extracted and summarized on standard mass storage media with speeds and efficiency that exceed human scanners by three orders of magnitude.[13] Nevertheless, it took more than 18 months to process calibrate all of the sheets. This processing was done in parallel with the trigger selection from the electronic data, which was done in the U.S. Scanning of the emulsion is done for three different phases of the analysis, event location, decay search and momentum measurement.

4.1 Event Location

Prior to this experiment, the standard technique for locating a vertex in the emulsion was to reconstruct a high momentum track in the electronic spectrometer and follow this track into the emulsion modules until it ends, presumably at the interaction vertex from which it originated. This method, called "Scan Back", also used in the CHORUS experiment,[11] is appropriate for less than 50% of the data in DONUT. Because the DONUT emulsion targets are very thick ($\sim$6cm), this method of following tracks from the spectrometer is less reliable for vertices in the upstream part of the target.

A new method of event location, called the "Net Scan" technique[14] was developed for this experiment. A "location" scan volume of 5mm$\times$5mm$\times$20mm is defined around the vertex position which has been predicted by the tracks reconstructed in the fiber tracker. All track segments in each emulsion layer are reconstructed using a dedicated automatic emulsion read-out system. Track segment positions and angles are measured by locating emulsion grains in 16 depths in the top 100μm of emulsion. Space tracks in the entire scan volume are reconstructed by linking segments in each layer. A typical

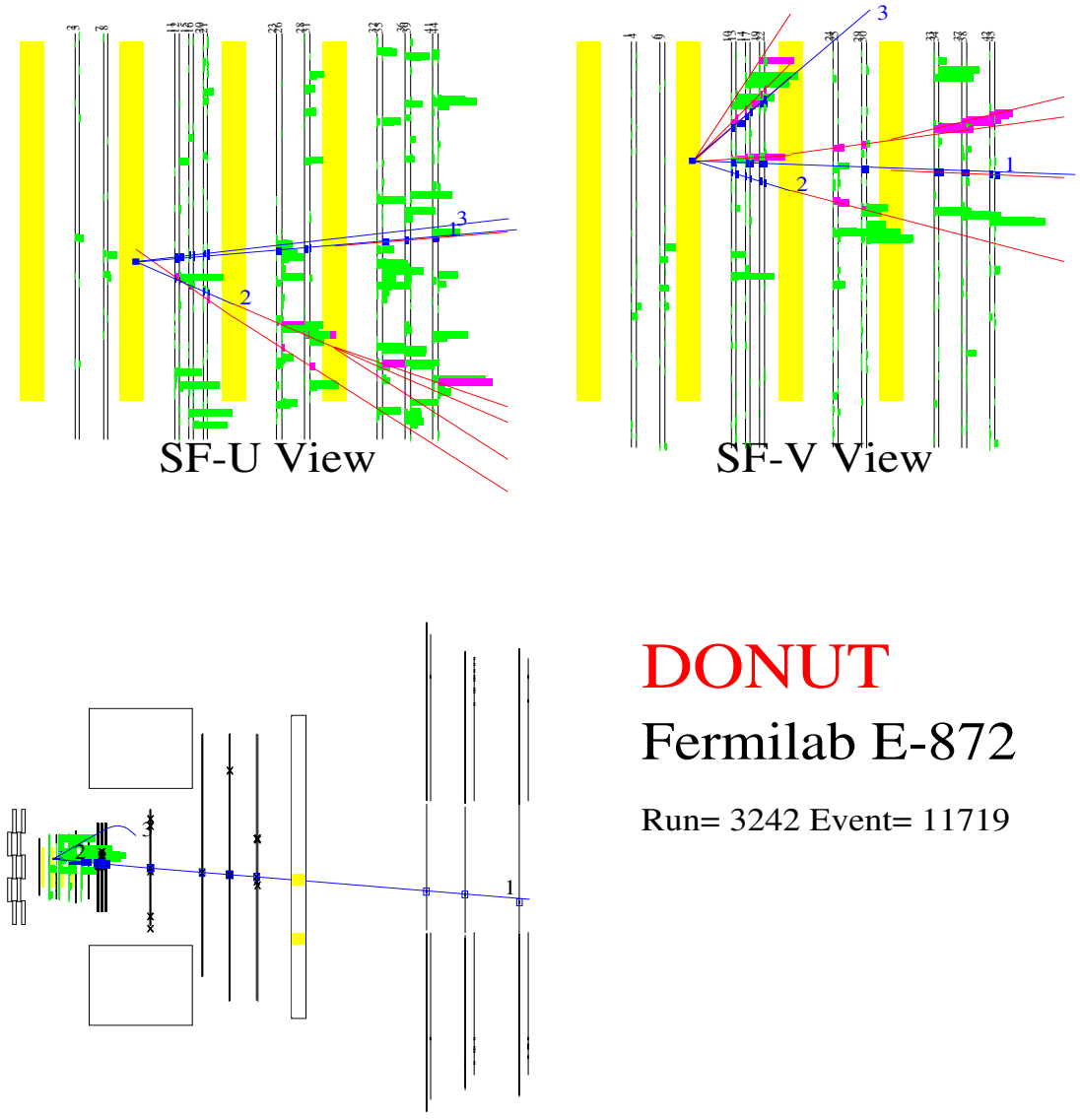

Fig. 6. A typical ν_μ charged current interaction.

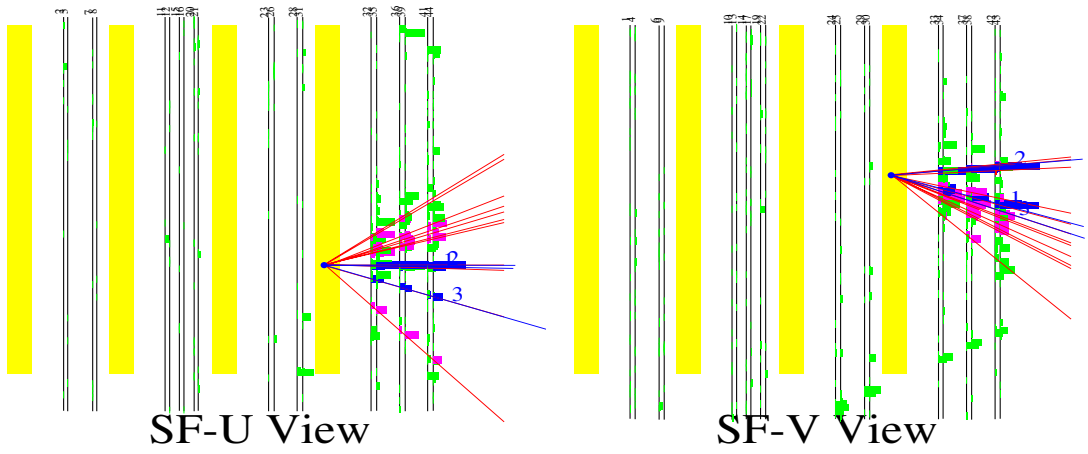

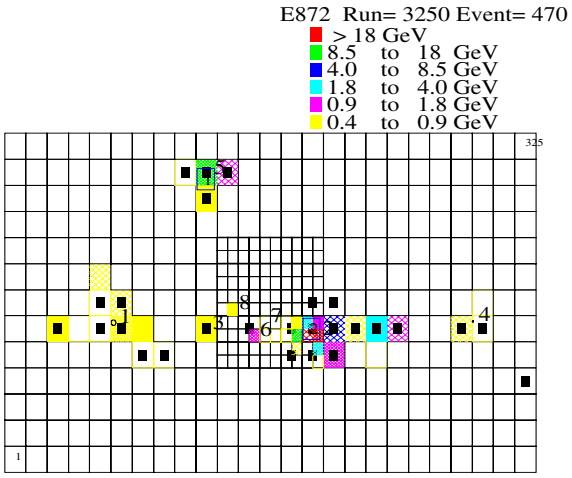

DONUT

Fermilab E-872

Run= 3250 Event= 470

Fig. 7. A typical ν_e charged current interaction.

scan volume will contain $\sim 10^5$ tracks. This number is easily reduced by removing all one and two segment "tracks" and all tracks which traverse the entire scan volume. The number of remaining tracks is $\sim 10^3$. Candidate interaction vertices have 3 or more space tracks that start in the same layer or in an adjacent layer and have an impact parameter less than 10μm. True interaction vertices are confirmed by matching emulsion tracks to the SFT.

This powerful method of vertex location is only possible because of the speed of the present generation of scanning stations. Nevertheless, until March 1999 it required more than 10 hours to process one event in this way. Today at Nagoya University the next generation of scanning machines are now on-line and have proven speed increases if 8 to 10 over the previous generation.

4.2 Decay Search

Emulsion plates for located events are rescanned by the automated optical system with a scan volume defined by a transverse area of 2.6mm$\times$2.6mm centered on the located vertex with a longitudinal dimension of 20 emulsion planes downstream and 2 planes upstream of the vertex. Tracks in the volume were aligned in both position and angle by using the straight through tracks previously identified. After this fine alignment 203 events satisfied the criteria that the track resolution was better than 0.6μm. The efficiency for linking tracks is shown in figure 8. The distribution of the position resolution of each emulsion plate is shown in figure 9. This fine resolution then allows for a precision of $\sim$1μm in the vertex finding accuracy, shown in figure 10.

4.3 Event Classification

Special scan data was taken for electron identification and to extend the accuracy of measuring a charged particle's momentum using its trajectory through the emulsion due to multiple scattering.

5 Decay (Kink) Search

The kink decay search is divided into two separate analysis. One is for long *(L)* decays where the kink is outside of the plate in which the interaction occurred. For a long decay, illustrated in figure 11, the parent track is recorded in the emulsion data explic-

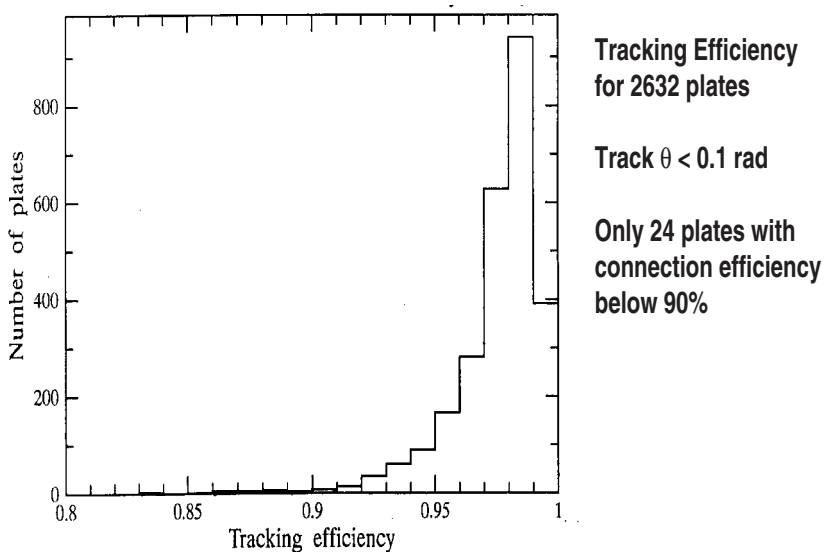

Fig. 8. Emulsion plate tracking efficiency. Note that for a total of 2632 plates scanned and aligned, only 24 plates had a connection efficiency of $< 90\%$.

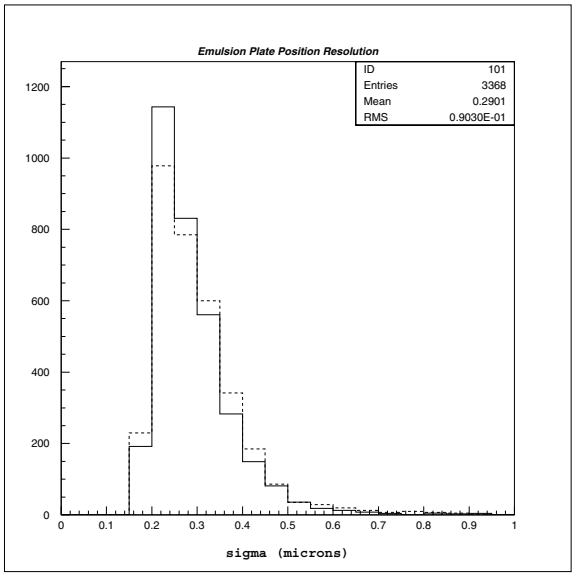

Fig. 9. Emulsion position resolution, determined by calculating the plate to plate residuals using through going muon tracks.

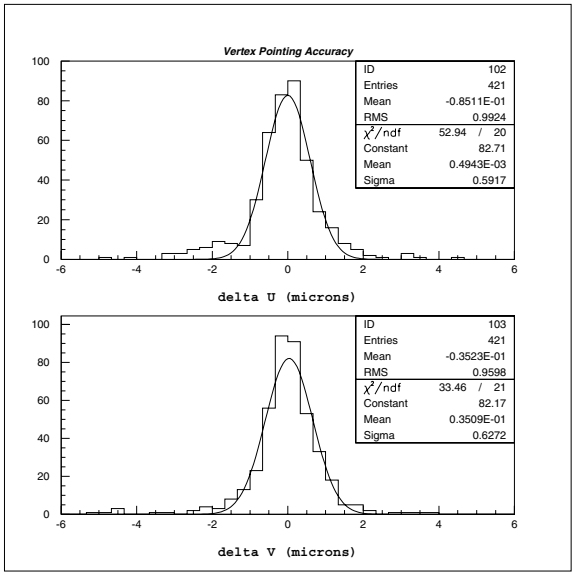

Fig. 10. Vertex pointing accuracy

itly. Additionally, if the kink is from a τ decay there will be no electron or muon from the primary vertex. For the target configurations used in DONUT, about 75% of all τ decays are expected to be long.

The second analysis is for short *(S)* decays in which the kink is in the same plate as the primary vertex, which for ECC-type modules means tha τ decay would be within steel and the event would have to be identified as a τ based on the impact parameter and minimum transverse momentum (p_T) of the daughter track. Only the results of the long decay search are presented here.

The following selection criteria were used to select kink candidates:

- At least one segment of the parent track is identified in the emulsion data.
- The daughter angle with respect to the parent track was $>$10 mrad and $<$ 400 mrad.
- The impact parameter of the daughter to the parent track was $< 5\mu$m.
- The impact parameter of the parent track to the interaction vertex was < 10 μm.
- The impact parameter of the daughter track to the primary vertex was $< 500\mu$m.

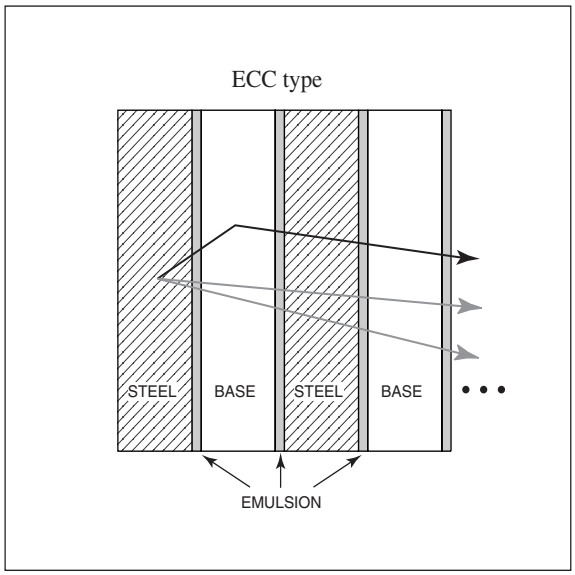

Fig. 11. Long decay topology

Cut	Kinks	$\%\tau$ remaining
none	7642	100
$0.01 <$ kink angle < 0.250	450	78
Parent angle < 0.200 rad	280	90
IP(Parent) < 5 μm	142	> 99
IP(kink) < 5 μm	65	> 99

Table 2. Kink selection in 680 primary tracks (from 203 interactions). Note that the $\%\tau$ remaining are not cumulative cuts.

6 Potential Backgrounds

Kinked tracks may be classified in the following categories: (1) random association of background tracks, (2) re-scattering, (3) charm decays in charged current interactions, and (4) τ decays.

The following selection criteria, which retained 50% of simulated τ events, were used to identify tau decay candidates from the kink candidates:

- Only one daughter track was associated with a parent track.
- The parent track was $<$ 5mm long.
- The daughter track momentum was $>$ 1 GeV/c.
- The transverse momentum of the decay was $>$ 250 MeV/c.
- None of the tracks originating at the primary interaction vertex was identified as a muon or electron.

6.1 Random Tracks

To determine the probability that an observed kink actually resulted from the mislinking of random background tracks, for each event the impact parameter of each track starting within one plate of the primary vertex was calculated. The distribution of these impact parameters is shown in figure 12. It can be seen that, with the exception of tracks known to be associated with the primary vertex, the shape of the distribution is characteristic of an uncorrelated, uniform distribution. On average there are 40 long tracks/mm^2/event which start near a random point in any layer. The fraction of primary tracks which stop within 5mm of the primary vertex is 0.14. The probability that the random track will be within 5μm of a stopping vertex track is 0.1. Requiring that the "daughter" matches in the SFT system reduces this background by a factor of five, to a negligible level, and it is not included in the final background number.

6.2 Charm Decays

Charged charm decays with a kink topology are a background if the lepton from the primary interaction is not identified. Charm is expected to be produced in 8.1% of the charged current ν_e and ν_μ events. The background is estimated by applying the branching ratios for charged charm and the one-prong kink topology, as well as the

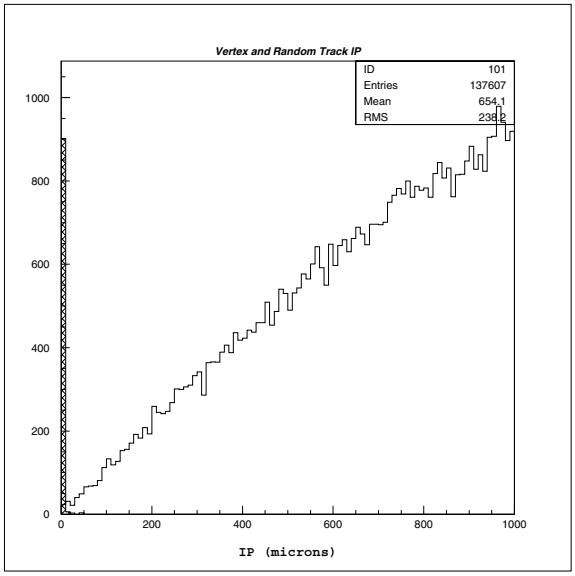

Fig. 12. Distribution of random track impact parameters. Tracks coming from the primary vertex were tagged independently.

cut efficiencies for "long decay", p_T, and lepton identification inefficiency. These cuts are summarized in Table 3. 2.4 charged charm events with correct lepton identification are expected, and 2 events are found. One of these charm events has a kink topology, consistent with the expectation of 0.9 ± 0.2 events.

However, the charm signal events would constitute a background to the τ sample if and only if the primary lepton is not identified. To estimate this potential background in the DONUT experiment, the muon identification efficiency was estimated to be 79% (82% acceptance $\times$ 96% efficiency). The electron efficiency was estimated (conservatively) to be 75%, giving a total lepton identification *inefficiency* of 23%. This leads to 0.21 ± 0.04 background charm events.

6.3 Interactions

A τ decay may be faked by re-scattering of a primary track in a) a neutral current event, or b) a charged current event where the lepton is not identified. The probability of re-scattering decreases rapidly with transverse momentum (p_T), in contrast to τ decays in which p_T peaks near 0.4 GeV/c. The re-scattering background is estimated by GEANT simulation of both of these processes. We find that the background due to re-scattering with a cut on $p_T \geq 250$ MeV/c is 0.2 ± 0.06 event, with a τ selection efficiency of 56%.

		no. of CC interactions
assume $\nu_\mu \sim \nu_e$		168±18
charm production	0.081±0.008	13±1.3
charged charm	0.47±0.05	6.4 ±0.9
"Long" decay and $<$ 5mm	0.66±0.06	4.2±0.7
kink detection ϵ	0.56±0.06	2.4±0.5
charm $\rightarrow$ kink (C1)	0.38±0.02	0.9±0.2

Table 3. Summary of charm background estimation.

The comparison of signal and background p_T is shown in figure 13.

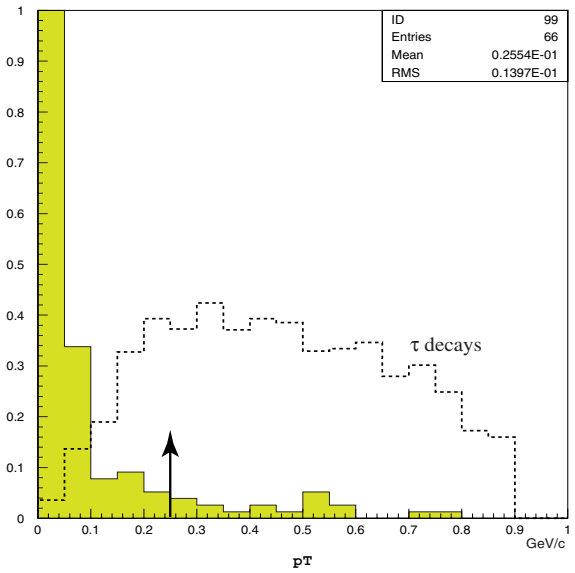

Fig. 13. Distribution of p_T for scattering background and τ decays.

For all kinks where it was possible to make a determination of the daughter momentum, the p_T was calculated. The distribution is shown in figure 14.

7 The Large p_T Events

Five events are well separated from a low p_T re-scattering background. One of these events has a clearly identified electron from the primary vertex, and is classified as the previously mentioned single-prong charm event. Each of the other four events are described and illustrated.

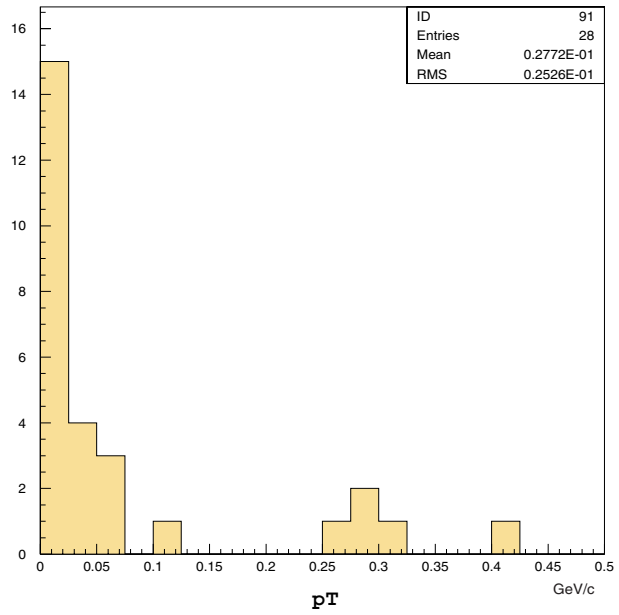

Fig. 14. P_T of kinks

7.1 Event 3333-17665

See figure 15. The track closest to the beam direction has a 13 milliradian kink, 0.54 mm from the primary vertex. The decay is located in the 800 μm thick plastic base. The daughter is identified as an electron. The momentum of the electron was measured to be 21^{+14}_{-6} GeV/c by multiple scattering measurement. Because of the continuous energy loss of the electron, this value must be considered as a lower limit. The corresponding decay p_T limit is $\geq 0.27^{+0.19}_{-0.08}$ GeV/c.

7.2 Event 3263-25102

See figure 16. One track has a 130 milliradian kink, 1.8 mm from the primary vertex. The decay is located in the steel plate. The daughter momentum is estimated to be $1.9^{+1.6}_{-0.6}$ GeV/c. The corresponding p_T is $0.25^{+0.21}_{-0.08}$ GeV/c.

7.3 Event 3039-01910

See figure 17. One track, isolated from the others, has a 90 milliradian kink angle, 0.28 mm from the primary vertex. This track is isolated from the other charged tracks and is emitted opposite to the other tracks in the plane perpendicular to the beam. The decay is

located in the plastic base (200 μm thickness). The daughter momentum was measured to be $4.6^{+1.6}_{-0.9}$ GeV/c. The estimated decay p_T is $0.41^{+0.14}_{-0.08}$ GeV/c. The daughter track was identified as a hadron since a secondary interaction is seen after 1.5 cm.

7.4 Event 3024-30175: $\tau \rightarrow e + \nu_\tau + \nu_e$.

See figure 18. This event has three tracks from the primary vertex. One track has a 93 mrad kink 4.5 mm from the primary vertex in the plastic substrate. No other tracks including nuclear evaporation tracks from this kink vertex are found. The kink daughter track was identified as an electron, because an electron pair accompanying this track was found in the emulsion, and a shower is observed in the SFT. The energy was estimated by measuring the multiple scattering of the daughter particle and by the shower development in the SFT. The former method gives $3.3^{+3.7}_{-1.2}$ GeV/c, but this value should be considered as a lower limit, as the electron loses energy continuously in the target. The latter method gives a value of 6.5 ± 2.5 GeV.

8 Conclusion and Future Analysis

The decay search for kinks from tau decays has been completed on 203 neutrino interactions using the emulsion data. For the long decay search method, four tau candidates are found. Each of these four events have a track that meets all the criteria for tau decays, with no evidence of another lepton from the primary vertex. The daughter impact parameter to the primary vertex and the kink p_T for the signal events are shown in comparison to the expected distributions for τ events in figure 19. The expected number of τ events in the 203 set, summarized in Table 4 is 4.1$\pm$1.4

The total background is estimated to be 0.42 ± 0.15 events. Kinks are found in the plastic emulsion substrate in three of the four events, however we expect the 0.2 scattering background to be dominated by kinks in the steel plates. Two events are identified as $\tau \rightarrow e\nu_\tau\nu_e$ decays and have negligible level of background from scattering. The probability that the four events are from backgound sources is 8×10^{-4}, and we conclude that tau neutrino charged current interactions have been observed.

The results which have been presented represent the analysis of one-third of the neutrino interactions which occurred in the emulsion targets. The collaboration plans to continue the process of event location and the subsequent decay search. It appears feasible to double the number of located interactions.

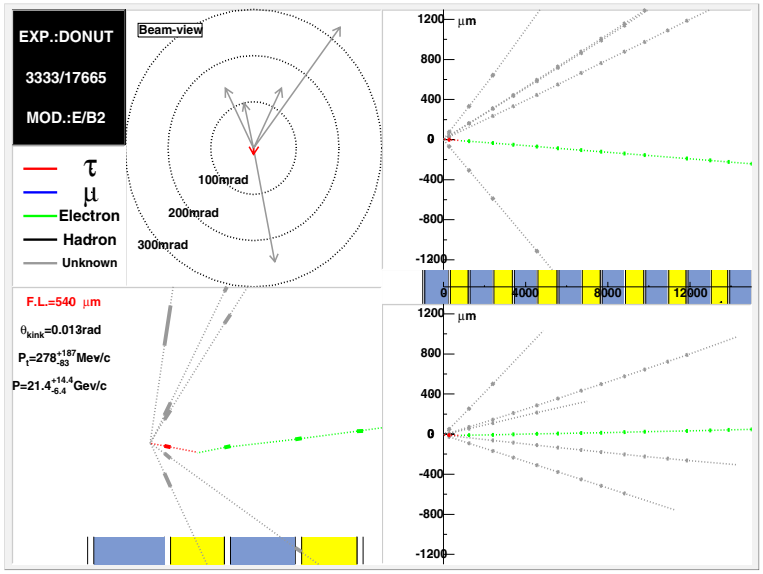

Fig. 15. Event 3333-17665: $\tau \rightarrow e + \nu_\tau + \nu_e$

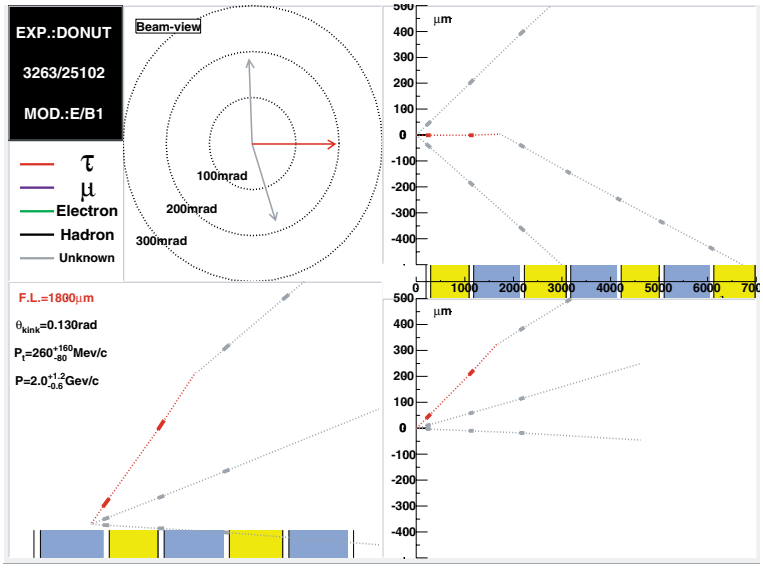

Fig. 16. Event 3263-25102: $\tau \rightarrow h + \nu_\tau + X$

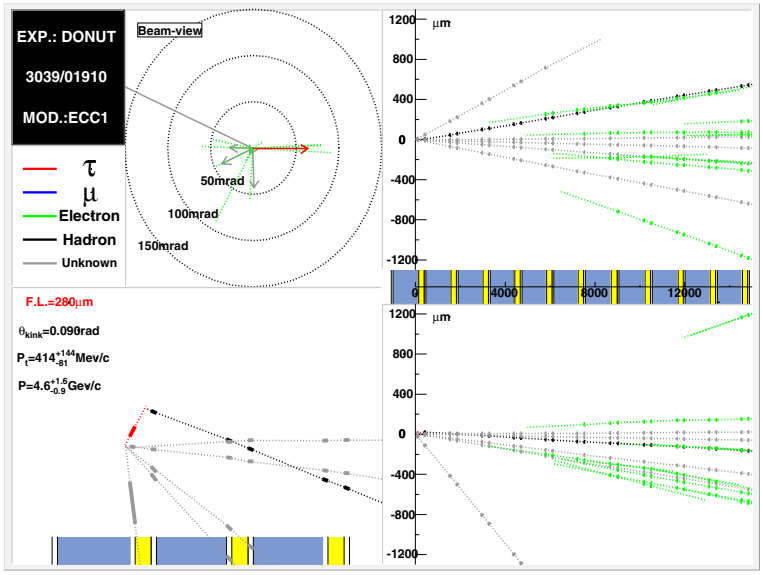

Fig. 17. Event 3039-01910: $\tau \rightarrow h + \nu_\tau + X$

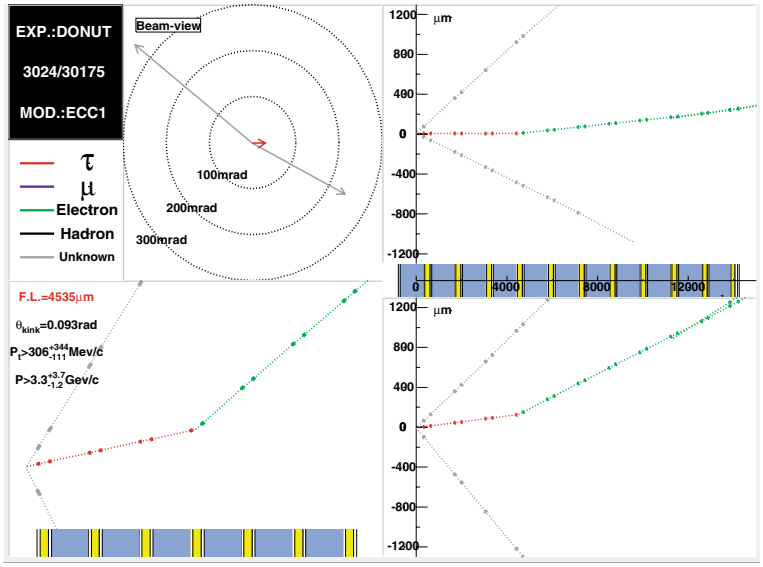

Fig. 18. Event 3024-30175: $\tau \rightarrow e + \nu_\tau + \nu_e$.

Number of interactions	203
fraction from ν_τ	0.048
C1 decay	0.86
Long decay	0.76
τ kink finding efficiency	0.65
Expected number of τs	4.1 ± 1.4

Table 4. Expected number of τ events in the 203 set

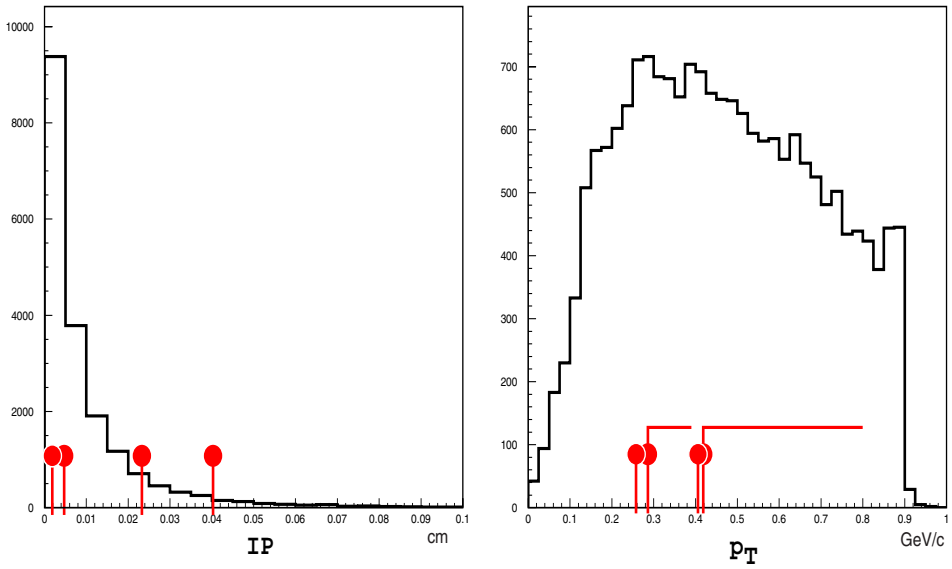

Fig. 19. Impact Parameter (IP) and p_T for tau candidates, compared to expected distributions. The data point for the p_T measurement uses the daughter momentum as determined from multiple scattering in the emulsion. The line indicates the corresponding measurement determined by the energy deposited in the SFT.

References

[1] M.L. Perl *et al.*, Phys. Rev. Lett. **35**, 1489 (1975).

[2] K. Kodama *et al.*, Phys. Rev. Lett. **57**, 2897 (1986).

[3] D. Decamp *et al.*, Z. Phys. **C53**, 1 (1992).

[4] Y. Fukuda *et al.*, Phys. Rev. Lett. **81**, 1562 (1998).

[5] C.L. Cowan, Jr., F. Reines, F.B. Harrison, H.W. Krue and A.D. McGuire, Science **124**, 103 (1956).

[6] G. Danby *et al.*, Phys. Rev. Lett. **9**, 36 (1962).

[7] E.S. Hafen *et.al.*, *Neutrino Interaction Studies Using a Beam Dump Technique to Produce the Neutrino Beam* (1980).

[8] H.H. Bingham *et.al.*, *Search for the ν_τ and Study of ν_e and $\bar{\nu}_e$ interactions* (1980).

[9] B. Lundberg *et.al.*, *Measurement of τ Lepton Production from the Process $\nu_\tau + N \to \tau + X$* (1993).

[10] K. Kodama *et al.*, Nucl. Instrum. Meth. **B93**, 340 (1994).

[11] E. Eskut *et al.*, Nucl. Instrum. Meth. **A401**, 7 (1997).

[12] M. Nakamura *in:* Proceedings of SCIFI93, (1995), p. 194; T. Nakano *et al., in:* Proceedings of SCIFI93, (1995), p. 525; T. Nakano *et al.*, IEEE on NS, **NS39**, 680 (1992).

[13] T. Nakano, Ph.D. Thesis, Nagoya University (1997).

[14] T. Nonaka *et al.*, to be submitted to Nucl. Instrum. Meth.

RECENT RESULTS FROM THE MUON $(g-2)$ EXPERIMENT

B. Lee Roberts*
Department of Physics
Boston University, Boston, MA 02215

Representing the Muon $(g-2)$ collaboration[1]

ABSTRACT

The status of the muon $(g-2)$ experiment at the Brookhaven AGS is reviewed. An accuracy of 5 ppm on the μ^+ anomalous magnetic moment has been achieved and published. Data with a statistical error of about 1.5 ppm are being analyzed with a result expected by the end of 2000 or early 2001. Additional data on tape should give a statistical error of about 0.5 ppm. A data run in 2001 will permit the measurement of the μ^- anomalous magnetic moment.

*Supported in part by the US National Science Foundation.

1 Introduction

Measurements of the *gyromagnetic ratios* of elementary particles have been intimately tied to the development of our understanding of subatomic physics. The gyromagnetic ratio, g, relates the spin and magnetic moment of an elementary particle through the relationship

$$\vec{\mu}_s = g(\frac{e}{2m})\vec{S}. \tag{1}$$

In the Dirac theory, the gyromagnetic ratio, or g-factor, is equal to 2. Since the g-factors of spin $\frac{1}{2}$ particles are not exactly equal to 2, is convenient to define an anomalous magnetic moment

$$a = \frac{(g-2)}{2}. \tag{2}$$

The proton, neutron and other baryons have large anomalous moments, which reflect their internal structure. The electron and muon are special in that they appear to be point-like. The small anomalous moments of these two leptons are dominated by the lowest order radiative correction $\frac{\alpha}{2\pi}$, which was first calculated by Schwinger[2] in 1948. QED calculations of the electron and muon anomalies have been carried out to eight-order (with an estimate of tenth-order) by Kinoshita.[3,4]

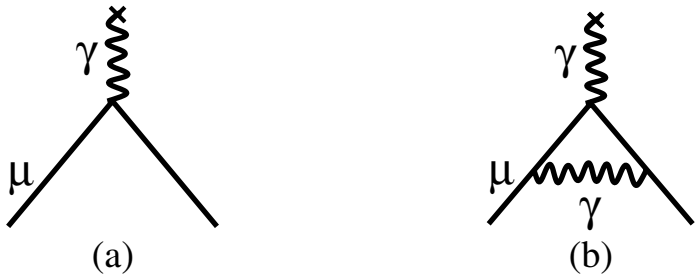

Fig. 1. The Feynman graphs for (a) $g = 2$; and (b) the lowest order radiative correction (Schwinger term)

The electron anomalous moment is now measured to an experimental accuracy of a few parts per billion,[5] and is well described by QED calculations.[3,4] To the level of measurement, only photons and electrons contribute, and $a \simeq 1 \times 10^{-3}$. There is no evidence to date, either from g-factor measurements or e^+e^- scattering, to indicate that the electron has any internal structure.

While the g-factor of the electron has provided a testing ground for QED, the anomalous magnetic moment of the muon has provided an even richer source of in-

formation, since the contribution of heavy virtual particles to the anomaly scales with the mass of the lepton squared. In a series of three elegant experiments at CERN,[6–8] virtual muons and hadrons have been shown to contribute at measurable levels. At present there is good agreement between experiment and theory,[3,9–11] and there is no indication of any muon substructure.

The famous CERN experiments measured $\mu_\mu = [1.001\ 165\ 9230(85)]\ (e\hbar/2m_\mu)$, a precision of ± 7.3 parts per million (ppm) for a_μ. While this result tested QED to a high level, and showed for the first time the contribution of virtual hadrons to the magnetic moment of a lepton, the sensitivity was not sufficient to observe the electroweak contribution from virtual $W^\pm$ and Z^0 gauge bosons. The goal of our experiment is an overall accuracy of ± 0.35 ppm which allows sufficient sensitivity to measure the electroweak contribution, as well as to search for physics beyond the standard model.

The theoretical value of a_μ consists of contributions from QED,[3] virtual hadrons,[12–17] and virtual electroweak gauge bosons.[18–21] Taking the value of α from the electron $(g-2)$ experiment,[22] the total QED contribution is $a_\mu^{QED} = 116\ 584\ 706(2)\ \times 10^{-11}$. The QED contribution is calculated to a precision of a few parts per billion. The agreement between the calculated and measured $(g-2)$ values for the electron gives us great confidence in the QED calculation.

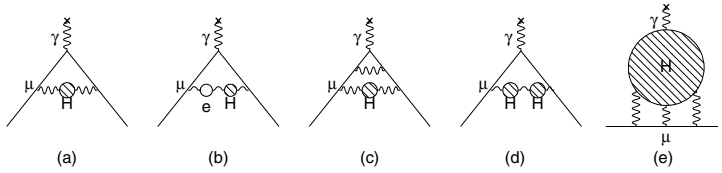

Fig. 2. Hadronic contributions to the muon anomalous moment. In these diagrams, H refers to a loop with hadrons (quarks). (a) The lowest order hadronic vacuum polarization, which is the dominant diagram.[14] (b) (c) (d) Higher order hadronic vacuum polarization diagrams.[15] (e) The light-on-light hadronic contribution.[14,17] The $\times$ indicates the virtual photon originating from the magnetic field.

Virtual hadrons contribute to the muon anomaly through vacuum polarization at a measurable level. The most important diagrams are shown in Fig. 2. The largest contribution (and the largest uncertainty) comes from the hadronic vacuum polarization diagram (Fig. 2(a)), which cannot be calculated from first principles. Instead measure-

ments of $R(s)$, the ratio

$$R(s) = \frac{e^+e^- \to \text{Hadrons}}{e^+e^- \to \mu^+\mu^-} \tag{3}$$

are used as input to the dispersion integral

$$a_\mu^{hadronic} = (\frac{\alpha m_\mu}{3\pi})^2 \int_{4m_\pi^2}^{\infty} \frac{ds}{s^2} K(s) R(s) \tag{4}$$

where

$$K(s) = \frac{3s}{m_\mu^2}\left[x^2(1-\frac{x^2}{2}) + (1+x)^2(1+\frac{1}{x^2})\left[\ln(1+x) - x + \frac{x^2}{2}\right] + \frac{1+x}{1-x}x^2\ln x\right] \tag{5}$$

is a kinematic factor, with

$$x = \frac{1-\beta}{1+\beta}, \qquad \beta = \sqrt{1-\frac{4m_\mu^2}{s}}. \tag{6}$$

The higher order hadronic contributions (Figs. 2(b-d)) are also calculated from these data,[15] but the hadronic light-on-light contribution[16,17] (Fig. 2(e)) must be obtained from a model calculation.

The total hadronic vacuum polarization contribution is $a_\mu^{Had} = 6882(154) \times 10^{-11}$ (~ 60 ppm of a_μ), where the error is dominated by the errors on the experimental data. The total hadronic contribution is given by[14] $a_\mu(\text{had}) = 6738(70) \times 10^{-11}$ which is 57.79 ± 0.60 ppm of a_μ.

The error quoted above does not reflect recent progress in $R(s)$ measurements at Novosibirsk and BES, reported in preliminary form at the ICHEP2000 conference in Osaka. Data at center-of-mass energies between 2 and 5 GeV from BES are likely to reduce the error from that region to a negligible level. In the energy region between 0.4 and 1.4 GeV, newly analyzed data from Novosibirsk should reduce the corresponding error in a_μ to 0.29 ppm. Data from hadronic τ decays should further reduce the error in roughly the same kinematic region. Finally, the region between 1.4 and 2.0 GeV will be addressed by the VEPP-2000 project at Novosibirsk, which will raise the collider's center-of-mass energy to 2 GeV. The uncertainty on the standard model value of a_μ will likely be reduced to about $\sim \pm 0.35$ ppm in the near future.

The one-loop electroweak contributions to a_μ (see Fig. 3(a),(b)) have been available for some time.[18] Recent higher order calculations, which include both fermionic[19,20] and bosonic[21] two-loop terms, have been confirmed by an independent calculation.[23] These authors obtain second order contributions which turn out to be surprisingly large.

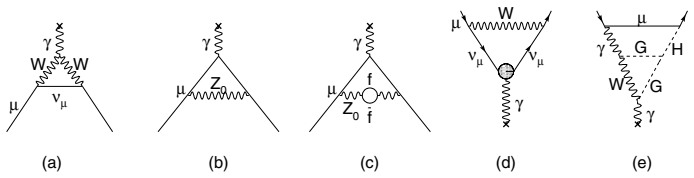

Fig. 3. Weak contributions to the muon anomalous magnetic moment. Single-loop contributions from (a) virtual W and (b) virtual Z gauge bosons. These two contributions enter with opposite sign, and there is a partial cancellation. The single-loop standard model Higgs contribution is negligible. The two-loop contributions fall into three categories: (c) fermionic loops which involve the coupling of the gauge bosons to quarks, (d) bosonic loops which appear as corrections to the one-loop diagrams, and (e) a new class of diagrams involving the Higgs where *G* is the longitudinal component of the gauge bosons. See reference [21] for details. The $\times$ indicates the virtual photon originating from the magnetic field.

The first order weak contribution of 195×10^{-11} is reduced to $151(4) \times 10^{-11}$ (1.3 ppm of a_μ) when the second order terms are included.

The total theoretical prediction is $a_\mu^{Theory} = 116\ 591\ 63\ (8)\ \times 10^{-10}$ where the theoretical error of ± 0.7 ppm is dominated by the uncertainty on the hadronic vacuum polarization contribution.

Theoretical interest in possible non-standard model contributions to the muon $(g-2)$ value has risen substantially in the past five years, and a great deal has been written about possible contributions to the muon $(g-2)$ value from non-standard model physics.[24,9] In Table 1 the sensitivities to several examples of new physics are given, assuming that the experimental error on a_μ is ± 0.35 ppm, and the error on the hadronic contribution is significantly less.

For example, just as proton substructure produces a g-value which is not equal to two, muon (or W) substructure would also contribute to the anomalous moment, the critical issue being the scale of the substructure.[25] A standard model value for $(g-2)$ at the 0.35 ppm level would restrict the substructure scale to around 5 TeV. If leptoquarks exist, they too could contribute to the non-standard model value of $(g-2)$.[26] The muon $(g-2)$ obtains its sensitivity to W substructure and anomalous gauge couplings through the $WW\gamma$ triple gauge vertex in Fig. 3(a). The combined sensitivity of LEP1,

LEP2 and $(g-2)$, and the unique contribution which $(g-2)$ makes in constraining the existence of such anomalous couplings, is described by Renard et al.[27]

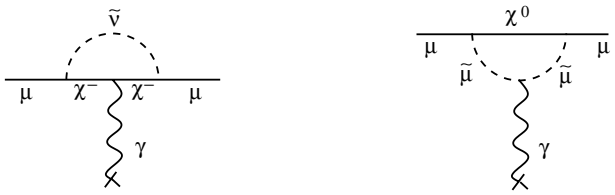

Fig. 4. The lowest order supersymmetric contributions to $(g-2)$.

Supersymmetry has become a serious candidate for physics beyond the standard model. There is a large sensitivity to almost any supersymmetric model with large $\tan\beta$ (the ratio of the vacuum expectation value of the two Higgs fields).[24] The SUSY contribution is shown in Fig. 4. In the case of large $\tan\beta$, the chargino (χ^-) diagram dominates the contribution to $(g-2)$ from SUSY, and is given by[24]

$$a_\mu(\mathrm{SUSY}) \simeq \frac{\alpha}{8\pi \sin^2\theta_W}\frac{m_\mu^2}{\tilde{m}^2}\tan\beta \simeq 140\times 10^{-11}\,(\frac{100\ \mathrm{GeV}}{\tilde{m}})^2\tan\beta, \qquad (7)$$

where $\tilde{m}$ is the largest mass in the loop. The goal of E821 is to reach a precision of $\pm 40\times 10^{-11}$ (± 0.35 ppm), so the factor of 140 in Eq. 7 corresponds to 1.2 ppm in a_μ. For $\tilde{m}=750$ GeV and $\tan\beta=40$, $a_\mu(\mathrm{SUSY})=100\times 10^{-11}$, a contribution which is 2.5 times larger than the sensitivity we hope to achieve. For $\tilde{m}=500$ GeV, the effect is 224×10^{-11} or 5.6 ppm.

Several measurements in addition to that of the muon anomalous moment will be made in our experiment. We expect to improve the limit on the muon electric dipole moment (EDM) by an order of magnitude over the current limit of $d<3.7\pm 3.4\times 10^{-19}$ e-cm, which was placed by the CERN $(g-2)$ experiment. An EDM would produce a spin motion out of the plane of the storage ring, so the signal would be a change in time of the vertical position of the decay positrons on the detectors. Since this small (the standard model value for the EDM is 10^{-38} e-cm) spin motion rides on top of a very large $(g-2)$ precession, the EDM measurement from E821 will be dominated by systematic errors. To obtain much more than an order of magnitude improvement over the CERN EDM result, it will be necessary to do an optimized EDM measurement, and preliminary studies show that we might reach a sensitivity of 10^{-24} e-cm. If there is non-standard model physics such as SUSY present, the EDM would be sensitive to it.

New Physics	E821 Sensitivity	Comments
μ substructure[a]	$\Lambda \geq 5\ TeV^{\dagger}$	LHC domain
μ Form factors[b] $(1 - k^2/\Lambda^2)$	$(W^{\pm})\ \Lambda > 450GeV$ $(Z^0)\ \Lambda > 64GeV$ $(\gamma)\ \Lambda > 180GeV$	$\Lambda_{LEP\ I} > 300GeV$
excited muon	$m_{\mu^*} \geq 400\ GeV$	LEPII comparable
$W^{\pm}$ substructure[c]	$\Lambda \geq 400\ GeV^{\dagger}$	LEPII $\sim 100 - 200\ GeV$
$\frac{(g_W - 2)}{2} \neq 0$	$\geq 0.02^{\ddagger}$	LEPII~ 0.05, LHC~ 0.2

†Scales as the square root of the error.

‡Scales linearly with error.

[a]For substructure $\Delta a_\mu \sim m_\mu^2/\Lambda^2$.

[b]See P. Méry, S.E. Moubarik, M. Perrottet, F.M Renard, Z. Phys. **C46**, 229 (1990).

[c]Goes to 0 if $M_W \to 0$ to get proper coupling to conserved current.

Table 1. Sensitivity to new physics other than SUSY if $\sigma_{a_\mu} = 0.35\ ppm$ (This table is taken primarily from Kinoshita and Marciano.[9])

However, unlike $(g-2)$, the standard model contribution ($\sim 10^{-38}$ e-cm) to the EDM is negligible compared to that predicted by SUSY models, and the interpretation would not be subject to any uncertainties in our knowledge of the standard model contribution.

We will measure $(g-2)$ for both μ^+ and μ^- thus providing a test of CPT (the CERN experiment[8] obtained values for these two which differed by over one σ). The experiment also tests special relativity, since the dilated muon lifetime in the storage ring is one of the parameters which comes out of the fit to the positron time distribution.

2 The Experimental Technique

A charged particle moving transverse to a uniform magnetic field will go in a circle with the orbital cyclotron frequency

$$\omega_c = \frac{(eB)}{(m\gamma)}. \tag{8}$$

The spin precession frequency in this same magnetic field is given by

$$\omega_s = \frac{geB}{2m} + (1-\gamma)\frac{eB}{m\gamma}. \tag{9}$$

Thus the spin vector of a charged particle moving transverse to a uniform magnetic field will precess relative to the momentum vector with a frequency ω_a, which is given by the difference between the orbital cyclotron frequency ω_c and the spin precession frequency ω_s. The frequency is

$$\omega_a = \omega_s - \omega_c = \frac{e}{m}a_\mu B, \tag{10}$$

where ω_a is directly proportional to the anomalous moment and is independent of the particle's momentum.

Vertical focusing must be provided to keep the muon beam stored, which can be accomplished with magnetic multipoles, or with an electrostatic quadrupole field. However, if magnetic multipoles are used, it is difficult to determine the average B field to the accuracy needed for a precision measurement of a_μ. In a region in which both magnetic and electric fields are present, the relativistic formula for the precession is given by[28]

$$\vec{\omega}_a = \frac{d\Theta_R}{dt} = -\frac{e}{m}\left[a_\mu \vec{B} - \left(a_\mu - \frac{1}{\gamma^2-1}\right)\vec{\beta}\times\vec{E}\right], \tag{11}$$

where Θ_R is the angle between the muon spin direction in its rest frame and the muon velocity direction in the laboratory frame. The other quantities refer to the laboratory frame. If the muon beam has the "magic" value of $\gamma = 29.3$, then the coefficient of the $\vec{\beta}\times\vec{E}$ term is zero, and the electric field does not cause spin precession. Thus the precession of the spin relative to the momentum is determined entirely by the magnetic field, and one can use electrostatic quadrupoles for vertical focusing.

Because the muon's lifetime is relatively long, and because muons are produced fully-polarized along their direction of motion in pion decay at rest, it is possible to store large numbers of polarized muons in a storage ring. In the three-body decay $\mu^+ \rightarrow e^+\bar{\nu}_\mu\nu_e$, the highest energy positrons are preferentially emitted parallel to the muon spin direction in the muon rest frame. Also, the highest energy electrons in the muon rest frame, when emitted parallel to the muon momentum, are Lorentz boosted to become the highest energy electrons in the lab frame. Therefore, the number of high energy electrons is a maximum when the muon spin is parallel to the momentum, and a minimum when it is anti-parallel, thus making it possible to measure the spin (or anomalous) precession frequency by counting high energy electrons as a function of

time. This time spectrum will show the muon lifetime modulated by the spin precession frequency.

The muon beam for storage in our storage ring is obtained from a bunched proton beam extracted from the AGS and directed onto a production target, which produces a secondary beam of charged pions. The AGS beam contains either six (1999) or twelve (2000, 2001) proton bunches ($\sigma \simeq 30ns$), with a bunch intensity limited to $\leq 7 \times 10^{12}$ protons by shock considerations in the production target. The total proton intensity in a single AGS cycle with 12-bunch operation was $\sim 60 \times 10^{12}$ protons.

The secondary beam momentum is set with dipoles and a momentum slit, and the beam is brought down a 100 m beamline which has a straight 74 m long quadrupole decay channel to collect muons from pion decay. Just upstream of the storage ring, a second momentum slit permits us to select a pion beam or, by adjusting the momentum lower by $\simeq 1\%$, a muon beam. Initially we injected pions into the ring and used the $\pi \rightarrow \mu\nu$ decay to kick the muons onto stored orbits.[10] Since the summer of 1998, we have injected muons into the storage ring, storing them with a 10 mrad magnetic kick.

With muon injection, about 10^4 muons were stored in the ring per proton bunch, and the number of detected positrons per hour was increased by an order of magnitude over the pion-injection method employed previously. Furthermore, the injection-related background (flash) in the positron detectors was reduced by a factor of about 50, since most of the pions were removed from the beam before it entered the storage ring.

The storage ring is a 600 ton, superferric magnet with 14 m diameter coils which excite the B field.[29] (See Fig. 5.) The ring functions as a weak focusing betatron, with a field index of 0.137. After a rigorous program of shimming, the B field uniformity is better than ± 2 ppm, integrated over azimuth. The storage ring parameters are given in Table 2.

The muon decay electrons, having lower momenta than the stored muons, are swept by the B-field into twenty-four scintillating-fiber-Pb calorimeters, which are spaced evenly around the interior of the ring. The calorimeter pulses were continuously sampled by custom 400 MHz waveform digitizers (WFDs), which provided both timing and energy information for the positrons. Both the NMR (magnetic field) and WFD clocks were phase-locked to the same LORAN-C frequency signal.[30] The waveforms were zero-suppressed, and stored in memory in the WFD until the end of the AGS cycle. Between AGS acceleration cycles the WFD data were written to tape for off-line analysis, as were the calorimeter calibration data and the magnetic field data.

We measure the frequency of oscillation in the number of high energy decay elec-

Fig. 5. The 700 ton muon $(g-2)$ storage ring during a maintenance period. The magnet yoke is covered with (white) thermal insulation, except at 9:00 o'clock where it is pulled back. The lighter colored inner-radius ring at 9:00 is the top cryostat for the inner-radius coil, and the bottom inner-radius cryostat can also be seen below the magnet gap at 2 o'clock. Most of the 24 electron calorimeter stations are installed. The muon kicker modulators are the three "cannon-like" objects at 1:00 o'clock. Two sets of tracks the detectors ride on can be seen to the right of the third kicker modulator, since these detectors have been removed.

trons, which is the same as the anomalous precession frequency. In the time histogram of high-energy decay electrons one observes the exponential lifetime expected from muon decay, modulated by the $(g-2)$ frequency,

$$N(t) = N_0 e^{-t/\gamma\tau}(1 + A\cos(\omega_a t + \phi)), \tag{12}$$

where *A*, the product of the decay asymmetry and the stored muon polarization, is about 0.4 for electrons above 1.8 GeV (the maximum electron energy is 3.1 GeV). The full data set from the 1999 run is shown below in Fig. 6. Ultimately $(g-2)$ plans to collect about 2×10^{10} decay positrons with energy above 1.8 GeV, spread over more than ten

Parameter	Value	Comments
(g-2) Frequency	$f_a \sim 0.23 \times 10^6/s$	$\omega_a = 2\pi f_a$ $\tau_a = 1/f_a = 4.37\ \mu$ s
Muon Lifetime	$\gamma\tau = 64.4\ \mu$ s	
Muon kinematics	$p_\mu = 3.094$ Gev/c $\gamma_\mu = 29.3$	The Central Momentum = The Magic Momentum
Cyclotron Period	$\tau_{cyc} = 149$ ns	
Central Radius	$\rho = 7112$ mm — $(280'')$	
Magnetic Field	$B = 1.4513$ T	
Storage Aperture	9.0 cm circle	
In one lifetime:	432 revolutions around ring	14.7 *(g-2)* periods

Table 2. Storage Ring Parameters

time-dilated muon lifetimes (640 μs).

In our storage ring, the magnetic field (see Eqn. 11) is a nearly pure dipole field which can be measured to a precision of a few parts in 10^7 with NMR. At the edge of the 9 cm diameter storage aperture, the quadrupole and higher multipole strengths are at the few ppm level relative to the vertical dipole field. There is a small second order correction from the electric field because the cancellation only occurs for the central momentum of the storage ring. Because of the vertical betatron motion of the stored muons, there is also a "pitch" correction[32] from the vertical betatron motion, since $\vec{\beta} \cdot \vec{B}$ is not exactly zero.

3 Beam Dynamics

A knowledge of beam dynamics is important to the ω_a analysis. The magnetic field which enters into Eq. 10 (and Eq. 11) is the magnetic field in the storage ring averaged over the muon distribution. Thus we need to measure the field very well, and we need to have some knowledge of the muon distribution in the ring. Furthermore, both the electric field and "pitch" corrections require some knowledge of the muon distribution. The electric-field correction, 0.5 ppm in the 1999 run, is proportional to the rms momentum spread of the stored muon beam, which we can measure by examining the rate at which the beam debunches at early times.

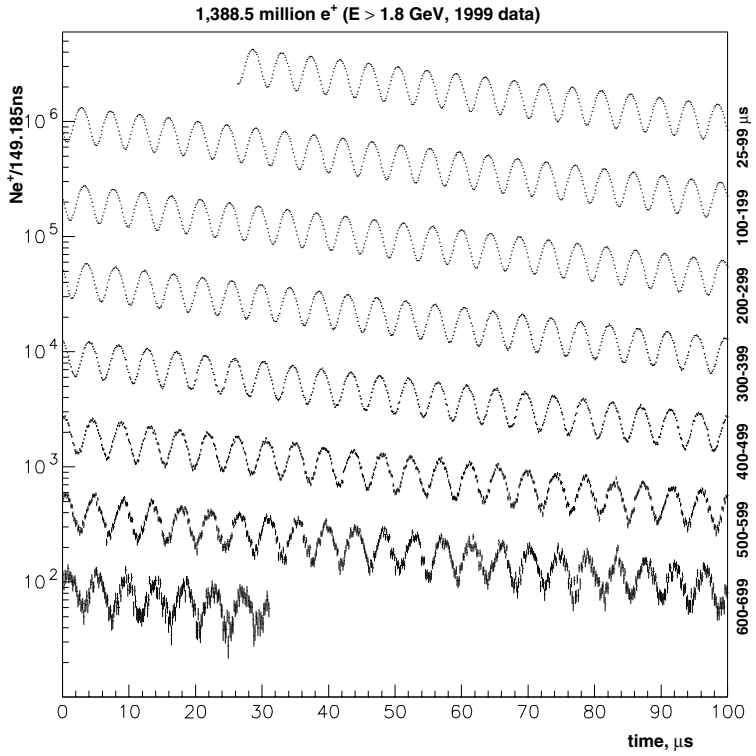

Fig. 6. The 1999 data. Because we accumulate data over many lifetimes, the time scale is folded back over every 100 μs. These data clearly show the exponential muon lifetime modulated by the spin precession.

The $(g-2)$ storage ring functions as a weak focusing betatron,[33] with an average field index $n = 0.137$. With the assumption that the vertical focusing is provided by a uniform quadrupole field spread around the storage ring, the horizontal and vertical betatron oscillations obey the equations

$$\ddot{x} + \omega_x^2 x = 0, \quad \text{horizontal (radial)} \tag{13}$$

and

$$\ddot{y} + \omega_y^2 y = 0, \quad \text{vertical}, \tag{14}$$

which are harmonic oscillator equations with the frequencies

$$\omega_x = \omega_c\sqrt{1-n}; \qquad \omega_y = \omega_c\sqrt{n}. \tag{15}$$

ω_c is the cyclotron frequency. We use the standard accelerator coordinates, x for radial position, y for vertical, and s for arc length around the ring. The point $x = y = 0$ is the center of the storage region. From Eqn. 15 one sees that the requirement for stable orbits is $0 < n < 1$.

For a uniform quadrupole gradient, the field index n is defined by

$$n = -\frac{\rho}{B_{0y}}\frac{\partial B_y}{\partial x} \tag{16}$$

where ρ is the storage ring radius, B_{0y} is the vertical dipole magnetic field, $\partial B_y/\partial x$ is the magnetic gradient term which provides the quadrupole focusing. If both magnetic and electric gradient terms are present, the effective field index becomes[34]

$$n_{\rm eff} = -\frac{\rho}{B_{0y}}\frac{\partial B_y}{\partial x} - \frac{\rho}{\beta B_{0y}}\frac{\partial E_x}{\partial x}. \tag{17}$$

In E821, only an electric field is used to provide vertical focusing with the magnetic field as pure a dipole field as possible.

Eqns. 13 and 14 represent the motion of single particles in our storage ring. An alternate way of looking at the beam motion is to view the ring as a spectrometer. With a field index of 0.137, the horizontal betatron frequency is $f_{\rm rad} = 0.93 f_C$, which means that in one betatron wavelength $\lambda_{\rm rad} = 1.075(2\pi\rho)$, the particle returns to its starting radial position. In ~ 13.3 turns, the the betatron oscillation returns to the same radial (x) and azimuthal (s) position in the storage ring. We return to this point below.

In order to deliver the beam to the edge of the storage region, an iron-free superconducting septum magnet called an inflector[35] produces a 1.5 T dipole field which opposes the main storage ring field, thus permitting the beam to arrive at the edge of the storage volume essentially undeflected. The inflector aperture is 18 mm wide and 53 mm high, and the region inside the ring available for beam storage is a 90 mm diameter circle. While this small injection aperture, which does not match the storage ring aperture, is contrary to usual storage ring practices, ordinary storage rings do not have magnetic fields uniform to a few ppm. The usual technique of a storage ring composed of separate elements is not possible here, and a hole cut into the magnet for injection would spoil the excellent field uniformity. Thus the storage ring magnet is a circular "C" dipole magnet, 14 m in diameter, with a pole gap of 180 mm.[29] The opening of the "C" faces the circle center, and the beam enters through a small hole in the magnet yoke. The geometry showing the inflector exit and the storage region between the magnet pole pieces is shown in Fig. 7.

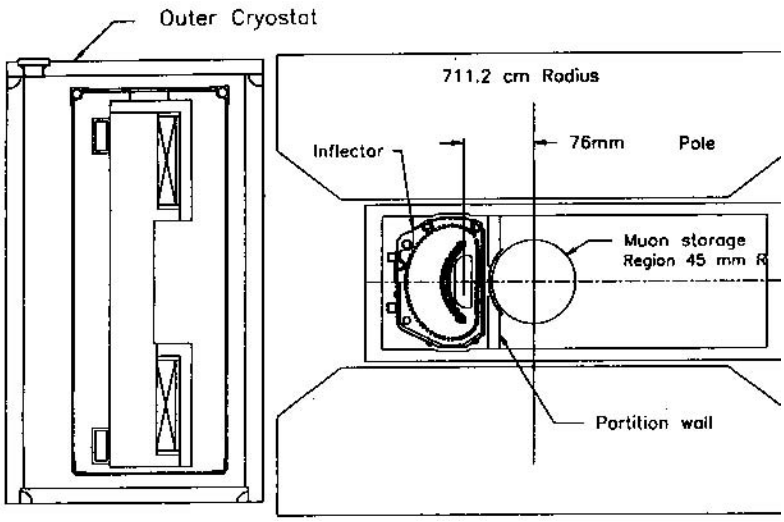

Fig. 7. An elevation view of the geometry of the inflector and the storage ring magnet. The beam vacuum chamber and the inflector cryostat are a coupled package. The chamfered pole pieces can be seen immediately above and below the inflector and storage region. The beam enters through the "backward D"-shaped aperture 77 mm (not 76 as shown) from the storage ring center. The large Xs at the top and bottom of the outer cryostat are the superconducting coils which excite the magnetic field.

At the inflector exit the beam is 77 mm (not 76 as is indicated in the drawing) from the center of the storage region. Since the beam will travel in a circle, without a kick it will return to hit the side of the inflector and be lost. A 0.1 T-m (10 mrad) kick must be applied a quarter of a betatron wavelength after the inflector exit to place the beam at the center of the storage region. The usual kicker techniques with ferrite core magnets cannot be employed here, because of the precision magnetic field. The magnetic kick was generated with a pulsed current, which had a peak current of 4100 A and a half period of 400 ns.

Three pulse-forming networks powered three identical 1.7 m long one-loop kicker sections consisting of 95 mm high parallel plates on either side of the beam. The current pulse was formed by an under-damped LCR circuit. The kicker plate geometry and composition were chosen to minimize eddy currents. The residual eddy current effect on the total field seen by the muons was less than 0.1 ppm 20 μs after injection. The time-varying magnetic field from the eddy currents was calculated with the program OPERA[36] and was measured in a full-size straight prototype vacuum chamber

with the use of the Faraday effect.[37] Since the muons circulate in 149 ns, they were kicked several times before the kicker pulse died out. Simulations show that because of the phase-space mismatch between the inflector and the storage region, a perfect kick would result in 7.5% of the beam being stored. With the actual kicker waveforms these calculations predict a storage efficiency of 6.6%. While not exactly at the level of efficiency expected in the usual accelerator application, this injection efficiency more properly should be compared with the pion injection efficiency of 3×10^{-6} muons stored per pion injected into the ring. Thus the order of magnitude improvement in stored muons and the substantial reduction in background over that obtainable with pion injection show the real success of this new technique.

During injection, and for 16 μs following injection, the electrostatic quadrupoles are powered asymmetrically, so that the beam is lifted and displaced sideways in the storage ring. This permits the beam to be scraped on circular collimators placed at several locations inside of the ring. After scraping, the quadrupole plates are returned to symmetric potentials with an RC time-constant of 5 μs.

The beam of particles enters the ring in a bunch. Since all muons are traveling at essentially the same velocity, those with larger radii will be overtaken by those at smaller radii, and the beam will debunch. This can be seen clearly in the positron time spectra from the detectors.

Fig. 8(a) shows the high energy positron time spectrum early in the data-taking cycle. The interval between the peaks is the beam's 150 ns "fast rotation" time around the storage ring. Fig. 8(b) shows the time spectrum about 30 μs later, by which time the debunching of the beam has noticeably washed out the fast rotation structure. Figure 8(c) shows the inferred equilibrium radius distribution which peaks at the radius corresponding to the magic gamma, 711.2 cm, but is not symmetric about it, having something of a high side shoulder. Two independent analyses, one using Fourier techniques, arrive at distributions which are virtually identical.

The tracking code mentioned above has also been used to calculate the average magnetic field seen by the stored muons, as well as the pitch and radial-E-field correction. The distribution of equilibrium radii calculated from tracking is overlaid with the "fast rotation analysis" (discussed below) in Fig. 8(c). The radial E-field calculation and pitch correction calculations are consistent with our expectations.

The beam exiting the inflector has a narrow waist imposed on it by the aperture of the inflector. This waist will be reformed one betatron wavelength later around the ring. In ~ 13 turns, this waist will travel around the ring. If there were no momentum disper-

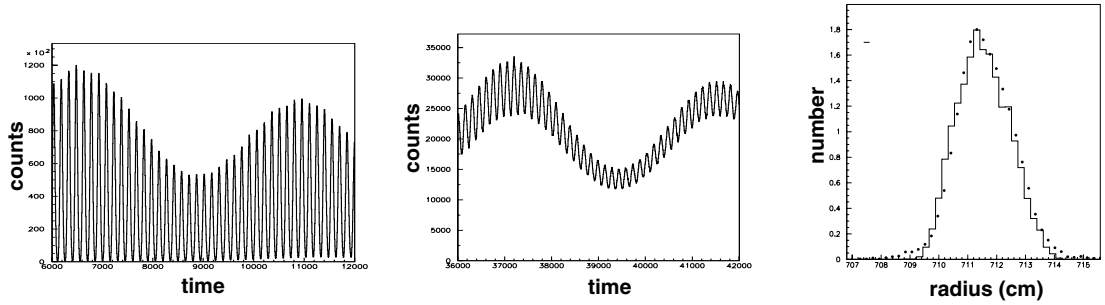

(a) (b) (c)

Fig. 8. The time spectrum of positrons at early times. The narrow structure is from the bunched beam structure, and the slower "wiggle" is from the $(g-2)$ precession. (a) Clear fast rotation structure about 6 microseconds after injection. (b) Faded fast rotation structure about 36 microseconds after injection. (c) The equilibrium radius distribution calculated using the tracking code (histogram) and obtained from an analysis of the beam debunching at early times (points) (1998 data).

sion in the storage ring, the waist would reform at 180° and return to the same azimuthal position every ~ 6.5 turns. In addition to the motion of this horizontal waist, the beam oscillates coherently about the central orbit because it is not kicked perfectly. Because the positron detector acceptance varies slightly with radius, we see both the radial coherent betatron motion, and the horizontal beam waist motion around the ring, in the 1999 high-statistics data. The width variation has a clear first- and second- harmonic dependence, as would be expected from the arguments above.

These betatron motion effects were first seen in data from the scintillating fiber harps which we have as beam diagnostic tools. The harps consist of seven 0.5 mm scintillating fibers strung either radially or horizontally, and are used to sample the beam profile. The measurement is destructive and is not performed during standard data runs, but it still gives a very reliable idea of the beam profile for many tens of microseconds.

Data from the harps are shown in figure 9. The two data sets, with beam scraping on and off, have different characteristic frequencies but send the same message: the beam undergoes a collective radial betatron motion, here of amplitude 0.4 cm. These coherent betatron oscillations are most prominent at early times but persist for more than 100 microseconds. The oscillations arise because the kick given to the incoming beam is not perfect. Instead of arriving on a stored circular orbit centered on the middle

of the storage ring, the beam describes a series of roughly circular orbits with a slowly moving center. A small radial acceptance bias transforms the oscillatory motion into a small modulation of the basic $(g-2)$ precession spectrum. The effect is small, but must be accounted for in our 1999 analysis.

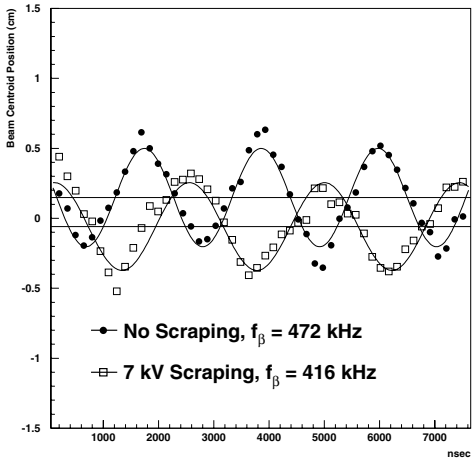

Fig. 9. Average beam radius vs. time. When the beam is first injected, the electrostatic quadrupoles are powered asymmetrically this moving the beam up and off-center horizontally, thus scraping it on collimators. This changes slightly the n-value of the weak-focusing storage ring during scraping.

4 Analysis

Experimentally, we determine the muon frequency ω_a from the detectors' positron time spectra, and the magnetic field from the proton NMR frequency ω_p (corrected to the free-proton value). ¿From the ratio $R = \omega_a/\omega_p$ we determine

$$a_\mu = \frac{R}{(\lambda - R)} \tag{18}$$

where $\lambda = \mu_\mu/\mu_p$ is measured independently.[38,39] The analysis is done blind, meaning that for each frequency analysis (ω_a and ω_p) an arbitrary offset is put into the data, so that without knowledge of the offsets one cannot determine a_μ. Since each offset is known by only one person, it is impossible for anyone doing the analysis to determine a_μ without the collaboration of these <u>two</u> people. Furthermore, the four independent

analyses of ω_a, and the two independent analyses of ω_p had additional offsets determined by the principals, which were removed late in the analysis process. Soon all offsets will be removed on the analysis of the 1999 data.

The heart of any precision experiment is the analysis of systematic errors. The most important errors in the analysis of the 1998 data are listed in Table 3. Limitations on our knowledge of the B-field are important. Some errors are related to the dynamics of the stored muon beam and others to the performance of the electron calorimeters and their associated PMTs, as well as to the procedures used to reconstruct the electron times and energies from the waveform record. With each new data set we have been able, thus far, to reduce the systematic errors well below the statistical errors. In the 1999 data set, the systematic errors are on the order of ~ 0.5 ppm with a statistical error of ~ 1.5 ppm.

Systematic Effect	ϵ (ppm)
1. Magnetic Field B	0.5
2. Timing Shifts	$<$0.1
3. Pileup	$<$0.6
4. Gain Changes	$<$0.1
5. Coherent Betatron Oscillations	0.2
6. Radial E Field, Pitch Correction	0.3
7. Backgrounds	$<$0.5
8. Lost Muons	$<$0.1
9. Fitting Start Time	0.3
10 Binning Effects	0.2
Total Systematic Error	1.0

Table 3. Systematic Errors for the 1998 run. The 1999 systematic error is about half a ppm.

The first and most important step in the analysis is forming positron times and energies from the waveform record. The algorithm agreed to is fast, reliable, stable, and largely insensitive to background. Its deadtime is less than 3 ns and, by itself, contributes nothing to the systematic error.

Excellent timing stability is required of the electronics. In particular, the average measured time must be stable to 20 ps over the first 200 μs of data-taking. For closely

related reasons, the gain must be stable to 0.2 percent over the same period. Using our laser calibration system, and for gain stability, the positron energy data itself, it has been demonstrated that both goals have been met.

At high rates, which come early in the data-taking cycle, pulse pileup is also a problem. Smaller pulses which follow close on the heels of a larger trigger pulse can be missed. Two small pulses which lie directly on top of one another can masquerade as a single high energy pulse. Because pileup occurs more often at early times than later on, it can produce a systematic error in ω_a, just like a shift in gain. In our 1998 analysis, pileup was the largest single systematic error. Since then, careful studies of our pulse and precession fitting procedures have made it possible to model and correct for the effect of pileup on ω_a.

For the past year, the systematic problems associated with fitting the $(g-2)$ precession to multi-parameter functions, have been investigated by a number of collaborators. Extensions of the classic 5-parameter function described above which include such effects as pileup, fast rotation and coherent betatron oscillations have been studied, and a consistent picture is emerging from the different analyses.

5 Results and Conclusions

We now have $\sim 10^{10}$ high-energy μ^+ decay positrons on tape (~ 5 terabytes of data), which we expect to give a statistical precision of $\sim \pm 0.5$ ppm. The CERN group observed the equivalent of about 4×10^7 of our high-energy events, which came from a data sample of a total of 1.4×10^8 detected positrons of all energies. We have now reported two new measurements[10,11] of $(g-2)$ and these results are shown graphically below in Fig. 10, along with the CERN results. Two large data sets are on tape from our 1999 and 2000 runs. Analysis of the 1999 data should be completed by the end of 2000, with a total error of ~ 1.4 ppm. The 2000 data should yield a statistical error of ~ 0.6 ppm.

After many years of construction and several years of engineering runs, the $(g-2)$ experiment has reached full maturity. A significant improvement on the 7.5 ppm result has now been published. With the world average one standard deviation above the standard model value, there is ample opportunity for the 1.4 ppm result to either agree with the standard model value, or be 4 standard deviations away, and still agree with all previous measurements.

I wish to acknowledge the many contributions made by my collaborators in $(g-2)$

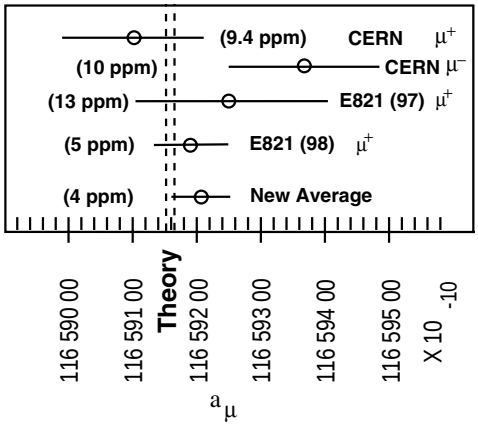

Fig. 10. Summary of the precise measurements of a_μ. The dashed lines show the standard model value.

in getting us to this point. This document is descended from a grant proposal written with my colleagues Jim Miller and Rob Carey, and I wish to thank them for letting me use it as the starting point for this manuscript, and for their comments. I also wish to thank Ivan Kronkvist, Ernst Sichtermann, and Yannis Semertzidis of the $(g-2)$ publications committee for helpful comments. This work was supported in part by the U.S. Department of Energy, the U.S. National Science Foundation, the German Bundesminister für Bildung und Forschung, The Russian Ministry of Science and the US-Japan Agreement in High Energy Physics.

References

[1] H.N. Brown[2], G. Bunce[2], R.M. Carey[1], P. Cushman[10], G.T. Danby[2], P.T. Debevec[7], H. Deng[12], W. Deninger[7], S.K. Dhawan[12], V.P. Druzhinin[3], L. Duong[10], W. Earle[1], E. Efstathiadis[1], F.J.M. Farley[12], G.V. Fedotovich[3], S. Giron[10], F. Gray[7], M. Grosse-Perdekamp[12], A. Grossmann[6], U. Haeberlen[8], M.F. Hare[1], E.S. Hazen[1], D.W. Hertzog[7], V.W. Hughes[12], M. Iwasaki[11], K. Jungmann[6], D. Kawall[12] M. Kawamura[11], B.I. Khazin[3], J. Kindem[10], F. Krienen[1], I. Kronkvist[10], R. Larsen[2], Y.Y. Lee[2], I. Logashenko[1,3], R. McNabb[10], W. Meng[2], J. Mi[2], J.P. Miller[1], W.M. Morse[2], C.J.G. Onderwater[7], Y. Orlov[4], C. Özben[2], C. Pai[2], J.M. Paley[1], C. Polly[7], J. Pretz[12], R. Prigl[2], G. zu Putlitz[6], S.I. Redin[12], O. Rind[1], B.L. Roberts[1], N. Ryskulov[3], S. Sedykh[7], Y.K. Semertzidis[2],

Yu.M. Shatunov[3], E. Solodov[3], M. Sossong[7], A. Steinmetz[12], L.R. Sulak[1], C. Timmermans[10], A. Trofimov[1], D. Urner[7], P. von Walter[6], D. Warburton[2], D. Winn[5], A. Yamamoto[9], D. Zimmerman[10]; [1]Department of Physics, Boston University, Boston, MA 02215, USA, [2]Brookhaven National Laboratory, Upton, NY 11973, USA, [3]Budker Institute of Nuclear Physics, Novosibirsk, Russia, [4]Newman Laboratory, Cornell University, Ithaca NY 14853, USA, [5]Fairfield University, Fairfield, CT 06430, USA, [6]Physikalisches Institut der Universität Heidelberg, 69120 Heidelberg, Germany, [7]Department of Physics, University of Illinois at Urbana-Champaign, IL 61801, USA, [8]MPI für Med. Forschung, 69120 Heidelberg, Germany, [9]KEK, High Energy Accelerator Research Organization,Tsukuba, Ibaraki 305-0801, Japan, [10]Department of Physics, University of Minnesota, Minneapolis, MN 55455, USA, [11]Tokyo Institute of Technology, Tokyo, Japan, [12]Department of Physics, Yale University, New Haven, CT 06511, USA.

[2] J. Schwinger, Phys. Rev. **73**, 416 (1948), and and Phys. Rev. **75**, 898 (1949).

[3] See the review by V.W. Hughes and T. Kinoshita, Rev. Mod. Phys. **71**, S133 (1999), for a discussion of both the muon and electron g-factors.

[4] The earlier reivew of these calculations given in T. Kinoshita, *Quantum Electrodynamics* (Directions in High Energy Physics, Vol. 7), T. Kinoshita ed. (World Scientific 1990), p. 218, is also useful.

[5] R.S. Van Dyck, Jr., P. Schwinberg, and H. Dehmelt, Phys. Rev. Lett. **59**, 26 (1987), and in *Quantum Electrodynamics*, T. Kinoshita ed. (World Scientific, 1990), p. 322.

[6] G. Charpak, F.J.M. Farley, R.L. Garwin, T. Muller, J.C. Sens and A. Zichichi, Nuovo Cim. **37**, 1241 (1965).

[7] J. Bailey, W. Bartl, B. von Bochmann, R.C.A. Brown, F.J.M. Farley, M. Giesch, H. Jöstlein, S. van der Meer, E. Picasso and R.W. Williams, Nuovo Cim. **9A**, 369 (1972).

[8] J. Bailey, K. Borer, F. Combley, H. Drumm, C. Eck, F.J.M. Farley, J.H. Field, W. Flegel, P.M. Hattersley, F. Krienen, F. Lange, G. Lebée, E. McMillan, G. Petrucci, E. Picasso, O. Runolfsson, W. von Rüden, R.W. Williams and S. Wojcicki, Nucl. Phys. **B150**, 1 (1979).

[9] T. Kinoshita and W.J. Marciano in *Quantum Electrodynamics* (Directions in High Energy Physics, Vol. 7), T. Kinoshita ed. (World Scientific, 1990), p. 419.

[10] R.M. Carey et al., $(g-2)$ Collaboration, Phys. Rev. Lett. **82**, 1632 (1999).

[11] H.N. Brown, et al., $(g-2)$ Collaboration, Phys. Rev. **D62**, 091101 (2000) [hep-ex/0009029].

[12] S. Eidelman and F. Jegerlehner, Z. Phys. **C67**, 585 (1995).

[13] W.A. Worstell and D.H. Brown, Phys. Rev. **D54**, 3237 (1996), and Muon (g-2) technical note # 220 (1995).

[14] M. Davier and A. Höcker, Phys. Lett. **B435**, 427 (1998), and refs. therein.

[15] Bernd Krause, Phys. Lett. **B390**, 392 (1997).

[16] M. Hayakawa and T. Kinoshita, Phys. Rev. **D57**, 465 (1998), and refs. therein.

[17] J. Bijnens, E. Pallante and J. Prades, Nucl. Phys. **B474**, 379 (1996), and refs. therein.

[18] W.A. Bardeen, R. Gastmans and B Lautrup, Nucl. Phys. **B46**, 319 (1972); R. Jackiw and S. Weinberg, Phys. Rev. **D5**, 157 (1972); I. Bars and M. Yoshimura, Phys. Rev. **D6**, 374 (1972).

[19] A. Czarnecki, B. Krause and W.J. Marciano, Phys. Rev. **D52**, R2619 (1995).

[20] S. Peris, M. Perrottet and E. de Rafael, Phys. Lett. **B355**, 523 (1995).

[21] A. Czarnecki, B. Krause and W.J. Marciano, Phys. Rev. Lett. **76**, 3267 (1996).

[22] T. Kinoshita, Phys. Rev. Lett. **75**, 4728 (1995).

[23] G. Degrassi and G.F. Giudice, Phys. Rev. **D58**, 53007 (1998).

[24] A. Czarnecki and W. Marciano, *Lepton anomalous magnetic moments - a theory update*, Nucl. Phys. **S76**, 245 (1999), and refs. therein.

[25] S. Brodsky and S. Drell, Phys. Rev. **D22**, 2236 (1980).

[26] G. Couture and H. Konig, Phys. Rev. **D53**, 555 (1996).

[27] F. Renard, et al., Phys. Lett. **B409**, 398 (1997).

[28] V. Bargmann, L. Michel and V.L. Telegdi, Phys. Rev. Lett. **2**, 435 (1959), are generally given credit for this formula. As noted by J.D. Jackson in *Classical Electrodynamics*, (John Wiley & Sons, New York, 1975), p. 556, Thomas published an equivalent equation in 1927.

[29] G.D. Danby, et al. ($(g-2)$ collaboration), Nucl. Instrum. Meth., in press (2000).

[30] LORAN-C User's Handbook, 1992, Superintendent of Documents, U.S. Government Printing Office #050-012-00331-9.

[31] S. Sedykh, et al., *Nucl. Instrum. Methods*, in press (2000).

[32] F.J.M. Farley and E. Picasso in *Quantum Electrodynamics*, ed. T. Kinoshita, (World Scientific, Singapore, 1990), p. 479.

[33] See Helmut Wiedemann, *Particle Accelerator Physics* V. 1, Springer-Verlag, 1993, p. 54 for a discussion of the weak focusing betatron.

[34] F. Combley and E. Picasso, Phys. Reports **C14**, 1 (1974).

[35] F. Krienen, D. Loomba and W. Meng, Nucl. Inst. and Met. **A283**, 5 (1989).

[36] Vector Fields Limited, 24 Bankside, Kidlington, Oxford OX5 1JE, England.

[37] Muon $(g-2)$ note #286 *The* $(g-2)$ *Muon Kicker: Design and Status*, E. Efstathiadis et al., (1997) and E. Efstathiadis et al., *The Muon* $(g-2)$ *Muon Kicker*, to be submitted to *Nucl. Instrum. Methods*.

[38] W. Liu, et al., Phys. Rev. Lett. **82**, 711 (1999).

[39] Particle Data Group, Eur. Phys. J. **C15**, 1 (2000).

THE ROLE OF SUPERSYMMETRY PHENOMENOLOGY IN PARTICLE PHYSICS

James D. Wells*
Physics Department, University of California, Davis, CA 95616
Theory Group, Lawrence Berkeley National Lab, Berkeley, CA 94720

ABSTRACT

Supersymmetry phenomenology is an important component of particle physics today. I provide a definition of supersymmetry phenomenology, outline the scope of its activity, and argue its legitimacy. This essay derives from a presentation given at the 2000 SLAC Summer Institute.

*Supported in part by the Department of Energy and the Alfred P. Sloan Foundation

1 Introduction

The talk I delivered on "Supersymmetry Phenomenology" at the 2000 SLAC Summer Institute was a relatively standard talk on the definitions, motivations and research activities associated with supersymmetry phenomenology. Being the energetic conference that SSI is, much of the interesting discussion occurred after my talk. Participants asked me many challenging questions about supersymmetry and supersymmetry phenomenology. I enjoyed these exchanges and think they were at least as useful to me and the participants as was the talk. In this proceedings write-up, I would therefore like to emphasize the relevant post-talk issues as an addendum to the actual talk.[1]

The purpose of this write-up is not to restate the meaning of supersymmetry and the basic moving parts of the theory. Some of this was covered in the talk, and much of it is covered admirably in pedagogical reviews of the subject.[2] Instead, I wish to enter quickly and directly into my view of supersymmetry phenomenology.

We should start with a definition of "supersymmetry phenomenology" that is accurate, useful, and inclusive for all those who view themselves as working on the subject. **Supersymmetry phenomenology attempts to answer four questions: (1) How can supersymmetry account for phenomena already measured and quantified? (2) How can supersymmetry resolve its own induced problems? (3) How can supersymmetry be found at future experiments? And, (4) how can supersymmetry be killed?**

If we look at any one of those four elements of supersymmetry phenomenology in isolation, the field appears unmoored and speculation chasing. For example, if the field were interested only in question **(3)**, the whole study would be without motivation. If the field were only concerned with question **(1)** practitioners would be charged with engaging in post-facto natural philosophy rather than scientific inquiry. The legitimacy of supersymmetry phenomenology derives from its commitment to address *all* questions raised above, and, just as important, the studies to date demonstrate very encouraging answers to those questions.

I would like to discuss, essay style, each of the questions in turn, and try to convince and remind the reader how much progress has been made answering them, and how much more work is still required.

2 How can supersymmetry account for the known?

I would not say any known phenomena begs for supersymmetry, but a supersymmetric theory appears to make the natural world more understandable. For example, we know that the Higgs sector in the standard model has quadratic divergences and is likely unstable to non-trivial physics at high mass scales. Supersymmetry elegantly solves this instability problem by protecting hierarchies with a symmetry.[2]

Furthermore, the renormalization group evolution of Higgs masses in supersymmetry naturally induces electroweak symmetry breaking. This is often called "radiative electroweak symmetry breaking" because the radiative corrections (RGE evolution) propel the Higgs mass squared to negative values. And most interestingly, the minimal supersymmetric standard model, with a large top Yukawa coupling, generically predicts only one scalar mass squared going negative (up-Higgs), whereas all the remaining scalar masses (Squarks, sleptons, sneutrinos) remain positive. One can almost raise electroweak symmetry breaking to the level of a prediction of an $SU(3)\times SU(2)\times U(1)$ supersymmetric theory with our known particle content and Yukawa couplings. This is perhaps too strong, but one should realize that radiative electroweak symmetry breaking was discovered and understood[3] well after supersymmetry was introduced as a possible component to nature. As we will see in several other examples, this pattern of finding good things flowing from a supersymmetry hypothesis is encouraging.

Another example of supersymmetry's success is the explanation for the ratios of gauge couplings and Yukawa couplings we measure. Gauge coupling unification and Yukawa unifications are based on model dependent assumptions extending beyond the simplest supersymmetrizing of the standard model. Namely, they imply unification — either Grand Unifications (GUTs) or some type of string unification. Yukawa unification, and the predictions derived from that are highly sensitive to matter content at the high scale. For this reason I will not attempt to force my positive opinions about this on others. However, I think the success of gauge coupling unification is extraordinary and wish to make a few comments on this.

Most of us have seen ad nauseum the graphs of the three gauge couplings unifying at a high scale in supersymmetry but not in the standard model. I think this suggests supersymmetry is the right way to go. Of course, it could be an accident that all three gauge couplings crossed at the same place in supersymmetry. Let's for a moment as-

sume that there is nothing significant about that. Observers must also witness another accident: the three gauge coupling RGE trajectories cross at a scale that is not too low to be ruled out by proton decay experiments *and* cross not too high to be meaningless when combined with gravity. To me, this constitutes another interesting accident. Just like on the roadways, one accident is a curiosity, two accidents side-by-side is a real effect requiring deeper understanding of what happened.

It is true that the more accurate measurements of the last few years at LEP and SLC clearly show that extrapolation to high scales gives a small mismatch of couplings at the unification scale in a supersymmetric theory. That does not mean there is a problem with gauge coupling unification. It is almost certain that there are threshold corrections at the high-scale that will not enable one to simply take low-scale couplings and get exact unification at the high scale. There *must* be a slight mismatch. However, if the unification is perturbative, and the GUT group does not contain extraordinary amounts of matter, the mismatch should only be a few percent. Indeed, this is what is found.

The success of gauge coupling unification in a particular theory is measured by the three gauge couplings being "within specs" (within the variations inducible by threshold corrections) at the high scale. Supersymmetry easily passes this test, theories springing from the standard model do not.

3 How can supersymmetry resolve its own problems?

As with many things in life, an apparent solution to one problem can lead to even more problems. Buying a dog to protect you from burglars may only lead to your couch being chewed up. Whenever you introduce a new theory (supersymmetry) to supplant an old theory (standard model), you run the risk of spoiling all the successful predictions and explanations that we've held dear for so long. For example, small flavor changing neutral currents (FCNC) seen by experiments are mostly natural within the standard model. Supersymmetric descriptions, on the surface, have no preference for small FCNC effects over large effects. This is a potential problem.

However, the resolution to many of these questions is wrapped up in supersymmetry breaking. Some supersymmetry breaking mechanisms, such as gauge mediated supersymmetry breaking, automatically solve many of these types of problems.[4] Some

theories do not automatically, or naturally, solve the problems. What we must keep in mind is that supersymmetry is not one theory — it's a multitude of related theories (with only some non-negotiable properties in common) that each have strengths and weaknesses in describing what we already know. The supersymmetric theories that only have weaknesses get ignored over time.

As one illustration of how supersymmetry phenomenology studies have better understood how internal inconsistencies can be resolve, we turn to proton stability. In the standard model, lepton number conservation and baryon number conservation is an accidental global symmetry at the renormalizable level. For this reason, the proton is remarkably stable within the standard model framework.

In supersymmetry, as is the case in most beyond-the-standard model theories, proton stability is not even approximately automatic. The most general gauge invariant, Lorentz invariant lagrangian does not respect baryon and lepton number conservation. Somehow they must be banished. We all have a sense of what it means to solve a problem, and part of that solution is not to add epicycles to a theory that is apparently breaking down. However, supersymmetry phenomenologists have identified several elegant explanations for proton stability. One such explanation is R-parity.

R-parity is well-motivated in that it is a simple Z_2 symmetry that has no discrete gauge anomalies, and so could be derivable from a gauge symmetry.[5] This is important for our confidence that the discrete symmetry has a solid underpinning, and won't be violated by quantum gravity effects. Furthermore, the requisite continuous gauge symmetry is $U(1)_{B-L}$ which is contained in many of our formulations of grand unified theories. We can see R-parity as coexisting nicely with grand unified theories, gauge coupling unification, and proton stability, all within the same theoretical framework. For these reasons, R-parity is not an ad hoc assumption in my view.

The introduction of R-parity has another important, non-trivial implication: the lightest supersymmetric particle is stable. Of course, stable particles can be cosmological relics, and the first discussion of stable LSP relics exclaimed relief that it was not a cosmological disaster.[6] Quickly after that, it became apparent that not only is the LSP allowed by cosmology, but it might be preferred since its interaction strength with other particles can be just right to provide a good cold dark matter candidate.[7]

I would say that the above story parallels the successful beginning history of many

good ideas. The LSP was not dreamed up to solve the cold dark matter problem like other candidate particles were, but rather fell out of a self-consistent complete picture of the supersymmetric theory when attempting to solve its own consistency issues. And keep in mind, dark matter is a real observational and experimental problem that does not seem to be explainable within the standard model. Nevertheless, it remains to be seen if the LSP is truly the dark matter.

4 How can supersymmetry be discovered?

Post-facto explanations for electroweak symmetry breaking, Higgs sector quantum stability, Yukawa coupling ratios, and gauge coupling unification are encouraging, but they are not the end of the story. Additional phenomena confirming the explanations are required. Supersymmetry in fact has many unique and discerning signatures at high energy colliders, and elsewhere, to solidify its claims on nature. This is in stark contrast to many speculative theories that have no correlating phenomena and follow the "one observation, one explanation" pattern.

I will not attempt to go into any detail how supersymmetry could be found at high-energy colliders. My approach here is somewhat paradoxical because more studies and more solid analysis have been plied to this question than any other, in my estimation. I simply refer the reader to the many excellent reviews on the subject.[8] These studies show that careful predictions and anticipations combined with careful experimental preparation and analysis are all needed to find supersymmetry and accurately interpret new signals. Theorists and experimentalists engaged in any of these aspects contribute substantially to the resolution of the question posed for this section.

We should not forget that many smaller scale experiments, such as electric dipole moment measurements and $g-2$ measurements, contribute to our understanding of the natural world, and by implication the allowed form of a valid supersymmetric theory. Another important non-collider experiment includes the search for dark matter. These searches take on many guises, including cryogenic table top experiments, annihilations into photons in the galactic halo, and antiproton searches in the galactic halo. The prediction of many supersymmetric models is that evidence of LSP scattering would appear when the experiments get an order of magnitude or two more sensitive.

5 How can supersymmetry be killed?

A common concern for any new theory is how it can be killed, or falsified. This is a complex issue that must combine technological capabilities (accelerators) with theoretical prejudices (what scale is supersymmetry?). This question, in my view, has value only inasmuch as it forces the respondent to formulate more detailed questions on the theory. For example, an easier subsidiary question would be "How can we rule out the bino LSP as an explanation for the dark matter?" or "How can we rule out supersymmetry as having an important role in electroweak symmetry breaking?" or "How can we determine if apparent unification of gauge couplings in supersymmetry is indeed just an accident?" These questions are still hard but they are easier breakdowns of the looming question: how do we determine if all of this is bunk?

These questions necessarily take on a negative tone, and are not pleasant to confront for a supersymmetry enthusiast. An unacceptable answer, but a technically correct answer, would be "we will never know." As scientists, we must make value judgements on how best to lasso natural law and try our best to figure it all out. Quixotic pursuits of nonviable theories run counter to these goals.

The community has set several standards on answering these questions. One is the careful evaluation of supersymmetric parameter space measured against a naturalness or finetuning criteria. For example, if supersymmetry governs electroweak symmetry breaking, the couplings and masses, it is argued, must be within reasonable bounds. Numerous papers have studied these questions in detail.[9] Although they are oftened phrased positively ("We should see supersymmetry at future collider X"), they set the tone for when people should give up on supersymmetry. Let's call this the "relevance standard," because if supersymmetry parameters are outside the specified range for relevance to a problem, it is no longer motivated.

We are currently far from straying outside the "relevance standard", as judged by criteria set forth in the current literature *and* the criteria implied in the original works on supersymmetry phenomenology.[10] If the parameter space of relevant supersymmetry were mapped as a long drive between San Francisco and New York City, our current experiments have taken us only about as far as lowly Elko, Nevada.

Note also, it is vitally important to the integrity of the "relevance standard" that

question **(3)** is answered in utter completeness, since we continue to find forms of supersymmetry that are extremely difficult to discover at colliders. For example, in many forms of anomaly mediated supersymmetry breaking, the lighter sparticles are nearly degenerate, and the lightest sparticle is invisible to the detectors.[11] Therefore, all that is produced in high energy collisions at, say, the LHC are a couple of very soft pions swamped by enormous backgrounds that cannot be overcome. Partial progress has been made on this issue, but other difficulties have been recognized and there are surely more discovery subtleties that we have not yet contemplated.

An even stricter application of the "relevance standard" can be found in considering the question, "What experiments must be performed to rule out supersymmetric theories that produce a bino with cosmologically significant cold dark matter density?" Depending on the precise nature of the theory, very detailed answers can be given and predictions on the success of colliders in finding such theories can be promulgated.[12]

There is one other standard, which I will call the "technology standard." This is a very practical standard, where you might hear it being applied when someone says, "If the LHC and NLC do not find supersymmetry I will give up on supersymmetry." On the surface it sounds silly, because nature does not care if the accelerator guy can only squeeze 7 TeV out of the beams. But without additional planned accelerators in the lifetime of that physicist, there may not be need to address the prospects of supersymmetry manifesting itself at higher energies. All questions related to supersymmetry become moot to such a hardline phenomenologist. I do not like this standard for many reasons, some of which are implicit above. The main argument against it is that each generation applying it puts an arbitrary divider line on theory viability based on what they think the last machine, or last probing experiment can be accomplished in their professional lifetime. There is room to motivate and encourage better technology and better ideas, and supersymmetry might be a part of that argument in the future, or it might not. But the argument will always need to be made.

6 Conclusion

There remain several more questions presented to me at the Institute meeting that I would like to address in the conclusion. Many people would like to know from super-

symmetry phenomenologists what percentage chance we give supersymmetry of being right. I have no idea. Supersymmetry is not running for city council against other well-defined candidates. The only thing I would say is that it appears to be the most attractive next step in our quest to get a deeper understanding of the natural world. I could never feel confident in judging its potential success on a more absolute scale because I am certain that I have not imagined all possibilities.

The next most asked question at the Institute along these lines was "What if supersymmetry isn't right? Doesn't that mean a lot of people have really wasted their time?" One answer to this question is that supersymmetry phenomenologists who study how supersymmetry should show up at experiments in general, and high energy colliders in particular, play a major role in helping experiments. The helpful input spans the full range from detector design to better techniques for data analysis and signal extraction. Remember, these experiments are multi-million dollar machines, sometimes multi-billion dollar machines, and having a few theorists around who are actively helping in this regard can only be a good thing. It increases the chances of finding a new signal, whether it be supersymmetry or not, and it helps maximize the interpretative scope of the data already taken (e.g., are $\mu = 0$ theories viable?). These skills and activities are then transferrable over a wide range of theory-experiment searches for new physics, whatever the underlying theory might be.

A more substantive reply to this question must quarrel with the premise. The subtle premise of the question is that all worthwhile activity must be guaranteed at the start to terminate in a usable product or textbook theory. A quick survey of the entire scientific endeavor, not just particle physics, demonstrates the folly of this attitude. For example, if you are attempting to find a drug that cures a disease, you do not require a guarantee of success before starting. You start your work with a thorough knowledge of all the past sputtered attempts and you make regular evaluations of your work to determine if your approach can still lead to success. You get even more encouraged, and the pharmaceutical company gives you raises, if it is clear that your approach appears to be not only viable but more promising than anyone else's. In the end, some of us will find the drugs that work, some of us won't, and hopefully very few of us will kill our trial subjects. But progress is made as a community of researchers trying to answer well-posed questions from different angles.

Our field is the high-energy frontier, and our questions are "What causes elec-

troweak symmetry breaking?", "What is the dark matter?", "Why are the neutrinos so light?", "What causes CP violation?", and "What's next on the horizon?" Although many of us work in different aspects of supersymmetry phenomenology because we think it is promising, the experiments are what keep us tethered.

We are wed to the questions, not the hypothesized answers.

References

[1] The talk is meant to be readable and can be found at `http://walden.ucdavis.edu/jwells/archive/ssi00.ps`.

[2] For example, S. P. Martin, "A supersymmetry primer," hep-ph/9709356.

[3] L. Ibanez and G. G. Ross, Phys. Lett. **B110**, 215 (1982); L. Ibanez, Phys. Lett. **B118**, 73 (1982); J. Ellis, D. V. Nanopoulos and K. Tamvakis, Phys. Lett. **B121**, 123 (1983); L. Alvarez-Gaume, J. Polchinski and M. B. Wise, Nucl. Phys. **B221**, 495 (1983).

[4] G. F. Giudice and R. Rattazzi, Phys. Rept. **322**, 419 (1999) [hep-ph/9801271].

[5] L. M. Krauss and F. Wilczek, Phys. Rev. Lett. **62**, 1221 (1989); L. E. Ibanez and G. G. Ross, Phys. Lett. **B260**, 291 (1991); R. N. Mohapatra, Phys. Rev. **D34**, 3457 (1986); A. Font, L. E. Ibanez and F. Quevedo, Phys. Lett. **B228**, 79 (1989); S. P. Martin, Phys. Rev. **D46**, 2769 (1992) [hep-ph/9207218].

[6] S. Weinberg, Phys. Rev. Lett. **50**, 387 (1983).

[7] H. Goldberg, Phys. Rev. Lett. **50**, 1419 (1983).

[8] For example, M. Carena, R. L. Culbertson, S. Eno, H. J. Frisch and S. Mrenna, Rev. Mod. Phys. **71**, 937 (1999) [hep-ex/9712022].

[9] J. Ellis, K. Enqvist, D. V. Nanopoulos and F. Zwirner, Mod. Phys. Lett. **A1**, 57 (1986); R. Barbieri and G. F. Giudice, Nucl. Phys. **B306**, 63 (1988); G. W. Anderson and D. J. Castano, Phys. Rev. **D52**, 1693 (1995) [hep-ph/9412322]; J. L. Feng, K. T. Matchev and T. Moroi, Phys. Rev. **D61**, 075005 (2000) [hep-ph/9909334].

[10] For example, the Haber-Kane Physics Report on supersymmetry phenomenology from 1985 implied a "relevance standard" of superpartners being lighter than about 1 TeV, which is far from the current experimental limits: "We emphasize

that the solution to the naturalness (fine-tuning) problem necessarily predicts that new physical phenomena must exist at a scale of $m_w/g \sim \mathcal{O}(1\,\mathrm{TeV})$ or below. In the case of supersymmetry, this new physics consists of a spectrum of new supersymmetric particles (partners of the ordinary particles) which have masses no greater than about 1 TeV and in some cases may be substantially lighter." H. Haber, G.L. Kane, Phys. Rep. 117, 75 (1985), quote from page 82.

[11] T. Gherghetta, G. F. Giudice and J. D. Wells, Nucl. Phys. **B559**, 27 (1999) [hep-ph/9904378]; J. L. Feng, T. Moroi, L. Randall, M. Strassler and S. Su, Phys. Rev. Lett. **83**, 1731 (1999) [hep-ph/9904250]; J. F. Gunion and S. Mrenna, Phys. Rev. **D62**, 015002 (2000) [hep-ph/9906270].

[12] For example, J. Ellis, G. Ganis and K. A. Olive, Phys. Lett. **B474**, 314 (2000) [hep-ph/9912324].